Engineering of Metal Organic Framework Catalysts

Jana Juan Alcañiz

Author: Jana Juan Alcañiz

PhD Thesis, Delft University of Technology

The Netherlands, July 2013

Cover design: Jorge Gascon / Alfonso Bravo Ivorra

Engineering of Metal Organic Framework Catalysts

Proefschrift

ter verkrijging van de graad van doctor

aan de Technische Universiteit Delft,

op gezag van de Rector Magnificus prof. ir. K.C.A.M. Luyben,

voorzitter van het College voor Promoties,

in het openbaar te verdedigen

op maandag 15 juli 2013

om 10.00 uur

door

Jana JUAN ALCAÑIZ

Ingeniera Química

Universidad Politécnica de Valencia

geboren te Elche, Spain

Dit proefschrift is goedgekeurd door de promotor:

Prof. dr. F. Kapteijn
Dr. J. Gascon, copromotor

Samenstelling promotiecommissie:

Rector Magnificus,	voorzitter
Prof. dr. F. Kapteijn,	Technische Universiteit Delft, promotor
Dr. J. Gascon,	Technische Universiteit Delft, copromotor
Prof. dr. U. Hanefeld,	Technische Universiteit Delft
Prof. dr. H. van Bekkum,	Technische Universiteit Delft
Prof. dr. N. Stock,	Christian-Albrechts Universitat zu Kiel, Institut für Anorganische Chemie
Dr. F.X. Llabrés i Xamena,	Universidad Politécnica de Valencia, Instituto de Tecnología Química
Dr. S. Furukawa,	Kyoto University, Institute for Integrated Cell-Material Sciences
Prof. dr. I.W.C.E. Arends,	Technische Universiteit Delft, reservelid

The research reported in this thesis was conducted in the Catalysis Engineering section of the Chemical Engineering department, Faculty of Applied Sciences (TNW) of the Delft University of Technology.

Dr. E.V. Ramos-Fernández heeft als begeleider in belangrijke mate aan de totstandkoming van het proefschrift bijgedragen.

Proefschrift, Technische Universiteit Delft
Met samenvatting in het Nederlands

ISBN/EAN 978-94-6186-182-5
Copyright © 2013 by Jana Juan Alcañiz
All rights reserved. No part of the material protected by this copyright notice may be reproduced or utilized in any form of by any means, electronic or mechanical, including photocopying, recording, or by any information storage and retrieval system, without the prior permission of the author.

Printed by Wohrmann Print Service B.V.

To my family

"Curriculum vitae" de JACINTO ALCAÑIZ BAEZA: autor novel, pero no joven.

Mi estilo, si es que lo tengo, es periodístico, de frases cortas y escasos alardes retóricos. Más que una virtud, es un defecto: el de mi escasa formación. Soy introvertido, poco observador -mala cosa para el que escribe- de esa clase de perezosos que se pasan un día entero escribiendo, con tal de estar una semana sin dar golpe. Las colaboraciones y mi empleo....y el pluriempleo, me ocupan todo el tiempo que me gustaría poder emplear en lo que más me gusta: LEER.

Cinto Baez

Content

Hydrofluoric Acid (HF)safety

Very Toxic [T+] 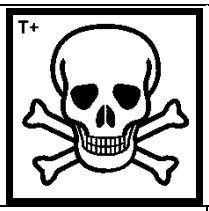	**Corrosive [C]** 
R-phrase(s)	**S-phrase(s)**
R26/27/28 Very toxic by inhalation, in contact with skin and if swallowed. R35 Causes severe burns.	S 7/9 Keep container tightly closed and in a well-ventilated place. S26 In case of contact with eyes, rinse immediately with plenty of water and seek medical advice. S36/37 Wear suitable protective clothing and gloves. S45 In case of accident or if you feel unwell, seek medical advice immediately (show the label where possible).
FIRST AIDS	**HANDLING, STORAGE AND FIRE-FIGHTING MEASURES**
General advice Consult a physician. Show this safety data sheet to the doctor in attendance. **If inhaled** If breathed in, move person into fresh air. If not breathing give artificial respiration. **In case of skin contact** Take off contaminated clothing and shoes immediately. Wash off with soap and plenty of water. Take victim immediately to hospital. **In case of eye contact** Rinse thoroughly with plenty of water for at least 15 minutes. **If swallowed** Do NOT induce vomiting. Never give anything by mouth to an unconscious person. Rinse mouth with water.	**Suitable extinguishing media** Use water spray, alcohol-resistant foam, dry chemical or carbon dioxide. **Special protective equipment for fire-fighters** Wear self-contained breathing apparatus for fire fighting if necessary. **Handling** Avoid contact with skin and eyes. Avoid inhalation of vapour or mist. Normal measures for preventive fire protection. **Storage** Store in cool place. Keep container tightly closed in a dry and well-ventilated place. Containers which are opened must be carefully resealed and kept upright to prevent leakage.
ACCIDENTAL RELEASE MEASURES	**EXPOSURE CONTROLS/PERSONAL PROTECTION**
Personal precautions Wear respiratory protection. Avoid breathing vapors, mist or gas. Ensure adequate ventilation. Evacuate personnel to safe areas. **Environmental precautions** Prevent further leakage or spillage if safe to do so. Do not let product enter drains. **Methods for cleaning up** Soak up with inert absorbent material and dispose of as hazardous waste. Keep in suitable, closed containers for disposal.	**Respiratory protection** Where risk assessment shows air-purifying respirators are appropriate use a full-face respirator with multipurpose combination (US) or type ABEK (EN 14387) respirator cartridges as a backup to engineering controls. If the respirator is the sole means of protection, use a full-face supplied air respirator. Use respirators and components tested and approved under appropriate government standards such as NIOSH (US) or CEN (EU). **Hand protection** The selected protective gloves have to satisfy the specifications of EU Directive 89/686/EEC and the standard EN 374 derived from it. Handle with gloves. **Eye protection** Tightly fitting safety goggles. Faceshield (8-inch minimum). **Skin and body protection** Choose body protection according to the amount and concentration of the dangerous substance at the work place.
Inhalation May be fatal if inhaled. Material is extremely destructive to the tissue of the mucous membranes and upper respiratory tract. **Skin** Causes severe skin burns. May be fatal if absorbed through skin. **Eyes** Causes severe eye burns. **Ingestion** May be fatal if swallowed. Causes severe burns. **Target Organs** Liver and Kidney.	

Abbreviations

MOF : metal organic framework

NP@MOF : nanoparticles encapsulated in MOF pores

SURMOF : on-surface growth of MOFs

MOF-5 [$Zn_4O(bdc)_3$

IRMOF-3[$Zn_4O(NH_2\text{-}bdc)_3$]

MOF-235(Al) : $Al_3O(bdc)_6(dmf)_3(AlCl_4)$

MIL-47(M) [MO(bdc)]

POST-1 : homochiral MOF $[M_3(\mu_3\text{-}O)(O_2Cr)_6(H_2O)_3]^{n+}$

Basolite® A100 [MIL-53(Al)as - $Al_2(bdc)_3$]

MIL-53(M) [MOH(bdc)]

MIL-101(M) $[M_3F(H_2O)_2O(bdc)_3]$

MIL-100(M) $[M_3F(H_2O)_3O(btc)_2]$

NENU-*n* : POM/HKUST-1 composites

UiO-66(Zr) $[Zr_6O_4(OH)_4(bdc)_6]$

NH_2-MOF : NH_2 in the benzene ring of the linker, usually NH_2-bdc or NH_2-btc

$Cu(2\text{-}pymo)_2$

$Cu(im)_2$

HKUST-1 $[Cu_3(btc)_2]$

rho-ZMOF : indium-imidazoledi-carboxylate zeolite-*like* MOF $[In_{48}(HImDC)_{96}]^{48-}$

TMPyP : tetrakis(N-methyl-4-pyridinio)prophine

POM : polyoxometalate

PTA : phosphotungstic acid $[H_3PM_{12}O_{40}]$

M : divalent or trivalent transition metal ions

CR : organic carboxylate anions

BINOL-derivated tetracarboxylic acid : 4,4',6,6'-substituted 1,1'-bi-2-naphthol

NH_2-bdc : 2-amino-benzene-1,4-dicarboxylic acid

bdc : benzene-1,4-dicarboxylic acid

2-pymo : 2-pyrimidinolate

im : imidazolate

HImDC : 4,5-imidazoledicarboxylate

btc : benzene-1,3,5-tricarboxylic acid : trimesic acid (TMA)

dmf : N,N-dimethylformamide

DME : dimethyl ether

Chapter 1

Engineering of metal–organic framework catalysts: Introduction

This chapter is partially based on the following publication:

J. Juan–Alcañiz, J. Gascon, F. Kapteijn, Journal of Material Chemistry, 22 (2012) 10102–10118

Abstract In the catalysis community, the topic of MOF catalysis has been traditionally looked at with a critical or even sometimes sceptical attitude. The examples discussed in this chapter demonstrate that these opinions cannot be justified anymore, and that MOFs will eventually find the application niche where other nano−structured materials are unsuitable. In this spirit, both the homogeneous and the heterogeneous catalysis community should regard MOFs as a golden opportunity to develop a large number of applications, where till now non−recyclable catalysts are used. There is now sufficient knowledge to deal with issues like leaching and lattice stability; and many of the catalytically interesting MOFs are based on affordable and commercial linker molecules. The tunability of the MOF catalysts and their easy recyclability are sufficient assets to apply these materials in industry. It is still a challenge for the MOF community to demonstrate the full potential of these fascinating solids.

1.1. METAL ORGANIC FRAMEWORKS

1.1.1. Definitions, properties and structures

Synthetic crystalline micro− and mesoporous materials have been extensively researched during the last centuries. They find applications in many different fields such as catalysis, adsorption/separation/storage, electronics, health, semiconductors, the food industry, and in detergents. Several unique aspects of these materials are responsible for their success: since they have a very high and tunable adsorption capacity, active sites of different strengths can be generated in the frameworks, the size of their channels and cavities falls within the range of that of many molecules of interest, and many materials present excellent ion exchange capabilities and exciting electronic properties, ranging from insulators to conductors and semiconductors. In addition, owing to their periodic nature, these materials are excellent playgrounds for scientists, since macroscopic events may be explained on the basis of interaction at the molecular level. The prime example is the development of synthetic zeolites that resulted in numerous industrial applications. More recently, a new class of nano−structured materials drew the attention of scientists from university and industry: metal−organic frameworks (MOFs). The first reports on MOFs or, [1] more widely speaking, on coordination polymers date from the late 1950s [2, 3] and early 1960s, [4-7] although it was not until the end of the last century when Robson and co−workers, [8, 9] followed by Kitagawa *et al*., [10, 11] Yaghi and co−workers, [1] and Férey *et al*. [12] rediscovered and boosted the field. The term MOF was firstly introduced by Yaghi and co−workers, with the best known example being the structure of MOF−5, published in 1999 in Nature. [13] Especially since then we have witnessed an explosion of publications on the topic during the last decade. [14]

Metal−organic frameworks (or coordination polymers) are hybrid crystalline porous materials, built up from the combination of an inorganic subunit (metal cluster) and organic linker (ligand), [15] displaying a vast chemical versatility and a plethora of possible structures compared to conventional used microporous inorganic materials such as zeolites. [16] These structures allow, in theory, rational design through control of the architecture and functionalization of the pores. The initial MOFs exhibited a very poor stability, collapsing in the absence of guest molecules, such as solvents, resulting in no permanent porosity. Later MOF structures were developed with acceptable stability that display permanent porosity, [17, 18] and extremely high surface areas and pore volumes, which can be fine−tuned towards specific applications, [19, 20] and even present flexible behaviours like breathing or gate−opening phenomena. [21-23] Different types of synthesis methods have been applied in the literature for MOF materials. Among them, classical hydro(solvo)thermal synthesis, microwave and electrochemical synthesis, diffusion and ultrasonic techniques. [24]

Stock and co−workers have recently reviewed synthesis methods and high−throughput techniques for the discovery of new MOF structures. [25] Several reports have also focused on understanding the crystallization mechanism of MOFs. [26, 27]

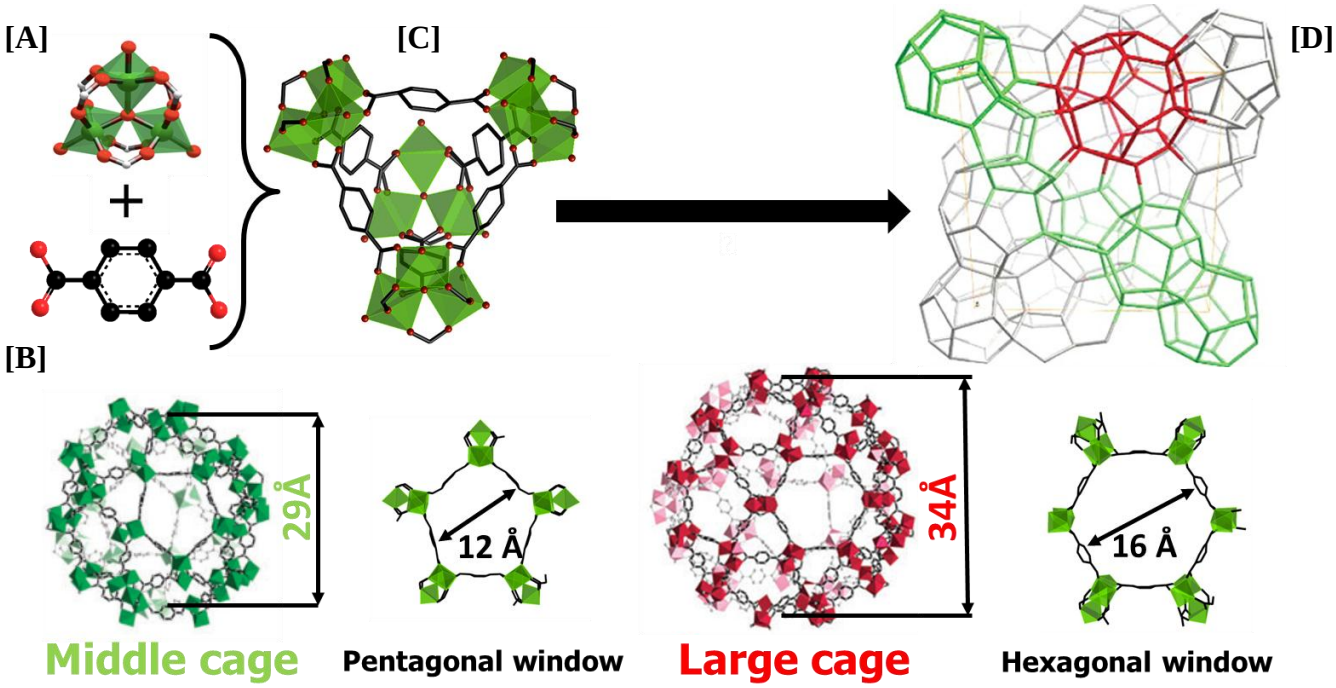

Figure 1 - 1 Schematic representation of MIL−101 structure. (*Top*) [A] Trimeric building block chelated by three carboxylic functions, [B] benzene−1,4−dicarboxylic acid, combined in a supertetrahedra (ST) unit [C], and [D] is the 3D representation of the MTN zeotype architecture (the vertices represent the centers of each ST). (*Bottom*) Description of types of cages: middle cage (29 Å) consisting only of pentagonal windows (12 Å) and large cage (34 Å) displaying also hexagonal windows (16 Å).

One of the best−known and most widely used MOF structures is MIL−101(Cr) (Fig. 1−1), discovered by the group of Férey in 2005, where MIL stands for Materiaux d'Institute Lavoisier. MIL−101 is an excellent example of the rich topological variety of these materials. Displaying an MTN topology, the MIL−101 structure consists of the combination of a metal trimer (Al, Cr or Fe), and benzene−1,4−dicarboxylic (terephthalic) acid, forming supertetrahedral primary building blocks (small cages) resulting in two different types of nano−cages: (*i*) middle cages of 29 Å internal diameter, displaying only pentagonal windows of 12 Å diameter; (*ii*) large cages of 34 Å internal diameter, having also hexagonal windows with 16 Å diameter. [28]

1.1.2. Major applications

Possible MOF applications have been broadly discussed in the areas of gas storage, [29, 30] gas separation, [31, 32] or gas purification [33-35], membranes and coatings [25, 36-38] and lately gas chromatography. [39] MOFs with magnetic [40] or luminescence properties [41] can be potentially utilized in sensor devices. [42, 43] The use of MOFs for the storage and delivery of pharmaceuticals has also been reported. [44, 45]

With the discovery and explosion of interest in MOFs, it was only a matter of time until the first catalytic applications were explored. First reports mostly consisted of demonstrating that a certain MOF contained the necessary catalytic centers to catalyze a given reaction. In many cases, the performance of the material was poor and many concerns existed regarding the stability of the materials under reaction conditions. Nowadays, the field has developed to a more mature state where catalytic applications vary from those of traditional heterogeneous catalysis to electro−, [46] photo−, and chiral catalysis. [47-51]

As mentioned before, MOFs contain three well distinguishable parts: the metallic nodes, the organic linker and the porous system. In the following sections, it will be shown that it is possible to prepare MOFs in which the catalytic function is located at any of these three parts. Moreover MOFs are known for containing simultaneously two or more types of catalytic sites. The main idea of the following sections is to give the reader a flavor of the different approaches that can be followed for the engineering of MOF catalysts at the molecular level. Special emphasis is put on encapsulation, since a large part of this Thesis deals with this approach.

1.2. CATALYSIS AT THE METAL NODES

The presence of highly dispersed metaloxy clusters as an intrinsic part of the MOF structures has boosted intensive investigations on the use of such nodes as potential active sites for catalysis. [52, 53]

In most cases, the development of metal reactive MOFs involves the use of metal centers that are not completely coordinated with the organic linkers, since labile ligands (usually solvent molecules) can be removed during activation. One of the most relevant examples is the HKUST–1 ($Cu_3(btc)_2$) structure, where copper sites are known to lose reversibly their coordinated water molecules upon thermal activation, leaving an accessible coordination vacancy on the Cu. [54] More complex situations might be found where solvents like dimethyl formamide need to be exchanged first by another solvent that can be easier removed thermally (like ethanol) with no structural damage.

In a limited number of MOFs, open metal sites are available, or become available after a proper pretreatment. [54-56] Increasingly, it becomes clear that also structural defects at the outer surface or inside the pores of MOFs can dote the MOF with catalytic activity. For instance, although the Zn atoms in MOF−5 are in principle inaccessible for ligation, catalytic activities have been reported for this material, for instance for alkylation of large polyaromatic compounds; in the case of benzene alkylation, the preference for *p*−products over *o*−products has been interpreted as an intraporous reaction. [57] Most probably Zn–OH defects, as consequence of moisture adsorption, [58] or ZnO impurities might be present in the pores, resulting in acidic species. [59, 60] Other MOFs lacking coordinatively unsaturated metal sites in the crystalline structure have been reported to demonstrate

significant catalytic activity as well, for instance in a series of Zn–MOFs used for alkylation and benzylation reactions, [61] in Basolite® A100, which surprisingly catalyzes the reduction of carbon–carbon multiple bonds with hydrazine or the N–methylation of aromatic amines, [62, 63] or in MIL–47 for the epoxidation of cyclohexene. [64, 65] Another approach to promote catalytic activity is the controlled formation of defects in the framework by post–synthetic treatment. [66]

Extensive reports have focused on the catalytic properties of MOFs featuring transition metal ions like Cu^{2+}. [67] For instance, copper coordinated to four N atoms belonging to heterocyclic rings, thus forming CuN_4 centers like [Cu(2–pymo)$_2$] and [Cu(im)$_2$] showed excellent performance for three–component coupling reaction to obtain propargylamines. [68] More broadly, Cu–MOFs have shown to be active and regioselective catalysts for "click" reactions (1,3–dipolar cycloadditon reactions) similar to homogeneous systems. [69] Co, Fe, V and Cr containing MOFs have also been reported to catalyze oxidation reactions. [70-74] Reduction reactions have been investigated in several MOF structures, like a 3D indium terephthalate MOF or aluminum terephthalate structures. [62, 75]

Alternatively, unsaturated sites can also be used as grafting sites. Pioneered by Hwang *et al.*, ethylenediamine was grafted onto the coordinatively unsaturated sites of MIL–101(Cr) and later used in base catalyzed reactions and for the incorporation of palladium nanoparticles. [76] More recently, Arnanz *et al.* developed a bifunctional MOF by the addition of a palladium complex introduced in aminopyridine compounds grafted in the unsaturated sites of HKUST–1. [77] A new approach is the post–synthetic exchange of metal clusters. [78] This leads to the possibility of developing MOFs with more than one type of metal center (M), which simultaneously act as a structural building component and as catalytic active site.

1.3. CATALYSIS AT THE ORGANIC LIGANDS

Catalytic activity in MOFs can also be introduced at the functional groups of the organic component (linker). In this case, the organic ligands in the final MOF must present two different types of functional groups: (*i*) coordinating groups, which are required for constructing the MOF structure through coordination to the metal node, and (*ii*) reactive groups, which will be responsible for the catalytic properties of the material. In addition, there are some reports of partial destruction of the coordination between organic and metal clusters to obtain additional organic functionalities, like carboxylic acid groups. [66]

There are two ways of functionalizing the organic component of MOFs: (*a*) pre–functionalization, where the linker already possesses a Functional Organic Site (FOS) before synthesizing the MOF; (*b*) post–functionalization, in this case, the FOS is created after MOF synthesis.

Several matters need to be considered for the synthesis of pre–functionalized MOF structures: (*i*) the starting building blocks should have both coordinating sites and FOS, (*ii*) under synthesis conditions the FOS should not participate in the coordination of the metal, and (*iii*) the FOS need to be stable under synthesis conditions. Eddaoudi *et. al.* described a number of isoreticular (IRMOF–X) structures systematically designed to tune pore size and functionalities of MOF−5, however its application was focused on methane storage and not on catalytic behaviour. [79] Seo *et al.* reported in 2000 the first example describing the catalytic activity of a homochiral MOF (POST–1) containing ligands with reactive groups such as a carboxylic acid and a pyridine group, active for transesterification reactions. [49] During the last years, a lot of work has focused on organic functionalities present at commercially available benzene–based linkers, like amino groups for base–catalyzed reactions. [80, 81] Recently, the development of mixed–linker MOFs has been reported [82, 83] together with post–synthetic linker–exchange approaches to form structures with different organic functionalized ligands in the same framework. [78, 84]

On the other hand, plenty of effort is also focused on the design of more complex MOF linkers with advanced functionalities for their use during the synthesis procedure. [85, 86] The combination of metallo–ligands with simpler organic linkers has been extensively reviewed by Das *et al.* [87] In addition, porphyrins with terminal coordination sites have been used to build new types of MOF structures, leaving uncoordinated porphyrins for post–synthetic metallation. [88] The possibility of shape– and size–selectivity in catalytic reactions, especially in oxidation reactions, make porphyrinic MOFs to be one of the most promising materials in practical applications.

Chirality has been postulated as one of the main advantages of hybrid frameworks in comparison with their inorganic counterparts. Several reviews have described the most significant studies on chiral MOFs. [48, 50, 89] A remarkable example is the development by Ma *et al.* of a series of isoreticular chiral MOFs constructed from copper paddle–wheels and BINOL–derived tetracarboxylic acid bridging ligands and the subsequent grafting of Ti(IV) complexes at the chiral dihydroxy group as a tuneable platform for asymmetric catalysis. [90]

In principle, the introduction of functional groups in MOFs should be more straightforward compared to that in other materials, especially inorganic catalyst supports. However, preparation of highly functional MOFs has been largely limited by the solvothermal synthetic methods used to prepare most MOFs. Under solvothermal conditions, linkers generally cannot contain functional groups that are thermally labile, poorly soluble, or likely to coordinate metal ions. In this sense, post–functionalization offers more freedom. Usually post–functionalization is carried out on materials having functional groups not directly coordinated to the metal sites. Cohen and co−workers have reviewed extensively

the topic of Post−Synthetic Modification (PSM), however for many of these modifications no catalytic applications have yet been developed. [91, 92]

Early PSM reports mainly focused on the reactivity of amine− or aldehyde− tagged MOFs. [93] For example, Garibay *et al.* modified amino groups with a set of cyclic anhydrides producing carboxylic acid functional groups that facilitate the methanolysis of several small epoxides. [94] Savonnet *et al.* developed a wide number of basic functionalities over amino group transformations, [95] for instance, using "click" chemistry reaction and appling the resulting catalysts in transesterification reactions. [96]

The incorporation of reactive metal complexes by the modification of amino groups of IRMOF–3 with salicylaldehyde to form the corresponding imine has been explored by Rosseinsky and co–workers to complexate vanadyl acetylacetonate, [97] and by Corma and co–workers to incorporate Au(III) sites coordinated to the Schiff−base complex. [98]

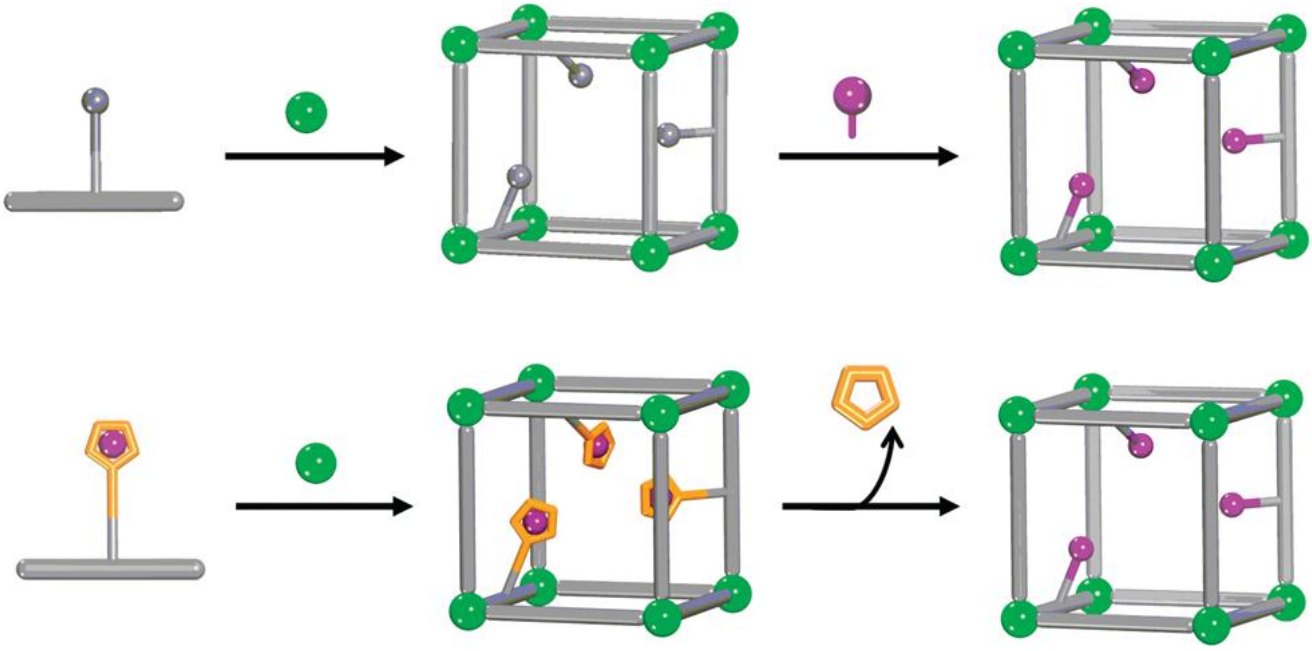

Figure 1 - 2 Generic schemes for (*top*) covalent post−synthetic modification, (*bottom*) post−synthetic deprotection. Reprinted with permission from [92]. Copyright (2011) American Chemical Society.

In addition to post−synthetic functionalization, there is another method to incorporate additional functionalitites in the organic ligands of MOFs: Post−Synthetic Deprotection (PSD) (Fig. 1−2). [92] The concept behind PSD is that a protected or "masked" functional group is introduced on an organic linker, then the linker is incorporated into a MOF under standard solvothermal conditions, and after that the protecting group is removed to liberate the desired functionality. After Kitagawa and co−workers demonstrated this concept [99] other groups followed, like Telfer and co−workers, who used bulky thermolabile Boc protecting groups for proline moieties. After removal of the Boc group, proline moieties can be applied in asymmetric aldol reactions. [100]

1.4. ENCAPSULATION

The concept of encapsulation is by no means young. Initially born as a process where a continuous thin coating is formed around solid particles, liquid droplets, or gas bubbles, fully contained within the capsule wall. [101] It rapidly became a topic of interest in a wide range of scientific and industrial areas varying from pharmaceutics [102, 103] to agriculture [104] and from pesticides [105] to enzymes. [106] Encapsulation technology has been used in food industry for more than 60 years as a way to provide liquid and solid ingredients with an effective barrier from environmental and/or chemical interactions until release is desired. [107, 108] The concept of encapsulation was later expanded to inorganic supports like zeolites. [109] The first examples using zeolites as scaffolds for encapsulation, dates from the late 1970s and opened the door to the encapsulation of gaseous species on small pore zeolites and clathrates, [110-112] and to the encapsulation of more attractive moieties like large homogeneous catalysts, molecular wires or semi–conductors. [113-119] It is worth clarifying that when dealing with encapsulated species in a porous material, the application scope differs from that of other approaches such as self–assembly encapsulation. In the latter, protection and eventual release of the encapsulated moieties is envisaged. In contrast, when active species are encapsulated in the pores of a support, the active moieties cannot leave the support but their main properties (catalytic, opto–electronic …) can be used and even enhanced by confinement effects in the resulting material.

To satisfy the condition of encapsulation in a porous matrix, the entrapped species must be small enough to fit the pores of the support material, and at the same time larger than the openings that give access to these pores, where techniques such as impregnation cannot be used. Therefore, two different synthetic approaches can be followed (Fig. 1–3):

1) Assembling the active species within the pores of the support, known as "*ship in bottle*" approach.
2) Assembling the support around the active species, also known as "*bottle around ship*" or "*templated synthesis*" approach.

The route used for the encapsulation is dictated by the chemistry of the support and the system to be encapsulated. If the targeted species are to be assembled within the pores of the support, then the support needs to be stable under the reaction conditions used. If the support is assembled around the active species, then the active species needs to be stable to the synthesis conditions of that support. Hence, if the active species can be made easily in a small number of steps then assembly within the pores is preferred. If the active species are difficult to synthesize but are intrinsically stable then the assembly of the support around the active species is preferred.

The almost unlimited topological richness of MOFs opens the door to the encapsulation of a much larger variety of moieties than inorganic supports. Furthermore, MOFs are synthesized in most cases

under milder conditions than zeolites, as no structure–directing agent other than the synthesis solvent is needed and therefore post–synthetic calcination steps are not required. Several reports summarize the promising steps achieved on encapsulation of guest species in MOF scaffolds. [52, 120]

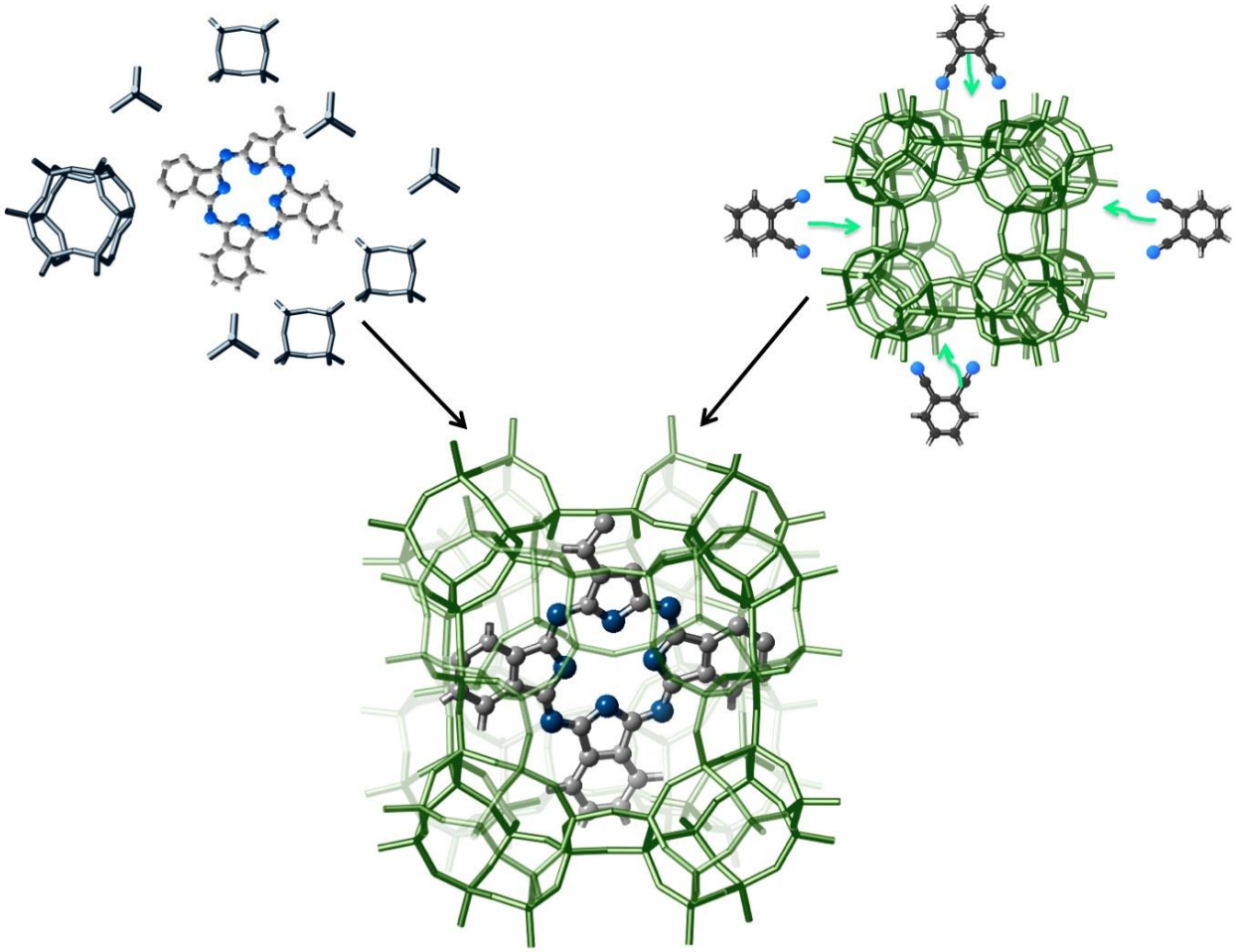

Figure 1 - 3 Different strategies for the encapsulation of a polycyclic ligand (phthalocyanine) in a porous host: "*bottle around ship*" or "*templated synthesis*" approach (*top left*) and "*ship in bottle*" approach (*top right*). The final system after encapsulation by either method is depicted in the bottom. Adapted from [120].

1.4.1. "Ship in a bottle" encapsulation approach

1.4.1.1. Nanoparticles and Metal oxides

The use of MOFs as nano–molds for hosting functional inorganic nanoparticles has attracted increasing attention during the last years. [121-124] As it is the case for other supports, the strategy for the assembly of nano–clusters always starts by the deposition of precursors in the MOF pore space. Several approaches can be followed:

- Impregnation: a solution of the metal precursor (usually in the form of a salt) is contacted with the porous substrate. [125] When the amount of impregnation solution is equal to the pore volume of the MOF the method is called "incipient wetness". One of the main drawbacks of this method is the necessity of a subsequent transformation of the precursor to form the

corresponding desired nano–particles. In order to avoid high temperatures and possible MOF decomposition, chemicals like hydrazine or $NaBH_4$ can be used as reducing agents under mild conditions. Special attention should be put on the precursor type, *i.e.*, nitrates or chlorides that must be washed out (before or after reduction) to avoid future poisoning of the active phase.

- Solvent free gas phase loading: chemical vapor deposition precursors can be incorporated into the pores or channels of MOFs by a sublimation process. [126] Since the method is solvent free, it allows high metal loadings. The decomposition of the precursor can be achieved by a thermal or chemical treatment, like the use of UV irradiation, or a reactive gas atmosphere. A variation of this method is the so–called solid grinding. [127] In this case, the metal precursors are firstly carefully ground together with the MOF and later infiltrated into the MOF porosity and reduced by a mild temperature treatment in a reducing atmosphere. With zeolites this is sometimes referred to as 'solid ion exchange'.

Depending on the method and the conditions applied for the loading and decomposition of precursors, nano–particle encapsulation might only be partially successful. Three possible cases have been defined when classifying metal nano–particle size distribution in MOFs (Fig. 1–4): [121]

- ❖ In class A most of the nano–particles are preferentially deposited at the outer surface of a MOF crystal, resulting in a wide particle size distribution and a poor metal dispersion, especially in the case of high loadings.
- ❖ In class B most of the nano–particles are deposited in the pores of the MOF but they display a broad particle size distribution that might arise from partial destruction of the MOF skeleton.
- ❖ In class C, nano–particles with a homogeneous particle size distribution close to that of the MOF pores or cavities are evenly dispersed throughout the porous host.

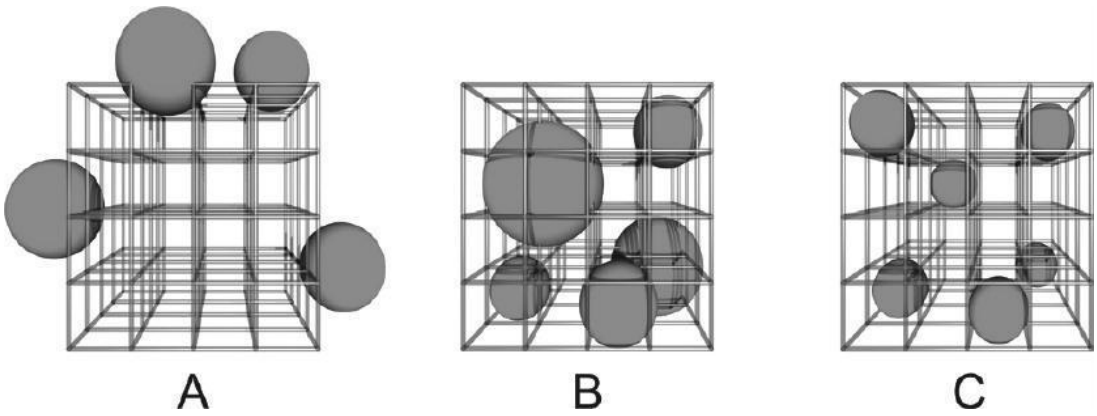

Figure 1 - 4 Limiting cases A, B and C of metal nanoparticles supported by MOFs. Reprinted with permission from [121]. Copyright (2010) WILEY-VCH Verlag GmbH & Co. KGaA, Weinheim.

Both systems A and B cannot be considered as nanoreactors, since the active species are not located in the confined spaces (A) or the confined spaces have been partially damaged (B), leading to a broad particle size distribution.

An important point addressed by Fischer and co–workers [121] and clearly exemplified by Allendorf *et al.* [128] deals with artifacts during widely used TEM characterization of metal catalysts. MOFs are particularly sensitive to electron beam imaging, quite in contrast to zeolites and other purely inorganic porous matrices. Collapse of the whole framework and/or chemical degradation together with coalescence of nanoparticles may occur under the high energetic electron doses in TEM analysis. All information on the internal versus external location of guests on MOFs from electron microscopy must therefore be interpreted cautiously. Additional characterization techniques like UV–Vis, infra–red, solid state NMR and X–Ray absorption spectroscopies together with PXRD and, if applicable, chemisorption methods need to be used in order to fully characterize NanoParticles@MOF systems.

1.4.1.2. Enzymes

The use of enzymes in industrial applications is often handicapped by their narrow range of application conditions, difficult recovery, and deactivation due to aggregation under reaction. Immobilization of enzymes on solid supports can enhance enzyme stability as well as facilitate product separation and catalyst recovery. [129-132] In many cases, immobilized enzymes show higher specific activity than free enzymes, since deactivation by aggregation can be prevented. [133] Crucial aspects to consider enzyme immobilization are structural deformations and host–guest interactions, responsible for loss in specific activity and leaching, respectively. [134-136]

Several features have been delineated for an ideal host matrix: (*a*) large pores for enzyme access and to reduce to the minimum the structural deformation, (*b*) high surface area to ensure high enzyme loading, (*c*) large cages decorated with functional organic groups to enhance interactions reducing leaching issues, and (*d*) sustained framework integrity under typical reaction conditions. [137] Intensive attention has been paid to the immobilization of enzymes in porous solids like mesoporous silicas, carbons or ceramics. [138-141] In spite of the great potential of MOFs for the immobilization of enzymes, only few works have been published in this field. [142, 143] Although, in principle, the microporous nature of many MOFs makes it difficult to incorporate macromolecules like enzymes, recent advances in the synthesis of robust mesoporous MOFs (such as MILs with MTN topologies and Tb–mesoMOFs) open the door for enzyme immobilization. [144]

1.4.2. "Bottle around a Ship" encapsulation approach

1.4.2.1. Polyoxometalates

Polyoxometalates (POMs) present several advantages as catalysts that make them economically and environmentally attractive. [80] POMs are complex Brønsted acids that consist of metal–oxygen octahedra as the basic structural units assembled to heteropolyanions. The first characterized and the best known of these structures is the Keggin–type heteropolyacid, typically represented by the formula

$XM_{12}O_{40}^{x-8}$ where X is the central atom (usually P^{5+} or Si^{4+} or B^{3+}). With a very strong Brønsted character, approaching the superacidic region, and exhibiting fast reversible multi–electron redox transformations under rather mild conditions, POMs represent a serious alternative to other acid systems. Their acid–base and redox properties can be widely varied by changing the chemical composition. On top of that, POMs have a good thermal stability in the solid state, better than other strong acids like ion exchange resins. [80]

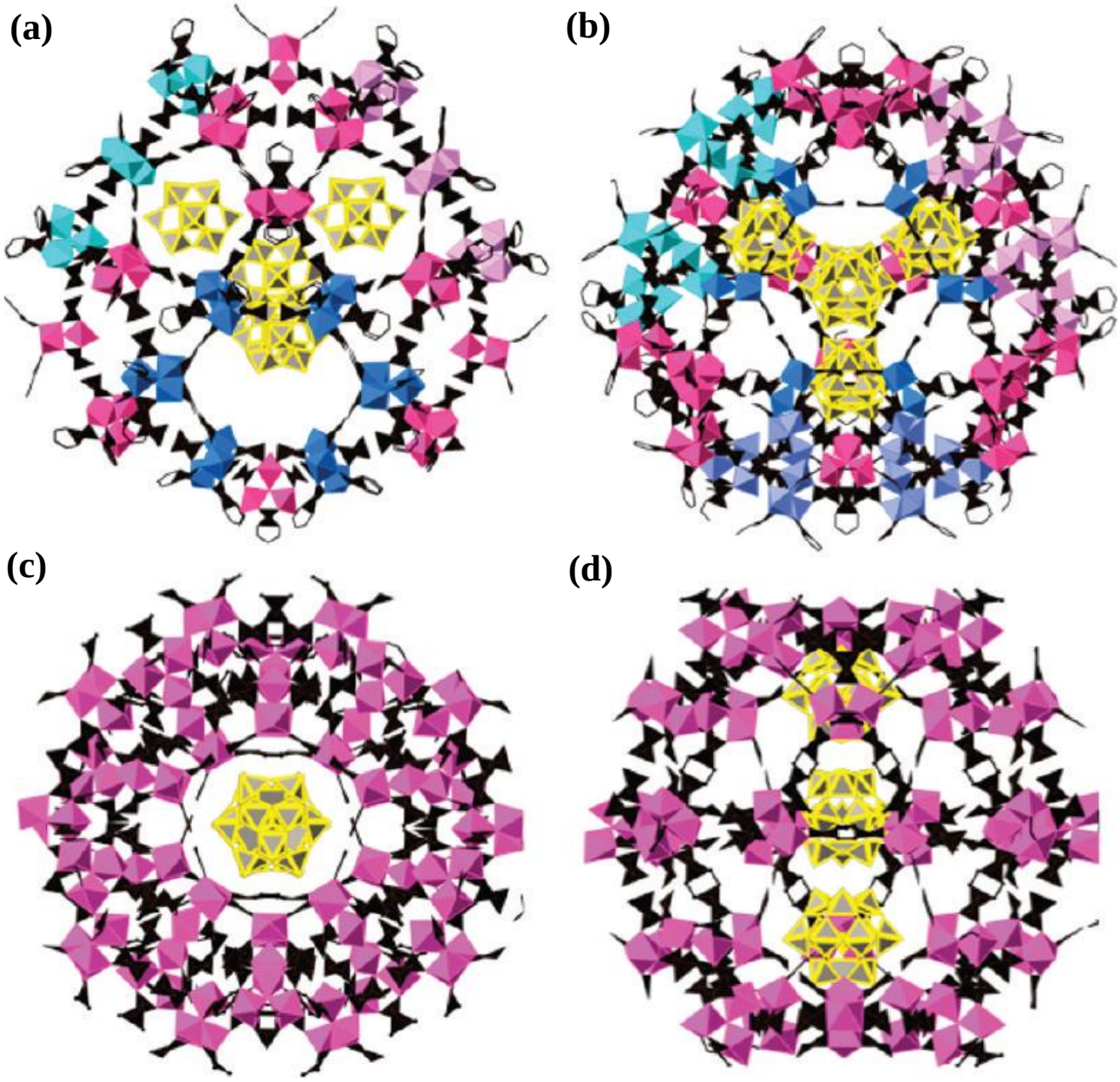

Figure 1 - 5 Proposed crystal structure of PTA/MIL−101(Cr) using the CrystalMaker 2.3.6 software. (a, b) The yellow PTA tetrahedron in a large cage of MIL–101 corresponding with the model of ordered PTA. Each of the four six–carbon rings is colored differently, each aligned with a PTA molecule. (c, d) A possible configuration of three PTA molecules in a small cage of MIL−101(Cr). The three PTA molecules were allowed to rotate around their shared axis. Cage views in the right side are top representations of the left–side figures. Reprinted with permission from [145]. Copyright (2012) American Chemical Society.

Supporting POMs is crucial for catalytic applications because most bulk POMs have a low specific surface area (1–5 m^2/g). Acidic or neutral porous solids such as SiO_2, Al_2O_3 and activated carbons have been explored as carriers. [146-150] The acidity and catalytic activity of supported POMs depend mainly on the type of carrier and the loading, *i.e.*, the interaction with activated carbons is so strong that the activity of the final catalyst is much lower than that of the POM itself, while weak interactions POM–support lead to dramatic leaching. Encapsulation of POMs inside zeolitic cavities has been achieved by direct synthesis of the Keggin structures inside the zeolite cavities (FAU). This approach is shown to solve the problem of leaching, since the POM clusters are bigger than the windows of the zeolitic cavities, but only low loadings can be utilized (<5 wt%) if diffusion limitations are to be avoided. [151] Phosphotungstic acid (PTA) is one of most well−known Keggin type POM structures, widely used in the encapsulation in porous solids, consisting of $H_3PW_{12}O_{40}$ formula.

The incorporation of POMs in MOF cavities has been widely studied (Fig 1−5), specially PTA. [52, 120] One–pot synthesis approach has also been extensively followed, using especially HKUST–1 and MILs as host for "ship in a bottle" catalyst. [152-154] Impregnation of the K/PTA salts was firstly performed by Férey and co–workers in MIL–101(Cr) as an original method to prove such large cavities. [28] Although the direct impregnation of PTA moieties into the large cavities of MIL–101 is straightforward, a number of drawbacks can be solved by one–pot encapsulation: [155, 156] (*a*) the maximal achievable loading of PTA is to a certain extent low, a maximum of ~10 wt% PTA can be obtained; (*b*) homogeneity of the sample is low; (*c*) dispersion of the active species is little, since only the large cavities of MIL–101 are filled with PTA; (*d*) leaching has been observed for certain reactions since immobilization is based on adsorption equilibrium. [157, 158]

1.4.2.2. Metal–organic macromolecules

Porphyrins and metalloporphyrins provide an extremely versatile basis for a large variety of applications. The fundamental properties of these materials come from their interaction with applied electric, magnetic or electromagnetic fields and with other chemical species. Porphyrins and metalloporphyrins have been broadly studied as field–responsive materials, particularly for potential optoelectronic applications and as chemoselective catalysts. [159] However, homogeneous metalloporphyrin–based catalysts present several drawbacks like limited life–time activity as a result of dimerization and self–degradation. Therefore, immobilization in solid matrices is expected to overcome such downsides by enhancing stability and by protecting the active site from deactivation. Several attempts on supporting metalloporphyrins include the use of mixed oxide surfaces and porous inorganic solids like zeolites, mesoporous silicates or silica surfaces. [109, 160, 161] Nevertheless, aggregation, limited catalyst loading, heterogeneous distribution, and/or leaching of the metalloporphyrins are some of the current limitations. [159]

Confined spaces have been proposed as an efficient environment to protect porphyrins from aggregation, heterogeneous distribution and leaching. A suitable host matrix providing such confinement effects should offer appropriate topological characteristics: large cavity dimensions (one guest porphyrin molecule per cavity) and relatively reduced opening windows preventing catalyst leaching while preserving reactants diffusion. It goes without saying that, when following this approach, stability of the metalloporphyrins during the matrix synthesis and the framework through possible post–synthetic metalation treatments might be considered. In the last decade of the twentieth century, zeolites were used to encapsulate metalloporphyrins through direct "bottle around a ship" synthesis. Such structures offered many opportunities for the development of selective catalysis, illustrating the stabilizing effect of zeolites. [8, 116, 119, 162-166] In a similar approach, the encapsulation of metalloporphyrins in metal–organic frameworks is expected to offer several advantages over other nano–molds, although only few proofs of concept have been published up to date. [88, 167]

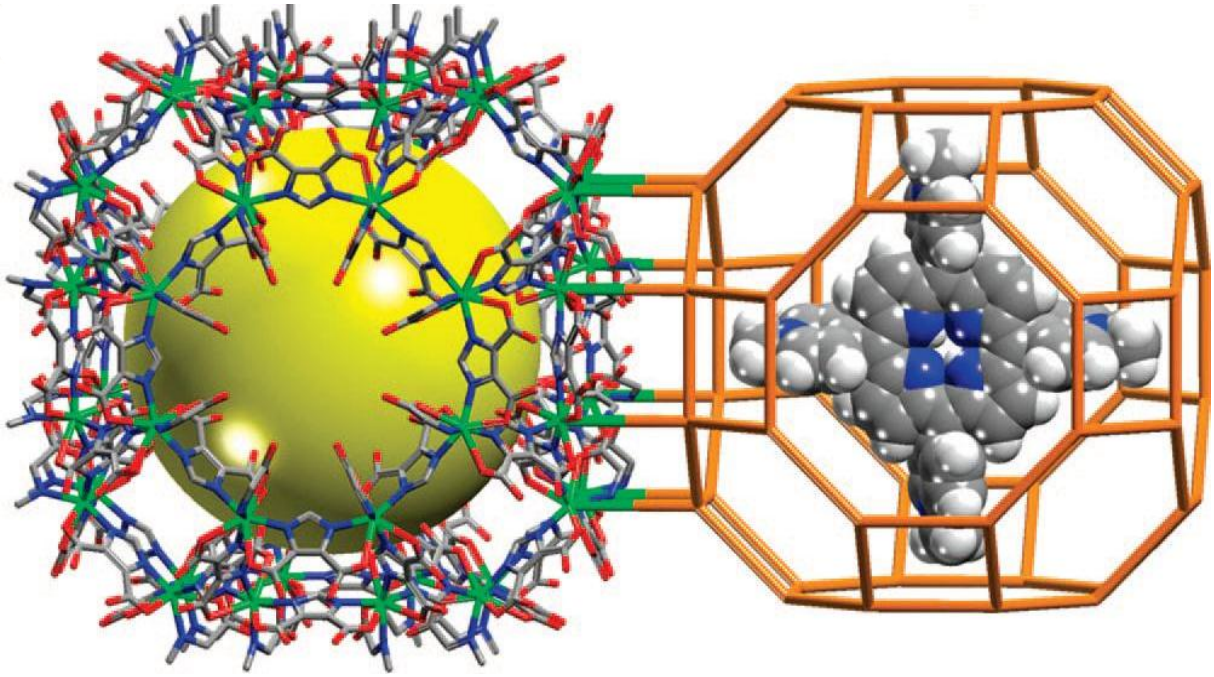

Figure 1 - 6 Crystal structure of *rho*–ZMOF (left), hydrogen atoms omitted for clarity, and schematic representation of $[H_2TMPyP]^{+4}$ porphyrin ring enclosed in *rho*–ZMOF α–cage (right, drawn to scale). Reprinted with permission from [168]. Copyright (2008) American Chemical Society.

Eddaoudi and co–workers pioneered the direct encapsulation of different porphyrins moieties in MOFs, for example, during the synthesis of zeolite–*like* MOF (ZMOF) Indium–based structure (Fig. 1–6). [168] After reporting these results, several publications describe further investigations of different porphyrin/MOF systems and their catalytic performances. [169, 170] In 2011, Larsen *et al.* described the encapsulation of M(3+)tetrakis(4–sulphonatophenyl)porphyrin (M_4SP, M=Fe or Mn)

within the octahedral cages of HKUST–1(Cu or Zn) forming MOMzyme–1, used for the monooxygenation of organic substrates. [171] After this work, two more publications from Zaworotko's group have reported templation effects of porphyrins during HKUST–1 and the formation of Porph@MOM–10 from CdTMPyP directly encapsulated and their performance in oxidation reactions. [172, 173]

1.5. OUTLINE OF THE THESIS

This Thesis focuses on the development of new approaches for the controlled incorporation of catalytic functionalities in MOFs and the use of the resulting functional solids as heterogeneous catalysts. To reach this goal, specific knowledge has been developed: (*i*) the development of several synthetic and post–synthetic methodologies for the encapsulation and/or grafting of active catalytic species; (*ii*) extensive use of a wide range of characterization techniques of the resulting porous solids; and (*iii*) development of specific catalytic applications depending on the incorporated active site. Considerable attention has been dedicated to the complete understanding of engineering active functional MOF catalysts from the molecular to the macro–scale levels.

A review of the current state of MOFs as catalysts is provided in **Chapter 1**. Definitions are very important to introduce the reader in the topic, and then an extensive review compiles the most interesting approaches for the functionalization of MOFs for catalytic purposes.

In **Chapter 2**, the one–pot encapsulation of phosphotungstic acid (PTA), a well–known Keggin polyoxometalate structure, in MIL–101(Cr) framework is presented. Next to extensive characterization to demonstrate the presence of the heteropolyacid in the MOF, a large study of the catalytic performance is given with the Knoevenagel condensation, esterification and etherification as acid catalysed test reactions. **Chapter 3** describes an *in situ* crystallization study of NH_2–MIL–101(Cr) and the differences observed with the presence of PTA in the reaction mixture. Another structure with the MTN topology, MIL–100(Cr), has also been used as scaffold for the encapsulation of PTA. In this case a biphasic medium and microwave irradiation have been used for the one–pot synthesis, the results are explained in **Chapter 4**. The metal (Pt) anchoring properties of encapsulated PTA have been explored in **Chapter 5** using CO oxidation, CO–PROX and toluene hydrogenation as model reactions.

Pre–functionalized sulfonic MOFs are described in **Chapter 6**. Sulfonic acid functionality in benzene–1,4–dicarboxylic acid has been used to synthesize Cr and Zr MOFs. Extensive characterization helps understanding the observed stability issues during esterification. **Chapter 7** reports one of the first examples of post–synthetic functionalization of robust MOFs by attaching sulfoxy groups at the terephthalate linkers of MIL–53(Al) and MIL–101(Cr). Proton conductivity and acid–catalyzed reactions are the applications studied in this chapter. **Chapter 8** presents the results of a combined pre–

and post– functionalization (covalent and dative) approach in MIL–101(Cr). A chelating agent has been formed at the benzene ring of the MOF structure and later used for the incorporation of Cu or Pd complexes, and the stabilization of Au nanoparticles. The resulting catalysts are applied in carbon–carbon coupling and oxidation reactions. **Chapter 9** addresses another very important aspect of catalysis engineering: the formulation of the MOF catalyst for application. MIL–101(Cr) is immobilized on a ceramic monolith and applied in a monolithic stirrer reactor for the oxidation of tetralin. The last chapter demonstrates that immobilization of the MOF catalysts solves attrition issues commonly found in the use of MOFs in slurry reactors.

Note that all chapters have been written as individual publications and can be read independently. Because of this, some overlap may be present.

REFERENCES

[1] O.M. Yaghi, H. Li, Hydrothermal synthesis of a metal-organic framework containing large rectangular channels, Journal of the American Chemical Society, 117 (1995) 10401-10402.
[2] Y. Kinoshita, I. Matsubara, T. Higuchi, Y. Saito, The Crystal Structure of Bis(adiponitrilo)copper(I) Nitrate, Bulletin of the Chemical Society of Japan, 32 (1959) 1221-1226.
[3] F.W. Knobloch, W.H. Rauscher, Coordination polymers of copper(II) prepared at liquid-liquid interfaces, Journal of Polymer Science, 38 (1959) 261-262.
[4] A.A. Berlin, N.G. Matveeva, Polymeric chelate compounds, Russian Chemical Reviews, 29 (1960) 119-128.
[5] B.P. Block, S.H. Rose, C.W. Schauman, E.S. Roth, J. Simkin, Coordination polymers with inorganic backbones formed by double-bridging of tetrahedral elements, Journal of the American Chemical Society, 84 (1962) 3200-3201.
[6] M. Kubo, M. Kishita, Y. Kuroda, Polymer molecules involving coordination links in the crystals of cupric oxalate and related compounds, Journal of Polymer Science, 48 (1960) 467-471.
[7] E.A. Tomic, Thermal stability of coordination polymers, Journal of Applied Polymer Science, 9 (1965) 3745-3752.
[8] S.R. Batten, B.F. Hoskins, R. Robson, Two interpenetrating 3D networks which generate spacious sealed-off compartments enclosing of the order of 20 solvent molecules in the structures of $Zn(CN)(NO_3)(tpt)_{2/3}\cdot$solv (tpt = 2,4,6-tri(4-pyridyl)-1,3,5-triazine, solv = $3/4C_2H_2Cl_4\cdot 3/4CH_3OH$ or $3/2CHCl_3\cdot 1/3CH_3OH$), Journal of the American Chemical Society, 117 (1995) 5385-5386.
[9] B.F. Hoskins, R. Robson, Design and construction of a new class of scaffolding-like materials comprising infinite polymeric frameworks of 3D-linked molecular rods. A reappraisal of the $Zn(CN)_2$ and $Cd(CN)_2$ structures and the synthesis and structure of the diamond-related frameworks $[N(CH_3)_4]$ [Cu(I)Zn(II)KCN_4], Journal of the American Chemical Society, 112 (1990) 1546-1554.
[10] S. Kitagawa, S. Matsuyama, M. Munakata, T. Emori, Synthesis and crystal structures of novel one-dimensional polymers, $[\{M(bpen)X\}_\infty]$ [M = Cu^I, X = PF_6^-; M = Ag^I, X = ClO_4^-; bpen = trans-1,2-bis(2-pyridyl)ethylene] and $[\{Cu(bpen)(CO)(CH_3CN)(PF_6)\}_\infty]$, Journal of the Chemical Society, Dalton Transactions, (1991) 2869-2874.
[11] S. Kitagawa, S. Kawata, Y. Nozaka, M. Munakata, Synthesis and crystal structures of novel copper(I) co-ordination polymers and a hexacopper(I) cluster of quinoline-2-thione, Journal of the Chemical Society, Dalton Transactions, (1993) 1399-1404.
[12] D. Riou, G. Férey, Hybrid open frameworks (MIL-n). Part 3: Crystal structures of the HT and LT forms of MIL-7: A new vanadium propylenediphosphonate with an open-framework. Influence of the synthesis temperature on the oxidation state of vanadium within the same structural type, Journal of Materials Chemistry, 8 (1998) 2733-2735.
[13] H. Li, M. Eddaoudi, M. O'Keeffe, O.M. Yaghi, Design and synthesis of an exceptionally stable and highly porous metal-organic framework, Nature, 402 (1999) 276-279.
[14] J.R. Long, O.M. Yaghi, The pervasive chemistry of metal-organic frameworks, Chemical Society Reviews, 38 (2009) 1213-1214.
[15] S.Y. Yang, H.B. Yuan, X.B. Xu, R.B. Huang, Influential factors on assembly of first-row transition metal coordination polymers, Inorganica Chimica Acta, 403 (2013) 53-62.
[16] M. O'Keeffe, O.M. Yaghi, Deconstructing the crystal structures of metal-organic frameworks and related materials into their underlying nets, Chemical Reviews, 112 (2011) 675-702.
[17] M. Kondo, T. Yoshitomi, H. Matsuzaka, S. Kitagawa, K. Seki, Three-Dimensional Framework with Channeling Cavities for Small Molecules: $\{[M_2(4,4'\text{-bpy})_3(NO_3)_4]\cdot xH_2O\}n$ (M = Co, Ni, Zn), Angewandte Chemie International Edition in English, 36 (1997) 1725-1727.
[18] H. Li, M. Eddaoudi, T.L. Groy, O.M. Yaghi, Establishing Microporosity in Open Metal−Organic Frameworks: Gas Sorption Isotherms for Zn(BDC) (BDC = 1,4-Benzenedicarboxylate), Journal of the American Chemical Society, 120 (1998) 8571-8572.
[19] W. Xuan, C. Zhu, Y. Liu, Y. Cui, Mesoporous metal-organic framework materials, Chemical Society Reviews, 41 (2012) 1677-1695.
[20] C. Janiak, J.K. Vieth, MOFs, MILs and more: Concepts, properties and applications for porous coordination networks (PCNs), New Journal of Chemistry, 34 (2010) 2366-2388.
[21] C. Serre, F. Millange, C. Thouvenot, M. Nogues, G. Marsolier, D. Louer, G. Férey, Very large breathing effect in the first nanoporous chromium(III)-based solids: MIL-53 or CrIII(OH)$\{O_2C\text{-}C_6H_4\text{-}CO_2\}\{HO_2C\text{-}C_6H_4\text{-}CO_2H\}xH_2Oy$, Journal of the American Chemical Society, 124 (2002) 13519-13526.
[22] T. Loiseau, C. Serre, C. Huguenard, G. Fink, F. Taulelle, M. Henry, T. Bataille, G. Férey, A Rationale for the Large Breathing of the Porous Aluminum Terephthalate (MIL-53) Upon Hydration, Chemistry - A European Journal, 10 (2004) 1373-1382.
[23] C. Gucuyener, J. Van Den Bergh, J. Gascon, F. Kapteijn, Ethane/ethene separation turned on its head: Selective ethane adsorption on the metal-organic framework ZIF-7 through a gate-opening mechanism, Journal of the American Chemical Society, 132 (2010) 17704-17706.
[24] G. Férey, Hybrid porous solids: Past, present, future, Chemical Society Reviews, 37 (2008) 191-214.

[25] N. Stock, S. Biswas, Synthesis of metal-organic frameworks (MOFs): Routes to various MOF topologies, morphologies, and composites, Chemical Reviews, 112 (2012) 933-969.
[26] E.A. Flugel, A. Ranft, F. Haase, B.V. Lotsch, Synthetic routes toward MOF nanomorphologies, Journal of Materials Chemistry, 22 (2012) 10119-10133.
[27] A. Umemura, S. Diring, S. Furukawa, H. Uehara, T. Tsuruoka, S. Kitagawa, Morphology Design of Porous Coordination Polymer Crystals by Coordination Modulation, Journal of the American Chemical Society, 133 (2011) 15506-15513.
[28] C. Férey, C. Mellot-Draznieks, C. Serre, F. Millange, J. Dutour, S. Surblé, I. Margiolaki, Chemistry: A chromium terephthalate-based solid with unusually large pore volumes and surface area, Science, 309 (2005) 2040-2042.
[29] M.P. Suh, H.J. Park, T.K. Prasad, D.-W. Lim, Hydrogen storage in metal-organic frameworks, Chemical Reviews, 112 (2011) 782-835.
[30] R.B. Getman, Y.-S. Bae, C.E. Wilmer, R.Q. Snurr, Review and analysis of molecular simulations of methane, hydrogen, and acetylene storage in metal–organic frameworks, Chemical Reviews, 112 (2011) 703-723.
[31] Y. He, W. Zhou, R. Krishna, B. Chen, Microporous metal-organic frameworks for storage and separation of small hydrocarbons, Chemical Communications, 48 (2012) 11813-11831.
[32] J.-R. Li, J. Sculley, H.-C. Zhou, Metal-organic frameworks for separations, Chemical Reviews, 112 (2011) 869-932.
[33] K. Sumida, D.L. Rogow, J.A. Mason, T.M. McDonald, E.D. Bloch, Z.R. Herm, T.-H. Bae, J.R. Long, Carbon dioxide capture in metal-organic frameworks, Chemical Reviews, 112 (2011) 724-781.
[34] H. Wu, Q. Gong, D.H. Olson, J. Li, Commensurate adsorption of hydrocarbons and alcohols in microporous metal-organic frameworks, Chemical Reviews, 112 (2012) 836-868.
[35] S. Cavenati, C.A. Grande, A.E. Rodrigues, C. Kiener, U. Müller, Metal-organic framework adsorbent for biogas upgrading, Industrial and Engineering Chemistry Research, 47 (2008) 6333-6335.
[36] A. Bétard, R.A. Fischer, Metal-organic framework thin films: from fundamentals to applications, Chemical Reviews, 112 (2011) 1055-1083.
[37] C. Munuera, O. Shekhah, H. Wang, C. Wöll, C. Ocal, The controlled growth of oriented metal-organic frameworks on functionalized surfaces as followed by scanning force microscopy, Physical Chemistry Chemical Physics, 10 (2008) 7257-7261.
[38] D. Zacher, O. Shekhah, C. Wöll, R.A. Fischer, Thin films of metal-organic frameworks, Chemical Society Reviews, 38 (2009) 1418-1429.
[39] Z.-Y. Gu, C.-X. Yang, N. Chang, X.-P. Yan, Metal-organic frameworks for analytical chemistry: from sample collection to chromatographic separation, Accounts of Chemical Research, 45 (2012) 734-745.
[40] W. Zhang, R.-G. Xiong, Ferroelectric metal-organic frameworks, Chemical Reviews, 112 (2011) 1163-1195.
[41] Y. Cui, Y. Yue, G. Qian, B. Chen, Luminescent functional metal-organic frameworks, Chemical Reviews, 112 (2011) 1126-1162.
[42] L.E. Kreno, K. Leong, O.K. Farha, M. Allendorf, R.P. Van Duyne, J.T. Hupp, Metal-organic framework materials as chemical sensors, Chemical Reviews, 112 (2011) 1105-1125.
[43] B. Chen, S. Xiang, G. Qian, Metal-organic frameworks with functional pores for recognition of small molecules, Accounts of Chemical Research, 43 (2010) 1115-1124.
[44] P. Horcajada, T. Chalati, C. Serre, B. Gillet, C. Sebrie, T. Baati, J.F. Eubank, D. Heurtaux, P. Clayette, C. Kreuz, J.S. Chang, Y.K. Hwang, V. Marsaud, P.N. Bories, L. Cynober, S. Gil, G. Férey, P. Couvreur, R. Gref, Porous metal-organic framework nanoscale carriers as a potential platform for drug delivery and imaging, Nature Materials, 9 (2010) 172-178.
[45] P. Horcajada, R. Gref, T. Baati, P.K. Allan, G. Maurin, P. Couvreur, G. Férey, R.E. Morris, C. Serre, Metal-organic frameworks in biomedicine, Chemical Reviews, 112 (2011) 1232-1268.
[46] X. Zheng, Y. Li, Y. Xu, Z. Hong, M. Wei, Metal-organic frameworks: Promising materials for enhancing electrochemical properties of nanostructured Zn_2SnO_4 anode in Li-ion batteries, CrystEngComm, 14 (2012) 2112-2116.
[47] Y. Liu, W. Xuan, Y. Cui, Engineering homochiral metal-organic frameworks for heterogeneous asymmetric catalysis and enantioselective separation, Advanced Materials, 22 (2010) 4112-4135.
[48] M. Yoon, R. Srirambalaji, K. Kim, Homochiral metal-organic frameworks for asymmetric heterogeneous catalysis, Chemical Reviews, 112 (2011) 1196-1231.
[49] J.S. Seo, D. Whang, H. Lee, S.I. Jun, J. Oh, Y.J. Jeon, K. Kim, A homochiral metal-organic porous material for enantioselective separation and catalysis, Nature, 404 (2000) 982-986.
[50] M.P. Yutkin, D.N. Dybtsev, V.P. Fedin, Homochiral porous metal-organic coordination polymers: Synthesis, structure and functional properties, Russian Chemical Reviews, 80 (2011) 1009-1034.
[51] L. Wenbin, Homochiral porous metal-organic frameworks: Why and how?, Journal of Solid State Chemistry, 178 (2005) 2486-2490.
[52] A. Corma, H. García, F.X. Llabrés i Xamena, Engineering metal-organic frameworks for heterogeneous catalysis, Chemical Reviews, 110 (2010) 4606-4655.
[53] M. Ranocchiari, J.A. van Bokhoven, Catalysis by metal-organic frameworks: Fundamentals and opportunities, Physical Chemistry Chemical Physics, 13 (2011) 6388-6396.

[54] L. Alaerts, E. Séguin, H. Poelman, F. Thibault-Starzyk, P.A. Jacobs, D.E. De Vos, Probing the Lewis acidity and catalytic activity of the metal-organic framework $[Cu_3(btc)_2]$ (btc = Benzene-1,3,5-tricarboxylate), Chemistry - A European Journal, 12 (2006) 7353-7363.
[55] F. Vermoortele, R. Ameloot, A. Vimont, C. Serre, D. De Vos, An amino-modified Zr-terephthalate metal-organic framework as an acid-base catalyst for cross-aldol condensation, Chemical Communications, 47 (2011) 1521-1523.
[56] P. Horcajada, S. Surblé, C. Serre, D.Y. Hong, Y.K. Seo, J.S. Chang, J.M. Greneche, I. Margiolaki, G. Férey, Synthesis and catalytic properties of MIL-100(Fe), an iron(III) carboxylate with large pores, Chemical Communications, (2007) 2820-2822.
[57] U. Ravon, M.E. Domine, C. Gaudillère, A. Desmartin-Chomel, D. Farrusseng, MOFs as acid catalysts with shape selectivity properties, New Journal of Chemistry, 32 (2008) 937-940.
[58] L. Huang, H. Wang, J. Chen, Z. Wang, J. Sun, D. Zhao, Y. Yan, Synthesis, morphology control, and properties of porous metal-organic coordination polymers, Microporous and Mesoporous Materials, 58 (2003) 105-114.
[59] J. Hafizovic, M. Bjørgen, U. Olsbye, P.D.C. Dietzel, S. Bordiga, C. Prestipino, C. Lamberti, K.P. Lillerud, The Inconsistency in Adsorption Properties and Powder XRD Data of MOF-5 Is Rationalized by Framework Interpenetration and the Presence of Organic and Inorganic Species in the Nanocavities, Journal of the American Chemical Society, 129 (2007) 3612-3620.
[60] G. Calleja, J. Botas, M.G. Orcajo, M. Sánchez-Sánchez, Differences between the isostructural IRMOF-1 and MOCP-L porous adsorbents, Journal of Porous Materials, 17 (2010) 91-97.
[61] P.K. Thallapally, C.A. Fernandez, R.K. Motkuri, S.K. Nune, J. Liu, C.H.F. Peden, Micro and mesoporous metal-organic frameworks for catalysis applications, Dalton Transactions, 39 (2010) 1692-1694.
[62] A. Dhakshinamoorthy, M. Alvaro, H. Garcia, Metal-Organic Frameworks (MOFs) as Heterogeneous Catalysts for the Chemoselective Reduction of Carbon-Carbon Multiple Bonds with Hydrazine, Advanced Synthesis & Catalysis, 351 (2009) 2271-2276.
[63] A. Dhakshinamoorthy, M. Alvaro, H. Garcia, Metal organic frameworks as heterogeneous catalysts for the selective N-methylation of aromatic primary amines with dimethyl carbonate, Applied Catalysis A: General, 378 (2010) 19-25.
[64] K. Leus, M. Vandichel, Y.Y. Liu, I. Muylaert, J. Musschoot, S. Pyl, H. Vrielinck, F. Callens, G.B. Marin, C. Detavernier, P.V. Wiper, Y.Z. Khimyak, M. Waroquier, V. Van Speybroeck, P. Van Der Voort, The coordinatively saturated vanadium MIL-47 as a low leaching heterogeneous catalyst in the oxidation of cyclohexene, Journal of Catalysis, 285 (2012) 196-207.
[65] K. Leus, I. Muylaert, M. Vandichel, G.B. Marin, M. Waroquier, V. Van Speybroeck, P. Van Der Voort, The remarkable catalytic activity of the saturated metal organic framework V-MIL-47 in the cyclohexene oxidation, Chemical Communications, 46 (2010) 5085-5087.
[66] F. Vermoortele, R. Ameloot, L. Alaerts, R. Matthessen, B. Carlier, E.V.R. Fernandez, J. Gascon, F. Kapteijn, D.E. De Vos, Tuning the catalytic performance of metal-organic frameworks in fine chemistry by active site engineering, Journal of Materials Chemistry, 22 (2012) 10313-10321.
[67] D. Jiang, T. Mallat, F. Krumeich, A. Baiker, Copper-based metal-organic framework for the facile ring-opening of epoxides, Journal of Catalysis, 257 (2008) 390-395.
[68] I. Luz, F.X. Llabrés i Xamena, A. Corma, Bridging homogeneous and heterogeneous catalysis with MOFs: Cu-MOFs as solid catalysts for three-component coupling and cyclization reactions for the synthesis of propargylamines, indoles and imidazopyridines, Journal of Catalysis, 285 (2012) 285-291.
[69] I. Luz, F.X. Llabrés I Xamena, A. Corma, Bridging homogeneous and heterogeneous catalysis with MOFs: "Click" reactions with Cu-MOF catalysts, Journal of Catalysis, 276 (2010) 134-140.
[70] F.X. Llabrés i Xamena, O. Casanova, R. Galiasso Tailleur, H. Garcia, A. Corma, Metal organic frameworks (MOFs) as catalysts: A combination of Cu^{2+} and Co^{2+} MOFs as an efficient catalyst for tetralin oxidation, Journal of Catalysis, 255 (2008) 220-227.
[71] I. Luz, A. León, M. Boronat, F.X. Llabrés I Xamena, A. Corma, Selective aerobic oxidation of activated alkanes with MOFs and their use for epoxidation of olefins with oxygen in a tandem reaction, Catalysis Science and Technology, 3 (2013) 371-379.
[72] J. Kim, S. Bhattacharjee, K.E. Jeong, S.Y. Jeong, W.S. Ahn, Selective oxidation of tetralin over a chromium terephthalate metal organic framework, MIL-101, Chemical Communications, (2009) 3904-3906.
[73] N.V. Maksimchuk, K.A. Kovalenko, V.P. Fedin, O.A. Kholdeeva, Cyclohexane selective oxidation over metal-organic frameworks of MIL-101 family: superior catalytic activity and selectivity, Chemical Communications, 48 (2012) 6812-6814.
[74] A. Phan, A.U. Czaja, F. Gándara, C.B. Knobler, O.M. Yaghi, Metal-organic frameworks of vanadium as catalysts for conversion of methane to acetic acid, Inorganic Chemistry, 50 (2011) 7388-7390.
[75] B. Gomez-Lor, E. Gutiérrez-Puebla, M. Iglesias, M.A. Monge, C. Ruiz-Valero, N. Snejko, $In_2(OH)_3(bdc)_{1.5}$ (bdc = 1,4-benzendicarboxylate): An In(III) supramolecular 3D framework with catalytic activity, Inorganic Chemistry, 41 (2002) 2429-2432.
[76] Y.K. Hwang, D.Y. Hong, J.S. Chang, S.H. Jhung, Y.K. Seo, J. Kim, A. Vimont, M. Daturi, C. Serre, G. Férey, Amine grafting on coordinatively unsaturated metal centers of MOFs: Consequences for catalysis and metal encapsulation, Angewandte Chemie - International Edition, 47 (2008) 4144-4148.

[77] A. Arnanz, M. Pintado-Sierra, A. Corma, M. Iglesias, F. Sánchez, Bifunctional metal organic framework catalysts for multistep reactions: MOF-Cu(btc)-[Pd] catalyst for one-pot heteroannulation of acetylenic compounds, Advanced Synthesis and Catalysis, 354 (2012) 1347-1355.
[78] M. Kim, J.F. Cahill, H. Fei, K.A. Prather, S.M. Cohen, Post-synthetic ligand and cation exchange in robust metal-organic frameworks, Journal of the American Chemical Society, 134 (2012) 18082-18088.
[79] M. Eddaoudi, J. Kim, N. Rosi, D. Vodak, J. Wachter, M. O'Keeffe, O.M. Yaghi, Systematic design of pore size and functionality in isoreticular MOFs and their application in methane storage, Science, 295 (2002) 469-472.
[80] J. Gascon, U. Aktay, M.D. Hernandez-Alonso, G.P.M. van Klink, F. Kapteijn, Amino-based metal-organic frameworks as stable, highly active basic catalysts, Journal of Catalysis, 261 (2009) 75-87.
[81] P. Serra-Crespo, E.V. Ramos-Fernandez, J. Gascon, F. Kapteijn, Synthesis and Characterization of an Amino Functionalized MIL-101(Al): Separation and Catalytic Properties, Chemistry of Materials, 23 (2011) 2565-2572.
[82] J.A. Thompson, C.R. Blad, N.A. Brunelli, M.E. Lydon, R.P. Lively, C.W. Jones, S. Nair, Hybrid zeolitic imidazolate frameworks: Controlling framework porosity and functionality by mixed-linker synthesis, Chemistry of Materials, 24 (2012) 1930-1936.
[83] S. Marx, W. Kleist, J. Huang, M. MacIejewski, A. Baiker, Tuning functional sites and thermal stability of mixed-linker MOFs based on MIL-53(Al), Dalton Transactions, 39 (2010) 3795-3798.
[84] M. Kim, J.F. Cahill, Y. Su, K.A. Prather, S.M. Cohen, Post-synthetic ligand exchange as a route to functionalization of 'inert' metal-organic frameworks, Chemical Science, 3 (2012) 126-130.
[85] F.A. Almeida Paz, J. Klinowski, S.M.F. Vilela, J.P.C. Tome, J.A.S. Cavaleiro, J. Rocha, Ligand design for functional metal-organic frameworks, Chemical Society Reviews, 41 (2012) 1088-1110.
[86] J.-P. Zhang, Y.-B. Zhang, J.-B. Lin, X.-M. Chen, Metal Azolate Frameworks: From Crystal Engineering to Functional Materials, Chemical Reviews, 112 (2011) 1001-1033.
[87] M.C. Das, S. Xiang, Z. Zhang, B. Chen, Functional mixed metal-organic frameworks with metalloligands, Angewandte Chemie International Edition, 50 (2011) 10510-10520.
[88] C. Zou, C.-D. Wu, Functional porphyrinic metal-organic frameworks: crystal engineering and applications, Dalton Transactions, 41 (2012) 3879-3888.
[89] L. Ma, C. Abney, W. Lin, Enantioselective catalysis with homochiral metal-organic frameworks, Chemical Society Reviews, 38 (2009) 1248-1256.
[90] L. Ma, J.M. Falkowski, C. Abney, W. Lin, A series of isoreticular chiral metal-organic frameworks as a tunable platform for asymmetric catalysis, Nature Chemistry, 2 (2010) 838-846.
[91] Z. Wang, S.M. Cohen, Postsynthetic modification of metal-organic frameworks, Chemical Society Reviews, 38 (2009) 1315-1329.
[92] S.M. Cohen, Post-synthetic methods for the functionalization of metal-organic frameworks, Chemical Reviews, 112 (2011) 970-1000.
[93] S.J. Garibay, Z. Wang, K.K. Tanabe, S.M. Cohen, Postsynthetic modification: A versatile approach toward multifunctional metal-organic frameworks, Inorganic Chemistry, 48 (2009) 7341-7349.
[94] S.J. Garibay, Z. Wang, S.M. Cohen, Evaluation of heterogeneous metal-organic framework organocatalysts prepared by postsynthetic modification, Inorganic Chemistry, 49 (2010) 8086-8091.
[95] M. Savonnet, D. Bazer-Bachi, N. Bats, J. Perez-Pellitero, E. Jeanneau, V. Lecocq, C. Pinel, D. Farrusseng, Generic post-functionalization route from amino-derived metal-organic frameworks, Journal of the American Chemical Society, 132 (2010) 4518-4519.
[96] M. Savonnet, A. Camarata, J. Canivet, D. Bazer-Bachi, N. Bats, V. Lecocq, C. Pinel, D. Farrusseng, Tailoring metal-organic framework catalysts by click chemistry, Dalton Transactions, 41 (2012) 3945-3948.
[97] M.J. Ingleson, J. Perez Barrio, J.B. Guilbaud, Y.Z. Khimyak, M.J. Rosseinsky, Framework functionalisation triggers metal complex binding, Chemical Communications, (2008) 2680-2682.
[98] X. Zhang, F.X. Llabrés i Xamena, A. Corma, Gold(III) – metal-organic framework bridges the gap between homogeneous and heterogeneous gold catalysts, Journal of Catalysis, 265 (2009) 155-160.
[99] T. Yamada, H. Kitagawa, Protection and deprotection approach for the introduction of functional groups into metal-organic frameworks, Journal of the American Chemical Society, 131 (2009) 6312-6313.
[100] D.J. Lun, G.I.N. Waterhouse, S.G. Telfer, A general thermolabile protecting group strategy for organocatalytic metal-organic frameworks, Journal of the American Chemical Society, 133 (2011) 5806-5809.
[101] G. Langer, G. Yamate, Encapsulation of liquid and solid aerosol particles to form dry powders, Journal of Colloid and Interface Science, 29 (1969) 450-455.
[102] K. Kita, C. Dittrich, Drug delivery vehicles with improved encapsulation efficiency: Taking advantage of specific drug-carrier interactions, Expert Opinion on Drug Delivery, 8 (2011) 329-342.
[103] T. Ishihara, T. Mizushima, Techniques for efficient entrapment of pharmaceuticals in biodegradable solid micro/nanoparticles, Expert Opinion on Drug Delivery, 7 (2010) 565-575.
[104] R. Ravichandran, Nanotechnology Applications in Food and Food Processing: Innovative Green Approaches, Opportunities and Uncertainties for Global Market, International Journal of Green Nanotechnology: Physics and Chemistry, 1 (2010) 72-96.

[105] D. Trimnell, B.S. Shasha, R.E. Wing, F.H. Otey, Pesticides encapsulation using a Starch-Borate complex as wall material, Journal of Applied Polymer Science, V 27 (1982) 3919-3928.
[106] D. Avnir, S. Braun, O. Lev, M. Ottolenghi, Enzymes and other proteins entrapped in sol-gel materials, Chemistry of Materials, 6 (1994) 1605-1614.
[107] L. Rashidi, K. Khosravi-Darani, The applications of nanotechnology in food industry, Critical Reviews in Food Science and Nutrition, 51 (2011) 723-730.
[108] B.F. Gibbs, S. Kermasha, I. Alli, C.N. Mulligan, Encapsulation in the food industry: A review, International Journal of Food Sciences and Nutrition, 50 (1999) 213-224.
[109] D.E. De Vos, B.F. Sels, P.A. Jacobs, Heterogeneous enzyme mimics based on zeolites and layered hydroxides, CATTECH, 6 (2002) 14-29.
[110] D. Fraenkel, J. Shabtai, Encapsulation of hydrogen in molecular sieve zeolites [12], Journal of the American Chemical Society, 99 (1977) 7074-7076.
[111] D. Fraenkel, Zeolitic encapsulation. Part 1.-Hydrogen diffusion in A-type zeolite encapsulates, Journal of the Chemical Society, Faraday Transactions 1: Physical Chemistry in Condensed Phases, 77 (1981) 2029-2039.
[112] D. Fraenkel, Zeolitic encapsulation. Part 2.-Percolation and trapping of inert gases in A-type zeolites, Journal of the Chemical Society, Faraday Transactions 1: Physical Chemistry in Condensed Phases, 77 (1981) 2041-2052.
[113] A. Markus, I. Eger, M. Mhasalkar, Z. Pelah, A. Galun, Encapsulation of methyl bromide in zeolites, Journal of Colloid and Interface Science, 94 (1983) 284-285.
[114] T. Bein, P. Enzel, Encapsulation of polypyrrole chains in zeolite channels, Angewandte Chemie - International Edition in English, 28 (1989) 1692-1694.
[115] T. Bein, P. Enzel, Encapsulation of polyaniline in zeolite Y and mordenite, Synthetic Metals, 29 (1989) 163-168.
[116] K.J. Balkus Jr, A.K. Khanmamedova, K.M. Dixon, F. Bedioui, Oxidations catalyzed by zeolite ship-in-a-bottle complexes, Applied Catalysis A: General, 143 (1996) 159-173.
[117] K.J. Balkus Jr, A.A. Welch, B.E. Gnade, The preparation and characterization of Rh(III) salen complexes encapsulated in zeolites X and Y, Zeolites, 10 (1990) 722-729.
[118] X. Liu, K.K. Iu, J. Kerry Thomas, Encapsulation of TiO_2 in zeolite Y, Chemical Physics Letters, 195 (1992) 163-168.
[119] K.J. Balkus Jr, A.A. Welch, B.E. Gnade, The encapsulation of Rh(III) phthalocyanines in zeolites X and Y, Journal of Inclusion Phenomena and Molecular Recognition in Chemistry, 10 (1991) 141-151.
[120] J. Juan-Alcañiz, J. Gascon, F. Kapteijn, Metal-organic frameworks as scaffolds for the encapsulation of active species: state of the art and future perspectives, Journal of Materials Chemistry, 22 (2012) 10102-10118.
[121] M. Meilikhov, K. Yusenko, D. Esken, S. Turner, G. Van Tendeloo, R.A. Fischer, Metals@MOFs – Loading MOFs with Metal Nanoparticles for Hybrid Functions, European Journal of Inorganic Chemistry, 2010 (2010) 3701-3714.
[122] A. Dhakshinamoorthy, H. Garcia, Catalysis by metal nanoparticles embedded on metal-organic frameworks, Chemical Society Reviews, 41 (2012) 5262-5284.
[123] R. Das, P. Pachfule, R. Banerjee, P. Poddar, Metal and metal oxide nanoparticle synthesis from metal-organic frameworks (MOFs): finding the border of metal and metal oxides, Nanoscale, 4 (2012) 591-599.
[124] H.R. Moon, D.W. Lim, M.P. Suh, Fabrication of metal nanoparticles in metal-organic frameworks, Chemical Society Reviews, 42 (2013) 1807-1824.
[125] M. Sabo, A. Henschel, H. Fröde, E. Klemm, S. Kaskel, Solution infiltration of palladium into MOF-5: Synthesis, physisorption and catalytic properties, Journal of Materials Chemistry, 17 (2007) 3827-3832.
[126] S. Hermes, M.K. Schröter, R. Schmid, L. Khodeir, M. Muhler, A. Tissler, R.W. Fischer, R.A. Fischer, Metal@MOF: Loading of highly porous coordination polymers host lattices by metal organic chemical vapor deposition, Angewandte Chemie - International Edition, 44 (2005) 6237-6241.
[127] T. Ishida, M. Nagaoka, T. Akita, M. Haruta, Deposition of Gold Clusters on Porous Coordination Polymers by Solid Grinding and Their Catalytic Activity in Aerobic Oxidation of Alcohols, Chemistry – A European Journal, 14 (2008) 8456-8460.
[128] B.W. Jacobs, R.J.T. Houk, M.R. Anstey, S.D. House, I.M. Robertson, A.A. Talin, M.D. Allendorf, Ordered metal nanostructure self-assembly using metal-organic frameworks as templates, Chemical Science, 2 (2011) 411-416.
[129] R.J.R.W. Peters, I. Louzao, J.C.M. van Hest, From polymeric nanoreactors to artificial organelles, Chemical Science, 3 (2012) 335-342.
[130] M.T. Reetz, Entrapment of biocatalysts in hydrophobic sol-gel materials for use in organic chemistry, Advanced Materials, 9 (1997) 943-954.
[131] K.M. de Lathouder, J.J.W. Bakker, M.T. Kreutzer, S.A. Wallin, F. Kapteijn, J.A. Moulijn, Structured reactors for enzyme immobilization: A monolithic stirrer reactor for application in organic media, Chemical Engineering Research and Design, 84 (2006) 390-398.
[132] K.M. de Lathouder, D.T.J. van Benthem, S.A. Wallin, C. Mateo, R.F. Lafuente, J.M. Guisan, F. Kapteijn, J.A. Moulijn, Polyethyleneimine (PEI) functionalized ceramic monoliths as enzyme carriers: Preparation and performance, Journal of Molecular Catalysis B: Enzymatic, 50 (2008) 20-27.
[133] K. Renggli, P. Baumann, K. Langowska, O. Onaca, N. Bruns, W. Meier, Selective and Responsive Nanoreactors, Advanced Functional Materials, 21 (2011) 1241-1259.

[134] J.J. Davis, K.S. Coleman, B.R. Azamian, C.B. Bagshaw, M.L.H. Green, Chemical and biochemical sensing with modified single walled carbon nanotubes, Chemistry - A European Journal, 9 (2003) 3732-3739.
[135] R. Plagemann, L. Jonas, U. Kragl, Ceramic honeycomb as support for covalent immobilization of laccase from Trametes versicolor and transformation of nuclear fast red, Applied Microbiology and Biotechnology, 90 (2011) 313-320.
[136] Y. Yu, B. Chen, W. Qi, X. Li, Y. Shin, C. Lei, J. Liu, Enzymatic conversion of CO_2 to bicarbonate in functionalized mesoporous silica, Microporous and Mesoporous Materials, 153 (2012) 166-170.
[137] S. Hudson, J. Cooney, E. Magner, Proteins in mesoporous silicates, Angewandte Chemie - International Edition, 47 (2008) 8582-8594.
[138] M. Hartmann, Ordered mesoporous materials for bioadsorption and biocatalysis, Chemistry of Materials, 17 (2005) 4577-4593.
[139] K.M. de Lathouder, D. Lozano-Castelló, A. Linares-Solano, S.A. Wallin, F. Kapteijn, J.A. Moulijn, Carbon-ceramic composites for enzyme immobilization, Microporous and Mesoporous Materials, 99 (2007) 216-223.
[140] S. Mitchell, J. Pérez-Ramírez, Mesoporous zeolites as enzyme carriers: Synthesis, characterization, and application in biocatalysis, Catalysis Today, 168 (2011) 28-37.
[141] J.F. Díaz, K.J. Balkus Jr, Enzyme immobilization in MCM-41 molecular sieve, Journal of Molecular Catalysis B: Enzymatic, 2 (1996) 115-126.
[142] V. Lykourinou, Y. Chen, X.-S. Wang, L. Meng, T. Hoang, L.-J. Ming, R.L. Musselman, S. Ma, Immobilization of MP-11 into a Mesoporous Metal–Organic Framework, MP-11@mesoMOF: A New Platform for Enzymatic Catalysis, Journal of the American Chemical Society, 133 (2011) 10382-10385.
[143] Y. Chen, V. Lykourinou, C. Vetromile, T. Hoang, L.-J. Ming, R.W. Larsen, S. Ma, How Can Proteins Enter the Interior of a MOF? Investigation of Cytochrome c Translocation into a MOF Consisting of Mesoporous Cages with Microporous Windows, Journal of the American Chemical Society, 134 (2012) 13188-13191.
[144] Y.K. Park, B.C. Sang, H. Kim, K. Kim, B.H. Won, K. Choi, J.S. Choi, W.S. Ahn, N. Won, S. Kim, H.J. Dong, S.H. Choi, G.H. Kim, S.S. Cha, H.J. Young, K.Y. Jin, J. Kim, Crystal structure and guest uptake of a mesoporous metal-organic framework containing cages of 3.9 and 4.7 nm in diameter, Angewandte Chemie - International Edition, 46 (2007) 8230-8233.
[145] L. Bromberg, Y. Diao, H. Wu, S.A. Speakman, T.A. Hatton, Chromium(III) terephthalate metal organic framework (MIL-101): Hf-free synthesis, structure, polyoxometalate composites, and catalytic properties, Chemistry of Materials, 24 (2012) 1664-1675.
[146] S.S. Wu, J. Wang, W.H. Zhang, X.Q. Ren, Preparation of Keggin and Preyssler heteropolyacid catalysts on amine-modified SBA-15 and their catalytic performances in esterification of n-butanol with acetic acid, Catal. Lett., 125 (2008) 308-314.
[147] H. Atia, U. Armbruster, A. Martin, Dehydration of glycerol in gas phase using heteropolyacid catalysts as active compounds, J. Catal., 258 (2008) 71-82.
[148] M.A. Schwegler, P. Vinke, M. van der Eijk, H. van Bekkum, Activated carbon as a support for heteropolyanion catalysts, Applied Catalysis A: General, 80 (1992) 41-57.
[149] J. Haber, K. Pamin, L. Matachowski, D. Mucha, Catalytic performance of the dodecatungstophosphoric acid on different supports, Applied Catalysis a-General, 256 (2003) 141-152.
[150] I.V. Kozhevnikov, A. Sinnema, R.J.J. Jansen, K. Pamin, H. Bekkum, New acid catalyst comprising heteropoly acid on a mesoporous molecular sieve MCM-41, Catal. Lett., 30 (1994) 241-252.
[151] P. Ferreira, I.M. Fonseca, A.M. Ramos, J. Vital, J.E. Castanheiro, Esterification of glycerol with acetic acid over dodecamolybdophosphoric acid encaged in USY zeolite, Catalysis Communications, 10 (2009) 481-484.
[152] C.Y. Sun, S.X. Liu, D.D. Liang, K.Z. Shao, Y.H. Ren, Z.M. Su, Highly stable crystalline catalysts based on a microporous metal-organic framework and polyoxometalates, Journal of the American Chemical Society, 131 (2009) 1883-1888.
[153] F.J. Ma, S.X. Liu, C.Y. Sun, D.D. Liang, G.J. Ren, F. Wei, Y.G. Chen, Z.M. Su, A sodalite-type porous metal-organic framework with polyoxometalate templates: Adsorption and decomposition of dimethyl methylphosphonate, Journal of the American Chemical Society, 133 (2011) 4178-4181.
[154] J. Juan-Alcañiz, E.V. Ramos-Fernandez, U. Lafont, J. Gascon, F. Kapteijn, Building MOF bottles around phosphotungstic acid ships: One-pot synthesis of bi-functional polyoxometalate-MIL-101 catalysts, Journal of Catalysis, 269 (2010) 229-241.
[155] C.M. Granadeiro, A.D.S. Barbosa, P. Silva, F.A.A. Paz, V.K. Saini, J. Pires, B. De Castro, S.S. Balula, L. Cunha-Silva, Monovacant polyoxometalates incorporated into MIL-101(Cr): Novel heterogeneous catalysts for liquid phase oxidation, Applied Catalysis A: General, 453 (2013) 316-326.
[156] I. Ahmed, N.A. Khan, Z. Hasan, S.H. Jhung, Adsorptive denitrogenation of model fuels with porous metal-organic framework (MOF) MIL-101 impregnated with phosphotungstic acid: Effect of acid site inclusion, Journal of Hazardous Materials, 250-251 (2013) 37-44.
[157] Y. Zang, J. Shi, X. Zhao, L. Kong, F. Zhang, Y. Zhong, Highly stable chromium(III) terephthalate metal organic framework (MIL-101) encapsulated 12-tungstophosphoric heteropolyacid as a water-tolerant solid catalyst for hydrolysis and esterification, Reaction Kinetics, Mechanisms and Catalysis, 109 (2013) 77-89.

[158] X. Hu, Y. Lu, F. Dai, C. Liu, Y. Liu, Host–guest synthesis and encapsulation of phosphotungstic acid in MIL-101 via "bottle around ship": An effective catalyst for oxidative desulfurization, Microporous and Mesoporous Materials, 170 (2013) 36-44.
[159] K.S. Suslick, N.A. Rakow, M.E. Kosal, J.H. Chou, The materials chemistry of porphyrins and metalloporphyrins, Journal of Porphyrins and Phthalocyanines, 4 (2000) 407-413.
[160] D.E. De Vos, M. Dams, B.F. Sels, P.A. Jacobs, Ordered mesoporous and microporous molecular sieves functionalized with transition metal complexes as catalysts for selective organic transformations, Chemical Reviews, 102 (2002) 3615-3640.
[161] R.F. Parton, I.F.J. Vankelecom, M.J.A. Casselman, C.P. Bezoukhanova, J.B. Uytterhoeven, P.A. Jacobs, An efficient mimic of cytochrome P-450 from a zeolite-encaged iron complex in a polymer membrane, Nature, 370 (1994) 541-544.
[162] V. Faraon, R.M. Ion, Ship-in-bottle porphyrin - zeolite nanomaterials, Optoelectronics and Advanced Materials, Rapid Communications, 4 (2010) 1135-1140.
[163] M. Radha Kishan, V. Radha Rani, P. Sita Devi, S.J. Kulkarni, K.V. Raghavan, A novel zeolite based stationary phase for in situ synthesis and evaluation of porphyrins and calix (4) pyrroles, Journal of Molecular Catalysis A: Chemical, 269 (2007) 30-34.
[164] M. Moghadam, S. Tangestaninejad, V. Mirkhani, I. Mohammadpoor-Baltork, M. Moosavifar, Host (nanocavity of zeolite-Y or X)-guest (manganese (III) tetrakis[4-N-methylpyridinum]porphyrin) nanocomposite materials as efficient catalysts for biomimetic alkene epoxidation with sodium periodate: Shape-selective epoxidation of linear alkenes, Journal of Molecular Catalysis A: Chemical, 302 (2009) 68-75.
[165] F.C. Skrobot, A.A. Valente, G. Neves, I. Rosa, J. Rocha, J.A.S. Cavaleiro, Monoterpenes oxidation in the presence of Y zeolite-entrapped manganese(III) tetra(4-N-benzylpyridyl)porphyrin, Journal of Molecular Catalysis A: Chemical, 201 (2003) 211-222.
[166] F.C. Skrobot, I.L.V. Rosa, A.P.A. Marques, P.R. Martins, J. Rocha, A.A. Valente, Y. Iamamoto, Asymmetric cationic methyl pyridyl and pentafluorophenyl porphyrin encapsulated in zeolites: A cytochrome P-450 model, Journal of Molecular Catalysis A: Chemical, 237 (2005) 86-92.
[167] K. Ono, M. Yoshizawa, T. Kato, K. Watanabe, M. Fujita, Porphine dimeric assemblies in organic-pillared coordination cages, Angewandte Chemie - International Edition, 46 (2007) 1803-1806.
[168] M.H. Alkordi, Y. Liu, R.W. Larsen, J.F. Eubank, M. Eddaoudi, Zeolite-like metal-organic frameworks as platforms for applications: On metalloporphyrin-based catalysts, Journal of the American Chemical Society, 130 (2008) 12639-12641.
[169] R.W. Larsen, L. Wojtas, Photophysical studies of Ru(II)tris(2,2′ -bipyridine) confined within a Zn(II)-trimesic acid polyhedral metal-organic framework, The Journal of Physical Chemistry A, 116 (2012) 30.
[170] R. Sen, S. Koner, A. Bhattacharjee, J. Kusz, Y. Miyashita, K.I. Okamoto, Entrapment of $[Ru(bpy)_3]^{2+}$ in the anionic metal-organic framework: Novel photoluminescence behavior exhibiting dual emission at room temperature, Dalton Transactions, 40 (2011) 6952-6960.
[171] R.W. Larsen, L. Wojtas, J. Perman, R.L. Musselman, M.J. Zaworotko, C.M. Vetromile, Mimicking heme enzymes in the solid state: metal-organic materials with selectively encapsulated heme, Journal of the American Chemical Society, 133 (2011) 10356-10359.
[172] Z. Zhang, L. Zhang, L. Wojtas, P. Nugent, M. Eddaoudi, M.J. Zaworotko, Templated synthesis, post-synthetic metal exchange, and properties of a porphyrin-encapsulating metal-organic material, Journal of the American Chemical Society, 134 (2011) 924-927.
[173] Z. Zhang, L. Zhang, L. Wojtas, M. Eddaoudi, M.J. Zaworotko, Template-Directed Synthesis of Nets Based upon Octahemioctahedral Cages That Encapsulate Catalytically Active Metalloporphyrins, Journal of the American Chemical Society, 134 (2011) 928-933.

Chapter 2

Building MOF bottles around phosphotungstic acid ships: One–pot synthesis of bifunctional polyoxometalate/MIL–101(Cr) catalysts

This chapter is based on the following publication:

J. Juan–Alcañiz, E. V. Ramos–Fernandez, U. Lafont, J. Gascon, F. Kapteijn, Journal of Catalysis, 269 (2010) 229–241

Abstract A new strategy has been developed for the direct encapsulation of polyoxometalates (POMs) into MIL–101(Cr). The addition of phosphotungstic acid (PTA) to the synthesis mixture of MIL–101 yields the direct encapsulation and good distribution of polyoxometalates (POMs) over the MOF crystals. X–ray diffraction indicates the formation of the right MOF structure despite the POM presence. ICP–OES and TGA proves the presence of PTA in the sample, while vibrational spectroscopy (DRIFT, Raman, UV–Vis) reveals structural changes after washing with NH_4F. The medium–sized cavities of MIL–101 are occupied by POM units bigger than their pentagonal windows when this one–pot approach is followed, and no leaching is observed. These new catalysts show the highest activities reported to date at 313 K for the Knoevenagel condensation of benzaldehyde with ethyl cyanoacetate when using apolar toluene as solvent as well as when using polar DMF and ethanol, with TOFs exceeding 15 turnovers per minute. In addition, they exhibit significant activity in two acid–catalyzed reactions, the esterification of 1–butanol with acetic acid in liquid phase slurry operation and the dimethyl ether production from methanol in a fixed bed gas phase reactor. In contrast, poor or no activity is observed for the catalysts prepared via POM impregnation in MIL–101, where the agglomeration of the POM only in the large cages deteriorates the catalytic performance.

2.1. INTRODUCTION

Heterogeneous catalysis using MOFs is one of the most promising applications. [1] As pointed out by Lee *et al.* [2] catalysis was one of the most underdeveloped areas of the MOF research, where mainly proofs of principle were reported. [3, 4] During the last years, MOF catalysts have grown tremendously, boosting the number of approaches and applications, including screening of different reaction conditions and few examples long–term utilization. [5-8] However, the use of MOFs in catalysis has been largely hampered by their relatively low thermal and chemical stability. In this sense, the MOF community is indebted to Férey's group for discovering thermally and chemically robust structures. [9, 10] The development of MIL structures with MTN topology provides an excellent playground for heterogeneous catalysis that has yet hardly been explored. [11-15]

Indeed, materials like MIL–101 offer tremendous possibilities for catalyst engineering. [9] The presence of coordinatively unsaturated metal sites (CUS) in MIL–101 allows their use as a mild Lewis acid and, more importantly, allows their post–functionalization via grafting of active species. In pioneering work, Hwang and co–workers demonstrated the possibility of post–functionalization of the MIL–101 framework with different amines and applied the obtained basic catalyst in a Knoevenagel condensation and for immobilizing metals. [16] The zeotype cavities of two different sizes, the fully accessible porosity, and therefore outstanding sorption properties, together with a high thermal and chemical stability make MIL–101 an excellent candidate for supporting catalytic species. In this sense mainly two post–synthetic approaches have been followed: the deposition of palladium nanoparticles for the use of MIL–101 in hydrogenation reactions [11] and the impregnation of polyoxometalate anions in the large cavities for their later use as an oxidation catalyst. [7]

Polyoxometalates (POMs) present several advantages as catalysts that make them economically and environmentally attractive. [17] POMs are complex Brønsted acids that consist of heteropolyanions having metal–oxygen octahedra as the basic structural units. The first characterized and the best known of these is the Keggin heteropolyanion, typically represented by the formula $(XM_{12}O_{40})^{x-8}$ where X is the central atom. With a very strong Brønsted acidity, approaching the superacid region, and exhibiting fast reversible multi–electron redox transformations under rather mild conditions, POMs represent a serious alternative to other acid systems. Their acid–base and redox properties can be varied by changing the chemical composition. This unique structure exhibits extremely high proton mobility, while heteropolyanions can stabilize cationic organic intermediates. On top of that POMs have a good thermal stability in the solid state, far better than other strong acids like ion exchange resins. [17]

Supporting POM catalysts is important for future applications since bulk POMs have a low specific surface (1–5 m^2/g). Acidic or neutral substances such as SiO_2, Al_2O_3, and activated carbons have been explored as carriers. [18-22] The acidity and catalytic activity of the supported POMs depend mainly on the type of carrier and on the loading, *e.g.*, the interaction with activated carbons is so strong that the activity of the final catalyst is much lower than that of the POM itself, while low interactions of POM–support lead to dramatic leaching. [23, 24] Encapsulation of POMs inside zeolitic cavities has been achieved by direct synthesis of the Keggin structures inside the zeolite cavities (like FAU). [25] This approach is shown to solve the problem of leaching, since the POM clusters are bigger than the windows of the zeolitic cavities, but only very low loadings can be utilized (<5 wt%) if diffusion limitations are to be avoided. [26] As explained before, polyoxometalates with the Keggin structure have been impregnated into the large cavities of MIL–101. Lacunary $PW_{11}O_{40}^{7-}$ anions (one tungsten less than Keggin ion) were introduced in order to demonstrate the large volume of such cavities. [9] Following a similar approach, Maksimchuk *et al.* impregnated different Ti and Co Keggin anions into the large cavities of MIL–101 and the catalytic performance of the resulting materials was assessed in the oxidation of three representative alkenes using molecular oxygen and aqueous hydrogen peroxide as oxidants. The catalysts could be reused several times without significant activity loss and they showed to be stable under mild operation conditions. [7] In one of the first works on this topic, a series of POMs were encapsulated by means of a one–step hydrothermal reaction of copper nitrate, benzene 1,3,5 tricarboxylate (btc), and different Keggin polyoxometalates. In these compounds, the catalytically active Keggin polyanions were alternately arrayed as non–coordinating guests in the cube–octahedral cages of a Cu–btc MOF host matrix (HKUST–1), showing activities similar to that of the bare acid in the hydrolysis of some esters, although diffusion limitations seem to be a problem in the case of HKUST–1 due to the comparable size of the Keggin anions and the MOF cavities. [27]

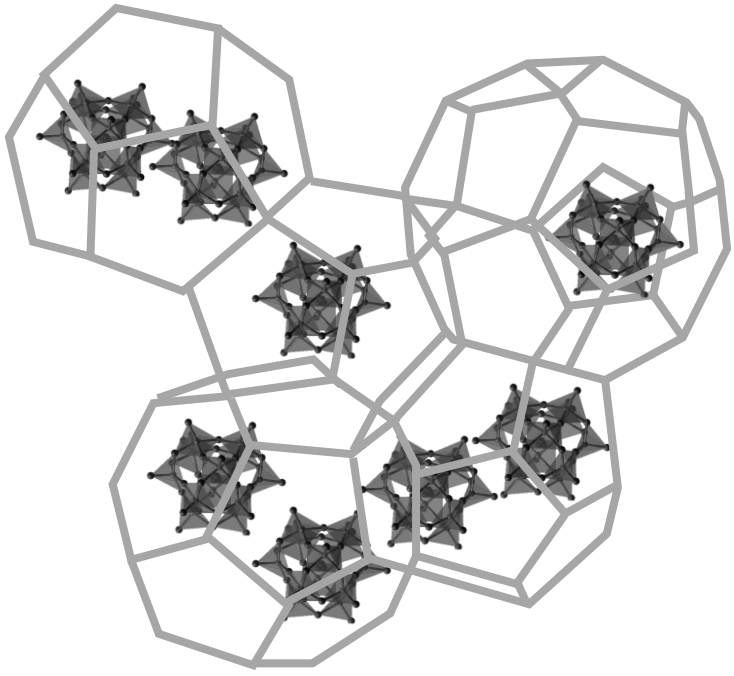

Figure 2 - 1 Phosphotungstic acid (PTA) encapsulated in middle and large cavities of the MIL-101(Cr) structure (*grey lines*).

In the case of MIL–101, the impregnation approach has demonstrated to be successful, but only the large cavities of MIL–101 can be accessed by Keggin–like structures (13–14 Å diameter). Taking into account that the medium–sized cavities represent 2/3 of the total number of cavities in MIL–101 and that the window openings of these cavities are smaller than the diameter of the Keggin structures, it is obvious that the encapsulation of such active species into the medium cavities would offer many advantages, like a better dispersion and utilization of the POMs. Moreover, if contained in the medium cavities, leaching of the polyoxometalates would never be a problem, since they are bigger than the windows of these cavities (Fig. 2–1).

In this work, we present a new, direct synthetic encapsulation of active species into MOFs. [27, 28] We demonstrate that it is possible to incorporate highly dispersed POMs into MIL–101 by following a one–pot synthesis approach. In addition to a complete characterization of the POM encapsulated samples, their catalytic performance is shown for reactions involving proton–abstraction (Knoevenagel), and acid–catalyzed liquid phase esterification (acetic acid with 1–butanol) and gas phase etherification (methanol dehydration).

2.2. EXPERIMENTAL

2.2.1. Catalyst preparation

2.2.1.1. PTA/MIL–101(Cr) encapsulated

MIL–101(Cr)$_{HF}$ Acidic medium: the reaction mixture was prepared from 1.63 g of chromium (III) nitrate ($Cr(NO_3)_3.9H_2O$, 97%), 0.7g of terephthalic acid (C_6H_4–1,4–$(CO_2H)_2$, 97%), 0.15g of hydrofluoric acid (HF, 47–51%) and 20g of distilled water (H_2O). The mixture was placed in a teflon container, and heated at 493 K for 8 h under static or rotational conditions. The solid product was filtered and washed through two procedures: (*a*) using ethanol (95% EtOH with 5% water) at 353K for 24h, and (*b*) with 1M of NH_4F aqueous solution (pH from 1 to 4) at 343K for 24h. Then, the solid was filtered, washed with hot water, and finally dried overnight at 423K under air atmosphere. [9, 29]

MIL–101(Cr)$_{TMAOH}$ Basic medium: the same reactant amounts as for the acidic synthesis were added to a basic water solution prepared from 0.364 g of tetramethylammonium hydroxide solution (TMAOH 25 wt%) and 19.5 ml of water (H_2O). The mixture was placed in a teflon container, and heated at 453 K for 24 h under static or rotational conditions. [30, 31] The green solid product was filtered and only washed thoroughly using ethanol (95% EtOH with 5% water) at 353K for 24h.

POM encapsulation: the same synthesis and cleaning procedure is followed, respectively for acidic and basic media, but different amounts of phosphotungstic acid (50 wt% or 1.5g, 20 wt% or 0.8g and 10 wt% or 0.4g of $H_3PW_{12}O_{40}$, Sigma–Aldrich) were added to the reaction mixture.

2.2.1.2. PTA/MIL–101(Cr) impregnated

POM adsorption was performed after the MOF synthesis and activation (basic or acid conditions as described above), following the procedure described by Férey *et al.* [9] 100 mg (50 and 25 mg) of PTA previously dissolved in 10 mL of distilled water were added to 100 mg of the MIL–101(Cr) sample in an Erlenmeyer flask at room temperature and stirred for 12 h. The resulting solid was then filtrated and washed three times with a large amount of deionized water and dried at room temperature.

2.2.2. Characterization techniques

(a) High–Resolution Transmission Electron Microscopy (HRTEM): was carried out on a Philips CM30T (150–300kV) microscope. In order to study dispersion in the crystals interior, cryo–slicing was applied. A dispersion of MOF crystals in ethanol was frozen with liquid N_2, ensuring minimal disturbance of the structure of the catalysts. The frozen catalyst samples were subsequently sectioned into 0.2 mm slices that present a better stability under the HRTEM beam. Although this technique has been widely applied in life sciences, this example represents, to the best of our knowledge, its first application to MOFs. *(b) Scanning Electron Microscopy (SEM):* was measured in a JEOL JSM 6500F setup coupled to an Energy Dispersive Spectrometer (EDS) for microanalysis. *(c) Nitrogen adsorption at 77 K:* a Quantachrome Autosorb–6B unit gas adsorption analyzer was used to determine the textural properties as BET surface area between 0.05 and 0.15 relative pressure and pore volume at 0.95 relative pressure. *(d) Powder X–*R*ay Diffraction (PXRD):* was measured using a Bruker–AXS D5005 with CuKα radiation. *(e) Thermo–gravimetric Analysis (TGA):* was performed by means of a Mettler Toledo TGA/SDTA851e, under air flow of 60 mL min^{-1} and heating rates of 5 K min^{-1} up to 873 K. *(f) Inductively Coupled Plasma Optical Emission Spectroscopy (ICP–OES):* the samples were digested in duplo in a mixture of 1% HF and 1.25% H_2SO_4 under microwave irradiation, and then analyzed with an ICP–OES Perkin Elmer Optima 3000 dv. *(g) Diffuse Reflectance Infrared Fourier Transform Spectroscopy (DRIFTS):* were recorded in a Bruker model IFS66 spectrometer, equipped with a high–temperature cell with CaF_2 windows and a 633 nm laser. The spectra were registered after accumulation of 256 scans and a resolution of 4 cm^{-1}. A flow of helium of 20 mL min^{-1} was maintained during the measurements. Before collecting the spectra, the samples were pre–treated at 473 K for 60 min under helium. KBr was used as background. *(h) Raman spectroscopy:* was measured using a Renishaw Raman imaging microscope, system 2000. The green (λ = 514 nm) polarized radiation of an argon–ion laser beam of 20 mW was used for excitation. A Leica DMLM optical microscope with a Leica PL floutar L500/5 objective lens was used to focus the beam on the sample. The Ramascope was calibrated using a silicon wafer. Spectra were collected in the range 100–2000 cm^{-1}. *(i) UV–Vis Diffuse Reflectance Spectroscopy:* were measured with a Perkin–Elmer Lambda 900 spectrophotometer

equipped with an integrating sphere (‘‘Labsphere”) in the 200–800 nm range. The Kubelka–Munk function was used to convert reflectance measurements into equivalent absorption spectra using the reflectance of $BaSO_4$ as a reference, and to obtain absorption edge energies directly from the curves. *(j)* *^{31}P Magic Angle Spinning Nuclear Magnetic Resonance Spectroscopy (MAS NMR):* was measured on a Bruker Avance–400 spectrometer at 161.98 MHz, using a solid–state probe and zirconium sample holders with inner diameter of 3 mm, spinning at the magic angle with a rate of 11 kHz. The spectral width is 617.76 ppm, acquisition time of 12.5 ms and acquisition delay of 10 s. Chemical shifts are reported in ppm referring to an external standard: 85% of H_3PO_4 (0 ppm).

2.2.3. Catalytic Testing

2.2.3.1. Knoevenagel condensation reaction

In a typical batch experiment, 0.5 g of catalyst was added under stirring (external shaking agitation to avoid attrition) to a solution of 7 mmol ethyl cyanoacetate (ECA) in 5 mL of toluene as a solvent in an Erlenmeyer flask at 313 K. After temperature adjustment, benzaldehyde (8 mmol) was added.

Table 2 - 1 Reactants used and products formed during the mechanism study of Knoevenagel condensation reaction.

Reactant	Reactant	Product
Benzaldehyde purified by redistillation >99.5%	Malononitrile >99.0%	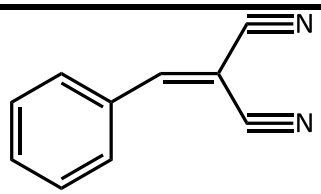
	Ethyl acetoacetate >99.0%	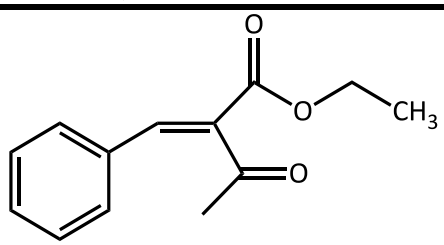
	Ethyl cyanoacetate >99.5%	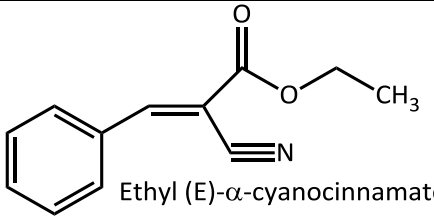 Ethyl (E)-α-cyanocinnamate
p-methoxy Benzaldehyde >98.0%		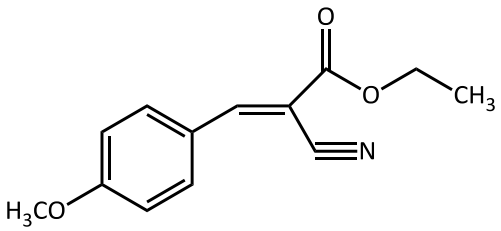

In the mechanistic study (Table 2–1) *p*–methoxybenzaldehyde was used instead of benzaldehyde, while ethyl cyanoacetate was replaced by malononitrile (two CN) and ethyl acetoacetate (none CN).
After recovering the catalyst by filtration, it was stored at 423 K and reused. 1,5,7–Triazabicyclo[4.4.0]dec–5–ene (Sigma–Aldrich) was used as a homogeneous organocatalyst under the same conditions in order to benchmark the activity of the synthesized MOF catalyst with a well–known strong base (30 mg, 0.2 mmol of catalyst). The samples of the reaction mixture were periodically analyzed by gas chromatography using a Chrompack GC CP–Sil 8CB Cat. No. 7453 equipped with an FID detector and a 50 m RTX®–1 (1% diphenyl–, 99% dimethylpolysiloxane) fused silica capillary column. *TOF*s and *TON*s were based on the total number of Keggin units (PW_{12}) present in each catalyst (as obtained from elemental analysis), and *TOF*s were calculated from the total reaction data in the batch experiments.

2.2.3.2. Esterification of acetic acid and 1–butanol

The esterification of acetic acid (HAc) and1–butanol (BUT) was performed without solvent using a molar ratio acetic acid: 1–butanol = 1:1. The mixture was introduced in a balloon flask, while being stirred under reflux at 383 K. A ratio of 3 g of catalyst per mol of acetic acid was used.

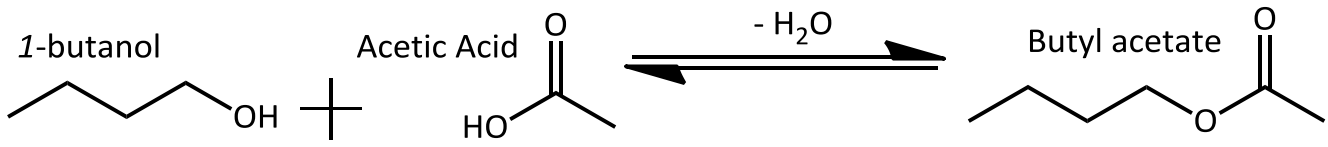

Scheme 2 - 1 Esterification reaction between 1–butanol and acetic acid.

Nafion® NR50 was used to benchmark the acidity of the resulting catalysts. After recovering the catalyst, it was filtered, stored at 423 K, and reused. The samples of the reaction mixture were periodically analyzed by gas chromatography using a Chrompack GC CP–Sil 8CB Cat. No. 7453 equipped with an FID detector and a 50 m RTX®–1 (1% diphenyl–, 99% dimethylpolysiloxane) fused silica capillary column, using decane (anhydrous, > 99%) as internal standard.

2.2.3.3. Dehydration of methanol to dimethyl ether (DME)

Experiments were performed in a 1/4 in. stainless steel reactor with a length of 2 cm. Pressed catalyst (0.1 g) with a mesh size around 0.75–1 mm was loaded in the reactor. Quartz wool was placed on the top of the bed for better catalyst packing. An ISCO liquid pump was used to feed the liquid methanol to the reactor together with N_2 (5.6 or 9.16 ml min^{-1}) by a mass flow controller. Methanol was fed to the reactor at a flow rate of 0.25, 0.5, and 1 ml h^{-1} resulting in WHSV range of 2–8 h^{-1}. The temperature of the reactor was varied between 523 and 643 K. The pressure drop over the reactor was

around 0.25 bar. The product mixture was analyzed online with an Interscience Compact GC over a 50 m RTX®–1 (1% diphenyl–, 99% dimethylpolysiloxane) column at 300 K.

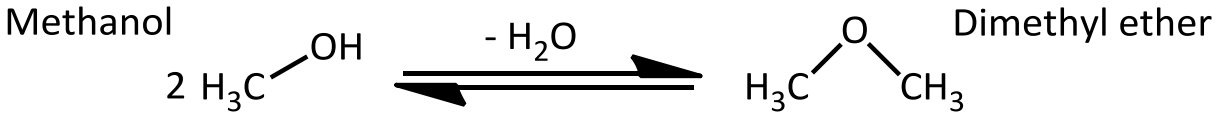

Scheme 2 - 2 Dehydration of methanol to dimethyl ether.

2.3. RESULTS

2.3.1. Catalysts characterization

2.3.1.1. Electron Microscopy and Energy Dispersive Spectroscopy

Figure 2–2 shows the comparison between HRTEM micrographs corresponding to two samples synthesized under acidic (HF) conditions in static and rotating ovens, respectively, together with EDS analysis at different areas of the crystals.

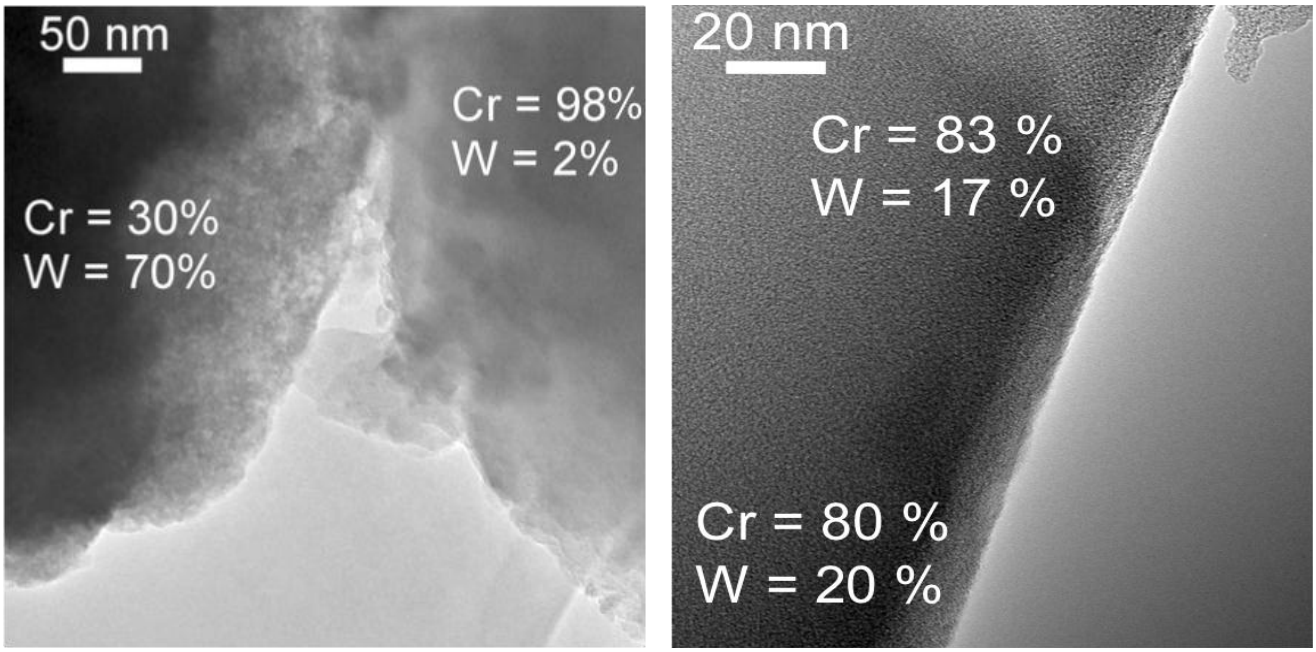

Figure 2 - 2 High–Resolution Transmission Electron Microscopy (HRTEM) images and Energy Dispersive Spectroscopy (EDS) mapping (wt% elemental analysis of W from the PW_{12} and Cr from the MOF framework) of the 50 wt% encapsulated POM sample. (*Left*) Static and (*Right*) rotational synthesis.

The dispersion of the tungsten in the samples prepared under static conditions is very inhomogeneous; the concentration of tungsten in some particles is really high, while other crystals do not contain any. In contrast, when applying rotating conditions, a homogeneous distribution of tungsten over the particles can be observed, in agreement with ICP results that indicate the percentage of PTA in the total sample. Consequently, rotating synthesis was applied as standard synthesis condition in all following results, assuming a decrease in concentration gradients.

In Figure 2–3 a comparison between two cryo–sliced samples of encapsulated POM system in acidic media and pristine MIL–101 is made. An excellent dispersion of the complex within the cavities of MIL–101 is reached through encapsulation, with most of the POM present in the interior of the crystals, as shown by the difference in contrast between the edge and the core of the particles.

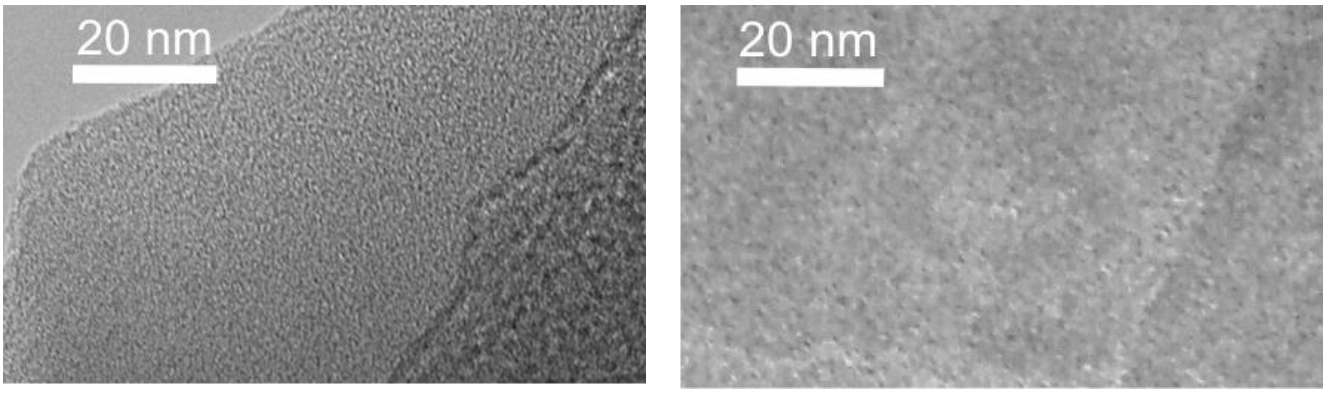

Figure 2 - 3 HRTEM micrographs of cryo–sliced samples: (*Left*) 20 wt% PTA/MIL–101(Cr) and (*Right*) MIL–101(Cr).

Figure 2–4 shows the EDS mapping of different elements in 20 wt% PTA/MIL–101(Cr)$_{HF}$. The good distribution of all analyzed elements is in agreement with the TEM results.

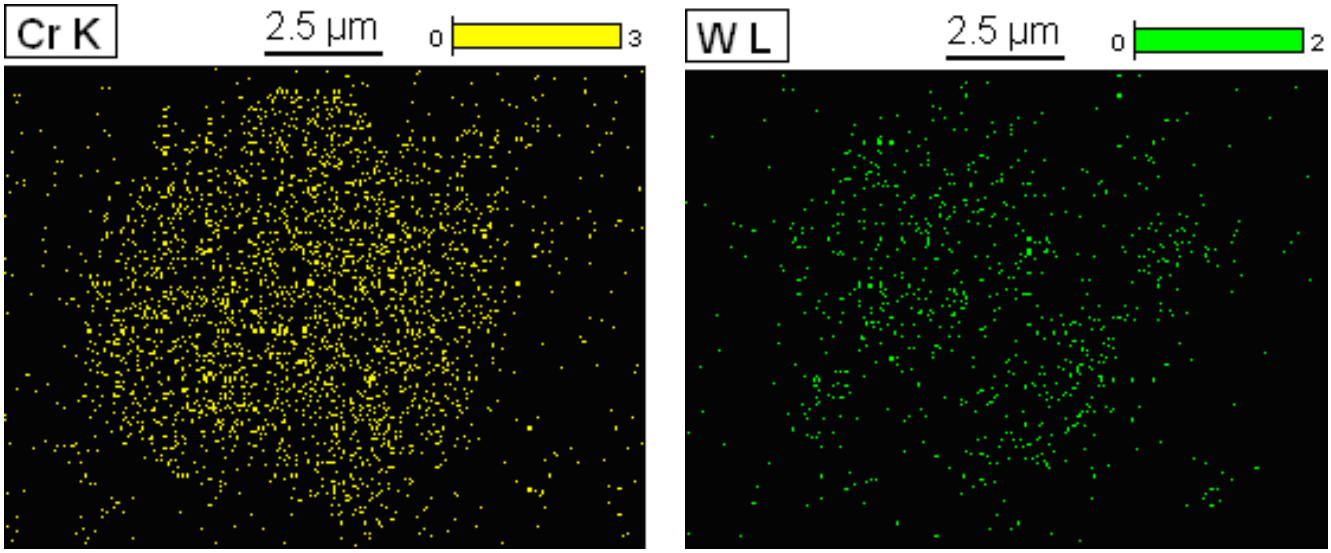

Figure 2 - 4 EDS analysis of Chromium from MIL–101(Cr) and W from 20 wt% encapsulated PTA.

2.3.1.2. Textural Properties: nitrogen adsorption isotherms

Table 2–2 shows BET surface area and total pore volume values of different MOF samples synthesized under acidic condition, on a mass basis and re–calculated per gram of MIL–101.

Surface area of pristine MIL–101(Cr) is smaller than reported values, [9] which may be explained by the pressure region used for the BET calculation. In this study, BET surface area values have been calculated between 0.05 and 0.15 relative pressure, excluding the corresponding filling of the MIL–

101 cavities characteristic for two steps in the isotherm at 0.15 and 0.20 relative pressure. The stepwise filling of such cavities should not be included in the monolayer calculation of the BET area.

Table 2 - 2 BET surface area (between 0.05 and 0.15 relative pressure)and pore volume (between 0.95-0.96 relative pressure) are calculated per gram of sample and per gram of MIL–101(Cr).
[a] Composition of the samples are obtained according to ICP-OES results, considering 12 W atoms per Keggin unit and 3 Cr atoms per MIL-101(Cr).

		PTA [wt%][a]	MIL–101(Cr) [wt%][a]	S_{BET} [m^2/g_{solid}] (m^2/g_{MOF})	V_p [cm^3/g_{solid}] (cm^3/g_{MOF})
MIL–101(Cr)$_{HF}$		0	100	2800	1.5
PTA/MOF	Encapsulation	9.7	90.3	2340 (*2600*)	1.1 (*1.2*)
		17.6	82.4	3047 (*3809*)	1.6 (*2.0*)
		48.2	51.8	2445 (*4890*)	1.3 (*2.6*)
	Impregnation	50.3	49.7	1460 (*2920*)	0.7 (*1.4*)

The encapsulated samples display BET values per total amount of sample similar to the bare MIL–101(Cr) used as a reference, with any observable trend. Interestingly when comparing BET values per gram of MOF, the encapsulated samples show a much higher specific surface area, increasing with PTA loading, indicative of a better crystallization when using PTA and decreasing the pH. Impregnated sample with 50 wt% PTA loading, used for comparison, exhibits larger decrease per total mass basis; however, similar BET values are observed per gram of MOF.

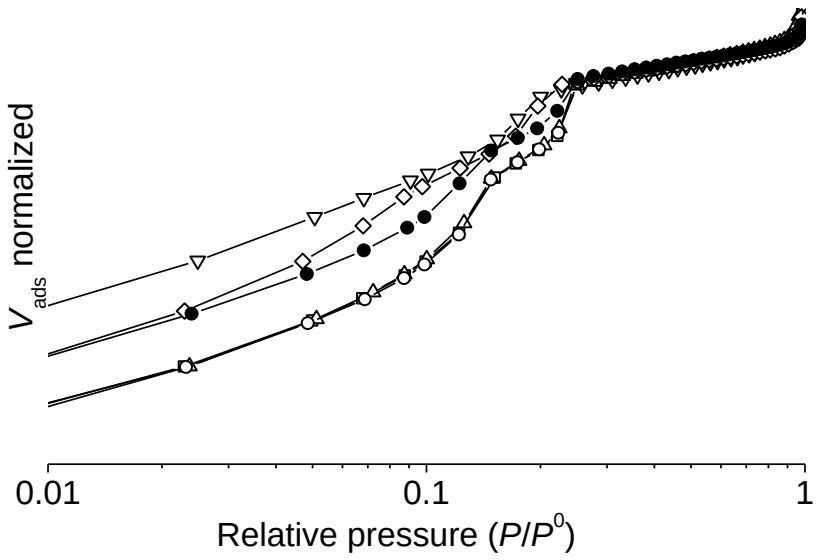

Figure 2 - 5 N_2 adsorption isotherms of different samples normalized at uptake at 0.4 relative pressure. Key: (□) MIL–101(Cr); (●,○,△) MIL–101(Cr) with 10, 20 and 50 wt% encapsulated POM, respectively; (▽,◇) MIL–101(Cr) with 30 and 50 wt% impregnated POM, respectively.

Comparison of the normalized isotherms at the maximum uptake (around 0.4 relative pressure) of the different samples is shown in Figure 2–5. The corresponding isotherms of the two encapsulated samples with the highest loadings (20 and 50 wt% PTA) overlap with that of the bare material, while a slight deviation is observed in the case of 10 wt% encapsulated samples. Despite the fact that the position of the characteristic MIL–101 steps is the same for all the encapsulated samples, in the case of impregnated system, both steps seem to be shifted to lower pressures, while the first step is more attenuated.

2.3.1.3. Powder X–Ray Diffraction

The PXRD patterns of the different samples synthesized with HF are illustrated in Figure 2–6, showing hardly any difference between the bare sample of MIL–101(Cr) and the samples with the PTA encapsulated. The MOF crystal structure seems to remain unchanged through POM encapsulation, while no signs of POM crystalline planes are observed, as previously reported for POM/HKUST–1 composite. [27]

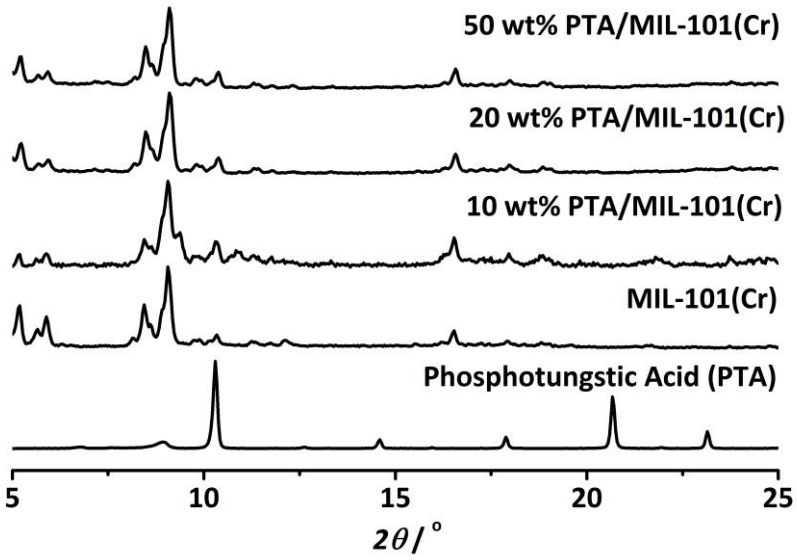

Figure 2 - 6 CuKα powder X–ray diffraction pattern normalized of different samples.

2.3.1.4. Thermo–gravimetric Analysis

The thermo–gravimetric analysis of samples containing different loadings of PTA encapsulated and pristine MIL–101(Cr) are shown in Figure 2–7. TG profiles display water desorption at around 373 K, in a similar weight percentage for every sample. On the other hand, residual masses are very different and directly dependent on the amount of PTA encapsulated, since it rises with increasing loading. The PTA percentage loading for each sample has been used to calculate a theoretical amount of W_2O_3 generated as residual mass. Considering 25 wt% Cr_2O_3 generated from the pristine MOF and

recalculating this amount for 90, 80 and 50 wt% MOF, the final residual mass is 30, 35 and 52 wt%, respectively as increasing PTA loading. The calculated values are very close to the residual mass observed experimentally as 32, 38 and 52 wt%, respectively for each increasing PTA loading sample.

The temperature of framework collapse is higher than 600 K for every sample. The thermal stability does not seem to be strongly influence by the PTA encapsulated presence. In addition, a trend seems to be followed, since decomposition temperature is lower when increasing PTA loading, suggest oxidation promotion by the encapsulated species. Encapsulated PTA under basic conditions and impregnated samples display very similar results to the ones reported for encapsulated acidic systems, residual mass follows the same increasing trend with loading, thermal stability remains constant, and loading calculations obtained from TGA are in agreement with the results observed in ICP–OES.

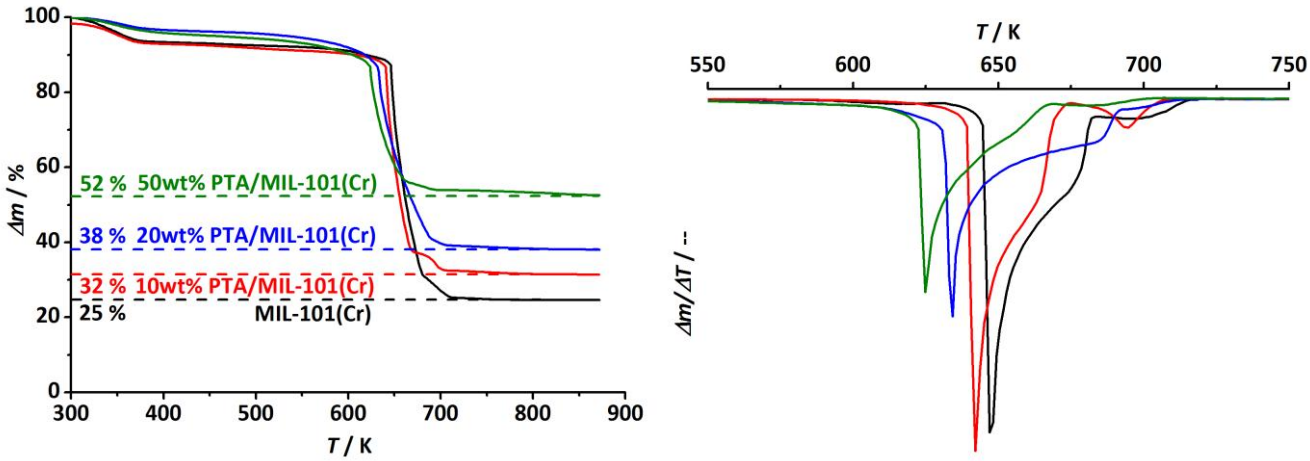

Figure 2 - 7 (*Left*) TG and (*Right*) DTG profiles in air (5 K/min) of 10, 20 and 50 wt% PTA loading encapsulated in the samples compared with the pristine MIL–101(Cr).

2.3.1.5. UV–Visible Spectroscopy

Figure 2–8 compares the UV–Vis spectra in Kubelka–Munk function intensity of the different PTA containing samples with the pristine MIL–101 and the bulk PTA. Impregnated PTA sample and PTA encapsulated both acidic and basic syntheses washing only with ethanol, do not present significant differences from the pristine MOF (Fig. 2–8A). Especially when comparing with experimentally measured PTA, where two main absorptions are observed: the first centered at 255 nm, attributed to the oxygen–tungsten charge–transfer absorption band for Keggin anions; [32-34] and the second at 360 with a shoulder at 345 nm with maximum intensity.

In the case of the encapsulated samples (Fig. 2–8B), two new bands arise strongly when increasing PTA loading. The samples with 20 and 50 wt% PTA encapsulated display two specific absorption bands between 350–400 nm, which are only observed after washing the sample with NH_4F, remaining

unchanged in the rest of the spectra. At low PTA loading (10 wt%), the sample does not present new features, although the MIL–101 bands around 450 and 625 nm are strongly decreased.

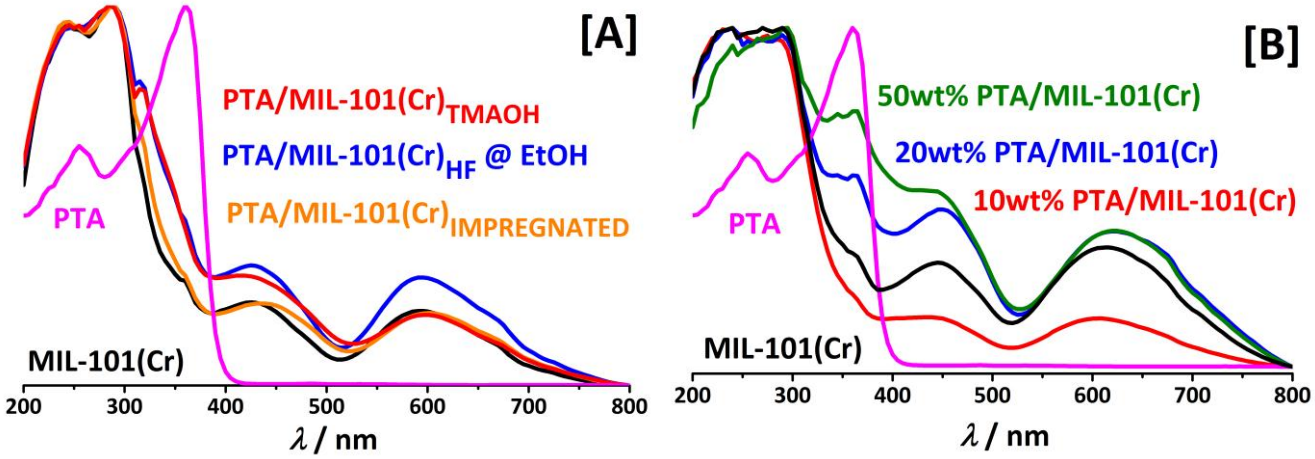

Figure 2 - 8 UV–Vis spectra of PTA/MIL–101(Cr) samples. (*A*) Impregnated samples compared with encapsulated samples only washed with EtOH. (*B*) Encapsulated samples with 10, 20 and 50wt% PTA loading washed with EtOH and NH_4F.

2.3.1.6. Diffuse Reflectance Infrared Fourier Transform Spectroscopy

Figure 2–9 shows several DRIFT spectra focused on unraveling the PTA nature. Differences can be mainly found at low wavenumber regions (1200–900 cm^{-1}), when POM encapsulated samples are compared with impregnated systems and the pristine MOF. The typical IR vibration bands of PTA are observed at 1080 (P–O in the central tetrahedron), 982 (terminal W=O), 895 and 810 cm^{-1} (W–O–W) asymmetric vibrations associated with Keggin ions, indicative of the preserved primary polyoxometalate structure. [23, 25, 35, 36]

Impregnated samples of MIL–101(Cr) contain 10, 20 and 50 wt% PTA loading, and the DRIFT spectra are compared with the pristine MOF in Figure 2–9A. The main PTA vibrations at 1080 and 980 cm^{-1} are clearly visible and increasing with PTA loading, as well as a shoulder at 965 shifted to 975 cm^{-1} for higher loadings. On the other hand, characteristic bands of the MOF at 1163 and 1020 cm^{-1} assigned to the Cr–O vibration are slightly altered by the inclusion of POMs, confirming that both MOF and PTA nature remain after impregnation.

Figure 2–9B shows the comparison of PTA encapsulated samples with different loading after washing with EtOH and NH_4F. In this case, main PTA vibrations are very weak and seem to be shifted in different directions. The band at 982 cm^{-1} corresponds to the W=O stretching and is known to shift with changing the counter–cation, while the sharpness and exact position are also related to the content of water bonded to the POM. [37]

Basic synthesis conditions where used to synthesize 50 wt% encapsulated POM in MIL–101(Cr)$_{TMAOH}$, and compared in Figure 2–9C with 10 wt% PTA impregnated in MIL–101(Cr)$_{TMAOH}$, while only ethanol washing was used as cleaning procedure. However, the presence of the main PTA vibrations after encapsulation under basic conditions and EtOH washing suggests the successful entrapment of guest species, remaining nature.

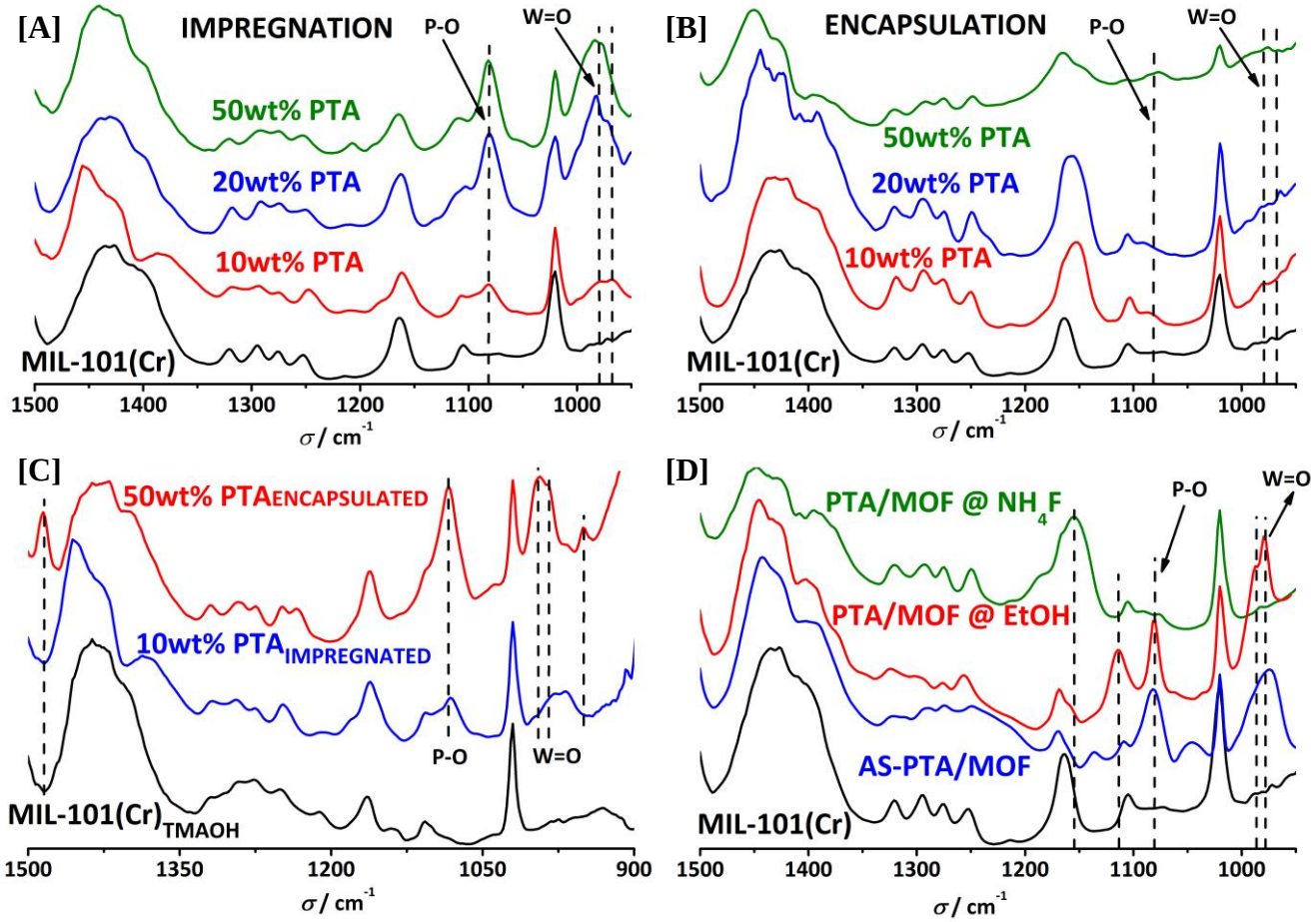

Figure 2 - 9 DRIFT spectroscopy of PTA/MIL–101(Cr) samples. [A] Impregnated [B] encapsulated 10, 20 and 50 wt% PTA in MIL–101(Cr). [C] 50 wt% encapsulated and 10 wt% impregnated PTA in MIL–101(Cr), synthesized by TMAOH route. [D] 20 wt% PTA encapsulated after washing steps.

Figure 2–9D shows DRIFT spectra of 20 wt% PTA encapsulated in MIL–101(Cr)$_{HF}$ after every step of the acid synthesis procedure: as synthesized, after boiling ethanol washing and after refluxed overnight with NH_4F (1M solution in water). As–synthesized sample displays very similar spectra as the impregnated systems, where the main PTA vibrations can be observed, while more distinct change occurs at 1163 cm^{-1} of Cr–O vibration splitting into less intense bands. When washing with boiling ethanol overnight the same PTA vibrations and splitting of the Cr–O band are observed, but a new band arises at 1110 cm^{-1}. However, after refluxing with NH_4F 1M solution overnight, most of the PTA vibrations are shifted or disappeared, while complete deformation of Cr–O band is detected, since the maximum is observed now at 1155 cm^{-1}.

2.3.1.7. Raman Spectroscopy

Figure 2–10 shows the spectra collected for the different MOF structures and the bulk POM. Crystalline PTA shows characteristic bands at 1007 cm^{-1} (stretching vibration of P–O), 986 cm^{-1} (stretching of W=O), 900 cm^{-1} (bending of W–O_c–W), and 550 cm^{-1} (bending of O–P–O). [38] However, encapsulated PTA only displays small differences from the pristine MOF with small visible bands at 1007 and 986 cm^{-1}, which seem to increase with PTA loading. Nevertheless, as observed for DRIFTS no more bands of PTA are visible in the spectra when washing PTA encapsulated samples with NH_4F. Impregnated samples display very similar results with very small indication of PTA presence from Raman spectra.

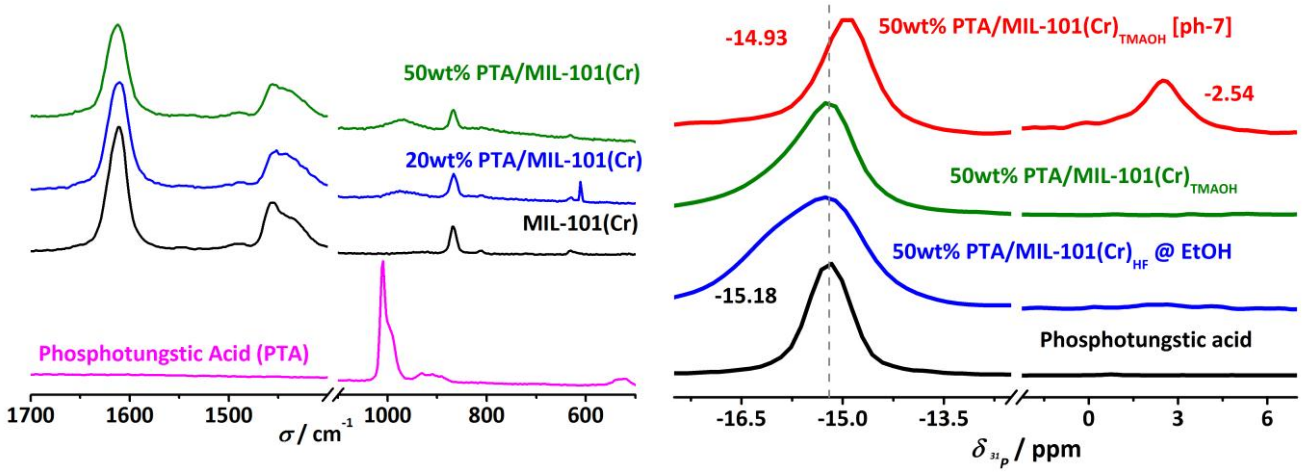

Figure 2 - 10 (*Left*) Raman spectra of 20 and 50 wt% PTA loaded MIL–101(Cr) samples compared with pure PTA and the pristine MOF pretreated overnight in an oven under 433 K.(*Right*) ^{31}P MAS–NMR spectra of different PTA containing samples.

2.3.1.8. ^{31}P Magic Angle Spinning Nuclear Magnetic Resonance Spectroscopy

The POM nature has also been studied by observing the nature of the central atom, which in this particular case is Phosphorus. Figure 2–10 shows the ^{31}P MAS–NMR spectra of different POM encapsulated comparing with the self–standing phosphotungstic acid.

Samples with 50 wt% POM loading encapsulated under basic and acidic conditions are very similar, resulting in one single peak comparable with the one observed for simple phosphotungstic acid. However, slight broadening and shifting can be depicted and assigned as an interaction between the encapsulated PTA and the MOF framework. When a higher amount of TMAOH is added reaching pH 7 at the synthesis mixture, a bigger shift is observed in the resulting solid as well as a secondary peak arises around –2.54 ppm. This result suggests the formation of a secondary POM nature, due to the presence of the strongly basic medium. A second NMR spectrum was measured at the sample synthesized under acidic conditions after washing it with NH_4F, but no signal was observed.

2.3.2. *Catalytic performance*

2.3.2.1. *Knoevenagel condensation of benzaldehyde and ethyl cyanoacetate*

2.3.2.1.1. *Catalytic performance and solvent effects*

The Knoevenagel condensation reaction between benzaldehyde and ethyl cyanoacetate in toluene was selected to test the different MOF catalysts. Although little has been published on the use of POMs in this C–C bond formation reaction, Yoshida *et al.* utilized Knoevenagel condensation to benchmark the basic character of several POMs after dimerization in organic solvents forming 'closed' dimers in a resulting non–protonated form. [39]

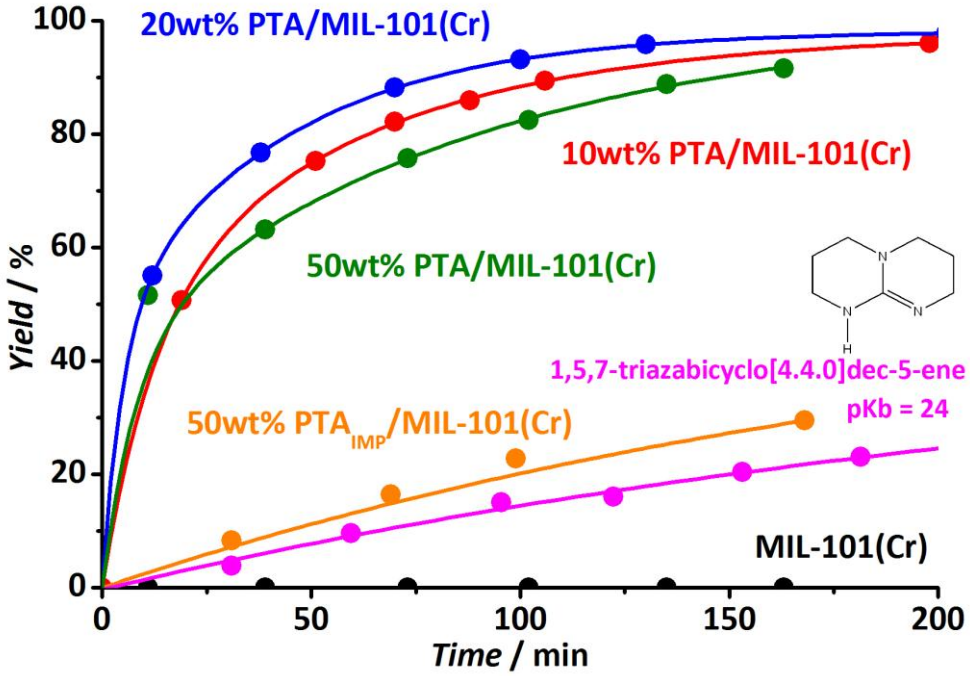

Figure 2 - 11 Knoevenagel condensation reaction of 8 mmol benzaldehyde and 7 mmol ethyl cyanoacetate over different MOF catalysts (0.5 g) in 5 mL of toluene as a solvent at 313 K.

Figure 2–11 displays the evolution with time of the yield of ethyl (E) –α–cyanocinnamate based on the ethyl cyanoacetate conversion (100% selectivity was achieved in every case) achieved for different catalysts at 313 K using toluene as a solvent. However, it should be considered that a fixed amount of catalyst was used in every case, implying different amounts of theoretically available active sites, *ca.* 12/1000, 5/1000 or 2.5/1000 molar ratios of encapsulated POM (50 wt%, 20 wt% and 10 wt% POM loading respectively) with respect to the amount of ethyl cyanoacetate used as a reactant.

1,5,7–Triazabicyclo[4.4.0]dec–5–ene was used as a homogeneous catalyst under the same conditions in order to benchmark the activity of the synthesized catalyst with a well–known strong base. [40] Bulk POM was also tested, although no conversion could be achieved, since it is insoluble in toluene. The bare MIL–101(Cr) sample gave hardly any conversion either. The encapsulated samples are clearly

much more active catalysts (conversion values over 90%) than those obtained by POM impregnation (reaching 20% conversion after 100 minutes of reaction), and the homogeneous base (20% conversion after 150 minutes of reaction).

A further insight into the catalytic process yields comparison of the turnover frequencies of the different catalysts at 313 K based on the theoretical number of active sites, mol POM or mol guanidine used (Table 2–3). TOFs of 775 mol ECA/mol POM h^{-1} are obtained for the 10 wt% encapsulated sample, almost two times higher than the values found for the 20% (410 h^{-1}) and far better than data obtained for the 50% loaded catalysts (130 h^{-1}), presenting much better activities than those obtained for the impregnated samples (12 h^{-1}) and the bi–cyclo guanidine base (4 h^{-1}).

Table 2 - 3 *TON* and *TOF* values obtained for the different catalysts in the Knoevenagel condensation of 8 mmol benzaldehyde and 7 mmol ethyl cyanoacetate over different MOF catalysts (mass: 0.5 g) in 5 mL of solvent at 313 K.

	$mmol_{active\ site}.g_{solid}^{-1}$	Solvent	$TON_{t\ =\ 165\ min}$	*TOF* (h^{-1})
10wt% PTA/MIL–101(Cr)$_{ENCAPSULATED}$	3.4	DMF	390	920
		EtOH	375	590
		Toluene	380	775
20wt% PTA/MIL–101(Cr) $_{ENCAPSULATED}$	6.1	Toluene	195	410
50wt% PTA/MIL–101(Cr) $_{ENCAPSULATED}$	16.7	Toluene	75	130
50wt% PTA/MIL–101(Cr) $_{IMPREGNATED}$	17.5	Toluene	23	12
1,5,7-Triazabicyclo[4.4.0]dec-5-ene	7.2	Toluene	7	4

On the other hand, the character of the solvent used in Knoevenagel condensations may have a strong effect on the reaction rate, and therefore has been further studied. [41] The polarity of the solvent affects the transition state and the capacity of the catalyst for proton transfer: when polar reagents are involved, the transition–state complex is better solvated by the polar solvent molecules and the partition of the reactants at the solid–liquid interface is higher, decreasing the activation–free enthalpy and enhancing the reaction rate. Moreover, protic solvents such as ethanol act as nucleophiles that attack the positive charge of the carbonyl carbon of polar benzaldehyde, yielding a higher catalytic activity. [8, 41-43] To avoid solvent promotion, toluene (nearly apolar and non–protic) was chosen as standard for most of the catalytic tests, although also some experiments were performed using DMF (polar) and ethanol (protic and polar).

Figure 2–12 shows the performance of the 10 wt% encapsulated sample at 313 K when using different solvents: toluene, ethanol, and DMF under similar experimental conditions. In contrast to the common

trend for this reaction, the activity of the catalyst is similar in DMF (non–protic, polar) and toluene (non–protic, nearly apolar), but is lower in ethanol (protic, polar). Indeed, while TOFs up to 920 h^{-1} are found in DMF and toluene, values under 590 h^{-1} are found when using ethanol. Nevertheless, solvent effects do not seem to play an important role in the performance of the catalyst, since similar turn–over numbers are observed in the three cases.

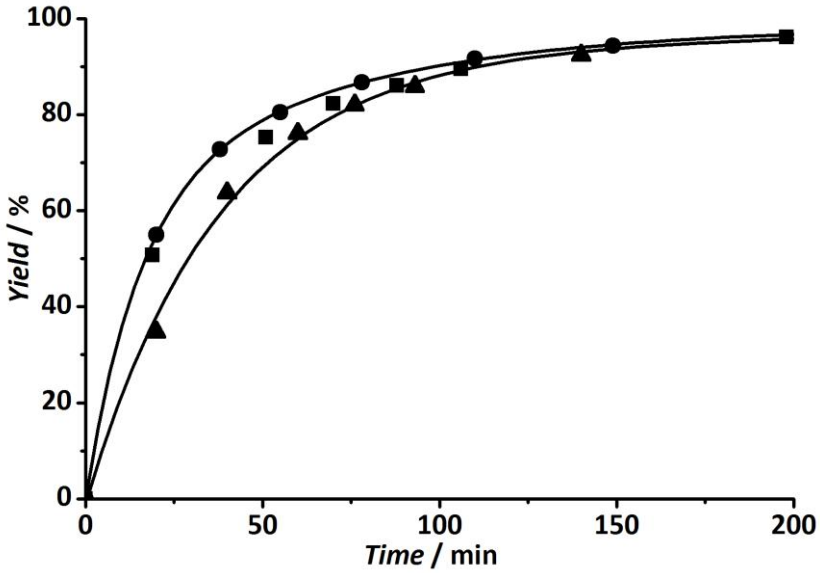

Figure 2 - 12 Effect of solvent on the performance of 0.5 g catalyst (10 wt% PTA/MIL–101(Cr)$_{ENCAPSULATED}$) in the Knoevenagel condensation of 8 mmol benzaldehyde and 7 mmol ethyl cyanoacetate, in 5 mL of solvent at 313 K. (■) Toluene. (▲) EtOH. (●) DMF.

2.3.2.1.2. Re–usability and hot filtration experiments

Apart from presenting a good catalytic activity, long–term stability and the absence of leaching are of primary importance for solid catalysts. MOF samples were reused several times in order to determine if the catalysts suffer from permanent deactivation. The standard procedure, described in the experimental section, was followed to perform the first run. After 3 h of reaction the solid was filtered off and dried in an oven at 423 K overnight. Then the catalyst was tested in consecutive runs using the same catalyst to reactants molar ratios. The possible leaching of the active phase was also studied by hot filtration experiments, where the catalyst is filtered off during the reaction and possible catalytic activity in the solution mixture is followed under the same reaction conditions.

Figure 2–13 shows the catalytic activity of consecutive runs for different MOF catalyst, as well as the hot filtration experiment. The sample with 20 wt% of POM encapsulated (Fig. 2–13A&B) exhibited the same catalytic activity in both runs, indicating no deactivation neither in non–polar nor in polar solvents. After hot filtration of the catalyst (time of filtration indicated by an arrow) no further reaction is observed in the reaction mixture, showing the truly heterogeneous behavior of the solids. Similar results were observed for the 50 wt% encapsulated sample (Fig. 2–13C) and for the 50 wt% impregnated catalyst (Fig. 2–13D) performance in toluene, for at least two cycles. The hot filtration experiment for the latter type also confirms the absence of leaching, as indicated before in oxidation reactions. [7, 9] Analysis of the liquid did not indicate any metal presence. Long–term use of these

catalysts should indicate a strong difference in deactivation, due to leaching of the PTA molecules from the large cages of the MIL–101(Cr) more evidence in impregnation than encapsulation systems (not studied in this thesis). The reaction conditions used at Knoevenagel condensation, are not enough to observe leaching from any of the systems, but dispersion has proven to be crucial parameter in the catalytic performance. The use of protic solvents, higher temperatures and longer reaction times, might force the leaching of the guest PTA molecules, and evidence differences between both systems.

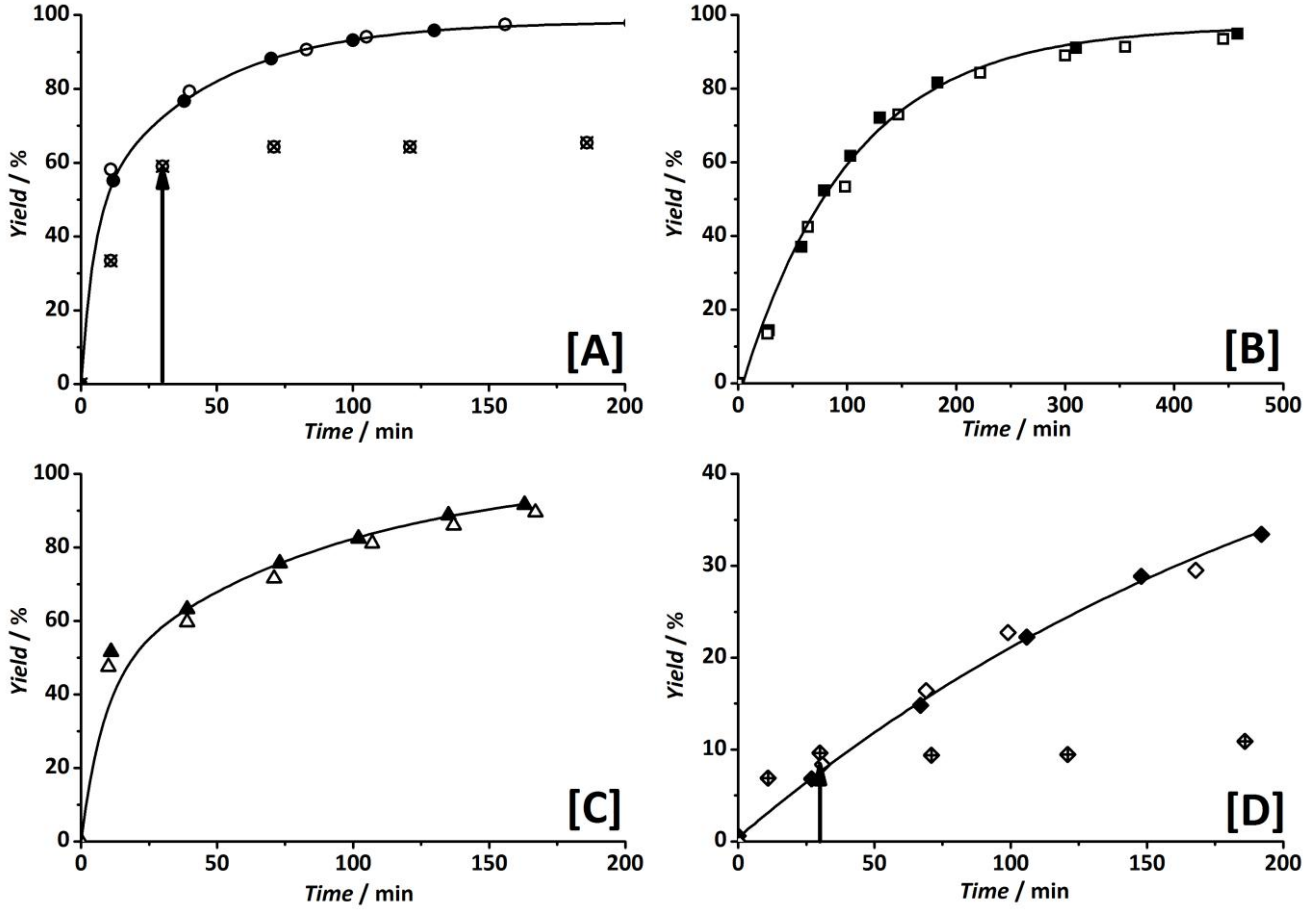

Figure 2 - 13 Knoevenagel condensation of 8 mmol benzaldehyde and 7 mmol ethyl cyanoacetate in 5 mL of solvent at 313 K over different MOF catalysts. [A] 20 wt% PTA/MIL–101(Cr)$_{ENCAPSULATED}$ in toluene. [B] 20 wt% PTA/MIL–101(Cr)$_{ENCAPSULATED}$ in ethanol. [C] 50 wt% PTA/MIL–101(Cr)$_{ENCAPSULATED}$ in toluene. [D] 50 wt% PTA/MIL–101(Cr)$_{IMPREGNATED}$ in toluene. (*Solid symbol*) 1st Run. (*Open symbol*) 2nd Run. (*Crossed symbol*) Hot filtration experiment, where arrow indicates moment of filtration.

2.3.2.1.3. Unraveling the reaction mechanism

The Knoevenagel condensation may proceed according to two different mechanisms that depend on the nature of the catalyst. For strong bases, certain transition metal complexes (*e.g.*, of ruthenium) and strong Lewis acids, direct activation of the methylene group on the catalyst surface may take place. When weaker bases, such as amino groups are involved in the catalytic process, the reaction proceeds through the formation of an imine intermediate: benzaldehyde reacts with an amino group to form a

benzaldimine with a higher basicity than one of the free amine. Afterwards, the deprotonation of the methylene group takes place followed by the condensation, regenerating the active site. [8, 44]

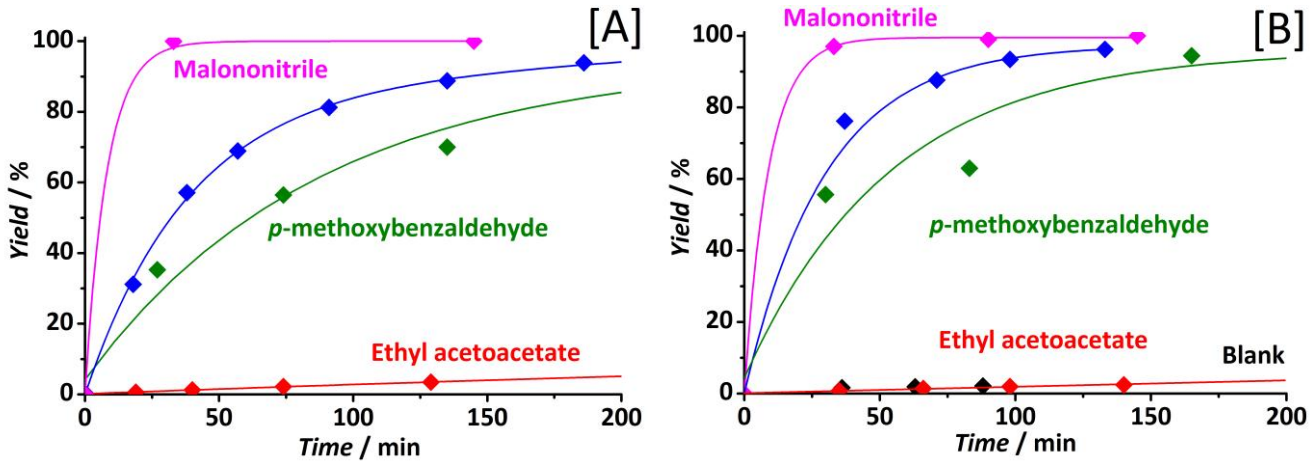

Figure 2 - 14 Knoevenagel condensation reaction of 7 mmol ethyl cyanoacetate and 8 mmol benzaldehyde (*blue*) in 5 ml toluene at 313 K, using 0.5 g of 50 wt% PTA/MIL–101(Cr)$_{ENCAPSULATED}$ catalyst and changing reactants: benzaldehyde by *p*–methoxybenzaldehyde (*green*), and ethyl cyanoacetate by ethyl acetoacetate (*red*) and malononitrile (*pink*). [A] HF sample. [B] TMAOH sample.

Different reactants were used in the testing of catalyst in order to elucidate the reaction mechanism (Figure 2–14). Benzaldehyde was replaced by *p*–methoxybenzaldehyde, and ethyl cyanoacetate was changed by malononitrile (with two cyano groups) and ethyl acetoacetate (no cyano groups).

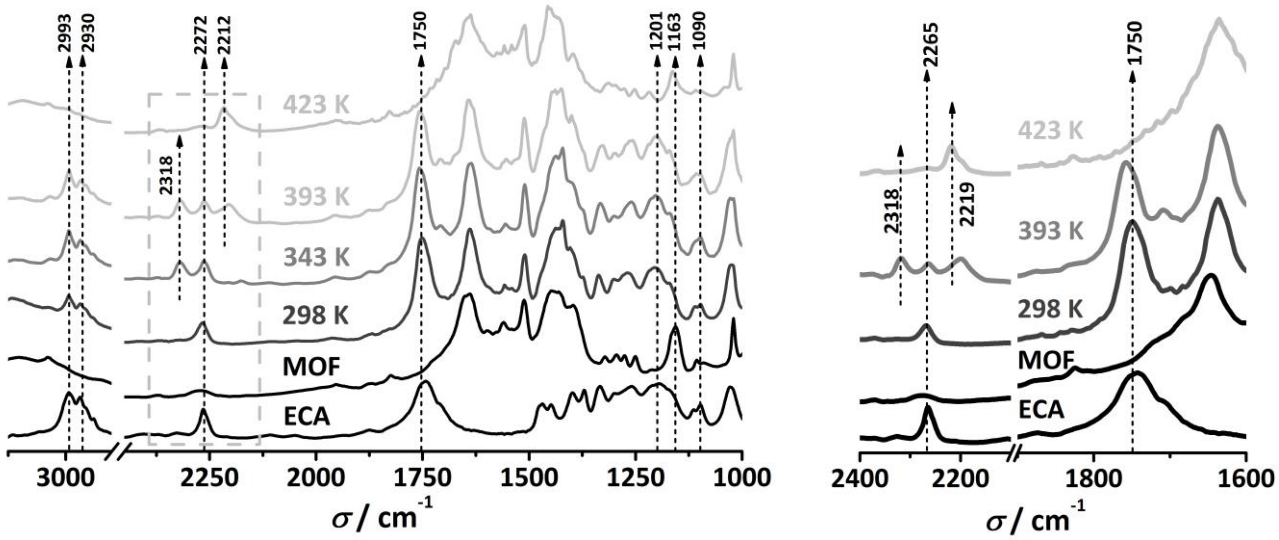

Figure 2 - 15 DRIFTs spectra of activated 20 wt% PTA/MIL–101(Cr)$_{ENCAPSULATED}$ (*left*) and 50 wt% PTA/MIL–101(Cr)$_{ENCAPSULATED}$ (*right-zoom around 2250 cm^{-1}*) after contact with a solution of ethyl cyanoacetate in toluene (1.4 M) at different temperatures pre–treatment under helium flow.

In addition, DRIFTS were used to follow *in situ* heating after adsorption of the reaction reactants on the MOF samples. A solution of ethyl cyanoacetate in toluene (the same concentration as for the reaction experiments) was contacted in the cell with the 20 wt% PTA/MIL–101(Cr)$_{ENCAPSULATED}$

sample and the evolution of its infrared spectra was followed while increasing the temperature in the DRIFT cell (Fig. 2–15). After contacting at room temperature the solution of ethyl cyanoacetate with the MOF encapsulated sample, all the main vibrations from the active methylene compound are present while the catalyst bands related to the OH (3700cm^{-1}) and Cr–O (1163 cm^{-1}) stretching disappear. Upon raising the temperature, the formation of CO_2 is evident from the appearance of a new band at 2318 cm^{-1}. At the highest temperature, a new band appears at 2212 cm^{-1} while the ethyl cyanoacetate and CO_2 bands disappear and the catalyst vibrations are recovered. Similar DRIFTS experiments performed with a mixture of benzaldehyde and toluene revealed no chemical interaction with the catalysts. In addition, simple evaporation is observed when heating KBr sample impregnated with Ethyl cyanoacetate. These results indicate a strong interaction between ethyl cyanoacetate and the encapsulated active site, suggesting activation of the active methylene compound.

2.3.2.2. Esterification of 1–butanol and acetic acid

The esterification of 1–butanol with acetic acid was chosen to test the different catalysts in a liquid phase acid–catalyzed reaction at relatively mild temperature conditions. The acetic acid to 1–butanol molar ratio was 1:1. A total of 3 g of catalyst per mol of acetic acid was used, corresponds with 0.036 mmol (0.5 g) of POM in the 20 wt% of POM encapsulated sample used. Figure 2–16 shows the yield of butyl acetate based on the acetic acid conversion (100% selectivity) as a function of time at 383 K.

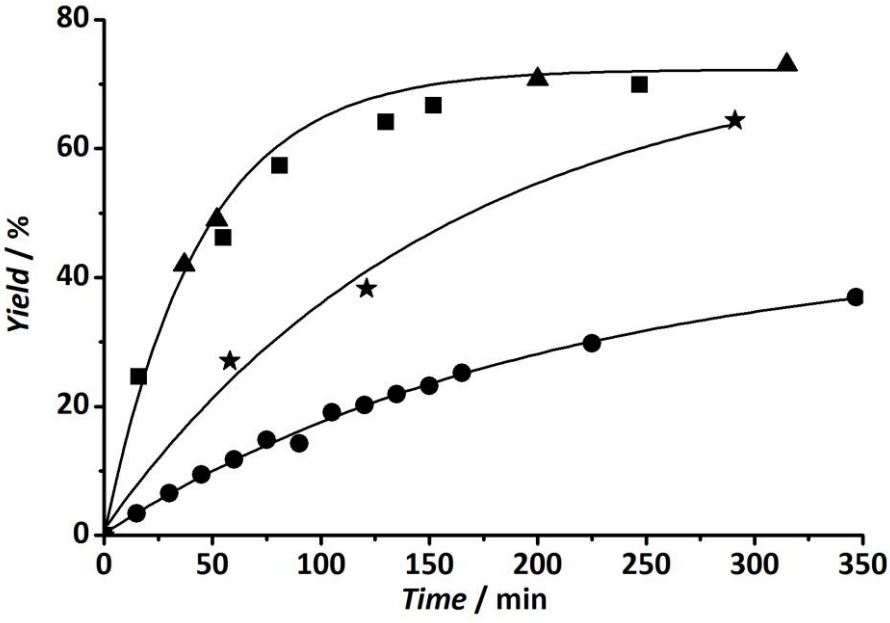

Figure 2 - 16 Esterification reaction of acetic acid and 1–butanol (1:1 molar ratio), using 3 g of catalyst per mol of acetic acid at 383 K. Yield of ester formation as a function of time. (★) 20wt% PTA/MIL–101(Cr)$_{ENCAPSULATED}$. (▲) 0.6 g of PTA per mol of acetic acid (equivalent to 20 wt% PTA in MIL–101 sample). (■) Nafion® NR50. (●) Blank.

The best catalytic activity was presented by the 20 wt% POM encapsulated sample, and it has been compared with that of dissolved POM acting as a homogeneous catalyst (the same amount used as present in the MOF sample, assuming that the 3 protons per POM are active, $H_3PW_{12}O_{40}$) and the performance of both have been benchmarked with Nafion® NR50 (the same mass of resin as MOF sample, 0.45 mmol H^+, since $[H^+]$=0.9 mmol/g). [45]

While experiments performed with the 10 and 50 wt% encapsulated catalysts showed conversions in the range of 50% after five reaction hours, the experiments with the impregnated POM samples did not show any differences with the blank runs (30% conversion after 5 h). In all other cases equilibrium is almost reached after 300 min, but both the Nafion® NR50 and the dissolved POM present higher catalytic performance, as is expected for non–porous materials.

Table 2 - 4 Kinetic rate constant, *TON* and *TOF* values for three different catalysts, calculated for the conditions specified in Figure 2 – 16.

	Nafion® NR50	PTA	20 wt% PTA/MOF
active sites (mmol H^+/g)	0.9 [(a)]	1 [(b)]	0.2 [(b)]
k [min^{-1}]	0.0213	0.225	0.0063
TOF [mol$_{converted}$. mol$_{active\ site}^{-1}$. min^{-1}]	8	36	10
TON$_{(t = 290\ min)}$ [mol$_{converted}$. mol$_{active\ site}^{-1}$]	270	1150	1025

(a) According to reference [45]. (b) Calculated theoretically, but in agreement with calculation obtained by acid–base titration in reference [46].

TON and *TOF* values calculated for the three different catalyst are presented in Table 2–4. Similar kinetic constants are observed for both Nafion® NR50 and phosphotungstic acid, while a significant decrease is displayed for the POMMOF catalyst. However, comparisons per catalytic active site (*TON* and *TOF*) display different results. While phosphotungstic acid as homogeneous system is still three times more active than the porous MOF, Nafion® NR50 values are slightly smaller than the new POMMOF system. *TON* values, calculated at the end of the followed reaction (t = 290 min), show similar values for the encapsulated and pristine PTA systems, while much lower numbers are shown for Nafion® NR50, assuming the same calculation of the active sites as explained before.

2.3.2.3. Dehydration of Methanol to Dimethyl Ether

The dehydration of methanol to dimethyl ether (DME) is a gas phase also acid–catalyzed reaction. The conversion and selectivity to DME at different temperatures are shown in Fig. 2–17 for three weight hourly space velocities (WHSVs) for the 20 wt% POM encapsulated in MIL–101(Cr) sample. Conversion is given after 30 reaction minutes, no deactivation of the catalyst was observed during the

experiments. At WHSV = 2 h^{-1} methanol conversion levels off at 70% and very low DME selectivity is achieved over the whole temperature range. When increasing the WHSV (4 h^{-1}) both selectivity and conversion increase with temperature. At the highest WHSV (8 h^{-1}) conversion is the lowest, but looking at the highest temperature the selectivity is the best.

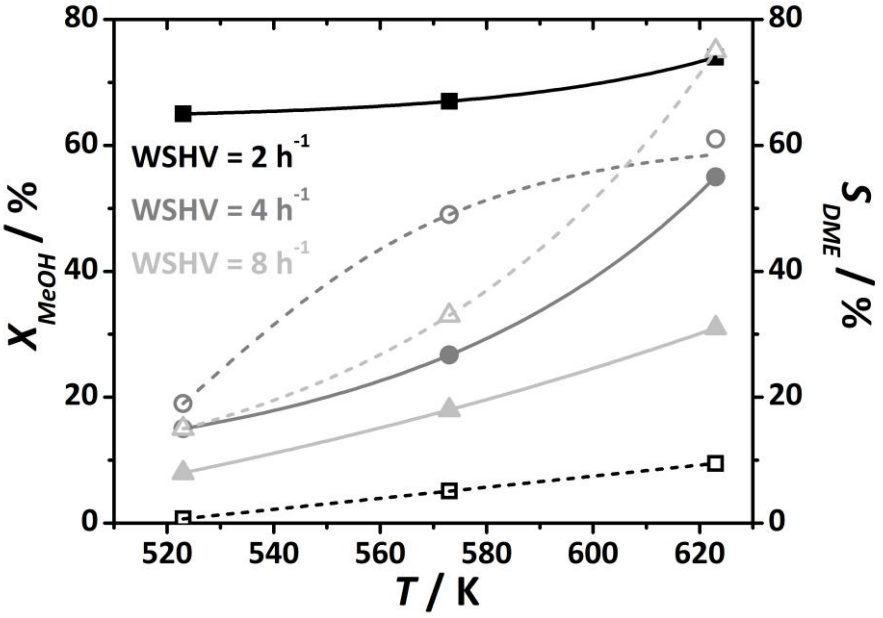

Figure 2 - 17 Methanol conversion and selectivity to DME in the dehydration of methanol as a function of temperature at different weight hourly space velocities. Catalyst: 100 mg of 20 wt% PTA/MIL–101(Cr)$_{ENCAPSULATED}$. Molar feed ratio N_2:MeOH = 5:1. (*Closed symbols*) Conversion. (*Open symbols*) Selectivity. WHSV = 2(■), 4(▲) and 8(●) h^{-1}.

2.4. DISCUSSION

The HRTEM analysis (Fig. 2–2 and 2–3) confirms that the direct encapsulation of POM in MIL–101(Cr) is possible through addition of the Keggin unit to the synthesis mixture and subsequent hydrothermal treatment, as already shown by Sun *et al.* for another MOF structure, HKUST–1. [27] Stirring the reaction mixture during the synthesis, however, improves dramatically the distribution of the POM in the MIL–101 matrix, as shown by the EDS analysis and mapping (Figs. 2–2 and 2–4).

Thermo–gravimetric analysis also indicates the presence of PTA, since residual mass increases with PTA loading in the sample and suiting the percentage given by ICP–OES. Furthermore, POMs have been reported to be excellent oxidation catalysts (Fig. 2–7). [37, 47] TG analysis confirms that the oxidation temperature of the encapsulated samples depends on the amount of POM, whereas the impregnated samples show oxidation profiles identical to the bare MIL–101. These results are in agreement with a better dispersion of the encapsulated POMs with respect to the impregnated systems, allowing air to diffuse faster through the pores and enhance the oxidation of the framework.

All samples synthesized showed the XRD pattern of pure MIL–101, while no reflections corresponding to crystalline POM were detected, demonstrating the absence of large POM crystals at the outer surface of the particles (Fig. 2–6). Moreover, the higher background appearing in the 10 wt% PTA encapsulated sample suggests an irregular occupation of the cavities, since only half of the cavities can be occupied by this low amount of Keggin units. Although the incorporation of W into the framework cannot be discarded, in this case we would expect changes in the positions of the main XRD peaks, that are not observed, however.

The better dispersion of the POM when directly encapsulated compared to the impregnated samples is additionally demonstrated by the comparison of the different N_2 isotherms (Fig. 2–5). The two characteristic steps in the MIL–101 isotherms are related with the filling of the mesoporous cavities. At very low relative pressures ($p/p^0 < 0.05$) only the supertetrahedra are filled. As pressure increases, the medium ($p/p^0 = 0.15$) and later the large cavities ($p/p^0 = 0.20$) are filled. [29] The fact that the encapsulated samples with high POM loadings show an adsorptive behavior similar to that of the bare material strongly suggests that the filling of the cavities is quite homogeneous, despite the POM presence (Table 2–2). Apparently, the arrangement of the POM in the impregnated samples is quite different: the ratio between the adsorbed amount of N_2 at low relative pressures (adsorption in the supertetrahedra) and the adsorbed amount at higher relative pressures (adsorption in the cavities) is relatively larger than for the bare MIL–101. It means that only a smaller fraction of the cavities is filled with POM and that most of these –large– cavities are blocked. In contrast, when encapsulated, the POM molecules may also be present in the medium–sized cavities, unlike impregnation techniques, since they are too big to enter through the pentagonal windows (Fig. 2–1). A much better dispersion results for the encapsulated samples, since no indication of cavities blockage is observed. Considering the amount of POM incorporated into the MIL–101, on average about 5.3 Keggin units should be present in every large cavity of the 50 wt% impregnated sample and up to two units would be present per cavity (medium and large) for the same loading on an encapsulated sample. [9] Considering the volumes of a Keggin unit (2250 $Å^3$) and the volume of the MIL–101 cages (20,600 and 12,700 $Å^3$, respectively), the difference in the adsorptive behavior between the encapsulated and the impregnated samples is not surprising: the volume of six Keggin units, even if they are very close to each other, may block completely a large cavity or at least block some of the windows. In the case of the other encapsulated samples, approximately one Keggin unit would be present in every cavity of the 20 wt% while only half of the cavities would be occupied by POM for the 10 wt% sample. This fact accounts for the differences found in the shape of the N_2 isotherms between the lowest loaded sample (10 wt%)

and the other encapsulated samples. A 10 wt% PTA is not enough to fill every cavity, resulting in empty spaces and therefore different isotherms.

With respect to the nature of the encapsulated species, every spectroscopic evidence points in the same direction: structural changes in the original PTA Keggin unit are most probably not taking place during the encapsulation process, but after washing the sample with NH_4F. The stabilization of lacunary POMs through exchange of tungsten with other transition metals has been widely reported in the literature. [21, 39, 48, 49] Metal–substituted polyoxometalates contain transition metals as addenda ions. The transition metal fits into the lacunary vacancy created in the otherwise complete Keggin structural unit. The lacunary or ‘‘defect structure” is created by the loss of an MO_6 octahedron (which is equivalent to stoichiometric loss of a MO^{n+} unit resulting in the formation of $XM_{11}O^{n-}$). [17] These species are usually synthesized at pH between 2 and 3, possibly obtained with a NH_4F solution, in fact at 373 K temperature Cr^{3+} may be incorporated in the Keggin structure.

UV–Vis spectroscopy shows clear evidences of the PTA nature change after washing with NH_4F (Fig. 2–8). The PTA peak centered at 255 nm is attributed to the oxygen–phosphor charge–transfer for Keggin anions, weakly observed in every sample due to strong MOF absorption in this region, and the one at around 360 nm for oxygen–tungsten charge–transfer. [23, 50] However, no change is specially observed for impregnated and encapsulated samples (acidic and basic media) only washed with ethanol, comparing with the pristine MIL–101(Cr). This result might indicate the good dispersion of PTA inside of the MOF cages as observed previously by XRD analysis. In the case of encapsulated samples after washing with NH_4F, new absorption bands arise at 360 and 345 nm, which increases with PTA loading. These bands can be related to interactions Cr–O–W, in analogy to Fe–containing POMs, [48] leading to some W atoms being substituted by Cr^{3+} forming the corresponding lacunary structures ($[PW_{11}O_{39}Cr(H_2O)]^{4-}$, $[(PW_{11}O_{39}Cr)_2O]^{10-}$, $([PW_{11}O_{39}Cr(OH)]^{5-}$). [37, 47] However, this result could also indicate the formation of WO_3. [51]

DRIFT spectra give additional information, upon comparison of encapsulated/impregnated samples under different synthesis and washing conditions (Fig. 2–9). The first main difference is the appearance of distortion in the OH bands of MIL–101 (3665 cm^{-1}) suggesting interaction between guest species and framework. While no significant changes take place comparing impregnated samples with encapsulated PTA under acidic and basic synthesis conditions, large differences are observed with respect to the main IR absorption vibrations of the POM after washing. Ethanol washing maintains the main PTA vibrations, but still a new peak at 1115 cm^{-1} appears, not assigned yet. Nevertheless, main differences appear after washing with NH_4F, where no vibrations of PTA are observed any longer. A broader band is formed for every PTA loading around 1150 cm^{-1} probably associated with a shift from

the P–O peak at 1080 cm^{-1}. No signs of shifting or splitting W=O and W–O–W stretchings are observed after washing with NH_4F. The fact that the main band is displaced or much less intense could be related with the fact that a part of the $H_3PW_{12}O_{40}$ has been exchanged with Cr^{3+} during the encapsulation, producing asymmetry in the PO_4 and W–O environment and therefore the splitting of a single band into several ones of less intensities. Moreover, the MIL–101(Cr) band at 1163 cm^{-1} assigned to the Cr–O vibration is altered by the encapsulation of POMs which also suggests the existence of further Cr–O vibrations, or even a second P–O vibration in the presence of Cr^{3+} . [37, 48] Thallium doped or Na salts of PTA do not show any change in the DRIFT vibrations, and therefore it should not be the cause for the disappearance of encapsulated PTA bands. [52, 53] But instead formation of amorphous WO_3 could be causing as well the disappearance of PTA vibrations.

^{31}P MAS–NMR is a useful technique for providing information about the integrity of the primary structure of phosphorus containing heteropolyacids and can evidence any changes in the chemical environment of phosphorus upon encapsulation. A broadening of the ^{31}P MAS–NMR peak centered at –15.18 ppm is indicative of less PTA rotational freedom by encapsulation inside the MOF cages, as previously reported for encapsulated POMs in zeolites (Fig. 2–10). [54] However, after NH_4F washing, the ^{31}P signal is no longer observed, suggesting a strong change in the nature of the PTA.

Further work is needed to fully understand if the changes observed in PTA after washing with NH_4F can only be assigned to cation exchange of protons by NH_4^+, or to a different modification of the POM structure influenced by the presence of extra F^-. However, cation exchange, for instance, by forming ionic liquids based on polyoxometalates, [55] or inclusion of organic molecules like carbonyls, amides, ureas, carbamates, and thiocarbamates into polyoxometallic structures, does not seem to alter the main spectroscopic features of the parent PTA. [56] Combination of spectroscopic techniques like XPS, EXAFS or XANES, might elucidate this question. [57]

The different dispersion of the POMs in the solid samples, is in harmony with the catalytic results, while differences in the nature of the PTA do not seem to affect reactivity. The encapsulated samples have been shown to be very active in the Knoevenagel condensation and quite active in the esterification reaction, while the impregnated samples show only a fair activity in the Knoevenagel and hardly any activity in the esterification, related with a stronger interaction MOF/POM and POM/POM when the active species are introduced by impregnation. Indeed, Férey *et al.* already reported the absence of counter anions (potassium) inside the MOF structure when impregnating the K–salt of the Keggin species, which is another evidence of a strong electrostatic interaction POM–support. It is well known that PTA is active when immobilized on several supports, but with increasing strength of the acid–support interaction, the acidity decreases dramatically, like in activated carbons. [58] Moreover,

the presence of more Keggin units per cavity might lead to stronger POM/POM interactions and to accessibility issues not present in the better dispersed encapsulated catalysts.

The catalysts are fully reusable and no activity loss was observed during consecutive tests (Fig. 2–13), some samples were reused up to eight times in different reactions (corresponding with a total *TON* > 3000 for 10 wt% encapsulated sample). The absence of leaching is concluded from the hot filtration experiments, and the absence of tungsten in the reaction medium is confirmed by elemental analysis after reactions in polar (1–butanol) and non–polar (toluene) media.

The performance of the encapsulated samples in the Knoevenagel condensation is outstanding when using toluene and DMF as a solvent, and is very good when using a polar solvent such as ethanol (Fig. 2–12). [8, 42, 43] The most active catalysts are the ones with the lowest loadings, the 10 wt% and 20 wt% encapsulated MIL–101's: almost 100% of conversion is reached after two hours of reaction. When comparing the turnover frequencies, the lower loaded samples are three times more active than the 50 wt% encapsulated system, 30 times more than the impregnated sample, and over 100 times more active than the bicycloguanidine, which is a state–of–the–art organic base. [40] Neither the bulk POM (insoluble) nor the bare MIL–101(Cr) showed any activity under the applied conditions. In addition, no difference depending on the POM nature is observed, since similar catalytic behaviors are observed for both encapsulated samples synthesized under acidic or basic conditions, and before and after washing the samples with NH_4F (Fig. 2–14). These results suggest the truly nature of the active phase should be related with W and O presence. In addition, the mechanism study indicates the need for a cyano group in the reactants for the reaction to proceed. These results are in agreement with infrared spectroscopy experiments presenting reactivity of ethylcyanoacetate impregnated in the MOF after heating up (Fig. 2–15), while no change is observed for benzaldehyde.

The Knoevenagel condensation is a two–step reaction in which the first step is a nuclophile addition of an active methylene compound to a carbonyl compound and the second step is a dehydration reaction leading to the formation of an α–β–conjugated enone. More evidences are needed to fully elucidate the role of the encapsulated polyoxometalates in the reaction mechanism for Knoevenagel condensation. However, we elucidate a possible mechanism similar to the one shown by certain metallic complexes and some strong Lewis acids for the proton abstraction at the methylene group [53, 59], where nitrile tautomer is formed (possibly responsible for vibrations observed in infrared).

It has been previously suggested that the redox properties of the lone–electron–pair–bearing oxygen of the polyoxometalate can attacks the electron–deficient methylene hydrogen abstracting a proton, thus forming a methylene carbanion in equilibrium with a nitrile tautomer. [60-62] This anion attacks the carbonyl group, and then hydrolyses to form the product and eliminate a water molecule (Scheme 2–3).

[53] In addition, the clear indication that the reaction does not proceed without the presence of a nitriles supports the proposed mechanism based on the initial activation of ethyl cyanoacetate, and was also observed by Zhang *et al.* for phosphotungstic ionic liquids. [53] When no aldehyde is present (Fig. 2–15), ethyl cyanoacetate can be broken by raising the temperature, liberating CO_2 (band at 2318 cm^{-1}), and producing the condensation of CN units on the active sites (band at 2212 cm^{-1}).

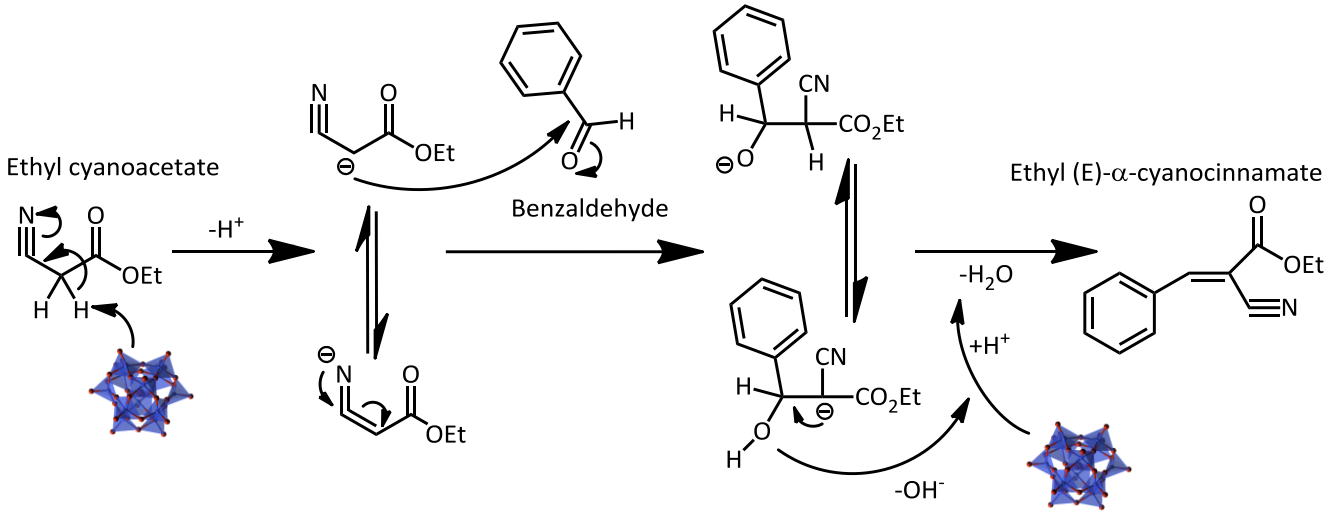

Scheme 2 - 3 Knoevenagel condensation mechanism acid catalysed *via* proton abstraction.

In the case of the esterification, the MOF initial activity is lower than that of the homogeneous POM counterpart on a molar basis and the Nafion® NR50 on a total weight basis, as comparing a non–porous and a highly porous system, the accessibility of the encapsulated POM might play a role in the initial rate of reaction. However calculations per active site display different conclusions. The encapsulated PTA shows higher *TOF* values than Nafion® NR50, but still lower reactivity than pristine PTA, indicating the remarkable acidity displayed by the encapsulated PTA, but also its strong interaction with the MOF structure affecting activity compared with the self–supported PTA. Similar *TON* numbers are observed for PTA encapsulated and pristine samples, while these numbers are much higher than the ones observed for Nafion® NR50. These results indicate a clear effect of the framework on the catalytic behavior, producing diffusional limitations and strong interaction with PTA, resulting in a slower system than the homogeneous counterpart, as primarily expected. PTA/MIL–101(Cr) also presents better catalytic results than those reported in the literature for POM immobilized on other supports like mesoporous silicas under similar reaction conditions, [18] demonstrating the presence of purely acid sites within the catalysts. Lately, PTA encapsulated in MIL–101(Cr) [46, 63] and HKUST–1 [27, 64-67] has been used for a wide number of acid–catalyzed reactions, showing the true nature of encapsulated PTA as acid–catalyst.

PTA/MOF systems are also active in the dehydration of methanol to DME at moderate reaction conditions, although a low selectivity to DME is obtained in comparison with other acid solids. [68-70] This is related with the formation of longer chain hydrocarbons that adsorb in the MIL–101 cavities. Indeed, the presence of negatively charged active sites together with large specific surface areas is not the best combination for reactions like DME formation.

Other polyoxometalates like $H_3PMo_{12}O_{40}$ (PMo) and $H_4SiW_{12}O_{40}$ (SiW) were encapsulated in the cages of MIL–101(Cr) through one–pot synthesis. DRIFT spectra show the main vibrations of each polyoxometalate (Fig. 2–18). The peak at 1080 cm^{-1} corresponding with $\nu(PO_4)$ vibration in the case of PTA, is shifted to 1060 cm^{-1} indicating the presence of these bonds within a change in the environment of tungsten by molybdenum, while $\nu(SiO_4)$ vibrations seem to be a lot more attenuated in this region. On the other hand, ν(W=O) vibrations present in the PTA spectrum are also shifted in the same way as $\nu(PO_4)$ for the case of ν(Mo=O), and splitting in two peaks much more attenuated for the SiW polyoxometalate. Finally, when looking at ν(W–O–W), the same behavior is observed for ν(Mo–O–Mo) vibrations shifted to lower wavenumbers, but in the SiW_{12} case, ν(W–O–W) vibrations are even more shifted close to the region at 800 cm^{-1}, probably due to the influence of Si instead of P. These polyoxometalates have not been used in catalysis due to the lack of time in the present project.

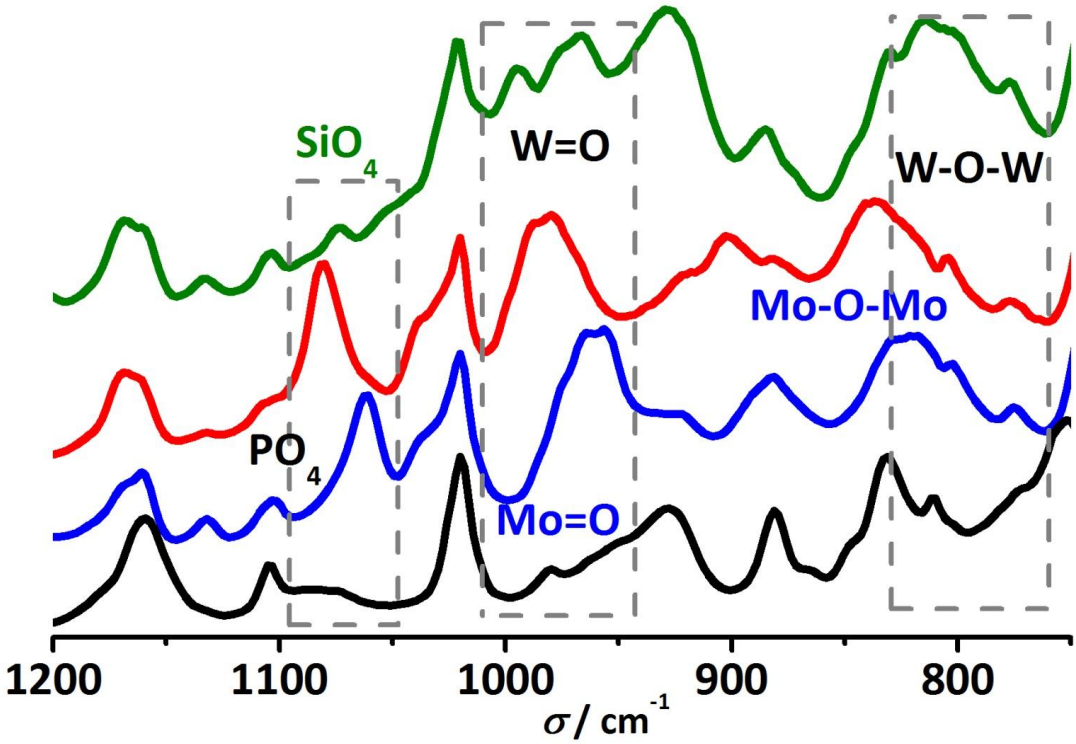

Figure 2 - 18 DRIFT spectra of different polyoxometalates encapsulated in the cages of MIL–101(Cr). (*Green*) $H_4SiW_{12}O_{40}$. (*Red*) $H_3PW_{12}O_{40}$. (*Blue*) $H_3PMo_{12}O_{40}$. (*Black*) MIL–101(Cr).

2.5. CONCLUSIONS

The addition of phosphotungstic acid to the synthesis mixture of MIL–101(Cr) yields the direct encapsulation of polyoxometalates of different nature into the MOF structure.

An excellent dispersion of the active species over the sample is obtained when combining the one–pot approach with synthesis under rotating conditions. N_2 adsorption results suggest that the ratio of medium to large cavities occupied by the POM is similar to the ratio in the bare MIL–101, demonstrating that both the large– and the medium–sized cavities may be used as host for the relatively large POM species. By contrast, when using impregnation techniques, only the larger cavities are accessed, and leaching might still be an issue regarding certain chemical reactions. Spectroscopic results indicate a change in the PTA nature after washing with aqueous NH_4F.

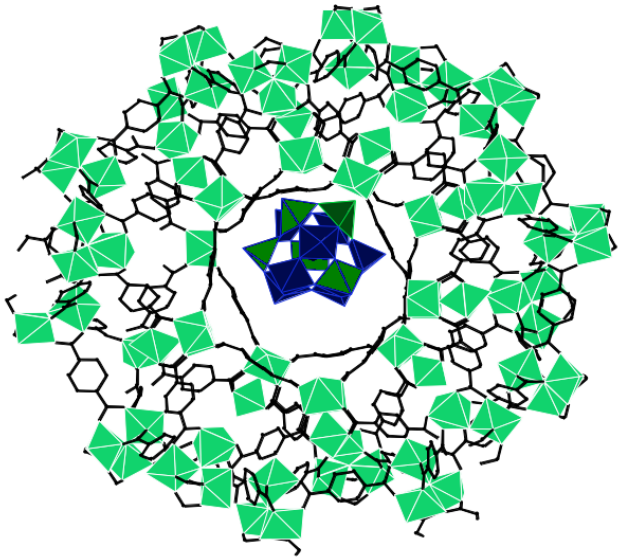

Figure 2 - 19 Phosphotungstic acid encapsulated in MIL-101(Cr)

The performance of these new catalysts in the Knoevenagel condensation of benzaldehyde and ethyl cyanoacetate is outstanding. No catalyst showing such high activity at 313 K in both apolar and polar solvents has been reported in the literature so far. The stabilization of encapsulated POMs in the MOF matrices may represent a new generation of catalysts with a high proton abstraction capability. The encapsulated catalysts show a remarkable activity in acid–catalyzed reactions, demonstrating the bifunctionality of these solids. In the catalysts prepared by impregnation, the strong interaction POM–MOF and the bad dispersion, deteriorate the acidity of the resulting solid, and hence the catalytic activity.

REFERENCES

[1] D. Farrusseng, S. Aguado, C. Pinel, Metal-organic frameworks: opportunities for catalysis, Angew. Chem Int Ed., 48 (2009) 7502-7513.
[2] J. Lee, O.K. Farha, J. Roberts, K.A. Scheidt, S.T. Nguyen, J.T. Hupp, Metal-organic framework materials as catalysts, Chemical Society Reviews, 38 (2009) 1450-1459.
[3] A. Corma, H. García, F.X. Llabrés i Xamena, Engineering metal-organic frameworks for heterogeneous catalysis, Chemical Reviews, 110 (2010) 4606-4655.
[4] J. Juan-Alcañiz, J. Gascon, F. Kapteijn, Metal-organic frameworks as scaffolds for the encapsulation of active species: state of the art and future perspectives, Journal of Materials Chemistry, 22 (2012) 10102-10118.
[5] F.X. Llabrés i Xamena, O. Casanova, R. Galiasso Tailleur, H. Garcia, A. Corma, Metal organic frameworks (MOFs) as catalysts: A combination of Cu^{2+} and Co^{2+} MOFs as an efficient catalyst for tetralin oxidation, Journal of Catalysis, 255 (2008) 220-227.
[6] F.X. Llabrés i Xamena, A. Abad, A. Corma, H. Garcia, MOFs as catalysts: Activity, reusability and shape-selectivity of a Pd-containing MOF, Journal of Catalysis, 250 (2007) 294-298.
[7] N.V. Maksimchuk, M.N. Timofeeva, M.S. Melgunov, A.N. Shmakov, Y.A. Chesalov, D.N. Dybtsev, V.P. Fedin, O.A. Kholdeeva, Heterogeneous selective oxidation catalysts based on coordination polymer MIL-101 and transition metal-substituted polyoxometalates, Journal of Catalysis, 257 (2008) 315-323.
[8] J. Gascon, U. Aktay, M.D. Hernandez-Alonso, G.P.M. van Klink, F. Kapteijn, Amino-based metal-organic frameworks as stable, highly active basic catalysts, Journal of Catalysis, 261 (2009) 75-87.
[9] C. Férey, C. Mellot-Draznieks, C. Serre, F. Millange, J. Dutour, S. Surblé, I. Margiolaki, Chemistry: A chromium terephthalate-based solid with unusually large pore volumes and surface area, Science, 309 (2005) 2040-2042.
[10] C. Serre, F. Millange, C. Thouvenot, M. Nogues, G. Marsolier, D. Louer, G. Férey, Very large breathing effect in the first nanoporous chromium(III)-based solids: MIL-53 or CrIII(OH){O_2C-C_6H_4-CO_2}{HO_2C-C_6H_4-CO_2H}xH_2Oy, Journal of the American Chemical Society, 124 (2002) 13519-13526.
[11] A. Henschel, K. Gedrich, R. Kraehnert, S. Kaskel, Catalytic properties of MIL-101, Chemical Communications, (2008) 4192-4194.
[12] Z. Sun, G. Li, L. Liu, H.O. Liu, Au nanoparticles supported on Cr-based metal-organic framework as bimetallic catalyst for selective oxidation of cyclohexane to cyclohexanone and cyclohexanol, Catalysis Communications, 27 (2012) 200-205.
[13] E. Kockrick, T. Lescouet, E.V. Kudrik, A.B. Sorokin, D. Farrusseng, Synergistic effects of encapsulated phthalocyanine complexes in MIL-101 for the selective aerobic oxidation of tetralin, Chemical Communications, 47 (2011) 1562-1564.
[14] J. Hermannsdörfer, R. Kempe, Selective palladium-loaded MIL-101 catalysts, Chemistry - A European Journal, 17 (2011) 8071-8077.
[15] J. Kim, S. Bhattacharjee, K.E. Jeong, S.Y. Jeong, W.S. Ahn, Selective oxidation of tetralin over a chromium terephthalate metal organic framework, MIL-101, Chemical Communications, (2009) 3904-3906.
[16] Y.K. Hwang, D.Y. Hong, J.S. Chang, S.H. Jhung, Y.K. Seo, J. Kim, A. Vimont, M. Daturi, C. Serre, G. Férey, Amine grafting on coordinatively unsaturated metal centers of MOFs: Consequences for catalysis and metal encapsulation, Angewandte Chemie - International Edition, 47 (2008) 4144-4148.
[17] I.V. Kozhevnikov, Catalysis by Heteropoly Acids and Multicomponent Polyoxometalates in Liquid-Phase Reactions, Chemical Reviews, 98 (1998) 171-198.
[18] S. Wu, J. Wang, W. Zhang, X. Ren, Preparation of Keggin and Preyssler heteropolyacid catalysts on amine-modified SBA-15 and their catalytic performances in esterification of 1-butanol with acetic acid, Catalysis Letters, 125 (2008) 308-314.
[19] H. Atia, U. Armbruster, A. Martin, Dehydration of glycerol in gas phase using heteropolyacid catalysts as active compounds, Journal of Catalysis, 258 (2008) 71-82.
[20] M.A. Schwegler, P. Vinke, M. van der Eijk, H. van Bekkum, Activated carbon as a support for heteropolyanion catalysts, Applied Catalysis A, General, 80 (1992) 41-57.
[21] J. Haber, K. Pamin, L. Matachowski, D. Mucha, Catalytic performance of the dodecatungstophosphoric acid on different supports, Applied Catalysis A: General, 256 (2003) 141-152.
[22] I.V. Kozhevnikov, A. Sinnema, R.J.J. Jansen, K. Pamin, H. van Bekkum, New acid catalyst comprising heteropoly acid on a mesoporous molecular sieve MCM-41, Catalysis Letters, 30 (1995) 241-252.
[23] C. Shi, R. Wang, G. Zhu, S. Qiu, J. Long, Synthesis, characterization, and catalytic properties of SiPW-X mesoporous silica with heteropolyacid encapsulated into their framework, European Journal of Inorganic Chemistry, (2005) 4801-4807.
[24] V. Dufaud, F. Lefebvre, G.P. Niccolai, M. Aouine, New insights into the encapsulation and stabilization of heteropolyacids inside the pore walls of mesostructured silica materials, Journal of Materials Chemistry, 19 (2009) 1142-1150.

[25] S. Anandan, S.Y. Ryu, W. Cho, M. Yoon, Heteropolytungstic acid ($H_3PW_{12}O_{40}$) - Encapsulated into the titanium-exchanged HY (TiHY) zeolite: A novel photocatalyst for photoreduction of methyl orange, Journal of Molecular Catalysis A: Chemical, 195 (2003) 201-208.
[26] P. Ferreira, I.M. Fonseca, A.M. Ramos, J. Vital, J.E. Castanheiro, Esterification of glycerol with acetic acid over dodecamolybdophosphoric acid encaged in USY zeolite, Catalysis Communications, 10 (2009) 481-484.
[27] C.Y. Sun, S.X. Liu, D.D. Liang, K.Z. Shao, Y.H. Ren, Z.M. Su, Highly stable crystalline catalysts based on a microporous metal-organic framework and polyoxometalates, Journal of the American Chemical Society, 131 (2009) 1883-1888.
[28] M.H. Alkordi, Y. Liu, R.W. Larsen, J.F. Eubank, M. Eddaoudi, Zeolite-like metal-organic frameworks as platforms for applications: On metalloporphyrin-based catalysts, Journal of the American Chemical Society, 130 (2008) 12639-12641.
[29] P.L. Llewellyn, S. Bourrelly, C. Serre, A. Vimont, M. Daturi, L. Hamon, G. De Weireld, J.S. Chang, D.Y. Hong, Y.K. Hwang, S.H. Jhung, G. Férey, High uptakes of CO_2 and CH_4 in mesoporous metal-organic frameworks MIL-100 and MIL-101, Langmuir, 24 (2008) 7245-7250.
[30] N.A. Khan, I.J. Kang, H.Y. Seok, S.H. Jhung, Facile synthesis of nano-sized metal-organic frameworks, chromium-benzenedicarboxylate, MIL-101, Chemical Engineering Journal, 166 (2011) 1152-1157.
[31] J. Yang, Q. Zhao, J. Li, J. Dong, Synthesis of metal-organic framework MIL-101 in TMAOH-$Cr(NO_3)_3$-H_2bdc-H_2O and its hydrogen-storage behavior, Microporous and Mesoporous Materials, 130 (2010) 174-179.
[32] M.H. Youn, H. Kim, J.C. Jung, I.K. Song, K.P. Barteau, M.A. Barteau, UV-vis spectroscopy studies of $H_3PMo_{12-x}W_xO_{40}$ heteropolyacid (HPA) catalysts in the solid state: Effects of water content and polyatom substitution, Journal of Molecular Catalysis A: Chemical, 241 (2005) 227-232.
[33] Y. Guo, Y. Wang, C. Hu, Y. Wang, E. Wang, Microporous polyoxometalates POMs/SiO_2: Synthesis and photocatalytic degradation of aqueous organocholorine pesticides, Chemistry of Materials, 12 (2000) 3501-3508.
[34] I.V. Kozhevnikov, Catalysis by Polyoxometalates, in: Catalysis for Fine Chemical Synthesis, Wiley, 2002.
[35] K.U. Nandhini, B. Arabindoo, M. Palanichamy, V. Murugesan, Synthesis, characterisation and catalytic evaluation of mesoporous AlPO supported phosphotungstic acid in the ethylation of ethylbenzene, Microporous and Mesoporous Materials, 81 (2005) 59-71.
[36] B. Li, W. Ma, J. Liu, C. Han, S. Zuo, X. Li, Synthesis of the well-ordered hexagonal mesoporous silicate incorporated with phosphotungstic acid through a novel method and its catalytic performance on the oxidative desulfurization reaction, Catalysis Communications, 13 (2011) 101-105.
[37] N.I. Kuznetsova, L.I. Kuznetsova, V.A. Likholobov, Catalytic properties of Cr-containing heteropolytungstates in H_2O_2 participated reactions: H_2O_2 decomposition and oxidation of unsaturated hydrocarbons with H_2O_2, Journal of Molecular Catalysis A: Chemical, 108 (1996) 135-143.
[38] E. Caliman, J.A. Dias, S.C.L. Dias, A.G.S. Prado, Solvent effect on the preparation of $H_3PW_{12}O_{40}$ supported on alumina, Catalysis Today, 107-108 (2005) 816-825.
[39] A. Yoshida, S. Hikichi, N. Mizuno, Acid-base catalysis by dimeric disilicoicosatungstates and divacant γ-Keggin-type silicodecatungstate parent: Reactivity of the polyoxometalate compounds controlled by step-by-step protonation of lacunary W=O sites, Journal of Organometallic Chemistry, 692 (2007) 455-459.
[40] Y.V. Subba Rao, D.E. De Vos, P.A. Jacobs, 1,5,7-triazabicyclo[4.4.0]dec-5-ene immobilized in MCM-41: A strongly basic porous catalyst, Angewandte Chemie (International Edition in English), 36 (1997) 2661-2663.
[41] A. Corma, S. Iborra, I. Rodríguez, F. Sánchez, Immobilized proton sponge on inorganic carriers: The synergic effect of the support on catalytic activity, Journal of Catalysis, 211 (2002) 208-215.
[42] M.J. Climent, A. Corma, I. Domínguez, S. Iborra, M.J. Sabater, G. Sastre, Gem-diamines as highly active organocatalysts for carbon-carbon bond formation, Journal of Catalysis, 246 (2007) 136-146.
[43] I. Rodriguez, G. Sastre, A. Corma, S. Iborra, Catalytic activity of proton sponge: Application to Knoevenagel condensation reactions, Journal of Catalysis, 183 (1999) 14-23.
[44] S.I. Murahashi, T. Naota, H. Taki, M. Mizuno, H. Takaya, S. Komiya, Y. Mizuho, N. Oyasato, M. Hiraoka, M. Hirano, A. Fukuoka, Ruthenium-catalyzed aldol and Michael reactions of nitriles. Carbon-carbon bond formation by α-C-H activation of nitriles, Journal of the American Chemical Society, 117 (1995) 12436-12451.
[45] M.A. Harmer, Q. Sun, Solid acid catalysis using ion-exchange resins, Applied Catalysis A: General, 221 (2001) 45-62.
[46] Y. Zang, J. Shi, X. Zhao, L. Kong, F. Zhang, Y. Zhong, Highly stable chromium(III) terephthalate metal organic framework (MIL-101) encapsulated 12-tungstophosphoric heteropolyacid as a water-tolerant solid catalyst for hydrolysis and esterification, Reaction Kinetics, Mechanisms and Catalysis, (2013) 1-13.
[47] L.I. Kuznetsova, L.G. Detusheva, N.I. Kuznetsova, M.A. Fedotov, V.A. Likholobov, Relation between structure and catalytic properties of transition metal complexes with heteropolyanion $PW_{11}O_{39}^{7-}$ in oxidative reactions, Journal of Molecular Catalysis A: Chemical, 117 (1997) 389-396.
[48] K. Nowinska, M. Sopa, A. Waclaw, D. Szuba, Transition metal modified lacunary heteropoly compounds as catalysts for oxidation of light paraffins, Applied Catalysis A: General, 225 (2002) 141-151.

[49] M.W. Droege, R.G. Finke, A novel triperoxyniobium-containing polyoxoanion, $SiW_9(NbO_2)_3O_{37}^{7-}$: synthesis, characterization, catalytic allylic epoxidations with H_2O_2 and preliminary kinetic studies, Journal of Molecular Catalysis, 69 (1991) 323-338.
[50] W. Zhu, W. Huang, H. Li, M. Zhang, W. Jiang, G. Chen, C. Han, Polyoxometalate-based ionic liquids as catalysts for deep desulfurization of fuels, Fuel Processing Technology, 92 (2011) 1842-1848.
[51] Q. Zhu, X. Chu, Z. Zhang, W.L. Dai, K. Fan, Effect of the tungsten precursor on the high activity of the WO_3/ZrO_2 catalyst in the oxidative lactonization of 1,2-benzenedimethanol, Applied Catalysis A: General, 435-436 (2012) 141-147.
[52] S.R. Mane, R.R. Kharadeb, R.M. Maneb, S.N. Gawale, S.M. Patilb, P.N. Bhosaleb, Influence of Tl^+ doping on opto-structural and electrical properties of chemically grown tungsten heteropolyoxometalate thin films, Digest Journal of Nanomaterials and Biostructures, 6 (2011) 451-466.
[53] M. Zhang, P. Zhao, Y. Leng, G. Chen, J. Wang, J. Huang, Schiff base structured acid-base cooperative dual sites in an ionic solid catalyst lead to efficient heterogeneous Knoevenagel condensations, Chemistry - A European Journal, 18 (2012) 12773-12782.
[54] B. Sulikowski, J. Haber, A. Kubacka, K. Pamin, Z. Olejniczak, J. Ptaszyński, Novel "ship-in-the-bottle" type catalyst: Evidence for encapsulation of 12-tungstophosphoric acid in the supercage of synthetic faujasite, Catalysis Letters, 39 (1996) 27-31.
[55] S. Uchida, R. Kawamoto, N. Mizuno, Recognition of Small Polar Molecules with an Ionic Crystal of α-Keggin-Type Polyoxometalate with a Macrocation, Inorganic Chemistry, 45 (2006) 5136-5144.
[56] J. Oble, B. Riflade, A. Noël, M. Malacria, S. Thorimbert, B. Hasenknopf, E. Lacôte, Carbonyl-Inserted Organo-Hybrids of a Dawson-Type Phosphovanadotungstate: Scope and Chemoselective Oxidation Catalysis, Organic Letters, 13 (2011) 5990-5993.
[57] P.G. Rickert, M.R. Antonio, M.A. Firestone, K.A. Kubatko, T. Szreder, J.F. Wishart, M.L. Dietz, Tetraalkylphosphonium polyoxometalate ionic liquids: Novel, organic-inorganic hybrid materials, Journal of Physical Chemistry B, 111 (2007) 4685-4692.
[58] T. Okuhara, N. Mizuno, M. Misono, Catalytic Chemistry of Heteropoly Compounds, Advances in Catalysis, 41 (1996) 113-252.
[59] R.A. Sheldon, H. Van Bekkum, Fine Chemicals through Heterogeneous Catalysis, Wiley-VCH, 2001.
[60] R.F. Renneke, M. Pasquali, C.L. Hill, Polyoxometelate systems for the catalytic selective production of nonthermodynamics alkenes form alkanes. Nature of excited-state deactivation processes and control of subsequent thermal processes in ploy oxometalate photoredox chemistry, Journal of the American Chemical Society, 112 (1990) 6585-6594.
[61] L.A. Combs-Walker, C.L. Hill, Use of excited-state and ground-state redox properties of polyoxometalates for selective transformation of unactivated carbon-hydrogen centers remote from the functional group in ketones, Journal of the American Chemical Society, 114 (1992) 938-946.
[62] A. Yokoyama, K. Ohkubo, T. Ishizuka, T. Kojima, S. Fukuzumi, Remarkable enhancement of catalytic activity of a 2:1 complex between a non-planar Mo(v)-porphyrin and a ruthenium-substituted Keggin-type heteropolyoxometalate in catalytic oxidation of benzyl alcohols, Dalton Transactions, 41 (2012) 10006-10013.
[63] Y. Zhang, V. Degirmenci, C. Li, E.J.M. Hensen, Phosphotungstic acid encapsulated in metal-organic framework as catalysts for carbohydrate dehydration to 5-hydroxymethylfurfural, ChemSusChem, 4 (2010) 59-64.
[64] F.J. Ma, S.X. Liu, C.Y. Sun, D.D. Liang, G.J. Ren, F. Wei, Y.G. Chen, Z.M. Su, A sodalite-type porous metal-organic framework with polyoxometalate templates: Adsorption and decomposition of dimethyl methylphosphonate, Journal of the American Chemical Society, 133 (2011) 4178-4181.
[65] D.D. Liang, S.X. Liu, F.J. Ma, F. Wei, Y.G. Chen, A crystalline catalyst based on a porous metal-organic framework and 12-tungstosilicic acid: Particle size control by hydrothermal synthesis for the formation of dimethyl ether, Advanced Synthesis and Catalysis, 353 (2011) 733-742.
[66] L.H. Wee, N. Janssens, S.R. Bajpe, C.E.A. Kirschhock, J.A. Martens, Heteropolyacid encapsulated in $Cu_3(btc)_2$ nanocrystals: An effective esterification catalyst, Catalysis Today, 171 (2011) 275-280.
[67] L.H. Wee, S.R. Bajpe, N. Janssens, I. Hermans, K. Houthoofd, C.E.A. Kirschhock, J.A. Martens, Convenient synthesis of $Cu_3(btc)_2$ encapsulated Keggin heteropolyacid nanomaterial for application in catalysis, Chemical Communications, 46 (2010) 8186-8188.
[68] J. Khom-in, P. Praserthdam, J. Panpranot, O. Mekasuwandumrong, Dehydration of methanol to dimethyl ether over nanocrystalline Al_2O_3 with mixed γ- and χ-crystalline phases, Catalysis Communications, 9 (2008) 1955-1958.
[69] F. Raoof, M. Taghizadeh, A. Eliassi, F. Yaripour, Effects of temperature and feed composition on catalytic dehydration of methanol to dimethyl ether over γ-alumina, Fuel, 87 (2008) 2967-2971.
[70] F. Yaripour, M. Mollavali, S.M. Jam, H. Atashi, Catalytic dehydration of methanol to dimethyl ether catalyzed by aluminum phosphate catalysts, Energy and Fuels, 23 (2009) 1896-1900.

Chapter 3

Live encapsulation of a Keggin polyanion in NH_2–MIL–101(Al) observed by *in situ* time resolved X–ray scattering

This chapter is based on the following publication:

J. Juan–Alcañiz, M. Goesten, A. Martinez–Joaristi, A. V. Petukhov, J. Gascon, F. Kapteijn, Chemical Communications, 47 (2011) 8578–8580

Abstract The templating effect of a well–known Keggin polyanion (phosphotungstic acid, PTA) during the synthesis of NH_2–MIL–101(Al) has been investigated by means of *in situ* small– and wide–angle X–ray scattering (SAXS/WAXS). Efficient PTA encapsulation has been observed upon crystallization. The WAXS range displays attenuation of specific diffraction peaks associated with the entrapped PTA molecules in the middle and large cages of this MOF. In addition, the performance of PTA as a nucleation site has been unraveled, leading to a complete model for the encapsulation mechanism. The SAXS time evolution regime suggests a mass fractal substance (surface and mass both when PTA is present, while smoother surface morphology is observed for bare NH_2–MIL–101(Al). Stabilization of the intermediate precursor phase NH_2–MOF–235(Al) is the initial step of the encapsulation process, with low temperature synthesis with PTA leading to the formation of only the intermediate phase. In contrast, in the absence of PTA, NH_2–MIL–101(Al) is the only product under the same reaction conditions. Kinetics of growth and nucleation have been measured in the presence and absence of PTA, surprisingly little differences have been found.

3.1. INTRODUCTION

During the last decade, metal–organic frameworks (MOFs) have attracted a great deal of attention in the field of nano–structured materials. [1] The combination of organic and inorganic subunits in these crystalline porous lattices has led to vast chemical versatility. In spite of initial skepticism owing to poor stability of the first MOF generation, impressive progress has been made during the last few years, yielding promising results in very different technological disciplines, such as adsorption and catalysis. [2-4] One of the most promising approaches towards catalytic applications of MOFs focuses on the encapsulation of active species by assembling the porous solid around it, via the so–called "*bottle around a ship*" or "*templated synthesis*" procedure. [5-7] In fact, the great topological richness of MOFs combined with relatively mild synthesis conditions offers excellent opportunities for hosting large catalytically active molecules. Among the various possibilities, [8] the stabilization and immobilization of polyoxometalates (POMs) through the formation of POM–containing coordination polymers have attracted a lot of attention. [9] Due to their rich structural and chemical variety, [10] POMs possess tuneable pore, shape, and size, a high negative charge in the anionic form, and are remarkably versatile building blocks in the construction of coordination supramolecules. [11] Frequently, POMs have been shown to act as anionic templates to build three–dimensional metal–organic frameworks, while the host MOF structure is not altered by this templating effect. Sun *et al.* [12] showed the encapsulation of POMs with the Keggin structure in the cavities of the well–known HKUST–1. Around the same time, we reported the successful encapsulation of a well–known Keggin type POM, phosphotungstic acid (PTA), in the large and medium cavities of the mesoporous MIL–101(Cr) by direct synthesis. [13] Canioni *et al.*, [14] following a similar one–pot hydrothermal approach, introduced various POMs into the cavities of MIL–100(Fe) and Bajpe *et al.* [15-17] reported the room temperature synthesis of different POM/HKUST–1 composites. In the latter work, the templating effect of the Keggin units was demonstrated by means of *ex situ* NMR/NIR/SAXS combination techniques. Even though the use of void–filling templates for synthesis of MOFs had been reported before, Bajpe *et al.* presented the first molecular–level mechanism of such a templating effect. [15, 18] The same group has studied the effect of POM template on several catalytic applications, like the solvent dependent solubility of HKUST–1 to use POMs as homogeneous catalysts and the recovery of the catalyst by encapsulation back in the MOF upon addition of hexane. [19] Later, the same group has reported the synthesis of a hierarchical variant of HKUST–1 with repetitive 5 nm wide mesopores, separated by uniform microporous walls, with PTA systematically occluded in the cavities forming the walls between the mesopores. [20]

Understanding how these materials are assembled will ultimately enable the rational design of new generations of MOFs and MOF based composites targeting specific morphology and properties. However little is known still about the mechanism that governs their crystallization: only a few *ex situ* [21-23] and *in situ* [24-27] studies on the crystallization of different prototypical MOFs have been reported up to date, while only one publication addresses templating effects. [15]

In this work, we report a combined *in situ* small– and wide– angle X–ray scattering (SAXS/WAXS) study on the crystallization of NH_2–MIL–101(Al) [28] in the presence of Keggin units of phosphotungstic acid (PTA). One–pot encapsulation is confirmed by results observed in the WAXS region where diffraction planes are attenuated due to electronic density fluctuations in the presence of PTA. Time evolution of the SAXS regime suggests a mass fractal nucleation when PTA is present, while smoother surface morphology is observed for bare NH_2–MIL–101(Al). Kinetic studies do not show any acceleration effects due to the PTA presence.

3.2. EXPERIMENTAL

3.2.1. MOF syntheses

NH_2–MIL–101(Al) was synthesized mixing 51 mg of aluminium chloride ($AlCl_3 \cdot 6H_2O$, Sigma Aldrich, 99%), 56 mg of 2–aminoterephthalic acid ($C_6H_3NH_2$–$(CO_2H)_2$, Sigma Aldrich, 99%) in 3 ml of N,N–dimethylformamide ($(CH_3)_2NCHO$, Sigma Aldrich, >99.9%). Phosphotungstic acid monohydrate ($H_3PW_{12}O_{40} \cdot H_2O$, 99.995%, 80 mg) was added in the PTA/NH_2–MIL–101(Al) synthesis. After vigorous stirring for 5 min, a 0.1 ml aliquot was transferred to the *in situ* cell.

3.2.2. Crystallization Cell

A specially designed synthesis cell was used for the experiments (Figure 3–1). The synthesis solution was loaded between two mica windows (10 mm diameter, 50–100 μm thickness) separated by PTFE spacers (1.5 mm height). Heating was provided by four chemically resistant cartridges and temperature was controlled at the external wall of the PTFE inserts.

Time resolved SAXS/WAXS experiments were performed at the beamline BM16 of the European Synchrotron Radiation Facility, ESRF (Grenoble, France), equipped with Roper Scientific CCD camera PI SCX90–1300 mounted on a Newport RV240PE goniometer, and X–Ray Research marCCD detector for WAXS and SAXS measurements, respectively. A complete description of the beamline is reported elsewhere. [29] With the high–intensity synchrotron radiation and position–sensitive detectors, SAXS and WAXS patterns could be collected simultaneously with an excellent signal to noise ratio every 20 s at different points of the crystallization cell. The data were normalized for the intensity of the X–ray beam, sample transmission and corrected for detector sensitivity prior to

background correction. The background scattering from the solvent (DMF) at the given reaction temperature was subtracted.

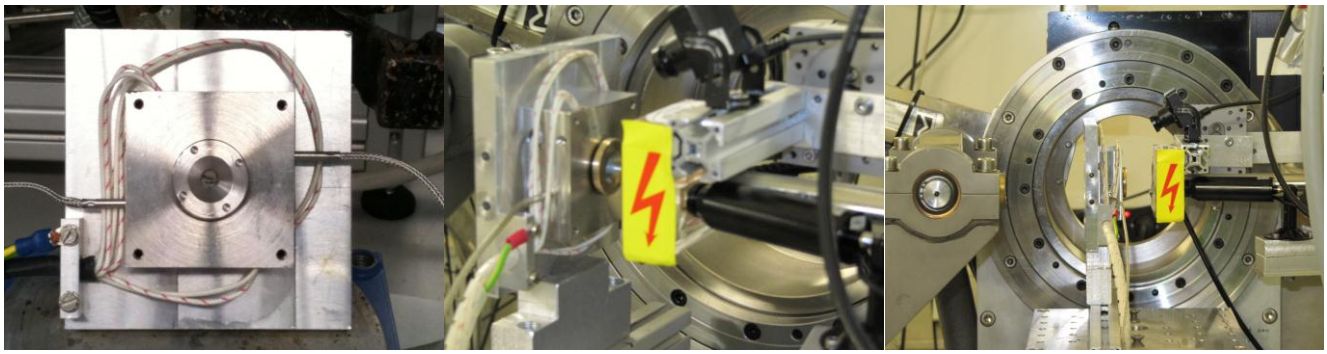

Figure 3 - 1 Crystallization cell used for the *in situ* SAXS/WAXS experiments. (*Left*) Top view. (*Centre and Right*) Cell mounted in the set–up at the ESRF.

3.2.3. SAXS analysis

Small–angle X–ray scattering has been the most commonly used technique to characterize the surface morphology of solid materials. The unit of resolution for the SAXS method is Q which is dependent on, and related to the scattering angle, θ, by the following equation, where λ is the X–ray wavelength:

$$Q = 4\pi\lambda^{-1}\sin\left(\theta/_2\right) \quad (1)$$

In a SAXS experiment, the intensity (*I*) of the scattered X–rays is measured as a function of the scattering angle which is usually expressed as the scattering vector, *Q*. The intensity as a function of *Q* (*I*(*Q*)) is related to *Q* by the power–law relationship described below:

$$I(Q) \propto Q^{-\alpha} \quad (2)$$

The magnitude of the exponent α is obtained from the slope of the log *I*(*Q*) vs log *Q* representation of the scattering data from the crystals, providing information about the morphology of the particles. If $\alpha \leq 3$ then the substance is a mass fractal, whose surface and mass are both characterized by fractal properties. If $3 < \alpha \leq 4$ then the substance is a surface fractal, where only the surface of the material exhibits fractal behavior. For smooth spherical particles with a homogeneous density, values around 4 are expected. [30, 31]

3.2.4. Kinetic Modelling

Analysis of the kinetic profiles was performed using the model developed by Gualtieri [32] and applied by Millange *et al.* [25] for the formation of several prototypical MOFs. This model is based on decoupling the nucleation and crystal growth processes.

In such a way, the extent of crystallization (C) with time (t) can be simulated according to the following equation:

$$C = \frac{1}{1+\exp\left(-\left(\frac{t-a}{b}\right)\right)} \cdot \left(1 - exp\left(-\left(k_g t\right)^n\right)\right) \quad (3)$$

Used in the modeling was fitting by Athena Visual Studio and the following mathematical model:

$$C = fac \cdot \frac{\left\{1-exp\left(-\left(k_g \cdot (t-dt)^n\right)\right)\right\}}{\left\{1+exp\left\{-\left(\frac{(t-dt)-a}{b}\right)\right\}\right\}} \quad (4)$$

Fitting a kinetic curve with the extent of crystallization, as the area below the most intense Bragg peak, yields the parameterization of:

Par1 = k_g, growth rate constant (s^{-1})

Par2 = *a*, reciprocal of nucleation constant $k_n = {}^1/_a$ (s)

Par3 = *b*, width of distribution of nuclei (s)

Par4 = *n*, growth dimensionality

Par5 = *fac*, factor introduced since normalization maybe off

Par6 = *dt*, time shift parameter that can be used to account for uncertainties in the start time, *e.g.*, when heating up time is not accounted for (s)

After having obtained the rate constants of growth and nucleation, activation energies (E_a) and pre–exponential factors (A) have been calculated through the Arrhenius equation, where R is the gas constant and T the temperature in Kelvin:

$$\ln(k) = \ln(A) - \frac{E_a}{R}\left(\frac{1}{T}\right) \quad (5)$$

3.3. EXPERIMENTAL RESULTS AND DISCUSSION

The scattering patterns recorded during the course of NH_2–MIL–101(Al) and PTA/NH_2–MIL–101(Al) formation at 413 K are shown in Figure 3–2. In both cases the Bragg reflections appear after an induction time, with positions of the diffraction maxima closely matching those predicted for the NH_2–MIL–101 structure ($Fd\bar{3}m$ cubic, a = 88.87 Å). Although some characteristic peaks of the MIL–101 structure are still present when PTA is added to the synthesis mixture, supporting formation of NH_2–MIL–101 structure, the intensity of the Bragg peaks decreased dramatically. In addition, the temporal evolution of small angle scattering patterns prior to the onset of crystallization is clearly different for these two cases.

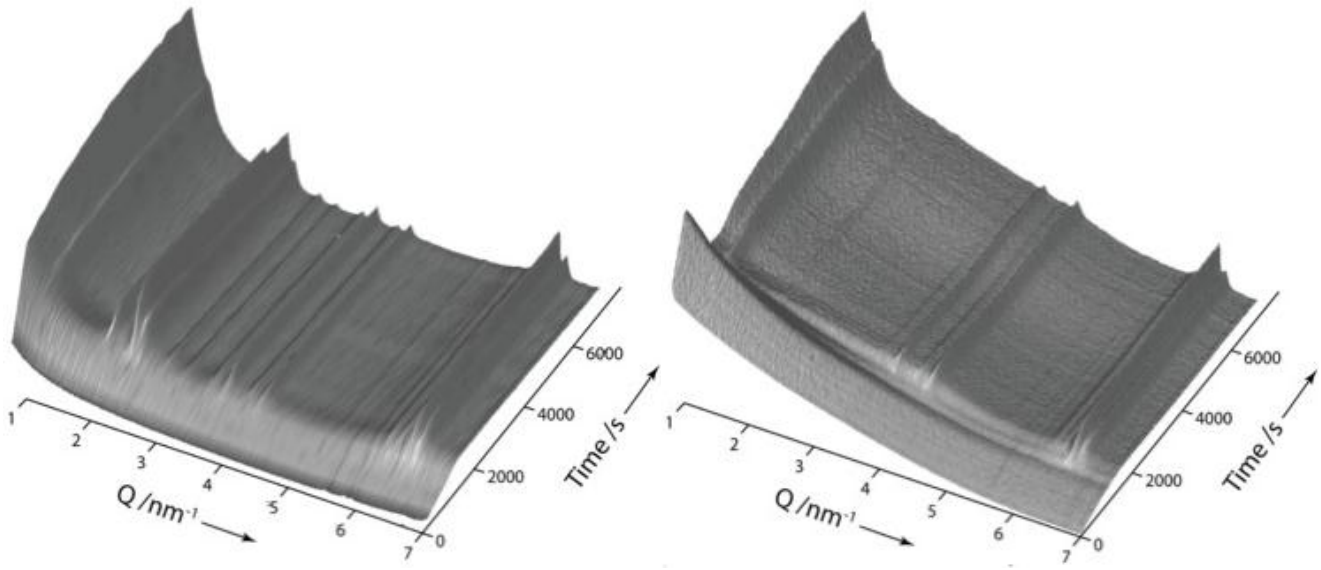

Figure 3 - 2 Time evolution X–ray scattering during the *in situ* synthesis of NH_2–MIL–101(Al) (*left-A*) and PTA/NH_2–MIL–101(Al) (*right-B*) at 413 K.

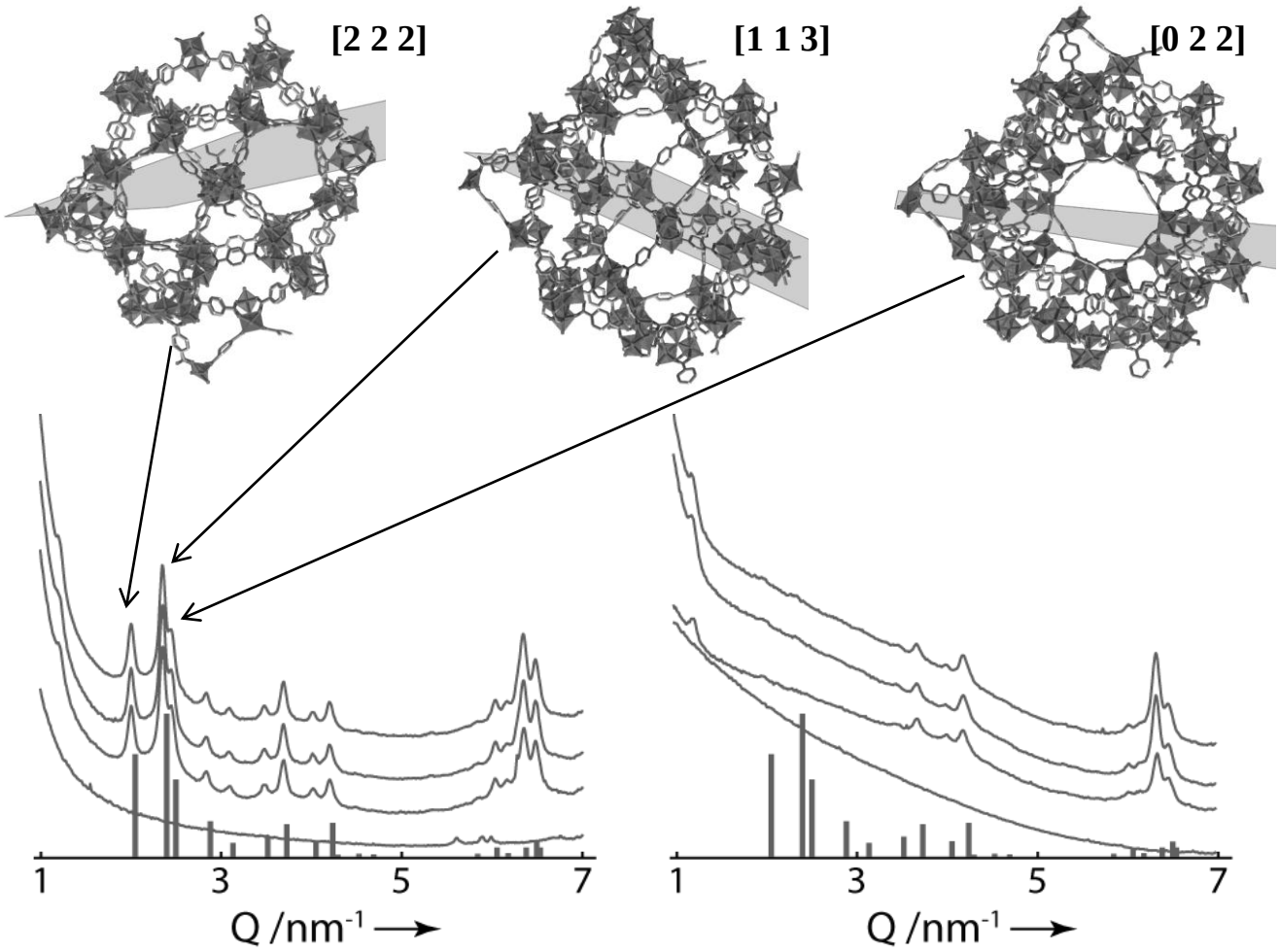

Figure 3 - 3 Comparison of X–ray diffraction pattern (500, 2500, 2600 and 2700s) of NH_2–MIL–101(Al) (*left*) and PTA/NH_2–MIL–101(Al) (*right*) at 413 K. Representation of the main planes attenuated by the PTA presence. (*Right*) [0 2 2] (Q = 1.96 nm^{-1}). (*Centre*) [1 1 3] (Q = 2.30 nm^{-1}). (*Left*) [2 2 2] (Q = 2.40 nm^{-1}).

Figure 3–3 shows four XRD spectra measured at different times for comparison between the NH_2–MIL–101(Al) and the PTA composite at 413 K. The intensity of the diffraction peaks at ~2 nm^{-1} is considerably lower when PTA is added: while the [1 1 1] Bragg reflection (Q = 1.20 nm^{-1}) is hardly affected, planes [0 2 2] (Q = 1.96 nm^{-1}), [1 1 3] (Q = 2.30 nm^{-1}) and [2 2 2] (Q = 2.40 nm^{-1}) almost disappear. The representation of the different attenuated diffraction planes is displayed in Figure 3–3. We attribute this intensity change to the successful encapsulation of the Keggin units in both medium and large cavities, in line with results presented earlier by Férey *et al.* after impregnation of similar moieties in MIL–101(Cr) [33] and by Canioni *et al.* after encapsulation of other POMs in MIL–100(Fe). [14] These results point to a very efficient encapsulation of the PTA [13] and suggest that the deprotonated, negatively charged, Keggin units act as nucleation sites for the MOF formation, while the influence of the amino groups in the linker cannot be evaluated from the results obtained. [15]

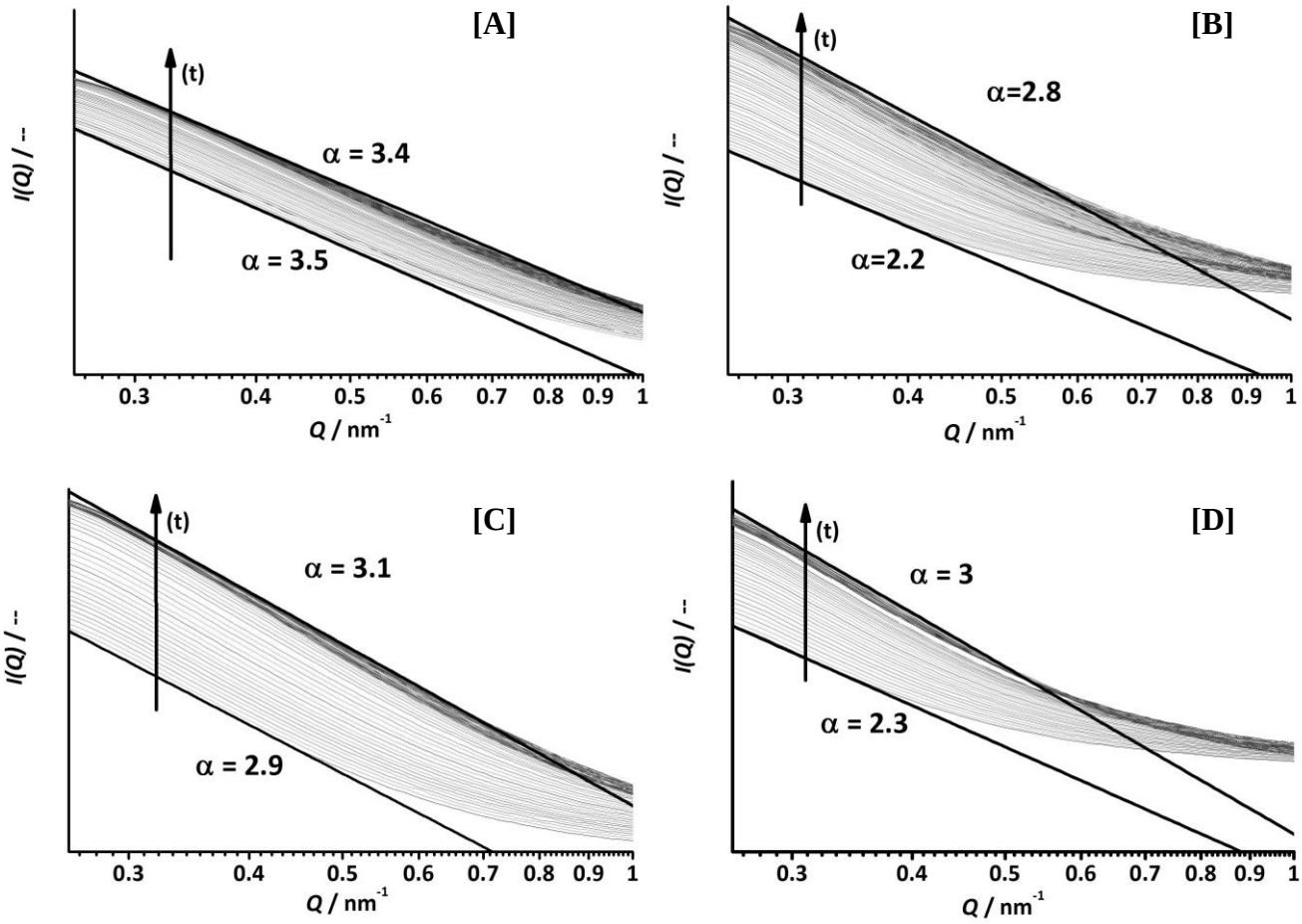

Figure 3 - 4 Selected $I(Q)$ profiles starting at time 0 until the beginning of the crystallization in log–log representation. Black lines illustrate the SAXS decay. (*Top*) T = 413 K. (*Bottom*) T = 403 K. (*Left*) NH_2–MIL–101(Al). (*Right*) PTA/NH_2–MIL–101(Al).

Time–resolved SAXS patterns show density fluctuations at early times that deserve special attention (Fig. 3–2). A more conspicuous view of changes in the scattering profile versus time is presented in

Figure 3–4, which shows a selection of the log $I(Q)$ – log Q plots measured at the beginning of the crystallization experiments at 413 (Fig. 3–4 *top*) and 403 K (Fig. 3–4 *bottom*) for both NH_2–MIL–101(Al) and PTA/NH_2–MIL–101(Al) before the appearance of the Bragg peaks. At 413 K, the SAXS intensity in both systems closely follows a power–law decay $Q^{-\alpha}$ with α between 3.5 and 3.4 for the NH_2–MIL–101(Al) and between 2.2 and 2.8 for the PTA containing system. The same trend is observed at lower temperatures (403 K) with α between 2.9 and 3.1 and from 2.3 to 3 for NH_2–MIL–101(Al) and PTA/NH_2–MIL–101(Al), respectively. In every case, the decay is slower than the asymptotic behavior of α = 4 predicted by the Porod law for a scatterer with smooth surfaces, [34] indicating that MOF systems have more complex multi–scale structures. [31]

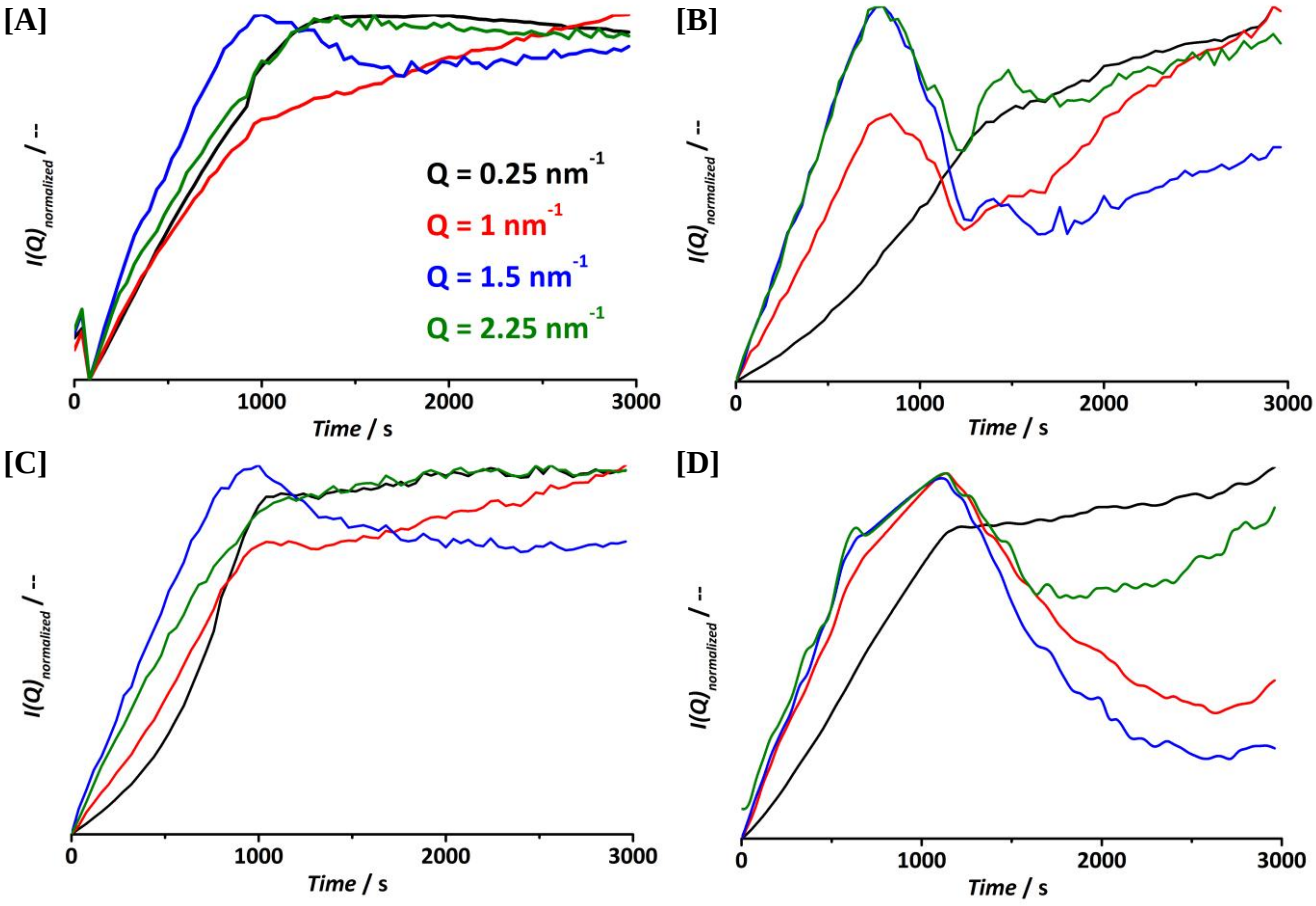

Figure 3 - 5 Development of the X–ray scattering with normalized intensities at different Q values. (*Black*) Q = 0.25 nm^{-1}. (*Red*) Q = 1 nm^{-1}. (*Blue*) Q = 1.5 nm^{-1}. (*Green*) Q = 2.25 nm^{-1}. (*Top*) T = 413 K. (*Bottom*) T = 403 K. (*Left*) NH_2–MIL–101(Al). (*Right*) PTA/NH_2–MIL–101(Al).

SAXS studies of the crystallization of different zeolites yielded α values of ~3, [35-38] suggesting that the formation of NH_2–MIL–101(Al) proceeds through an analogous precursor gel formation mechanism, with α values very similar and constant through the experiment. When PTA is added to the synthesis mixture, a clear change in the slope of the log $I(Q)$ *vs.* log Q plot can be observed, with α

values varying from 2 at the beginning of the experiment (mass fractal substance) [34, 39, 40] to almost 3 (only surface fractal and precursor gel formation mechanism) just before the onset of crystallization. The evolution of α values, when PTA is present, indicates two possible processes taking place, smoothening of the surface of the scattering particles and densification of the internal structure. [41] These results suggest that the PTA acts as a nucleation site, leading to complete efficiency of encapsulation.

The time development of the scattering intensity at 403 and 413 K is presented for different *Q* values in Figure 3–5. *Q* values were selected in such a way that they do not coincide with any Bragg reflection. In both temperature experiments for PTA/NH_2–MIL–101(Al) syntheses, the scattering intensity corresponding to *Q* values of 1, 1.5 and 2.25 nm^{-1} passes through a maximum. In contrast, NH_2–MIL–101(Al) experiments present an asymptotic evolution for all *Q* values except for Q = 1.5 nm^{-1}, in which a small decay takes place. In both cases, the decay in the slope of these scattering intensities coincides with the inflection in the scattering at Q = 0.25 nm^{-1} and with the onset of the development of MIL–101 Bragg reflection. In terms of local density fluctuations, the presence of PTA might form a higher number of primary units, which at the same time also form more aggregates, which need to be dissociated to boost crystallization. [30, 42] Temperature does not have any influence on the clusters dissolution occurring at *ca.* 800 seconds in both cases. However, the formation of new primary units is shown to be much faster with higher reaction temperatures, since *Q* values of 1 and 1.5 nm^{-1} only start growing around 3000 s. In fact, at lower temperatures (393 K) no formation of NH_2–MIL–101(Al) is observed, but its precursor phase NH_2–MOF–235(Al).

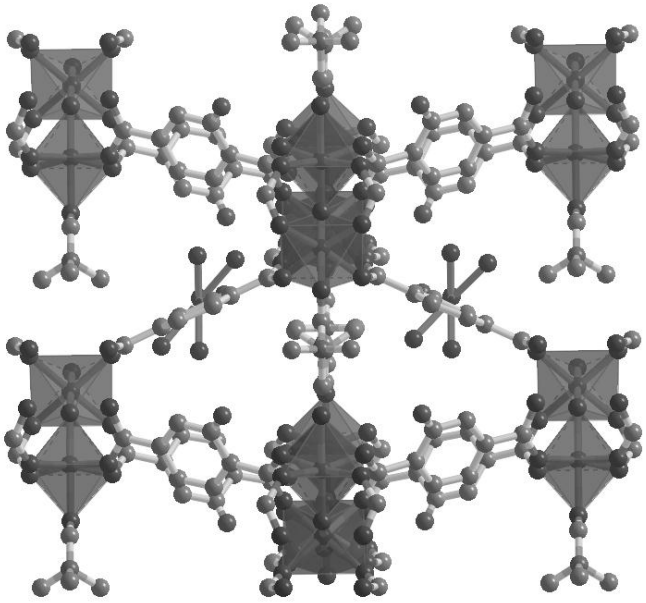

Figure 3 - 6 NH_2–MOF–235 (Al).

Very recently, we identified the NH_2–MOF–235(Al) (Fig. 3–6) structure as a precursor of the MIL–101 structure in the competitive formation of NH_2–MIL–101(Al) and NH_2–MIL–53(Al), [43] in agreement with Millange *et al.*, [26] who observed the formation of such MOF–235(Fe) phase prior to the formation of MIL–53(Fe). NH_2–MOF–235(Al) is composed of trimeric Al(III) clusters linked by amino–terephthalate in a similar fashion as MIL–101. [44]

The main Bragg reflection of this structure is predicted to appear at a *d*–spacing of 9.4 Å, corresponding to Q = 6.3 nm^{-1} and can be clearly identified at the beginning of every crystallization experiment (Fig. 3–7A and C). Notably, this reflection appears immediately at the onset of the crystallization and is the only observable reflection when PTA/NH_2–MIL–101(Al) is synthesized at 393 K (Fig. 3–7B and D). Along these lines, we attribute the evolution of the scattering shown in Figure 3–4 to the early formation of NH_2–MOF–235(Al) clusters with sizes in the range of 4–6 nm and 1–6 nm for NH_2–MIL–101(Al), and PTA/NH_2–MIL–101(Al), respectively. When no PTA is present, such clusters reconstruct into an ordered NH_2–MIL–101 phase, suggesting PTA stabilizes the intermediate stage. When PTA is present, a large number of the NH_2–MOF–235(Al) clusters at smaller typical length scales are formed, then re–dissolved and further reassembled into the NH_2–MIL–101(Al) phase. This can be deduced from the correlation between intensity decrease at small scales—NH_2–MOF–235(Al) breakdown—and, at the same time, growth of crystals at the larger scale—NH_2–MIL–101(Al) formation.

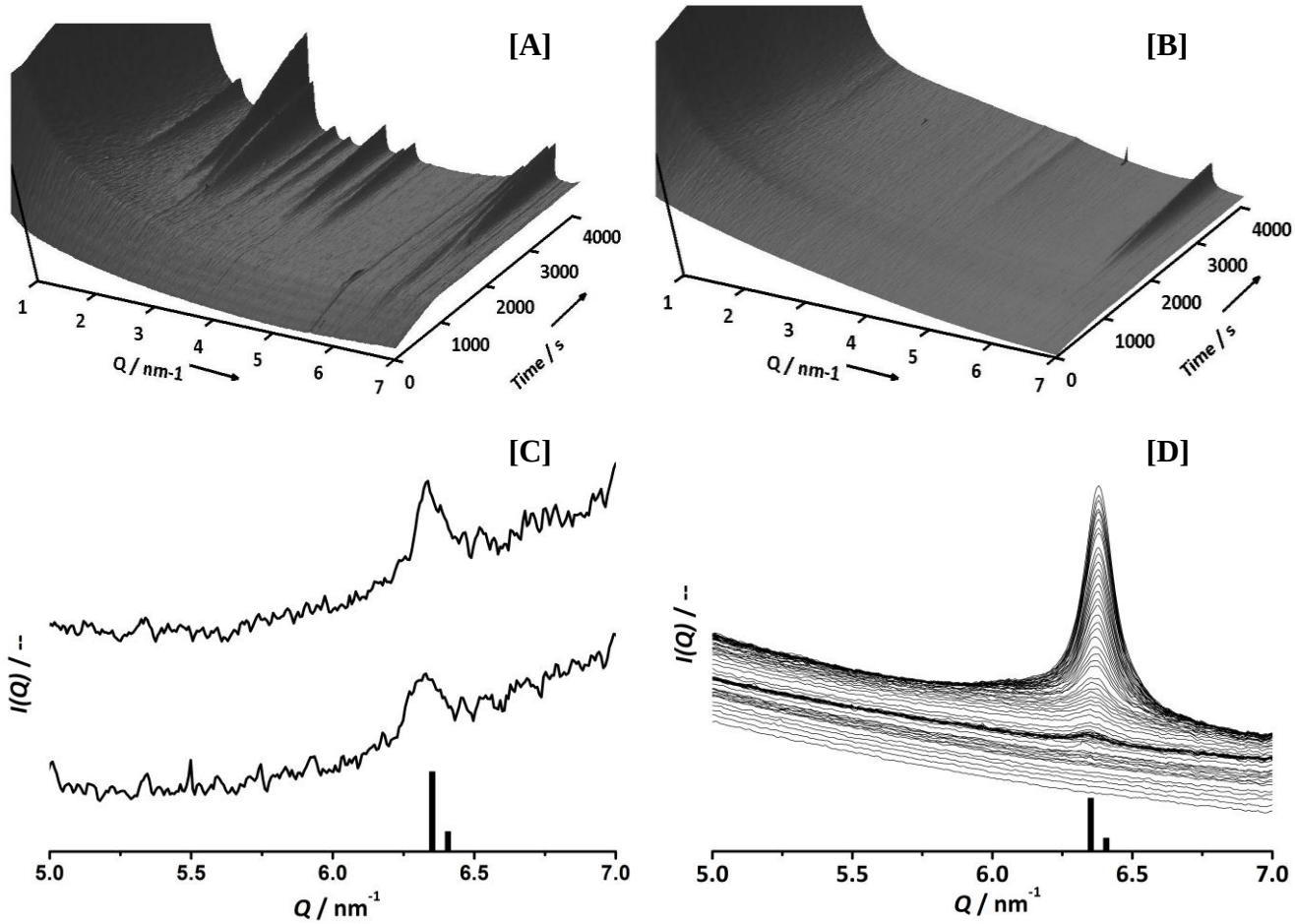

Figure 3 - 7 (*Top*) Time evolution X–ray scattering during the *in situ* synthesis of NH_2–MIL–101(Al) (*A*) and PTA/NH_2–MIL–101(Al) (*B*) at 393 K. (*C*) X–ray spectra taken during the first synthesis minutes of NH_2–MIL–101(Al) at 393 K. (*D*) X–ray spectra taken during the *in situ* synthesis of PTA/NH_2–MIL–101(Al) at 393 K. Solid bars are simulated MOF–235(Al) pattern.

Remarkably, the stability of both phases, NH_2–MIL–101(Al) and MOF–235(Al), seems to be enhanced in the presence of PTA, as inferred by the absence of decay in the Q = 0.25 nm^{-1} scattering and by the fact that experiments at lower temperature (393 K, Fig. 3–7) resulted in the selective formation of the MOF–235(Al) phase, while NH_2–MIL–101(Al) was formed at the same temperature in the PTA absence.

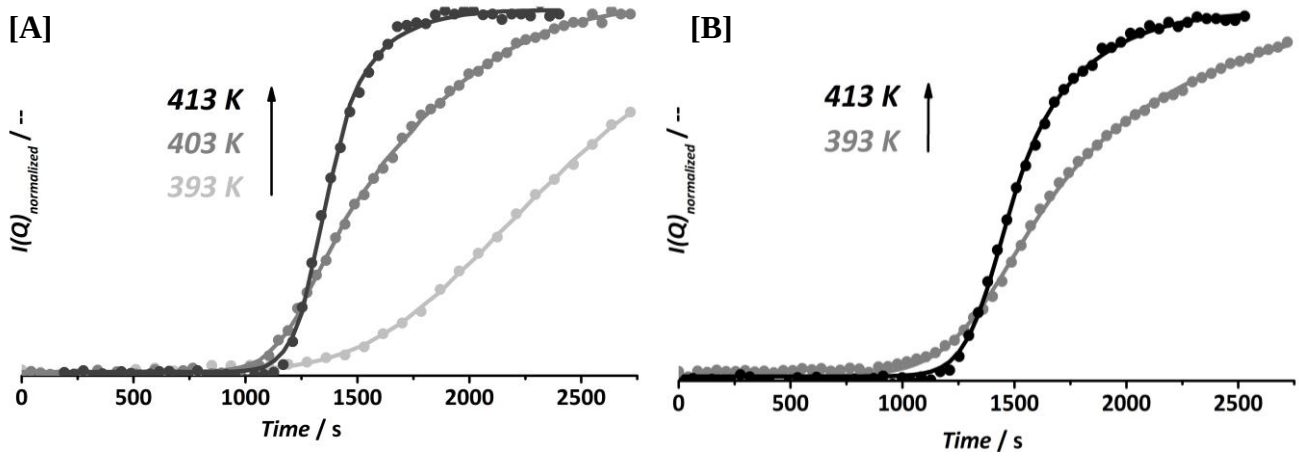

Figure 3 - 8 Extent of crystallization for 6.2 – 6.6 nm^{-1} profiles and fitting at different temperatures for: [A] NH_2–MIL–101(Al) and [B] PTA/NH_2–MIL–101(Al).

The crystallization was studied at different temperatures in order to quantify the kinetics of the process and the possible accelerating effects of the PTA in the MOF synthesis (Fig. 3–8). Analysis of the kinetic profiles was done by using the model developed by Gualtieri, as explained in the experimental section. [45] The fitting of the kinetic profiles yielded nucleation and growth rate constants, k_n and k_g, which are given in Table 3–1. From the Arrhenius plot (Fig. 3–9), the activation energies for nucleation and growth were found to be 50 and 17 kJ mol^{-1}, respectively, for the host MOF. Despite the fact that this values are within the range of previously reported data for HKUST–1 and MOF–14, [25] accuracy of this values is still very low since only three temperatures are measured.

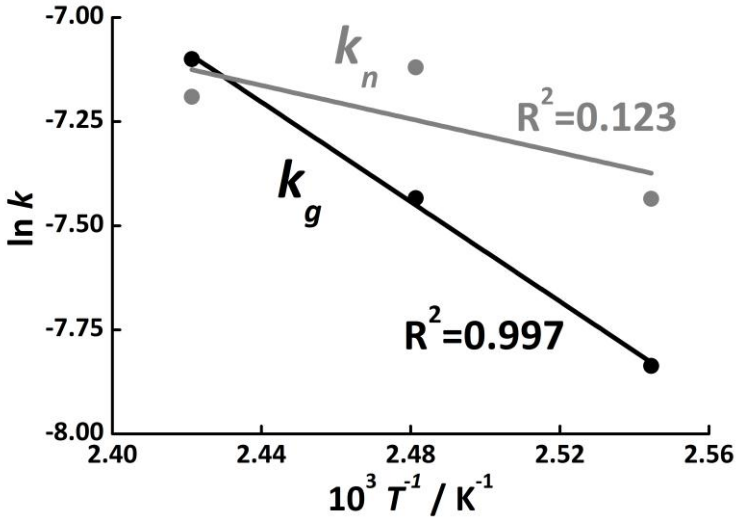

Figure 3 - 9 Arrhenius plot to calculate *Ea* of nucleation and growth constants of NH_2–MIL–101(Al).

On the other hand, values for the encapsulated POM/MOF composite could only be calculated for 393 and 413 K, where at the lowest temperature NH_2–MOF–235(Al) is formed, and the highest

temperature shows NH_2–MIL–101(Al) formation. Activation energies cannot be calculated, but comparing the values obtained for nucleation and growth constants (Table 3–1), the biggest differences are observed during growth, while nucleation seems to proceed very closely for both primary products PTA/NH_2–MIL–101(Al) and PTA/NH_2–MOF–235(Al).

Table 3 - 1 Crystal growth and nucleation rate constants for NH_2–MIL–101(Al) and PTA/NH_2–MIL–101(Al) crystallization estimated from the fitting of experimental profiles recorded at different temperatures. Values for activation energy and pre–exponential factors for growth and nucleation are included.

	T / K	n	b [s]	$k_g.10^4$ [s^{-1}]	A_g [s^{-1}]	$E_{a,g}$ [kJ mol^{-1}]	$k_n.10^4$ [s^{-1}]	A_n [s^{-1}]	$E_{a,n}$ [kJ mol^{-1}]
MOF	393	3	296 (±71)	3.9 (±0.64)	1632	50	5.9 (±0.44)	0.1	17
	403		101 (±9)	5.9 (±0.05)			8.1 (±0.07)		
	413		69 (±7)	8.2 (±0.27)			7.5 (±0.05)		
PTA / MOF-235	393	2	163 (±14)	5.6 (±0.26)	--	--	7.2 (±0.13)	--	--
PTA/MOF	413	3	86 (±7)	6.9 (±0.13)	--	--	7.1 (±0.04)	--	--

It has been suggested that together with a molecular templating effect, the addition of PTA to the synthesis mixture of HKUST–1 accelerates the rate of formation. [15] In contrast, for NH_2–MIL–101, this is clearly not the case: both nucleation and growth constants are hardly affected upon addition of PTA to the synthesis mixture, suggesting that once the primary units are formed, synthesis occurs at similar rates. Nevertheless, the results clearly indicate an effect of PTA in the formation of primary units, while temperature doesn't show strong influence in the first stages, but it becomes important in the growth of the nuclei.

One of the future challenges is to determine whether the PTA is already encapsulated in the MOF–235 in the early stage of the synthesis. In this light it is emphasized that other methods such as vibrational spectroscopy, X–ray absorption techniques and NMR should be combined with SAXS/WAXS in order to obtain complete chemical information of the different units assembled during crystallization.

3.4. CONCLUSION

Based on kinetic analysis of combined small– and wide–angle scattering profile analysis, the major events taking place during the encapsulation of PTA in NH_2–MIL–101 could be identified. The presence of PTA not only stabilizes the MOF–235 phase, but also promotes the fractal growth of this structure (α values starting from 2 and developing towards 3 values). Whereas in the absence of PTA, assembly of the disordered MOF–235 phase rapidly occurs to form small clusters of NH_2–MIL–101(Al) with smoother surfaces (α *ca.* 3.5 values).

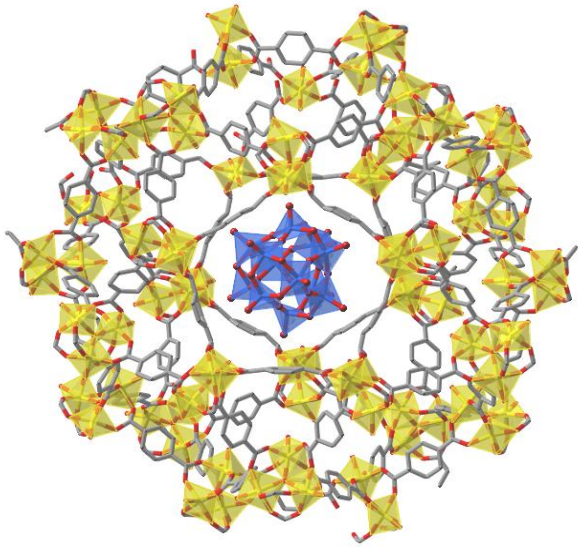

Figure 3 - 10 PTA encapsulated in MIL-101

Results infer that the high concentration of negatively charged PTA moieties in solution provides a large number of nucleation sites that promote fast formation of MOF–235 subunits that rapidly aggregate, giving rise to fractal–like structures. Once the crystallization of the MIL–101 phase begins, such agglomerates fall apart, and the PTA nuclei are encapsulated in the growing MIL–101 matrix.

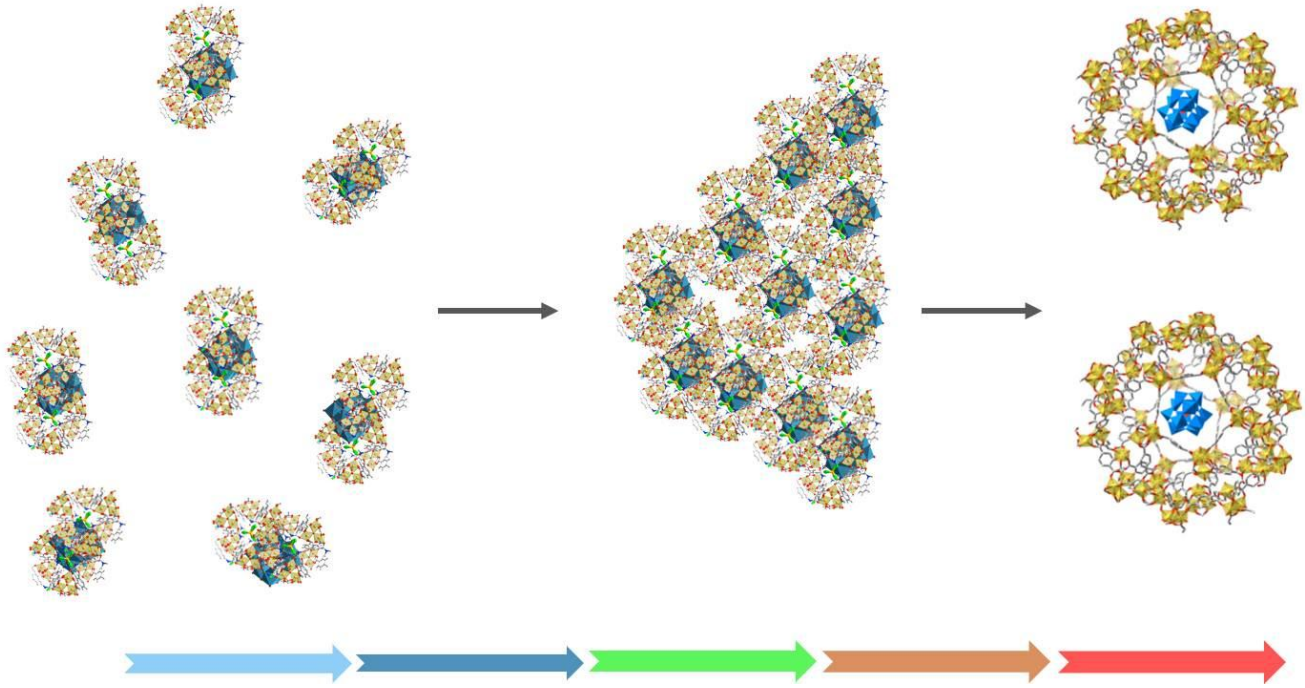

Figure 3 - 11 Crystallization mechanism hypothesis through fractal growth of PTA stabilizing NH_2–MOF–235(Al).

REFERENCES

[1] J.R. Long, O.M. Yaghi, The pervasive chemistry of metal-organic frameworks, Chemical Society Reviews, 38 (2009) 1213-1214.
[2] K. Sumida, D.L. Rogow, J.A. Mason, T.M. McDonald, E.D. Bloch, Z.R. Herm, T.-H. Bae, J.R. Long, Carbon dioxide capture in metal-organic frameworks, Chemical Reviews, 112 (2011) 724-781.
[3] A. Corma, H. García, F.X. Llabrés i Xamena, Engineering metal-organic frameworks for heterogeneous catalysis, Chemical Reviews, 110 (2010) 4606-4655.
[4] M.P. Suh, H.J. Park, T.K. Prasad, D.-W. Lim, Hydrogen storage in metal-organic frameworks, Chemical Reviews, 112 (2011) 782-835.
[5] J. Juan-Alcañiz, J. Gascon, F. Kapteijn, Metal-organic frameworks as scaffolds for the encapsulation of active species: state of the art and future perspectives, Journal of Materials Chemistry, 22 (2012) 10102-10118.
[6] Y. Yang, S. Liu, C. Li, S. Li, G. Ren, F. Wei, Q. Tang, A metal-organic framework based on Wells-Dawson polyoxometalates [As 2W 18O 62] 6 - template, Inorganic Chemistry Communications, (2012).
[7] J.Q. Sha, J.W. Sun, C. Wang, G.M. Li, P.F. Yan, M.T. Li, M.Y. Liu, Syntheses of POM-templated MOFs containing the isomeric pyridyltetrazole, CrystEngComm, 14 (2012) 5053-5064.
[8] M.H. Alkordi, Y. Liu, R.W. Larsen, J.F. Eubank, M. Eddaoudi, Zeolite-like metal-organic frameworks as platforms for applications: On metalloporphyrin-based catalysts, Journal of the American Chemical Society, 130 (2008) 12639-12641.
[9] Q. Chen, C. Xin, L.L. Lou, K. Yu, F. Ding, S. Liu, Polyoxometalate Supported Cinchona-Derived Chiral Amine for Asymmetric Organocatalysed Aldol Reaction, Journal of Inorganic and Organometallic Polymers and Materials, (2012) 1-5.
[10] I.V. Kozhevnikov, Catalysis by Heteropoly Acids and Multicomponent Polyoxometalates in Liquid-Phase Reactions, Chemical Reviews, 98 (1998) 171-198.
[11] D. Jiang, L.L. Keenan, A.D. Burrows, K.J. Edler, Synthesis and post-synthetic modification of MIL-101(Cr)-NH_2 via a tandem diazotisation process, Chemical Communications, 48 (2012) 12053-12055.
[12] C.Y. Sun, S.X. Liu, D.D. Liang, K.Z. Shao, Y.H. Ren, Z.M. Su, Highly stable crystalline catalysts based on a microporous metal-organic framework and polyoxometalates, Journal of the American Chemical Society, 131 (2009) 1883-1888.
[13] J. Juan-Alcañiz, E.V. Ramos-Fernandez, U. Lafont, J. Gascon, F. Kapteijn, Building MOF bottles around phosphotungstic acid ships: One-pot synthesis of bi-functional polyoxometalate-MIL-101 catalysts, Journal of Catalysis, 269 (2010) 229-241.
[14] R. Canioni, C. Roch-Marchal, F. Sécheresse, P. Horcajada, C. Serre, M. Hardi-Dan, G. Férey, J.M. Grenèche, F. Lefebvre, J.S. Chang, Y.K. Hwang, O. Lebedev, S. Turner, G. Van Tendeloo, Stable polyoxometalate insertion within the mesoporous metal-organic framework MIL-100(Fe), Journal of Materials Chemistry, 21 (2011) 1226-1233.
[15] S.R. Bajpe, C.E.A. Kirschhock, A. Aerts, E. Breynaert, G. Absillis, T.N. Parac-Vogt, L. Giebeler, J.A. Martens, Direct observation of molecular-level template action leading to self-assembly of a porous framework, Chemistry - A European Journal, 16 (2010) 3926-3932.
[16] L.H. Wee, S.R. Bajpe, N. Janssens, I. Hermans, K. Houthoofd, C.E.A. Kirschhock, J.A. Martens, Convenient synthesis of $Cu_3(btc)_2$ encapsulated Keggin heteropolyacid nanomaterial for application in catalysis, Chemical Communications, 46 (2010) 8186-8188.
[17] S. Kayaert, S. Bajpe, K. Masschaele, E. Breynaert, C.E.A. Kirschhock, J.A. Martens, Direct growth of Keggin polyoxometalates incorporated copper 1,3,5-benzenetricarboxylate metal organic framework films on a copper metal substrate, Thin Solid Films, 519 (2011) 5437-5440.
[18] S.R. Bajpe, E. Breynaert, D. Mustafa, M. Jobbágy, A. Maes, J.A. Martens, C.E.A. Kirschhock, Effect of Keggin polyoxometalate on Cu(II) speciation and its role in the assembly of $Cu_3(btc)_2$ metal-organic framework, Journal of Materials Chemistry, 21 (2011) 9768-9771.
[19] N. Janssens, L.H. Wee, S. Bajpe, E. Breynaert, C.E.A. Kirschhock, J.A. Martens, Recovery and reuse of heteropolyacid catalyst in liquid reaction medium through reversible encapsulation in $Cu_3(btc)_2$ metal-organic framework, Chemical Science, 3 (2012) 1847-1850.
[20] L.H. Wee, C. Wiktor, S. Turner, W. Vanderlinden, N. Janssens, S.R. Bajpe, K. Houthoofd, G. Van Tendeloo, S. De Feyter, C.E.A. Kirschhock, J.A. Martens, Copper benzene tricarboxylate metal-organic framework with wide permanent mesopores stabilized by keggin polyoxometallate ions, Journal of the American Chemical Society, 134 (2012) 10911-10919.
[21] N.A. Khan, S.H. Jhung, Phase-transition and phase-selective synthesis of porous chromium-benzenedicarboxylates, Crystal Growth and Design, 10 (2010) 1860-1865.
[22] M. Kim, J.F. Cahill, H. Fei, K.A. Prather, S.M. Cohen, Post-synthetic ligand and cation exchange in robust metal-organic frameworks, Journal of the American Chemical Society, 134 (2012) 18082-18088.
[23] A. Sutrisno, Y. Huang, Solid-state NMR: A powerful tool for characterization of metal-organic frameworks, Solid State Nuclear Magnetic Resonance, 49-50 (2012) 1-11.

[24] R. Ameloot, F. Vermoortele, J. Hofkens, F.C. De Schryver, D.E. De Vos, M.B.J. Roeffaers, Three-dimensional visualization of defects formed during the synthesis of metal-organic frameworks: a fluorescence microscopy study, Angewandte Chemie International Edition, 52 (2013) 401-405.
[25] F. Millange, R. El Osta, M.E. Medina, R.I. Walton, A time-resolved diffraction study of a window of stability in the synthesis of a copper carboxylate metal-organic framework, CrystEngComm, 13 (2011) 103-108.
[26] M.J. Ingleson, J.P. Barrio, J. Bacsa, C. Dickinson, H. Park, M.J. Rosseinsky, Generation of a solid Brønsted acid site in a chiral framework, Chemical Communications, (2008) 1287-1289.
[27] P. Horcajada, S. Surblé, C. Serre, D.Y. Hong, Y.K. Seo, J.S. Chang, J.M. Greneche, I. Margiolaki, G. Férey, Synthesis and catalytic properties of MIL-100(Fe), an iron(III) carboxylate with large pores, Chemical Communications, (2007) 2820-2822.
[28] P. Serra-Crespo, E.V. Ramos-Fernandez, J. Gascon, F. Kapteijn, Synthesis and Characterization of an Amino Functionalized MIL-101(Al): Separation and Catalytic Properties, Chemistry of Materials, 23 (2011) 2565-2572.
[29] J. Juanhuix, A. Labrador, D. Beltrán, J.F. Herranz, P. Carpentier, J. Bordas, The macromolecular crystallography station at beamline BM16 at the ESRF, Review of Scientific Instruments, 76 (2005) 1-4.
[30] P.P.E.A. De Moor, T.P.M. Beelen, R.A. van Santen, L.W. Beck, M.E. Davis, Si-MFI crystallization using a "dimer" and "trimer" of TPA studied with small-angle x-ray scattering, Journal of Physical Chemistry B, 104 (2000) 7600-7611.
[31] K. Malekani, J.A. Rice, J.S. Lin, Comparison of techniques for determining the fractal dimensions of clay minerals, Clays and Clay Minerals, 44 (1996) 677-685.
[32] A.F. Gualtieri, Synthesis of sodium zeolites from a natural halloysite, Physics and Chemistry of Minerals, 28 (2001) 719-728.
[33] C. Férey, C. Mellot-Draznieks, C. Serre, F. Millange, J. Dutour, S. Surblé, I. Margiolaki, Chemistry: A chromium terephthalate-based solid with unusually large pore volumes and surface area, Science, 309 (2005) 2040-2042.
[34] C. Serre, F. Millange, C. Thouvenot, M. Nogues, G. Marsolier, D. Louer, G. Férey, Very large breathing effect in the first nanoporous chromium(III)-based solids: MIL-53 or CrIII(OH){O_2C-C_6H_4-CO_2}{HO_2C-C_6H_4-CO_2H}xH_2Oy, Journal of the American Chemical Society, 124 (2002) 13519-13526.
[35] R. Yu, X.F. Kuang, X.Y. Wu, C.Z. Lu, J.P. Donahue, Stabilization and immobilization of polyoxometalates in porous coordination polymers through host-guest interactions, Coordination Chemistry Reviews, 253 (2009) 2872-2890.
[36] A.M. Beale, A.M.J. van der Eerden, S.D.M. Jacques, O. Leynaud, M.G. O'Brien, F. Meneau, S. Nikitenko, W. Bras, B.M. Weckhuysen, A Combined SAXS/WAXS/XAFS Setup Capable of Observing Concurrent Changes Across the Nano-to-Micrometer Size Range in Inorganic Solid Crystallization Processes, Journal of the American Chemical Society, 128 (2006) 12386-12387.
[37] X. Zhao, D. Liang, S. Liu, C. Sun, R. Cao, C. Gao, Y. Ren, Z. Su, Two Dawson-templated three-dimensional metal-organic frameworks based on oxalate-bridged binuclear cobalt(II)/nickel(II) SBUs and Bpy linkers, Inorganic Chemistry, 47 (2008) 7133-7138.
[38] S. Surblé, F. Millange, C. Serre, G. Férey, R.I. Walton, An EXAFS study of the formation of a nanoporous metal-organic framework: Evidence for the retention of secondary building units during synthesis, Chemical Communications, (2006) 1518-1520.
[39] M. Shoaee, M.W. Anderson, M.P. Attfield, Crystal growth of the nanoporous metal-organic framework HKUST-1 revealed by in situ atomic force microscopy, Angewandte Chemie - International Edition, 47 (2008) 8525-8528.
[40] S. Hermes, T. Witte, T. Hikov, D. Zacher, S. Bahnmüller, G. Langstein, K. Huber, R.A. Fischer, Trapping metal-organic framework nanocrystals: An in-situ time-resolved light scattering study on the crystal growth of MOF-5 in solution, Journal of the American Chemical Society, 129 (2007) 5324-5325.
[41] M.G. Goesten, E. Stavitski, J. Juan-Alcañiz, A. Martinez-Joaristi, A.V. Petukhov, F. Kapteijn, J. Gascon, Small-angle X-ray scattering documents the growth of metal-organic frameworks, Catalysis Today, 205 (2013) 120-127.
[42] P.P.E.A. De Moor, T.P.M. Beelen, B.U. Komanschek, L.W. Beck, P. Wagner, M.E. Davis, R.A. Van Santen, Imaging the assembly process of the organic-mediated synthesis of a zeolite, Chemistry - A European Journal, 5 (1999) 2083-2088.
[43] E. Stavitski, M. Goesten, J. Juan-Alcañiz, A. Martinez-Joaristi, P. Serra-Crespo, A.V. Petukhov, J. Gascon, F. Kapteijn, Kinetic control of metal-organic framework crystallization investigated by time-resolved in situ X-ray scattering, Angewandte Chemie International Edition, 50 (2011) 9624-9628.
[44] F. Millange, M.I. Medina, N. Guillou, G. Férey, K.M. Golden, R.I. Walton, Time-resolved in situ diffraction study of the solvothermal crystallization of some prototypical metal-organic frameworks, Angewandte Chemie - International Edition, 49 (2010) 763-766.
[45] G. Seeber, G.J.T. Cooper, G.N. Newton, M.H. Rosnes, D.L. Long, B.M. Kariuki, P. Kögerler, L. Cronin, Following the self assembly of supramolecular MOFs using X-ray crystallography and cryospray mass spectrometry, Chemical Science, 1 (2010) 62-67.

Chapter 4

Towards efficient polyoxometalate encapsulation in MIL–100(Cr): Influence of synthesis conditions

This chapter is based on the following publication:

J. Juan–Alcañiz, M. Goesten, E.V. Ramos–Fernandez, J. Gascon, F. Kapteijn, New J. Chem., 36 (2012) 977–987

Abstract The effect of synthesis conditions on the one–pot encapsulation of phosphotungstic acid (PTA, $H_3PW_{12}O_{40}.xH_2O$) in the porous structure named MIL–100(Cr) has been studied. Both conventional and microwave heating methods have been explored in three different solvent systems: pure aqueous or organic (DMF) phase and biphasic mixtures (water/2–pentanol). Biphasic systems yielded crystals with similar textural properties as those formed in water. The use of DMF as solvent promotes the formation of gel–like solids with dual porosity and enhanced accessibility. The addition of PTA to the MIL–100(Cr) synthesis mixture results in its direct encapsulation, confirmed by ^{31}P MAS NMR, elemental analysis, N_2 adsorption and DRIFT. The best combination for PTA/MIL–100(Cr) composite formation was obtained under microwave irradiation in biphasic solvent, with encapsulation loadings around 30 wt%. Microwave irradiation decreases the time of synthesis (from 4 days to 3 hours) while the use of biphasic media preserve PTA's integrity without affecting the MOF structure formation. The interaction of PTA with MIL–100(Cr) results in a loss of framework Lewis acidity, while the Brønsted acidity is hardly affected. Although PTA in its protonated form is considered as a super Brønsted acid molecule, after encapsulation in MIL–100(Cr) hardly any additional acidity is observed.

4.1. INTRODUCTION

One of the most promising methods towards catalytic applications of MOFs is the one–pot encapsulation of active species following the so–called ‘‘ship in a bottle’’ approach. [1-5] Among the different encapsulation possibilities, the stabilisation and immobilisation of Keggin–type polyoxometalates (POMs) through the formation of POM containing coordination polymers has recently attracted a lot of attention. [2, 6-9]

Keggin–type POMs are large and complex polyatomic ions, possessing very good thermal stability, excellent redox properties and often approaching the super–acid region in their protonic form. [10-12] However, the specific surface area of these solid materials is very low (generally in the range of 1 to 5 $m^2\ g^{-1}$) making dispersion on a good support crucial for eventual application. Several attempts at supporting Keggin POMs on materials like silica, activated carbons or zeolites have been made. [9, 13, 14] However, low POM loadings, agglomeration or leaching are still important limitations. Recently, several studies of POM based MOFs have been reported. Sun *et al.* presented the direct encapsulation of POMs in HKUST–1. [15] At the same time, we reported the successful one–pot encapsulation of similar POMs in the large and medium mesoporous cavities of MIL–101(Cr), achieving a highly dispersed material with outstanding catalytic performance in Knoevenagel condensation reactions and acid–catalysed reactions. [1] The same one–pot procedure was later used for the application of POM/MIL–101 in the dehydration of sugars and the use of NENU (POM/HKUST–1 composite) in methanol dehydration to DME and the formation of ethyl acetate from acetic acid and ethylene. [16, 17] Bajpe *et al.* studied POM templating properties observed during the one–step POM/HKUST–1 synthesis, while acidic catalytic properties in esterification reactions were also described by the same group. [18, 19] *In situ* time resolved X–ray scattering has been used lately to monitor POM templating effects. [5] Recently, Ma *et al.* made use of one–pot encapsulation for the adsorption and further hydrolysis of dimethyl methylphosphonate in the so–called NENU–11 [20] and Canioni *et al.* successfully incorporated different POMs in MIL–100(Fe) through microwave irradiation. [21]

Strikingly, POM encapsulation has been extensively studied in HKUST–1, but hardly in other MOF structures with bigger cavities and windows. Among the thousands of known structures, MIL–101 and MIL–100, that combine high surface areas and pore volumes with an excellent thermal and chemical stability, are of particular interest. [22, 23] Topologies incorporating mesoporous cages communicated by microporous windows present excellent opportunities for the encapsulation of relatively large active species. In particular, the MIL–100 structure is built up from trivalent metal oxide clusters (iron, aluminium and chromium) coordinated with benzene–1,3,5–tricarboxylate. Its extended MTN topology offers meso–cages of 25–29 Å connected through micro–windows of 5–9 Å. While POM

incorporation in MIL–101 might face leaching from the large cavities, as their windows are slightly larger than the critical diameter of a Keggin unit (16 Å versus 14 Å), the smaller window sizes in MIL–100 are ideal for the encapsulation of POMs while avoiding leaching.

Here, we report the successful encapsulation of a Keggin–type POM, the so–called phosphotungstic acid (PTA, $H_3PW_{12}O_{40}$), in the cavities of the highly stable MIL–100(Cr). An extensive study is provided on the main parameters that influence the MOF synthesis, as well as PTA stability upon encapsulation. Influence of solvent, heating methods and fluoride donor species are the investigated parameters. The resulting composites are thoroughly characterized by N_2 adsorption, thermo–gravimetric analysis and powder X–ray diffraction. PTA encapsulation has been proven by ^{31}P MAS NMR, elemental analysis and DRIFT spectroscopy.

4.2. EXPERIMENTAL

All the chemicals were obtained from Sigma–Aldrich and used without further purification, unless otherwise stated: N,N–dimethylformamide (DMF, 499.9%), 2–pentanol (98%), chromium oxide (CrO_3, ACS reagent, 498.0%), benzene–1,3,5–tricarboxylic acid (TMA, trimesic acid, 95%), hydrofluoric acid (HF, TraceSELECT, for trace analysis, 47–51% acidimetric), sodium fluoride (NaF, ACS reagent, 499%) and phosphotungstic acid hydrate (PTA, $H_3PW_{12}O_{40}.xH_2O$, reagent grade).

Three solvent systems were used for the hydrothermal and microwave synthesis of MIL–100(Cr): distilled water (24 g), DMF (24 g) and a biphasic system composed of distilled water (12 g) and rac–2–pentanol (12 g). In addition, two different fluoro donors were tested (5 mmol): aqueous HF and NaF.

4.2.1. Catalysts preparation

Hydrothermal synthesis: [24] was carried out by adding chromium(VI) oxide (0.5 g, 5 mmol) and trimesic acid (1.05 g, 5 mmol) to three different solvent systems and two fluoro donors. The reaction mixture was stirred for 10 min at room temperature, and then placed in a Teflon–lined stainless steel autoclave and heated up to 493 K (heating rate of 30 K min^{-1}) for 96 h in an oven under static conditions. The solid reaction product was then filtered off and washed with distilled water and acetone and dried at 433 K during 8 h.

Microwave synthesis: following the previously described mixture procedure, the reaction mixture was placed in a Teflon autoclave inside a microwave oven (Mycrosynth plus model ACT38) with automatic temperature control (ATC–TO). The synthesis was performed at 453 K for 3 h at a rate of 30 K min^{-1} while stirring the solution. The reaction product was then filtered off and washed with distilled water and acetone and dried at 433 K during 8 h.

One–pot synthesis of PTA encapsulated in MIL–100(Cr): was performed by adding two different quantities of PTA (0.8 g, 0.27 mmol or 0.4 g, 0.14 mmol) to the above mentioned synthesis solution, resulting in 14 mM (W/Cr molar ratio = 0.66) or 7 mM (W/Cr molar ratio = 0.33) PTA, respectively. Then, microwave or conventional heating syntheses were performed as explained above.

4.2.2. Characterization techniques

(a) Transmission Electron Microscopy (TEM): was carried out with a JEOL model JEM–210 electron microscope working at 200 kV and equipped with an INCA Energy TEM 100 analytical system and a SIS MegaView II camera. The samples were suspended in methanol and placed on a copper grid with a holey–carbon film support. *(b) Scanning Electron Microscopy (SEM):* was performed in a JEOL JSM 6500F setup. *(c) Nitrogen adsorption at 77 K:* was measured in a Quantachrome Autosorb–6B unit gas adsorption analyzer, determining textural properties like BET surface area (calculated from data between 0.05 and 0.15 relative pressure) and the nitrogen uptake volume (0.5 relative pressure). The samples were pre–treated under vacuum for 16 hours at 473 K. *(d) Powder X–Ray Diffraction (PXRD):* was analyzed using Bruker–AXS D5005 with CuKa or CoKa radiation (specified in each graph). *(e) Thermo–gravimetric Analysis (TGA):* was performed by means of a Mettler Toledo TGA/SDTA851e, under an air flow of 60 mL min^{-1} at heating rates of 10 K min^{-1} up to 873 K. *(f) Inductively Coupled Plasma Optical Emission Spectroscopy (ICP–OES):* the samples were digested in duplo in a mixture of 1% HF and 1.25% H_2SO_4 under microwave irradiation, and then they were analyzed with an ICP–OES Perkin Elmer Optima 5300dv. *(g) Diffuse Reflectance Infrared Fourier Transform Spectroscopy (DRIFTS):* was recorded on a Nicolet model 8700 spectrometer, equipped with a high–temperature DRIFT cell, DTGS–TEC detector and a 633 nm laser. The spectra were registered from 4000 to 600 cm^{-1} after accumulation of 256 scans and a resolution of 4 cm^{-1} under a helium flow of 20 mL min^{-1}. The samples were pre–treated under the same helium flow at 473 K for 60 min. KBr was used to perform background experiments. *(h) FT–IR transmission spectroscopy combined with CO adsorption:* was measured from 7.5 mg of self–supported MOF pellets. The pellets were placed in an IR quartz cell equipped with CaF_2 windows. A movable sample holder allows the sample to be placed in the infrared beam for the measurements or into the furnace for thermal treatments. The specimen is activated in vacuum at 453 K for two hours. After this step the samples were cooled down to 143 K and CO was dosed up to 2 mbar. Transmission spectra were recorded in the 400–4000 cm^{-1} range at 4 cm^{-1} resolution on a Nicolet Nexus spectrometer equipped with an extended KBr beam splitting and a mercury cadmium telluride (MCT) cryo–detector. *(i) ^{31}P Magic Angle Spinning Nuclear Magnetic Resonance Spectroscopy (MAS NMR):* was measured on a Bruker Avance–400 spectrometer at 161.98 MHz, using a solid–state probe and zirconium sample holders with inner diameter of 3 mm, spinning at

the magic angle with a rate of 11 kHz. The spectral width is 617.76 ppm, acquisition time of 12.5 ms and acquisition delay of 10 s. Chemical shifts are reported in ppm referring to an external standard: 85% of H_3PO_4 (0 ppm).

4.3. RESULTS

4.3.1. Solvent

The MIL–100(Cr) samples are synthesized in three different solvent systems, namely water, biphasic (H_2O/2–pentanol, 50/50 wt%) and DMF (using HF unless otherwise stated), denoted as: MIL–100(Cr) –water, –biphasic or –DMF, respectively.

4.3.1.1. Conventional Hydrothermal Syntheses

4.3.1.1.1. Powder X–Ray Diffraction

Figure 4–1 shows the PXRD patterns of hydrothermally synthesized MIL–100(Cr) according to the three different synthesis procedures. The diffraction patterns of all samples are assigned to the MTN topology and they are in agreement with literature data for MIL–100. [23] The crystallinity of MIL–100(Cr)–biphasic is lower than that of the water sample, but confirms the formation of pure MIL–100(Cr). MIL–100(Cr)–DMF as–synthesized displays—in contrast—a gel–like appearance with broader XRD reflections, due to the small particle size and to the possible parallel formation of an amorphous phase.

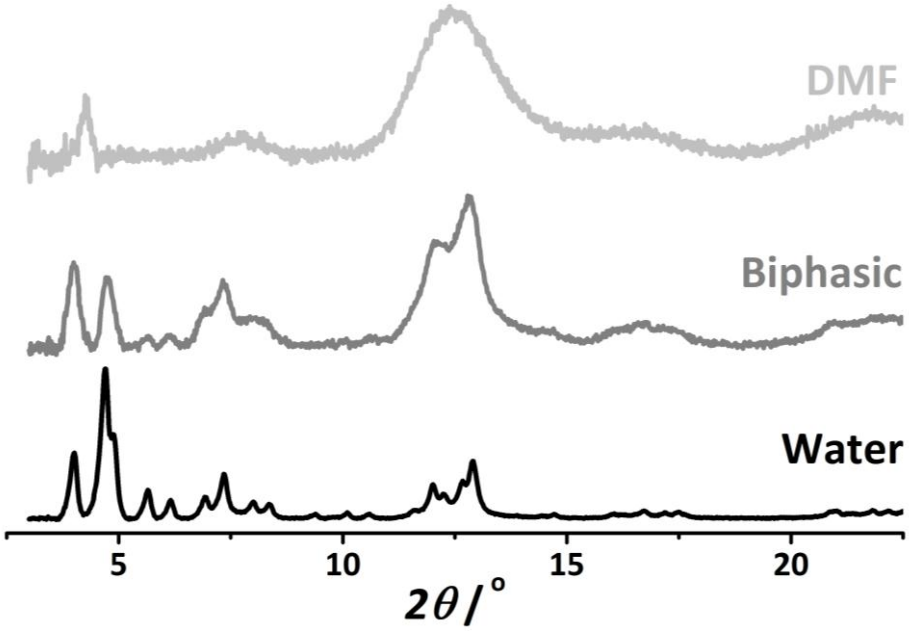

Figure 4 - 1 PXRD–CoKα pattern of different MIL–100(Cr) samples synthesized by conventional heating (static oven) using different solvent systems.

4.3.1.1.2. Electron Microscopy

SEM micrographs in Figure 4–2 show differentiated particles of around 500 nm in size for the water system, while smaller and less defined crystals, in the form of aggregates are observed for the biphasic sample.

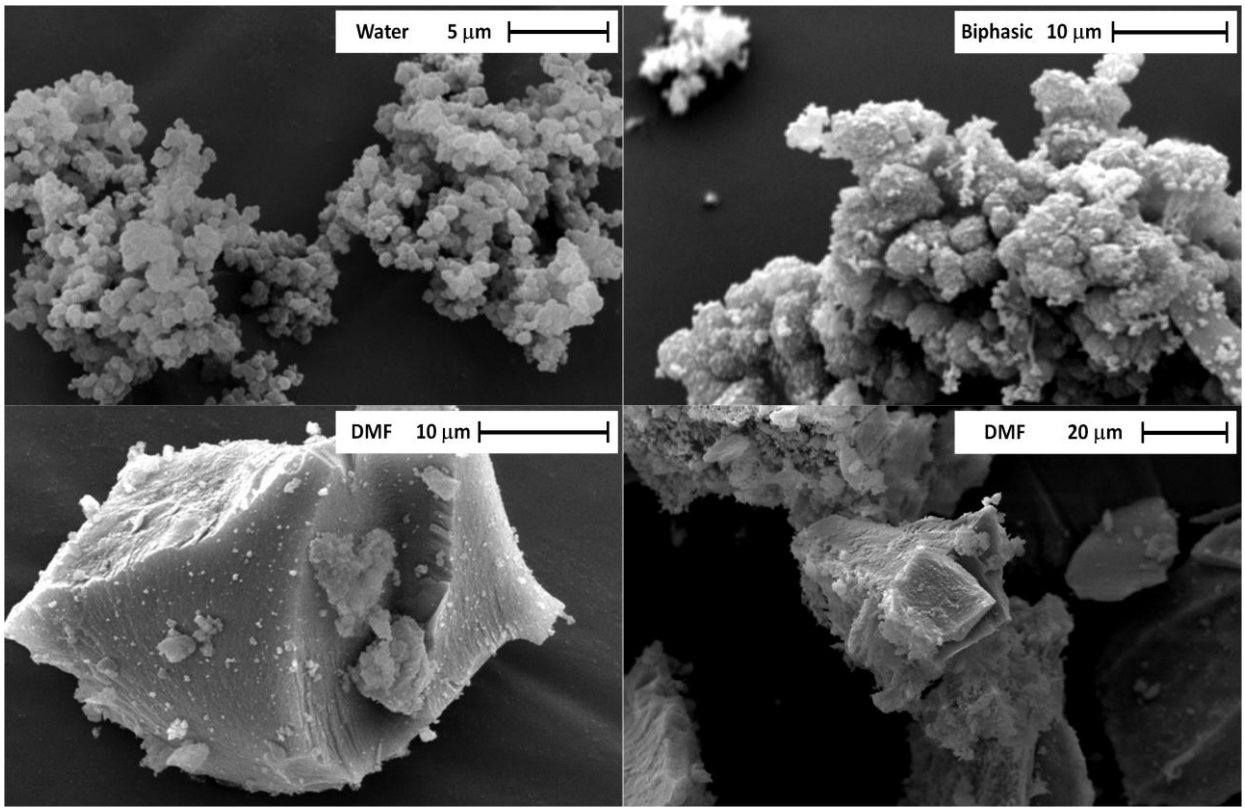

Figure 4 - 2 SEM pictures of different samples: MIL–100(Cr) synthesized by conventional heating using water, DMF or biphasic water/2–pentanol (*50:50* wt%) system as solvents.

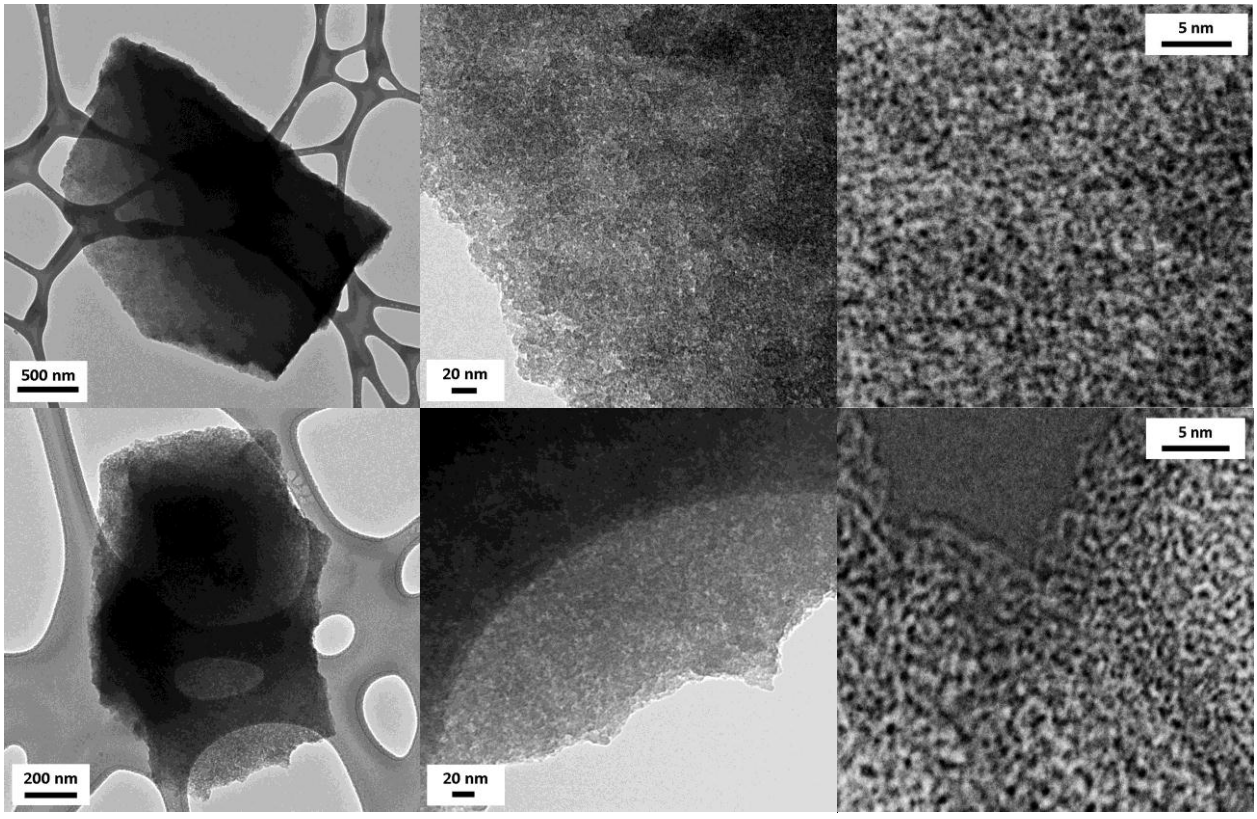

Figure 4 - 3 TEM micrographs of MIL–100(Cr) synthesized with DMF as solvent. (*Top*) Conventional heating. (*Bottom*) Microwave radiation

Big lumps appear when the solid is synthesized in DMF, while TEM pictures of these large agglomerates (Fig. 4–3) confirm the finely dispersed nature of the xerogel–like material. The MIL–100 structure synthesized in DMF presents textural properties similar to the so–called metal–organic gels, MOGs. [25] In addition, large zoom in the TEM images allows the observation of cavities, confirming the presence of the desired crystalline structure.

4.3.1.1.3. Thermo–Gravimetric Analysis

Figure 4–4 shows the comparison between the TGA profiles of the different solids. Similarities to the data previously reported are observed for MIL–100(Cr)–water. [23]

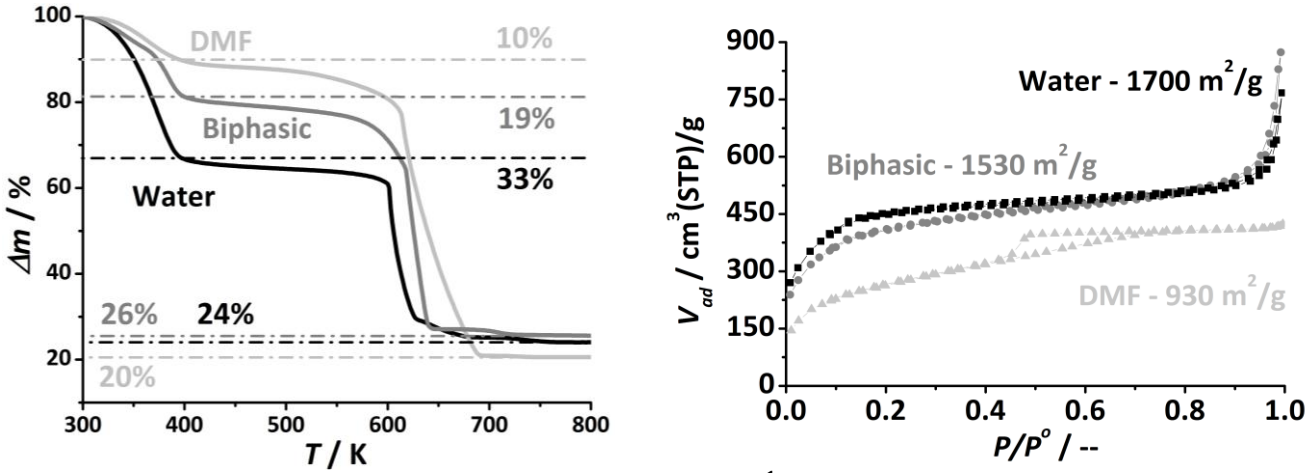

Figure 4 - 4 (*Left*) TG profile in flowing air (10 K min^{-1}) of MIL–100(Cr) samples synthesized by conventional heating in water, biphasic water/2–pentanol (*50:50* wt%) system or DMF. Residual mass (%) and water (%) content are specified. (*Right*) Adsorption isotherms of nitrogen at 77 K on different MOF samples: MIL–100(Cr) synthesized by conventional heating with (▲) DMF, (●) biphasic water/2–pentanol (*50:50* wt%) system or (■) water as solvent.

Water content is higher for samples synthesized in aqueous media. Around 30 wt% of the weight loss is associated with adsorbed water for MIL–100(Cr)–water, while this value decreases to 20 and 10 wt%, for biphasic and DMF samples, respectively. In the case of biphasic systems, the residual mass is similar to the water synthesis, while DMF sample presents a decrease of around 5 wt% in residual mass. Water content and residual mass results might suggest the presence of trapped trimesic acid (TMA) molecules within the cavities of the MOFs synthesized in the biphasic and DMF solvents. As calculated from TGA, a ratio TMA:Cr = 2:3 is found for the water sample, in good agreement with the unit cell formula. In contrast, 2.3/3 and 3.5/3 ratios are found for the biphasic and DMF samples, respectively.

4.3.1.1.4. Textural Analysis: Nitrogen adsorption isotherms

Figure 4–4 shows the N_2 isotherms and BET surface areas for each sample. Materials synthesized in water and in biphasic mixtures present quite similar isotherms, with two pronounced steps between 0.05 and 0.2 and a fairly similar BET area: 1700 and 1530 $m^2\,g^{-1}$. These values are slightly lower than those reported in the literature by Férey and co–workers. [23]

On the other hand, the material synthesized in DMF presents considerable differences. The nitrogen uptake is lower, although the BET surface area is still appreciable (930 $m^2 g^{-1}$). The isotherm has a Type IV shape, characteristic for materials presenting both micro– and meso–porosity. [26] At low relative pressure the micropores are filled, while the mesopores require higher relative pressures. In addition, a hysteresis loop is observed, with a pronounced step located at 0.45 in the desorption branch. This step in the hysteresis loop is usually associated with the fast desorption (cavitation) of N_2 molecules from mesopores between 2 and 6 nm in size. [27-29]

4.3.1.2. Microwave Syntheses

Sung *et al.* have already reported microwave synthesis of MIL–100(Cr) in water for 1 h, 2 h and 4 h at 493 K. [30] Our work focuses on the development of milder synthetic procedures, such as lower temperatures (423 K), that enhance the incorporation of Keggin polyoxometalates. Although synthesis in water was not successful under microwave irradiation, attributed to low synthesis temperatures, syntheses in organic solvents, MIL–100(Cr)–biphasic and –DMF produced solid powders, probably due to better linker solubility, and higher microwave sensitivity. BET areas of 1190 $m^2 g^{-1}$ and 1180 $m^2 g^{-1}$, respectively, were obtained and similar PXRD patterns as those observed for synthesis under conventional heating.

4.3.2. Fluoro donor influence

Two different fluoro donors were used during the synthesis of MIL–100(Cr). Both sodium fluoride (NaF) and hydrofluoric acid (HF) play the role of mineralizing agent and were used in order to reveal the influence of the pH on the synthesis. [24, 31]

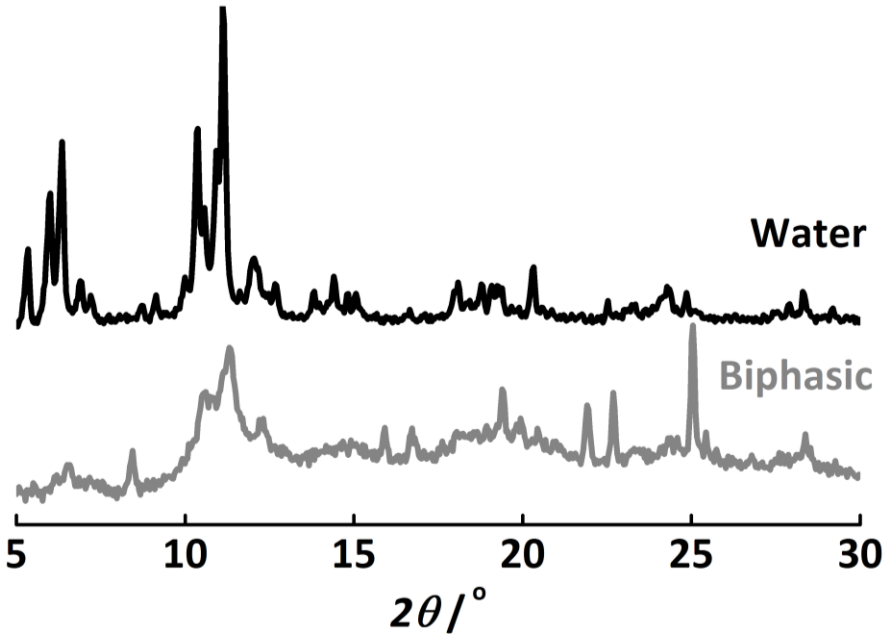

Figure 4 - 5 PXRD–CoKα pattern of different MOF samples: MIL–100(Cr) synthesized by conventional heating in biphasic water/2–pentanol (*50:50* wt%) system (*bottom*) or only water (*top*) as medium, and NaF used as mineralizing agent.

4.3.2.1. Powder X–Ray Diffraction

Figure 4–5 shows the PXRD pattern of water and biphasic systems synthesized with NaF as a mineralizing agent. The most remarkable result is the outstanding crystallinity achieved by the NaF/water system. Every reflection is well defined and narrower than in the case of the HF/water samples, suggesting a higher degree of crystallinity. In the case of biphasic and organic systems, crystallinity of the samples does not significantly improve.

4.3.2.2. Thermo–Gravimetric Analysis

Figure 4–6 compares the TG profiles of DMF systems with NaF and HF, hydrothermally synthesized. No clear differences are observed in TG profiles apart from residual mass differences.

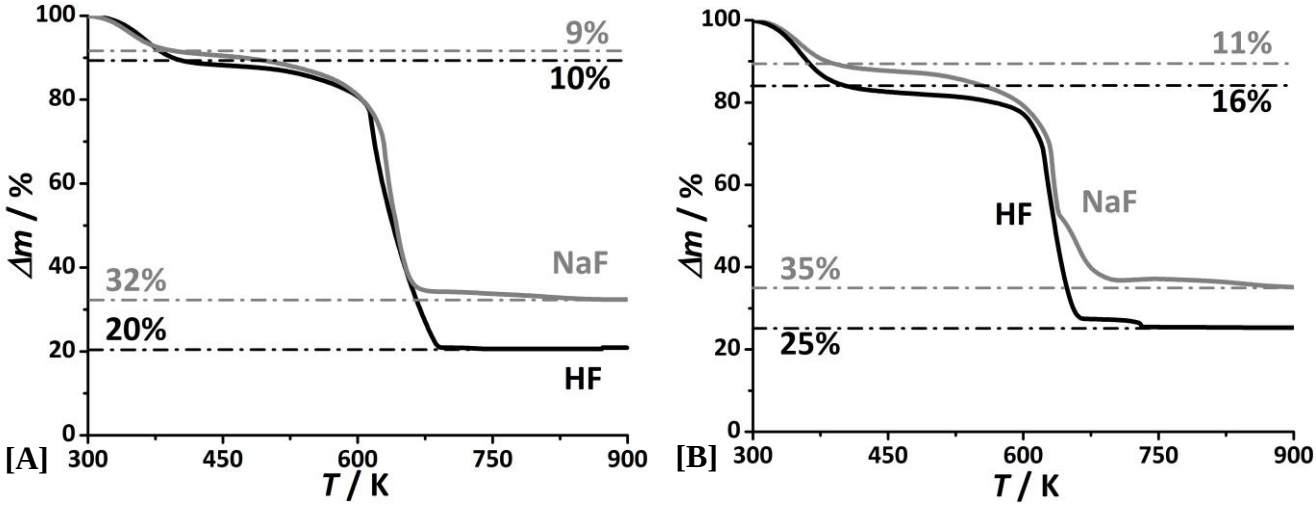

Figure 4 - 6 TG profile in air (10 K min^{-1}) of MIL–100(Cr)–DMF synthesized by [A] conventional heating and [B] microwave irradiation, with HF and NaF as fluoro donors.

The residual mass of the DMF/ NaF system is 12 wt% higher than in the case of DMF/HF. ICP–OES results (Table 4–1) show the presence of Na in the sample, and therefore sodium oxide formation during combustion results in an increase of residual mass. DMF/microwave synthesis using NaF and HF results in similar observations and the presence of Na in the NaF sample produces an increase in the residual mass (Table 4–1).

Table 4 - 1 ICP–OES chromium (Cr) and sodium (Na) weight percentage in different samples synthesized with NaF as mineralizing agent. The corresponding wt% oxide has been calculated.

Sample Description [a]	Cr / Cr_2O_3 [wt%]	Na / Na_2O[wt%]
MIL-100(Cr)-DMF/HT	13.8 / 20.2	6.4 / 10.8
MIL-100(Cr)-DMF/MW	13.8 / 20.2	5.4 / 9.1

[a] hydrothermal (HT) or microwave (MW) synthesis procedure with DMF as solvent.

4.3.2.3. Textural Analysis: Nitrogen adsorption isotherms

The use of NaF displays lower BET surface areas than those prepared with HF (Table 4–2) in every studied case. Solids synthesized in water are the least affected, even though surface areas are around 30% lower, while those from biphasic systems and DMF decrease by 60% and 50%, respectively.

Table 4 - 2 Overview of the most important MIL–100(Cr) synthesis conditions and N_2 BET areas of the obtained samples.

Solvent	Mineralizing Agent	Synthesis Procedure[a]	PTA loading (wt %)	S ($m^2\ g^{-1}$) [S ($m^2\ g^{-1}_{MOF}$)]
H_2O	HF	HT	–	1700
	NaF	HT	–	1200
	HF	MW	–	–
	NaF	MW	–	–
DMF	HF	HT	–	930
	NaF	HT	–	570
	HF	MW	–	1180
	NaF	MW	–	500
Biphasic	HF	HT	–	1530
	NaF	HT	–	540
	HF	MW	–	1190
	NaF	MW	–	490
	HF	MW	16.6	1080 [1295]
	HF	MW	29.8	650 [925]

[a] hydrothermal (HT) or microwave (MW) synthesis procedure.

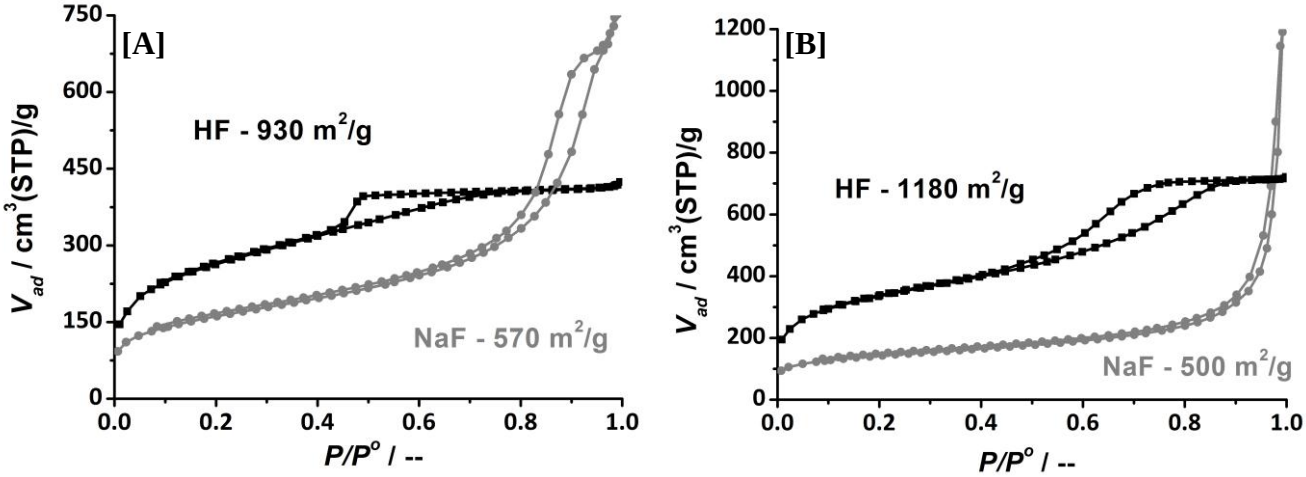

Figure 4 - 7 Adsorption isotherms of nitrogen at 77 K corresponding to MIL–100(Cr)–DMF synthesized by [A] conventional heating and [B] microwave irradiation, with HF or NaF as fluoro donors.

Figure 4–7 compares the isotherms obtained for the DMF synthesized solids using NaF or HF as a fluor donor. For hydrothermal synthesis (Fig. 4–7A), the mesoporosity of the sample is preserved, while the hysteresis loop moves to higher relative pressures when NaF is used, inferring the formation of larger mesopores or even macropores. The use of microwave irradiation using NaF as a mineralizing agent yielded similar results (Fig. 4–7B).

4.3.3. Encapsulation of PTA in MIL–100(Cr)

In view of the results obtained during the synthesis optimization, the biphasic protocol with HF as a mineralizing agent was selected for the encapsulation of PTA. Both conventional oven and microwave irradiation were used as heating methods.

4.3.3.1. Conventional heating vs. microwave synthesis

Encapsulation of PTA was tested in hydrothermal and microwave synthesis, resulting in very different PTA loadings. 'High' and 'low' loadings were designated using 14 mM (molar ratio W/Cr initial = 0.66) and 7 mM PTA (molar ratio W/Cr initial = 0.33) initial concentrations in the synthesis mixture, respectively. A summary of tungsten (W) weight percentages quantified in the solid products is shown in Table 4–3, as measured by elemental analysis after synthesis (ICP–OES).

Table 4 - 3 Tungsten analysis of high and low loadings of PTA/MIL–100(Cr) samples from different synthesis procedures.

	W / PTA (wt%)			
	HT/water	**HT/biphasic**	**MW/water**	**MW/biphasic**
High loading PTA [14 mM]	**0.6**	**1.3**	**[a]**	**22.8 / 29.8**
Low loading PTA [7 mM]	**[b]**	**[b]**	**[a]**	**12.7 / 16.6**

[a] No MOF was formed under these conditions. [b] Not synthesized as higher PTA concentrations gave already low loadings. (HT) conventional hydrothermal heating. (MW) microwave irradiation.

Even with the addition of large PTA amounts (initially 1 PTA molecule per 24 Cr atoms), only low tungsten loadings (0.6 wt%) were obtained with the hydrothermal/water system. Biphasic synthesis under solvothermal conditions slightly increased the tungsten loading up to 1.3 wt%. Opposite to that, using the biphasic/microwave combination led to much higher tungsten loadings (22.8 wt%) in very short synthesis times. Halving the PTA concentration (initially 1 PTA molecule per 52 Cr atoms) in biphasic/microwave conditions also resulted in halving the tungsten loading, 12.7 wt%. This confirms that control of the PTA encapsulated in MIL–100(Cr) is possible.

The 'high loading' sample corresponds to 29.8 wt% of PTA (0.5 W/Cr molar ratio), and the 'low loading' to 16.6 wt% PTA in the sample (0.23 W/Cr molar ratio). Here it is assumed that tungsten is only present in the form of PTA (one PTA molecule contains 12 tungsten atoms) and that chromium is only in the framework. The efficiency of encapsulation is remarkably high, reaching values around 70–75%, comparing initial and final molar W/Cr ratios. However, efficiencies might be even higher than these values, since chromium determined by ICP–OES might not only come from the MOF framework but possibly also from some chromium oxide formed during the synthesis. The high and low loading PTA/MIL–100(Cr), prepared in a biphasic system with microwave heating were further characterized.

4.3.3.2. Powder X–Ray Diffraction

XRD patterns of high and low PTA loadings are compared with the diffraction pattern of (hydrated) solid PTA and MIL–100(Cr)–biphasic/microwave. Lower intensities are shown for PTA containing samples, but no clear differences attributed to PTA loading. The diffraction pattern from PTA is not observed, indicating a good dispersion of PTA throughout the sample.

4.3.3.3. Thermo–Gravimetric Analysis

Figure 4–8 shows the TG profile of different PTA/MIL–100(Cr) samples in air, weight loss is represented as a function of temperature. No significant profile differences are observed, even after the inclusion of an oxidant like PTA, the samples display framework oxidation at the same temperature, around 600 K. As expected, more residual mass is observed for higher PTA loadings, attributed to tungsten oxide (WO_3) formation together with Cr_2O_3 from the MOF. High and low PTA loadings result in 34 and 43 wt% residual mass, respectively, higher than the bare sample (25 wt%) which is only associated with Cr_2O_3 formation. These results can be quantified and compared with ICP–OES elemental analysis data. Taking into account that high and low PTA loaded samples contain 70% and 83% of MOF, respectively, the related residual Cr_2O_3 percentages are 17.5 and 20.5 wt%. Subtracting these Cr_2O_3 wt% values from the residual mass, this yields 25.5 and 13.5 wt% WO_3 for the high and low PTA loading samples, respectively, or 20.2 and 10.7 wt% W, in good agreement with ICP–OES analysis (22.8 wt% and 12.7 wt% W, for high and low PTA loadings, respectively).

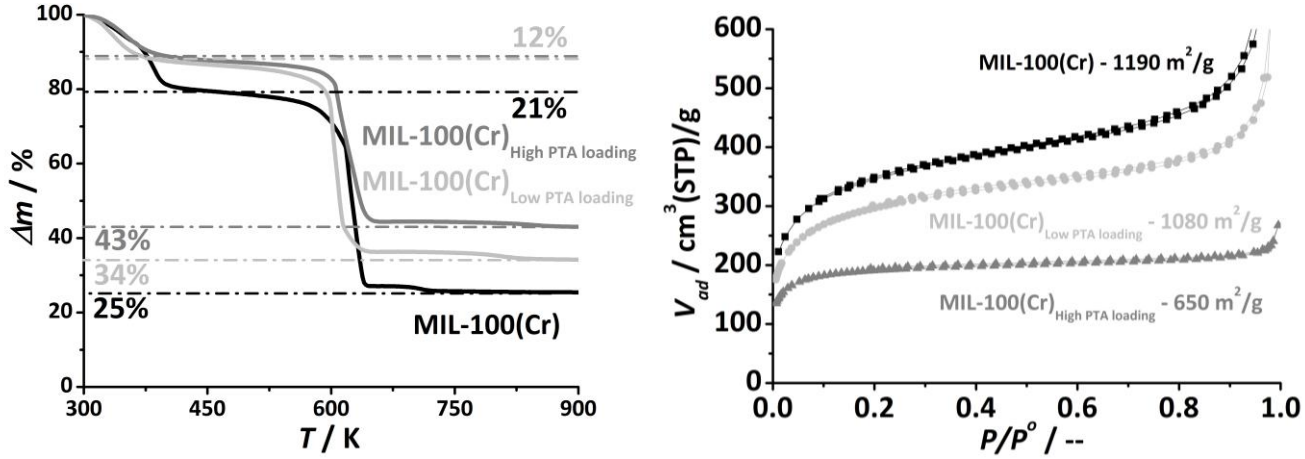

Figure 4 - 8 (*Left*) TG profiles of different MOF samples in air at heating rate of 10 K min^{-1}. Comparison of encapsulated PTA samples with bare MIL–100(Cr). (*Right*) Nitrogen adsorption isotherms at 77 K of different MIL–100(Cr) samples prepared in a biphasic water/2–pentanol system with microwave heating: (▲) High PTA loading (●) Low PTA loading (■) No PTA. Every isotherm has been normalized per total sample mass, including MOF and PTA.

4.3.3.4. Textural Analysis: Nitrogen adsorption isotherms

PTA encapsulation does not show any significant change in the isotherm shape (Fig. 4–8). On the other hand, it is clear that nitrogen uptake decreases when increasing PTA loadings. Table 4–2 summarizes the BET surface areas for encapsulated samples.

4.3.3.5. Diffuse Reflectance Infrared Fourier Transform Spectroscopy

Infrared spectroscopy confirms the presence of PTA in the sample. The Keggin unit is composed of a central PO_4 tetrahedron surrounded by twelve WO_6 octahedra. There are four types of oxygen atoms in the Keggin unit: four oxygen atoms of the central tetrahedron (O_a), twelve oxygen atoms that bridge tungsten atoms not sharing a central oxygen atom (corner–sharing, O_b), twelve oxygen atoms that bridge two tungsten atoms sharing the same central oxygen atom (edge–sharing, O_c), and twelve terminal oxygen atoms (O_d) associated with a single tungsten atom. According to the literature (simulations and experimental results), crystalline PTA shows characteristic bands at 1080 cm^{-1} (vibrational frequency of P–O_a), 978 cm^{-1} (stretching of W = O_d), 888 (vibrational frequency of W–O_b–W) and 815 cm^{-1} (vibration of W–O_c–W). [3, 32]

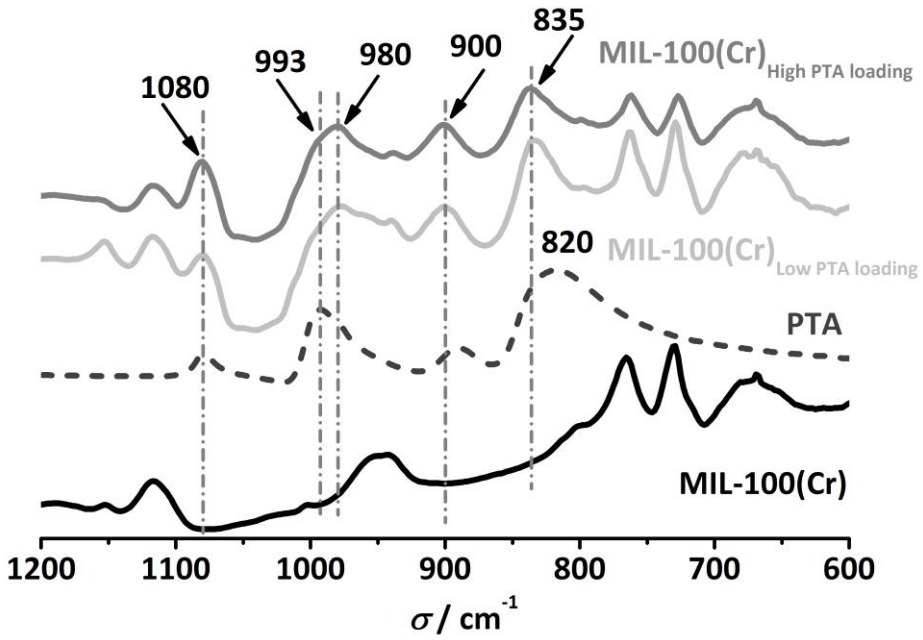

Figure 4 - 9 DRIFT spectra of several MIL–100(Cr) samples zoomed in the region of 1200 to 600 cm^{-1}. Key: (*Black*) MIL–100(Cr) bare sample; (*Dark Grey*) Phosphotungstic acid; (*Grey*) MIL–100(Cr) low PTA loading encapsulated; (*Light Grey*) MIL–100(Cr) low PTA loading encapsulated.

DRIFT spectra for different PTA loadings were compared with the unloaded MIL–100(Cr) sample and hydrated phosphotungstic acid (Fig. 4–9). All characteristic stretching bands of the polyoxometalate are present in the spectra of the PTA encapsulated samples. The bands corresponding to P–O_a vibration is perfectly visible at 1080 cm^{-1}, in good agreement with literature. The vibration corresponding with W = O_d appears shifted from literature values and it splits up into a maximum at 980 cm^{-1} with a pronounced shoulder at 993 cm^{-1}. Vibrations, associated with W–O_b–W and W–O_c–W, are observed at 900 and 835 cm^{-1}. Compared with the experimental spectrum of PTA, these vibrations are shifted 10–15 cm^{-1} due to interactions with the surface of MIL–100(Cr).

Figure 4–10 shows the DRIFT spectra of high and low PTA loading in MIL–100(Cr) before and after washing the sample with organic solvents (reaction mixture of *n*–butanol and acetic acid, molar ratio 1 : 1) at 393 K for 24 hours under vigorous stirring. When comparing the same characteristic peaks as in

Figure 4–10, no indication of PTA leaching is obtained. At both loadings, the vibration frequencies are present and similar intensities are observed.

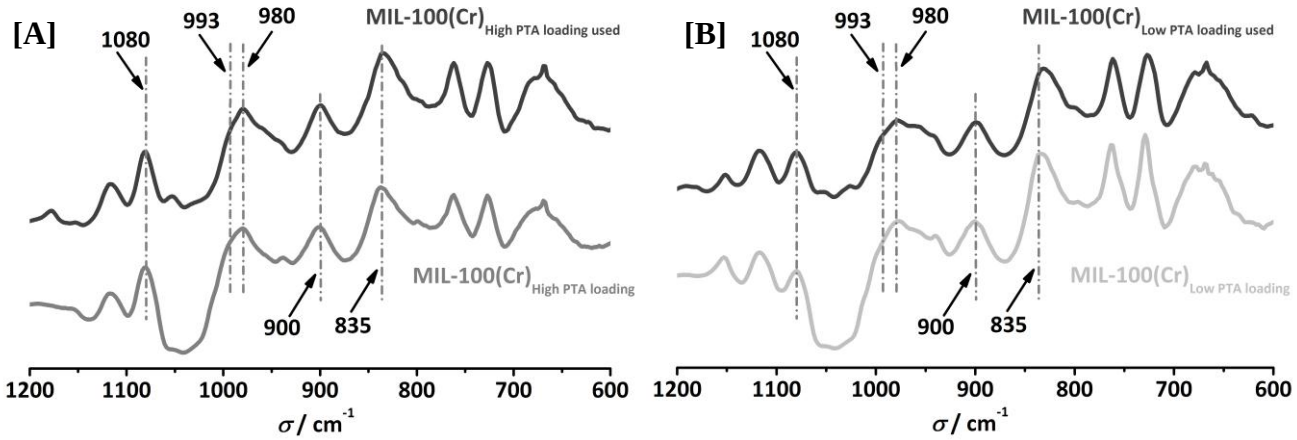

Figure 4 - 10 DRIFTS of different PTA/MIL–100(Cr) samples. Zoomed in on the region from 1200 to 600 cm^{-1}. Spectra (*Light grey*) before and (*grey*) after washing with organic solvent at 373 K during 24 hours under vigorous stirring. [A] MIL–100(Cr) high PTA loading. [B] MIL–100(Cr) low PTA loading.

Table 4–4 presents ICP–OES results of tungsten and chromium wt% values before and after washing the samples in an organic mixture at high temperatures for 24 h, suggesting no leaching of PTA.

Table 4 - 4 Tungsten and Chromium ICP–OES results for high and low PTA loadings in MIL–100(Cr) samples before and after washing with organic solvents (1–butanol and acetic acid (1:1 molar), esterification reaction mixture) at 373 K during 24 hours under vigorous stirring.

	W (wt%) / Cr (wt%)		Molar Ratio W/Cr	
	Fresh sample	Used sample	Fresh sample	Used sample
High loading PTA [14 mM]	22.8 / 12.8	21.2 / 13.9	0.50	0.43
Low loading PTA [7 mM]	12.7 / 15.6	12.6 / 16.3	0.23	0.22

4.3.3.6. ^{31}P Magic Angle Spinning Nuclear Magnetic Resonance

Figure 4–11 shows a comparison of the ^{31}P MAS NMR spectrum of the solid PTA hydrate and the high PTA loading MIL–100(Cr) sample. The chemical shift of solid PTA hydrate is centered at –15.18 ppm, whereas for PTA encapsulated in MIL–100(Cr) the signal is shifted to –14.72 ppm and is slightly broader.

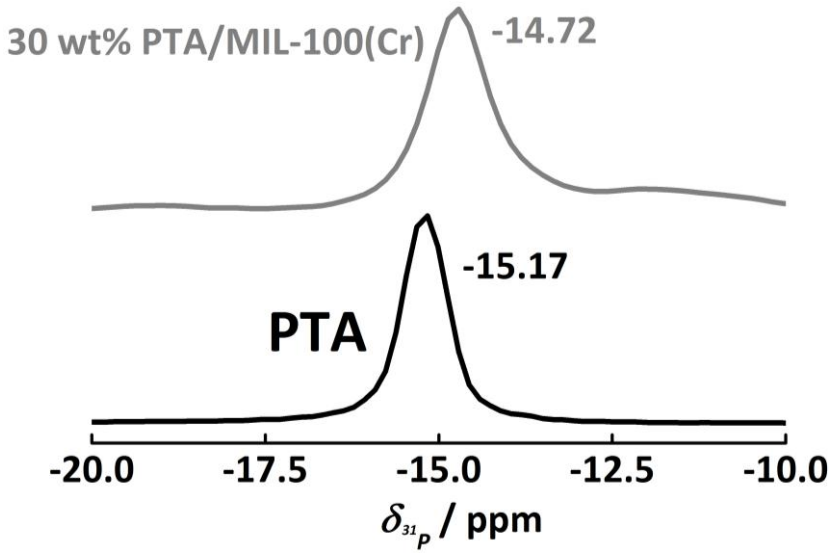

Figure 4 - 11 ^{31}P MAS NMR spectra of MIL–100(Cr) high PTA loading (*top*) compared with solid hydrated PTA (*bottom*).

4.3.3.7. Transmission Infrared Spectroscopy of CO Adsorption

In order to study acidity changes in MIL–100(Cr)–biphasic after PTA encapsulation, CO adsorption at low temperature has been performed and followed by transmission IR spectroscopy (Fig. 4–12). Vimont *et al.* reported CO adsorption experiments to evaluate the acidity of MIL–100(Cr)–water. [24]

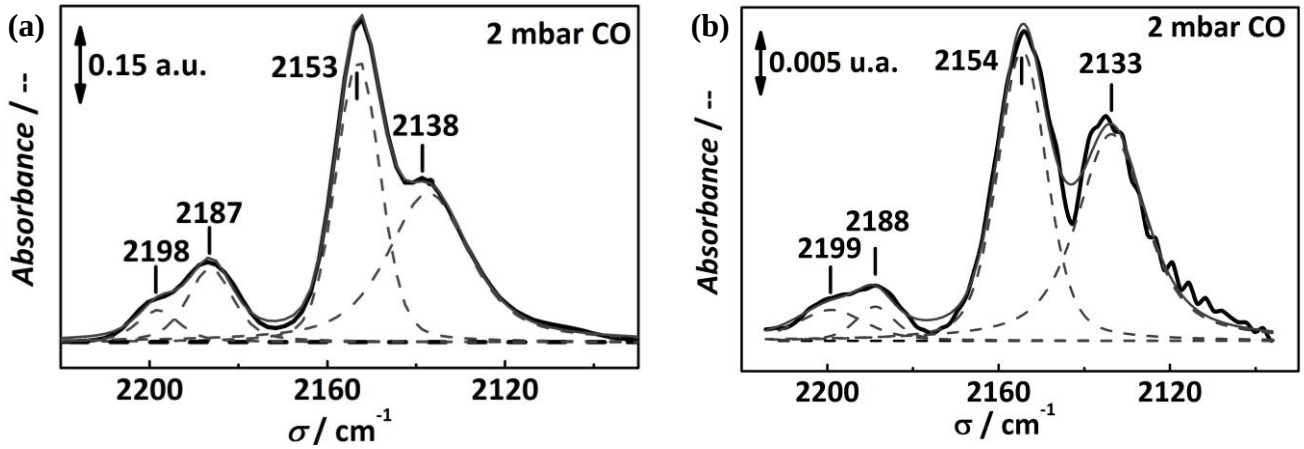

Figure 4 - 12 FTIR transmission spectra of CO adsorption at 143 K. Key: (*a*) MIL–100(Cr); (*b*) MIL–100(Cr) high PTA loading (30 wt%).

For MIL–100(Cr) synthesized under biphasic conditions, the main bands observed in the spectrum are in agreement with those reported for the water systems. Lewis acidity associated with coordinatively unsaturated sites (CUS) of chromium trimers is observed (bands at around 2199 and 2189 cm^{-1} shown after removal of the water coordinated to CUS). The most intense absorption centered at 2154 cm^{-1} corresponds to Brønsted acid sites such as –OH groups and water strongly coordinated with CUS and Keggin POMs [33], while the band around 2135 cm^{-1} is attributed to physically adsorbed CO.

Table 4 - 5 Intrinsic and relative areas (with respect to physically adsorbed CO) for each vibration frequency related to CO adsorbed in the MIL–100(Cr) bare and high PTA loading samples.

	MIL–100(Cr)		MIL–100(Cr) High PTA loading	
Vibration frequency / cm^{-1}	**Area**	**Relative area**	**Area**	**Relative area**
Physically adsorbed CO: 2135	**8.2731**	**1**	**0.4126**	**1**
Brønsted acid sites: 2154	**7.4751**	**0.90**	**0.3865**	**0.94**
Lewis acid sites: 2188	**2.1797**	**0.37**	**0.0381**	**0.22**
Lewis acid sites: 2199	**0.8864**		**0.0546**	

4.4. DISCUSSION

The synthesis of MIL–100(Cr) in water yields, as previously reported, the best sample in terms of crystallinity and surface area, but the use of alternative solvents like DMF and biphasic media offer several advantages, as discussed below, when studying inclusion of guest molecules like polyoxometalates.

As the crystallinity, the use of DMF as solvent always results in poorly crystalline materials (see Fig. 4–1). In addition, the textural properties of the sample seem to change dramatically. Nitrogen adsorption isotherms (Fig. 4–4) clearly show the appearance of mesoporosity when using the organic solvents, while a high microporosity is maintained. These properties are attributed to very small MIL–100(Cr)–DMF crystallites. SEM (Fig. 4–2) corroborates these findings, revealing particles of similar shape and size for water and biphasic systems, in contrast to the big lumps obtained in the DMF syntheses. The xerogel–like product is similar to that reported by Lohe *et al.* for MIL–100(Fe). [34] TEM images (Fig. 4–3) confirm the gel–like appearance of the agglomerates of nano–sized crystals. The synthesis of MIL–100 in DMF under microwave heating constitutes therefore an easy route to the production of gel bodies of this MOF, with prospective applications in, for instance, adsorption, drug delivery and heterogeneous catalysis. [25]

When using water media and microwave irradiation, no material is obtained at the studied temperature (423 K). Similar results have also been reported for other MOFs, like MOF–5, where a specific temperature is needed to form the crystalline structure. [35] In the chosen organic solvents, MOF nucleation takes place at the temperature selected. We attribute this result to the higher solubility of the organic precursor in 2–pentanol and DMF than in water, and to the higher microwave absorbance of both organic solvents. [36-38] The higher solubility of the organic linker in 2–pentanol strongly suggests that crystal formation in the biphasic system takes place at the solvents' interphase, as recently shown by Ameloot *et al.* [39]

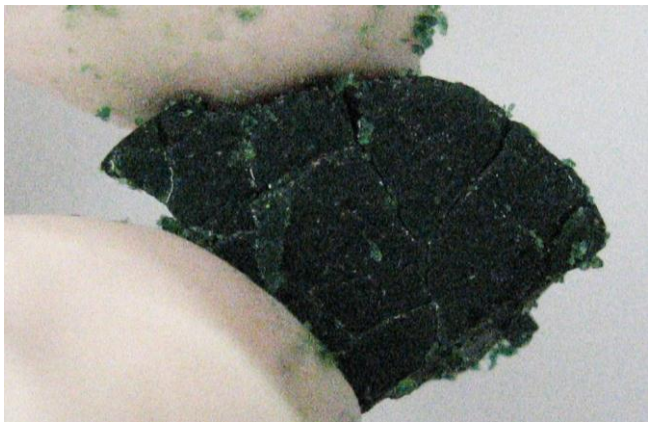

Figure 4 - 13 Images of MIL–100(Cr)–DMF as–synthesized, showing centimeter agglomerates of particles in a gel–like appearance, similar to previously reported MOGs (Metal–Organic Gels).

The effect of pH has been studied by modifying the fluoro donor used in the synthesis. Water systems displayed better crystallinity (Fig. 4–5) when substituting HF by NaF (maintained crystallinity for Biphasic and DMF samples). Again a higher solubility of the organic precursor at higher pH seems to enhance the crystallinity of the product. However, the higher pH by using NaF instead of HF also results in an increase of chromium oxide formation. ICP–OES results show the presence of Na in the

samples (Table 4–1), which is in agreement with TG profiles and an increase in residual mass (Fig. 4–6A). It might be trapped in the MOF cavities due to low solubility in the organic solvents, contributing to decreased surface areas. Similar results are observed when microwave irradiation is used: (1) a higher residual mass in TG profiles, due to more chromium oxide formation and sodium trapped in the MOF cavities (see Fig. 4–6B); (2) the isotherms shape, while HF samples show a hysteresis loop in the mesopores region, this is shifted for the NaF samples to the macropores region (Fig. 4–7). Therefore, HF is considered the best mineralizing agent possible (enhance nucleation), due to its contribution to a low pH in the synthesis solution and the benefits resulting from it (better adsorption properties).

The use of organic solvents in combination with microwave heating results in high PTA encapsulation yields (Table 4–3). Organic solvents have been reported to enhance the stability of PTA [40] and the use of microwave heating shortens the necessary synthesis time twelve–folds while using a lower temperature. The combination of these factors allows the almost complete encapsulation of the PTA added to the synthesis mixture.

Considering W and Cr percentages obtained by ICP–OES (Table 4–4), the average number of PTA Keggin units per cavity can be estimated. Only biphasic systems with different PTA loadings were analyzed. 'High' PTA concentration during the synthesis leads to on average 4.3 Keggin units per 1 big cavity and 2 medium ones, (30 wt% loading). In the case of 'low' PTA loadings, on average two Keggin units are present per 1 big cavity and 2 medium ones. Considering the available space in the large and medium cavities, indeed at high loading two and one Keggin units can be accommodated in the large and medium cavities, respectively, assuming a homogeneous distribution. For the case of low PTA loadings, one Keggin unit can be allocated per large cavity and one per 2 medium cavities. Nitrogen uptake is lower when the PTA loading is higher, if compared at a relative pressure of 0.5. Taking into account the Keggin unit volume (2250 $Å^3$) and the volume of the MIL–100 cages (medium 8100, maximum of 3.6 Keggin units, and large 12 700 $Å^3$, maximum of 5.6 Keggin units), a perceptive decrease in nitrogen uptake is expected of about 16% (84% of the initial volume available) for 'low' loadings (2 Keggin units per 1 big cage and 2 medium ones) and 33% (67% of the initial volume available) for 'high' loadings (4.3 Keggin units per 1 big cage and 2 medium ones) on the basis of the amount of MOF, respectively. Nitrogen adsorption volumes have been extracted at 0.5 relative pressures. Percentages of accessible volume have been calculated comparing PTA samples with the bare biphasic/microwave material. The low PTA loading sample shows an accessible volume of 84% from the initial bare MOF, in good agreement with the previous estimations. Only highly loaded samples deviate from the calculations above, probably related to PTA blocking of windows.

The presence of encapsulated PTA is confirmed by IR spectroscopy. The bands corresponding to W–O–W vibrations (O_c and O_d, respectively, at 900 and 835 cm^{-1}), 993 cm^{-1} associated to the W=O_b

stretching, and the band at 1080 cm^{-1} related to the P–O_a stretching are observed in both PTA loading samples (Fig. 4–9). Small differences are present with respect to the experimental solid hydrated PTA spectrum. W=O_b vibration splits into two peaks, while W–O–W frequencies are shifted, a strong indication for the interaction of the PTA with the surface of the MOF. These vibrations are still present after treating the samples with organic solvents (1–butanol and acetic acid 1:1 molar ratio) at elevated temperature (373 K) during 24 hours under vigorous stirring (Fig. 4–10), simulating a treatment in a liquid phase reaction. ICP–OES analysis confirms the absence of PTA leaching (Table 4–4).

DRIFT spectroscopy (see Fig. 4–9) in combination with ^{31}P MAS NMR (see Fig. 4–11) confirms that, by using biphasic/microwave synthesis, PTA has been successfully encapsulated without formation of lacunary structures or further damage of the polyoxometalate configuration. The chemical NMR shift observed for solid PTA centered at –15.17 ppm moves to –14.72 ppm for encapsulated PTA. This upfield shift of the phosphorus signal and the broadening of the NMR peak might suggest a slight interaction between PTA and the MOF environment. [35]

Species like $(H_xPW_{12}O_{40})^{-(3-x)}$ might be formed from the PTA interaction, as suggested in results obtained for impregnation procedures reported on other materials. [40] This interaction might take place with the –OH groups or the water strongly associated to Cr^{+3} CUS (still present in the MOF, as observed in the TG analysis), and causing the acidity loss of the PTA.

Furthermore, the direct interaction of PTA with the environment, as suggested by CO adsorption at low temperatures, also results in a decrease in the Lewis acidity compared to the bare sample (from 0.37 to 0.22 relative areas, see Fig. 4–12 and Table 4–5). MIL–100(Cr)–biphasic presents a similar CO adsorption spectrum as reported for water–based synthesis. [24] Here, only relative intensities of the adsorption peaks are compared, because of the strong decrease in transmission for the PTA samples, which hampers an absolute comparison with the parent sample.

When PTA is encapsulated, only a minor Brønsted acidity increase is revealed probably associated with the PTA. In contrast, Lewis acid sites decrease can be attributed to a better coordination of water to Cr sites in the presence of PTA that can stabilize them via hydrogen bonding.

It is anticipated that in view of the intrinsic properties of PTA, its high dispersion and the impossibility of its leaching, the resulting materials might find application in catalysis, adsorption and separation. The observed strong active phase–support interaction has implications for their potential application as acid catalysts and might explain the poor activities reported for similar systems. [19, 41]

4.5. CONCLUSIONS

Synthesis conditions like medium, mineralizing agent and the heating method determine the final textural properties of MIL–100(Cr). Despite the fact that water synthesis is the best way to obtain highly crystalline and high surface area MIL–100, synthesis in pure DMF combined with microwave heating at lower temperatures and much shorter times is a facile route for the formation of xerogel materials with a dual porosity. While mineralizing agent is used to enhance crystallinity of the structure, low pH values are needed (by using HF rather than NaF) to obtain higher surface areas.

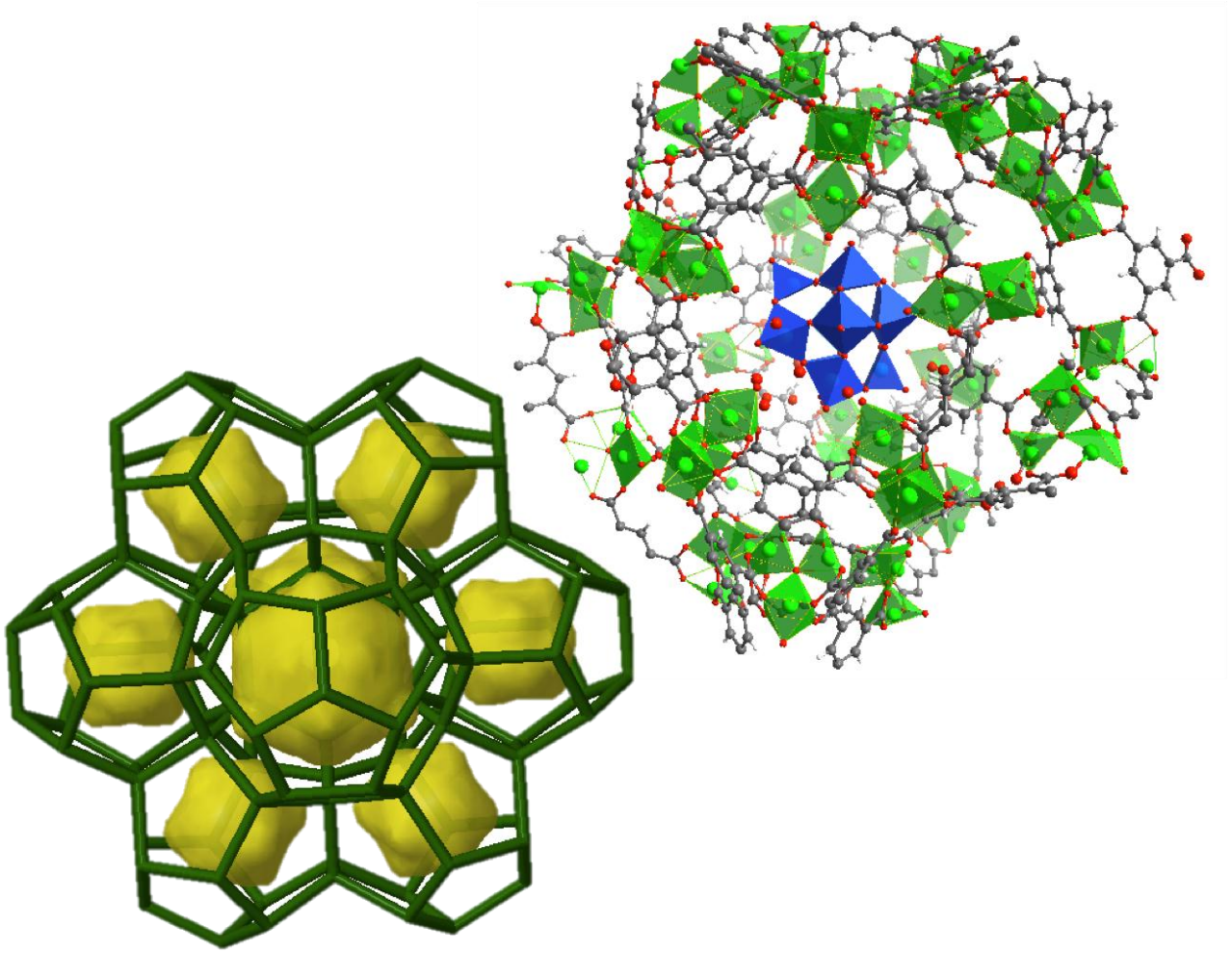

Figure 4 - 14 MTN topology and zoom of a MIL–100(Cr) cavity with PTA encapsulated.

The use of biphasic solvent systems allows the synthesis of MIL–100(Cr) at lower temperatures, while short synthesis times are obtained by using microwave irradiation. The one–pot encapsulation enables high PTA loadings (up to 30 wt%), not observed before for impregnated samples of structures like MIL–101(Cr). PTA leaching has not been detected from ICP–OES and DRIFTS. The chemical integrity of the Keggin structure of encapsulated PTA is confirmed by DRIFTS and ^{31}P MAS NMR, as is its interaction with the MIL–100 cage environment. This interaction decreases the Lewis acidity associated with the MOF framework and only slightly increases the Brønsted acidity.

REFERENCES

[1] J. Juan-Alcañiz, E.V. Ramos-Fernandez, U. Lafont, J. Gascon, F. Kapteijn, Building MOF bottles around phosphotungstic acid ships: One-pot synthesis of bi-functional polyoxometalate-MIL-101 catalysts, Journal of Catalysis, 269 (2010) 229-241.
[2] J. Lee, O.K. Farha, J. Roberts, K.A. Scheidt, S.T. Nguyen, J.T. Hupp, Metal-organic framework materials as catalysts, Chemical Society Reviews, 38 (2009) 1450-1459.
[3] B. Sulikowski, J. Haber, A. Kubacka, K. Pamin, Z. Olejniczak, J. Ptaszyński, Novel "ship-in-the-bottle" type catalyst: Evidence for encapsulation of 12-tungstophosphoric acid in the supercage of synthetic faujasite, Catalysis Letters, 39 (1996) 27-31.
[4] J. Juan-Alcañiz, J. Gascon, F. Kapteijn, Metal-organic frameworks as scaffolds for the encapsulation of active species: state of the art and future perspectives, Journal of Materials Chemistry, 22 (2012) 10102-10118.
[5] J. Juan-Alcañiz, M. Goesten, A. Martinez-Joaristi, E. Stavitski, A.V. Petukhov, J. Gascon, F. Kapteijn, Live encapsulation of a Keggin polyanion in NH_2-MIL-101(Al) observed by in situ time resolved X-ray scattering, Chemical Communications, 47 (2011) 8578-8580.
[6] A. Corma, H. García, F.X. Llabrés i Xamena, Engineering metal-organic frameworks for heterogeneous catalysis, Chemical Reviews, 110 (2010) 4606-4655.
[7] S. Bordiga, F. Bonino, K.P. Lillerud, C. Lamberti, X-ray absorption spectroscopies: Useful tools to understand metallorganic frameworks structure and reactivity, Chemical Society Reviews, 39 (2010) 4885-4927.
[8] V.I. Isaeva, L.M. Kustov, The application of metal-organic frameworks in catalysis (review), Petroleum Chemistry, 50 (2010) 167-180.
[9] A. Dolbecq, E. Dumas, C.R. Mayer, P. Mialane, Hybrid organic-inorganic polyoxometalate compounds: From structural diversity to applications, Chemical Reviews, 110 (2010) 6009-6048.
[10] T. Hsu-Yao, K.P. Browne, N. Honesty, Y.J. Tong, Polyoxometalate-stabilized Pt nanoparticles and their electrocatalytic activities, Physical Chemistry Chemical Physics, 13 (2011) 7433-7438.
[11] L.I. Kuznetsova, N.I. Kuznetsova, S.V. Koshcheev, V.A. Rogov, V.I. Zaikovskii, B.N. Novgorodov, L.G. Detusheva, V.A. Likholobov, D.I. Kochubey, Interaction of platinum and molybdophosphoric heteropoly acid under conditions of catalyst preparation for benzene oxidation to phenol with an O_2-H_2 gas mixture, Kinetics and Catalysis, 47 (2006) 704-714.
[12] G. Sun, Q. Li, R. Xu, J. Gu, M. Ju, E. Wang, Controllable fabrication of platinum nanospheres with a polyoxometalate-assisted process, Journal of Solid State Chemistry, 183 (2010) 2609-2615.
[13] S. Gao, Z. Wu, D. Pan, Z. Lin, R. Cao, Preparation and characterization of polyoxometalate-Ag nanoparticles composite multilayer films, Thin Solid Films, 519 (2011) 2317-2322.
[14] I.V. Kozhevnikov, Catalysis by Heteropoly Acids and Multicomponent Polyoxometalates in Liquid-Phase Reactions, Chemical Reviews, 98 (1998) 171-198.
[15] C.Y. Sun, S.X. Liu, D.D. Liang, K.Z. Shao, Y.H. Ren, Z.M. Su, Highly stable crystalline catalysts based on a microporous metal-organic framework and polyoxometalates, Journal of the American Chemical Society, 131 (2009) 1883-1888.
[16] Y. Zhang, V. Degirmenci, C. Li, E.J.M. Hensen, Phosphotungstic acid encapsulated in metal-organic framework as catalysts for carbohydrate dehydration to 5-hydroxymethylfurfural, ChemSusChem, 4 (2010) 59-64.
[17] D.D. Liang, S.X. Liu, F.J. Ma, F. Wei, Y.G. Chen, A crystalline catalyst based on a porous metal-organic framework and 12-tungstosilicic acid: Particle size control by hydrothermal synthesis for the formation of dimethyl ether, Advanced Synthesis and Catalysis, 353 (2011) 733-742.
[18] S.R. Bajpe, C.E.A. Kirschhock, A. Aerts, E. Breynaert, G. Absillis, T.N. Parac-Vogt, L. Giebeler, J.A. Martens, Direct observation of molecular-level template action leading to self-assembly of a porous framework, Chemistry - A European Journal, 16 (2010) 3926-3932.
[19] L.H. Wee, N. Janssens, S.R. Bajpe, C.E.A. Kirschhock, J.A. Martens, Heteropolyacid encapsulated in $Cu_3(btc)_2$ nanocrystals: An effective esterification catalyst, Catalysis Today, 171 (2011) 275-280.
[20] F.J. Ma, S.X. Liu, C.Y. Sun, D.D. Liang, G.J. Ren, F. Wei, Y.G. Chen, Z.M. Su, A sodalite-type porous metal-organic framework with polyoxometalate templates: Adsorption and decomposition of dimethyl methylphosphonate, Journal of the American Chemical Society, 133 (2011) 4178-4181.
[21] R. Canioni, C. Roch-Marchal, F. Sécheresse, P. Horcajada, C. Serre, M. Hardi-Dan, G. Férey, J.M. Grenèche, F. Lefebvre, J.S. Chang, Y.K. Hwang, O. Lebedev, S. Turner, G. Van Tendeloo, Stable polyoxometalate insertion within the mesoporous metal-organic framework MIL-100(Fe), Journal of Materials Chemistry, 21 (2011) 1226-1233.
[22] C. Férey, C. Mellot-Draznieks, C. Serre, F. Millange, J. Dutour, S. Surblé, I. Margiolaki, Chemistry: A chromium terephthalate-based solid with unusually large pore volumes and surface area, Science, 309 (2005) 2040-2042.
[23] G. Férey, C. Serre, C. Mellot-Draznieks, F. Millange, S. Surblé, J. Dutour, I. Margiolaki, A hybrid solid with giant pores prepared by a combination of targeted chemistry, simulation, and powder diffraction, Angewandte Chemie - International Edition, 43 (2004) 6296-6301.
[24] A. Vimont, J.M. Goupil, J.C. Lavalley, M. Daturi, S. Surblé, C. Serre, F. Millange, G. Férey, N. Audebrand, Investigation of acid sites in a zeotypic giant pores chromium(III) carboxylate, Journal of the American Chemical Society, 128 (2006) 3218-3227.

[25] S.K. Nune, P.K. Thallapally, B.P. McGrail, Metal organic gels (MOGs): A new class of sorbents for CO_2 separation applications, Journal of Materials Chemistry, 20 (2010) 7623-7625.
[26] J. Rouquerol, D. Avnir, C.W. Fairbridge, D.H. Everett, J.H. Haynes, N. Pernicone, J.D.F. Ramsay, K.S.W. Sing, K.K. Unger, Recommendations for the characterization of porous solids, Pure and Applied Chemistry, 66 (1994) 1739-1758.
[27] Y. Tao, H. Kanoh, L. Abrams, K. Kaneko, Mesopore-modified zeolites: Preparation, characterization, and applications, Chemical Reviews, 106 (2006) 896-910.
[28] T. Kyotani, Control of pore structure in carbon, Carbon, 38 (2000) 269-286.
[29] E. Robens, F. Rouquerol, J. Rouquerol, S. K., Adsorption by powders and porous solids, WILEY-VCH Verlag, San Diego, 1999.
[30] H.J. Sung, J.H. Lee, J.S. Chang, Microwave synthesis of a nanoporous hybrid material, chromium trimesate, Bulletin of the Korean Chemical Society, 26 (2005) 880-881.
[31] T. Loiseau, G. Férey, Crystalline oxyfluorinated open-framework compounds: Silicates, metal phosphates, metal fluorides and metal-organic frameworks (MOF), Journal of Fluorine Chemistry, 128 (2007) 413-422.
[32] M.J. Janik, K.A. Campbell, B.B. Bardin, R.J. Davis, M. Neurock, A computational and experimental study of anhydrous phosphotungstic acid and its interaction with water molecules, Applied Catalysis A: General, 256 (2003) 51-68.
[33] F.C. Jentoft, J. Kröhnert, R. Schlögl, IR spectroscopic investigation of heteropolymolybdate catalysts: Acidic properties and reactivity towards propene, Zeitschrift fur Physikalische Chemie, 219 (2005) 1019-1045.
[34] M.R. Lohe, M. Rose, S. Kaskel, Metal-organic framework (MOF) aerogels with high micro- and macroporosity, Chemical Communications, (2009) 6056-6058.
[35] B. Chen, X. Wang, Q. Zhang, X. Xi, J. Cai, H. Qi, S. Shi, J. Wang, D. Yuan, M. Fang, Synthesis and characterization of the interpenetrated MOF-5, Journal of Materials Chemistry, 20 (2010) 3758-3767.
[36] J.J. Harper, P. Janik, Terephthalic acid solubility, Journal of Chemical & Engineering Data, 15 (1970) 439-440.
[37] P. Long, H. Wu, Q. Zhao, Y. Wang, J. Dong, J. Li, Solvent effect on the synthesis of MIL-96(Cr) and MIL-100(Cr), Microporous and Mesoporous Materials, 142 (2011) 489-493.
[38] Q. Wang, H. Xu, X. Li, Solubilities of Terephthalic Acid in Dimethyl Sulfoxide + Water and in N,N-Dimethylformamide + Water from (301.4 to 373.7) K, Journal of Chemical & Engineering Data, 50 (2005) 719-721.
[39] R. Ameloot, F. Vermoortele, W. Vanhove, M.B.J. Roeffaers, B.F. Sels, D.E. De Vos, Interfacial synthesis of hollow metal-organic framework capsules demonstrating selective permeability, Nature Chemistry, 3 (2011) 382-387.
[40] I.V. Kozhevnikov, K.R. Kloetstra, A. Sinnema, H.W. Zandbergen, H. van Bekkum, Study of catalysts comprising heteropoly acid $H_3PW_{12}O_{40}$ supported on MCM-41 molecular sieve and amorphous silica, Journal of Molecular Catalysis A: Chemical, 114 (1996) 287-298.
[41] L.H. Wee, S.R. Bajpe, N. Janssens, I. Hermans, K. Houthoofd, C.E.A. Kirschhock, J.A. Martens, Convenient synthesis of $Cu_3(btc)_2$ encapsulated Keggin heteropolyacid nanomaterial for application in catalysis, Chemical Communications, 46 (2010) 8186-8188.

Chapter 5

Highly dispersed platinum NH_2-MIL-101(Al) containing phosphotungstic acid: Characterization and catalytic performance

This chapter is based on the following publication:

E. V. Ramos–Fernandez, C. Pieters, B. van der Linden, J. Juan–Alcañiz, P. Serra–Crespo, M.W.G.M. Verhoeven, H. Niemantsverdriet, J. Gascon, F. Kapteijn, Journal of Catalysis, 289 (2012) 42–52

Abstract The synthesis, characterization (FT–IR, XPS, NMR, UV–Vis), and catalytic performance of Pt supported on phosphotungstic acid (PTA) encapsulated in a metal–organic framework (MOF) have been extensively studied. The highly dispersed Keggin units of PTA encapsulated in NH_2–MIL–101(Al) cages by one–pot synthesis, act as anchoring sites for the Pt precursor species. After different post–treatments, the performance of the resulting catalysts have been tested in the oxidation of CO, the preferential CO oxidation in the presence of H_2, and in the hydrogenation of toluene. Reduction at 473 K results in the formation of both small Pt^0 clusters and Pt^{2+} species. Reduction at 573 K induces the formation of intermetallic Pt–W^{5+} species, which exhibit the best CO oxidation activity and a higher selectivity toward CO_2 than Pt supported on alumina, resembling the combination of a noble metal on a reducible support. In toluene hydrogenation, the MOF catalysts perform worse than Pt on alumina, ascribed to the very small size of the Pt clusters formed in the MOF catalysts.

5.1. INTRODUCTION

During the last few decades, polyoxometalates (POMs) have received a great deal of attention in the catalysis field. The combination of outstanding redox properties, high acidity, and good thermal and chemical stability makes POMs excellent candidates for a wide variety of catalytic applications. Among the different topologies that POMs may present, the most studied are those displaying the well–known Keggin structure $[XM_{12}O_{40}]^{n-}$ (X = P, Si, Al, *etc.* and M = W, Mo). [1-3] The specific surface area of these solid materials is, however, very low, in the range of 1–5 m^2 g^{-1}, becoming good dispersion on a support crucial for eventual application. Several attempts to support Keggin POMs on materials like silicas, activated carbons, or zeolites have been reported. [4-6] Nevertheless, low POM loadings, agglomeration of POM particles and POM leaching are still unresolved drawbacks.

Recently, several studies of Keggin POM based MOFs have been reported attracting great deal of attention. Sun *et al.* presented the direct encapsulation of POMs in HKUST–1. [7] At the same time, we reported the successful one–pot encapsulation of a similar POMs in the large and medium mesoporous cavities of MIL–101(Cr), achieving a highly dispersed material with outstanding catalytic performance in different Knoevenagel condensations and in two model gas and liquid phase acid–catalyzed reactions. [8] The same one–pot procedure was later used for the application of POM/MIL–101 composites in the dehydration of sugars and the use of NENU–n series (POM/HKUST–1) in methanol dehydration to DME and the formation of ethyl acetate from acetic acid and ethylene. [9, 10] Bajpe *et al.* studied the acidity of encapsulated POMs in HKUST–1, while templating effects of POM were described by extensive characterization. [11] These POM templating effects have lately been monitored by *in situ* time–resolved X–ray scattering. [12] Recently, Ma *et al.* made use of one–pot encapsulation for the adsorption and further hydrolysis of dimethyl methylphosphonate in the so–called NENU–11 (POM/HKUST–1), [13] and Canioni *et al.* successfully incorporated different POMs in MIL–100(Fe) through microwave heating. [14]

POMs redox chemistry allows for stepwise, multi–electron redox reactions, while the structure remains intact. They participate in catalytic redox processes as electron relays. [15] POMs can be reduced and oxidized very easily. Thus, POMs are used as efficient oxidation catalysts in many oxidation reactions [2, 16] or electro–catalytic processes such as methanol oxidation [17] or oxygen reduction. [18] Troupis *et al.* used their redox properties to reduce noble metal precursors and to produce well–dispersed nanoparticles. [19] Furthermore, other authors have proposed polyoxometalate anions as good stabilizers of metal nanoparticles. [17, 20-24] For instance, Legagneux *et al.* grafted platinum complexes on Keggin structures, demonstrating ionic interaction between the polyoxometalate and the platinum complex, with the charge being on the platinum atom. [25, 26] Similar findings were reported

by Kuznetsova *et al.* where Pt(II) and Pd(II) complexes were immobilized on different Keggin heteropolyanions. [2, 16]

This chapter reports the incorporation of Pt species on to the polyoxometalate phosphotungstic acid (PTA), which is highly dispersed in the NH_2–MIL–101(Al) framework and the application of the resulting composites in hydrogenation and oxidation reactions. In this way, sintering and leaching of the POM is eliminated and its properties for supporting active species are preserved. These results demonstrate that POM/MOF composites offer excellent possibilities for nanoparticle engineering.

5.2. EXPERIMENTAL

All the chemicals were purchased from Sigma–Aldrich and used without further purification: N,N–dimethylformamide (DMF, >99.9%), ethanol (98%), methanol (99%) aluminum trichloride ($AlCl_3.6H_2O$ > 98%) aminoterephthalic acid (95%), phosphotungstic acid hydrate (POM, $H_3PW_{12}O_{40}.nH_2O$, reagent grade), and hexachloroplatinic acid (H_2PtCl_6 37.4 wt.% Pt basis). As reference catalyst, 1 wt% Pt/Al_2O_3 catalyst (Sigma–Aldrich) was used.

5.2.1. Catalyst preparation

Microwave synthesis of PTA/NH_2–MIL–101(Al): the synthesis was carried out by dissolving 507 mg of $AlCl_3.6H_2O$ in 15 mL DMF. In addition, 564 mg of 2–aminoterephthalic acid were dissolved in 15 mL DMF and mixed with the previous solution. Finally, 0.34 mmol of PTA were added to the resulting synthesis mixture. The solution was placed in a Teflon insert, which was subsequently placed in a microwave oven. The temperature ramped in 5 min from room temperature to 403 K and subsequently maintained for one hour. The microwave oven operated at 400 W, under stirring conditions. The product was filtered off and washed with methanol under reflux overnight, and finally filtered and dried in an oven.

Platinum impregnation procedure: 1 g of NH_2–MIL–101(Al) or PTA/NH_2–MIL–101(Al) was dispersed in 30 ml of ethanol. A second solution containing 206 mg (0.40 mmol) of hexachloroplatinic acid in 20 mL of ethanol was prepared. The platinic solution was added drop–wise to the MOF slurry and stirred for 1 day at room temperature. The resulting material is recovered by filtration, washed twice with methanol and dried in air.

5.2.2. Characterization techniques

(a) Nitrogen adsorption at 77 K: Quantachrome Autosorb–6B unit gas adsorption analyzer was used to determine the textural properties as BET surface area between 0.05 and 0.15 relative pressures and pore volume at 0.95 relative pressures. The samples are pre–treated under vacuum at 423 K overnight.

(b) Powder X–Ray Diffraction (PXRD): was executed using a Bruker–AXS D5005 with CoKα radiation. *(c) Inductively Coupled Plasma Optical Emission Spectroscopy (ICP–OES):* the samples were digested in duplo in a mixture of 1% HF and 1.25% H_2SO_4 under microwave irradiation, and then analyzed with an ICP–OES Perkin Elmer Optima 3000 dv. *(d) Diffuse Reflectance Infrared Fourier Transform Spectroscopy (DRIFTS):* was carried out in a Bruker model IFS66 spectrometer, equipped with a high–temperature cell with CaF_2 windows and a 633 nm laser. The spectra were registered after accumulation of 256 scans and a resolution of 4 cm^{-1}. A flow of helium at 10 mL min^{-1} was maintained during the measurements. Before collecting the spectra, the samples were pre–treated in helium at 473 K for 60 min. KBr was used as background. *(e) UV–Vis Diffuse Reflectance Spectroscopy:* was performed with a Perkin–Elmer Lambda 900 spectrophotometer equipped with an integrating sphere (‘‘Labsphere”) in the 200–800 nm range. The Kubelka–Munk function was used to convert reflectance measurements into equivalent absorption spectra using the reflectance of $BaSO_4$ as a reference, and to obtain absorption edge energies directly from the curves. *(f) FT–IR transmission spectroscopy combined with CO adsorption:* Brønsted and Lewis acidities of the samples were determined by CO adsorption at low temperature. To this end, 7.5 mg of MOF were pressed (320 kg cm^{-2}, 60 s) into self–supporting wafers. The pellets were placed in an IR quartz cell equipped with CaF_2 windows. A movable sample holder allows the sample to be placed in the infrared beam for the measurements or into the furnace for thermal treatments. The cell is connected to a vacuum line for pre–treatment. The specimen is activated in vacuum at 453 K for two hours to remove any adsorbed species. After this step, the samples were cooled down to 143 K and CO was dosed up to 2 mbar. Transmission spectra were recorded in the 400–4000 cm^{-1} range at 4 cm^{-1} resolution on a Nicolet Nexus spectrometer equipped with an extended KBr beam splitter and a mercury cadmium telluride (MCT) cryodetector. The CO chemisorption experiments were done in the same set–up at room temperature, but the pre–treatment was done under hydrogen atmosphere (1.5 bar) at two different reduction temperatures, 473 and 573 K. *(g) ^{31}P Magic Angle Spinning Nuclear Magnetic Resonance Spectroscopy (MAS NMR):* ^{31}P NMR spectra were measured on a Bruker Avance–400 spectrometer at 161.98 MHz using a solid–state probe and zirconium sample holders with inner diameter of 3 mm, spinning at the magic angle with a rate of 11 kHz. The spectral width is 617.76 ppm, acquisition time of 12.5 ms, and acquisition delay of 10 s. Chemical shifts (δ) are reported in ppm referring to an external standard: 0.1 M aqueous solution of H_3PO_4 (0 ppm). *(h) X–Ray Photoelectron Spectroscopy (XPS):* was carried out on a Kratos AXIS Ultra spectrometer, equipped with a monochromatic X–ray source and a delay–line detector (DLD). Spectra were obtained using the aluminum anode (Al Kα = 1486.6 eV) operating at 150 W. Survey scans were measured at constant pass energy of 160 eV and region scans at 40 eV. The background

pressure was $2 \cdot 10^{-9}$ mbar. The intensities were estimated by calculating the integral of each peak, after subtraction of the S–shaped background, and by fitting the experimental curve to a combination of Lorentzian (30%) and Gaussian (70%) shaped peaks. All binding energies (*BE*) were referenced to the C 1*s* line at 284.6 eV, which provided BE values with an accuracy of ±0.2 eV. The surface atomic ratios were estimated from the integrated intensities corrected by the atomic sensitivity factors. [27]

5.2.3. Catalytic Testing

Toluene hydrogenation reaction: the reaction was tested in a microflow reactor at 0.15 MPa total pressure under different conditions. Before their catalytic performance was evaluated, the catalysts (*ca.* 0.1 g) were reduced in situ at 473 and 573 K in a flowing H_2/ N_2 mixture (20 mL min^{-1} each) for 1 h and then cooled to the reaction temperature (453 K), maintaining the flow. Then, the catalysts were contacted with the reaction mixture (total flow 40 cm^3 min^{-1}; H_2/toluene ratio 10). After each run, the catalysts were flushed with nitrogen, re–treated in air, reduced at the same reduction temperature and re–used. This procedure was carried out in order to check reproducibility and stability of the prepared catalysts. The products formed and the amount of unconverted feed were analyzed with a gas chromatograph (GC) equipped with a 30 m DB–1 column and FID detector. Based on the toluene conversion, the turnover frequency was calculated per total amount of Pt in the sample.

$$TOF = \frac{X_{toluene} \cdot F_{toluene}}{N_{Pt}} \left[{mol_{toluene}}/{h \cdot mol_{Pt}} \right] \quad (1)$$

CO oxidation reaction: was tested in a microflow reactor at 1 atm. Before reaction, the catalysts (*ca.* 0.05 g) were reduced in situ at 473 or 573 K in H_2/He flow (20 ml/min He and 20 ml/min H_2) for 1 h and then cooled in the helium flow to room temperature. Then, the catalysts were contacted with the reaction mixture of molar composition 1% O_2 and 0.5% CO in He (35 ml(STP)/min total flow), and the temperature was increased with 1 K/min until 523 K. The products were analyzed on–line over a ‘‘Poraplot Q’’ and a ‘‘Molsieve 5 A’’ column in a GC equipped with a TCD and FID detector.

Preferential CO oxidation reaction in the presence of H_2: was performed in the same micro–flow reactor as the CO oxidation. The molar reaction mixture composition in this case is 0.5% O_2, 7.3% H_2, 1% CO in He (35 ml(STP)/min). The oxygen selectivity toward CO_2 is defined as the fraction of O_2 converted to produce CO_2 divided by the total O_2 conversion:

$$S_{CO_2} = \frac{X_{O_2 \rightarrow CO_2}}{X_{O_2}} = \frac{{}^{1}/_{2} X_{CO}}{X_{O_2}} \cdot \frac{F_{CO}}{F_{O_2}} \quad (2)$$

5.3. RESULTS

5.3.1. Characterization of Pt@PTA/NH_2–MIL–101(Al)

We have recently reported the synthesis conditions to obtain a pure NH_2–MIL–101(Al) phase and studied *in situ* encapsulation of phosphotungstic acid (PTA) in the medium and large cavities of this MOF, resulting in both cases in materials with high porosity and good thermal stability. [12, 28] In addition, the presence of amino functionalities in the framework gives excellent possibilities for catalysis, separation, and post–synthetic functionalization. The synthesis involves a solvothermal treatment during 72 h at 403 K. Direct PTA encapsulation under the same synthesis conditions in attempts to synthesize NH_2–MIL–101(Al) containing PTA was unsuccessful. Using microwave irradiation (1 h at 403 K) for the synthesis of PTA/NH_2–MIL–101(Al) resulted in a high PTA encapsulation efficiency and quantitative loadings.

The grafting of platinum was performed via impregnation by contacting an ethanolic solution of hexachloroplatinic acid with a suspension of PTA/NH_2–MIL–101(Al) in ethanol for 1 h. After this process, the solution was filtered off, and the resulting powder was thoroughly washed with ethanol and dried in air at 333 K. The impregnation of the non–PTA containing NH_2–MIL–101(Al) with the Pt precursor solution resulted in the collapse of the framework and could not serve as a reference.

5.3.1.1. Powder X–Ray Diffraction

PXRD patterns of the as–synthetized and H_2PtCl_6 impregnated PTA/NH_2–MIL–101(Al) samples are shown in Figure 5–1. In both cases, the collected patterns match the extended MTN topology of MIL–101. [8, 29, 30] The crystallinity does not change significantly after Pt impregnation, in contrast to the pristine NH_2–MIL–101(Al) that collapses after a similar impregnation procedure, probably due to hydrolysis of the MOF.

5.3.1.2. Textural properties: Nitrogen adsorption isotherms

The N_2 adsorption isotherms for PTA/NH_2–MIL–101(Al) before and after impregnation with platinum (Fig. 5–1) show a Type IV shape, characteristic for materials presenting both micro– and mesoporosity. [31] At low relative pressures, two steps are displayed, attributed to the filling of the cavities. At very low relative pressures ($p/p^0 < 0.05$), only the supertetrahedra are filled. As pressure increases, the medium ($p/p^0 = 0.15$) and later the large cavities ($p/p^0 = 0.20$) are filled, while the mesopores are filled at higher relative pressure. In addition, a hysteresis loop is observed, with a pronounced step located at 0.45 relative pressure in the desorption branch. This step in the hysteresis loop is usually associated with the fast desorption (cavitation) of N_2 molecules from mesopores

between 2 and 6 nm in size. [32-34] The apparent surface area was calculated using the BET method, while the micropore volume was calculated using the Dubinin–Radushkevic equation (Table 5–1).

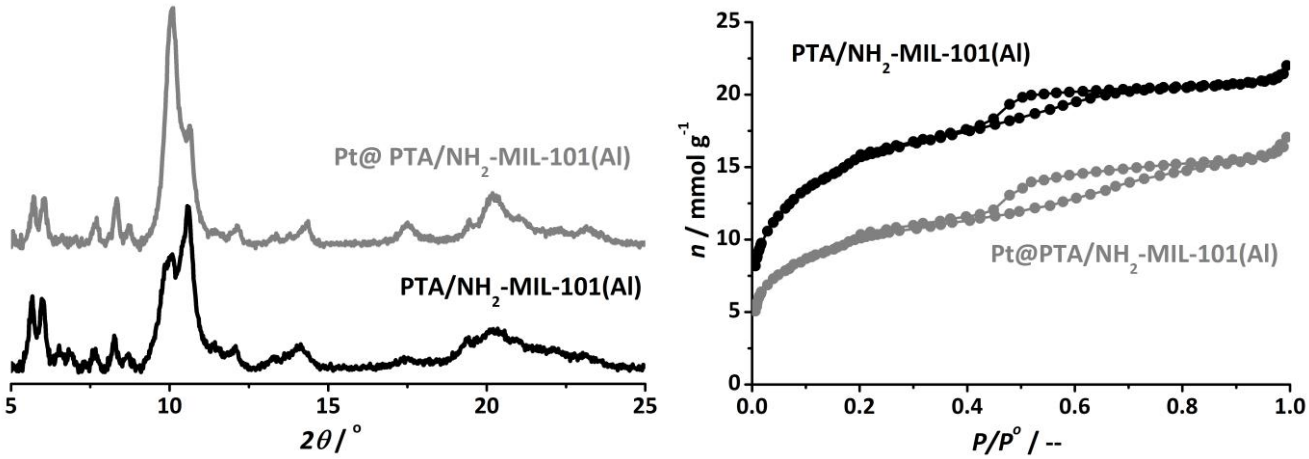

Figure 5 - 1 (*Left*) CoKα-XRD pattern: (*grey*) Pt(impregnated)@PTA/NH_2–MIL–101(Al), and (*black*) PTA/NH_2–MIL–101(Al). (*Right*) Nitrogen adsorption isotherms at 77 K: (*black*) PTA/NH_2–MIL–101(Al), and (*grey*) Pt(impregnated)@PTA/NH_2–MIL–101(Al).

Both the BET surface area and micropore volume decreased with the incorporation of platinum, while the amount of mesopores hardly changed. These results indicate that platinum incorporation partially blocks the microporosity of the material.

Table 5 - 1 Textural properties: Nitrogen adsorption isotherm calculations.

	S_{BET} [m^2/g]	$V_{micropore}$ [cm^3/g]	V_{total} [cm^3/g]	$V_{mesopore}$ [%]
PTA/NH_2–MIL–101(Al)	1260	0.45	0.72	38
Pt@PTA/NH_2–MIL–101(Al)	860	0.33	0.54	39

5.3.1.3. Diffuse Reflectance Fourier Transform Infrared Spectroscopy

The PTA Keggin unit is composed of a central PO_4 tetrahedron surrounded by twelve WO_6 octahedra. There are four types of oxygen atoms in the Keggin unit: four oxygen atoms of the central tetrahedron (O_a), 12 oxygen atoms that bridge tungsten atoms not sharing a central oxygen atom (corner-sharing, O_b), 12 oxygen atoms that bridge two tungsten atoms sharing the same central oxygen atom (edge-sharing, O_c), and 12 terminal oxygen atoms (O_d) associated with a single tungsten atom. According to literature, crystalline PTA shows characteristic bands at 1080 cm^{-1} (P–O_a), 978cm^{-1} (stretching of W=O_d), 888 (W–O_b–W), and 815 cm^{-1} (vibration of W–O_c–W). [35, 36]

In Figure 5–2, the IR spectra of PTA, PTA/MOF composite after subtracting the MOF background, and Pt containing samples (after impregnation and reduction at 473 or 573 K) after subtraction of the

PTA/MOF background are depicted. Substantial changes occur in the local environment of W, as shown by the shifts in the characteristic W–O bands after encapsulation and Pt impregnation. Upon encapsulation, the W–O_c–W stretching is split in two new features centered at 840 and 781 cm^{-1}. The W–O_b–W vibration is blue shifted to 905 cm^{-1}, while the W=O stretching is also split up in two new bands. The PO_4 vibrations do not change significantly. The results suggest a strong PTA/MOF interaction. [2, 37] After impregnation with hexachloroplatinic acid, all stretchings are red shifted, indicating the platinum complex (electron density on the platinum atom) is strongly interacting with the PTA. [25] After reduction in hydrogen at 473 and 573 K, the stretching vibrations associated with W=O and PO_4 are strongly modified which indicates a partial reduction of W in the PTA.

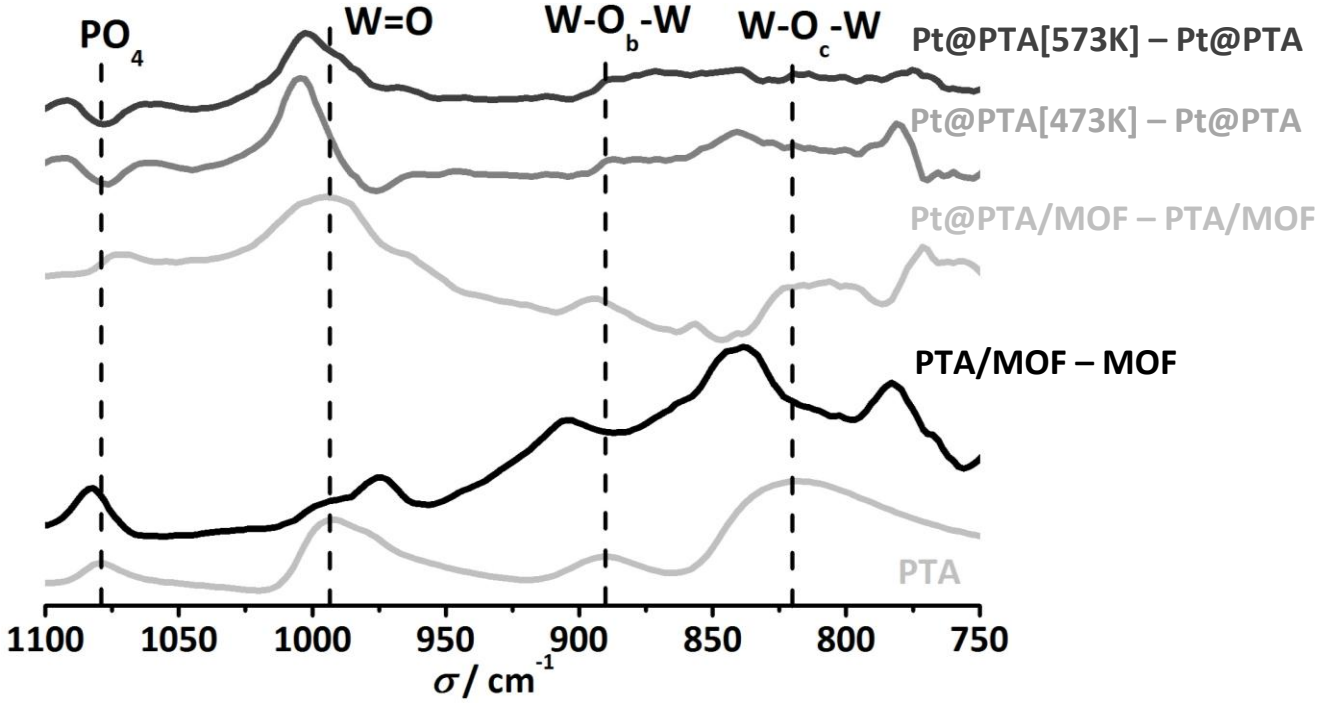

Figure 5 - 2 DRIFTS zoomed in at 1200–600 cm^{-1}. From the bottom to the top: PTA; PTA/NH_2–MIL–101(Al) subtracting NH_2–MIL–101(Al); Pt@PTA/NH_2–MIL–101(Al) subtracting PTA/NH_2–MIL–101(Al); Pt@PTA/NH_2–MIL–101(Al)[Red@473K] subtracting fresh Pt@PTA/MOF sample; Pt@PTA/NH_2–MIL–101(Al)[Red@573K] subtracting fresh Pt@PTA/MOF sample.

5.3.1.4. Infrared spectroscopy during CO adsorption at low temperature

Brønsted and Lewis acidity of NH_2–MIL–101(Al) and PTA/NH_2–MIL–101(Al) were evaluated by *in situ* IR spectroscopy during CO adsorption. The IR spectra were recorded at 143 K while gradually increasing the partial pressure of CO (Fig. 5–3).

When comparing the ν(OH) band for the NH_2–MIL–101(Al) and for PTA/NH_2–MIL–101(Al), two characteristic features can be observed. The first one is centered at 3708 cm^{-1} and corresponds to –OH linked to the aluminum oxide clusters. The second ν(OH) band centered at 3682 cm^{-1} is assigned to

similar –OH groups interacting by hydrogen bonding with the amino groups. [30, 38] When CO is dosed, the samples behave slightly different. In both cases, a new feature appears at 3664 cm^{-1} and grows while the absorption at 3708 cm^{-1} decreases due to the formation of –OH· · ·CO adducts. This phenomenon is a clear indication of the Brønsted acid character of this material, even though the red shift ($\Delta\nu$(OH) = 48 cm^{-1}) is not as large as for other Brønsted acid solids like zeolites. [39-41] Furthermore, the perturbation in the CO stretching region is also very small, corroborating the presence of weak Brønsted acidity.

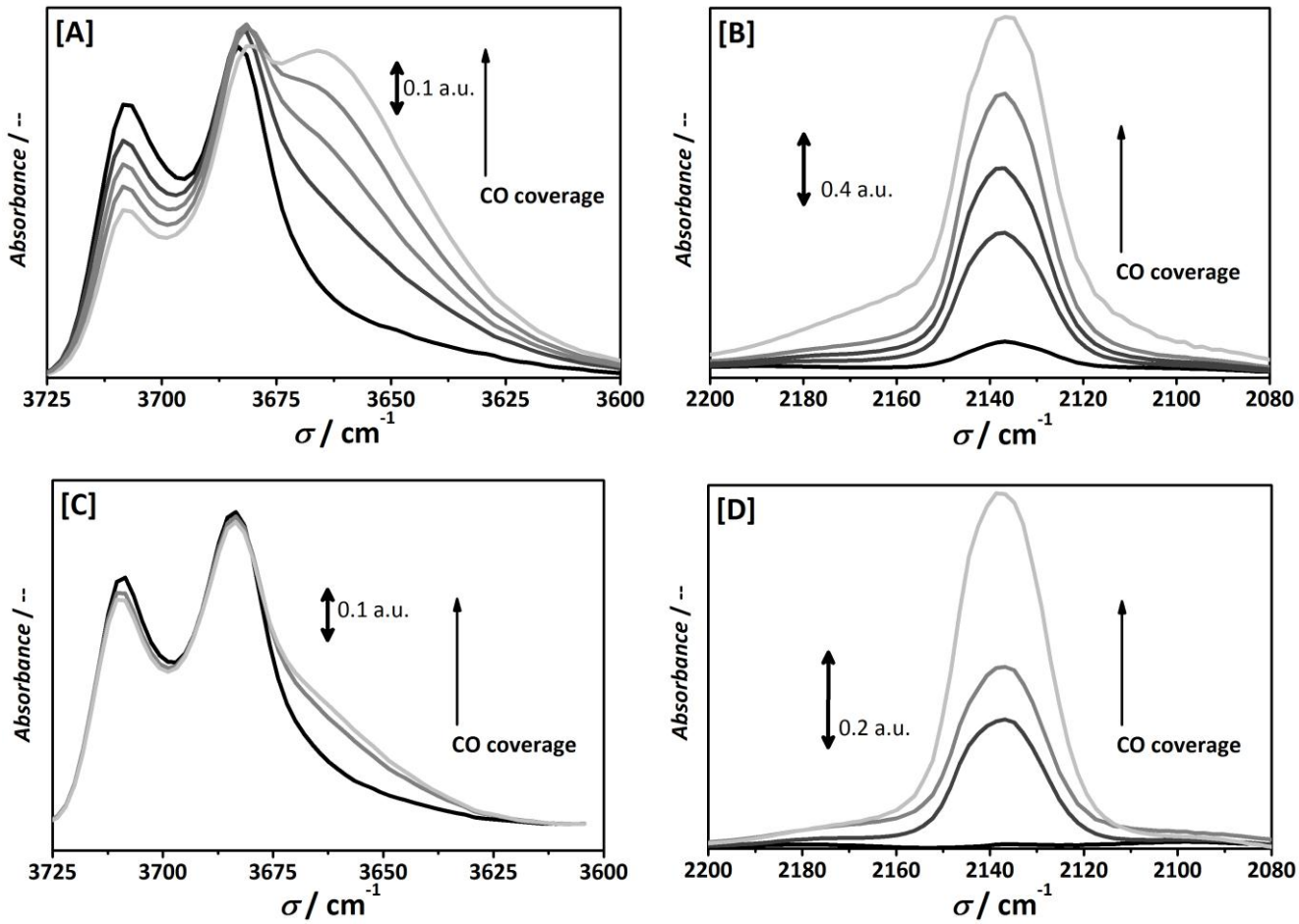

Figure 5 - 3 Transmission IR spectra of CO adsorption at 143 K. [A] NH_2–MIL–101(Al), OH region; [B] NH_2–MIL–101(Al), CO region; [C] PTA/NH_2–MIL–101(Al), OH region; [D] PTA/NH_2–MIL–101(Al), CO region.

The main difference between both samples is the intensity of ν(OH) associated with the Brønsted acidity. In the case of PTA/NH_2–MIL–101(Al), this vibration is less developed, due to low transmission values when PTA samples are measured, as well as to the interaction of the PTA with the MOF framework, reducing the Brønsted acid character of both PTA and MOF. Lewis acidity associated with coordinatively unsaturated sites (CUS) from aluminum trimers is not observed. This indicates that the aluminum trimers are fully saturated.

5.3.1.5. X–ray Photoelectron Spectroscopy and Elemental Analysis

The surface composition of the NH_2–MIL–101(Al), the PTA/MOF composite, and the Pt@PTA/MOF catalysts after different pre–treatments were analyzed by XPS. The spectra corresponding to O 1*s*, N 1*s*, C 1*s*, Al 2*p*, W 4*f*, and Pt 4*f* were collected. The survey results for the different Pt containing samples are depicted in Figure 5–4.

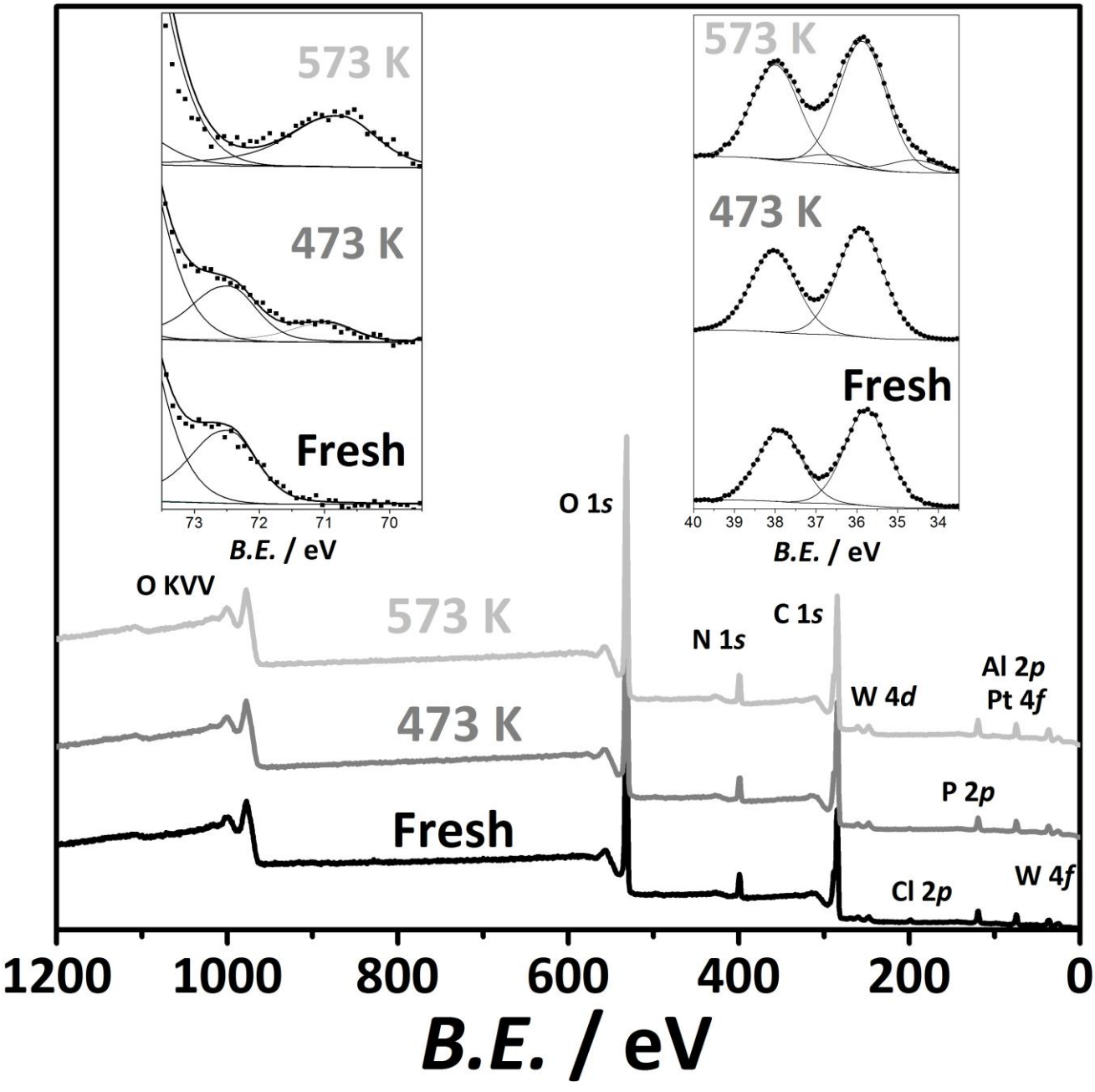

Figure 5 - 4 XPS survey spectra for the sample containing Pt before and after hydrogen reduction treatments. (*Left–insert*) zoom in the Pt $4f_{5/2}$ core–level. (*Right–insert*) Zoom in the W 4*f* core–level.

The binding energy value for Al 2*p* in all analyzed samples, before and after reduction, is 74.5 eV, which is typically assigned to Al^{3+}. It indicates that the oxidation state of the metal trimers does not

change upon reduction. The binding energy value for O 1*s* for the case of NH_2–MIL–101(Al) is deconvoluted in three contributions with values of 531.8, 533.0, and 529.9 eV. The main peak is centered at 531.8 eV, assigned to the terephthalate oxygen. [42] The other two peaks show a small contribution to the O 1*s* peak, and they are assigned to a small impurity of uncoordinated terephthalic acid (529 eV) and the hydroxyl groups present in the structure (533 eV). [43] When PTA and Pt are incorporated, no significant changes have been found, since the PTA oxygen atoms display similar binding energies. [44]

The Pt 4*f* level was analyzed after Pt impregnation and subsequent reductions at 473 and 573 K in H_2 atmosphere (Fig. 5–4). The untreated sample shows a binding energy of 75.7 eV for the $4f_{7/2}$ and 72.3 eV for the $4f_{5/2}$, which are typically assigned to Pt electron deficient species Pt^{n+}. After the treatment at 473 K, a new feature appears at 71.0 eV, which is ascribed to the $4f_{5/2}$ level for Pt^0, although the peak at 72.3 eV is still present, indicating that Pt is not fully reduced at 473 K. Complete Pt reduction was achieved after reduction at 573 K, as demonstrated by the presence of only one peak for the level $4f_{5/2}$ centered at 70.5 eV. [44, 45]

The binding energy values for the W 4*f* level in the PTA/MOF composite and in the non–reduced Pt sample are 35.7 eV ($4f_{5/2}$) and 37.8 eV ($4f_{7/2}$) (Fig. 5–4). These values are typically ascribed to W^{6+} in the Keggin structure. When the Pt sample is reduced at 473 K, the binding energy for W 4*f* level does not change, but after the treatment at 573 K under hydrogen, W^{6+} is partially reduced and two new peaks appear at 34.5 ($4f_{5/2}$) and 36.6 eV ($4f_{7/2}$). These peaks are assigned to W^{n+} with $n < 6$, indicating a modification of the W oxidation state. A colour change was also observed (the sample became blue) due to this treatment. PTAs are well–known to turn blue after reduction. [18, 19]

Table 5 - 2 Elemental information from XPS quantification and ICP–OES analysis.

	XPS			ICP–OES		
	Pt / Al	**W / Al**	**Pt / W**	**Pt / Al**	**W / Al**	**Pt / W**
Fresh	0.010	0.066	0.164	0.33	2.02	0.165
Red @ 473K	0.007	0.076	0.094			
Red @ 573K	0.006	0.079	0.085			

The atomic ratios calculated from the XPS data and those obtained by ICP–OES of the Pt@PTA/NH_2–MIL–101(Al) are shown in Table 5–2. In principle, the Pt/Al and W/Al XPS ratios can be an indication of the Pt and W dispersion. [53–55,57,58] The reduced samples present different atomic ratios, indicating Pt surface concentration decreases with increasing reduction temperature, while that of W increases. In all cases, the atomic ratios are lower than the ones calculated by ICP–OES, suggesting

that W and Pt are well inside the cavities. The Pt/W XPS atomic ratio of the unreduced sample is identical to the ICP–OES analysis, but the XPS ratio decreases with increasing the temperature of reduction. Most probably, platinum is being progressively buried into the Keggin POM, since no leaching during pre–treatments is likely to occur.

5.3.1.6. Infrared spectroscopy during CO chemisorption at room temperature

Figure 5–5 shows the transmission IR spectra of the three different Pt containing PTA/MOF catalysts upon CO adsorption at room temperature.

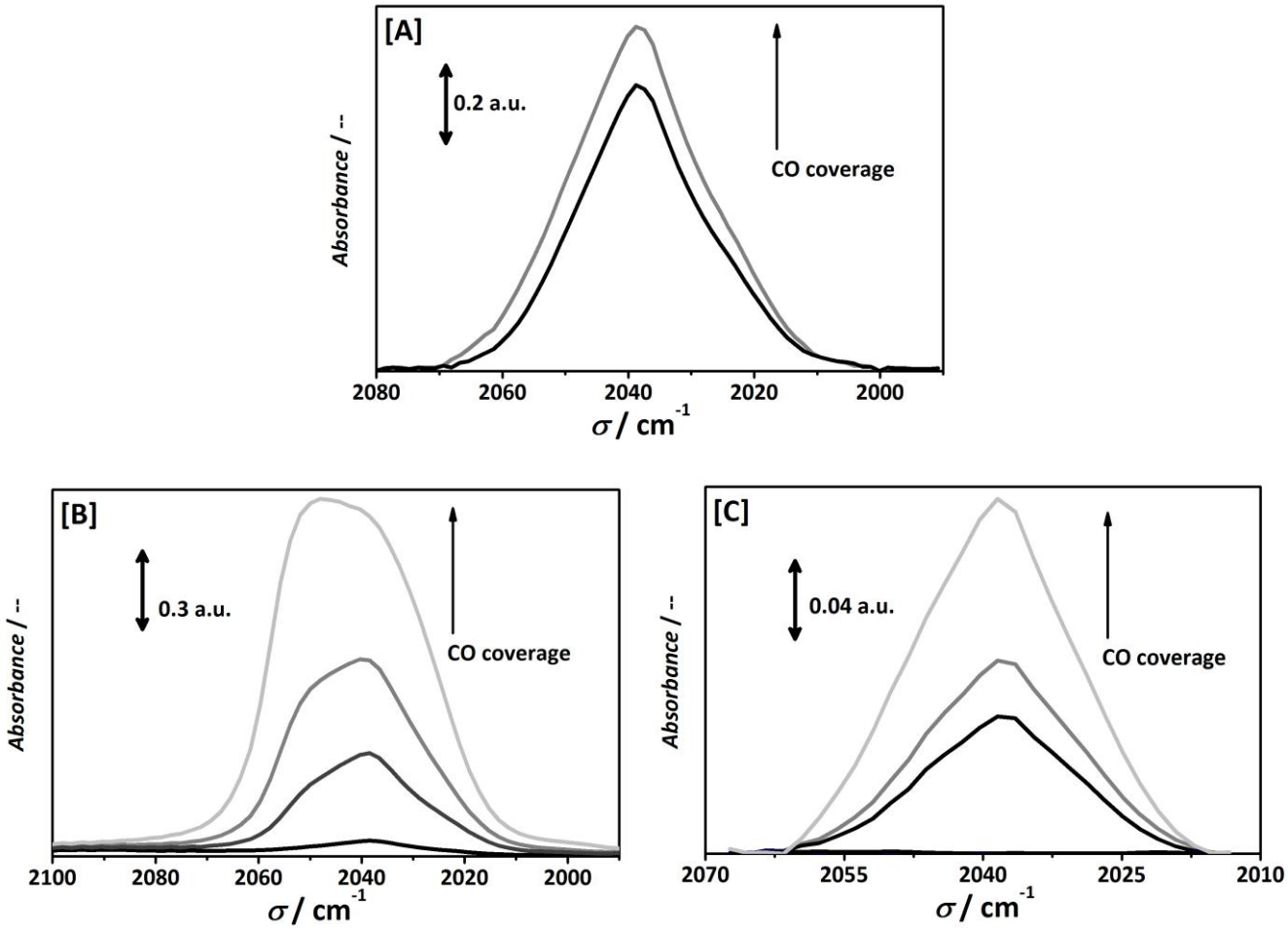

Figure 5 - 5 IR spectra after CO chemisorption at 300 K. (A) fresh sample; (B) after reduction at 473 K; (C) after reduction at 573 K.

While the as–synthesized sample displays one single ν(CO) band centered at 2035 cm^{-1}, in the case of the mild reduced sample (473K) two ν(CO), bands are observed at 2039 and 2051 cm^{-1}. These bands are assigned to linear CO adsorbed on two different Pt species, and no bridging CO adsorbed was detected. After reduction at 573 K, a similar spectrum as for the as–synthesized catalyst was obtained, but with a much lower intensity. Apparently, this lower CO adsorption capacity is associated with less exposed Pt atoms after reduction at high temperature.

5.3.1.7. ^{31}P Magic Angle Spinning Nuclear Magnetic Resonance

Figure 5–6 shows the ^{31}P MAS NMR spectra for the as–synthesized PTA/NH_2–MIL–101(Al) and for the impregnated Pt@PTA/NH_2–MIL–101(Al) samples. While the free PTA displays only one peak at ~15 ppm (shown in previous chapters), two chemical shifts, centered around ~13.5 and ~15.9 ppm, are found in the spectra of the PTA/MOF composites, suggesting a very strong interaction after encapsulation. Incorporation of Pt does not seem to introduce a large change on the state of P atoms.

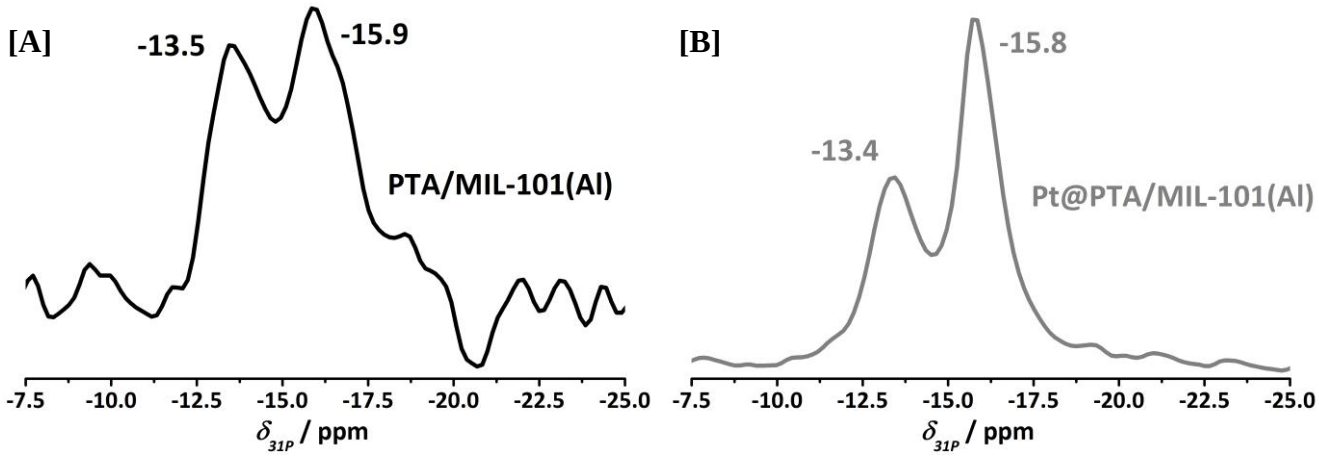

Figure 5 - 6 ^{31}P MAS NMR spectra. [A] PTA/NH_2–MIL–101(Al) and [B] Pt@PTA/NH_2–MIL–101(Al).

5.3.1.8. UV–Vis Spectroscopy

The UV–Vis spectra of the NH_2–MIL–101(Al) and the structures containing PTA and Pt@PTA have been measured in diffuse reflectance and are presented as Kubelka–Munk units in Figure 5–7.

The PTA/NH_2–MIL–101(Al) shows three new peaks centered at 290, 330, and 400 nm, belonging to the ligand to metal charge transfer (O to W) of the three different types of oxygen atoms present in the PTA structure. The sample containing Pt presents a new band centered at 520 nm assigned to the metal–to–metal charge transfer (Pt to W), which further reveals that Pt and W elements are indeed, in very close proximity.

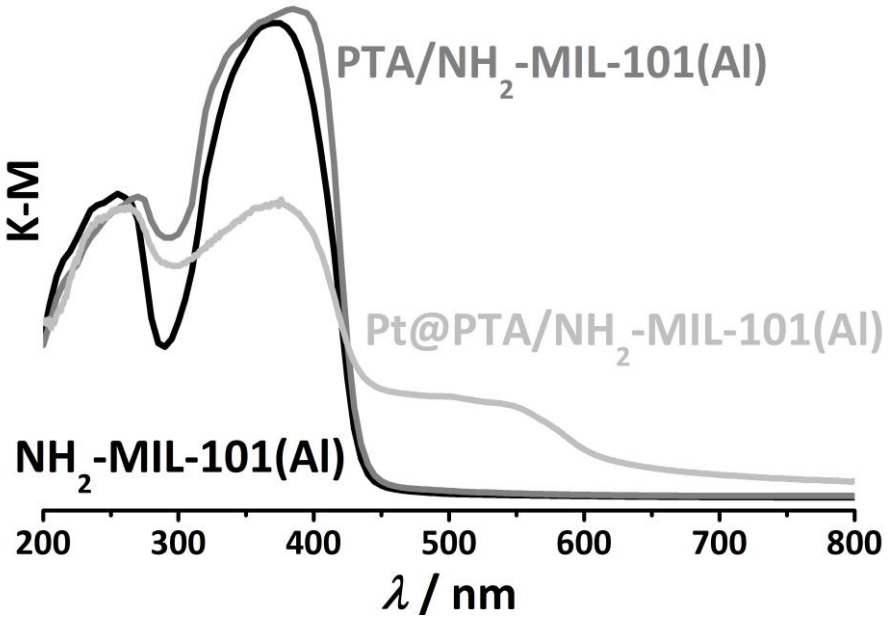

Figure 5 - 7 Kubelka–Munk transformation of UV–Vis diffuse reflectance spectra. (*Black*) NH_2–MIL–101(Al). (*Grey*) PTA/NH_2–MIL–101(Al). (*Light grey*) Pt@PTA/NH_2–MIL–101(Al).

5.3.2. Catalytic Performance

5.3.2.1. Toluene hydrogenation reaction

Toluene hydrogenation was carried out as a model reaction for hydrogenation activity. The performance of the Pt(1.3wt%)@PTA/MOF samples was benchmarked against the commercial Pt(1wt%)/Al_2O_3 catalyst in terms of turnover frequency values (*TOF*) (Fig. 5–8) during three consecutive runs (before every run activation upon reduction was performed).

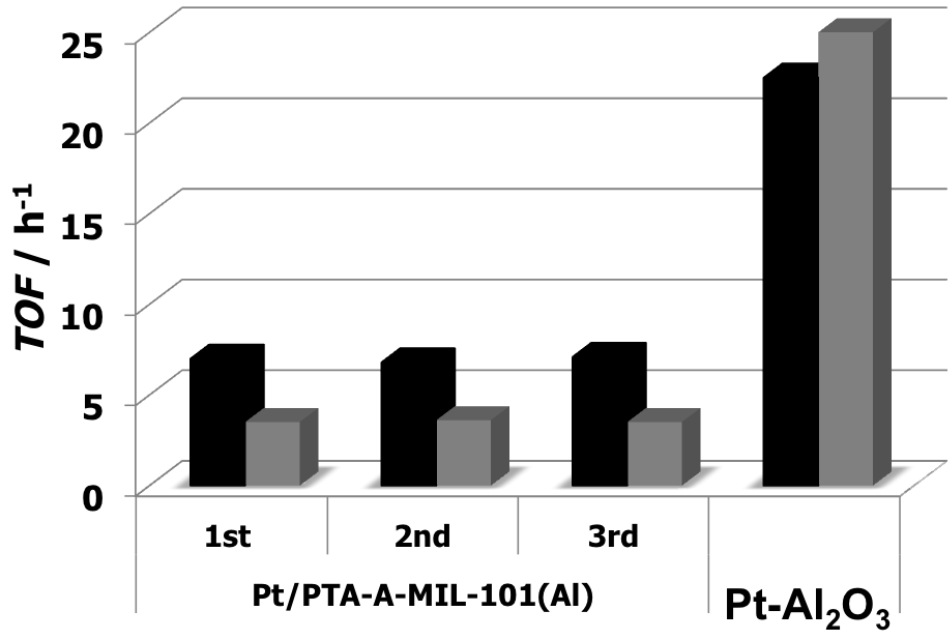

Figure 5 - 8 Turnover frequencies in the toluene hydrogenation at 423 K for Pt@PTA/NH_2–MIL–101(Al) for several consecutive runs and compared with Pt/Al_2O_3 reference catalyst, both reduced at 473 K (*Black*) and 573 K (*Grey*).

Even though dispersion of the active phase (Pt particle size) could not be quantified, the direct comparison with the commercial catalyst shows very little active for Pt@PTA/MOF. However, the catalysts can be re–used without any significant loss of activity, indicating good stability. When reducing the sample after every use, the Pt clusters might became smaller due to the formation of intermetallic species with W interaction and therefore displaying slightly lower catalytic activity for the reaction studied.

5.3.2.2. CO oxidation reaction

The catalytic activity of the synthesized materials for CO oxidation was determined in a typical light–off experiments (Fig. 5–9). The Pt@PTA/NH_2–MIL–101(Al) catalyst shows higher activity upon increasing reduction severity. Hence, the temperature at 50% CO conversion (T_{50}) was 70 K lower for the sample reduced at 573 K than for the fresh sample. In the absence of Pt, blank experiments performed with NH_2–MIL–101(Al), PTA or the PTA/MOF composite display negligible activity.

In contrast to the hydrogenation test reaction, the catalytic activity of the 1 wt% Pt/Al_2O_3 reference catalyst reduced at 573 K is lower than that of the Pt@PTA/MOF treated at the same reduction temperature. However, analysis of the catalyst stability after testing was impossible, due to impurities in the reactor, making very difficult the characterization of the used catalyst.

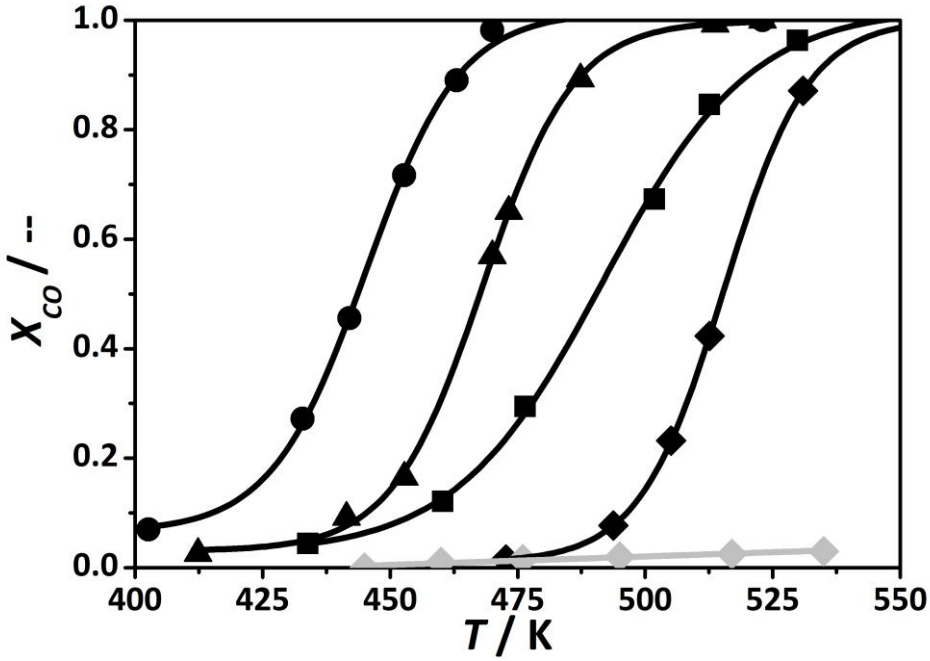

Figure 5 - 9 CO conversion as a function of temperature. (*Diamonds*) Unreduced sample; (*Squares*) Pt/Al_2O_3 reference catalyst reduced at 573 K; (*Triangles*) Pt@PTA/NH_2–MIL–101(Al) reduced at 473 K; and (*Circles*) reduced at 573 K; (*Diamonds–grey*) PTA/NH_2–MIL–101(Al) reduced at 573 K.

5.3.2.3. Preferential CO oxidation in H_2 presence

The CO oxidation activity of the catalysts in the presence of hydrogen (PROX reaction) differs from the previous case (Fig. 5–10).

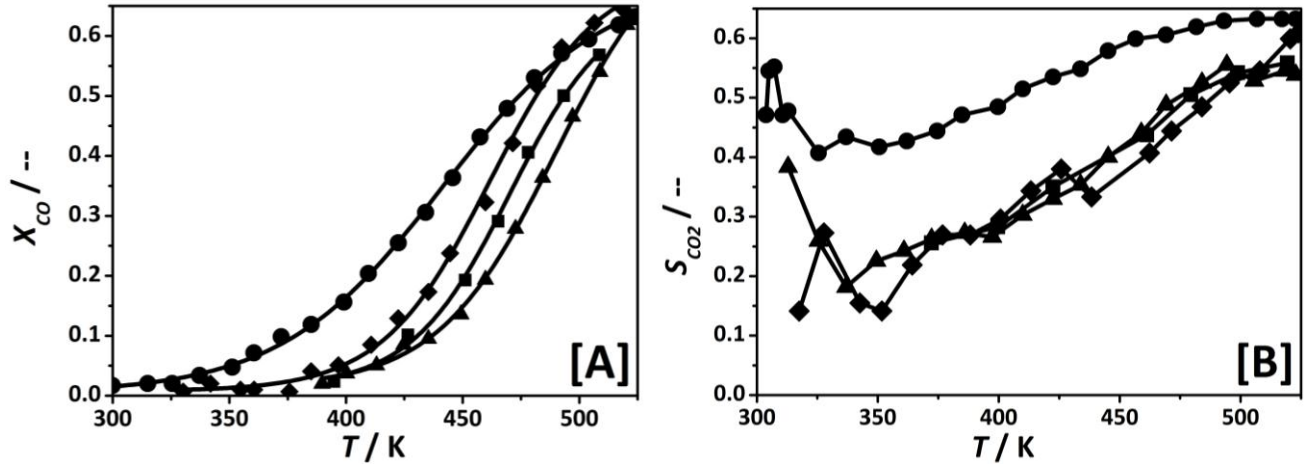

Figure 5 - 10 Preferential oxidation of CO in the presence of H_2. [A] CO conversion, and [B] selectivity toward CO_2 as a function of temperature. (*Diamonds*) Unreduced sample; (*Triangles*) Pt@PTA/NH_2–MIL–101(Al) reduced at 473 K; (*Circles*) and reduced at 573 K; (*Squares*) Pt/Al_2O_3 reference catalyst reduced at 573 K.

The sample reduced at 573 K oxidizes CO at lower temperatures and displays the highest selectivity toward CO_2. The fresh catalyst performs slightly better than the sample reduced at 473 K and the reference catalyst, being the three very similar and less active than the Pt@PTA/MOF sample reduced at higher temperature.

5.4. DISCUSSION

Microwave synthesis of the NH_2–MIL–101(Al) in the presence of PTA results in the incorporation of PTA with an excellent dispersion. The resulting composite is an exceptional support for anchoring highly dispersed Pt species, which depending on the subsequent hydrogen treatment, display different performances, as follows from the characterization and catalytic model reactions.

The one–pot encapsulation performed by microwave heating reveals that the formation of the MIL–101 structure is not affected by the PTA presence (Fig. 5–1). The absence of XRD reflections corresponding to PTA indicates its good dispersion over the sample. [46] These results are in agreement with the N_2 adsorption isotherms, where the two characteristic steps of MIL–101 at low relative pressure remain present. [8, 9, 29, 47-49] The encapsulation of PTA in the framework results in a pronounced decrease in the N_2 adsorption capacity, associated with the PTA loading (12 wt%). The obtained W content of 12 wt% corresponds to approximately one PTA molecule per cavity and reduces the accessible volume. The nitrogen adsorption isotherm for the PTA/NH_2–MIL–101(Al) shows a well–defined hysteresis loop attributed to agglomerates of nanocrystals. This has previously been reported for materials synthesized in DMF under microwave irradiation, the so–called metal organic gels. [50] The XPS results reveal that W/Al atomic ratio is much lower than the elementary composition determined by ICP–OES, indicating that Keggin are well dispersed inside the MOF crystal. Since XPS is a surface sensitive technique, while the Keggin units located inside the crystal are hardly detectable, and together with the N_2 adsorption and X–ray diffraction results, prove the presence of PTA inside the MOF cavities. The presence of the immobilized PTA is also confirmed by UV–Vis (Fig. 5–7), showing three new peaks at 290, 330, and 400 nm for the PTA containing MOF samples and ascribed to oxygen–to–tungsten charge characteristic transfer in the polyoxometalate. [51]

Through the one–pot encapsulation of the PTA, some of its physicochemical properties may be altered. The most important changes are highlighted below, based on the thorough characterization performed.

In the ^{31}P NMR spectra (Fig. 5–6), two different chemical shifts centered around ~15 ppm are found. The shift downfield is attributed either to partial dehydration (adsorbed water removal) of the PTA during the synthesis process [25, 43] or to interaction of the PTA with the MOF surface. The shift

upfield is attributed to partial deprotonation of the PTA. [52] The presence of both peaks strongly suggests that the PTA is deprotonated and strongly interacting with the MOF interior.

DRIFT spectra also point at changes in the PTA after encapsulation: the vibration of W–O_c–W is shifted to 840 cm^{-1}, W–O_b–W is blue shifted to 905 cm^{-1}, W=O stretching is also split in two new bands, while the PO_4 vibration does not change significantly. All these changes are assigned to the presence of PTA anions strongly interacting with the surface, [2] in good agreement with the ^{31}P MAS NMR observations. PTA/NH_2–MIL–101(Al) displays lower acidity than the pure NH_2–MIL–101(Al) indicating that encapsulated PTA is highly deprotonated and that the accessibility of the Al nodes is higher in the pristine NH_2–MIL–101(Al). In addition, the fact that the pristine MOF did not survive the impregnation with Pt points in the same direction. Indeed, the presence of polyoxometalate within different MOFs has shown to result in an enhanced thermal and chemical stability. [53]

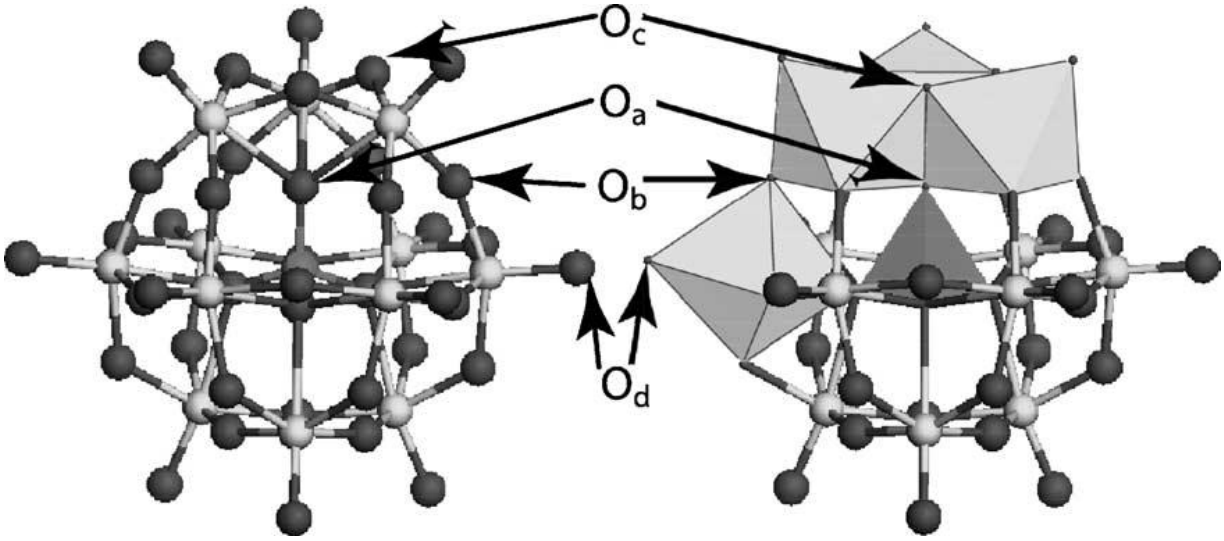

Figure 5 - 11 Representation of the Keggin structure of $PW_{12}O_{40}^{-3}$, indentifying the four types of oxygen in the structure. Copy from reference [35].

The incorporation of platinum produces remarkable changes in the chemical properties of the composites. ^{31}P MAS NMR suggests that the Keggin unit is surrounded by an electron–enriched environment, produced by the interaction of anionic platinum complexes ($(Pt^{n+}Cl_m)^{(m-n)}$ with $m > n$) with the PTA, as inferred from the increase in intensity of the upfield P species. This hypothesis is further supported by IR spectroscopy, where W=O_d, W–O_b–W and W–O_c–W stretching are clearly affected. These data together with the pronounced band observed at 530 nm in the UV–Vis (attributed to Pt–W charge transfer) confirms the hypothesis that platinum species are anchored to the PTA units. The uncoordinated adsorbed species are just washed out after the impregnation. The collapse of the pristine NH_2–MIL–101(Al) structure upon impregnation indicates that PTA plays an important role in the MOF stabilization. [53, 54] It has been proposed that PTAs electrostatically interact with the

metallic clusters, minimizing in this way the destruction of the framework by inhibiting the adsorption of corrosive species (water, acid compounds, etc.) at such nodes.

In situ infrared spectroscopy of adsorbed CO has been used to characterize metal dispersion and chemical nature of the metal species. In the case of the non–reduced catalysts, only a single, well defined, band centered at 2039 cm^{-1} can be observed. Both the extreme shift of the band and the absence of a coverage–dependent shift points at the formation of metal–carbonyl species rather than CO adsorption on a metal surface; suggesting the presence of monoatomically dispersed Pt located on the encapsulated PTA. Platinum carbonyls containing only CO ligands are unknown or very unstable; however, the oxygen atoms in the PTA framework may act as sigma–donor ligands and stabilizers of a structure like $O_mPt(CO)_y$. [44] The low stability of these carbonyl adducts is confirmed by their easy removal upon evacuation and the catalytic behavior of the sample in CO oxidation (discussed below).

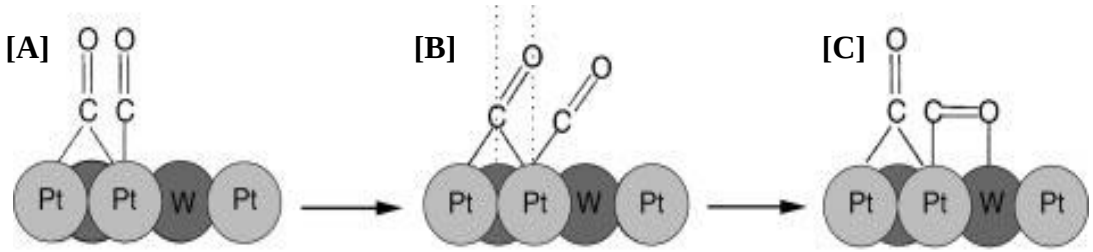

Figure 5 - 12 Suggested mechanism for the formation of C– and O–bonded surface species on platinum well dispersed on tungsten. Copy from reference [55]. [A] Linear complex. [B] Activated state. [C] Tilted complex.

When the sample is reduced at 473 K, a new absorbance appears at higher wavenumbers (2055 cm^{-1}), characteristic of CO adsorbed at small Pt^0 nanoclusters, as evidenced by XPS (new peak at 71 eV). [56] These results confirm the coexistence of two types of Pt species in the sample: isolated Pt^{2+} ion complexes and small clusters of Pt^0. After reduction at 573 K, only a single absorbance is observed at 2039 cm^{-1}, while only Pt^0 was found by XPS. Therefore, the presence of a carbonyl bond on nanoparticle surfaces is very unlikely, as this would yield absorbance at higher wavenumbers. Alexeev and co–workers have explained this unusual behavior for a similar system, PtW_2/Al_2O_3. [55] They relate this red–shifted absorption band to CO adsorbed on electron–rich platinum, with electron donation from CO 5σ molecular orbitals to vacant metal *d*–orbitals and back–donation from filled metal *d*–orbitals to CO $2\pi^*$ antibonding molecular orbitals. This suggests a strong Pt–W interaction and consequently an increase in Pt electron density. This strong Pt–W interaction is supported by the presence of a new peak in the W 4*f* level (XPS), confirming the partial reduction of tungsten. Furthermore, due to the Pt–W interaction, the formation of tilted CO species is facilitated, where the

carbon atom is bonded to the platinum and the oxygen is bonded to an oxophilic partially reduced tungsten cation.

Comparing the Pt composition in the surface of the material from XPS with the bulk composition from ICP–OES indicates that the surface concentration of Pt decreases with increased reduction temperature. The as–prepared sample contains monoatomically dispersed Pt, resulting in a Pt/W atomic XPS ratio similar to the bulk Pt/W atomic ratio (ICP–OES). When the temperature of reduction is increased, some Pt nanoclusters are formed and the Pt surface concentration decreases due to this agglomeration. It is worth to notice that particle size is very small, since the adsorption band at 2051 cm^{-1} is normally associated with CO adsorbed on high–uncoordinated platinum atoms. Furthermore, it is important to remark that after the impregnation, there are on average two platinum atoms per Keggin unit and one Keggin unit per cavity of MOF, so platinum sintering to form large particles is highly unlikely. The observed clusters will consist of only a few platinum atoms. If the temperature of reduction is further increased, a strong metal–support interaction occurs and Pt–W intermetallic species are formed, with a further decreased of the atomic Pt/W XPS ratio.

As to the catalytic activity of the different samples, in the case of toluene hydrogenation, the reduction treatment strongly affects the catalytic activity (Fig. 5–8). The sample reduced at 573 K shows a lower hydrogenation activity than the sample reduced at 473 K, in agreement with the decreased Pt/W XPS ratio with temperature. The higher activity of the commercial Pt/Al_2O_3 catalyst is not surprising considering that the platinum species deposited on the PTA are atomically dispersed or clusters of a few atoms. These ensembles are too small for toluene and hydrogen (co–)adsorption. Even though toluene hydrogenation is traditionally considered as a structure–insensitive reaction, this breaks down for too small Pt particles as is the case here with the high platinum dispersion. Furthermore, Alexeev *et al.* recently reported that small Pt clusters supported on WO_3/Al_2O_3 have a low activity for toluene hydrogenation. [45, 55] This was explained by the insufficient amount of sites on the small Pt clusters to accommodate the reactants and the close proximity of the Pt with cations of oxophilic metals diminishing the catalytic activity. [57] These thoughts resembles our findings with the atomically dispersed Pt in close proximity with oxophilic tungsten. Moreover, after reduction at 573 K, intermetallic species Pt–oxophilic W are formed, and the catalytic activity drops. These results further confirm the strong Pt–W interaction and the very small Pt particles formation. The stability and re–usability of the Pt@PTA/MOF composites is beyond question.

The light–off experiments in CO oxidation show increasing activity of the PTA supported Pt catalysts with reduction temperature (Fig. 5–9). The temperature where half conversion is reached, T_{50}, is 70 K lower for the sample reduced at 573 K than for the untreated sample, while all have a similar apparent

activation energy of ~120 kJ mol^{-1}. The reference catalyst exhibits an activity intermediate between the untreated and 473 K treated sample, with lower activation energy (~100 kJ mol^{-1}). The fresh sample does not have any Pt nanoparticles, which are the most active species for CO oxidation, although it displays some catalytic activity. As this occurs above 470 K, this is attributed to decomposition of the adsorbed complex, freeing up the Pt coordination sphere, and to some formation of active clusters. Pt–Cl species are known to migrate, a property used to re–disperse Pt on, *e.g.*, reforming catalysts. The reduction in hydrogen at 473 K accelerates the complex decomposition, and small Pt clusters are created on the surface of the PTA, increasing the catalytic activity. These clusters must consist of only a few Pt atoms, as the PTA units in the MIL–101 cages can accommodate only a few Pt complexes (null atoms per Keggin unit) in view of their valence. The further activity increase after reduction at 573 K is ascribed to the formation of Pt–W intermetallic species. These species favor tilted adsorption, which strongly weaken the CO molecules. [55] Furthermore, the presence of partially reduced W favors the adsorption of O_2 in close proximity to the CO, which enhances the oxidation activity.

The lower activity of the reference Pt/Al_2O_3 catalyst, also pre–treated at 573 K, is attributed to the strong chemisorption of CO, inhibiting the adsorption of oxygen. Higher temperatures are required to liberate sites before reaction can take place. [45] This inhibition is absent for the Pt@PTA catalysts as the CO chemisorbs less strongly on the Pt. The IR experiments showed that evacuation is enough to remove CO, which is impossible for the Pt/Al_2O_3 catalyst. [56] Inhibition generally increases the apparent activation energy of catalytic reactions, so the high activation energy of the Pt@PTA/MOF catalysts points to another kinetic process. Since PTA itself is a good oxidation catalyst, [17] it is speculated that the oxygen is adsorbed on the PTA, after which it reacts with the CO adsorbed on the Pt. The intermetallic Pt–W species formed after reduction at 573 K constitute then the optimal active site where both reactants adsorb next to each other without inhibiting one another. It points to a Mars van Krevelen mechanism where the oxygen is provided by the support and it is replenished in separate consecutive reaction, resembling the partially reducible supports used in the PROX reaction. [58]

PROX of CO is considered the simplest and most effective method for purifying H_2–rich gases. The key point is a catalyst displaying a good activity and high selectivity for CO oxidation in the presence of H_2 in a wide temperature–window, a high tolerance toward CO_2 and H_2O, usually present in reformed fuel, and a low activity for undesired side reactions like H_2 oxidation, reverse WGS, methanation, etc. Thus, partially reducible supports are used to enhance selectivity, [48, 59] since the noble metal can chemisorb the CO and the partially reduced support can enhance the O_2 adsorption, apart from the electronic density change on the noble metal. In contrast, pure noble metals will preferentially oxidize H_2. In this light and following the discussion on the CO oxidation above, the

higher activity and especially selectivity of the Pt@PTA/MOF composite containing the intermetallic Pt–W species than the other samples (Fig. 5–10) is completely in line with this interpretation. The selective oxidation to CO_2 of the latter catalysts ranges from ~45% at room temperature to ~65% at 500 K where all oxygen is converted. This suggests that at lower temperature, one oxygen atom is picked up by the CO, and the other by a hydrogen molecule. Apparently at lower temperature, the CO is not able to regenerate the oxidized W site. With increasing temperature this phenomenon is possible, as it enters the region where the CO oxidation occurs and hence the selectivity increases. Apparently, this changeover in reduction power of H_2 and CO with temperature results in the lower apparent activation energy (~50 kJ/mol). Consequently, in the oxidation of CO in the absence of hydrogen, the regeneration of the oxidized tungsten is the rate determining process. In view of the similar apparent activation energies, this holds for all Pt@PTA/MOF catalysts.

Summarizing, PTA/MOF composites offer excellent possibilities for metal nanoparticle engineering. On the one hand, the encapsulation of PTA, and probably polyoxometalates (POMs) in general, yields a good and stable support for a homogeneous metal distribution in the whole MOF network. On the other hand, the remarkable redox character of the PTA allows a fine–tuning of the metal species by pretreatment optimization, going from monodispersed cationic species to small nanoparticles to intermetallic species.

5.5. CONCLUSIONS

Highly dispersed PTA was successfully incorporated in NH_2–MIL–101(Al) in a single–step microwave synthesis. This PTA can be used as a support to accommodate molecularly dispersed Pt complexes, which, after the adequate pre–treatment, can be used as catalyst in hydrogenation and oxidation reactions. Reduction treatment in hydrogen decomposes these complexes and creates small Pt metal clusters. At 473 K, the platinum is only partially reduced and two different Pt species are present, Pt^0 and Pt^{2+}. Upon increasing the reduction temperature to 573 K, only Pt^0 is formed, and in addition, the tungsten is partially reduced to W^{5+}, resulting in the formation of Pt–W intermetallic species. In all catalysts, the CO adsorption is much weaker than on Pt surfaces.

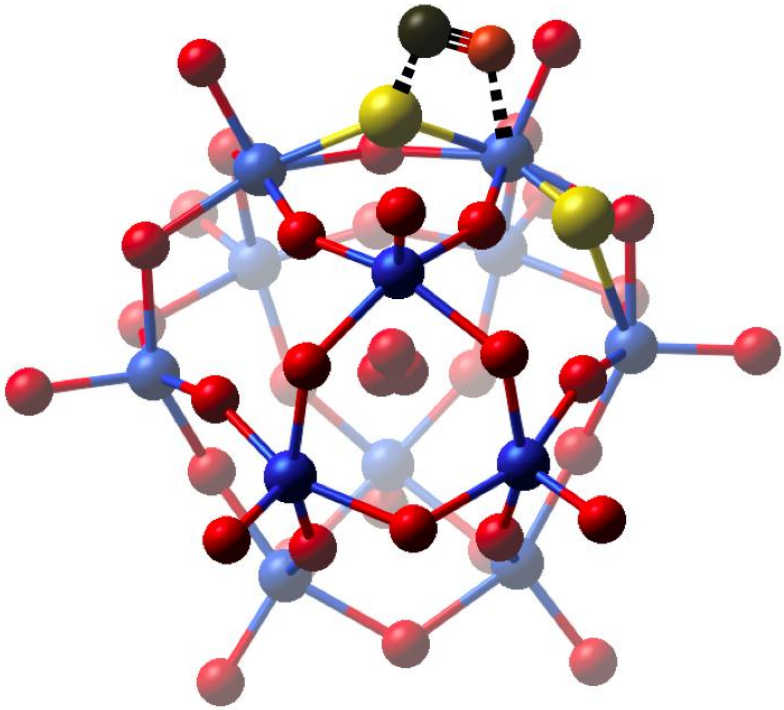

Figure 5 - 13 Platinum incorporated in the Keggin PTA structure with tilded CO adsorption. *Red*: oxygen. *Blue*: tungsten. *Yellow*: platinum. *Black*: carbon

In the CO oxidation in the absence or presence of H_2, the Pt–W species exhibit the highest catalytic activity and resemble noble metal catalysts on a reducible support. In all catalysts, the rate determining step (rds) is the reduction in the oxidized tungsten sites. In the particular case of the PROX reaction, the selectivity is also improved due to the formation of such intermetallic species facilitating CO tilted adsorption, which strongly weakens the CO bond and hinders the H_2 chemisorption. In both the CO oxidation and PROX reaction, the reduced Pt@PTA/MOF catalyst is more active than a commercial Pt/Al_2O_3 reference catalyst, but in toluene hydrogenation the reverse holds. In the latter case, the sufficiently large Pt ensembles needed are absent in the MOF–based catalysts.

REFERENCES

[1] T. Hsu-Yao, K.P. Browne, N. Honesty, Y.J. Tong, Polyoxometalate-stabilized Pt nanoparticles and their electrocatalytic activities, Physical Chemistry Chemical Physics, 13 (2011) 7433-7438.
[2] L.I. Kuznetsova, N.I. Kuznetsova, S.V. Koshcheev, V.A. Rogov, V.I. Zaikovskii, B.N. Novgorodov, L.G. Detusheva, V.A. Likholobov, D.I. Kochubey, Interaction of platinum and molybdophosphoric heteropoly acid under conditions of catalyst preparation for benzene oxidation to phenol with an O_2-H_2 gas mixture, Kinetics and Catalysis, 47 (2006) 704-714.
[3] G. Sun, Q. Li, R. Xu, J. Gu, M. Ju, E. Wang, Controllable fabrication of platinum nanospheres with a polyoxometalate-assisted process, Journal of Solid State Chemistry, 183 (2010) 2609-2615.
[4] S. Gao, Z. Wu, D. Pan, Z. Lin, R. Cao, Preparation and characterization of polyoxometalate-Ag nanoparticles composite multilayer films, Thin Solid Films, 519 (2011) 2317-2322.
[5] A. Dolbecq, E. Dumas, C.R. Mayer, P. Mialane, Hybrid organic-inorganic polyoxometalate compounds: From structural diversity to applications, Chemical Reviews, 110 (2010) 6009-6048.
[6] I.V. Kozhevnikov, Catalysis by Heteropoly Acids and Multicomponent Polyoxometalates in Liquid-Phase Reactions, Chemical Reviews, 98 (1998) 171-198.
[7] C.Y. Sun, S.X. Liu, D.D. Liang, K.Z. Shao, Y.H. Ren, Z.M. Su, Highly stable crystalline catalysts based on a microporous metal-organic framework and polyoxometalates, Journal of the American Chemical Society, 131 (2009) 1883-1888.
[8] J. Juan-Alcañiz, E.V. Ramos-Fernandez, U. Lafont, J. Gascon, F. Kapteijn, Building MOF bottles around phosphotungstic acid ships: One-pot synthesis of bi-functional polyoxometalate-MIL-101 catalysts, Journal of Catalysis, 269 (2010) 229-241.
[9] Y. Zhang, V. Degirmenci, C. Li, E.J.M. Hensen, Phosphotungstic acid encapsulated in metal-organic framework as catalysts for carbohydrate dehydration to 5-hydroxymethylfurfural, ChemSusChem, 4 (2010) 59-64.
[10] D.D. Liang, S.X. Liu, F.J. Ma, F. Wei, Y.G. Chen, A crystalline catalyst based on a porous metal-organic framework and 12-tungstosilicic acid: Particle size control by hydrothermal synthesis for the formation of dimethyl ether, Advanced Synthesis and Catalysis, 353 (2011) 733-742.
[11] S.R. Bajpe, E. Breynaert, D. Mustafa, M. Jobbágy, A. Maes, J.A. Martens, C.E.A. Kirschhock, Effect of Keggin polyoxometalate on Cu(II) speciation and its role in the assembly of $Cu_3(btc)_2$ metal-organic framework, Journal of Materials Chemistry, 21 (2011) 9768-9771.
[12] J. Juan-Alcañiz, M. Goesten, A. Martinez-Joaristi, E. Stavitski, A.V. Petukhov, J. Gascon, F. Kapteijn, Live encapsulation of a Keggin polyanion in NH_2-MIL-101(Al) observed by in situ time resolved X-ray scattering, Chemical Communications, 47 (2011) 8578-8580.
[13] F.J. Ma, S.X. Liu, C.Y. Sun, D.D. Liang, G.J. Ren, F. Wei, Y.G. Chen, Z.M. Su, A sodalite-type porous metal-organic framework with polyoxometalate templates: Adsorption and decomposition of dimethyl methylphosphonate, Journal of the American Chemical Society, 133 (2011) 4178-4181.
[14] R. Canioni, C. Roch-Marchal, F. Sécheresse, P. Horcajada, C. Serre, M. Hardi-Dan, G. Férey, J.M. Grenèche, F. Lefebvre, J.S. Chang, Y.K. Hwang, O. Lebedev, S. Turner, G. Van Tendeloo, Stable polyoxometalate insertion within the mesoporous metal-organic framework MIL-100(Fe), Journal of Materials Chemistry, 21 (2011) 1226-1233.
[15] A.M. Khenkin, G. Leitus, R. Neumann, Electron Transfer−Oxygen Transfer Oxygenation of Sulfides Catalyzed by the $H_5PV_2Mo_{10}O_{40}$ Polyoxometalate, Journal of the American Chemical Society, 132 (2010) 11446-11448.
[16] N.I. Kuznetsova, L.I. Kuznetsova, V.A. Likholobov, Catalytic properties of Cr-containing heteropolytungstates in H_2O_2 participated reactions: H_2O_2 decomposition and oxidation of unsaturated hydrocarbons with H_2O_2, Journal of Molecular Catalysis A: Chemical, 108 (1996) 135-143.
[17] M.H. Seo, S.M. Choi, H.J. Kim, J.H. Kim, B.K. Cho, W.B. Kim, A polyoxometalate-deposited Pt/CNT electrocatalyst via chemical synthesis for methanol electrooxidation, Journal of Power Sources, 179 (2008) 81-86.
[18] S. Li, X. Yu, G. Zhang, Y. Ma, J. Yao, P. De Oliveira, Green synthesis of a Pt nanoparticle/polyoxometalate/carbon nanotube tri-component hybrid and its activity in the electrocatalysis of methanol oxidation, Carbon, 49 (2011) 1906-1911.
[19] A. Troupis, A. Hiskia, E. Papaconstantinou, Synthesis of Metal Nanoparticles by Using Polyoxometalates as Photocatalysts and Stabilizers, Angewandte Chemie International Edition, 41 (2002) 1911-1914.
[20] G. Maayan, R. Neumann, Direct aerobic epoxidation of alkenes catalyzed by metal nanoparticles stabilized by the $H_5PV_2Mo_{10}O_{40}$ polyoxometalate, Chemical Communications, (2005) 4595-4597.
[21] R.G. Finke, S. Özkar, Molecular insights for how preferred oxoanions bind to and stabilize transition-metal nanoclusters: A tridentate, C3 symmetry, lattice size-matching binding model, Coordination Chemistry Reviews, 248 (2004) 135-146.
[22] S. Özkar, R.G. Finke, Nanocluster formation and stabilization fundamental studies: Ranking commonly employed anionic stabilizers via the development, then application, of five comparative criteria, Journal of the American Chemical Society, 124 (2002) 5796-5810.

[23] P.S. Kishore, B. Viswanathan, T.K. Varadarajan, Electrochemical oxygen reduction reaction by Pt nanoparticles on carbon support stabilized by polyoxometalates, Journal of nanoscience and nanotechnology, 9 (2009) 5188-5197.
[24] A. Corma, S. Iborra, F.X. Llabrés i Xamena, R. Montón, J.J. Calvino, C. Prestipino, Nanoparticles of Pd on Hybrid Polyoxometalate−Ionic Liquid Material: Synthesis, Characterization, and Catalytic Activity for Heck Reaction, The Journal of Physical Chemistry C, 114 (2010) 8828-8836.
[25] N. Legagneux, E. Jeanneau, A.l. Thomas, M. Taoufik, A. Baudouin, A. de Mallmann, J.-M. Basset, F.d.r. Lefebvre, Grafting Reaction of Platinum Organometallic Complexes on Silica-Supported or Unsupported Heteropolyacids, Organometallics, 30 (2011) 1783-1793.
[26] M. Boltz, A. Blanc, G. Laugel, P. Pale, B. Louis, Heterogenization of [Cu(2,2'-bpy)Cl_2] and [Cu(1,10-phen)Cl_2] on Polyoxometalates: New Catalysts for the Selective Oxidation of Tetralin, Chinese Journal of Catalysis, 32 (2011) 807-811.
[27] D.A. Shirley, High-resolution x-ray photoemission spectrum of the valence bands of gold, Physical Review B, 5 (1972) 4709-4714.
[28] P. Serra-Crespo, M.A. van der Veen, E. Gobechiya, K. Houthoofd, Y. Filinchuk, C.E.A. Kirschhock, J.A. Martens, B.F. Sels, D.E. De Vos, F. Kapteijn, J. Gascon, NH_2-MIL-53(Al): A High-Contrast Reversible Solid-State Nonlinear Optical Switch, Journal of the American Chemical Society, 134 (2012) 8314-8317.
[29] C. Férey, C. Mellot-Draznieks, C. Serre, F. Millange, J. Dutour, S. Surblé, I. Margiolaki, Chemistry: A chromium terephthalate-based solid with unusually large pore volumes and surface area, Science, 309 (2005) 2040-2042.
[30] P. Serra-Crespo, E.V. Ramos-Fernandez, J. Gascon, F. Kapteijn, Synthesis and Characterization of an Amino Functionalized MIL-101(Al): Separation and Catalytic Properties, Chemistry of Materials, 23 (2011) 2565-2572.
[31] J. Rouquerol, D. Avnir, C.W. Fairbridge, D.H. Everett, J.H. Haynes, N. Pernicone, J.D.F. Ramsay, K.S.W. Sing, K.K. Unger, Recommendations for the characterization of porous solids, Pure and Applied Chemistry, 66 (1994) 1739-1758.
[32] Y. Tao, H. Kanoh, L. Abrams, K. Kaneko, Mesopore-modified zeolites: Preparation, characterization, and applications, Chemical Reviews, 106 (2006) 896-910.
[33] T. Kyotani, Control of pore structure in carbon, Carbon, 38 (2000) 269-286.
[34] E. Robens, F. Rouquerol, J. Rouquerol, S. K., Adsorption by powders and porous solids, WILEY-VCH Verlag, San Diego, 1999.
[35] M.J. Janik, K.A. Campbell, B.B. Bardin, R.J. Davis, M. Neurock, A computational and experimental study of anhydrous phosphotungstic acid and its interaction with water molecules, Applied Catalysis A: General, 256 (2003) 51-68.
[36] B. Sulikowski, J. Haber, A. Kubacka, K. Pamin, Z. Olejniczak, J. Ptaszyński, Novel "ship-in-the-bottle" type catalyst: Evidence for encapsulation of 12-tungstophosphoric acid in the supercage of synthetic faujasite, Catalysis Letters, 39 (1996) 27-31.
[37] L.I. Kuznetsova, L.G. Detusheva, N.I. Kuznetsova, M.A. Fedotov, V.A. Likholobov, Relation between structure and catalytic properties of transition metal complexes with heteropolyanion $PW_{11}O_{39}^{7-}$ in oxidative reactions, Journal of Molecular Catalysis A: Chemical, 117 (1997) 389-396.
[38] W. Daniell, U. Schubert, R. Glöckler, A. Meyer, K. Noweck, H. Knözinger, Enhanced surface acidity in mixed alumina-silicas: A low-temperature FTIR study, Applied Catalysis A: General, 196 (2000) 247-260.
[39] Z. Shi, J. Peng, C.J. Gómez-García, S. Benmansour, X. Gu, Influence of metal ions on the structures of Keggin polyoxometalate-based solids: Hydrothermal syntheses, crystal structures and magnetic properties, Journal of Solid State Chemistry, 179 (2006) 253-265.
[40] E.V. Ramos-Fernández, A.F.P. Ferreira, A. Sepúlveda-Escribano, F. Kapteijn, F. Rodríguez-Reinoso, Enhancing the catalytic performance of Pt/ZnO in the selective hydrogenation of cinnamaldehyde by Cr addition to the support, Journal of Catalysis, 258 (2008) 52-60.
[41] A. Demessence, P. Horcajada, C. Serre, C. Boissière, D. Grosso, C. Sanchez, G. Férey, Elaboration and properties of hierarchically structured optical thin films of MIL-101(Cr), Chemical Communications, (2009) 7149-7151.
[42] D. Dybtsev, C. Serre, B. Schmitz, B. Panella, M. Hirscher, M. Latroche, P.L. Llewellyn, S. Cordier, Y. Molard, M. Haouas, F. Taulelle, G. Férey, Influence of $[Mo_6Br_8F_6]^{2-}$ cluster unit inclusion within the mesoporous solid MIL-101 on hydrogen storage performance, Langmuir, 26 (2010) 11283-11290.
[43] E. Grinenval, J.M. Basset, F. Lefebvre, Reactivity of anhydrous Keggin-type molybdenum heteropolyacids with alkylsilanes: Synthesis and characterization, Inorganica Chimica Acta, 370 (2011) 297-303.
[44] A.Y. Stakheev, E.S. Shpiro, N.I. Jaeger, G. Schulz-Ekloff, FTIR evidence of the formation of platinum carbonyls from Pt metal clusters encaged in KL zeolite, Catalysis Letters, 34 (1995) 293-303.
[45] O.S. Alexeev, G.W. Graham, M. Shelef, B.C. Gates, γ-Al_2O_3-supported Pt catalysts with extremely high dispersions resulting from Pt-W interactions, Journal of Catalysis, 190 (2000) 157-172.
[46] O.I. Lebedev, F. Millange, C. Serre, G. Van Tendeloo, G. Férey, First direct imaging of giant pores of the metal-organic framework MIL-101, Chemistry of Materials, 17 (2005) 6525-6527.
[47] A. Sonnauer, F. Hoffmann, M. Fröba, L. Kienle, V. Duppel, M. Thommes, C. Serre, G. Férey, N. Stock, Giant pores in a chromium 2,6-Naphthalenedicarboxylate Open-Framework structure with MIL-101 topology, Angewandte Chemie - International Edition, 48 (2009) 3791-3794.

[48] J. Beckers, G. Rothenberg, Sustainable selective oxidations using ceria-based materials, Green Chemistry, 12 (2010) 939-948.
[49] P.L. Llewellyn, G. Maurin, T. Devic, S. Loera-Serna, N. Rosenbach, C. Serre, S. Bourrelly, P. Horcajada, Y. Filinchuk, G. Férey, Prediction of the conditions for breathing of metal-organic framework materials using a combination of X-ray powder diffraction, microcalorimetry, and molecular simulation, Journal of the American Chemical Society, 130 (2008) 12808-12814.
[50] S.K. Nune, P.K. Thallapally, B.P. McGrail, Metal organic gels (MOGs): A new class of sorbents for CO_2 separation applications, Journal of Materials Chemistry, 20 (2010) 7623-7625.
[51] B.P. Macpherson, B.M. Alzoubi, P.V. Bernhardt, M. Martínez, P.A. Tregloan, R. Van Eldik, Pressure and temperature effects on metal-to-metal charge transfer in cyano-bridged CoIII-FeII complexes, Dalton Transactions, (2005) 1459-1467.
[52] F. Lefebvre, ^{31}P MAS NMR study of $H_3PW_{12}O_{40}$ supported on silica: Formation of $(AlSiOH^{2+})(H_2PW_{12}O_{40}^-)$, Journal of the Chemical Society, Chemical Communications, (1992) 756-757.
[53] D. Mustafa, E. Breynaert, S.R. Bajpe, J.A. Martens, C.E.A. Kirschhock, Stability improvement of $Cu_3(btc)_2$ metal-organic frameworks under steaming conditions by encapsulation of a Keggin polyoxometalate, Chemical Communications, 47 (2011) 8037-8039.
[54] J.B. Decoste, G.W. Peterson, M.W. Smith, C.A. Stone, C.R. Willis, Enhanced Stability of Cu-btc MOF via Perfluorohexane Plasma-Enhanced Chemical Vapor Deposition, Journal of the American Chemical Society, 134 (2012) 1486-1489.
[55] O.S. Alexeev, G.W. Graham, D.W. Kim, M. Shelef, B.C. Gates, γ-Al_2O_3-supported Pt-W catalysts prepared from molecular organometallic precursors: Characterization by infrared spectroscopy, Physical Chemistry Chemical Physics, 1 (1999) 5725-5733.
[56] M.M. Schubert, M.J. Kahlich, H.A. Gasteiger, R.J. Behm, Correlation between CO surface coverage and selectivity/kinetics for the preferential CO oxidation over Pt/γ-Al_2O_3 and Au/α-Fe_2O_3: An *in situ* DRIFTS study, Journal of Power Sources, 84 (1999) 175-182.
[57] D. Ferri, T. Biirgi, A. Baiker, Pt and Pt/Al_2O_3 thin films for investigation of catalytic solid-liquid interfaces by ATR-IR spectroscopy: CO adsorption, induced reconstruction and surface-enhanced absorption, Journal of Physical Chemistry B, 105 (2001) 3187-3195.
[58] J.L. Ayastuy, M.P. González-Marcos, A. Gil-Rodríguez, J.R. González-Velasco, M.A. Gutiérrez-Ortiz, Selective CO oxidation over CeXZr1-XO2-supported Pt catalysts, Catalysis Today, 116 (2006) 391-399.
[59] S. Huang, K. Hara, A. Fukuoka, Green catalysis for selective CO oxidation in hydrogen for fuel cell, Energy and Environmental Science, 2 (2009) 1060-1068.

Chapter 6

Towards acid MOFs: Catalytic performance of sulfonic acid functionalized architectures

This chapter is based on the following publication:

J. Juan–Alcañiz, R. Gielisse, A.B. Lago, E.V. Ramos–Fernandez, P. Serra–Crespo, T. Devic, N. Guillou, C. Serre, F. Kapteijn, J. Gascon, Catal. Sci. & Technol. (2013) *DOI: 10.1039/C3CY00272A*

Abstract In this work, the inclusion of free sulfonic acid groups in highly stable MOFs is explored. The synthesized catalysts have been applied in a model esterification reaction. Two metal organic frameworks bearing sulfonic acid moieties are investigated: HSO_3–MIL–101(Cr) synthesized following different approaches and a new structure based on HSO_3–bdc and Zr. The acidic properties, catalytic performance, deactivation and stability of the different structures is critically evaluated. In the case of MIL–101(Cr), deactivation of the sulfonic acid groups *via* formation of butyl sulfonic esters has been observed. Due to the strong interaction between $–SO_3^-$ and the Cr open metal site where usually fluoride (F^-) is located in the structure, the HSO_3–MIL–101(Cr) catalysts are not stable under acidic regeneration conditions. When using Zr as metal node, a new and stable sulfonic acid containing porous structure was synthesized. This structure showed high activity and full re–usability in the esterification of 1–butanol with acetic acid. In this case, deactivation of the catalyst due to sulfonic ester formation could be reversed by reactivation under acidic conditions.

6.1. INTRODUCTION

During the last few decades, much effort has been put into the development of acidic solid materials such as ion–exchange resins based on sulfonic acid groups, [1] sulfated oxides based on zirconia, silica, or alumina [2] and activated carbons with different surface functional groups. [3-5] However, the application window of such solids is limited: some exhibit swelling in solvents (polymers) or strong leaching (sulfated oxides and activated carbons), while none of them possesses a well–defined porosity. The development of strongly acidic nano–structured catalysts is a long–standing challenge for materials' researchers and is only partially solved by organic funtionalized mesoporous silicas. [6]

In the field of synthetic nano–structured materials, metal–organic frameworks, hereafter MOFs, are attracting a great deal of attention. Next to a high surface area and pore volume, the chemical environment in MOFs can be fine–tuned by selecting the appropriate building blocks and/or by post–synthetic treatment, resulting in nearly infinite design possibilities. [7]

When it comes to catalytic applications, as recently highlighted in several reviews, [8, 9] MOFs hold many promises: the inorganic connectors may hold certain functional sites by themselves, as shown for MOFs possessing coordinatively unsaturated sites (CUS), [10] or may display photoactivity. [11] Besides the intrinsic activity of such CUS, they can also be utilized as anchoring points for molecules to create catalytically active or sorption centers. [12] Regarding the organic linkers, it is generally anticipated that MOFs may bridge the gap between organic and inorganic catalysis, [13, 14] since almost any organic moiety of choice could be immobilized. The formation of guest–accessible functional organic sites (FOS) may be achieved following two different strategies: [15] direct incorporation of functionality during the synthesis [16] or post–functionalization. [17] Different approaches have been followed for the introduction of strong Brønsted acidity in MOFs, these include mainly post–synthetic and encapsulation routes, like controlled framework destruction to increase the number and acidity of CUS, [18] post–synthetic framework sulfation, [19] post–functionalization of amine groups with sultones [20] and encapsulation of heteropolyacids. [21] To date, Kitagawa and co–workers have reported the direct synthesis of free sulfonic acid functionalized MOFs, namely MIL–101(Cr) and doped UiO–66(Zr), *via* direct synthesis. [22-24] Very recently Biswas *et al.* presented a new direct synthesis procedure for HSO_3–UiO–66. [25] Several works describe the benefits of sulfonic MOFs for applications like catalysis, [26] proton conductivity or adsorption. [23, 24]

In this work, we explore two synthetic routes for the production of sulfonic structures like MIL–101(Cr) and a Zr based MOF, along with a thorough assessment of their acid catalytic activity, deactivation and the influence of synthesis conditions on framework stability and catalyst reusability.

6.2. EXPERIMENTAL

6.2.1. Syntheses

All the chemicals and reference catalyst were obtained from Sigma–Aldrich and used without further purification, unless otherwise stated.

HSO_3–MIL–101(Cr)$_{HCl}$: has been synthesized according to the procedure reported by Kitagawa and co–workers, a mixture of monosodium 2–sulfoterephthalic acid (2 g, 7.5 mmol), CrO_3 (0.75 g, 7.5 mmol), concentrated aqueous hydrochloric acid (12 M, 0.546 g) was dissolved in water (30 g), and was hydrothermally treated at 453 K for 168 h. [22]

HSO_3–MIL–101(Cr)$_{HF}$: has been synthesized by heating a mixture of chromium(III) nitrate nonahydrate (2.00 g, 5 mmol), monosodium 2–sulfoterephthalic acid (Tokyo Chemical Company, 2.70 g, 10 mmol), deionized water (30 g) and hydrofluoric acid (47–51 wt %, 0.3 g) by heating at 463 K for 24 h. The as–synthesized solid was washed with deionized water and dried in air at 393 K.

KSO_3–bdc*:* 25 g (0.134 mol) of 2,5–dimethylbenzenesulfonic acid dehydrated (Acros Organics, 99%) was dissolved in 100 mL of water and $KMnO_4$ (106 g, 0.67 mol) was slowly added. The reaction mixture was heated under reflux for 48 h, followed by filtration to remove the residual MnO_2. The solution was concentrated until approx. 80%, and 12 M hydrochloric acid was added to the filtrate (approx. 200 mL). Immediately, a precipitate of a mixture of 2–sulfoterephthalic acid and the monopotassium salt is formed. The white precipitate is washed with EtOH and dried at 373 K. ^{1}H NMR (dmso–d_6): δ 8.34 (s, ^{1}H), 7.99 (dd, ^{1}H, J=2 Hz, J= 8.6 Hz), 7.69(d, ^{1}H, J=8.5 Hz). MS–ESI: *m/z* (%) = 245 (100) $[HSO_3–bdc]^+$. EDS analysis: (K:S/0.6:1). IR(cm^{-1}) : 1710 vs, 1487 m, 1260 m, 1208 vs, 1120 m, 1386 m, 1200 w

HSO_3–ZrMOF: zirconium tetrachloride (1.17 g, 5 mmol) and *KSO_3*–bdc (2.50 g, 8.5 mmol) reacted in deionized water (25 g) at 423 K for 24 h. The resulting white solid was washed with hot deionized water and dried in air under ambient conditions.

6.2.2. Characterization techniques

(a) Scanning Electron Microscopy: SEM was measured in a JEOL JSM 6500F setup coupled to an Energy Dispersive Spectrometer (EDS) for micro elemental analysis. *(b) Nitrogen adsorption at 77 K:* measured in a Quantachrome Autosorb–6B unit gas adsorption analyzer. *(c) Carbon Dioxide adsorption at 273 K:* Low–pressure adsorption was measured in a Micromeritics TriStar II 3020 based on the volumetric technique. The samples were pre–treated under vacuum for 16 h at different temperatures depending on the sample. *(d) X–Ray Diffraction:* using a Bruker–AXS D5005 with CoKα radiation. For HSO_3–ZrMOF, high–resolution synchrotron data were collected at ID31, ESRF, France.

Subsequent pattern indexing and Le Bail structure–independent fits were performed using Topas software. *(e) ICP–OES:* samples were digested in duplo in a mixture of 8 mL *aqua regia* and 2 mL HF using microwave irradiation. After digestion, the samples were diluted to 50 mL with MQ, and analyzed with an ICP–OES Perkin Elmer Optima 5300dv. *(f) Diffuse Reflectance IR spectroscopy:* recorded on a Nicolet model 8700 spectrometer, equipped with a high–temperature DRIFT cell (KBr windows), DTGS–TEC detector and a 633 nm laser. The spectra were registered from 4000 to 600 cm^{-1} after accumulation of 128 scans and a resolution of 4 cm^{-1}. A flow of helium at 20 mL min^{-1} was maintained during the measurements. Before collecting the spectra, the different samples were pre–treated in the same helium flow at 393 K for 30 min. KBr was used to perform background experiments. *(g) X–Ray Photoelectron Spectroscopy (XPS):* using a VG–Microtech Multilab equipment, MgKα (*hν:* 1253.6 eV) radiation and a pass energy of 50 eV. The XPS system analysis pressure was kept at 5×10^{-10} mbar. The binding energy (BE) and the kinetic energy (KE) scales were adjusted by setting the C*1s* transition to 284.6 eV. BE and KE values were determined with the peak–fit software of the spectrometer. The intensities were estimated by calculating the integral of each peak, after subtraction of the S–shaped background, and by fitting the experimental curve to a combination of Lorentzian (30%) and Gaussian (70%) peak shapes. The surface atomic ratios were estimated from the integrated intensities corrected by the atomic sensitivity factors. [27] (h) *Acid–Base Titration:* volumes of known solutions of two different bases (NaOH and 1,5,7–triazabicyclo[4.4.0.]dec–5–ene) were added to 100 mg of MOF dispersed in 20 mL water, while analyzed by a pH–meter, at RT. The diffusion of the bases inside of the MOF was in agreement to their size, and in both cases long times were needed for pH stabilization (1 mL needs at least one hour).

$$Volume_{BASE} \cdot M_{BASE} = mol_{SO3H} \quad (1)$$

6.2.3. Esterification of acetic acid and 1–butanol

The reaction was performed without solvent, using a molar ratio mixture of acetic acid : 1–butanol of 1:1. The reaction mixture (25 mL) was introduced into a round bottom flask, while being stirred under reflux the temperature was increased to 343 K. A ratio of 3 g catalyst per mol of acetic acid was used. The samples of the reaction mixture were periodically analyzed by gas chromatography using a Chrompack GC CP–Sil 8CB Cat. No. 7453 equipped with an FID detector and a 50 m RTX®–1 (1% diphenyl–, 99% dimethylpolysiloxane) fused silica capillary column, using decane (anhydrous, > 99%) as internal standard. The catalyst was recovered by filtration, and treated with an acidic solution before use in consecutive runs. The acidic treatment was performed by putting the MOF catalyst in contact with a 0.2 M solution of HCl or pellets of an acidic ion exchange resins 1:1 mass ratio (DOWEX® 50W X8 hydrogen form) in water under stirring conditions for 30 minutes at room temperature.

6.3. EXPERIMENTAL RESULTS AND DISCUSSION

6.3.1. HSO_3–MIL–101(Cr)

HSO_3–MIL–101(Cr)$_{HCl}$ has been synthesized according to the procedure reported by Kitagawa and co–workers, while a new route has been developed for the synthesis of *HSO_3–MIL–101(Cr)$_{HF}$*. Both catalysts exhibit the PXRD pattern expected for MIL–101 structure (Fig. 6–1). N_2 adsorption isotherms (Fig. 6–1) show the two characteristic steps of MIL–101, related to the filling of the mesoporous cavities: at very low relative pressures (p/p^0 < 0.05) only the supertetrahedra are filled, as pressure increases, the medium (p/p^0 = 0.15) and later the large cavities (p/p^0 = 0.20) are filled. Slightly lower relative pressure are observed for the steps of the HCl route, which might suggest impurities like recrystallized linker in the cages, making them smaller for adsorption. Samples synthesized in the presence of HCl and at long synthesis times display a lower surface area (*circa* 1200 $m^2\ g^{-1}$, calculated between 0.05 and 0.10 relative pressure) than samples synthesized in shorter times and in the presence of HF (*circa* 1800 $m^2\ g^{-1}$). In both cases, the surface area is smaller than that of MIL–101(Cr) [28] but in good agreement with other functionalized MIL–101s. [29]

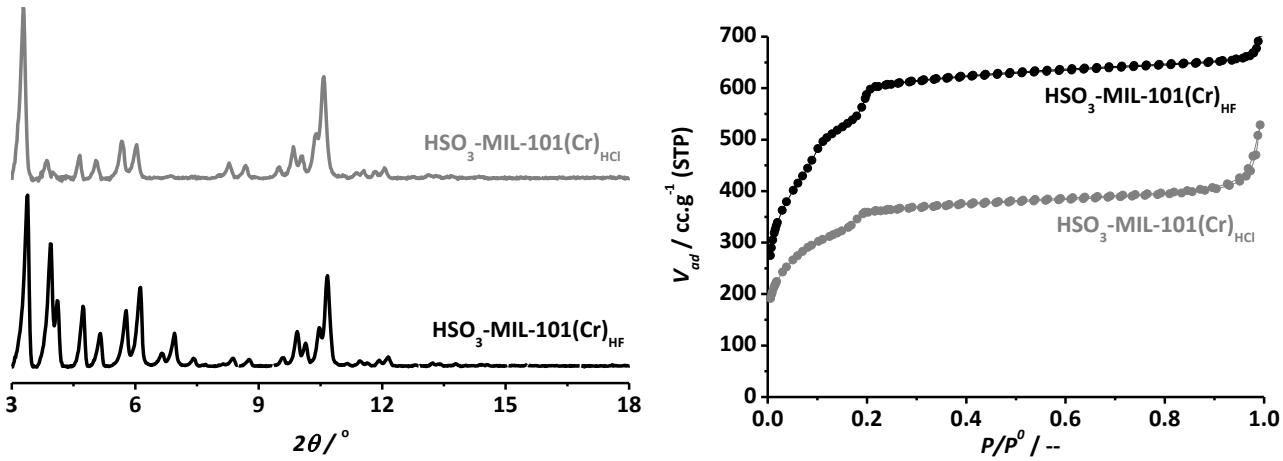

Figure 6 - 1 (*Left*) CoKα Powder X–Ray diffraction patterns. (*Right*) Nitrogen adsorption isotherms at 77 K. HSO_3–MIL–101(Cr) samples synthesized with HCl (*grey*) or HF (*black*) as described in the experimental section.

SEM pictures (Fig. 6–2) reveal a smaller particle size for HSO_3–MIL–101(Cr)$_{HCl}$ (≈ 200 nm) than for HSO_3–MIL–101(Cr)$_{HF}$ (≈ 700 nm). Elemental analysis of the evacuated samples demonstrates that ion exchange occurs during the synthesis, resulting in an exchange of Na^+ from the linker with protons, yielding a partial protonation of the sulfonic acid groups. This ion exchange is more effective for HSO_3–MIL–101(Cr)$_{HCl}$ (1.28 wt% Na resulting in 0.3 Na^+/SO_3^-) in contrast with HSO_3–MIL–101(Cr)$_{HF}$ (2.75 wt% Na resulting in 0.41 Na^+/SO_3^-), probably due to the longer synthesis times, the stronger acidity of the synthesis medium and to the smaller particle size.

Thermo–gravimetric analysis of both samples (Fig. 6–3) reveal a significantly higher amount of inorganic residue in the case of the HSO_3–MIL–101(Cr)$_{HCl}$. While the remaining 20 wt% in the case of HSO_3–MIL–101(Cr)$_{HF}$ is in good agreement with the expected molecular formula ($Cr_3OF(H_2O)_2[(O_2C)–C_6H_3(SO_3Na_xH_y)–(CO_2)]_3$), and the amount of water found in the sample (15 wt%), as indicated also by EDS with Cr/S of 1. The residue for HSO_3–MIL–101(Cr)$_{HCl}$ is higher than expected and can be attributed to the presence of Cr_2O_3 in the material.

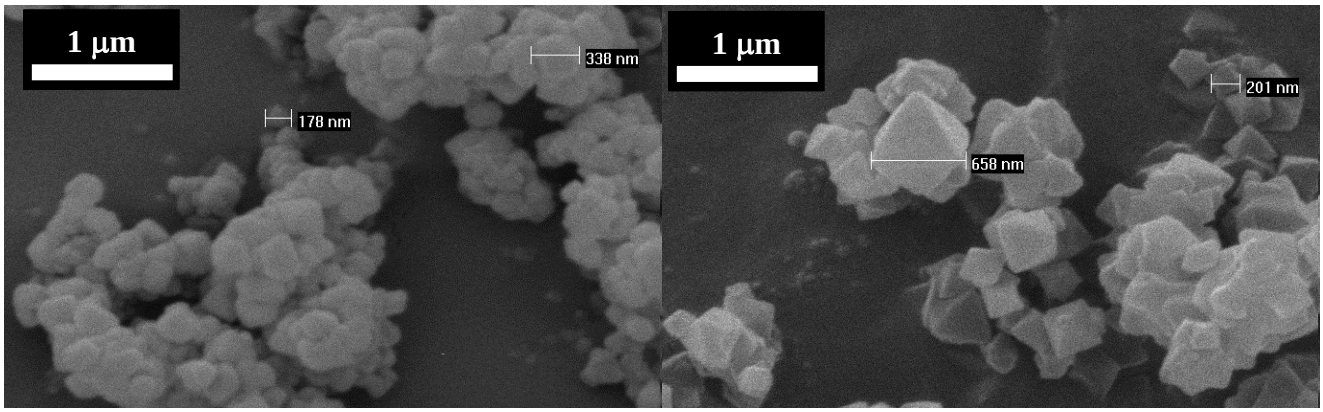

Figure 6 - 2 SEM images of HSO_3–MIL–101(Cr) samples. (*Left*) HCl, (*Right*) HF exchange treatment.

DRIFTS confirms the successful functionalization. Figure 6–4 shows a comparison between the pristine MIL–101(Cr) and both functionalized HSO_3–MIL–101(Cr). Clear differences are already revealed when observing the whole spectrum (4000–1000 cm^{-1}). The ν(OH) region (4000–3000 cm^{-1}) exhibits a broad band centered at 3400 cm^{-1} for the sulfonic acid materials, absent in the bare samples. This vibration corresponds to water molecules retained in the pores by strong hydrogen bonding with the sulfonic acid even after *in situ* treatment at 423 K for one hour. Specific sulfonic acid stretching can be observed in the fingerprint region (between 1800 and 1000 cm^{-1}).

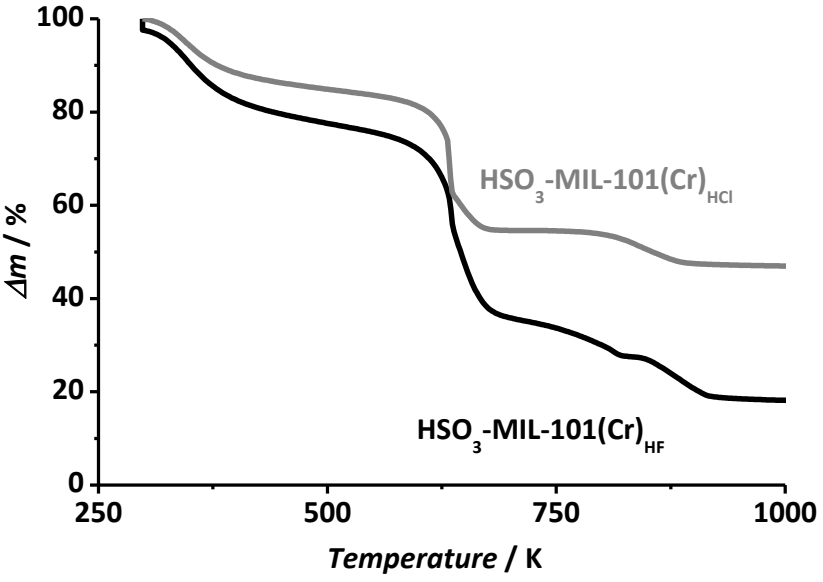

Figure 6 - 3 TG profile of HCl (*grey*) or HF (*black*) synthesized HSO_3–MIL–101(Cr) samples.

New bands at 1190 and 1240 cm^{-1}, are attributed to the O=S=O symmetric and asymmetric stretching modes. The peak at 1080 cm^{-1} corresponds to the S–O stretching vibration, with a slight shift of the band at 1020 to 1030 cm^{-1}, attributed to the influence of the SO_3H substituted aromatic ring. [30]

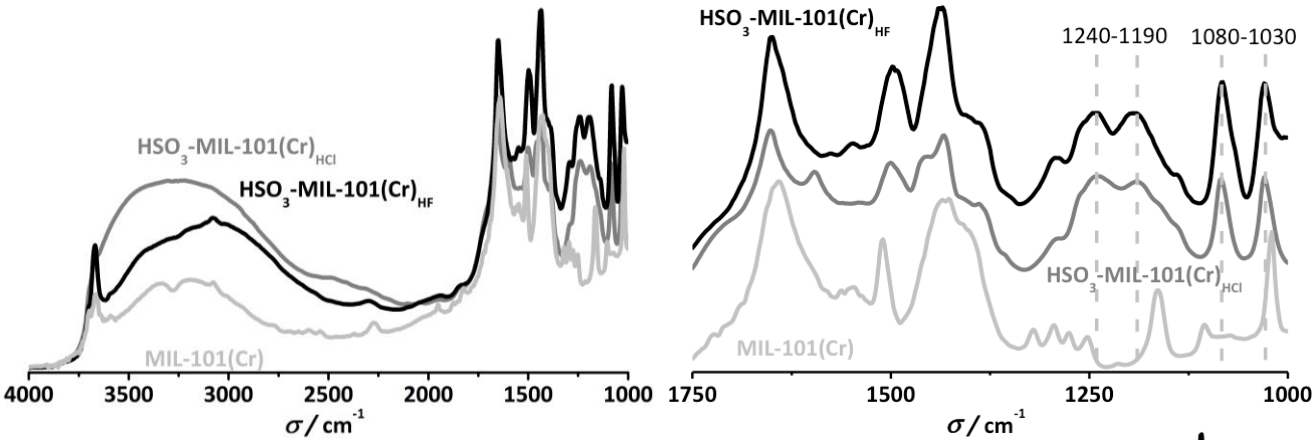

Figure 6 - 4 FTIR spectra of the different HSO_3–MIL–101(Cr) structures compared to that of non–functionalized MIL–101(Cr). Left: full spectral range. Right: detail of the 1000–1750 cm^{-1} region.

The catalytic activity of the HSO_3–MIL–101(Cr) materials has been benchmarked against Amberlyst®–15 (sulfonated polystyrene) by the liquid–phase stoichiometric esterification of 1–butanol and acetic acid at low temperatures (343 K). Experiments were performed using the same ratio of 3 g mol^{-1} reactant for all catalysts. The evolution of the butyl acetate yield (the only reaction product next to water) with time for all studied catalysts is plotted in Figure 6–5. The commercial catalyst displays a higher activity on a weight basis, while a clear difference in activity between both HSO_3–MIL–101(Cr) samples can be noticed. The latter can be explained based on the amount of protonated HSO_3 groups in the HSO_3–MIL–101(Cr)$_{HCl}$ catalyst. On the other hand, the difference in activity found between commercial and MOF based catalysts can be explained when the density of acid sites is considered: the amount of H^+ in Amberlyst®–15 is 4.2 mmol g^{-1}, higher than 1.9 and 2.2 mmol g^{-1} for HSO_3–MIL–101(Cr)$_{HF}$ and HSO_3–MIL–101(Cr)$_{HCl}$, respectively (Table 6–1).

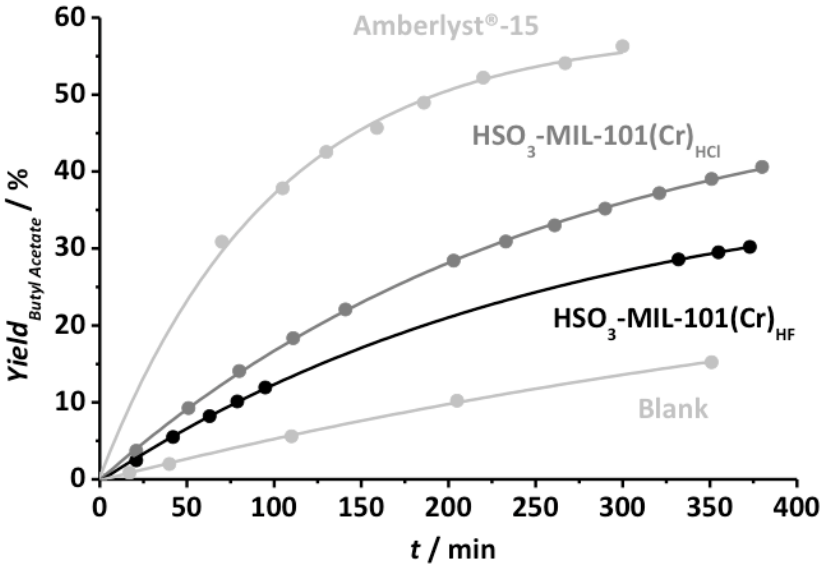

Figure 6 - 5 Esterification of 1–butanol and acetic acid (1:1 molar fraction) using 3 gram of catalyst (specified in the graph) per mol of reactant at 343 K.

TOF values were calculated based on the amount of protonated sulfonic acid groups for Amberlyst®–15, HSO_3–MIL–101(Cr)$_{HCl}$ and HSO_3–MIL–101(Cr)$_{HF}$, according to the theoretical molecular formula, and the amount of Na in the sample. The *TOF* values for the MOFs are systematically 15 to 30% lower, although equal values could be expected, since all three catalysts are based on benzene–

sulfonic moieties and therefore their acidic strength should not differ much. On the other hand, it has to be noted that *TOF* values obtained for the MOF catalysts are even higher than most heterogeneous catalysts reported in the literature, including sulfonic functionalized mesoporous silicas. [31, 32]

Table 6 - 1 Turn–over frequencies (*TOF*, min^{-1}) for the esterification of 1–butanol and acetic acid (1:1 molar ratio) using 3 gram of catalyst per mol of reactant at 343 K, for several catalytic runs.

Catalyst	*Acidity [mmol/g]*	*TOF* / min^{-1}			
		1st Run	2nd Run	3rd Run	4th Run
Amberlyst®-15	4.2 [(a)]	0.36	0.31	0.20	
HSO_3-MIL-101(Cr)$_{HF}$	1.9 [(b)]	0.23	0.12	0.11	
HSO_3-MIL-101(Cr)$_{HCl}$	2.2 [(b)]	0.30	0.22	0.13	
HSO_3-ZrMOF	2.6 [(c)]	0.29	0.23	0.20	0.33

[(a)] Obtained from reference [33]. [(b)] Obtained by molecular formula. [(c)] Obtained by the theoretical molecular formula, and confirmed accessibility of all protons by acid-base titration with NaOH and 1,5,7-triazabicyclo[4.4.0.]dec-5-ene.

Recycling tests were performed to assess the heterogeneous character of the samples. These experiments suggest a strong deactivation of both HSO_3–MIL–101(Cr) samples, in contrast to a somewhat less pronounced deactivation found for Amberlyst®–15. A large decrease in activity is observed for the MOF catalysts. Indeed, after 3 cycles, similar conversion levels as those in the blank run (in the absence of catalyst) were observed, demonstrating the complete deactivation of the HSO_3–MIL–101(Cr) samples.

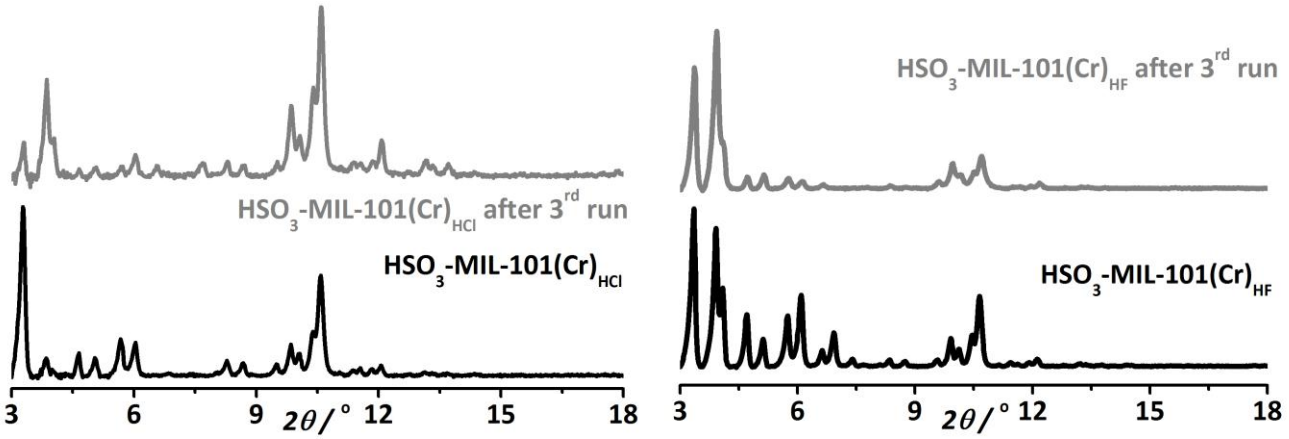

Figure 6 - 6 CoKα Powder X–Ray diffraction patterns of HSO_3–MIL–101(Cr) samples before (*black*) and after (*grey*) three reaction cycles. (*Left*) HCl. (*Right*) HF.

To unravel the nature of the deactivation, the different HSO_3–MIL–101(Cr) catalysts were analyzed after several reaction cycles: PXRD confirmed the integrity of the crystalline structure (Fig. 6–6), although some reflections are attenuated due to presence of reactants and products inside of the pores, while SEM did not show any strong attrition of the catalyst particles, both discounting framework collapse as a reason for the deactivation (Fig. 6–7).

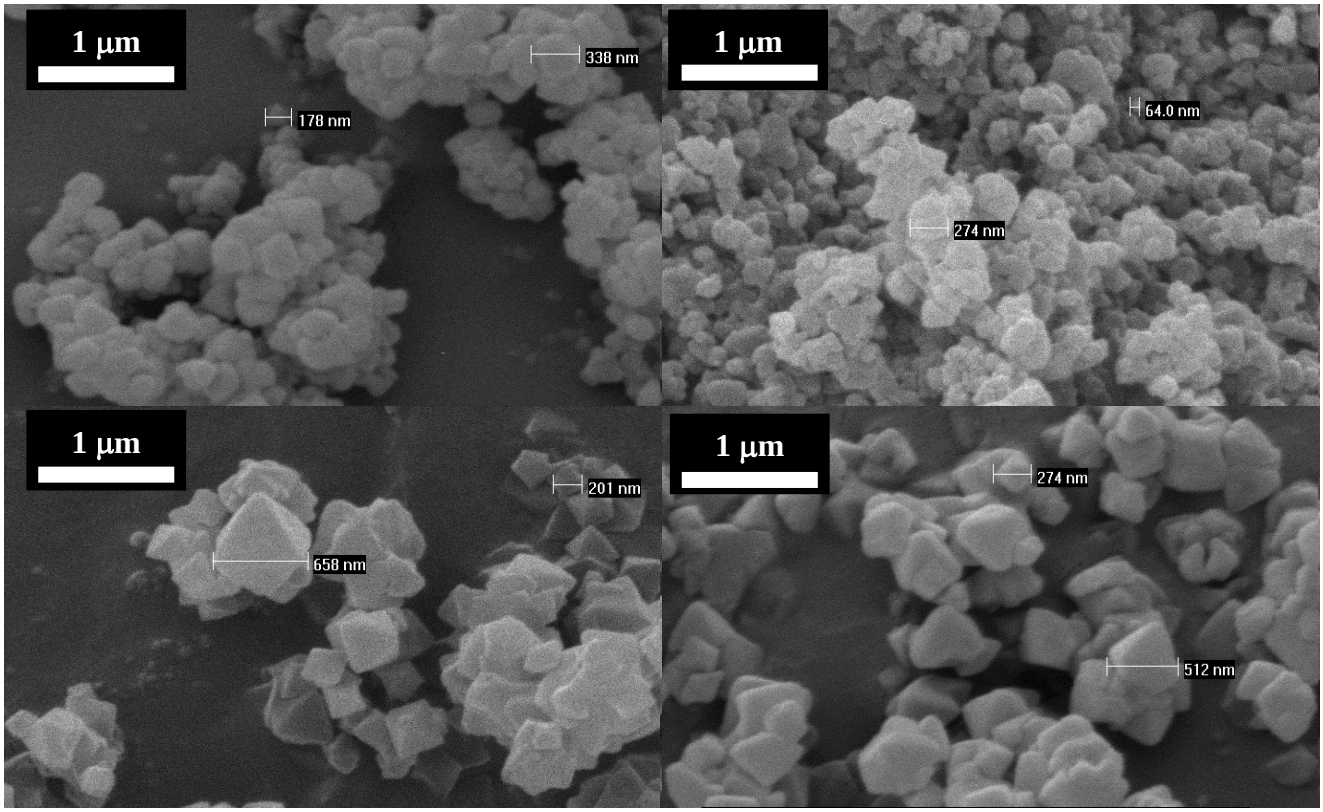

Figure 6 - 7 SEM images of HSO_3–MIL–101(Cr) samples before (*left*) and after (*right*) three reaction cycles. (*Top*) HCl, (*Bottom*) HF.

On the other hand, BET measurements (Fig. 6–8) show a substantial decrease in surface area after every reaction cycle, even after pre–treatment at 433 K under vacuum. This decrease in accessible pore volume and the absence of particle disintegration points at adsorbed reactants and products as a possible cause for deactivation.

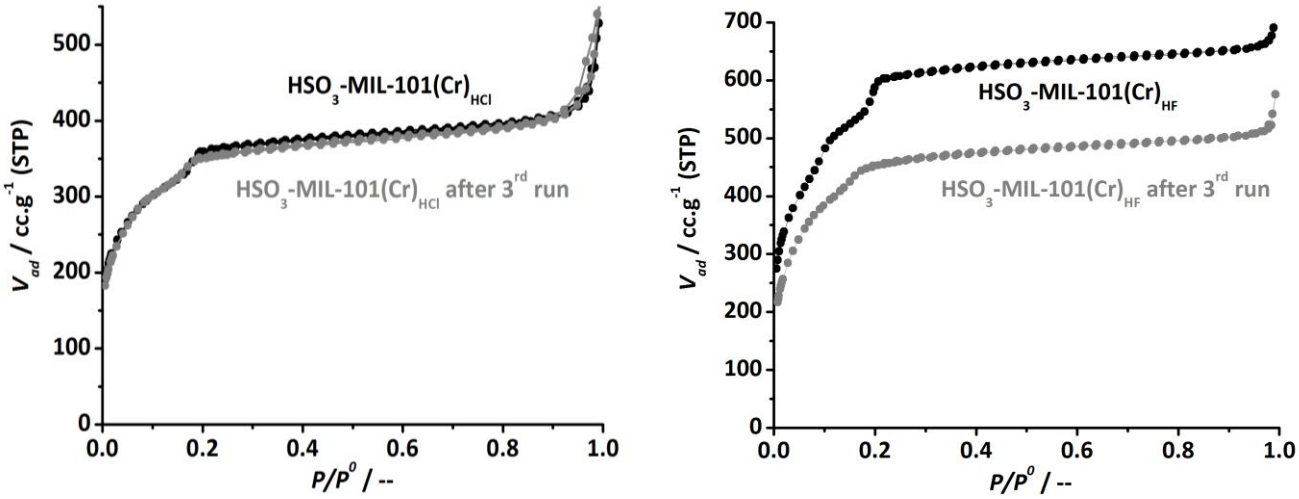

Figure 6 - 8 Nitrogen adsorption isotherm at 77 K of HSO_3–MIL–101(Cr) samples before (*black)* and after (*grey*) three reaction cycles.(*Left*) HCl, (*Right*) HF.

In order to gain insight into the specific interactions between both reactants and the HSO_3–MIL–101(Cr) framework, DRIFT spectroscopy has been performed during the adsorption and thermal

desorption of 1–butanol and acetic acid. Figure 6–9 shows the collected IR spectra at different temperatures. Impregnation with acetic acid does not result in the appearance of new vibrations other than those representative of the carboxylic acid group at 2650, 2575 and 1725 cm^{-1}. All bands disappear after heat treatment of the sample, demonstrating that the framework–acetic acid interaction is rather mild. In contrast, when the HSO_3–MIL–101(Cr) catalysts are contacted with 1–butanol, in addition to the CH_2 and CH_3, symmetric and asymmetric stretching modes, between 2960 and 2880 cm^{-1}, several new vibrations can be observed after heat treatment, namely a doublet at 2650 and 2575 cm^{-1} and a broadening of the 1725 cm^{-1} and S=O bands (1260 and 1180 cm^{-1}). Both the doublet and the broadening of the 1725 cm^{-1} bands can be ascribed to carbonyl vibrations resulting from the partial hydrolysis of terephthalate–Cr bonds, while the broadening of the S=O bands and the shoulder formed at 1065 cm^{-1} are attributed to a strong SO_3/butanol interaction.

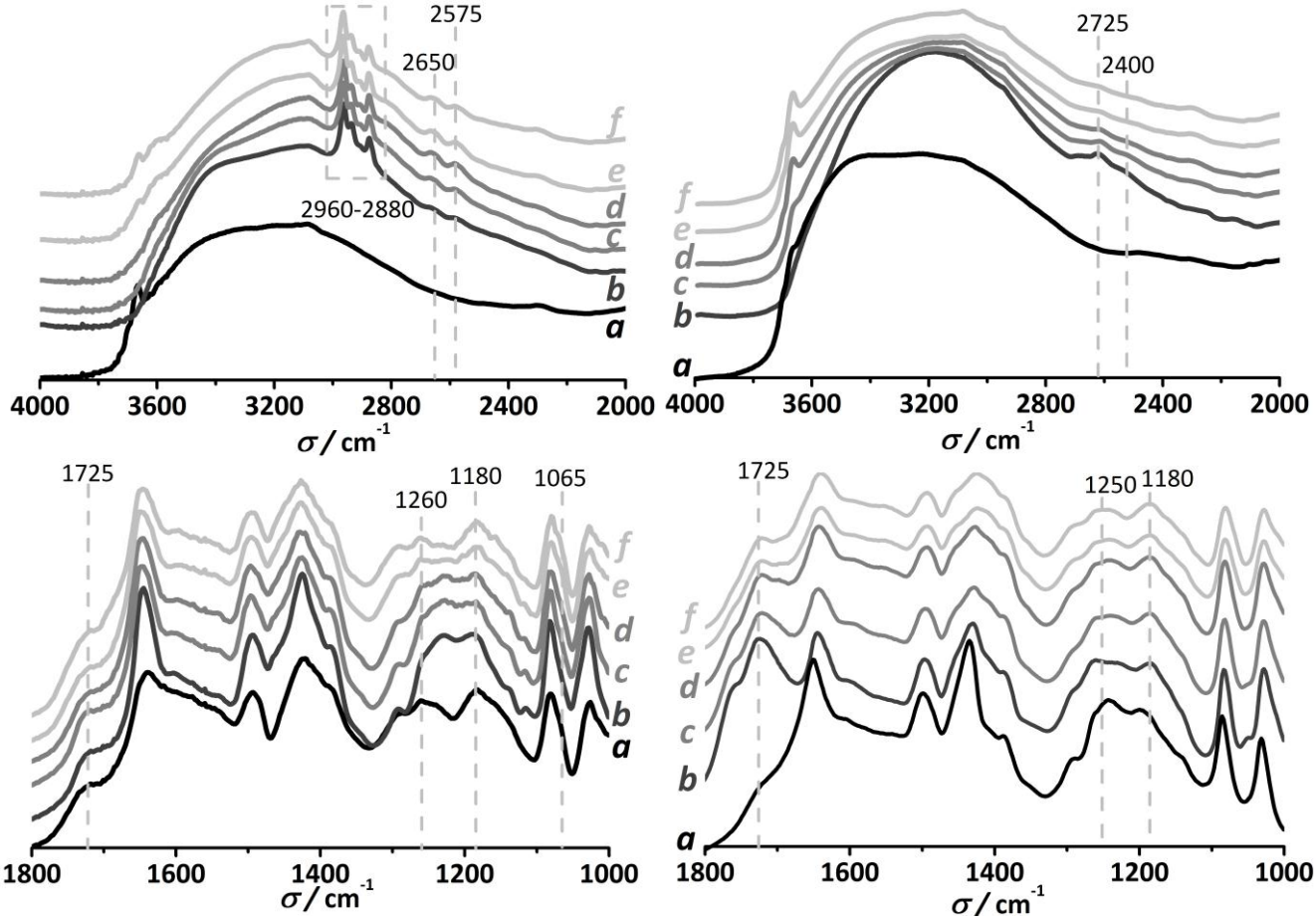

Figure 6 - 9 DRIFTS (a) HSO_3–MIL–101(Cr)$_{HF}$ (also observed for HCl samples) upon contact with an esterification reactant at RT (b) and desorption under helium at increasing temperature steps: (c) 30min at 323K, (d) 30min at 373K, (e) 30min at 423K, (f) 120min at 443K. *Left*: 1–butanol. *Right*: acetic acid.

Very recently, Fraile and co–workers [3] demonstrated that in the case of sulfonic acid functionalized microporous carbons the formation of sulfonate esters accounts for the deactivation of the catalysts in the presence of an alcohol. In our work, the infrared and adsorption results are in line with this

formation of sulfonate esters. [4] In view of such a strong chemical interaction, we re–activated the HSO_3–MIL–101(Cr) catalysts using either acidic ion exchange resins (DOWEX® 50W X8 hydrogen form) or very diluted HCl–water mixtures. Infrared spectra of the reactivated samples show the disappearance of all 1–butanol related bands, demonstrating the successful exchange. However, XRD and adsorptive characterization after several ion exchanges show a clear loss of crystallinity along with a reduced nitrogen uptake, inferring the partial collapse of the framework. These results demonstrate that although active during the first catalytic runs, the application window of HSO_3–MIL–101(Cr) is rather limited.

Kitagawa *et al*. claimed that electroneutrality in the HSO_3–MIL–101(Cr) framework is achieved by partial deprotonation of SO_3H groups, instead of halide or hydroxide inclusion in the Cr trimers, resulting in one out of three SO_3^- moieties in anionic form. [22] If this is the case, it is easy to envisage that, due to a strong interaction of these anionic moieties with 1–butanol and during the ion exchange with the acidic resin, charge neutrality may be compromised, resulting in a partial collapse of the framework. Two different approaches were followed to improve stability of the Cr^{3+} trimers and to achieve charge neutrality in the framework without using the SO_3^- functional groups: in the first approach, the as–synthesized catalysts were ion exchanged with NH_4F with the idea that F^- would stabilize the Cr^{3+} trimers and that NH_4^+ would act as counter ion for the SO_3^-, but this approach resulted in the collapse of the framework. In a second approach, we synthesized mixed linker MIL–101(Cr) using a 50:50 mixture of monosodium 2–sulfoterephthalic acid and terephthalic acid and the same synthesis conditions as in the case of HSO_3–MIL–101(Cr)$_{HF}$ (Fig. 6–10).

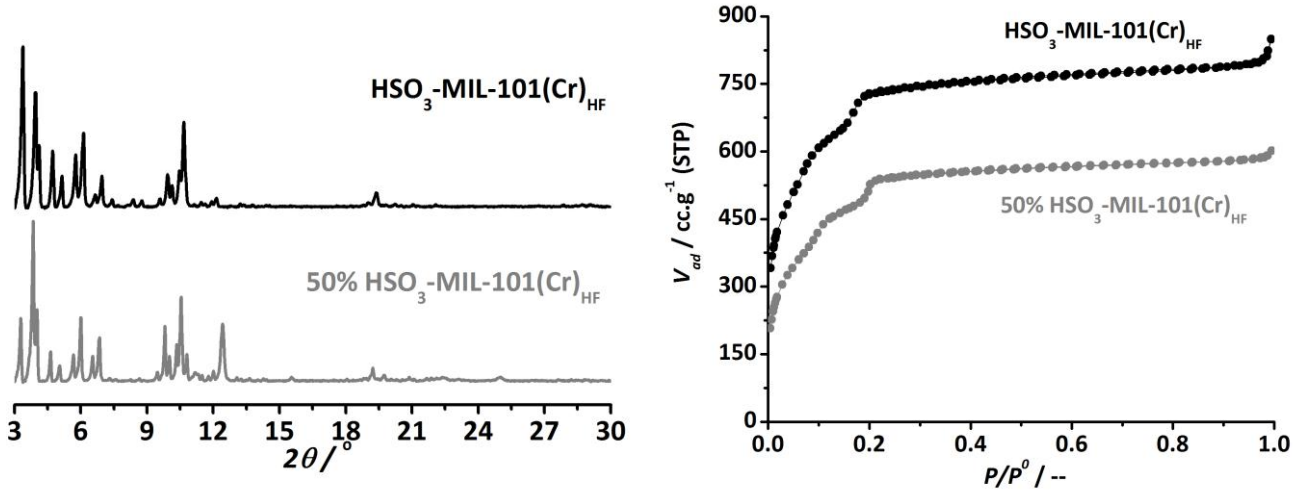

Figure 6 - 10 XRD (*left*) and N_2 adsorption isotherms at 77 K (*right*) of 50%HSO_3-MIL-101(Cr) (*grey*) compared with full HSO_3–MIL–101(Cr) (*black*).

Elemental analysis (XPS) on the resulting solids demonstrates that both linkers are present and that F^- incorporation in the framework took place during synthesis (Fig. 6–11). However, the resulting solids

did not display any activity in the esterification of 1–butanol and acetic acid, inferring that most SO_3^- moieties are used to stabilize the framework Cr trimers and confirming the rather limited availability of the protons in HSO_3–MIL–101(Cr) for catalysis.

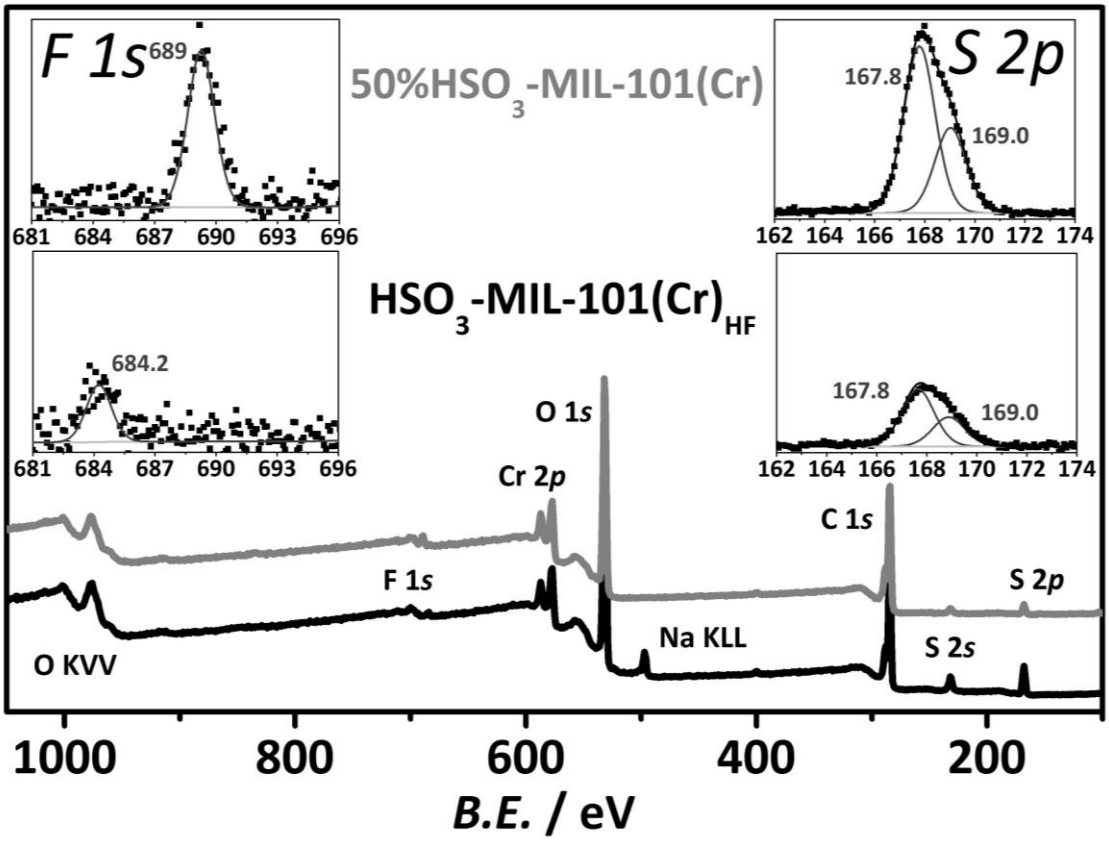

Figure 6 - 11 XPS survey spectra of HSO_3–MIL–101(Cr) full sulfonic linker and mixture of 50% with TBD. Zoom in at the F 1*s* and S 2*p* core–levels.

XPS analysis of the S 2*p* shows one peak centered at 168 eV, indicating the presence of sulfonic acid groups. [34] These peaks decrease significantly for the mix–linker system, suggesting the rather low inclusion of sulfonic linkers compared to the 100% functionalized linker sample. For both structures, contributions from two different S 2*p* peaks are observed after precise deconvolution: 169 eV and 167.8 eV. Although these binding energies are typically attributed to the S $2p_{3/2}$ and S $2p_{1/2}$ transitions of sulfonic acid groups (R–SO_3H), [35] several publications partially attribute this transition to sulfonic esters (R–SO_3–R') groups, [36] suggesting a possible interaction of sulfonic acid groups with another part of the framework. This hypothesis is emphasized when looking at the F 1*s* spectra. When full sulfonic linker is present in the synthesis, a very small amount of fluoro is found in the final solid, with a binding energy of 684.2 eV. Interestingly, in the case of pristine MIL–101(Cr) (no sulfonic acid groups) and when only half of the linkers are sulfonated, a much larger amount of fluoro, with a binding energy of 689 eV, is observed. [37, 38] These results demonstrate that in the fully sulfonic structure, SO_3^- play the same role as F^- in stabilizing the chromium trimmers and that full proton

exchange results in the collapse of the structure. It is indeed well known that fluoride is involved in the terminal bond of the trimeric chromium species and partly substitutes the terminal –OH molecules attached to chromium in MIL–100 and MIL–101. Although it is not fully clear yet, it seems that the use of fluorine provides a strong interaction with the chromium octahedral motif and enhances the formation of MIL–101 during the hydrothermal reaction. [39, 40] In our case, when a similar stabilization role is taken by the sulfonic acid groups, the final structure is more likely to collapse due to the weaker interaction with the sulfonic acid groups. [41]

6.3.2. HSO_3–ZrMOF

Zr–carboxylate MOFs like UiO–66(Zr) and other have been shown to be among the most stable MOFs. [42] Functionalization of UiO–66(Zr) has been extensively studied, both by direct synthesis for groups like $–NH_2$, $–NO_2$ or –Br, [43] and by post–synthetic treatment for more complex groups. [44-46] Several theoretical studies already proposed the benefits of sulfonic acid functionalization on the UiO–66(Zr) [47] framework, and very recently Kitagawa and co–workers and Biswas *et al.* described the first synthetic route towards fully sulfonated and mixed–linker UiO–66(Zr) as well as the effect of linker functionalization on adsorption properties. [24, 25] More precisely, whereas the mixed bdc/bdc–SO_3H linker based compounds were shown to present a rather high specific surface area, the fully substituted compound loses its crystallinity upon activation. Exploring the reactivity towards a MOF formation of zirconium– and potassium 2–sulfoterephthalic in water rather than DMF, a new crystalline porous solid could be isolated, denoted HSO_3–ZrMOF (Fig 6–12).

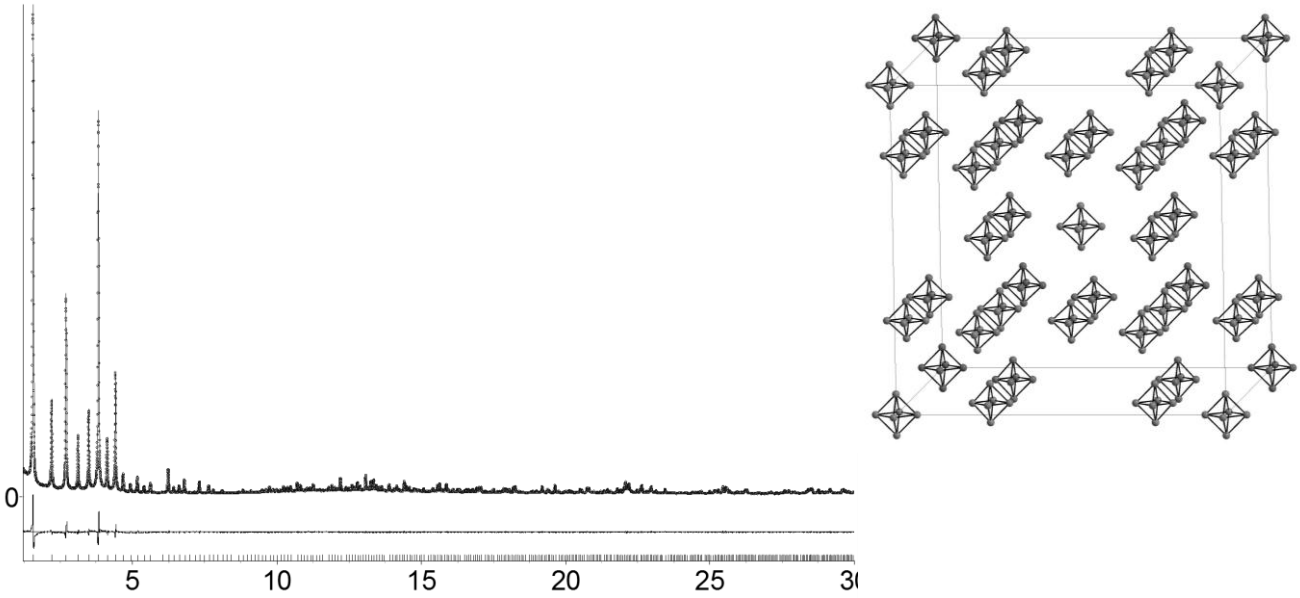

Figure 6 - 12 Structure pattern profile refinement of HSO_3–ZrMOF (*R*wp = 0.0495). Data collected on ID31 (ESRF), λ= 0.79989 Å. Cubic setting, space group *Im–3m*, *a* = 41.5331(2) Å. (*Insert*) Partial structural model of the HSO_3–Zr MOF: location of the Zr_6 clusters (*grey balls, black bonds*) within the unit–cell (*grey*).

The XRD powder pattern of the new structure could not be indexed (Fig. 6–12) within a *I cubic* unit–cell (*Im*$\bar{3}$*m*, *a* = 41.5331(2) Å), first indicating that the product is a single crystalline phase. Although this cell presents similarities with the one of UiO–66 (*cubic*, *SG: Fm*$\bar{3}$*m*, *a* = 20.7004(2) Å) with a doubling of the cell parameter, preliminary structural analysis suggests that it does not represent a UiO–66 type topology built up from 12–connected Zr_6 clusters solely, but is rather based on 8–connected Zr_6 clusters, similar to the ones observed in some very recently reported Zr–MOFs. [48-50] This is furthermore in accordance with the Zr/ligand ratio extracted from EDS analysis (Zr/S ~ 1.5, repeated at least 10 times with equal results), which suggest a $Zr_6(bdc–SO_3H)_4$ formula rather than a $Zr_6(bdc –SO_3H)_6$ one. Using state of the art structure solution methods (charge flipping), some Zr atoms could be allocated. This unambiguously confirms the presence of Zr_6 clusters similar to those found in many Zr–based MOFs (Fig. 6–12); one can nevertheless not preclude that some clusters are still missing in our model. Moreover, the ligands could not be localized yet. Nevertheless, the examination of the intercluster distances gives information about their connection. The shortest intercluster Zr–Zr distances (11.4 Å) are indeed almost identical to those found in UiO–66, indicating that at least one part of the clusters is connected in a similar way as in the UiO–66 solid, *i.e.*, through Zr–terephthalate–Zr bridges. This proves that at least one part of the sulfonic acid groups is not connected to Zr ions and thus available for catalysis.

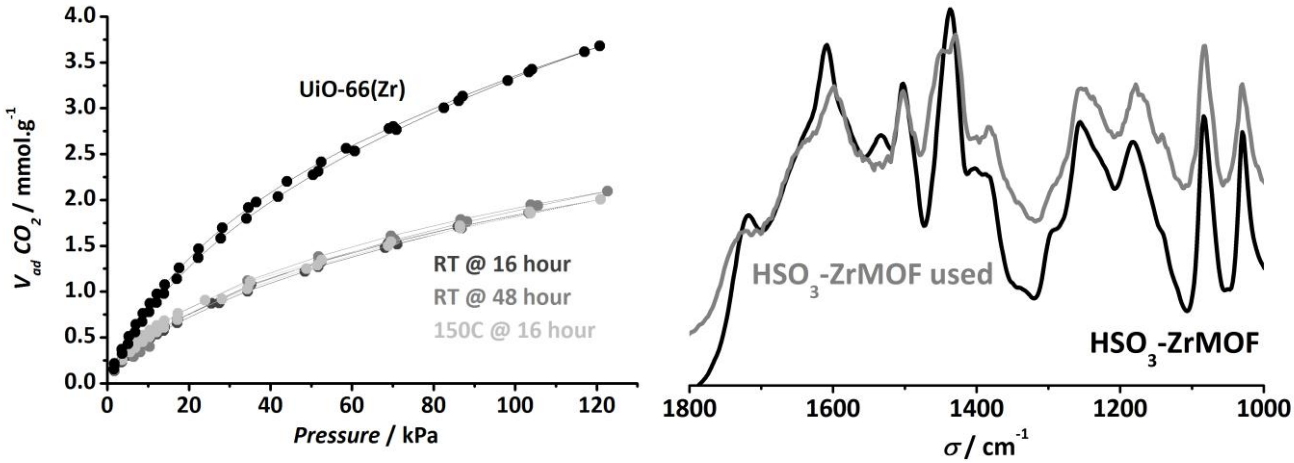

Figure 6 - 13 (*Left*) Carbon dioxide adsorption isotherms (273 K) of the HSO_3–Zr–MOF pre–treated under different conditions compared to UIO–66(Zr) pre–treated at 427 K for 16 hours. (*Right*) DRIFT spectra of HSO_3–ZrMOF before (*black*) and after (*grey*) use in the esterification reaction.

Nitrogen adsorption at 77 K proved not to be the best method to characterize porosity of the new Zr MOF: N_2 uptakes depend on the pre–treatment prior the measurement. For instance, after pre–treatment at room temperature under vacuum, samples presented a modest adsorption capacity (400 $cm^3\,g^{-1}$), whereas when pre–treated at 353 K under vacuum, samples did not show any N_2 uptake. In contrast, adsorption of carbon dioxide at 273 K demonstrated sample micro–porosity, independent of

the pre–treatment used (2 mmol CO_2 per g at 100 kPa, see Fig. 6–13). Compared to the pristine UiO–66(Zr), the accessible surface area is lower: 496 $m^2\ g^{-1}$ for UiO–66(Zr) *vs.* 339 $m^2\ g^{-1}$ for $Zr_6(bdc–SO_3H)_4$, as calculated from CO_2 adsorption data using the Dubinin Radushkevich model. This adsorption capacity is however higher than the values shown by fully sulfonated UiO–66(Zr) presented by Kitagawa *et al.* [24] In addition, since the synthesis takes place in the presence of the highly acidic precursor $ZrCl_4$, almost full K^+ exchange takes place during synthesis (~0.36 wt% residual K compared to the 2.5 wt% Na in the MIL–101 samples). In fact, after one single use of the catalyst in reaction all the K^+ is exchanged (<0.01 wt% K). DRIFT spectroscopy demonstrates the presence of sulfonic acid groups, with the same new vibrations related to $C_{aromatic}–SO_3$ bonds (Fig. 6–13) as observed for the MIL–101 sulfonic samples.

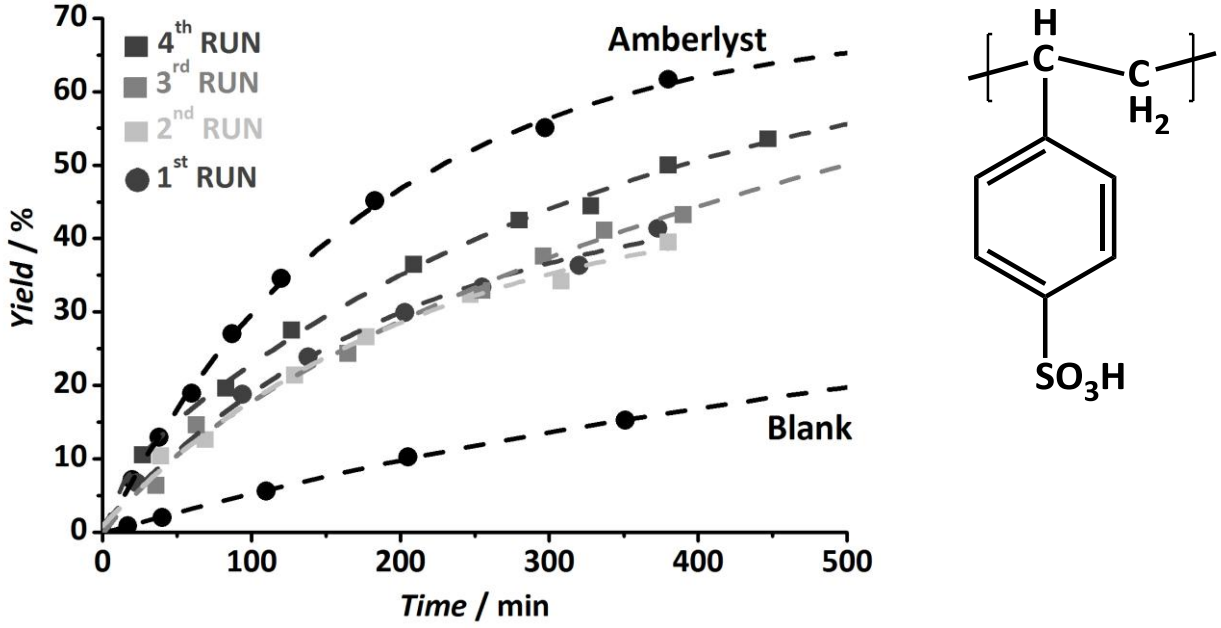

Figure 6 - 14 Esterification of 1–butanol and acetic acid (1:1 molar ratio) using 3 gram of catalyst per mol of reactant at 343 K. Before every use the catalyst has been pre–treated with 0.2 M HCl solution for 1 h at room temperature and thoroughly washed with H_2O until neutral pH. (*Right insert*) Amberlyst®–15.

In order to demonstrate that all sulfonic acid groups present in the new Zr structure are accessible for catalysis, titration experiments were performed using two different bases: sodium hydroxide and 1,5,7–triazabicyclo[4.4.0.]dec–5–ene; differing very much in size. Titration results indicated a similar consumption of both bases, and in agreement with the amount of sulfonic acid groups in the theoretical molecular formula (~3 mmol H^+ per g). These results demonstrate that even though pores are not accessible to N_2 adsorption after sample activation, in the liquid phase much bulkier molecules like triazabicyclo[4.4.0.]dec–5–ene can enter the pores and titrate all sulfonic acid groups. This result is in line with the observed textural properties, since CO_2 can be adsorbed at 273 K while N_2 (similar molecular size) is not adsorbed at 77 K, a strong proof of the microporous structure.

The acidic performance of the new Zr MOF has been assessed in the esterification of acetic acid and 1–butanol. Figure 6–14 shows a very high initial catalytic activity, well in comparison with the benchmark catalyst Amberlyst®–15.

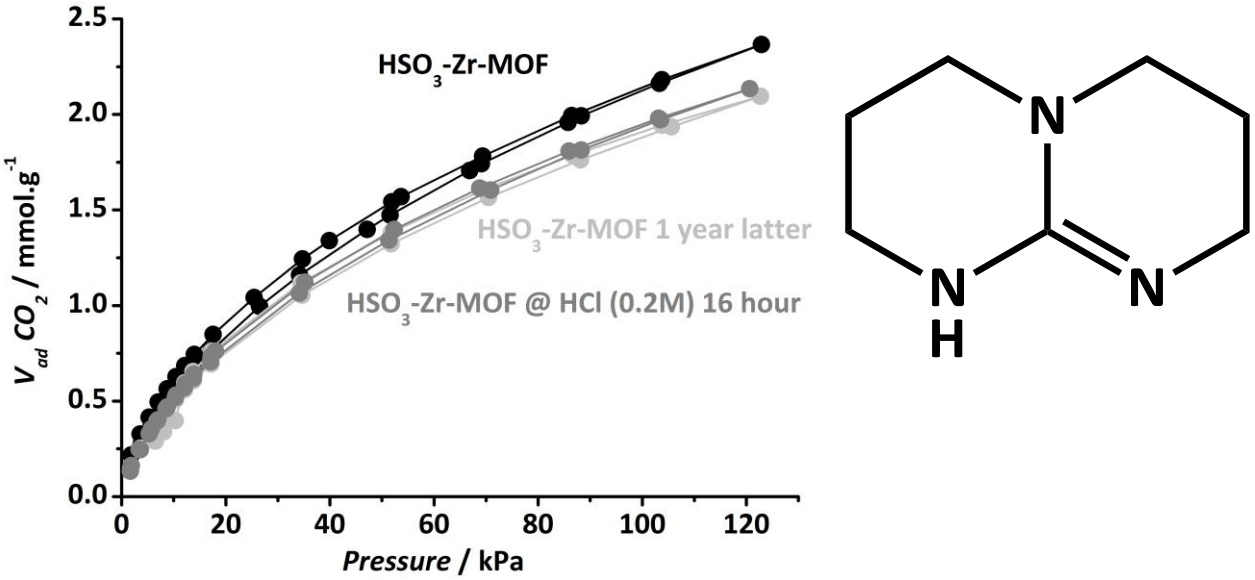

Figure 6 - 15 (*Left*) Carbon dioxide adsorption isotherms (273 K) of the HSO_3–Zr–MOF pre–treated under vacuum at RT overnight. (*Black*) HSO_3–Zr–MOF. (*Grey*) HSO_3–Zr–MOF activated with HCl (0.2 M) for 16 hours. (*Light grey*) HSO_3–Zr–MOF after one year from the synthesis, stored in air at RT. (*Right*) 1,5,7–triazabicyclo[4.4.0.]dec–5–ene.

Reusability of the catalyst was tested. Similar to that for MIL–101(Cr) samples, formation of sulfonic esters resulted in a strong decrease in catalytic activity. In addition, the Na^+ and K^+ salts of the sulfonic linker were tested in a blank experiment, and did not show any catalytic activity. In order to regenerate the spent catalyst, acid treatments were applied after each reaction cycle with a 0.2 M HCl solution at room temperature for one hour followed by thorough cleaning in water until pH 7 was reached. In the case of the Zr–MOF, re–usability and full recovery of the catalytic activity upon regeneration is possible (Fig. 6–14), with crystallinity and porosity being intact after 4 catalytic–regeneration cycles (Fig. 6–15), demonstrating the much higher chemical stability of the new MOF. Possible dissolution of the framework could be discarded by ^{13}C, ^{1}H NMR and infrared analysis of the reaction solution: the presence of sulfonic linker in solution could not be detected with any of the above mentioned techniques.

6.4. CONCLUSION

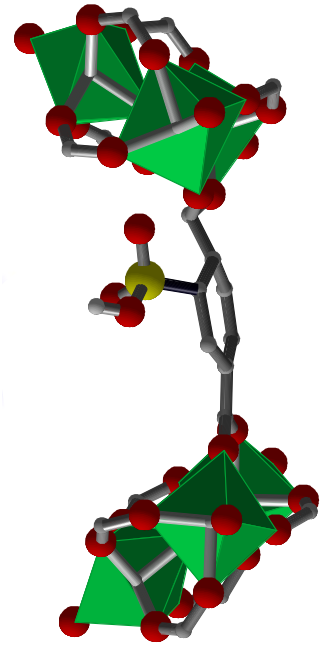

In this work the inclusion of free sulfonic acid groups is explored in supposedly highly stable MOFs. When applied in a model esterification reaction, deactivation of the sulfonic acid groups *via* formation of butyl sulfonic esters has been observed. In the case of MIL–101(Cr), due to the strong interaction between $–SO_3^-$ and the Cr open metal site where usually fluoride (F^-) is located in the structure, the catalysts are not stable under acidic regeneration conditions. When using Zr as metal node, a new and stable sulfonic acid containing porous structure was synthesized. This structure showed high activity and full reusability in the esterification reaction of 1–butanol with acetic acid. In this case, deactivation of the catalyst due to the formation sulfonic esters could be tackled by reactivation under acidic conditions.

Figure 6 - 16 SO_3H moiety at the benzene ring of MIL–101(Cr).

REFERENCES

[1] M.A. Harmer, Q. Sun, Solid acid catalysis using ion-exchange resins, Applied Catalysis A: General, 221 (2001) 45-62.
[2] T.A. Peters, N.E. Benes, A. Holmen, J.T.F. Keurentjes, Comparison of commercial solid acid catalysts for the esterification of acetic acid with butanol, Applied Catalysis A: General, 297 (2006) 182-188.
[3] J.M. Fraile, E. García-Bordejé, L. Roldán, Deactivation of sulfonated hydrothermal carbons in the presence of alcohols: Evidences for sulfonic esters formation, Journal of Catalysis, 289 (2012) 73-79.
[4] L. Peng, A. Philippaerts, X. Ke, J. Van Noyen, F. De Clippel, G. Van Tendeloo, P.A. Jacobs, B.F. Sels, Preparation of sulfonated ordered mesoporous carbon and its use for the esterification of fatty acids, Catalysis Today, 150 (2010) 140-146.
[5] J.H. Clark, V. Budarin, T. Dugmore, R. Luque, D.J. Macquarrie, V. Strelko, Catalytic performance of carbonaceous materials in the esterification of succinic acid, Catalysis Communications, 9 (2008) 1709-1714.
[6] G. Morales, R. van Grieken, A. Martín, F. Martínez, Sulfonated polystyrene-modified mesoporous organosilicas for acid-catalyzed processes, Chemical Engineering Journal, 161 (2010) 388-396.
[7] O.M. Yaghi, M. O'Keeffe, N.W. Ockwig, H.K. Chae, M. Eddaoudi, J. Kim, Reticular synthesis and the design of new materials, Nature, 423 (2003) 705-714.
[8] A. Corma, H. García, F.X. Llabrés i Xamena, Engineering metal-organic frameworks for heterogeneous catalysis, Chemical Reviews, 110 (2010) 4606-4655.
[9] A. Dhakshinamoorthy, M. Opanasenko, J. Čejka, H. Garcia, Metal Organic Frameworks as Solid Catalysts in Condensation Reactions of Carbonyl Groups, Advanced Synthesis & Catalysis, 355 (2013) 247-268.
[10] K. Schlichte, T. Kratzke, S. Kaskel, Improved synthesis, thermal stability and catalytic properties of the metal-organic framework compound $Cu_3(btc)_2$, Microporous and Mesoporous Materials, 73 (2004) 81-88.
[11] H. Khajavi, J. Gascon, J.M. Schins, L.D.A. Siebbeles, F. Kapteijn, Unraveling the optoelectronic and photochemical behavior of Zn_4O-based metal organic frameworks, Journal of Physical Chemistry C, 115 (2011) 12487-12493.
[12] Y.K. Hwang, D.Y. Hong, J.S. Chang, S.H. Jhung, Y.K. Seo, J. Kim, A. Vimont, M. Daturi, C. Serre, G. Férey, Amine grafting on coordinatively unsaturated metal centers of MOFs: Consequences for catalysis and metal encapsulation, Angewandte Chemie - International Edition, 47 (2008) 4144-4148.
[13] I. Luz, F.X. Llabrés i Xamena, A. Corma, Bridging homogeneous and heterogeneous catalysis with MOFs: Cu-MOFs as solid catalysts for three-component coupling and cyclization reactions for the synthesis of propargylamines, indoles and imidazopyridines, Journal of Catalysis, 285 (2012) 285-291.
[14] I. Luz, F.X. Llabrés I Xamena, A. Corma, Bridging homogeneous and heterogeneous catalysis with MOFs: "Click" reactions with Cu-MOF catalysts, Journal of Catalysis, 276 (2010) 134-140.
[15] S. Hasegawa, S. Horike, R. Matsuda, S. Furukawa, K. Mochizuki, Y. Kinoshita, S. Kitagawa, Three-dimensional porous coordination polymer functionalized with amide groups based on tridentate ligand: Selective sorption and catalysis, Journal of the American Chemical Society, 129 (2007) 2607-2614.
[16] J. Gascon, U. Aktay, M.D. Hernandez-Alonso, G.P.M. van Klink, F. Kapteijn, Amino-based metal-organic frameworks as stable, highly active basic catalysts, Journal of Catalysis, 261 (2009) 75-87.
[17] C. Volkringer, S.M. Cohen, Generating reactive MILs: Isocyanate-and isothiocyanate-bearing MILs through postsynthetic modification, Angewandte Chemie - International Edition, 49 (2010) 4644-4648.
[18] F. Vermoortele, R. Ameloot, L. Alaerts, R. Matthessen, B. Carlier, E.V.R. Fernandez, J. Gascon, F. Kapteijn, D.E. De Vos, Tuning the catalytic performance of metal-organic frameworks in fine chemistry by active site engineering, Journal of Materials Chemistry, 22 (2012) 10313-10321.
[19] M.G. Goesten, J. Juan-Alcañiz, E.V. Ramos-Fernandez, K.B. Sai Sankar Gupta, E. Stavitski, H. Van Bekkum, J. Gascon, F. Kapteijn, Sulfation of metal-organic frameworks: Opportunities for acid catalysis and proton conductivity, Journal of Catalysis, 281 (2011) 177-187.
[20] D. Britt, C. Lee, F.J. Uribe-Romo, H. Furukawa, O.M. Yaghi, Ring-opening reactions within porous metal-organic frameworks, Inorganic Chemistry, 49 (2010) 6387-6389.
[21] J. Juan-Alcañiz, J. Gascon, F. Kapteijn, Metal-organic frameworks as scaffolds for the encapsulation of active species: state of the art and future perspectives, Journal of Materials Chemistry, 22 (2012) 10102-10118.
[22] G. Akiyama, R. Matsuda, H. Sato, M. Takata, S. Kitagawa, Cellulose Hydrolysis by a New Porous Coordination Polymer Decorated with Sulfonic Acid Functional Groups, Advanced Materials, 23 (2011) 3294-3297.
[23] G. Akiyama, R. Matsuda, H. Sato, A. Hori, M. Takata, S. Kitagawa, Effect of functional groups in MIL-101 on water sorption behavior, Microporous and Mesoporous Materials, 157 (2012) 89-93.
[24] M. Lin Foo, S. Horike, T. Fukushima, Y. Hijikata, Y. Kubota, M. Takata, S. Kitagawa, Ligand-based solid solution approach to stabilisation of sulphonic acid groups in porous coordination polymer $Zr_6O_4(OH)_4(bdc)_6$ (UiO-66), Dalton Transactions, 41 (2012) 13791-13794.
[25] S. Biswas, J. Zhang, Z. Li, Y.-Y. Liu, M. Grzywa, L. Sun, D. Volkmer, P. Van Der Voort, Enhanced selectivity of CO_2 over CH_4 in sulphonate-, carboxylate- and iodo-functionalized UiO-66 frameworks, Dalton Transactions, 42 (2013) 4730-4737.

[26] Y. Zang, J. Shi, F. Zhang, Y. Zhong, W. Zhu, Sulfonic acid-functionalized MIL-101 as a highly recyclable catalyst for esterification, Catalysis Science & Technology, DOI: 10.1039/C3CY00044C (2013).
[27] D.A. Shirley, High-resolution x-ray photoemission spectrum of the valence bands of gold, Physical Review B, 5 (1972) 4709-4714.
[28] C. Férey, C. Mellot-Draznieks, C. Serre, F. Millange, J. Dutour, S. Surblé, I. Margiolaki, Chemistry: A chromium terephthalate-based solid with unusually large pore volumes and surface area, Science, 309 (2005) 2040-2042.
[29] P. Serra-Crespo, E.V. Ramos-Fernandez, J. Gascon, F. Kapteijn, Synthesis and Characterization of an Amino Functionalized MIL-101(Al): Separation and Catalytic Properties, Chemistry of Materials, 23 (2011) 2565-2572.
[30] P. Atorngitjawat, R.J. Klein, J. Runt, Dynamics of sulfonated polystyrene copolymers using broadband dielectric spectroscopy, Macromolecules, 39 (2006) 1815-1820.
[31] I. Díaz, F. Mohino, J. Pérez-Pariente, E. Sastre, Synthesis, characterization and catalytic activity of MCM-41-type mesoporous silicas functionalized with sulfonic acid, Applied Catalysis A: General, 205 (2001) 19-30.
[32] E. Cano-Serrano, G. Blanco-Brieva, J.M. Campos-Martin, J.L.G. Fierro, Acid-functionalized amorphous silica by chemical grafting-quantitative oxidation of thiol groups, Langmuir, 19 (2003) 7621-7627.
[33] A.S. Singh, B.M. Bhanage, J.M. Nagarkar, Formylation and acetylation of alcohols using Amberlyst-15® as a recyclable heterogeneous catalyst, Green Chemistry Letters and Reviews, 5 (2011) 27-32.
[34] W. Wang, X. Zhuang, Q. Zhao, Y. Wan, Self-assembly synthesis of a high-content sulfonic acid group functionalized ordered mesoporous polymer-based solid as a stable and highly active acid catalyst, Journal of Materials Chemistry, 22 (2012) 15874-15886.
[35] B. Brunetti, E. De Giglio, D. Cafagna, E. Desimoni, XPS analysis of glassy carbon electrodes chemically modified with 8-hydroxyquinoline-5-sulphonic acid, Surface and Interface Analysis, 44 (2012) 491-496.
[36] A.J. Crisci, M.H. Tucker, M.Y. Lee, S.G. Jang, J.A. Dumesic, S.L. Scott, Acid-functionalized SBA-15-type silica catalysts for carbohydrate dehydration, ACS Catalysis, 1 (2011) 719-728.
[37] P.C. Howlett, D.R. MacFarlane, A.F. Hollenkamp, High lithium metal cycling efficiency in a room-temperature ionic liquid, Electrochemical and Solid-State Letters, 7 (2004) A97-A101.
[38] I. Minami, T. Inada, R. Sasaki, H. Nanao, Tribo-chemistry of phosphonium-derived ionic liquids, Tribology Letters, 40 (2010) 225-235.
[39] T. Loiseau, G. Férey, Crystalline oxyfluorinated open-framework compounds: Silicates, metal phosphates, metal fluorides and metal-organic frameworks (MOF), Journal of Fluorine Chemistry, 128 (2007) 413-422.
[40] D.Y. Hong, Y.K. Hwang, C. Serre, G. Férey, J.S. Chang, Porous chromium terephthalate MIL-101 with coordinatively unsaturated sites: Surface functionalization, encapsulation, sorption and catalysis, Advanced Functional Materials, 19 (2009) 1537-1552.
[41] A. Vimont, J.M. Goupil, J.C. Lavalley, M. Daturi, S. Surblé, C. Serre, F. Millange, G. Férey, N. Audebrand, Investigation of acid sites in a zeotypic giant pores chromium(III) carboxylate, Journal of the American Chemical Society, 128 (2006) 3218-3227.
[42] J.H. Cavka, S. Jakobsen, U. Olsbye, N. Guillou, C. Lamberti, S. Bordiga, K.P. Lillerud, A new zirconium inorganic building brick forming metal organic frameworks with exceptional stability, Journal of the American Chemical Society, 130 (2008) 13850-13851.
[43] M. Kandiah, M.H. Nilsen, S. Usseglio, S. Jakobsen, U. Olsbye, M. Tilset, C. Larabi, E.A. Quadrelli, F. Bonino, K.P. Lillerud, Synthesis and stability of tagged UiO-66 Zr-MOFs, Chemistry of Materials, 22 (2010) 6632-6640.
[44] V. Guillerm, F. Ragon, M. Dan-Hardi, T. Devic, M. Vishnuvarthan, B. Campo, A. Vimont, G. Clet, Q. Yang, G. Maurin, G. Férey, A. Vittadini, S. Gross, C. Serre, A series of isoreticular, highly stable, porous zirconium oxide based metal-organic frameworks, Angewandte Chemie - International Edition, 51 (2012) 9267-9271.
[45] D. Feng, Z.Y. Gu, J.R. Li, H.L. Jiang, Z. Wei, H.C. Zhou, Zirconium-metalloporphyrin PCN-222: Mesoporous metal-organic frameworks with ultrahigh stability as biomimetic catalysts, Angewandte Chemie - International Edition, 51 (2012) 10307-10310.
[46] M. Kim, S.M. Cohen, Discovery, development, and functionalization of Zr(IV)-based metal-organic frameworks, CrystEngComm, 14 (2012) 4096-4104.
[47] Q. Yang, A.D. Wiersum, P.L. Llewellyn, V. Guillerm, C. Serre, G. Maurin, Functionalizing porous zirconium terephthalate UiO-66(Zr) for natural gas upgrading: a computational exploration, Chemical Communications, 47 (2011) 9603-9605.
[48] X. Feng, L. Liu, Y. Honsho, A. Saeki, S. Seki, S. Irle, Y. Dong, A. Nagai, D. Jiang, High-rate charge-carrier transport in porphyrin covalent organic frameworks: Switching from hole to electron to ambipolar conduction, Angewandte Chemie - International Edition, 51 (2012) 2618-2622.
[49] W. Morris, B. Volosskiy, S. Demir, F. Gándara, P.L. McGrier, H. Furukawa, D. Cascio, J.F. Stoddart, O.M. Yaghi, Synthesis, structure, and metalation of two new highly porous zirconium metal-organic frameworks, Inorganic Chemistry, 51 (2012) 6443-6445.
[50] V. Bon, V. Senkovskyy, I. Senkovska, S. Kaskel, Zr(IV) and Hf(IV) based metal-organic frameworks with reo-topology, Chemical Communications, 48 (2012) 8407-8409.

Chapter 7

Sulfated metal–organic frameworks: Opportunities for acid catalysis and proton conductivity

This chapter is based on the following publication:

M. Goesten, J. Juan–Alcañiz, , E.V. Ramos–Fernandez, K.B. Sai Sankar Gupta, E. Stavitski, H. Van Bekkum, J. Gascon, F. Kapteijn, Journal of Catalysis, 281 (2011) 177–187

Abstract A new post–functionalization method for metal–organic frameworks (MOFs) has been developed to introduce catalytic active sites. Upon treatment with a mixture of triflic anhydride and sulfuric acid, chemically stable MOF structures MIL–101(Cr) and MIL–53(Al) can be sulfated, resulting in a Brønsted hydrogen sulfate group attached to up to 20 and 50% of the aromatic terephthalate linkers of the structure, respectively. The sulfated samples have been extensively characterized by solid–state NMR, XANES, and FTIR spectroscopy. The functionalized acidic frameworks show catalytic activity similar to that of acidic polymers like Nafion® NR50 in the esterification of 1–butanol with acetic acid ($TOF \sim 1.75\ min^{-1}$ @ 343 K). Water adsorbs strongly up to 4 molecules per sulfoxy acid group, and an additional 2 molecules are taken up at lower temperatures in the 1D pore channels of sulfated MIL–53(Al). The high water content and Brønsted acidity provide the structure sulfated MIL–53(Al) with elevated proton conductivity up to moderate temperatures.

7.1. INTRODUCTION

The chemistry of metal–organic frameworks (MOF) has greatly advanced during the last few years. Nowadays, thousands of structures are known. [1] The great topological richness of this new class of materials resulting from the combination of metal ions and organic linkers is without precedent. [2] However, the absence of functionalities other than open metals or weak functional organic sites (*e.g.*, amines) in most of these structures limits to a certain extent their applicability. [3, 4] Practical solutions to create functional solids include direct synthesis or post–synthetic functionalization of MOFs, [5-7] grafting of active groups on the open metal sites of certain structures, [8] and encapsulation of active species. [9-11] In fact, the incorporation of ligands, including additional functional moieties, is not trivial, since such groups may directly coordinate to the metal ions. [12] One of the current challenges is the development of efficient functionalization methods that can be applied to MOFs without functional organic sites [13, 14] (in many cases, the most stable frameworks and usually most inert), *e.g.*, the direct functionalization of aryl carbons in terephthalate–linked MOFs.

During the last few decades, much effort has been put into the development of highly acidic solid materials such as ion–exchange resins based on sulfonic acid groups [15] or sulfated oxides based on zirconia, [16] silica, or alumina. [17] However, the application window of such materials is limited: some exhibit swelling in solvents (polymers) or strongly leaching issues (sulfated oxides), while none of them possess a defined porosity. Therefore, the development of nanostructured strongly acidic catalysts is still in the portfolio of materials' researchers.

In principle, MOFs offer a large amount of possibilities for the introduction of active moieties. Indeed, owing to their hybrid nature, functional groups could be included in such nanostructured materials by applying classical organic chemistry. However, in many cases, the limited chemical stability of MOFs does not allow harsh functionalization conditions, and terephthalate, perhaps the most used ligand in MOF synthesis, is deactivated for electrophilic substitution reactions at its aromatic ring due to the presence of carboxylate groups that diminish the density of electrons in the ring. Traditional sulfonation or sulfation methods are a clear example: [18] MOFs cannot be exposed to high concentrations of sulfuric acid since the framework would be destroyed. In this sense, several groups have tried to include sulfonic acid type of functionalities: Burrows *et al.* pioneered the incorporation of secondary sulfone moieties by using thiol–tagged linkers followed by a post–synthetic oxidation, [19] and Neofotistou *et al.* used a pre–modified linker already containing secondary sulfones: the ligand 4,4'–bibenzoic acid–2,2'–sulfone. [20] This approach leads to excellent properties for adsorption applications, but does not introduce acid functionality. Along the same line, Britt *et al.* reported the

post–synthetic modification of an amine containing MOF (IRMOF–3) with sultones, resulting in the opening of the sultone ring and the formation of terminal sulfonic acid groups. [21] In spite of the elegance of this method, sultones are among the most hazardous chemicals, forbidden in most developed countries. Unfortunately, no real applications for sulfonic acid/sulfonate–containing MOFs have seen the light up to now.

In this work, a different approach has been followed. Here, we report a room–temperature, homogeneously activated method to post–synthetically incorporate sulfoxy moieties into non–functional, chemically, and thermally stable MOFs (*e.g.*, MIL–101(Cr) [22] and MIL–53(Al) [23]). An extensive characterization demonstrates that by treating these stable MOFs with a mixture of sulfuric acid and trifluoromethanesulfonic anhydride (triflic anhydride), sulfoxy acid moieties are covalently bonded to the aromatic carbons of the organic linkers, and therefore widely distributed throughout the 3 dimensional framework. The resulting functionalized MOFs (denoted as S–MIL–101(Cr) and S–MIL–53(Al)) show excellent acid catalytic properties and high proton conductivity.

7.2. EXPERIMENTAL

7.2.1. Catalyst Preparation

All chemicals were obtained from Sigma–Aldrich and were used without further purification. MIL–53(Al) and Nafion® NR50 (0.5 mm pellets) were also purchased from Sigma–Aldrich, while MIL–101(Cr) was synthesized following the procedure described elsewhere. [22]

Stoichiometric sulfation was carried out with sulfuric acid in the presence of trifluoromethanesulfonic anhydride (triflic anhydride, Tf_2O), using nitromethane (CH_3NO_2) as solvent. The used molar ratio was bdc/H_2SO_4/Tf_2O = 1:1:1.5, where *bdc* is the benzene 1,4–dicarboxylic acid linker in the MOF structures. The mixture was continuously stirred in a water bath at room temperature. After 60 min, the solid product was filtered off, rinsed with ultrapure water and acetone, soaked in ethanol for 24 h at 343 K, and stored at 433 K.

7.2.2. Characterization techniques

(a) Nitrogen adsorption at 77 K: in a Quantachrome Autosorb–6B unit gas adsorption analyzer was used to determine the textural properties as BET surface area between 0.05 and 0.15 relative pressures and pore volume at 0.95 relative pressures. *(b) Water adsorption isotherms:* were measured using a Quantachrome Aquadyne DVS gravimetric water sorption analyzer. *(c) Powder X–Ray Diffraction (PXRD):* was measured using a Bruker–AXS D5005 with CuKα radiation. *(d) Thermo–Gravimetric Analysis (TGA):* was performed by means of a Mettler Toledo TGA/SDTA851e, under flowing air at 60 mL min^{-1} and heating rates of 5 K min^{-1} up to 873 K. *(e) Elemental analysis of Carbon and Sulfur:*

mass percentages were measured in a Leco CS induction oven. The samples were burnt in a continuous stream of O_2, while formed gases were analyzed by means of IR spectroscopy. The analysis is performed in duplicate after which the average concentration is reported. *(f) Fourier Transform Infrared Spectroscopy (FTIRS):* The infrared spectra were obtained using a Thermo Nicolet Nexus FTIR spectrometer. The samples (1 mg) were mixed with KBr and pressed into self–supported pellets (50 mg cm^{-2}). The spectra were taken in the transmission mode in an *in situ* cell equipped with CaF_2 windows. Prior to the measurements, the samples were degassed in vacuum (10^{-5} mbar) at 473 K for 30 min to remove adsorbed molecules. *(g) ^{27}Al, ^{13}C and ^{1}H Magic Angle Spinning Nuclear Magnetic Resonance Spectroscopy (MAS NMR):* were performed on a Bruker AV–750 spectrometer with a 17.6 T magnetic field, in which these nuclei resonate at 195.46, 188.64, and 750.13 MHz, respectively. A H/X/Y 2.5 mm MAS probe–head and a standard ZrO_2 rotor spun at 20 kHz were used. For the acquisition of ^{27}Al MAS NMR spectra, the RF field frequency, pulse duration, number of scans, and repetition time were 55 kHz, 1.5 μs, 1024 scans, and 1 s, respectively. The corresponding parameters were 78.1 kHz, 3.2 μs, 32 scans, and 1 s for ^{1}H MAS spectra. For ^{1}H to ^{13}C CPMAS with TPPM decoupling, we used 62.5 and 89 kHz RF field frequencies in the ^{13}C and ^{1}H channels, respectively, for cross–polarization (CP). The contact time was 3 ms, and the repetition time was 2 s for 1024 scans. Chemical shift references (0 ppm) are $Al(NO_3)_3$ in aqueous nitric acid solution for ^{27}Al and TMS for ^{1}H and ^{13}C. ^{27}Al spectra were fitted with the DMFIT software package [21] to obtain approximations for quadrupolar coupling constant C_q and asymmetry factor *eta*. *(h) Sulfur K–edge:* experiments were carried out at beam–line X19b, National Synchrotron Light source (NSLS) at Brookhaven National Laboratory (Upton, New York). Powder samples were finely ground to prevent scattering and mounted on 2.5 μm Mylar film to reduce the self–absorption effect that commonly occurs for thick samples with S content higher than 0.3 wt %. The incident X–ray energy was scanned over the range from 2430 to 2500 eV with a step size of 0.25 eV. Elemental sulfur (99.998%, Sigma–Aldrich, USA) was used as reference. Sample fluorescence was measured using a PIPS (passivated implanted planar silicon) detector (Canberra Industries, CT).

7.2.3. Proton Conductivity

The proton conductivity of the S–MIL–53(Al) pellets was measured by AC impedance spectroscopy, using an Autolab PGSTAT302N over a range of 10–10^7 Hz with controlled voltage. The pellets, pressed at 5 ton cm^{-2}, *ca.* 13.5mm Ø 0.9mm thick, were clamped between two pairs of electrodes and placed in a chamber under controlled humidity and temperature. No recording of bare MIL–53(Al) was made, as this material could not be pelletized.

The resistance *R* of the membrane was derived from the low intersection of the high–frequency semicircle on a complex impedance plane with the real Re (*Z*) axis. The conductivity is calculated using the relationship:

$$\sigma = {}^{d}/_{R \cdot S} \quad (1)$$

Where σ is the conductivity in S cm^{-1}, *R* the measured resistance of the membrane in Ω, *d* the distance between the two electrodes in cm, and *S* the contact surface, in cm^2. The σ values reported are an average of at least three measurements.

7.2.4. Catalytic testing

The esterification of acetic acid and 1–butanol was performed without solvent using a mixture with a molar ratio acetic acid/butanol = 1:1. The mixture was introduced in a round–bottom flask while being stirred under reflux. A ratio of 3 g catalyst per mol of acetic acid was used. Nafion® NR50 was used to benchmark the acidity of the resulting catalysts. After recovering the catalyst by filtration, it was stored at 423 K, and reused. The samples of the reaction mixture were periodically analyzed by gas chromatography using a Chrompack GC CP–Sil 8CB Cat. No. 7453 equipped with an FID detector and a 50 m RTX®–1 (1% diphenyl–, 99% dimethylpolysiloxane) fused silica capillary column, using decane (anhydrous, > 99%) as internal standard.

7.3. EXPERIMENTAL RESULTS

7.3.1. Characterization

7.3.1.1. Crystallinity, thermal stability and textural properties

After treatment of two different MOF structures, MIL–101(Cr) and MIL–53(Al), with stoichiometric amounts of H_2SO_4 and excess of Tf_2O for only 60 min at room temperature, a C/S weight ratio of 6 was determined by elemental analysis for MIL–53(Al). Assuming mono–benzene substitution, this would correspond to successful sulfation of a 50% of the aromatic terephthalate units. In the case of MIL–101(Cr), up to 20% of the linking terephthalate units could be mono–sulfated (one sulfoxy acid moiety per terephthalate linker) under similar reaction conditions.

No sulfation was observed of MOFs treated only with Tf_2O or with H_2SO_4 under similar reaction conditions, indicated by Tf_2O–MIL or H_2SO_4–MIL. XRD patterns of the sulfated samples (Fig. 7–1) demonstrate that the framework integrity is preserved after this mild post–treatment (despite some structural changes in S–MIL–53 discussed below).

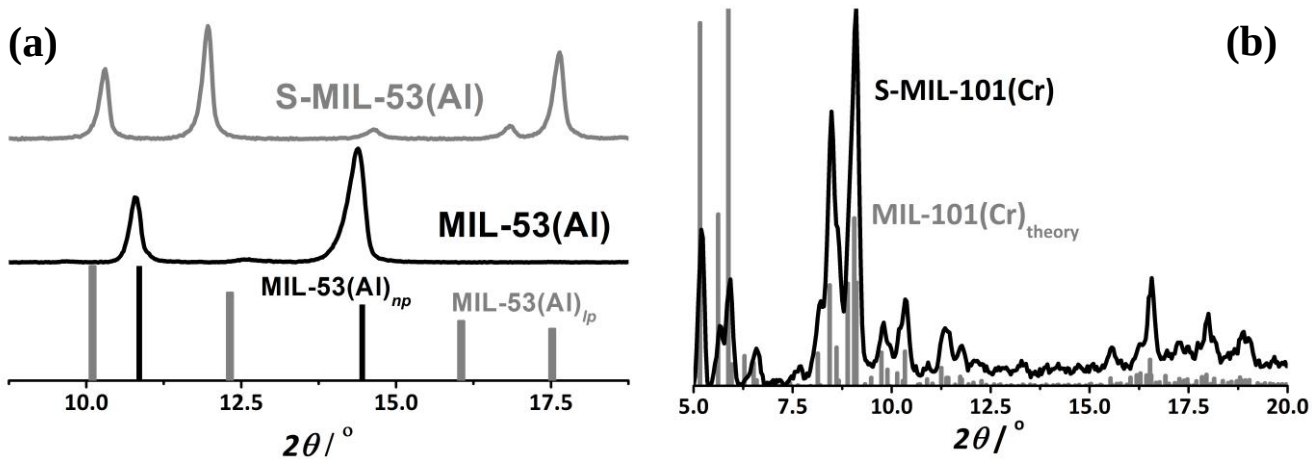

Figure 7 - 1 Power X–ray diffraction patterns for the sulfated samples compared with that of the bare MOFs. (a) MIL–53(Al) with simulated XRD reflections for the narrow (*np*) and large pore (*lp*) MIL–53(Al) phases. (b) MIL–101(Cr).

TGA results confirm the high thermal stability in air of the resulting materials (Fig. 7–2 and 3).

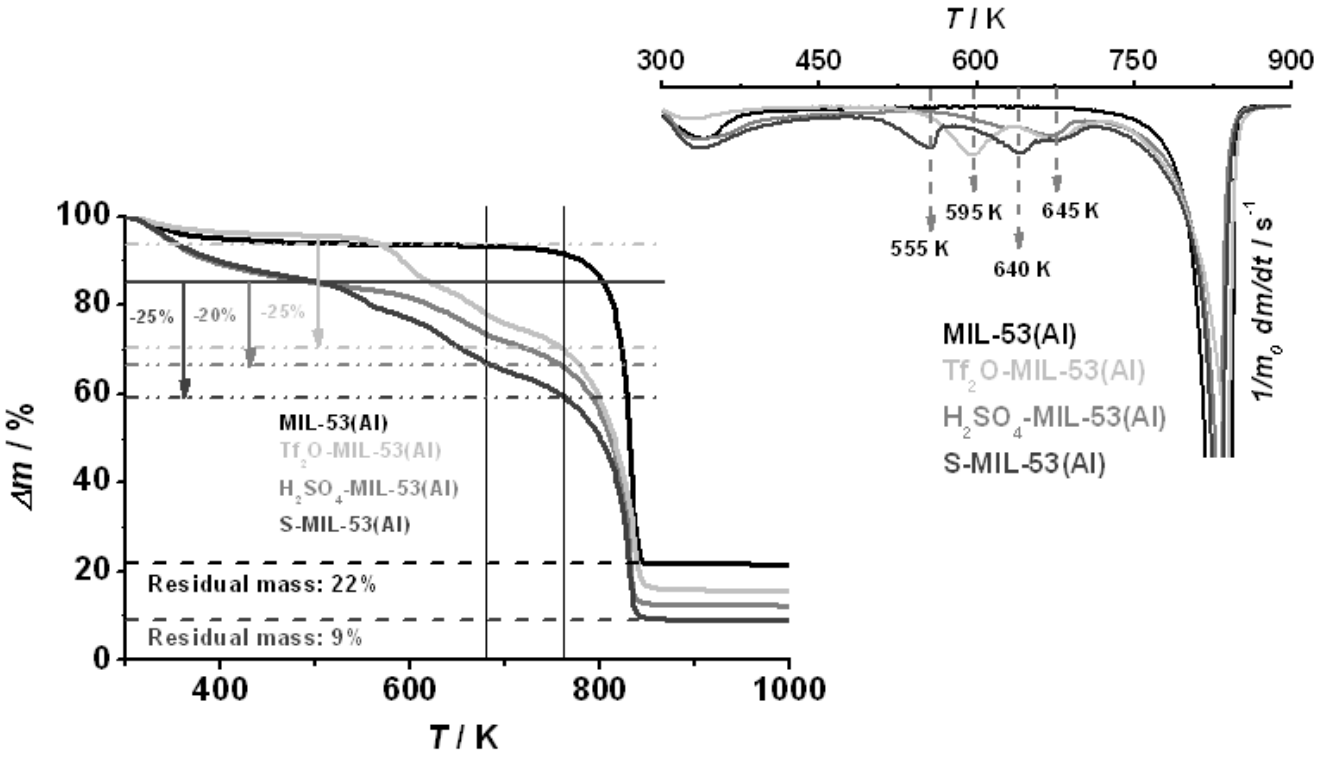

Figure 7 - 2 TGA (*left*) and DTG (*right*) profiles of the sulfated (*dark grey*) and pristine (*black*) MIL–53(Al) samples in air at a heating rate of 5 K min^{-1}, samples treated only with Tf_2O (*light grey*) or H_2SO_4 (*grey*) are also shown for comparison.

While several water desorption steps are observed in the TGA profile of S–MIL–53(Al), a gradual decrease between 400 and 600 K similar to the bare material is shown for S–MIL–101(Cr), and 50 K better thermal stability.

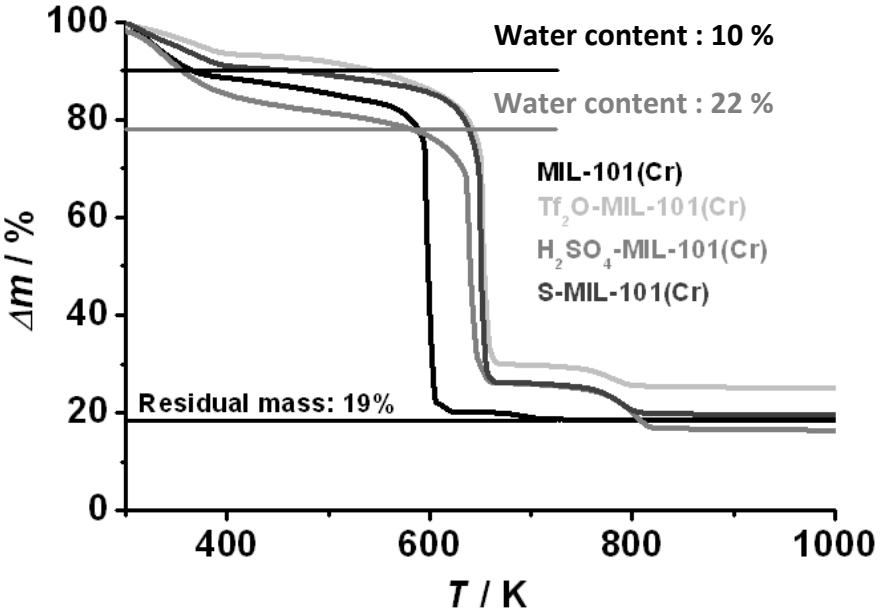

Figure 7 - 3 TGA profiles of the sulfated (*dark grey*) and pristine (*black*) MIL–101(Cr) samples in air at a heating rate of 5 K min^{-1}, samples treated only with Tf_2O (*light grey*) or H_2SO_4 (*grey*) are also shown for comparison.

In Figure 7–4, a comparison of the N_2 adsorption isotherms at 77 K is depicted.

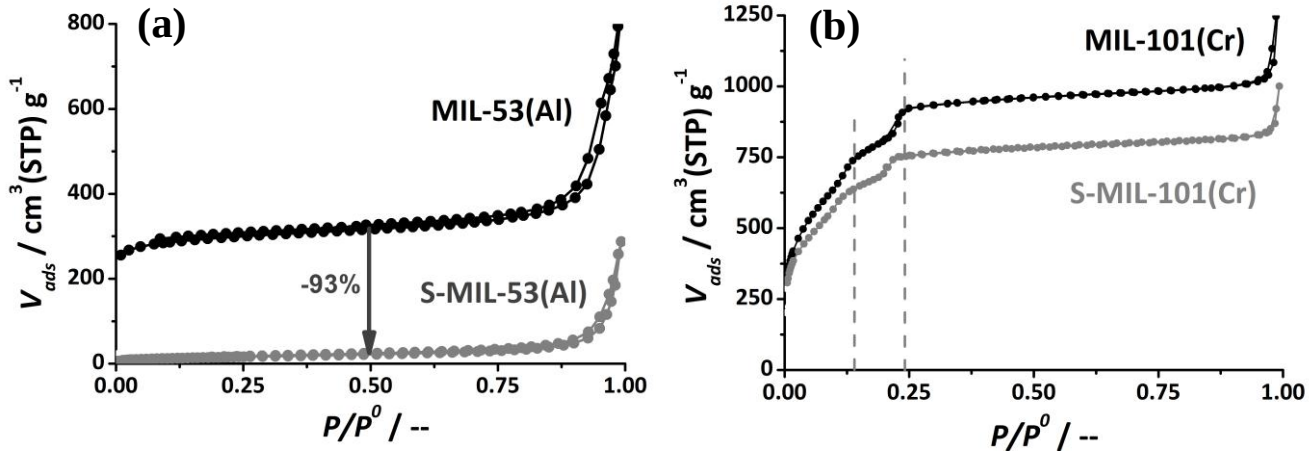

Figure 7 - 4 N_2 adsorption isotherms at 77 K for sulfated (*grey*) and pristine (*black*) samples. (a) MIL–53(Al). (b) MIL–101(Cr).

In the case of MIL–101(Cr), nitrogen adsorption reveals a decrease in the specific surface area from *ca.* 2750 $m^2 g^{-1}$ to 2230 $m^2 g^{-1}$. The shape of the isotherm is very similar with the two characteristic steps, but these are shifted to lower relative pressures, probably due to shrinking of the pores by the presence of the introduced sulfoxy acid groups. In the case of MIL–53(Al), the framework is not open for N_2 at 77 K after sulfate modification and evacuation at 513 K in high vacuum for 12 h. This result points at a large decrease in the pore size of the MIL–53(Al) caused by the volume of the sulfoxy groups, together with the presence of residual water within the framework (about 15 wt%), as shown in the TGA profile analyses (Fig. 7–2).

In order to demonstrate that, after sulfation, the MIL–53(Al) framework retains its intrinsic porosity, adsorption isotherms of H_2O at different temperatures were measured (Fig. 7–5). Even though the sulfated sample did not show any N_2 uptake at 77 K, water is able to access the pores. Two steps are observed during water adsorption. The onset of the first step clearly depends on the temperature and shifts to lower relative humidity (*RH*) with increasing temperature, while the adsorbed amount decreased in the case of T = 358 K. The second step occurs close to 100% *RH* at all instances, indicative of water inter–particle condensation. In every case, a remarkable adsorption–desorption hysteresis occurs. The whole set of isotherms was determined with the same sample, demonstrating the chemical stability of the framework upon (de) hydration.

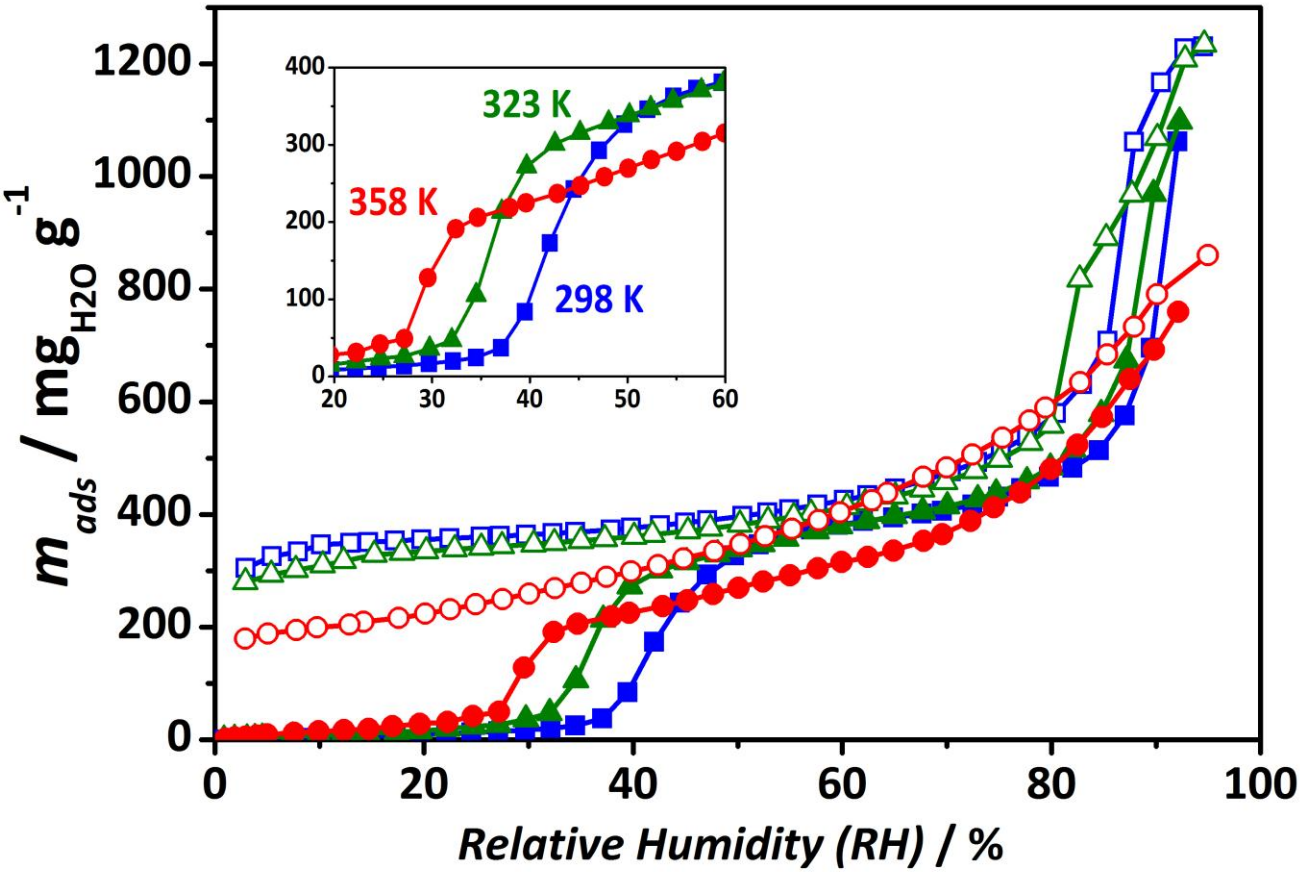

Figure 7 - 5 Water adsorption isotherms of the S–MIL–53(Al) framework at three different temperatures: (*squares*) 298K, (*triangles*) 323K and (*circles*) 358 K. Closed and open symbols correspond to adsorption and desorption, respectively.

These isotherms are arguably unique for microporous materials and completely different from the ones reported for non– or differently functionalized MIL–53(Al). [24] Indeed, the sulfated sample adsorbs twice as much water as unfunctionalized MIL–53(Al) and more than four times the amount adsorbed by NH_2–functionalized MIL–53(Al), underlining the hydrophilicity of the OSO_3H groups. [24]

7.3.1.2. Infrared Spectroscopy

A complete IR study on the sulfated structures confirms the successful functionalization of both MOFs. Figure 7–6 shows a comparison between untreated and sulfated samples. Each material was previously pre–treated under vacuum at 573 K for 60 min. Clear differences are already revealed when observing the whole spectra (4000–1000 cm^{-1}). The ν(OH) region (4000–3000 cm^{-1}) exhibits a broad band centered at 3400 cm^{-1} for the sulfated materials, absent in the bare samples. This vibration corresponds to water molecules retained in the pores by strong hydrogen bonds with the hydrogen sulfate. Specific sulfoxy acid stretching can be observed when zooming in at the region between 1800 and 1000 cm^{-1}. [25, 26]

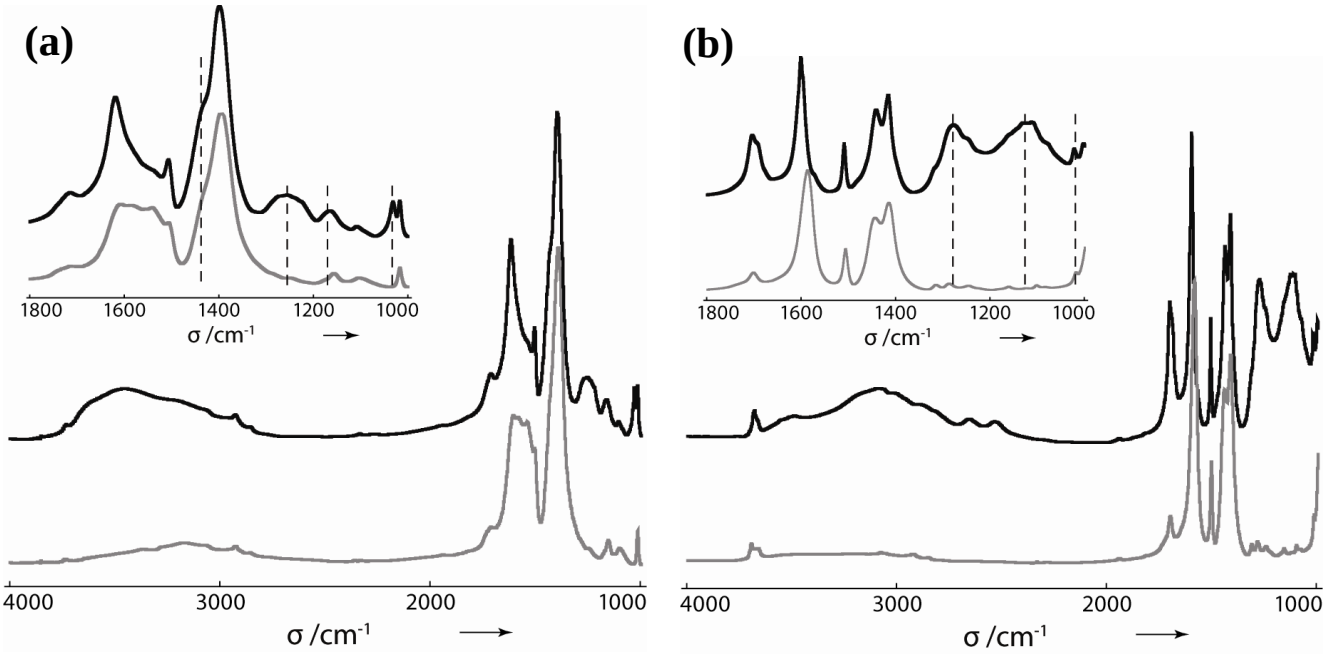

Figure 7 - 6 Comparison between the IR spectra of unfunctionalized (*grey*) and (*black*) S–MIL–101(Cr) (*a–left*) and S–MIL–53(Al) (*b–right*).

In the case of MIL–101(Cr), new bands appear at 1170 and 1260 cm^{-1} along with a shoulder at 1430 cm^{-1}, which can be attributed to the O=S=O symmetric and asymmetric stretching modes. [25, 26] The peak at 1100 cm^{-1} corresponds to the in–plane skeletal vibration of the benzene rings substituted by a hydrogen sulfate group, whereas the 1030 cm^{-1} can be assigned to the S–O stretching vibration. [25, 27]

In the case of S–MIL–53(Al), double and single S–O bond vibrations of sulfoxy acid groups are observed in the 1350–1000 cm^{-1} region. Upon pre–treating the sample, the presence of large amounts of remaining water within the S–MIL–53(Al) framework is evident from the bands appearing in the 3500–2750 cm^{-1} region. The broad band at 3000–2900 cm^{-1} is related to ν(O–H) stretching vibration mode of sulfoxy acid groups associated with cyclic dimers. [27] It is easy to envisage that within the

1D channel structure of S–MIL–53(Al), sulfoxy acid groups present in opposite channel walls might interact with each other, stacking via hydrogen bonding, as reported for polymers with a high density of sulfonic acid groups. [27] When comparing the infrared results with the TGA of S–MIL–53(Al) framework, the water still present in the framework corresponds to the third desorption step, water that is strongly H–bonded to the sulfoxy acid moieties.

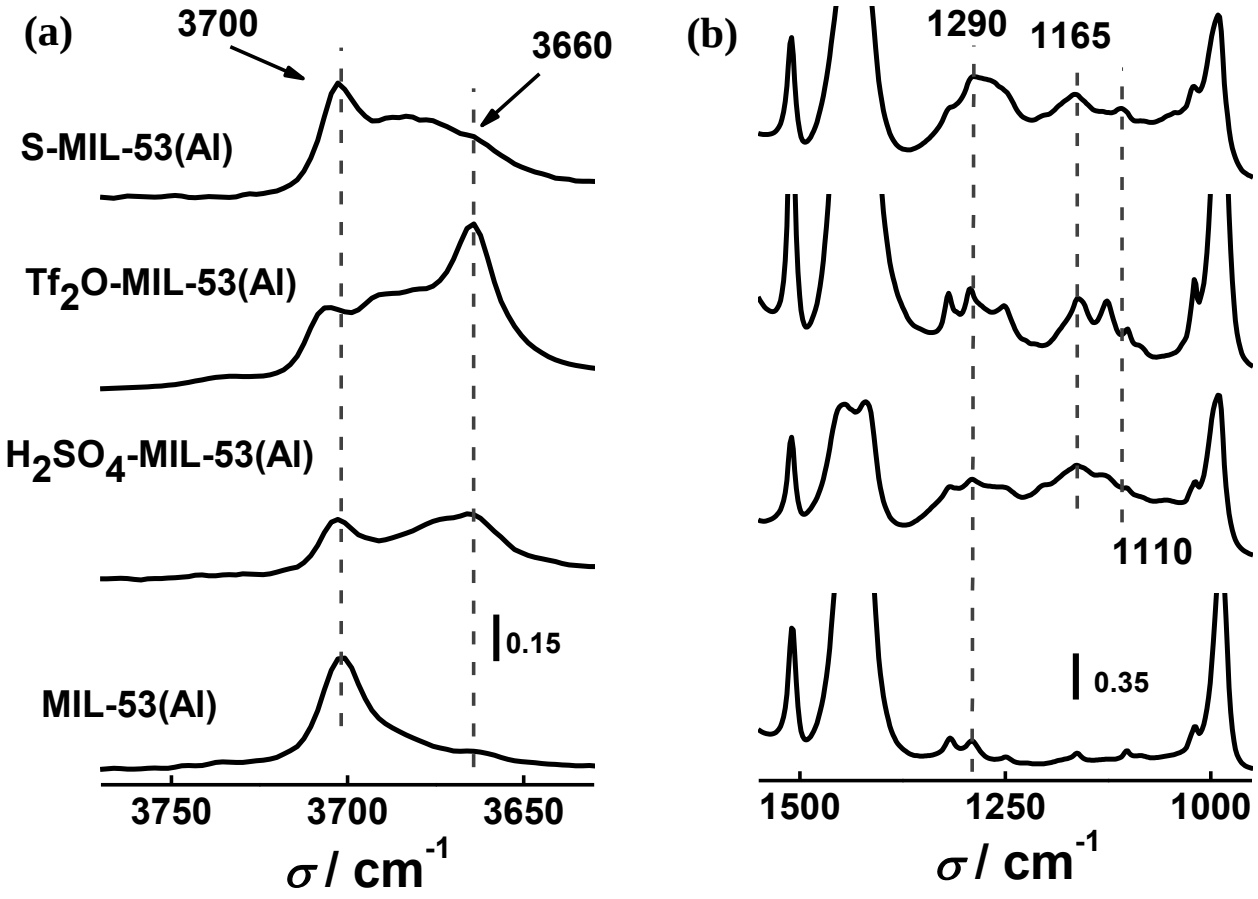

Figure 7 - 7 Infrared spectra in the regions 4000–3000 (a) and 1500–1000 cm^{-1} (b) for MIL–53(Al) samples (sulfated, Tf_2O, and H_2SO_4) treated under vacuum.

Figure 7–7 and 7–8 show the comparison between the IR spectra of samples treated with Tf_2O/H_2SO_4 mixtures and samples treated with only one of these reactants (Tf_2O or H_2SO_4), focused on two specific regions of the spectra, namely, 3800–3600 and 1550–950 cm^{-1}. Before recording, the samples were pre–treated at 573 K during 60 min in order to remove weakly adsorbed water and differentiate better the spectral features. In the ν(OH) region, two main stretching bands can be observed. MIL–53(Al) (Fig. 7–8a) reveals only one sharp stretching band at 3700 cm^{-1} related to ν(OH). This result is in line with previous reports, where this peak has been assigned to μ–hydroxo groups. [14] In the case of the modified samples, the stretching band at 3700 cm^{-1} remains, but its intensity decreases dramatically. Some μ–hydroxo groups are free, while other groups interact with guest moieties.

Hydrogen bond formation between the μ–hydroxo groups and S–O or –OH moieties (present in sulfoxy groups, H_2SO_4 and Tf_2O) might be the cause of a broad band between 3700 and 3660 cm^{-1} observed in the modified materials. The Tf_2O sample shows a higher intensity at 3660 cm^{-1}, indicating a higher density of S–O bonds (4 per molecule, while only 2 per moiety in the sulfated and H_2SO_4 samples). In the 1550–950 cm^{-1} region, where sulfoxy acid bands are present, similar features are observed for the modified materials. The maximum absorption at 1290 and 1165 cm^{-1} are related to the symmetric and asymmetric S=O stretching vibrations, respectively. In contrast, the band at 1110 cm^{-1}, only appearing in the sulfated sample, is related to the benzene rings substituted with an acid sulfoxy group. These results are in agreement with the data obtained for S–MIL–101(Cr).

On the basis of the catalytic activity and the fact that sulfated and their hydrated materials contain hydrated protons, [28] IR spectroscopy was applied *in situ* during dehydration of the same samples. At this point, it is of primary importance to show the main differences and similarities between samples sulfated and those treated only with H_2SO_4 or Tf_2O.

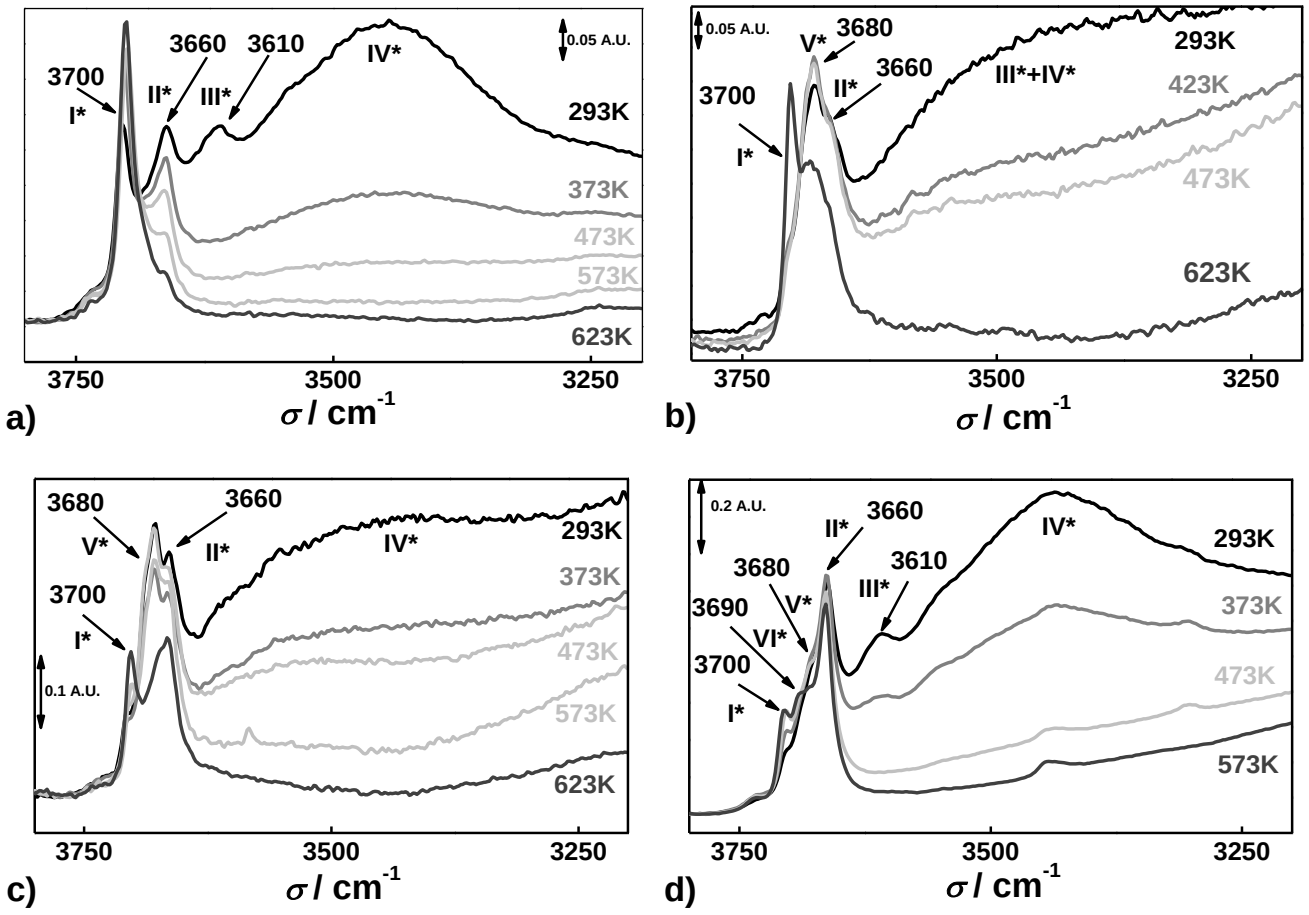

Figure 7 - 8 IR spectra in the ν(OH) (3800–3200 cm^{-1}) region. Study of dehydration by treating under vacuum and heating at different temperatures. (a) Parent MIL–53(Al), (b) S–MIL–53(Al), (c) H_2SO_4–MIL–53(Al) and (d) Tf_2O–MIL-53(Al).

Figure 7–8 shows the IR spectra recorded during the dehydration of the modified and bare materials. The samples were treated at the specified temperature under vacuum for 10 min before spectra were collected. In the case of MIL–53(Al) (Fig. 7–8a), the solid exhibits a breathing phenomenon upon hydration/dehydration, which involves atomic movements of ~5 Å. [23] In the hydrated form, the pores are slightly deformed due to interactions between the hydrogen atoms of adsorbed water and the μ–hydroxide groups, but when water is desorbed, the structure opens. [29] In vacuum at room temperature, three different types of –OH groups (I, II, and III) are present in the sample, apart from the physisorbed water (IV). The bands at 3660 (II) and 3610 cm^{-1} (III) can be assigned to interaction between the μ–hydroxide groups and water moieties in the pores. [13] In addition, the peak at 3700 cm^{-1} shows the ν(OH) of the μ–hydroxide group. In this situation, the pores of the structure are closed. After heating at 373 K under vacuum, the type III groups have already disappeared with most of the broad water band. As the pre–treatment temperature increases, strongly adsorbed water moieties desorb (disappearance of the 3660 cm^{-1} band). When reaching 623 K under vacuum, only the 3700 cm^{-1} band (μ–hydroxide groups) is left.

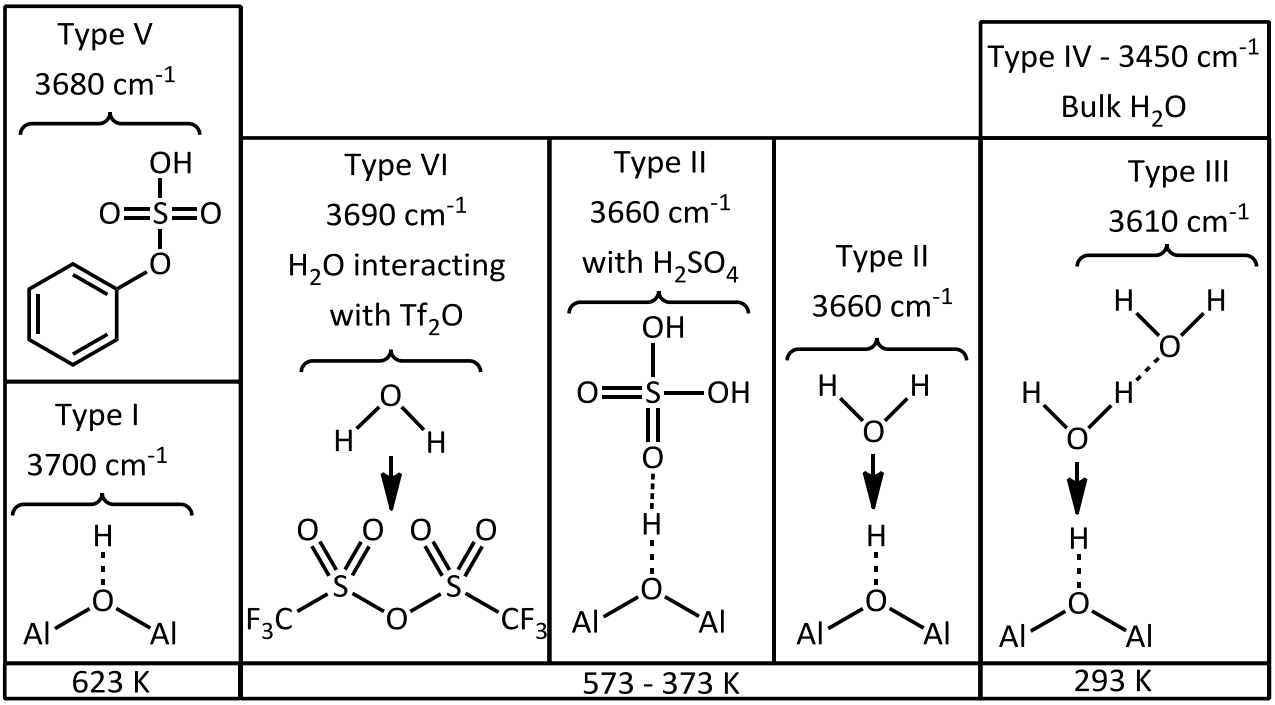

Scheme 7 - 1 Representation of the possible types of *ν*(OH) stretching observed during dehydration of MIL–53(Al) and the modified samples: sulphated, H_2SO_4 and Tf_2O.

Figure 7–8b shows the spectra obtained during the dehydration of S–MIL–53(Al). At room temperature, two main stretching bands appear: –OH group at 3680 (type V) and 3660 (type II) cm^{-1}. In addition, a shoulder is present at 3700 (type I) related to the free μ–hydroxide group. Upon heating, type I dominates the spectrum, whereas type II and V bands decrease drastically.

Figure 7–8c presents the dehydration study of the H_2SO_4–MIL–53(Al) sample, showing a similar behavior as S–MIL–53(Al). At room temperature, the main –OH bands observed are V (at 3680 cm^{-1}) and II (at 3660 cm^{-1}), with a shoulder at 3700 cm^{-1} (type I) corresponding to free μ–hydroxide groups. When the pre–treatment temperature increases, the absorbance at 3680 cm^{-1} decreases significantly, while the band at 3700 cm^{-1} is visible again showing a similar intensity as the also remaining band at 3660 cm^{-1}. Free μ–hydroxide groups are detectable again when most of the water is desorbed by dehydration (third peak in the DTA). Remaining –OH types V and II might be associated with –OH groups of H_2SO_4 interacting with water moieties and μ–hydroxide groups. Figure 7–8d shows the dehydration study of Tf_2O–MIL–53(Al). The main stretching band is observed at 3660 cm^{-1} (type II) with a shoulder at 3680 cm^{-1} (type V). No free μ–hydroxide groups at 3700 cm^{-1} (type I) are observed. When the sample is heated, the band at 3680 cm^{-1} is shifted to 3690 cm^{-1}, while the 3660 cm^{-1} (type II) band decreases in intensity and the vibration at 3700 cm^{-1} (type I) appears. For the bare MIL–53(Al) and Tf_2O–MIL–53(Al) materials, the absorbance at 3610 cm^{-1} disappears upon heating at 373 K under vacuum. In addition, the broad band (centered at 3400 cm^{-1}) associated with ν(OH) of water moieties almost disappears. In the case of H_2SO_4 and S–MIL–53(Al), the interaction of water with the hydroxyl groups exhibits a different behavior. The peak at 3610cm^{-1} is not visible due to a broader band centered at 3500cm^{-1} associated with the ν(OH) of adsorbed water. After pre–treating the samples at 473 K under vacuum, the broad band centered at 3500 cm^{-1} is still visible, in contrast to the bare and Tf_2O–MIL–53(Al) samples, showing a much stronger interaction (red shift and desorption at higher temperatures) between water and –OH groups of sulfuric acid and sulfated groups.

7.3.1.3. Magic Angle Spinning Nuclear Magnetic Resonance

In Figure 7–9 and 7–10, ^{27}Al MAS NMR, ^{13}C CPMAS NMR and ^{1}H MAS NMR spectra of S–MIL–53(Al) and unfunctionalized MIL–53(Al) are shown. Similar analyses could not be performed on Cr–based MIL–101 due to the paramagnetic nature of chromium, which sends its unpaired electrons through the linker, causing relaxation to be too fast to obtain an acquisition FID. ^{27}Al MAS NMR analysis shows interesting results as well as a duplet of peaks is obtained (Fig. 7–9). When fitted with DMFIT, it displays a quadrupolar coupling constant of 12.6 MHz which is significantly larger than the 8.5 and 9.2 MHz coupling constants reported by Lieder *et al.* [30] in their NMR analysis of dehydrated MIL–53(Al) and with different adsorbents, respectively. Quadrupolar coupling constants for solids are correlated with electronic field gradients within the crystal, and it would be reasonable to suppose that sulfoxy acid groups, binding in a non–symmetric way from a crystallographic perspective, enlarge electric field gradients and therefore quadrupolar coupling constants.

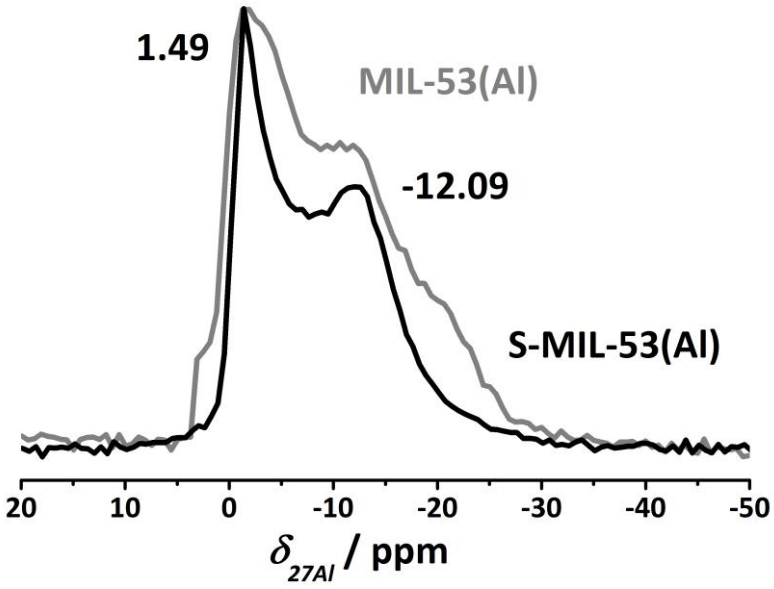

Figure 7 - 9 **^{27}Al MAS NMR spectra of S–MIL–53(Al) (*black*) and MIL–53(Al) (*grey*).**

The ^{13}C CPMAS NMR spectrum shows the removal of free terephthalic acid by the disappearance of the peak at 174 ppm present in the commercial sample (Fig. 7–10). Apparently, the reaction, cleaning, and drying procedure (*see experimental section*) of this sulfation treatment clears out free terephthalic acid. An extra aromatic carbon peak or rather a shoulder at 132–133 ppm is visible. [31] Whether this signal is caused by the aromatic carbon bonded to the sulfate group remains unclear, since Loiseau *et al.* have reported a similar shoulder for as–synthesized MIL–53(Al). [23] In this referred publication, this shoulder only occurs for as–synthesized MIL–53(Al) as does the terephthalic acid peak at 173–174 ppm, which would suggest it is terephthalic acid giving rise to this signal, but in our case of the S–MIL–53(Al) no free terephthalic acid carbon signal is found. Peaks at 130 and 137 ppm are unfunctionalized aryl carbons bonded to protons.

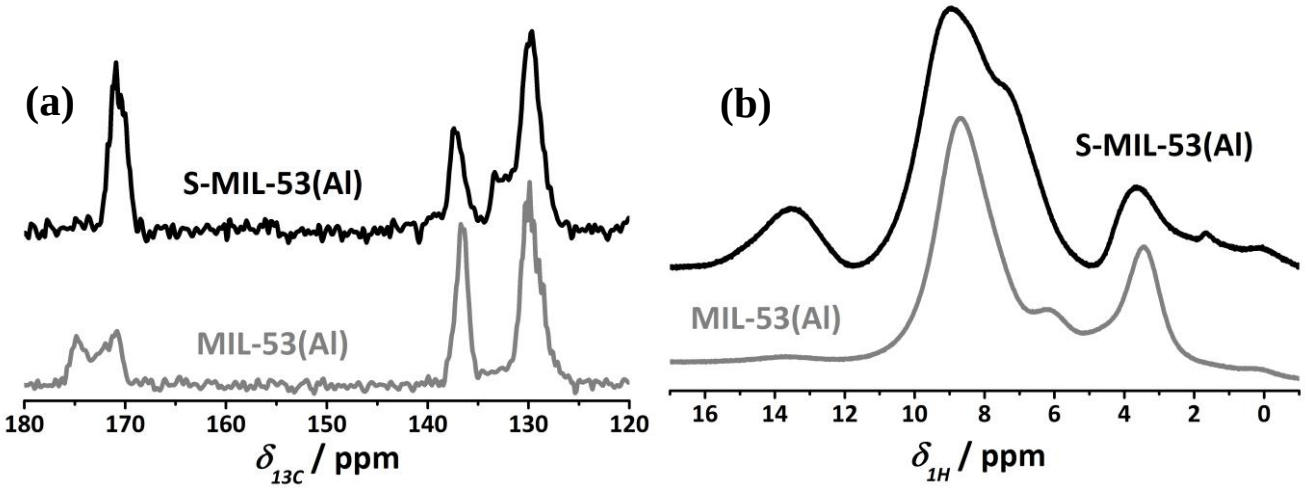

Figure 7 - 10 **(a) ^{13}C CPMAS NMR, (b) ^{1}H MAS NMR spectra of S–MIL–53(Al) (*black*) and MIL–53(Al) (*grey*).**

The ^{1}H MAS NMR spectrum is much more relevant though, with an acidic proton signal at 13–14 ppm. Theoretically, this proton signal could be attributed to free terephthalic acid, but ^{13}C CPMAS experiments and ^{1}H–^{13}C HETCOR experiments (Fig. 7–11) exclude this. In combination with XANES data, later on it is concluded that we deal with a sulfate proton. An extra proton peak at 1.7–1.8 ppm is visible too, which is in perfect correspondence with Al–OH–Al proton signals for heated MIL–53(Al) in Loiseau's work. [23] Apart from that, the peak caused by framework–coordinated water, at 6 ppm for the unfunctionalized sample, is increased and shifted downfield (~8 ppm) for the sulfated sample. This is because the sulfated sample coordinates to more water than the unfunctionalized sample, and sulfate–coordinated water protons are slightly more deshielded, giving rise to a larger chemical shift. Finally, ^{1}H–^{13}C HETCOR NMR (Fig. 7–11) shows that the acidic proton signal (at 13–14 ppm observed in ^{1}H MAS NMR) is not coming from terephthalic acid (extra peak at at 173–174 ppm in ^{13}C CPMAS NMR), since no cross–peak is visible in that region. All protons in the ^{1}H MAS NMR spectra only couple with the aromatic carbons. The distance between aryl carbons (shoulder at 132–133 ppm of modified aryl carbon and peaks at 130 and 137 ppm for unfunctionalized aryl carbons) and presumably sulfoxy acid protons (signal at 13–14 ppm) was too large to transfer magnetization and obtain cross–correlation.

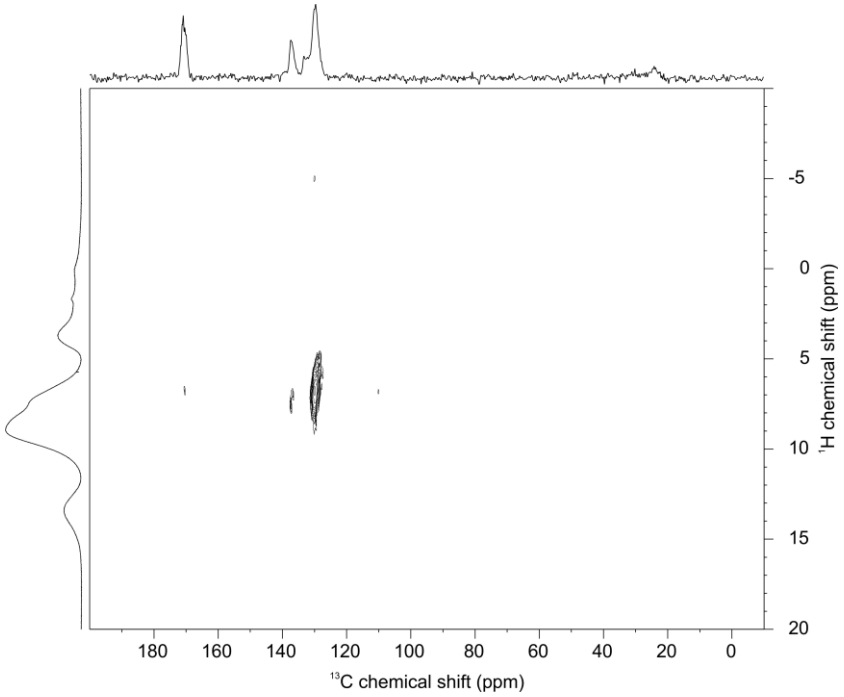

Figure 7 - 11 ^{1}H–^{13}C HETCOR spectra of S–MIL–53. [32]

7.3.1.4. X–Ray Absorption at the Sulfur K–edge

The successful functionalization of the framework with sulfur–containing acidic species has been demonstrated; however, the real nature of these sulfur species is not clear yet; indeed, our initial aim

was sulfonation (formal oxidation state of S^{+5}) rather than sulfation (formal oxidation of S^{+6}) functionality. In order to unravel the real nature of the active species, sulfur K–edge absorption spectra were recorded in the samples with the higher degree of functionalization (S–MIL–53(Al)). Sulfur K–edge absorption spectra are very sensitive to electronic structure, oxidation state, and the symmetry of the absorbing site. In particular, position of the white line is a very accurate indicator for the oxidation state, spanning across ~11 eV from 2469 eV for cystine (S^{2-}) to 2483 eV for inorganic sulfates (S^{6+}). [33] The line shape (features in the pre–edge and post–edge regions) may also be used for the identification of the sulfur–containing compounds. The traditional approach for speciation of multicomponent mixtures involves creating a spectral library of the possible components and analyzing the experimental spectra as their linear combination. [33, 34] We, however, limit ourselves to determination of the sulfur oxidation state in the sulfated MOF.

The XANES region of the K–edge absorption spectra for S–MIL–53(Al) is shown in Figure 7–12. Comparison of the white line position (2483 eV) with results reported in the literature points out the +6 oxidation state of sulfur (sulfate).

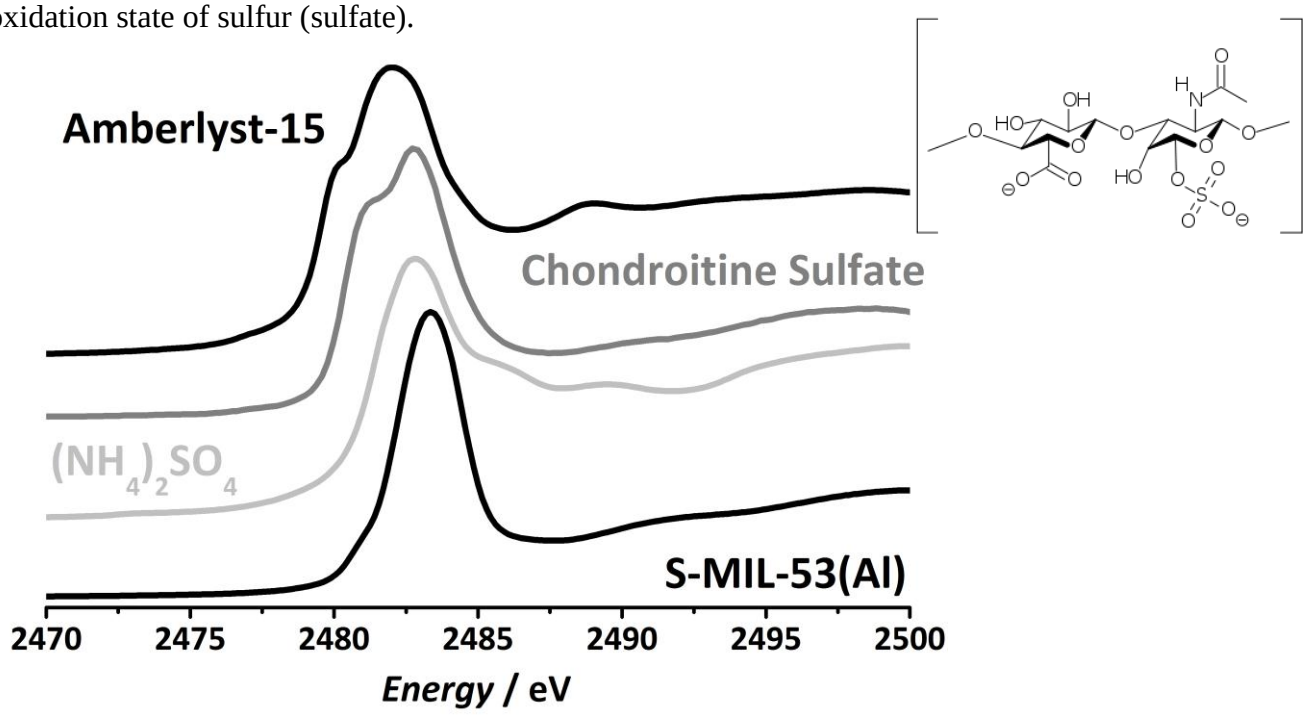

Figure 7 - 12 Sulfur K–edge XANES spectra. Spectra S–MIL–53(Al), $(NH_4)_2SO_4$ and Amberlyst®-15 are recorded in this work, spectrum of chondroitine sulfate (monomer represented) is adapted from Cuif *et al.* [32] All data had been normalized to the height of the white line.

This assumption is supported by the experimental spectra of $(NH_4)_2SO_4$ recorded under similar conditions (Fig. 7–12) as well as relevant model organic compound (chondroitine sulfate, [32]). In all three cases, the absorption maximum appears at nearly the same position. For the organic sulfonate group C–SO_3H, one would expect a shift to lower energy by ~1.5 eV. Indeed, the spectrum of Amberlyst (sulfonic–acid–functionalized polystyrene resin) shows a shift of 1.3 eV.

7.3.2. Proton conductivity:

Impedance spectroscopy was performed on the S–MIL–53(Al) to characterize its proton conduction properties and to compare them with those of acidic polymers. It turned out that the conductivity of a pellet as a function of temperature in the presence of N_2 saturated with H_2O at room temperature (Fig. 7–13) lies in the order of magnitude of Nafion® NR50 and several orders of magnitude higher than those reported for other proton–conducting MOFs, albeit measured under dry conditions. [35]

Above 353 K, however, the conductivity drops considerably, suggesting that when water is only adsorbed at the hydrogen sulfate groups, and not filling up the rest of the framework space, the proton conductivity decreases dramatically. Arguably, in this case, protons can only be conducted through the grain boundaries but not through the dry framework. In any case, the results indicate that model systems like S–MIL–53(Al) represent an excellent playground for studying proton conductivity in confined pores.

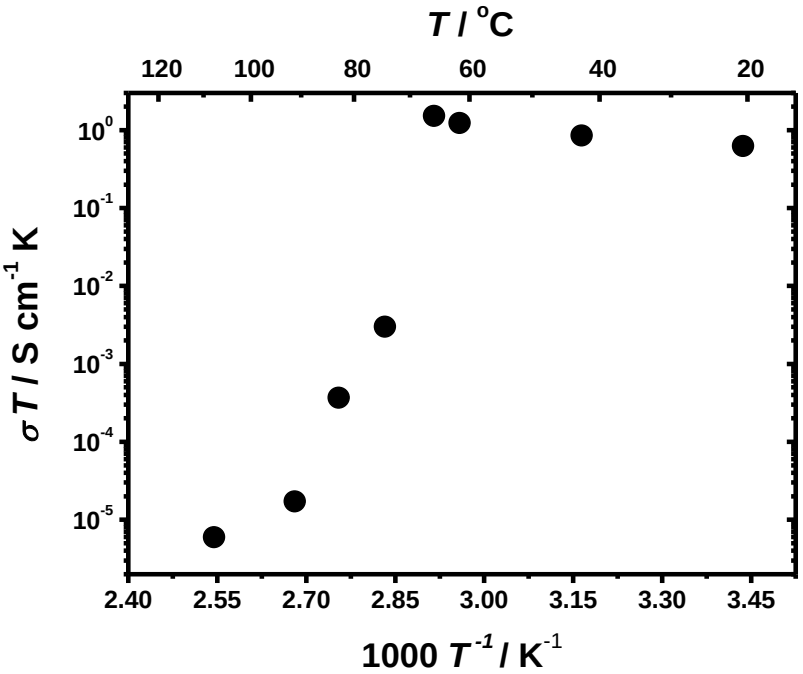

Figure 7 - 13 Conductivity of S–MIL–53(Al) framework as measured by impedance spectroscopy at different temperatures in the presence of humid N_2 (1.5 wt% H_2O).

7.3.3. Catalytic performance:

The catalytic activity of the functionalized frameworks has been benchmarked against Nafion® NR50 by the liquid–phase stoichiometric esterification (solvent free) of 1–butanol and acetic acid at low temperatures (343 K). The yield of the only reaction product, butyl acetate, is obtained using the same weight ratio (3g/mol reactant) of S–MIL–53(Al) and S–MIL–101(Cr) and Nafion® NR50. The functionalized samples show a high catalytic activity in the first run, due to adsorbed Tf_2O or H_2SO_4, which are very difficult to eliminate except under reaction conditions. Hence, the performance shown

in Figure 7–14 is related to the second use in case of the sulfated MOFs and compared with the first use of Nafion® NR50 as standard acid resin. Functionalized S–MIL–53(Al) shows an outstanding performance as acid catalyst and can be recycled without significant loss of activity (Fig. 7–15).

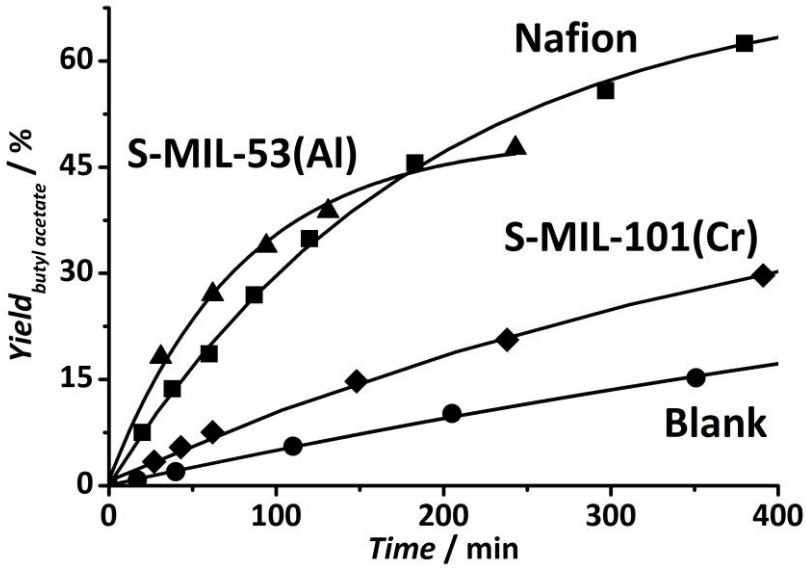

Figure 7 - 14 Esterification of acetic acid with 1–butanol (molar ratio 1:1) at 343 K with 3 g of catalyst per mol of acetic acid. Yield of butyl acetate as a function of time. (■) Nafion® NR50; (▲) S–MIL–53(Al); (◆) S–MIL–101(Cr) and(●) blank run (no catalyst).

Experiments with unfunctionalized MIL–53(Al) showed the same conversion profile as the blank run, demonstrating that the catalysis can be attributed to the presence of sulfoxy acid groups within the framework. S–MIL–101(Cr) shows catalytic behavior, but significantly lower, on a weight basis, than the previous described structure. The number of acidic protons per gram of framework should be considered for better comparison (Table 7–1).

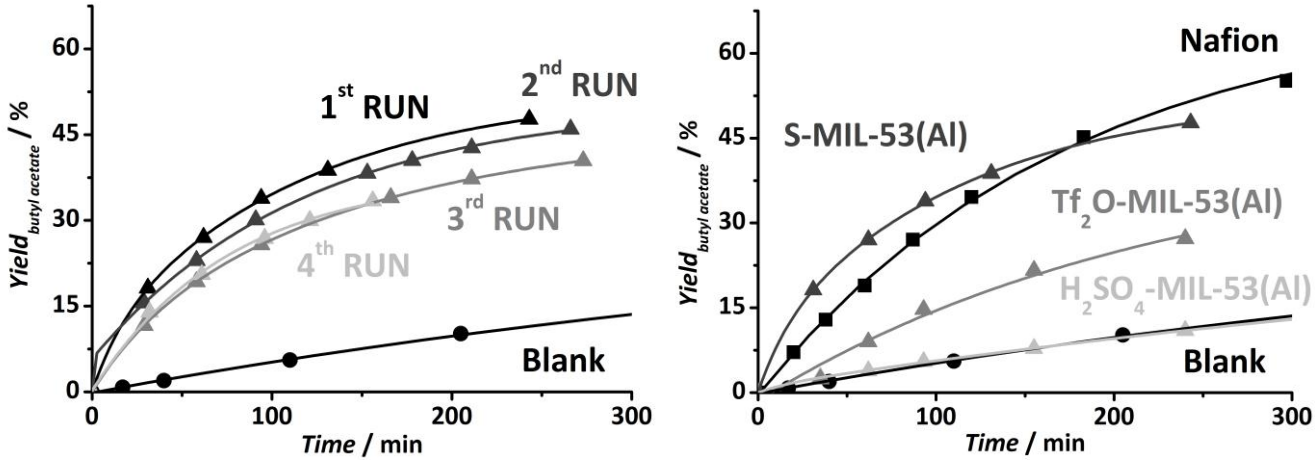

Figure 7 - 15 Esterification of acetic acid with 1–butanol (molar ratio 1:1) at 343 K with 3 g of catalyst per mol of acetic acid. Yield of butyl acetate as a function of time. *Left*: (▲)1st reuse S–MIL–53 (Al) (▲–*dark grey*) 2nd reuse (▲–*grey*) 3rd reuse (▲–*light grey*) 4th reuse and (●) Blank run (no catalyst). *Right*: (■) Nafion® NR50 (▲–*dark grey*) 1st reuse S–MIL–53 (Al) (▲–*grey*) 1st reuse H_2SO_4–MIL–53(Al) (▲–*light grey*) 1st reuse Tf_2O–MIL–53(Al) and (●) Blank run (no catalyst).

Figure 7–15 compares the second use (first reuse) of S–MIL–53(Al) with the same material treated with only one of the reactants (Tf_2O or H_2SO_4). While S–MIL–53(Al) maintains its outstanding performance, Tf_2O and H_2SO_4–MIL–53(Al) drop in activity due to desorption of the active species. These results show the presence of stable active sites in S–MIL–53(Al) formed by the combination of Tf_2O and H_2SO_4 in the sulfation procedure. A slightly higher turn–over–frequency (*TOF*) per acid group is found for the S–MIL–53(Al) sample as 1.75 mol of acetic acid reacts per mol of sulfur per minute against 1.33 for the acidic resin (Table 7–1). *TOF* values are maintained even after 5 reuses of the S–MIL–53(Al) catalyst, while for samples treated only with Tf_2O or H_2SO_4, the activity ceased upon reuse. In the case of S–MIL–101(Cr), a lower *TOF* and activity on a weight basis are observed, 0.54 mol reacted per sulfur and minute.

Table 7 - 1 Summary of kinetic constants, *TOF* and *TON* values obtained in the esterification of acetic acid with 1–butanol (molar ratio 1:1) at 343 K with 3 g of catalyst per mol of acetic acid.

Catalyst	active sites $\left[mmol\ H^+/g\right]$	Use	k [min^{-1}]	TOF $\left[\frac{mol_{converted}}{mol_{active\ site}\ min}\right]$	$TON_{accumulative\ (t = 250\ min)}$ $\left[\frac{mol_{converted}}{mol_{active\ site}}\right]$
Nafion® NR50	0.9[(a)]	1st	0.0036	1.33	188
S–MIL–53(Al)	2.40[(b)]	2nd	0.0126	1.75	67
		3rd	0.0112	1.55	129
		4th	0.0099	1.38	183
		5th	0.0131	1.81	237
S–MIL–101(Cr)	0.8[(b)]	2nd	0.0013	0.54	89

(a) According to reference [17]. (b) Calculated theoretically from the molecular formula.

7.4. DISCUSSION

The extensive characterization of the functionalized MOF samples demonstrates that it is possible to sulfate stable MOF structures using relatively mild conditions. It has to be stressed that the applicability of this method is limited to MOFs with a high chemical stability, similar treatment performed on less stable MOFs like UiO–66 [36] or MIL–68 [37] resulted in the destruction of the framework. The content of sulfur in the different MOF samples after post–functionalization has been measured by elemental analysis, suggesting 50% of linker functionalization for S–MIL–53(Al) and 20% for S–MIL–101(Cr). The different loading between structures can be assigned to the variation in framework inertness, since MIL–101(Cr) is described as one of the least reactive MOF systems upon alteration. [38, 39] Such sulfur content is designated to the formation of sulfoxy acid moieties at the aromatic ring supported by IR confirmation from O=S=O and S–O stretching vibrations, and particularly evidenced by NMR and XANES analyses for S–MIL–53(Al).

The appearance of new vibration bands after MOF post–functionalization (Fig. 7–6) reveals the presence of O=S=O and S–O stretching vibrations in both structures. In addition, the impossibility to fully dehydrate the samples suggests a very strong interaction of water molecules with very hydrophilic moieties. Comparison of IR spectra after sulfation or individual reactants treatment concedes a wider study on the S–MIL–53(Al) differences with respect to adsorbed reactants. Very similar spectra are observed throughout the high wavenumber region (–OH groups) comparing S–MIL–53(Al) with individual H_2SO_4 treated sample (Fig. 7–7), as expected. However, the new band at 1100 cm^{-1} only appearing in the case of S–MIL–53(Al) proves a different sulfo configuration from adsorption of individual reactants. IR measurements upon *in situ* dehydration of the samples have encountered more differences at the high wavenumber region between sulfated and single reactant treatment (Fig. 7–8). Similarities are very strong between individual H_2SO_4 treated and S–MIL–53(Al) samples before dehydration, however while heating proceeds differences arise leading to a unique ν(OH) at 3680 cm^{-1} only for the sulfated sample.

From comparison between the sulfur K–edge absorption spectra of the S–MIL–53(Al) sample and the different standards, it is clear that the oxidation state of sulfur in the MOF sample is +6 rather than +5 (Fig. 7–12). The XANES line shape (featuring in the pre–edge and post–edge regions) is similar to that reported for aryl sulfates (chondroitin sulfate). Together with the absence of any free terephthalic acid species in the functionalized material, which is confirmed by ^{1}H–^{13}C HETCOR and ^{1}H NMR, this points at hydrogen sulfate acidity. ^{27}Al MAS NMR shows that no aluminum salt residue is present in the sulfated framework and hence no sulfated aluminum oxide clusters. A partial destruction of the framework and possible sulfate formation of the linker at the carboxylic group is also discarded since it would result in partially coordinated aluminum that should be well visible in the ^{27}Al MAS NMR spectrum. NMR analysis was impossible to be performed for S–MIL–101 (Cr) due to the paramagnetic character of the chromium present in the framework.

The mechanistic side of the reaction deserves some special care since we deal with the implementation of a non–ordinary electrophile. The first step is traditional triflic anhydride chemistry in which triflic anhydride reacts with sulfuric acid to produce the mixed anhydride SO_4H–O–SO_2Tf. This mixed anhydride then has the sulfur bonded to the Tf group much more strongly polarized than the other sulfur and decomposes into triflate and $O^{+}SO_3H$ cations, an electrophillic oxygen, and a reagent for electrophilic ring attack and following substitution.

The most common approach for the construction of sulfated aryl systems is sulfation of hydroxyl group–containing aromatics using sulfur trioxide–amine complexes or chloro–sulfonic acid. [40] Due to the high reactivity of the acid proton, sulfated organics are usually produced in the form of alkaline

sulfates and it is not common to find sulfate–containing organic compounds. In contrast, when such groups are anchored to porous solids, like inorganic oxides, it has been shown that both SO_4^{2-} and HSO_4^- species are present at the catalyst surface, resulting in a mixed Lewis–Brønsted acid.

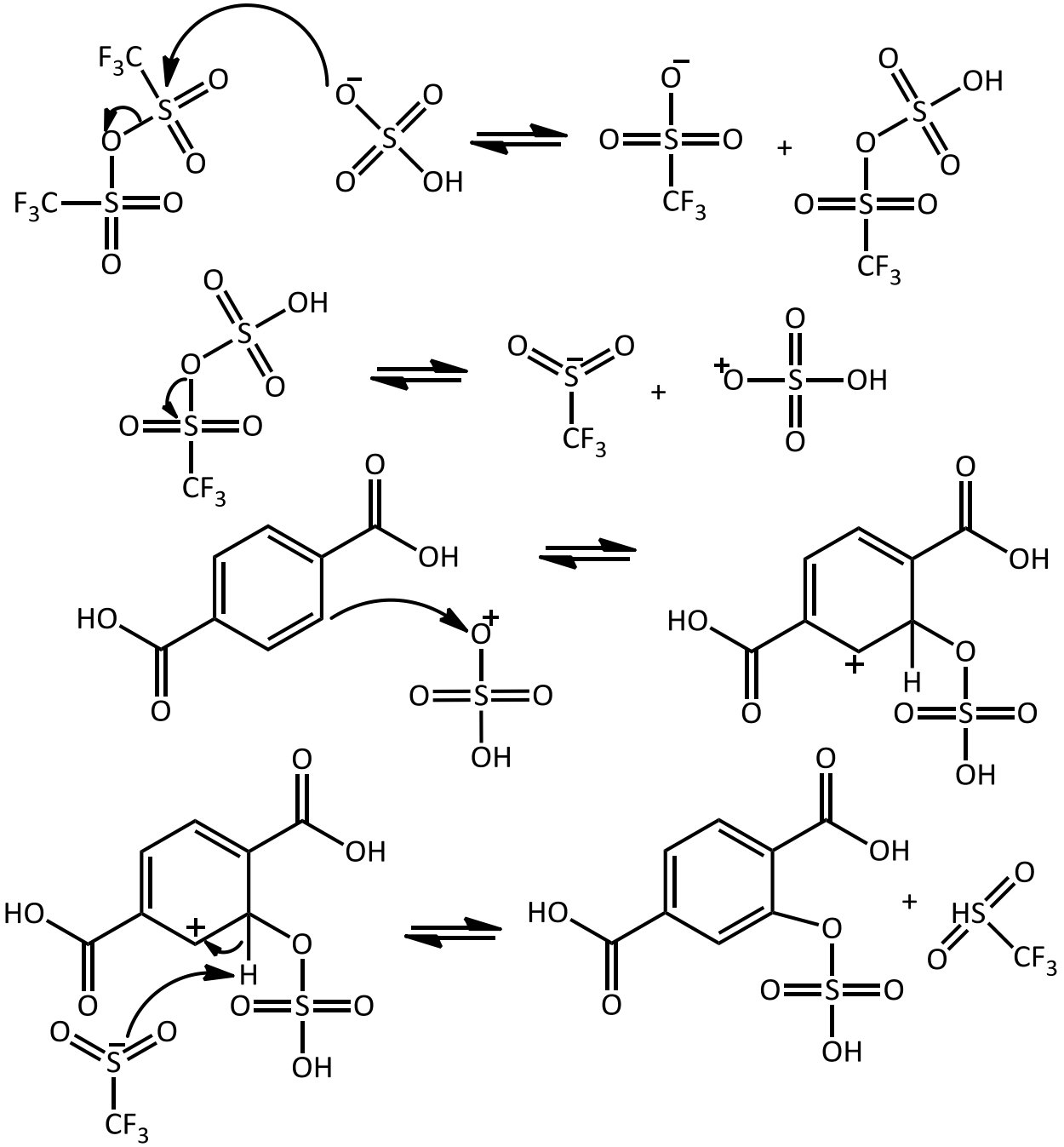

Figure 7 - 16 Proposed mechanism for the sulfation of terephthalic acid MOFs linker.

For example, in the case of sulfated zirconia, the positive charge of exposed Zr^{4+} cations is enhanced by the electron–acceptor nature of adjacent SO_4^{2-} groups and results in strong Lewis acid centers, while hydrogen sulfate/sulfoxy groups and OH^- groups interacting with electron acceptors such as adjacent Zr^{4+} cations have been identified as Brønsted acid sites. [17] In the functionalization of the MOFs, the combination of Tf_2O and sulfuric acid allows the direct formation of sulfoxy acid moieties covalently

bonded to the aromatic linkers, while the porosity of the material stabilizes the acidic proton of the sulfoxy acid groups, by interacting and stabilizing its charge in the spatial environment. The sulfoxy acid groups in the MOFs present a good thermal stability. TG analysis indicates that such functionalities are stable up to 555 K for S–MIL–53(Al) and 650 K for S–MIL–101(Cr) framework. However, their chemical stability needs attention: a S–MIL–53(Al) sample was boiled in water at pH 10 for 12 h leaving OH groups after hydrolysis of the sulfoxy groups.

When it comes to the properties of the sulfated materials, the effect of functionalization on the MIL–53(Al) framework is specifically interesting. MIL–53 is the best–known example of flexible MOFs, which, depending on both the presence of guests and the temperature, evolves from a narrow pore (‘*closed*’) to a large pore (‘*open*’) form with a variation of the cell volume without any bond breaking. [14] The adsorption of water (Fig. 7–5) is responsible for the switch between the open and the closed structure, with hydrogen bonding interactions playing the primary role. [23] The difference between this ‘breathing’ behavior among differently functionalized MIL–53 frameworks and the consequences for separation have recently been reported, demonstrating that the presence of functional organic sites at the aromatic rings strongly disturbs the framework breathing. [41, 42] In the case of S–MIL–53(Al), strong hydrogen bonding already occurs in the absence of water. This is in line with the TGA and IR results showing desorption of water at high temperatures and with the XRD pattern (Fig. 7–1): after pre–treating the sulfated sample at 373 K in inert atmosphere, most of the structure remains in the narrow pore form, as concluded from the half–open/half–closed crystallographic pattern. [43] Only Kusgens *et al.* [44] reported a somehow similar isotherm shape for the metal–organic framework DUT–4, but in that case, the shape of the isotherm was related to the irreversible collapse of the framework through the addition of water. We attribute the first step in the isotherm to the breathing of the framework: in the low–temperature isotherm, up to six molecules of water are reversibly adsorbed per sulfoxy acid group. The uptake at the highest temperature (358 K) corresponds with around four water molecules per sulfoxy acid moiety. This demonstrates that at lower temperatures, water is adsorbed both at the sulfoxy acid groups and in the remaining pore space; while at increased temperatures, only the sulfoxy acid groups are able to attract water. These adsorption results match the TGA data very well, where similar amounts of released water were observed after sample exposure to ambient conditions. In both cases, the framework has to expand to accommodate the water. In the case of samples treated only with H_2SO_4 or Tf_2O, slightly different TGA profiles are found: none of them show the first H_2O desorption step at around 555K, related to strongly bonded water to hydrogen sulfate moieties. In the case of S–MIL–101(Cr) framework, the incorporation of sulfoxy moieties bonded to the organic ligands leads to a decrease in nitrogen adsorption uptake, corresponding with a reduction of the pore volume due to the presence of a bulky functionality. At the same time, the

characteristic steps of the nitrogen isotherm are shifted to lower relative pressure, suggesting also the presence of sulfoxy groups in the framework. TGA profiles describe an increase in thermal stability of 50 K for every functionalized MIL–101(Cr) framework.

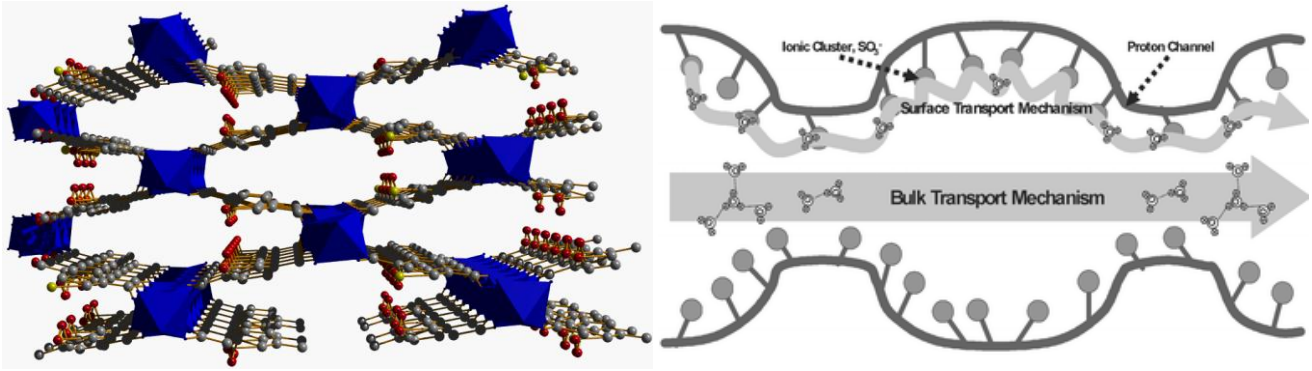

Figure 7 - 17 (*Left*) Sulfated MIL-53(Al) structure. (*Right*) Proton transfer mechanism in Nafion membranes. Adapted from [45].

The proton transfer mechanism in the S–MIL–53(Al) sample may be very similar to the situation described for Nafion® NR50 self–standing membranes. Proton conductivity is strongly dependent upon its nanostructure and water content. Two different water environments are usually distinguished. For instance, the water in the middle region of the pore is referred to as "*bulk water*", through which the mobility of the protons is fast (Grotthus mechanism). However, water near the pore surface along the array of SO_3^- groups is referred to as "*surface water*", and the proton transport along the negatively charged surface is smaller than in the "*bulk*" of a pore, due to strong electrostatic attractions and higher activation energy of SO_3^- groups, but a higher concentration of charge carriers are present. Therefore, the measured proton conductivity at given water content is the result of weighted average of the surface and bulk conductivities, depending upon the radial distribution of protons and water content. At high water contents, the properties of proton transfer in Nafion® NR50 are similar to those of "*bulk water*". Al low water contents, not all acid sites are dissociated and the relative population of clusters of hydrogen bonded water decreases, resulting in a low rate of proton transfer limited to the surface region, providing very low conductivity. [46, 47] We assume that the transport of protons in S–MIL–53(Al) sample is carried out via *(i)* a surface diffusion mechanism occurring close to the pore wall under low water activity, and *(ii)* a bulk diffusion mechanism prevailing in the central region of the pore under high water content. Therefore, under the presence of water below 353 K the proton conductivity is in the same order of magnitude as Nafion® NR50. Regrettably, when the presence of water within the pores of the material decreases, the proton conductivity is lost.

The catalytic behavior tested for the esterification of acetic acid and 1–butanol of the sulfated samples is displayed in Figures 7–14 and 15. Significant catalysis is observed when using S–MIL–101(Cr), however far lower than that of the S–MIL–53(Al) framework, which presents similar activities as

those of Nafion® NR50. On the other hand, MIL–53(Al) samples treated with only one of the reactants, display very poor catalytic performances during the first reuse. *TOF* values have been calculated for proper comparison of catalytic activity per active site (Table 7–1). Calculations of the number of active sites per gram of Nafion® NR50 have been obtained from literature, however MOF values have been calculated from the theoretical molecular formula (assuming that all sulfonic groups of the formula are available). Better catalysis per active site is detected for S–MIL–53(Al) comparing with Nafion® NR50 (*TOF* MOF ~ 1.75 > *TOF* Nafion® NR50 ~ 1.33), with stable performance through at least four cycles (*TON accumulative* > 235). These results demonstrate that, when anchored to an ordered structure, sulfoxy acid groups are stable and display excellent acidic properties. However, lower values are observed for S–MIL–101(Cr), suggesting similarities with Chapter 6, where sulfonic groups interact with the chromium trimmers reducing their accessibility for catalytic purposes.

Whether the breathing behavior of S–MIL–53(Al) affects the catalytic performance is not clear. For instance, MIL–53(Fe) breathes through adsorption of different solvents, but the extent of breathing varies with the nature of the solvent. [42] With regard to the pore opening observed through water adsorption (Fig. 7–5), it is reasonable to assume that the S–MIL–53(Al) framework will also be open in the reaction mixture, ensuring the full sulfoxy groups' accessibility inside the channels.

7.5. CONCLUSION

A new post–synthetic functionalization method for metal–organic frameworks has been developed. Upon treatment with a stoichiometric mixture of triflic anhydride and sulfuric acid, it is possible to sulfate the aromatic ring of the terephthalic linker in stable MOF structures. The applicability of this method is, however, limited to MOFs with a high chemical stability like MIL–53(Al) and MIL–101(Cr).

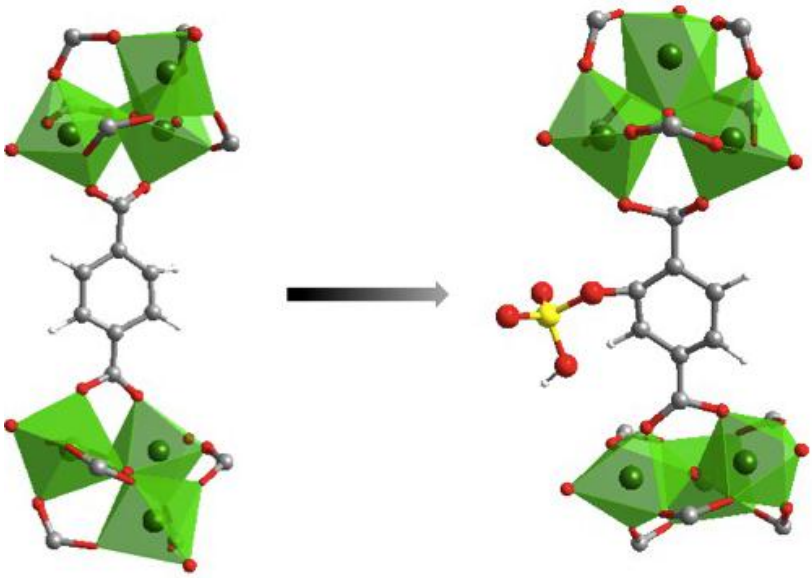

Figure 7 - 18 Schematic view of the sulfation post–synthetic modification in the benzene ring of MIL–101(Cr).

The functionalized frameworks, up to 50% of their aromatic ligands for S–MIL–53(Al) and 20% for S–MIL–101(Cr) were sulfated, show outstanding acid catalytic activity in esterification of 1–butanol with acetic acid (*TOF* ~1.75) and stability (*TON accumulative* > 235). The new IR vibration band appearing only in the case of S–MIL–53(Al) together with the NMR and XANES results, and the fact that for samples treated with only H_2SO_4 the catalytic activity disappears after thorough washing of the material, demonstrates that aryl carbon functionalization only takes place when a mixture of Tf_2O and H_2SO_4 is used. Furthermore, S–MIL–53(Al) shows a high proton conductivity up to moderate temperatures with adsorbed water acting as conductor in a continuous phase.

This work might form the basis for the development of highly acid and multifunctional metal–organic frameworks that might find applications in fuel cells, separation of molecules, and catalytic processes.

REFERENCES

[1] G. Férey, Hybrid porous solids: Past, present, future, Chemical Society Reviews, 37 (2008) 191-214.
[2] J.J. Perry, J.A. Perman, M.J. Zaworotko, Design and synthesis of metal-organic frameworks using metal-organic polyhedra as supermolecular building blocks, Chemical Society Reviews, 38 (2009) 1400-1417.
[3] D. Farrusseng, S. Aguado, C. Pinel, Metal-organic frameworks: opportunities for catalysis, Angew. Chem Int Ed., 48 (2009) 7502-7513.
[4] A. Corma, H. García, F.X. Llabrés i Xamena, Engineering metal-organic frameworks for heterogeneous catalysis, Chemical Reviews, 110 (2010) 4606-4655.
[5] J. Gascon, U. Aktay, M.D. Hernandez-Alonso, G.P.M. van Klink, F. Kapteijn, Amino-based metal-organic frameworks as stable, highly active basic catalysts, Journal of Catalysis, 261 (2009) 75-87.
[6] X. Zhang, F.X. Llabrés i Xamena, A. Corma, Gold(III) – metal-organic framework bridges the gap between homogeneous and heterogeneous gold catalysts, Journal of Catalysis, 265 (2009) 155-160.
[7] Z. Wang, S.M. Cohen, Postsynthetic modification of metal-organic frameworks, Chemical Society Reviews, 38 (2009) 1315-1329.
[8] D.Y. Hong, Y.K. Hwang, C. Serre, G. Férey, J.S. Chang, Porous chromium terephthalate MIL-101 with coordinatively unsaturated sites: Surface functionalization, encapsulation, sorption and catalysis, Advanced Functional Materials, 19 (2009) 1537-1552.
[9] J. Juan-Alcañiz, E.V. Ramos-Fernandez, U. Lafont, J. Gascon, F. Kapteijn, Building MOF bottles around phosphotungstic acid ships: One-pot synthesis of bi-functional polyoxometalate-MIL-101 catalysts, Journal of Catalysis, 269 (2010) 229-241.
[10] F.J. Ma, S.X. Liu, C.Y. Sun, D.D. Liang, G.J. Ren, F. Wei, Y.G. Chen, Z.M. Su, A sodalite-type porous metal-organic framework with polyoxometalate templates: Adsorption and decomposition of dimethyl methylphosphonate, Journal of the American Chemical Society, 133 (2011) 4178-4181.
[11] M.H. Alkordi, Y. Liu, R.W. Larsen, J.F. Eubank, M. Eddaoudi, Zeolite-like metal-organic frameworks as platforms for applications: On metalloporphyrin-based catalysts, Journal of the American Chemical Society, 130 (2008) 12639-12641.
[12] G.K.H. Shimizu, R. Vaidhyanathan, J.M. Taylor, Phosphonate and sulfonate metal-organic frameworks, Chemical Society Reviews, 38 (2009) 1430-1449.
[13] C. Serre, S. Bourrelly, A. Vimont, N.A. Ramsahye, G. Maurin, P.L. Llewellyn, M. Daturi, Y. Filinchuk, O. Leynaud, P. Barnes, G. Férey, An explanation for the very large breathing effect of a metal-organic framework during CO2 adsorption, Advanced Materials, 19 (2007) 2246-2251.
[14] C. Serre, F. Millange, C. Thouvenot, M. Nogues, G. Marsolier, D. Louer, G. Férey, Very large breathing effect in the first nanoporous chromium(III)-based solids: MIL-53 or CrIII(OH){O_2C-C_6H_4-CO_2}{HO_2C-C_6H_4-CO_2H}xH_2Oy, Journal of the American Chemical Society, 124 (2002) 13519-13526.
[15] S.S. Kaye, J.R. Long, Matrix isolation chemistry in a porous metal-organic framework: Photochemical substitutions of N_2 and H_2 in $Zn_4O[(\eta^6$-1,4-benzenedicarboxylate)$Cr(CO)_3]_3$, Journal of the American Chemical Society, 130 (2008) 806-807.
[16] M.G. Goesten, K.B. Sai Sankar Gupta, E.V. Ramos-Fernandez, H. Khajavi, J. Gascon, F. Kapteijn, Chloromethylation as a functionalisation pathway for metal-organic frameworks, CrystEngComm, 14 (2012) 4109-4111.
[17] M.A. Harmer, Q. Sun, Solid acid catalysis using ion-exchange resins, Applied Catalysis A: General, 221 (2001) 45-62.
[18] A.D. Burrows, C.G. Frost, M.F. Mahon, C. Richardson, Sulfur-tagged metal-organic frameworks and their post-synthetic oxidation, Chemical Communications, (2009) 4218-4220.
[19] N. Katada, J.I. Endo, K.I. Notsu, N. Yasunobu, N. Naito, M. Niwa, Superacidity and catalytic activity of sulfated zirconia, Journal of Physical Chemistry B, 104 (2000) 10321-10328.
[20] L. Hamon, P.L. Llewellyn, T. Devic, A. Ghoufi, G. Clet, V. Guillerm, G.D. Pirngruber, G. Maurin, C. Serre, G. Driver, W. Van Beek, E. Jolimaetre, A. Vimont, M. Daturi, G. Férey, Co-adsorption and separation of CO_2-CH_4 mixtures in the highly flexible MIL-53(Cr) MOF, Journal of the American Chemical Society, 131 (2009) 17490-17499.
[21] D. Britt, C. Lee, F.J. Uribe-Romo, H. Furukawa, O.M. Yaghi, Ring-opening reactions within porous metal-organic frameworks, Inorganic Chemistry, 49 (2010) 6387-6389.
[22] C. Férey, C. Mellot-Draznieks, C. Serre, F. Millange, J. Dutour, S. Surblé, I. Margiolaki, Chemistry: A chromium terephthalate-based solid with unusually large pore volumes and surface area, Science, 309 (2005) 2040-2042.
[23] T. Loiseau, C. Serre, C. Huguenard, G. Fink, F. Taulelle, M. Henry, T. Bataille, G. Férey, A Rationale for the Large Breathing of the Porous Aluminum Terephthalate (MIL-53) Upon Hydration, Chemistry - A European Journal, 10 (2004) 1373-1382.
[24] Y.K. Hwang, D.Y. Hong, J.S. Chang, S.H. Jhung, Y.K. Seo, J. Kim, A. Vimont, M. Daturi, C. Serre, G. Férey, Amine grafting on coordinatively unsaturated metal centers of MOFs: Consequences for catalysis and metal encapsulation, Angewandte Chemie - International Edition, 47 (2008) 4144-4148.
[25] F. Kučera, J. Jančář, Homogeneous and heterogeneous sulfonation of polymers: A review, Polymer Engineering and Science, 38 (1998) 783-792.

[26] D.S. Warren, A.J. McQuillan, Infrared spectroscopic and DFT vibrational mode study of perfluoro(2-ethoxyethane) sulfonic acid (PES), a model nafion side-chain molecule, Journal of Physical Chemistry B, 112 (2008) 10535-10543.
[27] B. Ostrowska-Gumkowska, J. Ostrowska-Czubenko, Property-structure relationships in partially sulphonated poly(ethylene terephthalate)-I. Infrared studies, European Polymer Journal, 30 (1994) 869-874.
[28] A. Zecchina, G. Spoto, S. Bordiga, Probing the acid sites in confined spaces of microporous materials by vibrational spectroscopy, Physical Chemistry Chemical Physics, 7 (2005) 1627-1642.
[29] P.L. Llewellyn, S. Bourrelly, C. Serre, Y. Filinchuk, G. Férey, How hydration drastically improves adsorption selectivity for CO_2 over CH_4 in the flexible chromium terephthalate MIL-53, Angewandte Chemie - International Edition, 45 (2006) 7751-7754.
[30] C. Lieder, S. Opelt, M. Dyballa, H. Henning, E. Klemm, M. Hunger, Adsorbate effect on $AlO_4(OH)_2$ centers in the metal-organic framework MIL-53 investigated by solid-state NMR spectroscopy, Journal of Physical Chemistry C, 114 (2010) 16596-16602.
[31] M.J. Cánovas, I. Sobrados, J. Sanz, J.L. Acosta, A. Linares, Proton mobility in hydrated sulfonated polystyrene. NMR and impedance studies, Journal of Membrane Science, 280 (2006) 461-469.
[32] P. Atorngitjawat, R.J. Klein, J. Runt, Dynamics of sulfonated polystyrene copolymers using broadband dielectric spectroscopy, Macromolecules, 39 (2006) 1815-1820.
[33] G. Sarret, J. Connan, M. Kasrai, G.M. Bancroft, A. Charrié-Duhaut, S. Lemoine, P. Adam, P. Albrecht, L. Eybert-Bérard, Chemical forms of sulfur in geological and archeological asphaltenes from Middle East, France, and Spain determined by sulfur K- and L-edge X-ray absorption near-edge structure spectroscopy, Geochimica et Cosmochimica Acta, 63 (1999) 3767-3779.
[34] J. Prietzel, J. Thieme, M. Salomé, H. Knicker, Sulfur K-edge XANES spectroscopy reveals differences in sulfur speciation of bulk soils, humic acid, fulvic acid, and particle size separates, Soil Biology and Biochemistry, 39 (2007) 877-890.
[35] J.A. Hurd, R. Vaidhyanathan, V. Thangadurai, C.I. Ratcliffe, I.L. Moudrakovski, G.K.H. Shimizu, Anhydrous proton conduction at 150 °C in a crystalline metal-organic framework, Nature Chemistry, 1 (2009) 705-710.
[36] J.H. Cavka, S. Jakobsen, U. Olsbye, N. Guillou, C. Lamberti, S. Bordiga, K.P. Lillerud, A new zirconium inorganic building brick forming metal organic frameworks with exceptional stability, Journal of the American Chemical Society, 130 (2008) 13850-13851.
[37] C. Volkringer, M. Meddouri, T. Loiseau, N. Guillou, J. Marrot, G. Ferey, M. Haouas, F. Taulelle, N. Audebrand, M. Latroche, The Kagome topology of the gallium and indium metal-organic framework types with a MIL-68 structure: Synthesis, XRD, solid-state NMR characterizations, and hydrogen adsorption, Inorganic Chemistry, 47 (2008) 11892-11901.
[38] M. Kim, J.F. Cahill, H. Fei, K.A. Prather, S.M. Cohen, Post-synthetic ligand and cation exchange in robust metal-organic frameworks, Journal of the American Chemical Society, 134 (2012) 18082-18088.
[39] M. Kim, J.F. Cahill, Y. Su, K.A. Prather, S.M. Cohen, Post-synthetic ligand exchange as a route to functionalization of 'inert' metal-organic frameworks, Chemical Science, 3 (2012) 126-130.
[40] Y. Liu, I.F.F. Lien, S. Ruttgaizer, P. Dove, S.D. Taylor, Synthesis and Protection of Aryl Sulfates Using the 2,2,2-Trichloroethyl Moiety, Organic Letters, 6 (2004) 209-212.
[41] S. Couck, J.F.M. Denayer, G.V. Baron, T. Rémy, J. Gascon, F. Kapteijn, An amine-functionalized MIL-53 metal-organic framework with large separation power for CO_2 and CH_4, Journal of the American Chemical Society, 131 (2009) 6326-6327.
[42] F. Millange, C. Serre, N. Guillou, G. Ferey, R.I. Walton, Structural effects of solvents on the breathing of metal-organic frameworks: An in situ diffraction study, Angewandte Chemie - International Edition, 47 (2008) 4100-4105.
[43] D. Farrusseng, C. Daniel, C. Gaudillère, U. Ravon, Y. Schuurman, C. Mirodatos, D. Dubbeldam, H. Frost, R.Q. Snurr, Heats of adsorption for seven gases in three metal-organic frameworks: Systematic comparison of experiment and simulation, Langmuir, 25 (2009) 7383-7388.
[44] P. Kusgens, M. Rose, I. Senkovska, H. Frode, A. Henschel, S. Siegle, S. Kaskel, Characterization of metal-organic frameworks by water adsorption, Microporous and Mesoporous Materials, 120 (2009) 325-330.
[45] S.P. Tung, B.J. Hwang, Synthesis and characterization of hydrated phosphor-silicate glass membrane prepared by an accelerated sol-gel process with water/rapor management, Journal of Materials Chemistry, 15 (2005) 3532-3538.
[46] K.A. Mauritz, R.B. Moore, State of understanding of Nafion, Chemical Reviews, 104 (2004) 4535-4585.
[47] P. Choi, N.H. Jalani, R. Datta, Thermodynamics and proton transport in Nafion II. Proton diffusion mechanisms and conductivity, Journal of the Electrochemical Society, 152 (2005) E123-E130.

Chapter 8

The oxamate route, a versatile post–functionalization for metal incorporation in MIL–101(Cr): Catalytic applications of Cu, Pd and Au systems

This chapter is based on the following publication:

J. Juan–Alcañiz, J. Ferrando–Soria, I. Luz, P. Serra–Crespo, E. Skupien, V.P. Santos, E. Pardo, F.X. Llabrés i Xamena, F. Kapteijn, J. Gascon (2013) submitted

Abstract A new consecutive post–functionalization method has been developed for the inclusion of additional metal functionalities in Metal Organic Frameworks (MOFs) through oxamate as chelating agent. This may result in catalytic centers of metal–organic complexes or in controlled formation of metal nanoparticles, demonstrated for Cu, Pd and Au, in the highly stable MIL–101(Cr) framework. In a first post–synthesis step, reduction of the NO_2–MIL–101(Cr) leads to the formation of NH_2–MIL–101(Cr). The second functionalization consists of a straightforward condensation of the amino groups of the ligand with ethyl chloro–oxoacetate resulting in formation of free oxamates attached to the linker. Two different copper complexes have been coordinated through the oxamate ligand, attaining loadings as high as 9 wt% and showing similar performance as the best reported copper MOFs (HKUST–1, [Cu(2–pymo)$_2$] and [Cu(im)$_2$]) in "click chemistry" catalysis (1,3–dipolar cycloaddition reactions) and multicomponent coupling reactions (propargylamine formation). Highly dispersed palladium and gold nano–particles can be incorporated and stabilized in the MOF. The resultant Pd–catalysts are very active and selective in Suzuki–Miyaura condensation, although palladium leaching is observed. After reduction of the Au–catalysts, immobilized gold nanoparticles are formed, that maintain a good performance in benzyl alcohol oxidation to benzaldehyde for at least 4 consecutive runs. No side reactions (further oxidation and esterification) are observed, attributed to the absence of any cationic gold species. TEM studies and DRIFTS analysis during CO adsorption show the very uniform size, ~2 nm, and metallic character of these gold particles encapsulated in the MIL–101 cages.

8.1. INTRODUCTION

Along with perspective MOF applications, several authors have highlighted possible limitations of this new class of materials, both with respect to framework stability, and with the possibilities for incorporating very reactive moieties in the MOF scaffold. The latter is especially important in the case of metal catalysis, since the coordination sphere of the inorganic component is in most cases almost or fully occupied. First studies into the development of functional MOFs focused on grafting organic molecules onto coordinatively unsaturated sites (CUS) of the structural metals [1, 2] and on the use of organic ligands bearing different functionalities. [3] The first example of a MOF with reactive organic ligands was reported in 2000 by Seo *et al.* [4] After that, extensive work was devoted to the less stable IRMOF series bearing different functionalized organic ligands. [5, 6] Stability issues were solved by combining late transition metals and functional benzene 1,4–dicarboxylates (X–bdc; X= $–NO_2$, $–NH_2$, –Br, $–OCH_3$, $–CH_3$, –F, –Cl). [7-9] The use of several Functional Organic Sites (FOS) within a single MOF crystal by approaches like mix–linker or post–synthetic exchange has also attracted a lot of interest during the last few years. [2, 10-15] More complex pre–functionalized linkers, like homochiral ligands for asymmetric catalysis and enantioselective separation, [16, 17] or metallo–ligands enabling immobilization of a wide variety of active open metal sites have also been explored by several research groups. [18-20] Protective groups have been used to avoid coordination of additional functionalities and to allow the direct synthesis of MOFs with functional groups that can be easily activated. [21] Progress in the direct synthesis of functional MOFs has been highlighted in a number of high quality reviews. [22-25]

In spite of the rich MOF chemistry, the main drawbacks associated to the direct scaffold functionalization are: (*i*) functional ligands must be stable under MOF synthesis conditions (*ii*) the ligand must be soluble under synthesis conditions and (*iii*) coordination to the metal ions by the functional ligand has to be avoided. In order to address these limitations, different post–synthetic modifications (PSM) have been developed to allow the preparation of highly functional MOF structures regardless of the synthesis method. [26-30]

When it comes to the application of PSM in the field of catalysis, one of the most interesting catalytic examples is the generation of additional reactive metal sites by post–synthetic incorporation of chelating agents. In 2008, Rosseinsky and co–workers reported the formation of Schiff base groups appended to the MOF ligands *via* condensation of salicylaldehyde and the amine groups of IRMOF–3. NMR spectroscopy studies suggested about 13% amine modification, and the formed chelating group was used to incorporate $VO(acac)_2.H_2O$. The resulting catalyst showed activity in the oxidation of cyclohexene using *t*–BuOOH along with framework degradation under reaction conditions. [31]

Similar strategy was followed by Corma *et al.*, where Au(III) (2 wt%) was anchored to a similarly modified IRMOF–3 and tested in domino coupling and cyclization to indoles. [6] More recently, Bhattacharjee *et al.* described the immobilization of a manganese(II) acetylacetonate complex by PSM of the amine linker in IRMOF–3. [32] The $Mn(acac)_2$ Schiff base complex attached to the organic ligand of the MOF was active in the epoxidation of different alkenes using molecular oxygen. Although these works highlight the potential of PSM for metal incorporation, the use of more stable MOF structures will facilitate the development of post–functionalization protocols that require harsher conditions (*i.e.*, the use of high concentrated acids or bases). One of the current challenges is the development of stable MOFs bearing functional organic sites that could be used for PSM. To date, most of the examples existing in the literature on PSM have been performed on MOFs with a limited stability. One of the most stable MOF structures, which also provides nanometer size pores and high surface areas useful for catalysis, [33] is MIL–101. Iron [34, 35], aluminium [36, 37] and vanadium [38] based NH_2–MIL–101 have been directly synthesized by reacting the corresponding metals with NH_2–bdc, but until very recent there was no procedure for its analogous, more stable, chromium form. [39] Chen and co–workers reported the synthesis of this material from a hydroxide–assisted hydrothermal synthesis, [40] whereas Jiang *et al.* [41] described the direct hydrothermal synthesis from a very specific metal–ligand ratio. At the same time, Stock and co–workers have developed another route towards NH_2–MIL–101(Cr) via the reduction of NO_2–MIL–101(Cr). Main advantages of the latter method are higher surface areas and better crystallinity. [42]

In this work, we report a novel PSM route to form an oxamate chelating agent, opening the door to the immobilization of active metal ion sites and to the stabilization of small metal nanoparticles, as demonstrated for Cu, Pd and Au, in the highly stable MIL–101(Cr) framework. In a first step, Stock's approach is used to produce high quality NH_2–MIL–101(Cr). After production of the amine containing framework, a second post–functionalization step is applied consisting of a nucleophilic substitution of primary amines with acyl chloride (ethyl chloro–oxoacetate) to form amides (oxamates) attached to the framework ligands as chelating agents. The experimental results demonstrate that the high stability of MIL–101(Cr) allows PSMs with conversions approaching 100%. The resulting catalysts have been demonstrated for several reactions: click chemistry, carbon–carbon forming *via* Suzuki–Miyaura, and the selective oxidation of benzyl alcohol.

8.2. EXPERIMENTAL

All the chemicals were obtained from Sigma–Aldrich and used without further purification. AUROlite^{TM} (1 wt% Au/Al_2O_3) was obtained from STREM Chemicals.

8.2.1. Oxamate formation in MIL–101(Cr)

Hydrothermal synthesis of NO_2–MIL–101(Cr): 1.63 g (4.1 mmol) of chromium (III) nitrate nonahydrate ($Cr(NO_3)_3.9H_2O$, 99%), 0.89 g (4.2 mmol) 2–nitroterephthalic acid (NO_2–C_6H_3–1,4–$(CO_2H)_2$, 99%) and 0.16 g (4 mmol) of hydrofluoric acid (HF, 47–51 %) were placed in a 40 mL teflon vessel with 20 g of distilled water. The Teflon vessel was inserted into a stainless steel autoclave and heated up at a rate of 20 K min^{-1} in an oven under static conditions to 493 K, keeping it for 8 h, followed by cooling to room temperature. The green product (*ca.* 350 mg) was filtered off, activated by washing in boiling ethanol during 24 h, and finally dried overnight at 343 K under ambient conditions.

Chemical Reduction of NO_2–MIL–101(Cr) to NH_2–MIL–101(Cr): the procedure of chemical reduction used was taken from the stated reference. [42] Slightly longer times (16 h) were used to ensure complete reduction when scaled up (2 g per batch).

Post–synthetic modification of NH_2–MI–-101(Cr) to PMA–MIL–101(Cr): 1 g (3.9 mmol NH_2) of dried NH_2–MIL–101(Cr) were dispersed in 20 mL of tetrahydrofuran (THF anhydrous, containing 250 ppm BHT as inhibitor, ≥99.9%). Then, 875 µl of ethyl chloro–oxoacetate ($ClCOCOOCH_2CH_3$, 98%) was added, and the solution was heated at 343 K during different times, with a maximum of 2 days. The product was filtered and washed in a Soxhlet extraction system with THF for 16 h, and finally dried at 433 K overnight. The material is named PMA, from phenylene–mono(oxamate).

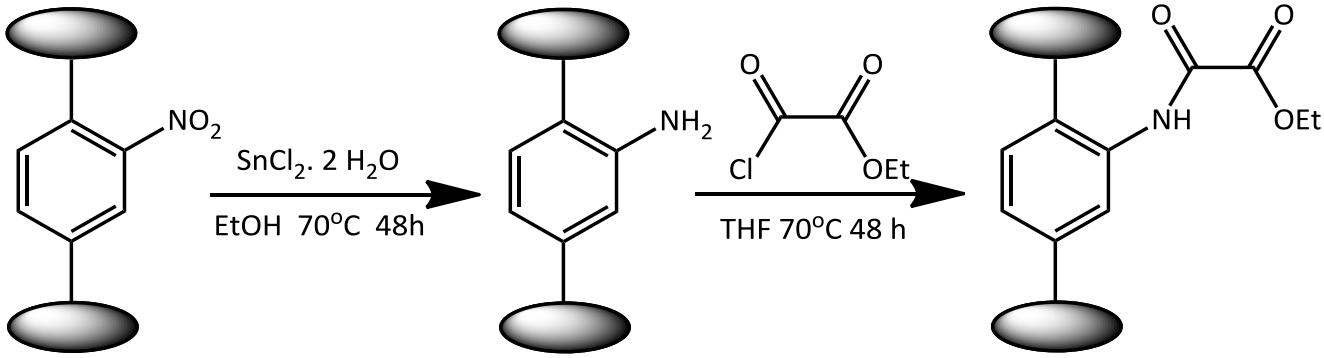

Scheme 8 - 1 Post–functionalization procedures: (a) Reduction of –NO_2 to –NH_2 and (b) transformation of –NH_2 to an oxamate group.

8.2.2. Metal incorporation

Copper complex incorporation: 1 g (2.8 mmol PMA) of PMA–MIL–101(Cr) was dispersed in 80 mL of deionized water and 780 µl (5.6mmol) of triethylamine (NEt_3, 99%) was added to hydrolyze the ester. Two different copper solutions were prepared separately: (A–*[Cu/PMA–MIL–101(Cr)]*) 650 mg (2.8 mmol) of copper (II) nitrate ($Cu(NO_3)_2 \cdot 2.5H_2O$, 98%) in 20 mL of deionized water turning out to colorful blue, and (B–*[CuEDA/PMA–MIL–101(Cr)]*) previous solution with 170 mg (2.8 mmol) of

ethylenediamine (EDA, 99%) added, becoming colorful purple. The different copper solutions were added drop–wise to the MOF dispersion and stirred for 24 h at room temperature. The samples were filtered and washed thoroughly with water, and finally dried at 433 K overnight.

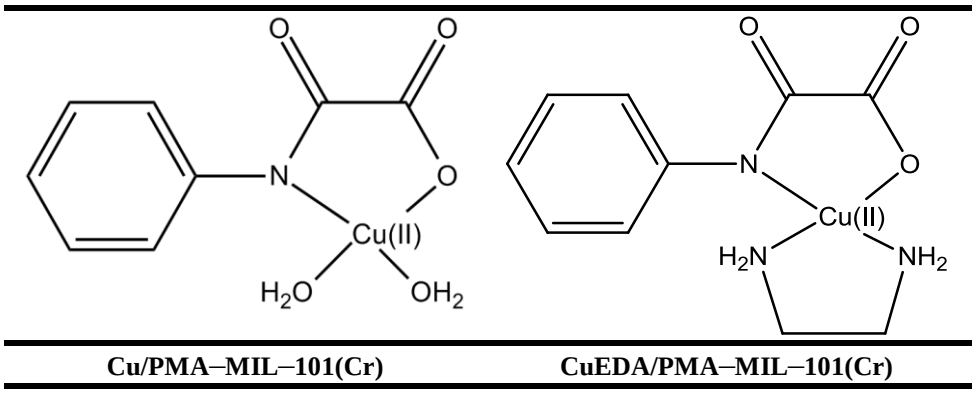

Cu/PMA–MIL–101(Cr) **CuEDA/PMA–MIL–101(Cr)**

Scheme 8 - 2 Copper complex attached to the oxamate group of the MIL–101(Cr) ligand.

Palladium incorporation [Pd/PMA–MIL–101(Cr)]: 1 g (2.8 mmol PMA) of PMA–MIL–101(Cr) was suspended in 25 mL of acetonitrile (ACN, anhydrous 99.8%), and 780 μl (5.6mmol) of triethylamine (NEt_3, 99%) was added. On the other hand, a solution of 492 mg (1.4 mmol) of palladium chloride ($PdCl_2$ powder, 99%) in 50 mL acetonitrile was prepared under heating (333 K) until full dissolution, and then added to the MOF dispersion. Finally, the mixture was stirred at 343 K for 5 h. The brownish solid was filtered off and washed with THF in a Soxhlet extraction during 12 h, and finally dried at 373 K overnight.

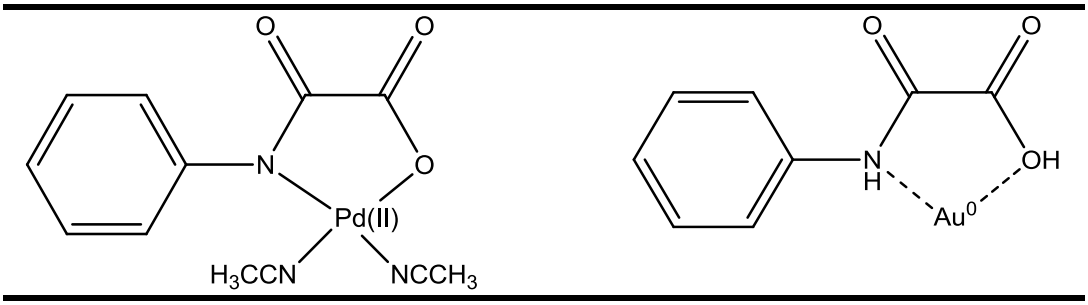

Pd/PMA–MIL–101(Cr) **Au/PMA–MIL–101(Cr)**

Scheme 8 - 3 Palladium complex and representation of gold nanoparticles attached or interacting with the oxamate group of the MIL–101(Cr) ligand, respectively.

Gold incorporation in PMA or NH_2–MIL–101(Cr): 1 g (2.8 mmol PMA or 3.9 mmol NH_2) of PMA or NH_2–MIL–101(Cr) was suspended in 25 mL of acetonitrile (ACN, anhydrous 99.8%). Then 0.15 mmol of potassium gold (III) chloride ($KAuCl_4$ powder, 98%) per mmol of functional site (PMA or NH_2) was dissolved in 15 mL of acetonitrile and added drop–wise, and stirred for 5 h at room temperature. Finally, 780 μl (5.6 mmol) of triethylamine (NEt_3, 99%) was incorporated in the solution and stirred for 30 min at room temperature.

8.2.3. Characterization techniques

(a) Transmission Electron Microscopy (TEM): was carried out using a FEI Technai TF20 electron microscope with a field emission gun as the source of electrons operated at 200 kV. Samples were mounted on a Quantifoil® carbon polymer supported on a copper grid by placing a few droplets of a suspension of the ground sample in ethanol on the grid, followed by drying at ambient conditions. Energy Dispersive X–ray Spectroscopy (EDS) was performed using an Oxford Instruments system. *(b) Nitrogen adsorption at 77 K:* was measured in a Quantachrome Autosorb–6B unit gas adsorption analyzer. The samples were pre–treated under vacuum for 16 h at 473 K. *(c) Powder X–Ray Diffraction (PXRD):* was analyzed using Bruker–AXS D5005 with CoKα radiation. *(d) Inductively Coupled Plasma Optical Emission Spectroscopy (ICP–OES):* carried out with an ICP–OES Perkin Elmer Optima 3000dv, after digesting in duplo in a mixture of 1 mL HF and 4 mL Aqua Regia, under microwave irradiation and diluted 50 mL with MQ water. *(e) Diffuse Reflectance Infrared Fourier Transform Spectroscopy (DRIFTS):* recorded on a Nicolet model 8700 spectrometer, equipped with a high–temperature DRIFTS cell, DTGS–TEC detector and a 633 nm laser. The spectra were recorded from 4000 to 600 cm^{-1} with 256 scans and a resolution of 4 cm^{-1} under a helium flow of 20 mL min^{-1}. The samples were pre–treated under the same helium flow at 473 K for 60 min. KBr was used to perform background experiments. *(f) Infrared Spectroscopy of adsorbed CO:* spectra were recorded at room temperature on a Nicolet model 8700 spectrometer equipped with a high–temperature DRIFTS cell, and a MCT/A detector with a spectral resolution of 4 cm^{-1}. Prior to CO adsorption, the sample was pre–treated *in situ* in helium at 373 K for 1 h, and then cooled to room temperature. An initial infrared spectrum was recorded and was used as background for further spectra. 5% CO in helium was introduced in the cell for 30 minutes at room temperature. Subsequently, the system was flushed with helium at same temperature, to remove physisorbed CO. Spectra of adsorbed CO were recorded at room temperature 323 and 373 K. Each reported spectrum is an average of 128 scans. *(g) UV–Vis Spectroscopy:* spectra were measured with a Perkin–Elmer Lambda 900 spectrophotometer equipped with an integrating sphere ("Labsphere") in the 200–800 nm range. The Kubelka–Munk function was used to convert reflectance measurements into equivalent absorption spectra using the reflectance of $BaSO_4$ as reference. *(h) X–Ray Photoelectron Spectroscopy (XPS):* measurements were made using a VG–Microtech Multilab equipment, a MgKα (1253.6 eV) radiation and a pass energy of 50 eV. The XPS system analysis pressure was kept at 5×10^{-10} mbar. The binding energy (*BE*) and the kinetic energy (*KE*) scales were adjusted by setting the C*1s* transition to 284.6 eV. *BE* and *KE* values were determined with the peak–fit software of the spectrometer. The intensities were estimated by calculating the integral of each peak fitting the experimental curve to a combination of Lorentzian

(30%) and Gaussian (70%) shaped peaks, and after S–shape background subtraction and corrections for differences in escape depth and photoionization cross sections. Surface atomic ratios were estimated from the integrated intensities corrected by the atomic sensitivity factors. [43] *(i) Nuclear Magnetic Resonance spectroscopy (NMR):* solution spectra were recorded after decomposition of the MIL–101(Cr) materials using a basic solution (NaOH 2M). After removing precipitated $Cr(OH)_3$ by filtering, the terephthalic acid and its derivatives can be precipitated under acidic conditions. After centrifugation and washing with acetone, the yellowish precipitate is dissolved using concentrated deuterated sodium hydroxide solution.

8.2.4. Catalytic performance testing

Turn–over frequency is calculated according to the following equation, where active site refers to the total number of moles metal determined by ICP, and the amount of converted reactant is obtained from the GC analysis:

$$Turnover\ frequency(TOF) = \frac{[mol\ reactant\ converted]}{[mol\ active\ site].[unit\ time]} \quad (1)$$

When nanoparticles are the active sites:

$$[mol\ active\ site] = \frac{m_{cat}.{wt\%M}/_{100}.D_M}{M} \quad (2)$$

$$D_M = \frac{6 \cdot n_S \cdot M}{\rho \cdot N \cdot d_p} \quad (3)$$

Table 8 - 1 Parameters for the quantification of active sites based on nanoparticles.

	Parameter	***Units***	***Palladium***	***Gold***
m_{cat}	Catalyst mass	mg	80	700
wt % M	Weight percent of metal	%	6	1.5
n_s	Number or atoms per surface	m^{-2}	1.27 E19	1.15 E19
M	Molecular mass	g mol^{-1}	106.4	196.97
ρ	Density	g cm^3	12.02	19.30
d_p	Mean particle size diameter	nm	~2	~2.5
N	Avogadro's number	mol^{-1}	6.022 E23	
D_M	Dispersion	—	0.555	0.468

1,3–dipolar cycloaddition of benzyl azide to phenylactetylene: Copper–MOFs (0.1 mmol Cu or 10 mol% with respect to phenylacetylene) was dispersed in ethanol (6 mL) and heated up to 343 K. Benzyl azide (2 mmol) was added to this mixture with a syringe. After 10 min, phenylacetylene (1 mmol) was also added to the reaction mixture. Samples were taken at different reaction times and

analyzed by GC using *n*–dodecane as external standard. Reusability of the catalysts was performed after filtration and drying.

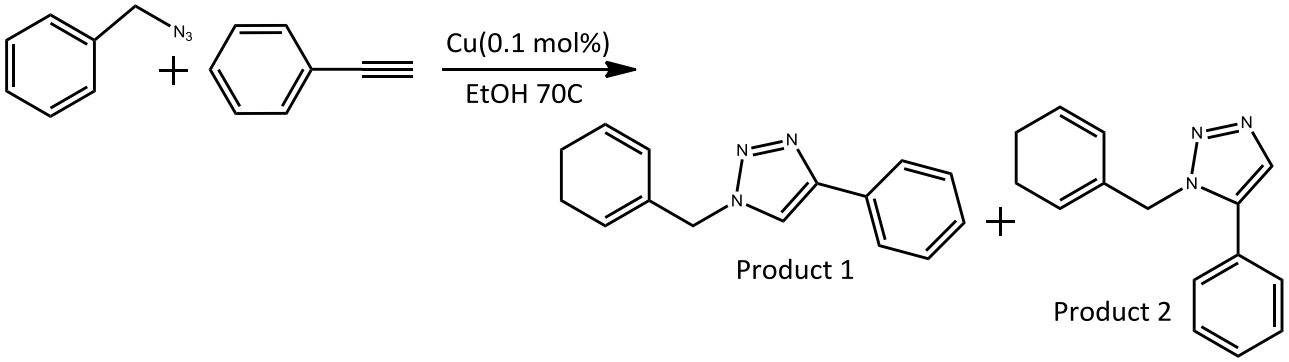

Scheme 8 - 4 1,3–dipolar cycloaddition of benzyl azide to phenylacetylene.

Formation of propargylamines by one–pot three–component coupling reactions: Paraformaldehyde (1.2 mmol) and the copper–catalyst (1 mol% Cu, 0.01 mmol Cu) were dispersed in 1 mL of dioxane as solvent. Then piperidine (1.1 mmol) and phenylacetylene (1 mmol) were added to the solution and heated to 313 K. Sample aliquots were taken during the course of the reaction and analyzed by GC using *n*–dodecane as external standard.

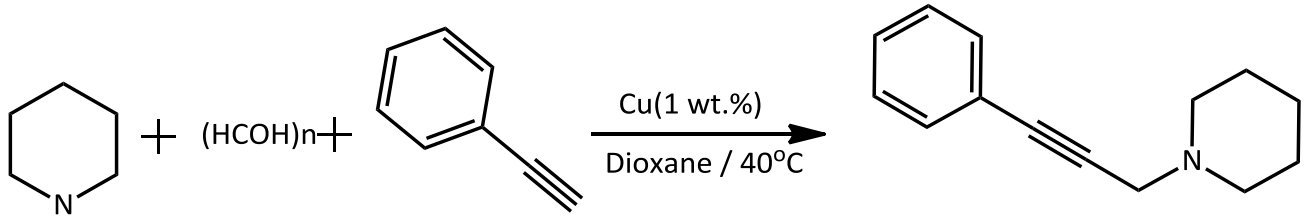

Scheme 8 - 5 Formation of propargylamines by a one–pot three–component coupling reaction.

Suzuki–Miyaura cross coupling between bromobenzene and phenylboronic acid: 1.5 g (11 mmol) of K_2CO_3 (ACS reagent, 99.0%), and *ca.* 80 mg Pd/MOF catalyst was dispersed in 4 mL N,N–dimethylformamide (DMF, anhydrous 99.8%), 670 mg (5.5 mmol) of phenylboronic acid ($PhB(OH)_2$, 95%) were added to the previous mixture and heated at 403 K. After the given temperature is reached, 550 mg (3.5 mmol) of bromobenzene (BB, 99%) are introduced in the reactor with a syringe. Reaction samples were analyzed by GC, using *n*–dodecane as external standard.

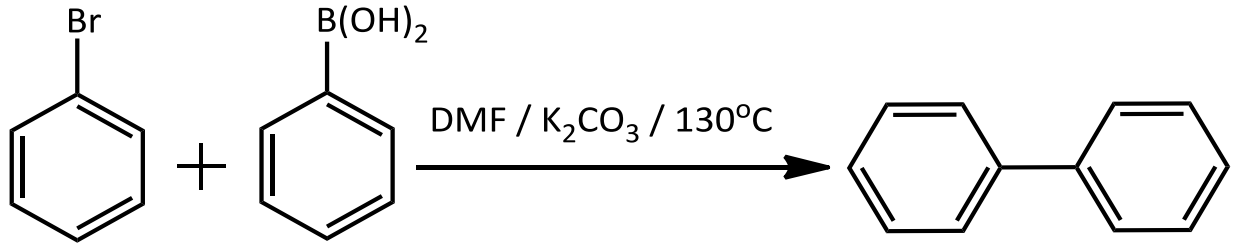

Scheme 8 - 6 Suzuki–Miyaura cross coupling between bromobenzene and phenylboronic acid.

Selective oxidation of benzyl alcohol to benzaldehyde and benzoic acid: 3 g (22 mmol) of K_2CO_3 (ACS reagent, 99.0%), 80 mL toluene (anhydrous, 99,8%) and the catalyst were introduced in a round bottom flask reactor with refrigerated condenser at 253 K. The reaction mixture was heated to 353 K and bubbled with 200 mL min^{-1} air flow. When the reaction temperature was reached, 2.4 g (22 mmol) of benzyl alcohol (ACS reagent, 99.0%) was added, constituting the start of the reaction. The reaction was followed by periodically sampling and GC analysis, with tetradecane as external standard.

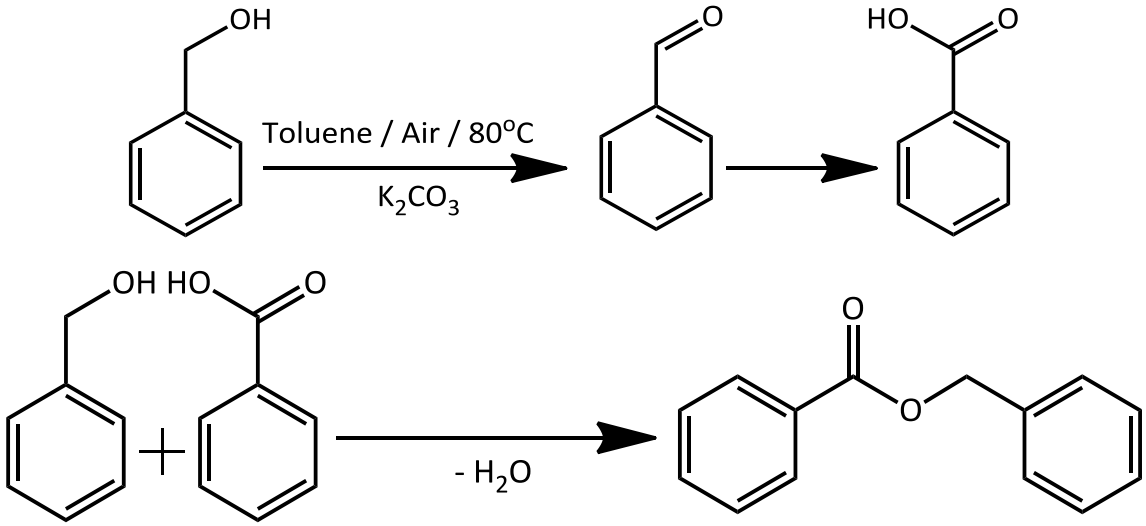

Scheme 8 - 7 (*Top*) Selective oxidation of benzyl alcohol to benzaldehyde and benzoic acid. (*Bottom*) Side reaction during the selective oxidation of benzyl alcohol to benzaldehyde, consisting on the esterification of benzyl alcohol and benzoic acid to form benzyl benzoate.

8.3. RESULTS

8.3.1. Synthesis and reduction of NO_2–MIL–101(Cr)

The pre–functionalized linker NO_2–H_2bdc (2–nitroterephthalic acid) was directly used in the hydrothermal synthesis of NO_2–MIL–101(Cr) under the same reaction conditions as reported by Férey *et al.* [39] for the synthesis of pristine MIL–101(Cr) (see section *8.2.1. catalyst preparation*).

Crystallinity is in agreement with the simulated pattern (Fig. 8–1). The nitrogen uptake at 77 K (Fig. 8–1) after ethanol activation is higher than previously reported data, [42] but still lower than the pristine MIL–101, attributed to the presence of bulky –NO_2 groups. The procedure to reduce –NO_2 to –NH_2 groups has been performed as described by Bernt *et al.* [42] Framework is stable after the complete reduction procedure with $SnCl_2.2H_2O$ for 24 h and washing with HCl (37 wt% in H_2O), ICP–OES did not show rests of Sn. Nitrogen uptake (Fig. 8–1) increases after reduction, in agreement with a decrease in the atomic diameter from oxygen to hydrogen and its lower atomic mass. [42]

Vibrational characteristics of both systems and specific changes after reduction have been analyzed by infrared spectroscopy (Fig. 8–2). In the high wavenumber region of the spectra, clear symmetric and asymmetric stretching vibrations specific for the –NH_2 groups are present, centered at 3520 and 3370

cm^{-1}, respectively. Differences are also observed in the O–H stretching region at slightly higher wavenumbers.

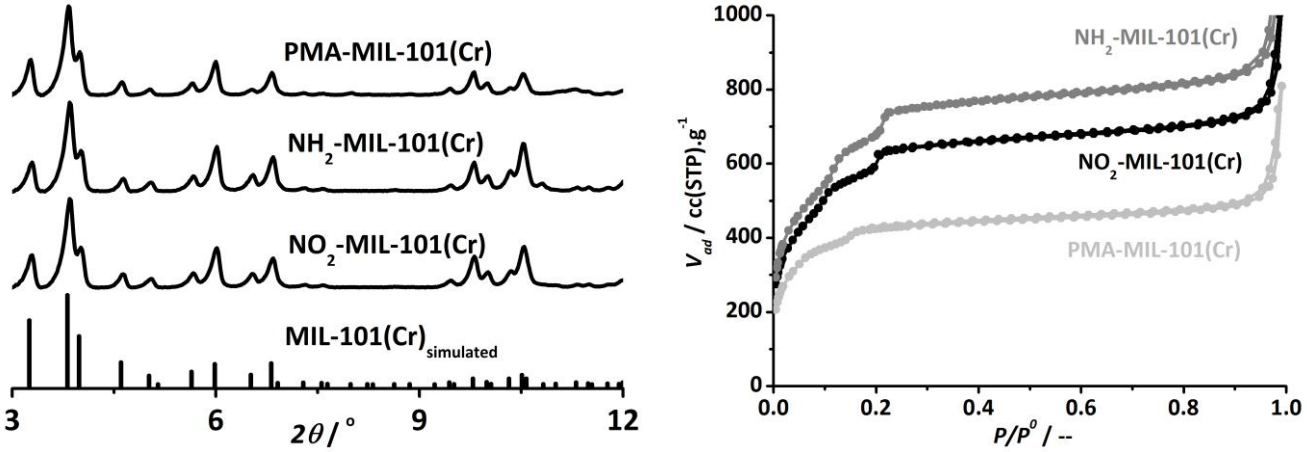

Figure 8 - 1 (*Left*) CoKα X–ray diffraction patterns of NO_2–MIL–101(Cr) throughout cascade post–functionalization (NH_2 and PMA) compared with the simulated MIL–101(Cr) pattern. (*Right*) Nitrogen adsorption isotherm at 77 K of (black) NO_2–, (grey) NH_2– and (light grey) PMA– versions of MIL–101(Cr), after pre–treatment at 423 K in vacuum for 16 h.

For the nitro sample a broad band is observed from 3600 to 3300 cm^{-1}, which is typical for OH groups of residual adsorbed water. Nevertheless it also stretches up to 3700 cm^{-1}, suggesting strong interactions between OH and $–NO_2$ groups.

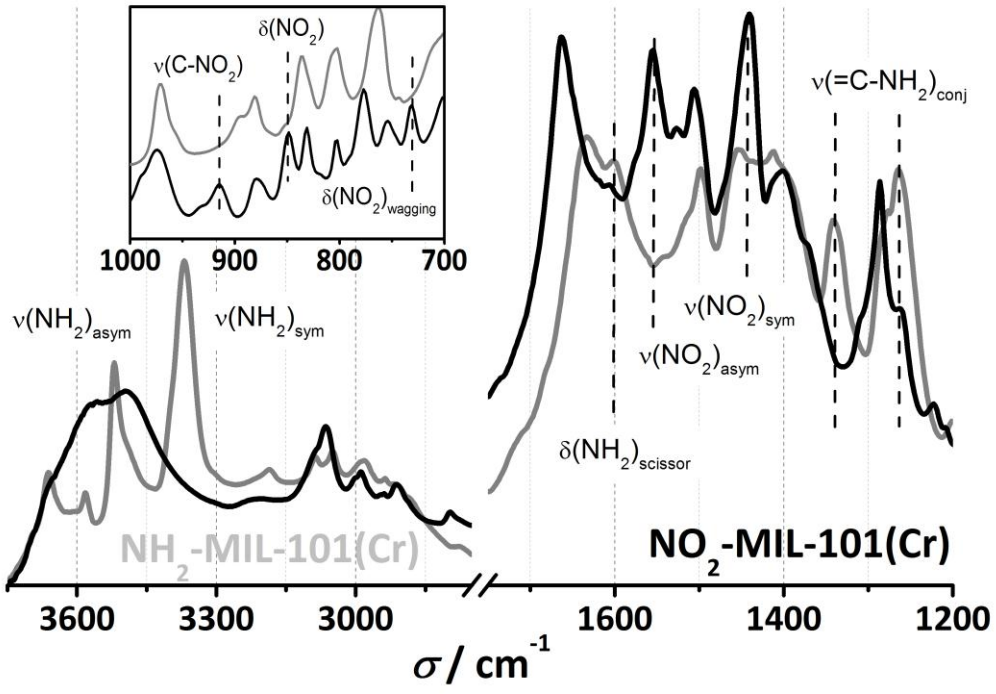

Figure 8 - 2 DRIFTS of (black) NO_2–and (grey) NH_2–MI–101(Cr) samples. The samples were pre–treated *in situ* at 473 K for 1 h in helium flow of 20 mL min^{-1}.

After sample reduction, the broad band has decreased, pointing to a reduced hydrophilicity upon reduction, while two defined bands become visible at 3660 and 3580 cm^{-1}. The main two ν(OH)

vibrations correspond to Cr–OH groups of the supertetrahedra, being the first band associated to Cr–OH and the second to water molecules interacting with these sites: Cr–OH···H_2O. [44, 45]

In the low wavenumber region of the spectra, symmetric and asymmetric stretching vibrations of –NO_2 are observed at 1440 cm^{-1} and 1555 cm^{-1}, respectively, which disappear after reduction. Weaker vibrational deformations have also been assigned to –NO_2, *i.e.*, the band at 850 cm^{-1} or the wagging at 730 cm^{-1}, which also vanished after reduction. The C–N stretching with vibration is very difficult to assign since it has a broad range of appearance, but it could be associated to the band at 915 cm^{-1}.

After reduction, a very characteristic vibrational deformation (scissoring) of the amino groups appears at 1600 cm^{-1}. For aromatic amines ν(=C–N), two bands are also observed at 1340 and 1260 cm^{-1} due to conjugation of the electron pair of the nitrogen with the ring, imparting double–bond character to the C–N bond. [46] Taken together, all the observed differences between both samples points towards the complete reduction of the nitro to the amino groups. These results are in agreement with ^{1}H NMR studies of the linkers after MOFs digestion and previous results by Bernt *et al.* [42]

8.3.2. Oxamate post–functionalization

The second post–functionalization step consists of amine transformation into an oxamate by reacting NH_2–MIL–101(Cr) with ethyl chloro–oxoacetate for 48 h, followed by thorough cleaning *via* Soxhlet extraction with THF. After oxamate post–functionalization, nitrogen uptake is reduced, since bulky molecules are incorporated into the pores (Fig. 8–1), while no changes are observed in terms of framework crystallinity (Fig. 8–1).

This second post–functionalization step was also examined by infrared spectroscopy, which allowed determining the optimum time (16, 24 or 48 h) necessary for complete transformation (Fig. 8–3).

In the ν(OH) region, the band at 3680 cm^{-1} associated with ν(Cr–OH) decreases and is partially covered by the presence of strongly adsorbed water, overlapping the asymmetric ν(NH_2) bands that become difficult to analyze. Nevertheless, one can follow the evolution of symmetric ν(NH_2) band with reaction time (48 h of reaction), while shorter reaction times confirm that the band is still present though with low intensity. New vibrations appear at 3490 and 3300 cm^{-1}, which can be correlated with ν(N–H) of an aromatic secondary amine, present in the formed oxamate. In addition, higher intensities of the ν(CH_3) bands at 2910 and 2990 cm^{-1} symmetric and asymmetric respectively, and ν(CH_2) at 2880 and 2945 cm^{-1}, symmetric and asymmetric respectively, can be observed. At the low wavenumber region, strong differences confirm the very high degree of transformation. The most intense vibrational band is present at 1720 cm^{-1} associated with the C=O stretching, while vibrational bands also arise between 1520 to 1590 cm^{-1}. Other specific vibrations appear in the fingerprint region of the spectra characteristic of ketones or esters, as highlighted in Fig. 8–3.

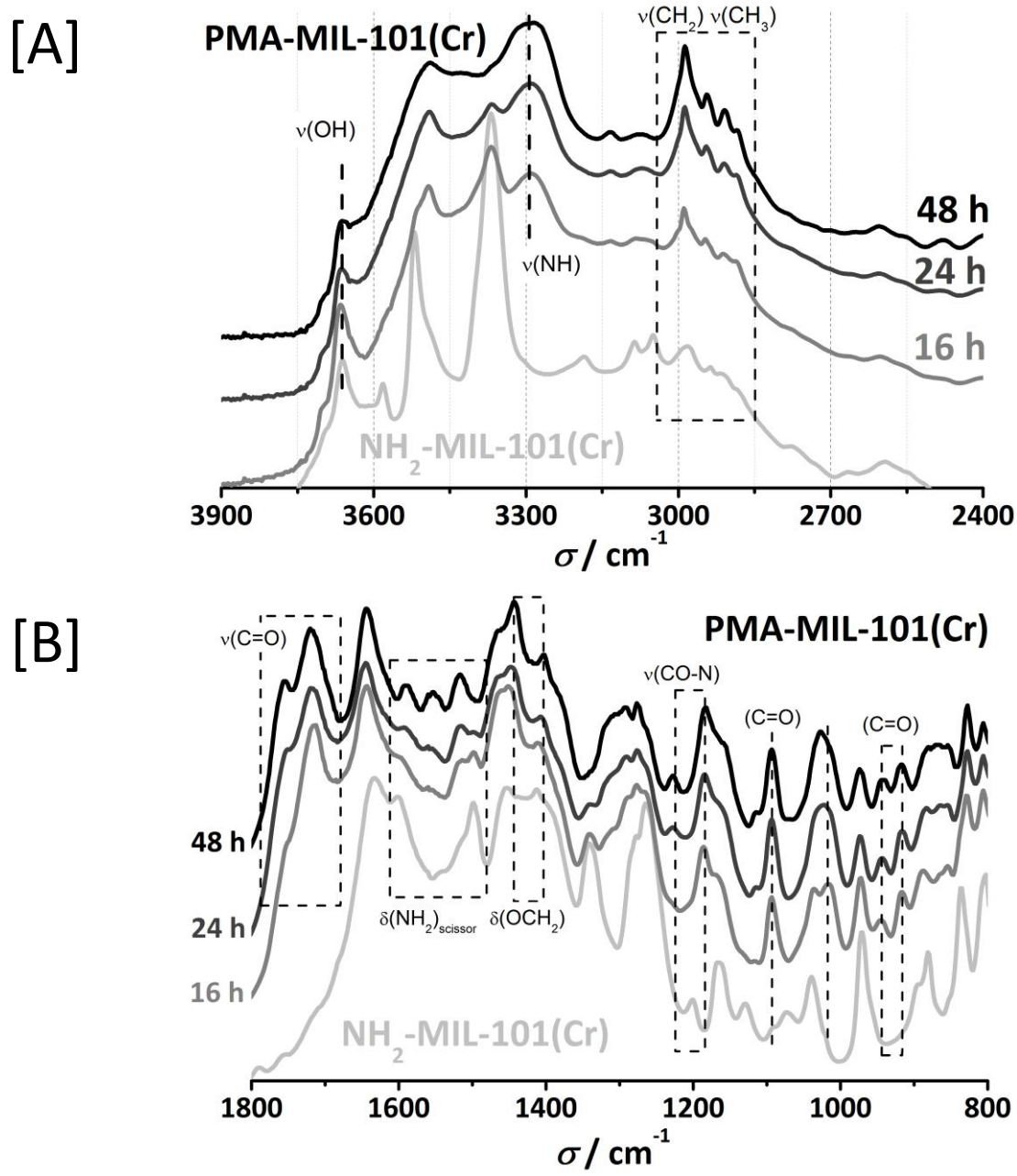

Figure 8 - 3 DRIFTS of (light grey) NH_2- to (black) PMA-MIL-101(Cr) transformation at different times of post-functionalization. The samples were pre-treated in situ at 473 K for 1 h under helium from of 20 mL min^{-1}: [A] high wavenumber region, from 3900 to 2400 cm^{-1}. [B] low wavenumber region, from 1800 to 800 cm^{-1}.

8.3.3. Cu incorporation

Once the covalent bonding of the chelating agent to the organic linker was confirmed, copper incorporation was performed using two different precursors: copper nitrate [*Cu/PMA–MIL–101(Cr)*], and copper–ethylenediamine [*CuEDA/PMA–MIL–101(Cr)*].

ICP–OES analysis confirms the incorporation of circa 9 wt% copper in both cases, while XPS indicates the presence of cationic copper (figure 8–4): the presence of the shake–up peaks indicate the presence of Cu^{2+}. [47]

The broad major Cu $2p_{3/2}$ peak, which can be deconvoluted into two components at 935.5 and 933.3 eV, corresponds excellently with oxamate complexed Cu^{2+} for the former binding energy, [48] while the latter can be attributed to reduction damage by the X–ray beam. [49] In contrast, when NH_2–MIL–101(Cr) was used as support under similar synthetic conditions, no incorporation of Cu could be observed after thorough sample washing.

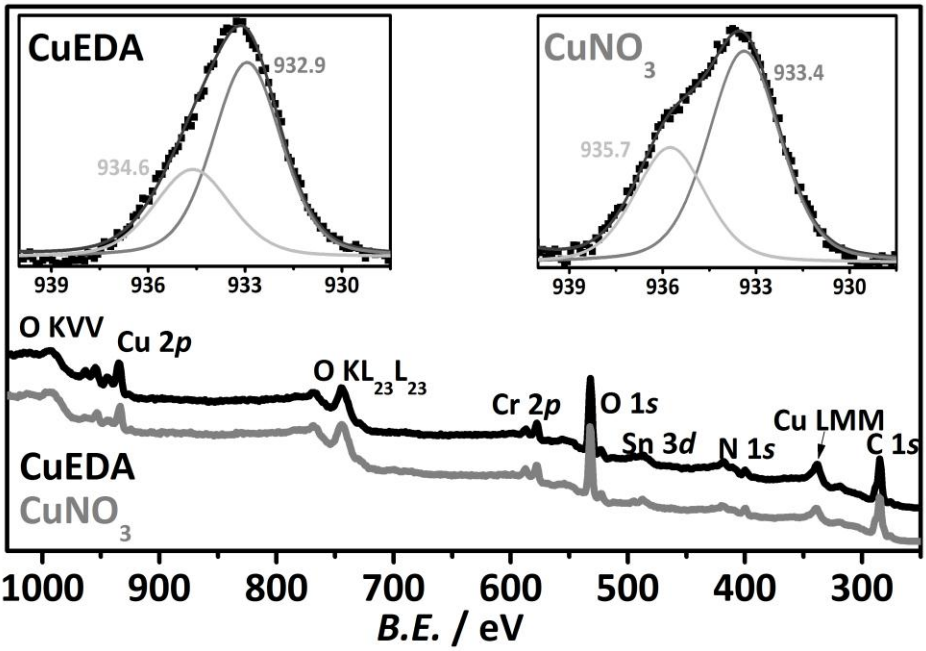

Figure 8 - 4 XPS survey and Cu 2*p* core level spectra of Cu complexes incorporated in PMA-MIL-101(Cr) sample (grey: $CuNO_3$, black CuEDA).

Powder XRD spectra do not show specific differences after copper incorporation, confirming the good stability of the framework (Fig. 8–5), but slightly lower diffraction intensities are observed when using ethylene diamine.

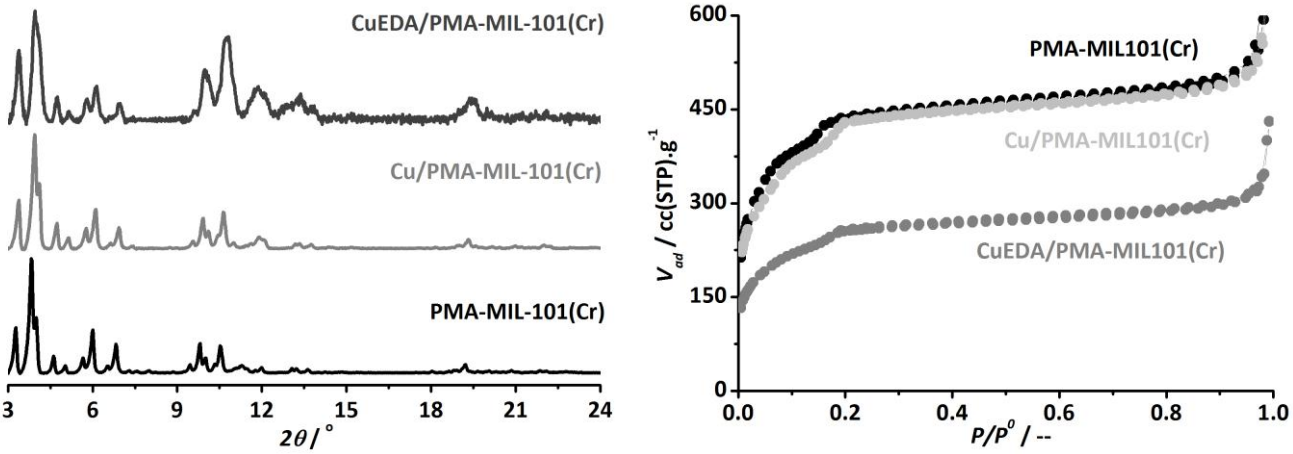

Figure 8 - 5 (*Left*) CoKα X–ray diffraction pattern of PMA–MIL–101(Cr) and both copper coordination complexes (Cu and CuEDA/PMA–MIL–101(Cr)). (*Right*) Nitrogen adsorption isotherms at 77 K for (*black*) PMA–MIL–101(Cr) and both copper coordination complexes: (*light grey*) Cu and (*grey*) CuEDA/PMA–MIL–101(Cr)).

On the other hand, clear differences between both Cu samples are found in the textural properties (Fig. 8–5). While nitrogen uptake barely changes when using copper nitrate, a decrease is observed when using the ethylenediamine–copper complex.

Figure 8–6 shows the infrared spectra of the CuEDA/PMA–MIL–101(Cr) catalyst compared with the initial PMA and NH_2 counterparts. Primary amine vibrations arise again due to the presence of ethylene diamine in the complex. However, significant differences are observed at the stretching modes of secondary PMA amine of PMA MIL–101. ν(NH) centered at 3285 cm^{-1} is reduced suggesting that part of the secondary amines are dehydrogenated to accommodate the Cu complex (Scheme 8–2). Vibrational bands characteristic of $\nu(CH_3)$ completely disappear after copper incorporation, suggesting successful hydrolysis of the ester, which is required for the copper coordination. In addition, $\nu(CH_2)$ bands at 2955 and 2895 cm^{-1} are associated with the ethylenediamine.

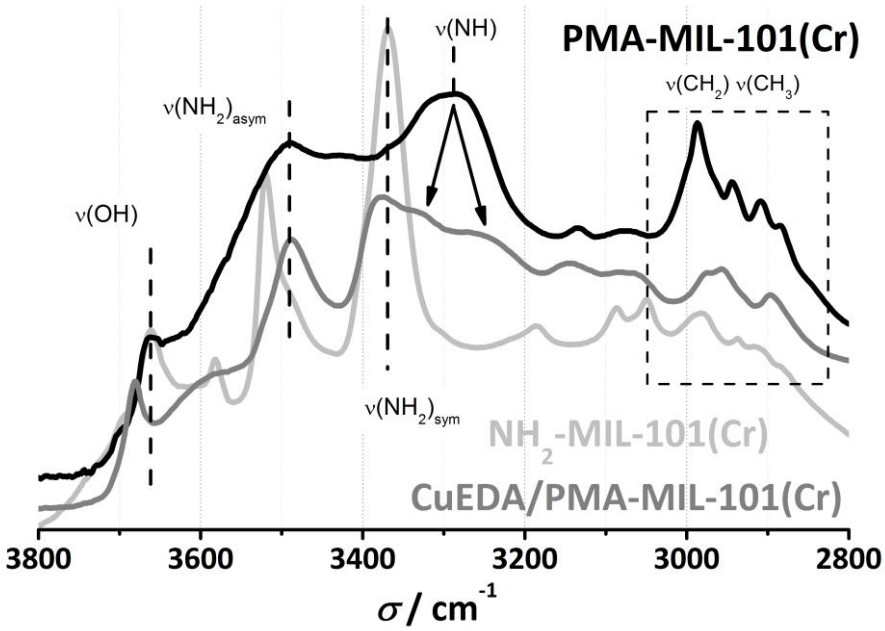

Figure 8 - 6 DRIFTS comparison of (light grey) NH_2–MIL–101(Cr), (black) PMA–MIL–101(Cr) and (grey) CuEDA/PMA–MIL–101(Cr) samples. The samples were pre–treated *in situ* at 473 K for 1 h in a helium flow of 20 mL min^{-1}.

The catalytic performance of both complexes has been tested for two typical copper catalyzed reactions: (*a*) 1,3–dipolar cycloaddition of alkynes and azides for the preparation of 1,2,3–triazole derivatives, and (*b*) the formation of propargylamines by one–pot three–component coupling reaction.

The catalytic performance of the different copper containing MOFs in the 1,3–dipolar cycloaddition is shown in Fig. 8–7. Both catalysts yield 100% conversion of phenylacetylene after 4 h, both in ethanol and toluene as solvents (as confirmed by isolated products), kinetic profiles are different (only studied using ethanol as solvent). When copper nitrate is used as precursor, a significant deactivation is observed during the first three uses, probably due to leaching of weakly bound Cu. However, after the

third catalytic cycle activity remains constant. In the case of ethylenediamine copper complex, only a minor deactivation is observed and stable catalytic performance is achieved after the second use.

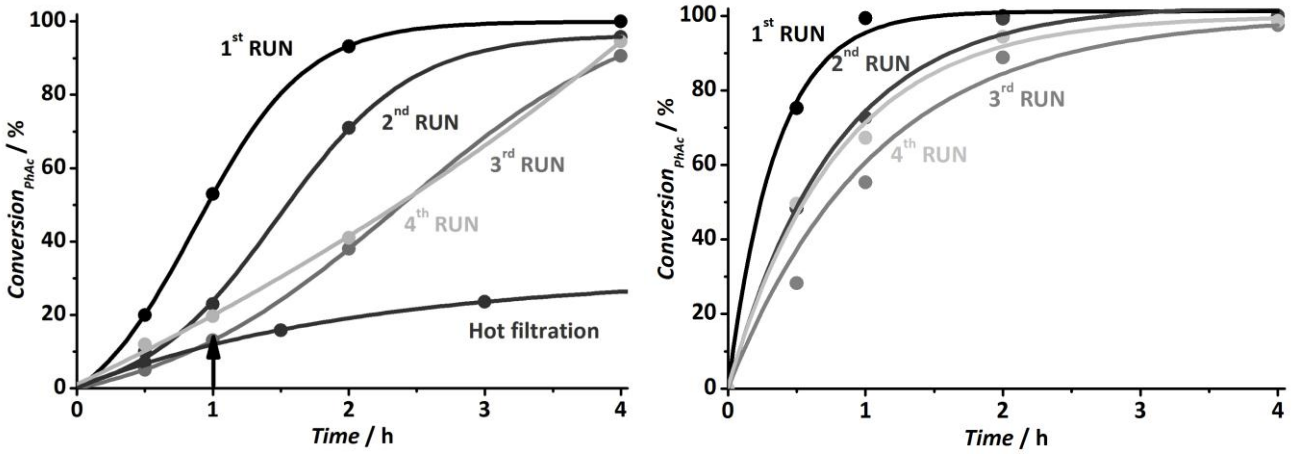

Figure 8 - 7 Phenylacetylene (1 mmol) conversion in 1,3–dipolar cycloaddition reaction with benzyl azide (2 mmol) using Cu(9 wt%)/MOF (0.1 mmol Cu) catalysts in ethanol (6 mL) at 343 K for several consecutive runs. (*Right*) Cu/PMA–MIL–101(Cr), and hot filtration; (*left*) CuEDA/PMA–MIL–101(Cr).

Both catalysts were also active in the formation of propargylamines by one–pot three–component coupling reaction, achieving 60% conversion of phenylacetylene after 17 h in both cases, with full selectivity to the expected propargylamine.

8.3.4. Pd incorporation

Palladium incorporation was performed using palladium chloride as precursor and triethylamine to drive ester hydrolysis and complex coordination. However, by using this base, precipitation of the palladium precursor and formation of nanoparticles occurred.

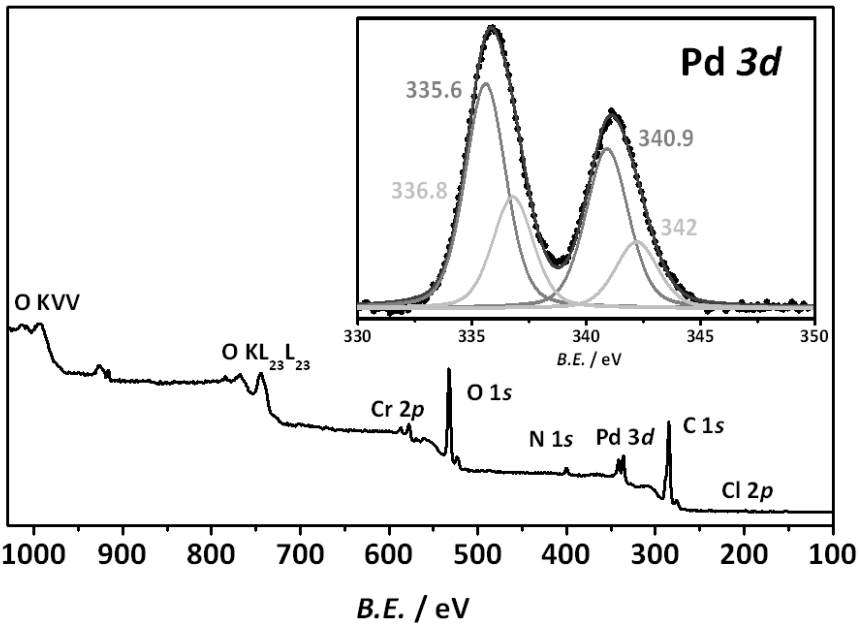

Figure 8 - 8 Pd *3d* XPS survey and core level spectra of Pd(6 wt%)/PMA–MIL–101(Cr) sample.

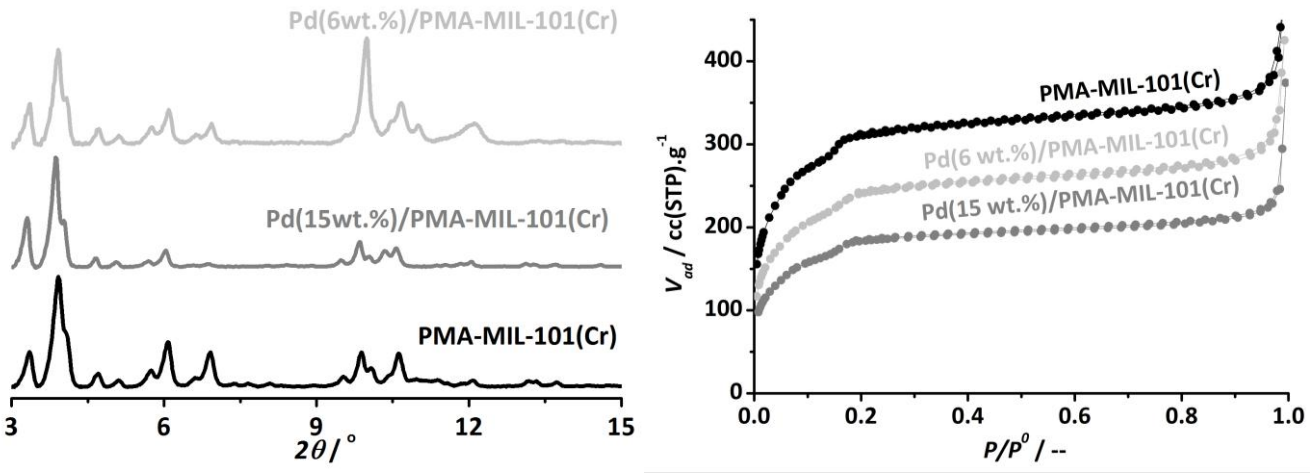

Figure 8 - 9 (*Left*) CoKα X–ray diffraction pattern of PMA–MIL–101(Cr) and the two different palladium loaded samples. Comparison of main reflections with PMA–MIL–101(Cr). (*Right*) Nitrogen adsorption isotherm at 77 K for PMA–MIL–101(Cr) and the two different palladium loaded samples.

Figure 8–8 shows the XPS analysis of the as–synthesized catalyst. Both, metallic (335.6 and 340.9 eV binding energies) and cationic Pd species are observed (336.8 and 342 eV binding energies). [10, 50, 51] Structural stability of the samples after palladium incorporation is demonstrated by XRD analysis and higher decrease in the pore volume is observed with higher palladium content (Fig. 8–9).

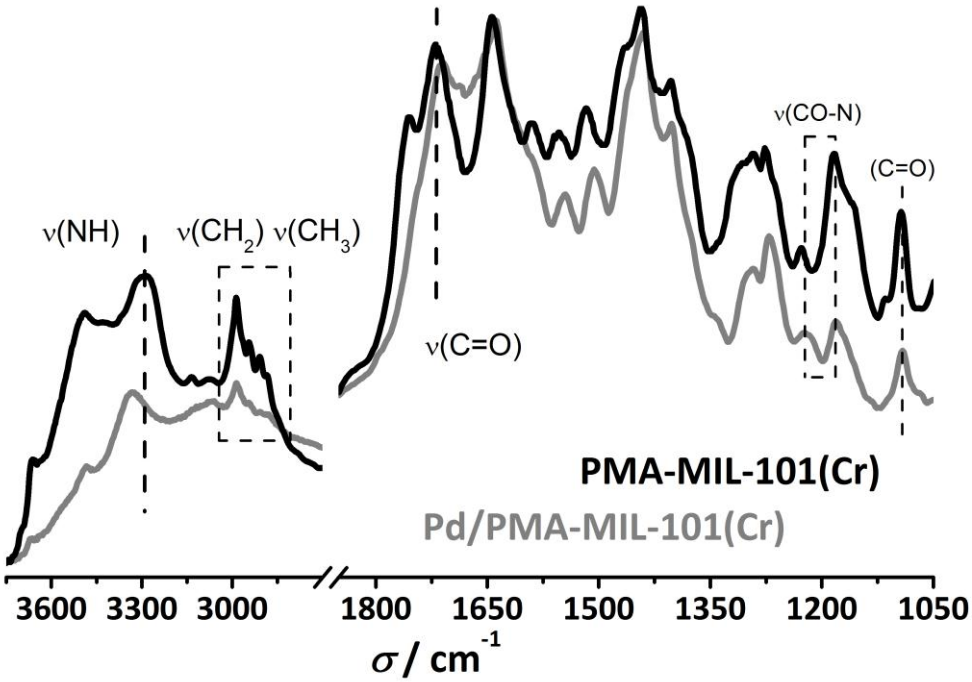

Figure 8 - 10 DRIFTS of (*black*) PMA–MIL–101(Cr) and (*grey*) 15 wt% palladium sample. The samples were pre–treated in situ at 473 K for 1 h in a helium flow of 20 mL min^{-1}.

DRIFTS shows the successful incorporation of Pd (Fig. 8–10): ν(C=O) at 1700 cm^{-1} and ν(N–C=O) between 1230 and 1185 cm^{-1} bands remain very intense. Ester hydrolysis partially occurs, as evidenced by the attenuation of the $\nu(CH_2)$ and $\nu(CH_3)$ bands. In addition, interesting differences are observed in

the ν(NH) region: the secondary amine stretching decreases and shifts towards higher wavenumbers, while vibrations at 3665 cm^{-1} from ν(OH) and at 3485 cm^{-1} of ν(NH) are significantly weakened.

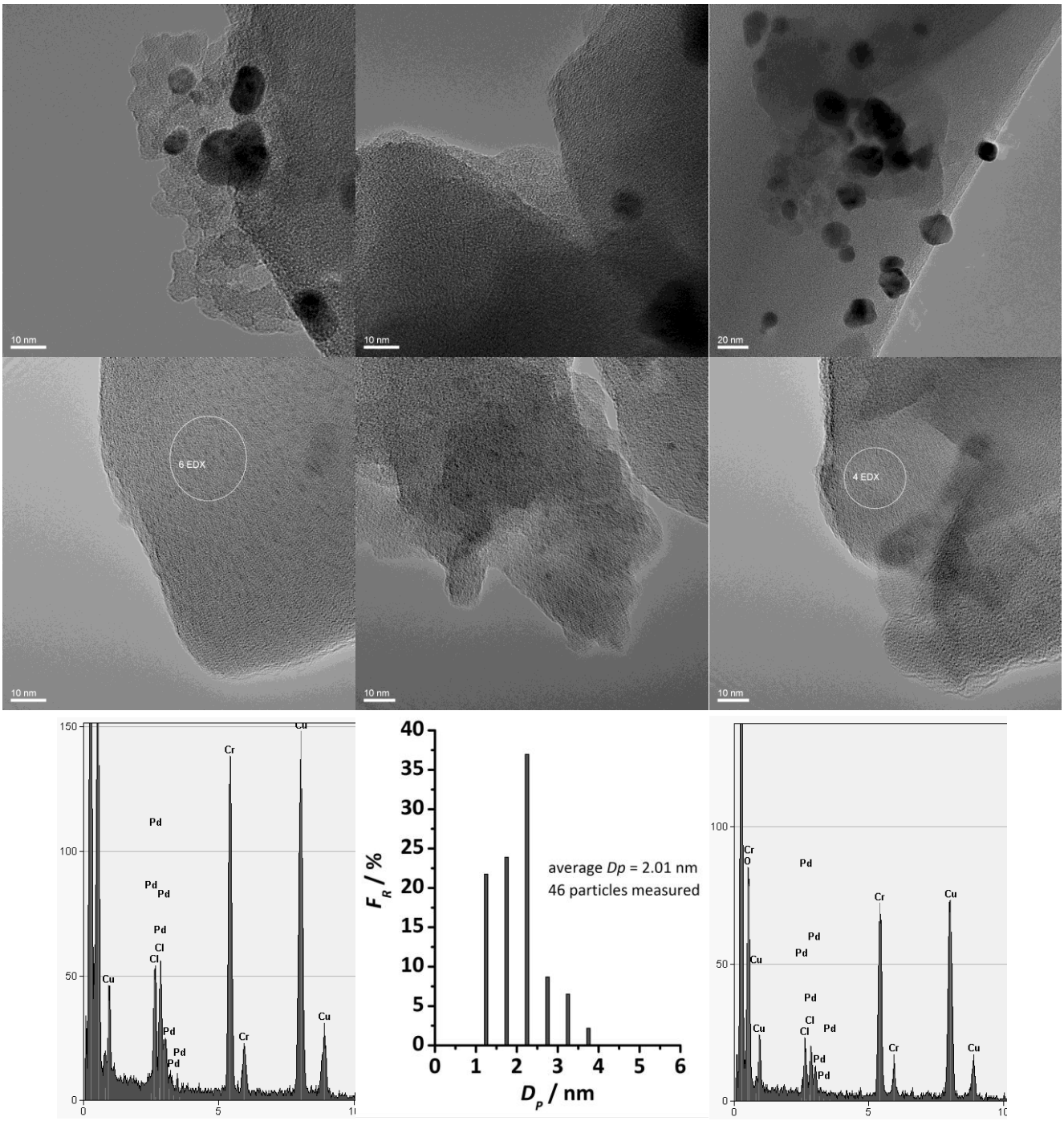

Figure 8 - 11 TEM images of Pd/PMA–MIL–101(Cr) with different palladium loading, particle size distribution and EDX analysis for low loading particles. (*Top*) 15 wt%. (*Bottom*) 6 wt%.

By changing the initial precursor concentration it is possible to fine tune Pd dispersion, particle size and the formation of nanoparticles: when higher Pd concentrations were used, loadings as high as 15 wt% are achieved with large aggregates of nanoparticles outside the MOF crystals (Fig. 8–11*top*). When lower precursor concentrations were used, moderate Pd loadings (~6 wt%) were obtained. In

this case, TEM images (Fig. 8–11*bottom*) do not show the formation of large aggregates, but well dispersed and small palladium nanoparticles (≈ 2 nm).

The 6 wt% loaded palladium–containing samples were tested for their catalytic activity in the Suzuki–Miyaura cross–coupling of bromobenzene and phenylboronic acid, using dimethylformamide as solvent and in the presence of potassium carbonate at 403 K (Fig. 8–12 and Table 8–2).

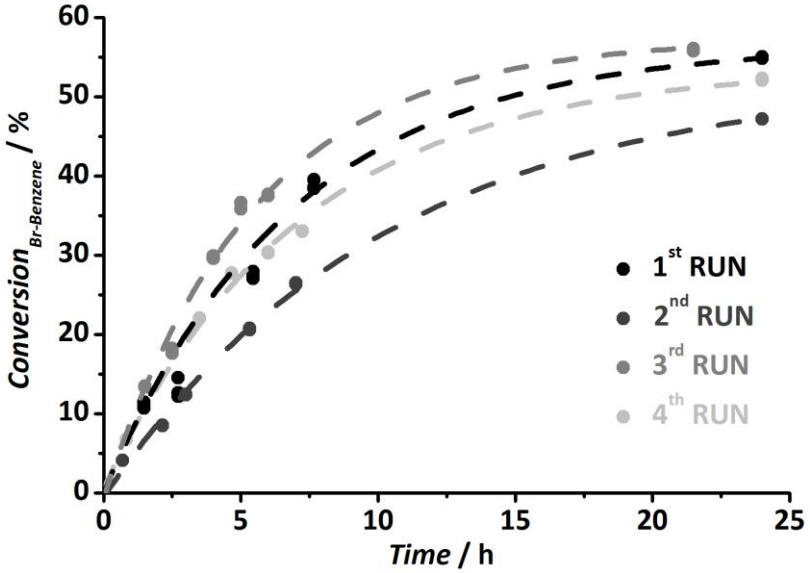

Figure 8 - 12 Conversion of Br–benzene (3.5 mmol) as a function of time in the Suzuki–Miyaura coupling using 80 mg (0.045 mmol Pd) of Pd(6 wt%)/PMA–MIL–101(Cr) sample, 1.5 g (11 mmol) of K_2CO_3, and 670 mg (5.5 mmol) of phenylboronic acid in 4 mL N,N–dimethylformamide at 403 K.

Ca. 50% conversion after 24 h is achieved under these relatively mild reaction conditions, with *TOF* values in the order of 10 h^{-1}, with very similar catalytic performance for the first 4 uses. However, a hot filtration experiment performed after the fourth run (not shown) shows a similar catalytic profile, indicating palladium leaching. Low palladium concentrations in the order of ppm are catalytically active, and therefore it is very difficult to demonstrate the heterogeneous character of the MOF catalysts. Nevertheless, the presence of the oxamate linker in the modified MOF is probably stabilizing the Pd^{2+} species to some extent, thus acting as slow–release reservoir for metallic Pd species.

Table 8 - 2 Rate constant (assuming first order reaction order), *TOF* and cumulative *TON* values for the Suzuki–Miyaura coupling over Pd(6 wt%)/PMA–MIL–101(Cr) sample. Calculated at 150 min for the conversion of bromobenzene (3.5 mmol), using 80 mg of catalyst, 1.5 g (11 mmol) of K_2CO_3, and 670 mg (5.5 mmol) of phenylboronic acid in 4 mL N,N–dimethylformamide at 403 K.

	1st use	2nd use	3rd use	4th use
k (h^{-1})	0.062	0.044	0.084	0.07
TOF ($mol_{converted}/mol_{Pd}h$)	10.4	7.1	13.7	11.4
TON cumulative ($mol_{converted}/mol_{Pd}$)	90	167	260	345

8.3.5. Au incorporation

Gold chloride is readily reduced in the presence of a base; however, a base is necessary to de–protect the oxoacetate by ester hydrolysis. In this work the base (NEt_3) has been used also as reductant, but in order to avoid gold formation of nanoparticles outside the MOF crystals, the gold precursor was initially adsorbed in the MOF (5 h) and then triethylamine was added drop–wise to the oxamate gold impregnated MOF. The same procedure was performed for the NH_2–MIL–101(Cr) used as benchmark.

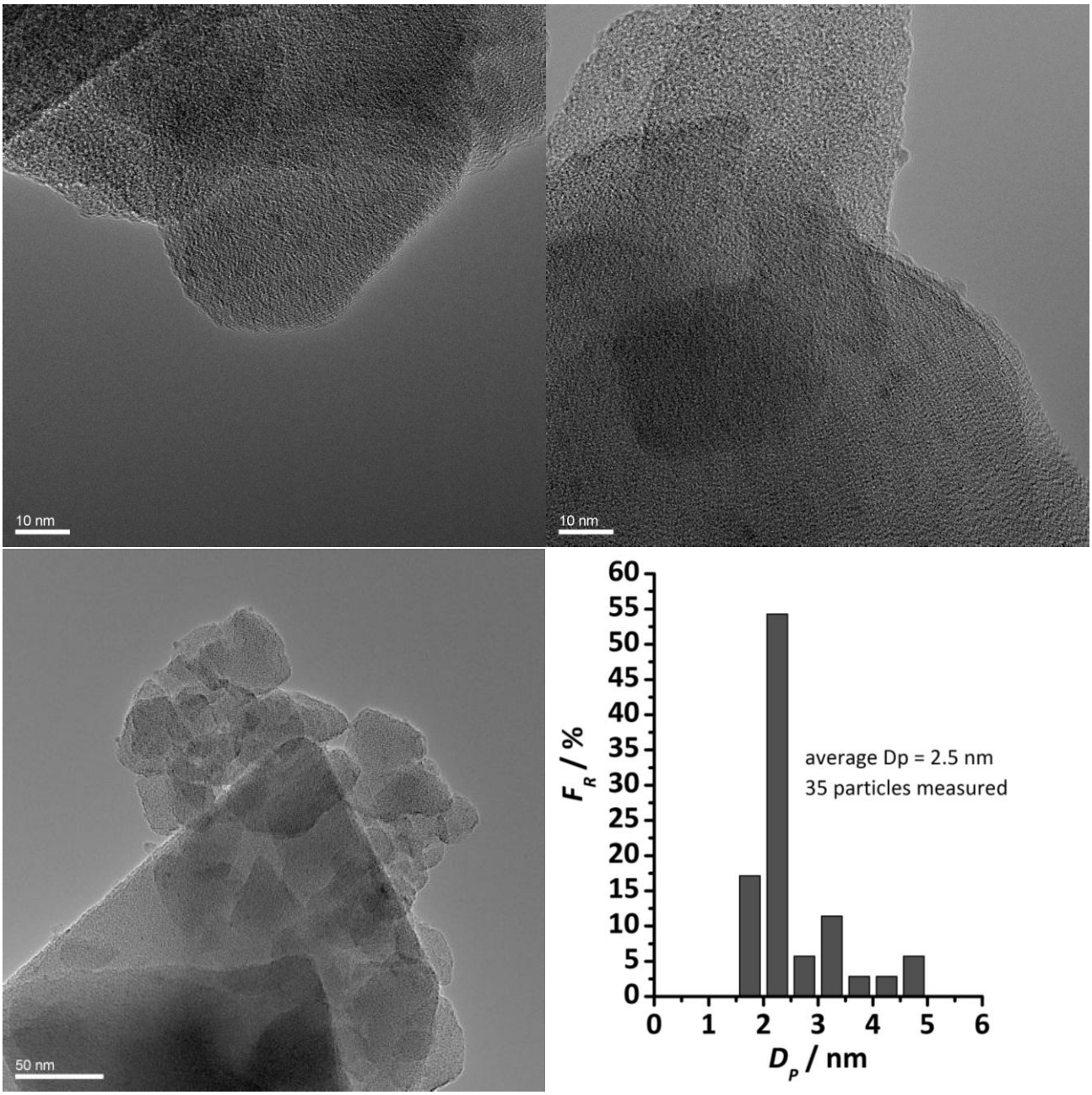

Figure 8 - 13 TEM images of *in situ* impregnated/reduced gold in Au(1.5 wt%)/PMA–MIL–101(Cr) and particle size distribution.

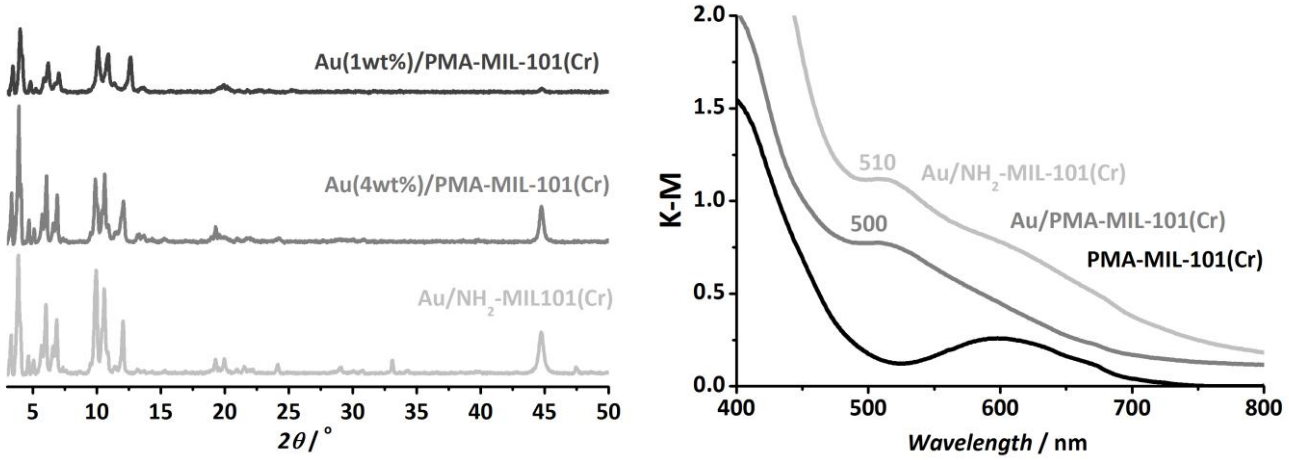

Figure 8 - 14 UV–Vis absorption spectra of (*black*) PMA–MIL–101(Cr), (*grey*) Au/PMA–MIL–101(Cr) and (*light grey*) Au/NH_2–MIL–101(Cr).

In both cases, the formation of gold nanoparticles was observed in few minutes by a color change from green (characteristic for MIL–101 chromium) to brown–purple. UV–Vis measurements reveal gold plasmon resonance centered at 500 nm for Au/PMA and at 510 nm for Au/NH_2, suggesting very small nanoparticles (Fig. 8–14). X–ray diffraction does not show any sign of framework degradation after impregnation and base precipitation (Fig. 8–14). ICP–OES measured after thorough washing (colorless supernatant) showed gold contents of 1.5 wt% for the oxamate sample, which implies that originally 5% of the oxamate groups would be coordinated with atomic gold. TEM images also support the formation of very small gold particles (≈ 2.5 nm, unimodal distribution) well dispersed throughout the Au/PMA sample (Fig. 8–13).

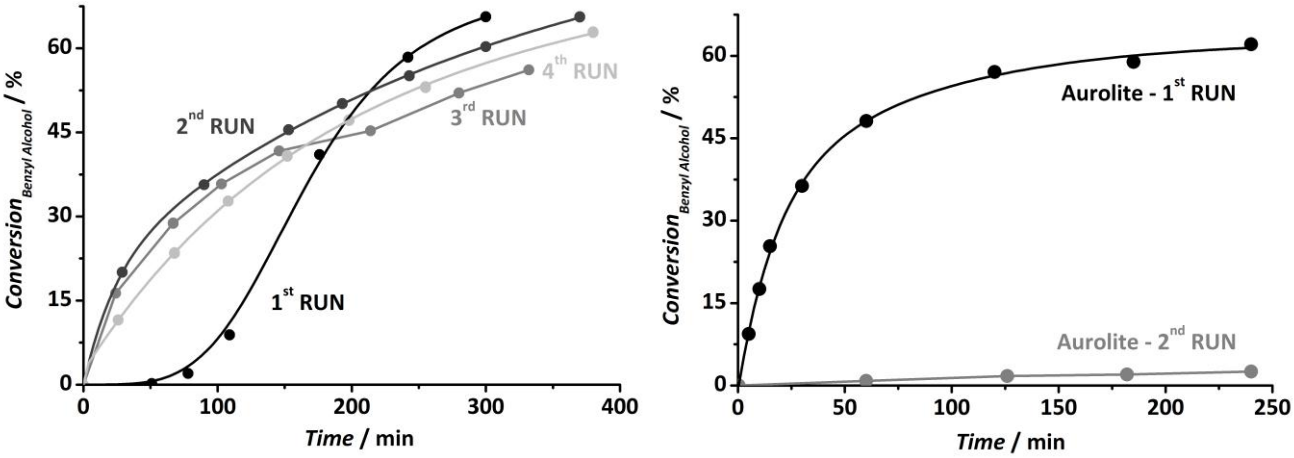

Figure 8 - 15 Benzyl alcohol (22 mmol) oxidation to benzaldehyde, using 3 g (22 mmol) of K_2CO_3, 80 mL toluene (anhydrous, 99.8%) at 353 K and bubbled with 200 mL min^{-1} air flow. [A] 700 mg of Au(1.5 wt%)/PMA–MIL–101(Cr): (*black*) 1st use, (*dark grey*) 2nd use, (*grey*) 3rd use, and (*light grey*) 4th use. [B] 800 mg AUROlite™ (1 wt% Au/Al_2O_3).

The oxidation of benzyl alcohol to benzaldehyde using toluene as solvent and air as oxidant was used to assess the catalytic performance of the gold samples. Figure 8–15 shows four consecutive runs of

Au/PMA–MIL–101(Cr) catalyst under the same conditions (*TOF* ≈ 7 min^{-1}), washing and drying the recovered catalyst after each use (*TON* ≈ 2150). Selectivities are 100% towards benzaldehyde, without any sign of benzoic acid or further condensation to benzyl benzoate. The sample displays an induction time during the first use, which is not observed in subsequent runs, and the catalytic activity remains constant during 4 recycling uses. AUROlite™ (1 wt% Au/Al_2O_3) was also tested in the same reaction set–up as a benchmark catalyst for the oxidation of benzyl alcohol. After a very active first catalytic run (*TOF* ≈ 23 min^{-1}), the catalyst has deactivated (*TON* ≈ 760).

Table 8 - 3 Rate constant, *TOF* and accumulative *TON* values for the benzyl alcohol oxidation over Au/PMA–MIL–101(Cr) sample and commercial AUROlite™ catalyst.

	AUROlite™	Au/PMA-MIL-101(Cr)			
		1st use	2nd use	3rd use	4th use
k (min^{-1})	0.0194	--	0.0077	--	--
TOF ($mol_{converted}/mol_{Au}min$)	23	--	7	--	--
TON $_{cumulative\ (t = 300\ min)}$ ($mol_{converted}/mol_{Au}$)	760	580	1120	1640	2150

TOF values were calculated assuming similar dispersion values of gold for AUROlite™ as for Au/MOF, since smaller but also bigger particle size diameter are found in the former (Table 8–3). The benchmark catalyst is initially more active than the Au/MOF, but only during the first reaction use, since deactivation is a major issue for this commercial catalyst. In this case also benzoic acid and the ester of benzyl alcohol and benzoic acid were observed (Fig. 8–16).

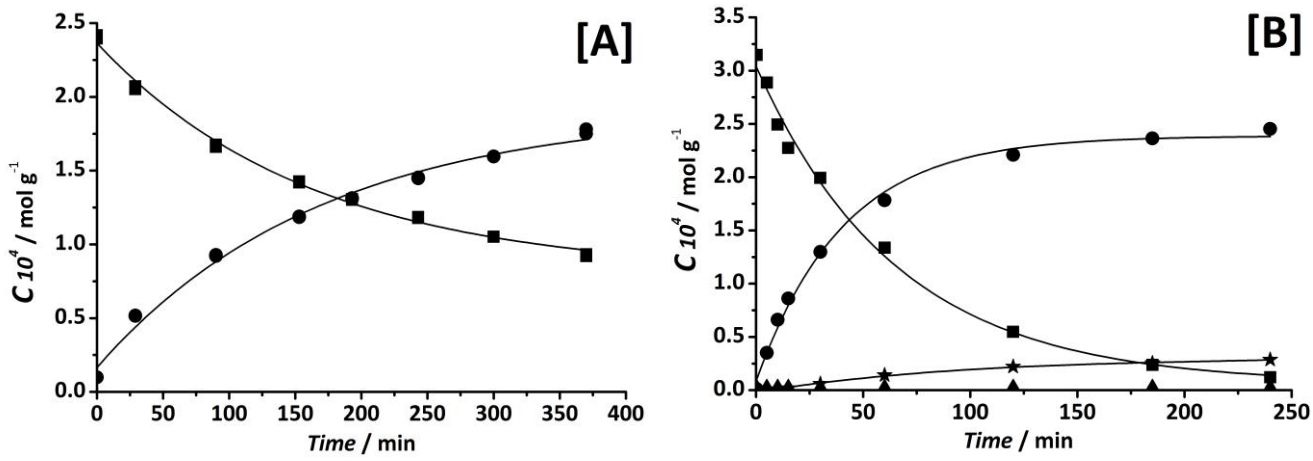

Figure 8 - 16 Concentration profiles of benzyl alcohol and its oxidation products: (■) benzyl alcohol, (●) benzaldehyde, (▲)benzoic acid, (★) benzyl benzoate .[A] Au(1.5 wt%)/PMA–MIL–101(Cr) 2nd use. [B] AUROlite™ 1st use.

8.4. DISCUSSION

An improved synthesis route has been successfully developed for the formation of NO_2–MIL–101(Cr). Synthesis conditions differ from previously reported methods, [42] *i.e.*, we used higher synthesis temperatures (493 K *vs.* 453 K), leading to shorter reaction times (8 h instead of 96 h). In addition, we did not observe any need for long cooling times. Microwave irradiation has proven to yield very small nanocrystals (50 nm) in only 3 h of synthesis at 453 K. On the other hand, the use of HF in the improved synthesis route does not affect the stability of the $–NO_2$ functionalized linker, as observed by NMR, but enhances framework stability. [39] Nitrogen uptake is, to the best of our knowledge, the highest reported for a NO_2–MIL–101(Cr) sample (Fig. 8–1), while thermal stability remains the same as for pristine MIL–101(Cr).

In the first post–functionalization step, amine functionalities can be easily formed using $SnCl_2$ as reducing agent. [42] The subsequent cleaning under concentrated HCl does not affect crystallinity, demonstrating the high stability of the framework (Fig. 8–1). The successful reduction of most NO_2 groups to NH_2 is clear from Fig. 8–2. In the high wavenumber region of the spectra, the symmetric and asymmetric stretching vibrations specific of $–NH_2$ groups appear, centered at 3370 and 3520 cm^{-1}, respectively. In the fingerprint region, symmetric and asymmetric stretching vibrations of $–NO_2$ groups are observed at 1440 cm^{-1} and 1555 cm^{-1}, respectively, which disappear after reduction. In addition, a very characteristic vibrational deformation (scissoring) of the amino groups appears at 1600 cm^{-1}, as observed previously for similar structures like NH_2–MIL–101(Al). [52] For aromatic amines ν(=C–N), two bands are also observed at 1340 and 1260 cm^{-1} due to conjugation of the electron pair of the nitrogen with the ring, imparting double–bond character to the C–N bond. [46]

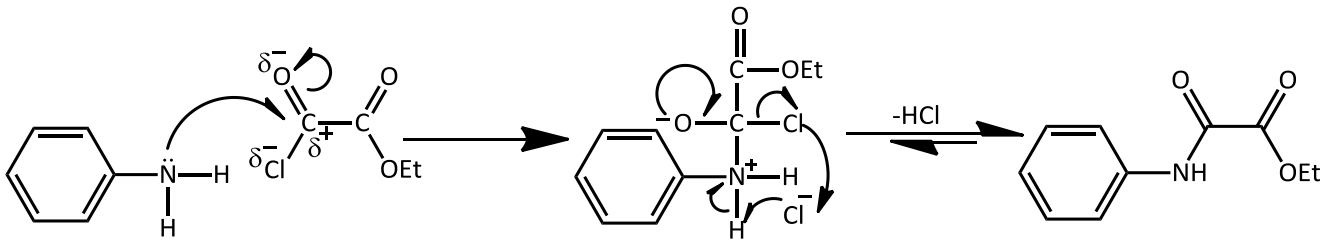

Scheme 8 - 8 Mechanism of nucleophilic substitution of aromatic primary amines with ethyl chloro–oxo acetate to form amides and hydrochloric acid.

The reaction between acyl chloride and amines from the framework during the second functionalization step proceeds through the nucleophilic attack of the aromatic primary amine to the halide carbonyl (Scheme 8–8) to form the corresponding amide and hydrochloric acid. The reaction is favored by using chloride as halide leaving group linked to the strongly polarized carbon in the oxoacetate system. On the other hand, the formation of hydrochloric acid, might reverse the reaction to

form $–NH_3^+$ (impossible to observed by infrared, due to overlapping with the amine and imine region) and consequently back to the amine functionalization. To some extent, back reaction might occur, reducing the efficiency of the post–functionalization, but the use of an excess of solvent and the strong chloride leaving group should limit the back reaction, showing still very high degree of post–functionalization, as discussed later. [53]

PXRD and Infrared analysis demonstrate that crystallinity preserved (Fig.8–1) and the successful oxamate formation (Fig.8–3), reaching very high conversion after 48 h. [54, 55] The higher hydrophilicity of the PMA samples can be noticed in the ν(OH) region of the spectra, where the band at 3680 cm^{-1} associated with ν(Cr–OH) decreases and is partially covered by the presence of strongly adsorbed water. Even the asymmetric $\nu(NH_2)$ vibration is completely overlapped and very difficult to distinguish. However, the symmetric $\nu(NH_2)$ clearly disappears after 48 h of post–functionalization. In addition, new vibrations appear at 3490 and 3300 cm^{-1}, which can be related to ν(N–H) of an aromatic secondary amine, present in the formed oxamate. The increasing intensities of the symmetric and asymmetric $\nu(CH_3)$ (2910 and 2990 cm^{-1}) and $\nu(CH_2)$ (2880 and 2945 cm^{-1}) together with the appearance of a new band at 1720 cm^{-1} (associated with the ν(C=O)), all point to the successful oxamate modification. [54, 55] UV–Vis spectroscopy analyses also confirm the transformation of NH_2 groups, since the characteristic absorption associated with NH_2–bdc around 410 nm, decreases drastically after modification (Fig. 8–17).

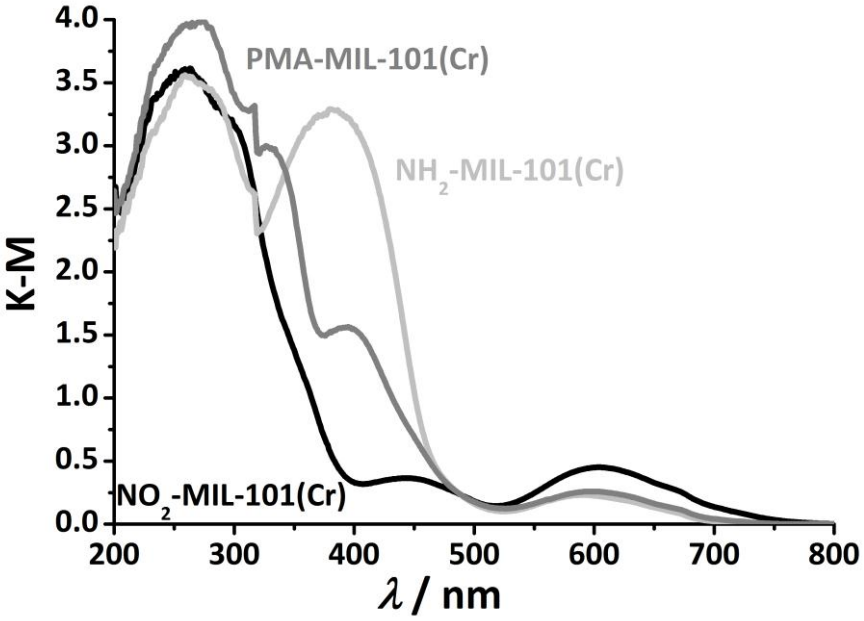

Figure 8 - 17 UV–Vis (Kubelka–Munk transform) absorption spectra of bare MIL–101(Cr) and functionalized (–NO_2, –NH_2, –PMA) samples.

The post–functionalization proposed in this work has proven to be far more efficient than previously reported methods, among other reasons, because the use of a very stable framework such as MIL–

101(Cr) allows long reaction times and harsh conditions, which is not possible with most amino functionalized MOFs reported so far. The usefulness of the integration of oxamate moieties has been demonstrated with the incorporation of three different metals in different configurations: copper using two different precursor configurations, cationic Pd in combination with nanoparticles and Au nanoparticles. In all cases characterization demonstrates the preservation of the framework after metal incorporation.

Copper catalysts contain *ca.* 9 wt%, where *ca.* 60% of the oxamate groups contain copper. The catalytic performance of both copper complexes was tested in the 1,3–dipolar cycloaddition reaction between benzyl azide and phenylacetylene (Fig. 8–7). Reaction kinetics was very difficult to follow, due to strong adsorption of azides, probably at the chromium sites of the structure. Reactions performed using an equimolar reaction mixture, an excess of benzyl azide or an excess of phenylacetylene resulted in 80%, 70% and 95% product yield, respectively (isolated yields of the propargylamine measured after thorough washing the catalyst and column purification). These results suggest that irreversible adsorption of the substrates (and particularly the azide) takes place. Therefore, an excess of azide was used for all reactions in order to saturate adsorption sites in the framework.

Both complex catalysts yield 100% conversion of phenylacetylene after 4 h with 100% selectivity for product 1 (Scheme 8–4) in both ethanol and toluene as solvents (confirmed by isolated products). Copper nitrate catalysts display higher conversion levels than $Cu_3(btc)_2$ structures after 4 h of reaction. [56] Copper ethylenediamine catalysts present higher activity than $Cu_3(btc)_2$ and similar as the best MOF reported in literature ($Cu(2–pymo)_2$) and to the best homogeneous catalyst, copper acetate. [56]

Table 8 - 4 ICP–OES analysis of chromium and copper in Cu/PMA-MIL-101(Cr) before and after several reuses.

	Cr [wt %]	Cu [wt %]	Cu/Cr [mass ratio]	Cu/Cr [molar ratio]	Leaching [%]
1st use	12.09	8.79	0.727	0.6	--
2nd use	9.9	6.9	0.697	0.575	4
3rd use	9.82	6.73	0.685	0.565	1.7
4th use	8.78	5.97	0.680	0.561	0.7

In addition, hot filtration experiments confirm and leaching studies confirm the true heterogeneous character of the MIL–101(Cr) based Cu catalysts. According to elemental analysis the initial sample contains 0.6 Cu mol per mol of chromium, after the first use this ratio decreases *ca.* 4 % to 0.575 Cu mol, and 1.7 % (0.565 Cu mol) and 0.7 % (0.561 Cu mol) for the second and third reuses, respectively (Table 8–4). Using for instance 0.4 % $Cu(OAc)_2$, as homogeneous catalyst, per mol of reactant

(corresponding with 4% leaching from a 10 wt% Cu catalyst used) in the reaction medium, this copper amount is not responsible for a significant part of the catalytic activity observed in the experiments. Therefore, the activity decrease monitored after reuses is not attributed to the leaching of Cu species, but to the adsorption of reactants and products on the active sites that slightly deactivate the catalyst in the first stages of the reaction. The second catalytic test was the formation of propargylamines by a one–pot three–component–coupling reaction (experimental section). Phenylacetylene conversion observed was similar for both copper complexes, around 60% conversion after 17 h. In this case, lower activities per copper site are obtained compared to other copper MOFs and homogeneous systems. [57] We attribute this effect to the fact that in the case of MIL–101(Cr) based solids catalysis takes place only inside the pores of the material (no external surface Cu sites), resulting in serious diffusion limitations for the bulky reaction product.

The incorporation of palladium using palladium chloride as precursor and triethylamine to favor ester hydrolysis was only partially successful. From the XPS analysis (Fig. 8–8) we conclude that Pd is partially reduced upon base addition. In spite of the reduction of a large part of the incorporated Pd, DRIFT spectra demonstrate a certain degree of coordination to the chelating oxamate groups along with ester hydrolysis, as well as complete stability of the framework (Fig. 8–10). The catalytic performance was explored in the Suzuki–Miyaura cross–coupling between bromobenzene and phenylboronic acid (Fig. 8–12 and Table 8–2). Dimethylformamide was used as solvent because the solubility of potassium carbonate in this solvent is low. Surprisingly, the use of other solvents like water or alcohols resulted in the complete dissolution of both the base and the MOF catalyst, probably due to the complexation of the metal nodes by the carbonate in solution. Experiments performed with other carboxylate based MOFs under similar conditions also resulted in the complete dissolution of the framework. These results are in evident contradiction with and shed serious doubts on some recently published works where different carboxylate based MOFs have been used as Pd supports and claimed to be stable under Suzuki–Miyaura conditions using potassium carbonate as base in the presence of water or alcohols. [58, 59] When the reaction was performed in DMF, similar results were obtained for several catalyst recycles. However, hot filtration experiments clearly show leaching of palladium as a contribution of homogeneous catalysis in the solution.

Gold incorporation in PMA–MIL–101(Cr) has also been compared with the benchmark catalyst AUROlite^{TM} (1wt% Au/Al_2O_3). The AuMOF sample, after *in situ* formation of gold nanoparticles by base precipitation, exhibits gold plasmon resonance at 500–510 nm, suggesting very small gold nanoparticles (Fig. 8–14). TEM image analysis of the Au/PMA–MIL–101(Cr) sample also support the formation of very small gold particles of around 1.5–2.5 nm, and well dispersed throughout the sample (Fig. 8–13). As the size of the nanoparticles is smaller than that of the MIL–101(Cr) cavities this

suggests encapsulation of the gold nanoparticles in MOF cages. Additional information about the dispersion and oxidation state of gold, was provided by studying the CO adsorption behavior of Au/PMA–MIL–101(Cr) using *in situ* infrared spectroscopy.

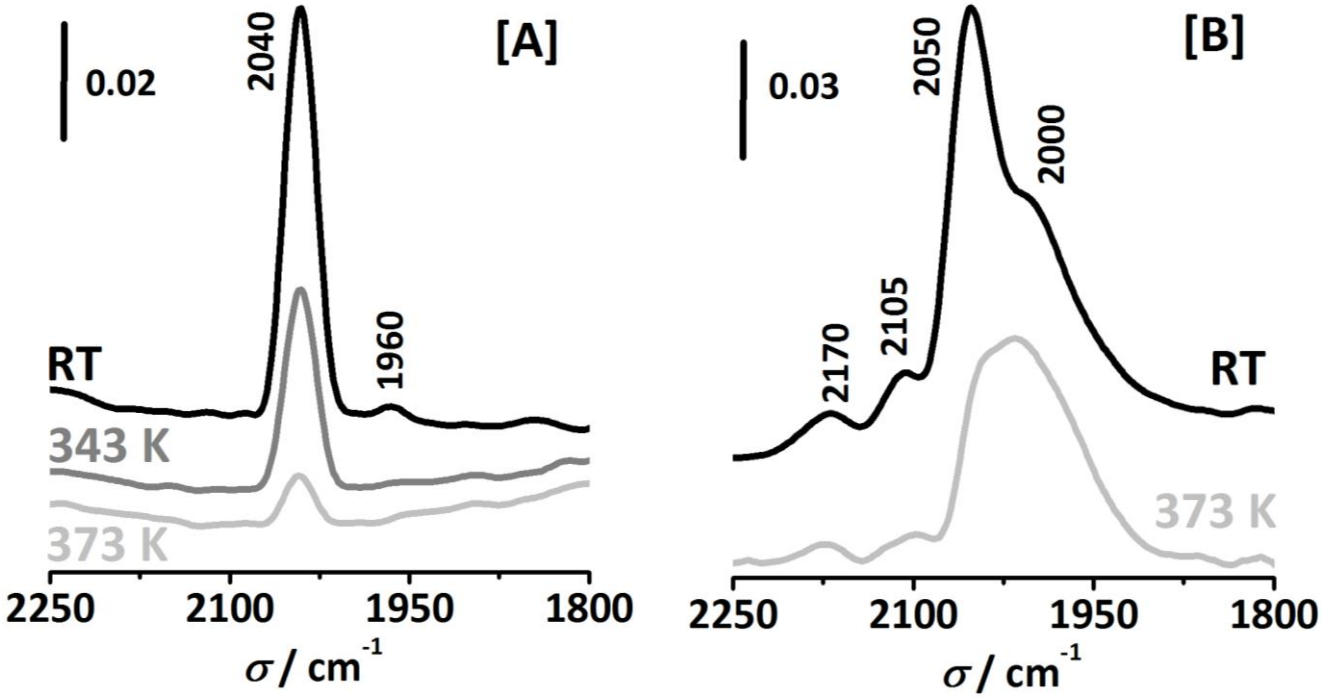

Figure 8 - 18 Infrared spectra of CO adsorbed on [A] Au(1.5 wt%)/PMA–MIL–101(Cr), and [B] AUROlite™ (1 wt% Au/Al_2O_3).

Figure 8–18 shows the infrared spectrum of adsorbed CO after evacuation at RT, 323 and 373 K. At room temperature, a strong absorption band at 2040 and a weak band contribution at 1960 cm^{-1} are observed. Upon heating up to 323 and 373 K, the CO band at 1960 cm^{-1} disappears, while the intensity of the band at 2040 cm^{-1} decreases significantly. The main band at 2040 cm^{-1} can be ascribed to linearly bonded CO on Au^0 sites, while the contribution at 1960 cm^{-1} is caused by bridge adsorption of CO on gold. [60-64] The fact that one single band is found near 2040 is attributed to a very homogeneous Au particle size distribution. In comparison with other catalysts, the main CO band is blue shifted. Both bridge adsorption and a high blue shift are consistent with very small size of gold nano–particles, in agreement with TEM and UV–Vis experiments. [60-64] In addition, no cationic gold species are observed in this sample, due to the absence of bands in the 2280–2166 cm^{-1} region. [65, 66] For comparison, similar spectra are given for the commercial catalyst (Fig. 8–18B). In this case, three overlapping absorptions at 2105, 2050 and 2000 are observed, together with a small absorption contribution at about 2170 cm^{-1}. The three former bands correspond to linearly bonded CO on metallic gold particles with different sizes, while the band at 2170 cm^{-1} can be assigned to positively charged gold species. [66]

The catalytic oxidation of benzyl alcohol to benzaldehyde was performed in four consecutive cycles using both catalysts under similar reaction, washing and drying conditions (Fig. 8–15). In the case of the oxamate sample, the first run shows an induction period, which we attribute to the washing of Cl^- remaining from the gold precursor, as confirmed by XPS analysis of the sample and detection of chloride anions in the washing liquid. As from the second catalytic use, no induction is observed anymore. The selectivity towards benzaldehyde is 100% in the case of the MOF catalyst, while 10% of benzyl benzoate is observed for AUROlite™ due to consecutive oxidation and esterification (Fig. 8–16). This difference in selectivity might be crucial for the stability of the catalyst, since an activity loss is observed for the second catalytic use of benchmark AUROlite™ sample, even though it had a higher activity in the first catalytic use. The nature of this deactivation has tentatively been attributed to strong adsorption of benzoic acid or benzyl benzoate (product inhibition) on the AUROlite™ catalyst.

Similar differences have been observed after *ex situ* reduction of impregnated samples with gold precursors in a hydrogen stream. Gold nanoparticles supported on NH_2–MIL–101(Cr) show no catalytic activity after the second use, where probably aggregation is playing an important role. In contrast, Au nanoparticles in PMA–MIL–101(Cr) are sufficiently stable and maintain their activity and selectivity at least for 4 consecutive runs. The Au/PMA–MIL–101(Cr) sample shows no CO oxidation activity in the temperature range 298–473 K. Although the reaction mechanism of CO oxidation over gold nano–particles is still under debate, it has been proposed that especially cationic gold is the active species in combination with a reducible support. [67-69] Both the absence of these cationic species and a reducible support could explain why Au/PMA–MIL–101(Cr) shows no activity in the CO oxidation, and apparently also does not oxidize further the benzaldehyde.

Altogether, the presented results demonstrate that the developed post–synthetic modification is a versatile functionalization method for the incorporation of additional metal functionalities, resulting in high loadings in combination with a high dispersion and fine control over particle size distribution.

8.5. CONCLUSIONS

A new sequential post–functionalization method has been developed for the incorporation of catalytically active metal complexes and nanoparticles in Metal Organic Frameworks (MOFs). The starting MOF, NO_2–MIL–101(Cr) was successfully synthesized in short periods (8 h) under acidic conditions. In a first post–synthesis step, reduction of the NO_2 moieties leads to the formation of NH_2–MIL–101(Cr). The second functionalization step consists of a straightforward condensation of the amino groups of the ligand with ethyl chloro–oxoacetate resulting in free oxamate groups attached to the linker.

Two different copper complexes have been coordinated through the oxamate ligand, attaining loadings as high as 9 wt% and showing similar performance as other previously reported copper MOFs (HKUST–1, [Cu(2–pymo)$_2$] and [Cu(im)$_2$]) in "click chemistry" catalysis (1,3–dipolar cycloaddition reactions) and multicomponent coupling reactions (propargylamine formation). Small palladium and gold nanoparticles can be incorporated and stabilized by the oxamate ligand. The resulting catalysts are active and selective in Suzuki–Miyaura condensation and in the oxidation of benzyl alcohol, respectively. While Pd containing catalysts show leaching of the active phase, Au immobilized nanoparticles maintain an stable performance for at least 4 consecutive runs displaying 100% selectivity towards benzaldehyde, surpassing the stability and selectivity of the commercial Au catalyst AUROlite^{TM}. These particles are very uniform, both in size, ~2 nm, and metallic in character.

REFERENCES

[1] Y.K. Hwang, D.Y. Hong, J.S. Chang, S.H. Jhung, Y.K. Seo, J. Kim, A. Vimont, M. Daturi, C. Serre, G. Férey, Amine grafting on coordinatively unsaturated metal centers of MOFs: Consequences for catalysis and metal encapsulation, Angewandte Chemie - International Edition, 47 (2008) 4144-4148.
[2] A. Arnanz, M. Pintado-Sierra, A. Corma, M. Iglesias, F. Sánchez, Bifunctional metal organic framework catalysts for multistep reactions: MOF-Cu(btc)-[Pd] catalyst for one-pot heteroannulation of acetylenic compounds, Advanced Synthesis and Catalysis, 354 (2012) 1347-1355.
[3] S. Kitagawa, R. Kitaura, S.-I. Noro, Functional Porous Coordination Polymers, Angewandte Chemie International Edition, 43 (2004) 2334-2375.
[4] J.S. Seo, D. Whang, H. Lee, S.I. Jun, J. Oh, Y.J. Jeon, K. Kim, A homochiral metal-organic porous material for enantioselective separation and catalysis, Nature, 404 (2000) 982-986.
[5] M. Eddaoudi, J. Kim, N. Rosi, D. Vodak, J. Wachter, M. O'Keeffe, O.M. Yaghi, Systematic design of pore size and functionality in isoreticular MOFs and their application in methane storage, Science, 295 (2002) 469-472.
[6] X. Zhang, F.X. Llabrés i Xamena, A. Corma, Gold(III) – metal-organic framework bridges the gap between homogeneous and heterogeneous gold catalysts, Journal of Catalysis, 265 (2009) 155-160.
[7] F. Vermoortele, M. Vandichel, B. Van De Voorde, R. Ameloot, M. Waroquier, V. Van Speybroeck, D.E. De Vos, Electronic effects of linker substitution on Lewis acid catalysis with metal-organic frameworks, Angewandte Chemie - International Edition, 51 (2012) 4887-4890.
[8] P. Serra-Crespo, M.A. van der Veen, E. Gobechiya, K. Houthoofd, Y. Filinchuk, C.E.A. Kirschhock, J.A. Martens, B.F. Sels, D.E. De Vos, F. Kapteijn, J. Gascon, NH_2-MIL-53(Al): A High-Contrast Reversible Solid-State Nonlinear Optical Switch, Journal of the American Chemical Society, 134 (2012) 8314-8317.
[9] J. Gascon, U. Aktay, M.D. Hernandez-Alonso, G.P.M. van Klink, F. Kapteijn, Amino-based metal-organic frameworks as stable, highly active basic catalysts, Journal of Catalysis, 261 (2009) 75-87.
[10] Y. Huang, S. Gao, T. Liu, J. Lü, X. Lin, H. Li, R. Cao, Palladium nanoparticles supported on mixed-linker metal-organic frameworks as highly active catalysts for Heck reactions, ChemPlusChem, 77 (2012) 106-112.
[11] W. Kleist, M. Maciejewski, A. Baiker, MOF-5 based mixed-linker metal-organic frameworks: Synthesis, thermal stability and catalytic application, Thermochimica Acta, 499 (2010) 71-78.
[12] S. Marx, W. Kleist, J. Huang, M. MacIejewski, A. Baiker, Tuning functional sites and thermal stability of mixed-linker MOFs based on MIL-53(Al), Dalton Transactions, 39 (2010) 3795-3798.
[13] J.A. Thompson, C.R. Blad, N.A. Brunelli, M.E. Lydon, R.P. Lively, C.W. Jones, S. Nair, Hybrid zeolitic imidazolate frameworks: Controlling framework porosity and functionality by mixed-linker synthesis, Chemistry of Materials, 24 (2012) 1930-1936.
[14] M. Kim, J.F. Cahill, H. Fei, K.A. Prather, S.M. Cohen, Post-synthetic ligand and cation exchange in robust metal-organic frameworks, Journal of the American Chemical Society, 134 (2012) 18082-18088.
[15] H. Chun, D.N. Dybtsev, H. Kim, K. Kim, Synthesis, X-ray crystal structures, and gas sorption properties of pillared square grid nets based on paddle-wheel motifs: Implications for hydrogen storage in porous materials, Chemistry - A European Journal, 11 (2005) 3521-3529.
[16] L. Ma, C. Abney, W. Lin, Enantioselective catalysis with homochiral metal-organic frameworks, Chemical Society Reviews, 38 (2009) 1248-1256.
[17] Y. Liu, W. Xuan, Y. Cui, Engineering homochiral metal-organic frameworks for heterogeneous asymmetric catalysis and enantioselective separation, Advanced Materials, 22 (2010) 4112-4135.
[18] M.C. Das, S. Xiang, Z. Zhang, B. Chen, Functional mixed metal-organic frameworks with metalloligands, Angewandte Chemie International Edition, 50 (2011) 10510-10520.
[19] C. Zou, C.-D. Wu, Functional porphyrinic metal-organic frameworks: crystal engineering and applications, Dalton Transactions, 41 (2012) 3879-3888.
[20] A. Corma, M. Iglesias, F.X. Llabrés i Xamena, F. Sánchez, Cu and Au metal-organic frameworks bridge the gap between homogeneous and heterogeneous catalysts for alkene cyclopropanation reactions, Chemistry – A European Journal, 16 (2010) 9789-9795.
[21] D.J. Lun, G.I.N. Waterhouse, S.G. Telfer, A general thermolabile protecting group strategy for organocatalytic metal-organic frameworks, Journal of the American Chemical Society, 133 (2011) 5806-5809.
[22] F.A. Almeida Paz, J. Klinowski, S.M.F. Vilela, J.P.C. Tome, J.A.S. Cavaleiro, J. Rocha, Ligand design for functional metal-organic frameworks, Chemical Society Reviews, 41 (2012) 1088-1110.
[23] J.-P. Zhang, Y.-B. Zhang, J.-B. Lin, X.-M. Chen, Metal Azolate Frameworks: From Crystal Engineering to Functional Materials, Chemical Reviews, 112 (2011) 1001-1033.
[24] M.P. Yutkin, D.N. Dybtsev, V.P. Fedin, Homochiral porous metal-organic coordination polymers: Synthesis, structure and functional properties, Russian Chemical Reviews, 80 (2011) 1009-1034.
[25] M. Yoon, R. Srirambalaji, K. Kim, Homochiral metal-organic frameworks for asymmetric heterogeneous catalysis, Chemical Reviews, 112 (2011) 1196-1231.
[26] S.M. Cohen, Post-synthetic methods for the functionalization of metal-organic frameworks, Chemical Reviews, 112 (2011) 970-1000.

[27] H.L. Jiang, D. Feng, T.F. Liu, J.R. Li, H.C. Zhou, Pore surface engineering with controlled loadings of functional groups via click chemistry in highly stable metal-organic frameworks, Journal of the American Chemical Society, 134 (2012) 14690-14693.
[28] K.K. Tanabe, S.M. Cohen, Postsynthetic modification of metal-organic frameworks-a progress report, Chemical Society Reviews, 40 (2011) 498-519.
[29] M.G. Goesten, J. Juan-Alcañiz, E.V. Ramos-Fernandez, K.B. Sai Sankar Gupta, E. Stavitski, H. Van Bekkum, J. Gascon, F. Kapteijn, Sulfation of metal-organic frameworks: Opportunities for acid catalysis and proton conductivity, Journal of Catalysis, 281 (2011) 177-187.
[30] G. Tuci, A. Rossin, X. Xu, M. Ranocchiari, J.A. Van Bokhoven, L. Luconi, I. Manet, M. Melucci, G. Giambastiani, "click" on MOFs: A versatile tool for the multimodal derivatization of N_3-decorated metal organic frameworks, Chemistry of Materials, 25 (2013) 2297-2308.
[31] M.J. Ingleson, J. Perez Barrio, J.B. Guilbaud, Y.Z. Khimyak, M.J. Rosseinsky, Framework functionalisation triggers metal complex binding, Chemical Communications, (2008) 2680-2682.
[32] S. Bhattacharjee, D.A. Yang, W.S. Ahn, A new heterogeneous catalyst for epoxidation of alkenes via one-step post-functionalization of IRMOF-3 with a manganese(ii) acetylacetonate complex, Chemical Communications, 47 (2011) 3637-3639.
[33] J. Juan-Alcañiz, E.V. Ramos-Fernandez, U. Lafont, J. Gascon, F. Kapteijn, Building MOF bottles around phosphotungstic acid ships: One-pot synthesis of bi-functional polyoxometalate-MIL-101 catalysts, Journal of Catalysis, 269 (2010) 229-241.
[34] S. Bauer, C. Serre, T. Devic, P. Horcajada, J. Marrot, G. Férey, N. Stock, High-throughput assisted rationalization of the formation of metal organic frameworks in the iron(III) aminoterephthalate solvothermal system, Inorganic Chemistry, 47 (2008) 7568-7576.
[35] K.M.L. Taylor-Pashow, J. Della Rocca, Z. Xie, S. Tran, W. Lin, Post-synthetic modifications of iron-carboxylate nanoscale metal-organic frameworks for imaging and drug delivery, Journal of the American Chemical Society, 131 (2009) 14261-14263.
[36] P. Serra-Crespo, E.V. Ramos-Fernandez, J. Gascon, F. Kapteijn, Synthesis and Characterization of an Amino Functionalized MIL-101(Al): Separation and Catalytic Properties, Chemistry of Materials, 23 (2011) 2565-2572.
[37] M. Hartmann, M. Fischer, Amino-functionalized Basic Catalysts with MIL-101 Structure, Microporous and Mesoporous Materials, 164 (2012) 38-43.
[38] S. Biswas, S. Couck, M. Grzywa, J.F.M. Denayer, D. Volkmer, P. Van Der Voort, Vanadium analogues of nonfunctionalized and amino-functionalized MOFs with MIL-101 topology - Synthesis, characterization, and gas sorption properties, European Journal of Inorganic Chemistry, (2012) 2481-2486.
[39] C. Férey, C. Mellot-Draznieks, C. Serre, F. Millange, J. Dutour, S. Surblé, I. Margiolaki, Chemistry: A chromium terephthalate-based solid with unusually large pore volumes and surface area, Science, 309 (2005) 2040-2042.
[40] Y. Lin, C. Kong, L. Chen, Direct synthesis of amine-functionalized MIL-101(Cr) nanoparticles and application for CO_2 capture, RSC Advances, 2 (2012) 6417-6419.
[41] D. Jiang, L.L. Keenan, A.D. Burrows, K.J. Edler, Synthesis and post-synthetic modification of MIL-101(Cr)-NH_2 via a tandem diazotisation process, Chemical Communications, 48 (2012) 12053-12055.
[42] S. Bernt, V. Guillerm, C. Serre, N. Stock, Direct covalent post-synthetic chemical modification of Cr-MIL-101 using nitrating acid, Chemical Communications, 47 (2011) 2838-2840.
[43] D.A. Shirley, High-resolution x-ray photoemission spectrum of the valence bands of gold, Physical Review B, 5 (1972) 4709-4714.
[44] C. Volkringer, H. Leclerc, J.-C. Lavalley, T. Loiseau, G. Férey, M. Daturi, A. Vimont, Infrared spectroscopy investigation of the acid sites in the metal-organic framework aluminum trimesate MIL-100(Al), The Journal of Physical Chemistry C, 116 (2012) 5710-5719.
[45] A. Vimont, J.M. Goupil, J.C. Lavalley, M. Daturi, S. Surblé, C. Serre, F. Millange, G. Férey, N. Audebrand, Investigation of acid sites in a zeotypic giant pores chromium(III) carboxylate, Journal of the American Chemical Society, 128 (2006) 3218-3227.
[46] G. Socrates, Infrared and Raman Characteristic Group Frequencies: Tables and Charts, 3rd ed., John Wiley & Sons Ltd, England, 2001.
[47] C.C. Chusuei, M.A. Brookshier, D.W. Goodman, Correlation of relative X-ray photoelectron spectroscopy shake-up intensity with CuO particle size, Langmuir, 15 (1999) 2806-2808.
[48] G.A. Hope, R. Woods, G.K. Parker, A.N. Buckley, J. McLean, Spectroscopic characterisation of copper acetohydroxamate and copper n-octanohydroxamate, Inorganica Chimica Acta, 365 (2011) 65-70.
[49] E. Cano, C.L. Torres, J.M. Bastidas, An XPS study of copper corrosion originated by formic acid vapour at 40% and 80% relative humidity, Werkstoffe und Korrosion, 52 (2001) 667-676.
[50] Y.M.A. Yamada, S.M. Sarkar, Y. Uozumi, Self-assembled poly(imidazole-palladium): Highly active, reusable catalyst at ppm-ppb levels, Journal of the American Chemical Society, 134 (2012) 3190-3198.
[51] H. Li, Z. Zhu, F. Zhang, S. Xie, P. Li, X. Zhou, Palladium nanoparticles confined in the cages of MIL-101: An efficient catalyst for the one-pot indole synthesis in water, ACS Catalysis, 1 (2011) 1604-1612.

[52] P. Serra-Crespo, E. Gobechiya, E.V. Ramos-Fernandez, J. Juan-Alcañiz, A. Martinez-Joaristi, E. Stavitsky, C.E.A. Kirschhock, J.A. Martens, F. Kapteijn, J. Gascon, Interplay of metal node and amine functionality in NH_2-MIL-53: modulating breathing behaviour through intra-framework interactions, Langmuir, 28 (2012) 12916-12922.
[53] J. Ferrando-Soria, D. Cangussu, M. Eslava, Y. Journaux, R. Lescouëzec, M. Julve, F. Lloret, J. Pasán, C. Ruiz-Pérez, E. Lhotel, C. Paulsen, E. Pardo, Rational enantioselective design of chiral heterobimetallic single-chain magnets: Synthesis, crystal structures and magnetic properties of oxamato-bridged $M^{II}Cu^{II}$ chains (M=Mn, Co), Chemistry - A European Journal, 17 (2011) 12482-12494.
[54] J. Ferrando-Soria, M. Castellano, R. Ruiz-Garcia, J. Cano, M. Julve, F. Lloret, J. Pasan, C. Ruiz-Perez, L. Canadillas-Delgado, Y. Li, Y. Journaux, E. Pardo, Redox switching of the antiferromagnetic coupling in permethylated dicopper(II) paracyclophanes, Chemical Communications, 48 (2012) 8401-8403.
[55] J. Ferrando-Soria, E. Pardo, R. Ruiz-García, J. Cano, F. Lloret, M. Julve, Y. Journaux, J. Pasán, C. Ruiz-Pérez, Synthesis, crystal structures and magnetic properties of $M^{II}Cu^{II}$ chains (M=Mn and Co) with sterically hindered alkyl-substituted phenyloxamate bridging ligands, Chemistry - A European Journal, 17 (2011) 2176-2188.
[56] I. Luz, F.X. Llabrés I Xamena, A. Corma, Bridging homogeneous and heterogeneous catalysis with MOFs: "Click" reactions with Cu-MOF catalysts, Journal of Catalysis, 276 (2010) 134-140.
[57] I. Luz, F.X. Llabrés i Xamena, A. Corma, Bridging homogeneous and heterogeneous catalysis with MOFs: Cu-MOFs as solid catalysts for three-component coupling and cyclization reactions for the synthesis of propargylamines, indoles and imidazopyridines, Journal of Catalysis, 285 (2012) 285-291.
[58] B. Yuan, Y. Pan, Y. Li, B. Yin, H. Jiang, A highly active heterogeneous palladium catalyst for the Suzuki-Miyaura and Ullmann coupling reactions of aryl chlorides in aqueous media, Angewandte Chemie - International Edition, 49 (2010) 4054-4058.
[59] Y. Huang, Z. Zheng, T. Liu, J. Lü, Z. Lin, H. Li, R. Cao, Palladium nanoparticles supported on amino functionalized metal-organic frameworks as highly active catalysts for the Suzuki-Miyaura cross-coupling reaction, Catalysis Communications, 14 (2011) 27-31.
[60] M. Sterrer, M. Yulikov, T. Risse, H.-J. Freund, J. Carrasco, F. Illas, C. Di Valentin, L. Giordano, G. Pacchioni, When the Reporter Induces the Effect: Unusual IR spectra of CO on Au1/MgO(001)/Mo(001), Angewandte Chemie International Edition, 45 (2006) 2633-2635.
[61] T. Risse, S. Shaikhutdinov, N. Nilius, M. Sterrer, H.-J. Freund, Gold Supported on Thin Oxide Films: From Single Atoms to Nanoparticles, Accounts of Chemical Research, 41 (2008) 949-956.
[62] M. Manzoli, F. Boccuzzi, A. Chiorino, F. Vindigni, W. Deng, M. Flytzani-Stephanopoulos, Spectroscopic features and reactivity of CO adsorbed on different Au/CeO_2 catalysts, Journal of Catalysis, 245 (2007) 308-315.
[63] G.C. Bond, D.T. Thompson, Catalysis by Gold, Catalysis Reviews - Science and Engineering, 41 (1999) 319-388.
[64] J.Y. Lee, J. Schwank, Infrared spectroscopic study of NO reduction by H_2 on supported gold catalysts, Journal of Catalysis, 102 (1986) 207-215.
[65] M.Y. Mihaylov, J.C. Fierro-Gonzalez, H. Knbözinger, B.C. Gates, K.I. Hadjiivanov, Formation of nonclassical carbonyls of Au^{3+} in zeolite NaY: Characterization by infrared spectroscopy, Journal of Physical Chemistry B, 110 (2006) 7695-7701.
[66] M.A. Centeno, K. Hadjiivanov, T. Venkov, H. Klimev, J.A. Odriozola, Comparative study of Au/Al_2O_3 and Au/CeO_2-Al_2O_3 catalysts, Journal of Molecular Catalysis A: Chemical, 252 (2006) 142-149.
[67] C. Louis, Nanoparticles and Catalysis, in: D. Astruc (Ed.) Gold Nanoparticles: recent advances in CO oxidation, Wiley-VCH Verlag GmbH & Co. KGaA, 2008, pp. 475-503.
[68] J.C. Fierro-Gonzalez, B.C. Gates, Evidence of active species in CO oxidation catalyzed by highly dispersed supported gold, Catalysis Today, 122 (2007) 201-210.
[69] G.J. Hutchings, M.S. Hall, A.F. Carley, P. Landon, B.E. Solsona, C.J. Kiely, A. Herzing, M. Makkee, J.A. Moulijn, A. Overweg, J.C. Fierro-Gonzalez, J. Guzman, B.C. Gates, Role of gold cations in the oxidation of carbon monoxide catalyzed by iron oxide-supported gold, Journal of Catalysis, 242 (2006) 71-81.

Chapter 9

MOFs meet monoliths: Hierarchical structuring of metal–organic framework catalysts

This chapter is based on the following publication:

E.V. Ramos–Fernandez, M. Garcia–Domingos, J. Juan–Alcañiz, J. Gascon, F. Kapteijn, Applied Catalysis A: General, 391 (2011) 261-267

Abstract Structuring heterogeneous catalysts from the micro– to the macro–level is essential for efficient catalyst utilization. The optimized synthesis and the catalytic performance of MIL–101(Cr) immobilized on a monolithic structure are presented. Secondary seeded growth is the optimal procedure to obtain uniform coatings of ~9 wt% inside the monolith channels. A monolithic stirrer reactor has been used as playground for exploring the catalytic performance of MIL–101(Cr) in the liquid phase of selective tretralin oxidation, with *TOF* values around 4.5 h^{-1} and 75% selectivity to 1–tetralone. The presented results confirm the stability of the catalyst and coating, and the absence of any transport limitations in this reaction (*Ca* and *Φ* criteria). The easy recovery of the catalyst allows simple reusability, something impossible to realize when working in the often–practiced slurry operation mode. The reported results demonstrate that MIL–101(Cr) undergoes reversible deactivation attributed to the strong adsorption of products on the Cr sites. Applying the proper regeneration procedure (washing in chlorobenzene and air treatment @ 523 K) the initial performance is fully recovered.

9.1. INTRODUCTION

Metal–organic frameworks (MOFs) have been widely used as bulk (powder) materials, but it is obvious that the integration of MOFs as novel nano–materials raises the challenge to direct and controlled growth of MOFs at surfaces. In this sense, the immobilization of MOFs onto structured supports is of high importance, not only for gas storage [1] but also for other applications like catalysis and photocatalysis, [2, 3] separation, [4, 5] adsorbents for GC columns, [6, 7] or sensors. [8]

In particular, the synthesis of MOFs thin films is a domain that has only recently been initiated. However, because of the similarities with zeolites, widely used methods for zeolitic membrane syntheses have been adapted to MOFs, and several reviews have already reported excellent examples of MOFs immobilization onto structured supports for numerous applications. [4, 9-13]

The layer–by–layer (LBL) deposition involves repeated cycles of immersion in separated solutions of metal salt and organic linker, achieving homogeneous thickness and controlled orientation. [14] The LBL approach includes the use of pre–functionalized surfaces by self–assembled monolayers (SAMs) or small crystallites of surface attached MOFs (SURMOFs) in a very controlled manner to anchor MOF building units. Hermes *et al.* describe the growth of MOF–5 on SAM functionalized gold surfaces, and Shekhah *et al.* implement a similar approach to grow MOF–on–MOF layers, while Liu *et al.* apply SURMOFs for enantioselective adsorption. [15-17]

Direct growth approach consists of support immersion in the reaction solution (metal salt and organic linker). [18] Chemical modification of the support becomes indispensable for high quality films. Arnold *et al.* modified alumina under basic conditions and partially oxidized graphite while changing reaction conditions to enhance Mn–MOF coverage. [4] Caro and co–workers have reported a series of ZIF membranes on alumina supports modified with 3–aminopropyltriethoxysilane to promote heterogeneous nucleation and growth. [19, 20] In contrast, secondary growth is one of the most used techniques, which by decoupling nucleation and growth steps allows the control of membrane microstructure. Seeding of the support as initial step has been demonstrated as a simple and versatile approach to obtain high MOF coverage. Gascon *et al.* studied the seeding procedure to obtain dense coatings of HKUST–1 on α–alumina supports, [21] and Guerrero *et al.* used the system for hydrogen separation. [22] Hu *et al.* applied alumina porous supports as the inorganic source (reactive seeding (RS)) to grow continuous MIL–53(Al) membranes. [23] And Caro and co–workers synthesized high coverage ZIF membranes. [24, 25] Nevertheless, no catalytic reports on MOF coated supports were published before this work. Since then, Sachse *et al.* described the formation of HKUST–1 nanoparticles inside the mesopores of silica monoliths, and used the immobilized Cu catalyst for

continuous flow Friedlander reactions, [26] while Aguado *et al.* reported on SIM–2 prepared on alumina beads as catalysts performing for the Knoevenagel condensation reaction. [27]

In this work, MIL–101(Cr) is used, since it is one of the most stable frameworks reported so far, with cage sizes in the mesopores region. Chromium–based catalytic systems are well–known to be highly active and selective catalysts, while mesoporous supports improve mass transfer properties. [28-31] In this regard, MIL–101, having abundant atomically distributed accessible Cr(III) sites (after terminal water removal) and uniform mesopores, is an excellent candidate as catalyst. In pioneering work, Kim *et at.* [32] applied MIL–101(Cr) in a benzylic oxidation, Maksimchuk *et al.* deeply studied alkene oxidation, [33, 34] and Hwang *et al.* [35] described its use to selectively produce sulfoxides from aryl sulfides. Due to the operation in slurry mode, still some drawbacks have to be overcome, *e.g.*, catalysts recovery, attrition and regeneration. [36]

Here, we report the first example of MIL–101(Cr) hybrid structure successfully immobilized on a structured monolithic support, and its use in the selective oxidation of tetralin towards 1–tetralone. The easy recovery of the catalyst allows studying long–term utilization on a single catalyst batch, and therefore regeneration can be studied in detail. In addition, the advantages of immobilization in terms of absence of attrition and diffusion limitations (and therefore better catalytic performance) are discussed. Furthermore, the immobilization of MIL–101(Cr) on monoliths opens up the use of this catalyst for continuous reactor operation.

9.2. EXPERIMENTAL

9.2.1. Materials

All the reagents were purchased from Sigma–Aldrich and were used as received without further purification. The polished asymmetric α–alumina discs (25 mm diameter, 2 mm thickness, top layer pore size 80 nm, and support layer pore size 150 nm) were supplied by Pervatech. The cylindrical cordierite monolithic substrates (2.5 cm of length and 1 cm of diameter, square channels with a cell density of 62 cells cm^{-2} (400 cpsi) and a wall thickness of 0.18 mm) were supplied by Corning Inc.

MIL–101(Cr) seed synthesis: from a mixture of 1.63 g chromium (III) nitrate ($Cr(NO_3)_3 \cdot 9H_2O$, 97%), 0.7 g terephthalic acid, (C_6H_4–1,4– $(CO_2H)_2$, 97%), 0.20 g hydrofluoric acid (HF, 40%) and different water quantities, 20 g (standard conditions) and 1.5, 2, 2.5 times. [37] The mixture is heated under microwave irradiation for 2 h at 453 K. [38] The crystalline product is filtered and activated with: (a) ethanol 95% at 353 K for 24 h, and (b) ammonium fluoride (NH_4F, 1M) solution at 343 K for 24 h. Finally, the sample is filtered off rinsed with hot water, dried and stored at 423 K.

9.2.2. MIL–101(Cr) coated α–alumina discs

Two different procedures were applied to cover the discs with seeds, spin coating and dip coating. In both cases a dispersion of 100 mg of MOF crystals (size ~150 nm) and 100 mL of ethanol were sonicated during 12 h, needed to avoid agglomeration of particles. Ethanol was chosen as a solvent because its volatile character enables fast evaporation during the seeding procedures.

(A) Spin coating: ten drops of the previously described suspension were placed on the disc before starting the spinning at 1500 rpm for 1 min. The procedure was repeated five times for each disc.

(B) Dip coating: the disc is immersed in the solution containing the seed material at a constant speed. Then, it remains fully immersed and it stays motionless, afterwards the disc is raised at a constant speed. This procedure was repeated 10 times.

Once the discs were seeded, a secondary growth was performed in rotating autoclaves heated in a conventional oven for 8 h at 493 K. The synthesis mixture contained 1.63 g chromium (III) nitrate ($Cr(NO_3)_3 \cdot 9H_2O$, 97%), 0.7 g terephthalic acid, (C_6H_4–1,4–$(CO_2H)_2$, 97%), 0.20 g hydrofluoric acid (HF, 40%) and 25 g water. The activation procedure was as described for seeds synthesis.

9.2.3. MIL–101(Cr) coated monolith synthesis

Coating procedure A: the cordierite monoliths were pre–wetted with NaOH (0.1 M) solution. Followed by immersion in the α–alumina suspension, prepared by a slightly acidified (pH = 5) suspension of 50% water and 50% α–alumina (particles size of ~0.1 μm) under continuous stirring. Then, the monoliths were flushed with flowing air (air knife) and dried under rotation at room temperature during 12 h. The alumina–coated monoliths were calcined slowly at 1273 K for 4 h (heating rate 2 K min^{-1}), to avoid cracks of the α–alumina layer. Followed by seeding with MIL–101(Cr) nanocrystals (~150 nm size) by immersion in a seeding suspension (1 wt% MIL–101(Cr)/ethanol) for 1 h under stirring. After that, the monoliths were taken out from the solution and dried under vacuum during 1 h at room temperature. Then, the remaining solvent was removed via evaporation at 373 K. The procedure was adapted from optimized conditions based on [39]. The secondary growth was performed in an autoclave under rotation for 8 h at 493 K using the standard synthesis conditions and activation procedure described above (see seed synthesis section *9.2.1.*).

Coating Procedure B: similar to procedure *A*, but a mixture of α–alumina and MIL–101(Cr) nanoparticles was coated on the monolith, instead of separate seeding procedure. In this case the calcination step was done at 673 K in order to preserve the integrity of the MOF.

9.2.4. Characterization

(a) Spin coating: was performed on a SPS Spin 150 Spincoater at 1500 rpm. *(b) Powder X–Ray Diffraction (PXRD):* was measured using a Bruker–AXS D5005 with Cu Kα radiation. *(c) Scanning Electron Microscopy (SEM) and Energy Dispersive X–ray Spectroscopic (EDS) mapping:* were done using a JEOL JSM–840 scanning electron microscope equipped with secondary and backscattered electron detectors as well as an energy dispersive X–ray spectrometer. *(d) Thermo–Gravimetric Analysis (TGA):* was performed by means of a Mettler Toledo TGA/SDTA851e, under 60 mL min^{-1} flowing air at heating rates of 10 K min^{-1}. *(e) Nitrogen adsorption isotherms:* were performed using a Quantachrome gas adsorption analyzer. The samples were pre–treated under vacuum at 423 K overnight. *(f) Raman Spectroscopy:* was carried out by using a Renishaw Raman imaging microscope, system 2000. The green (λ = 514 nm) polarized radiation of an argon–ion laser beam of 20 mW was used for excitation. A Leica DMLM optical microscope with a Leica PL floutar L500/5 objective lens was used to focus the beam on the sample. The Ramascope was calibrated using a silicon wafer.

9.2.5. Catalytic test: selective oxidation of tetralin

In a typical batch oxidation experiment, a solution of 8 mmol tetralin, 16 mmol *t*–butyl hydroperoxide in 50 mL chlorobenzene was prepared. After temperature adjustment, the catalyst was added.

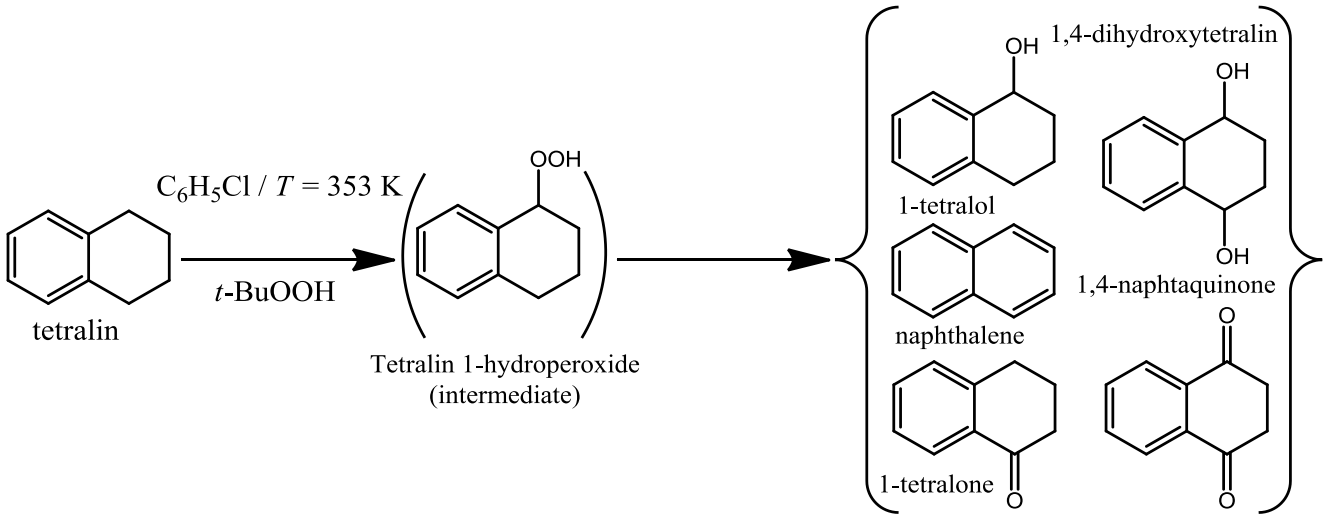

Figure 9 - 1 Scheme of tetralin oxidation reaction.

The reaction mixture was periodically analyzed by gas chromatography (Chrompack GC equipped with an FID detector) using *n*–decane as internal standard over a CP–Sil 8CB column. The analysis was carried out directly after sampling to avoid any additional conversion in the sample mixture. Carbon balances obtained in every case were > 97 %.

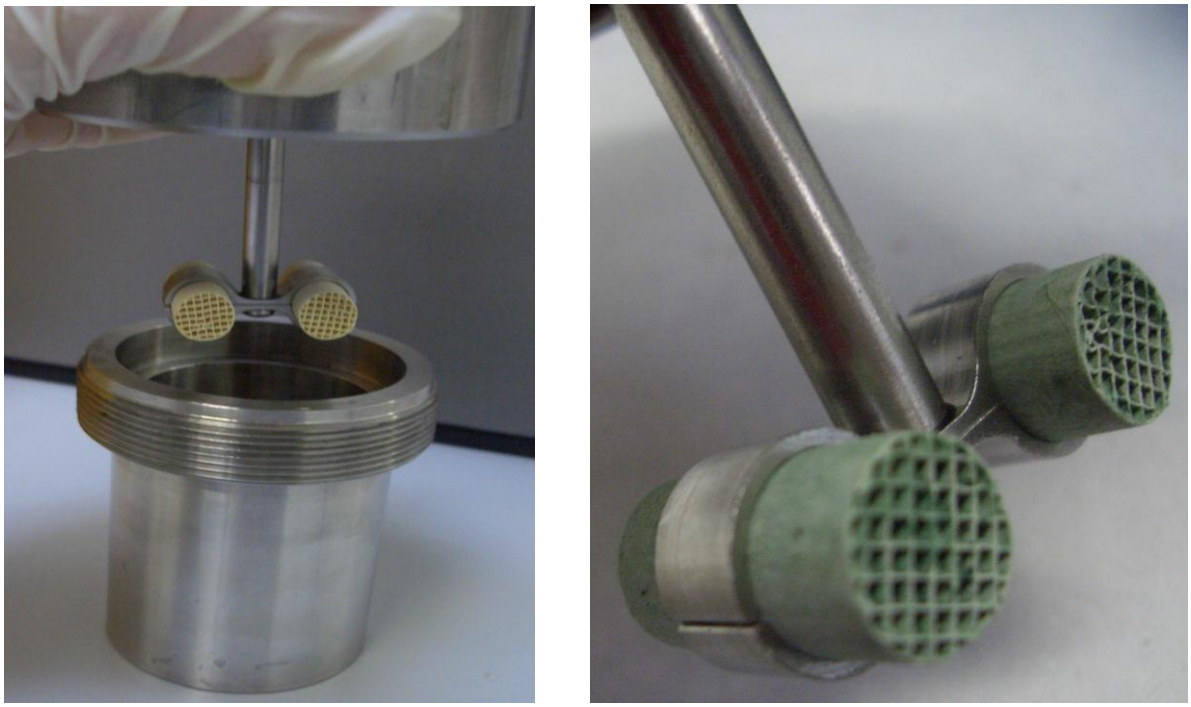

Figure 9 - 2 Monolithic Stirrer Reactor (MSR) experimental set–up. (*Left*) Reactor vessel and tap–stirrer in the position to be closed. (*Right*) Close look at the stirrer with coated monoliths.

The catalysts activity is presented as turn–over–frequency (*TOF*, mol tetralin converted per h per 2 out of 3 mol of Cr in the sample, corresponding with the CUS) determined from the initial conversions in the batch operation. The overall selectivity to 1–tetralone was calculated as the amount of 1–tetralone produced relative to 90% of tetralin converted.

9.3. EXPERIMENTAL RESULTS AND DISCUSSION

In order to obtain high quality coatings, it is crucial to promote the MOF/support interaction. The nature of the interaction is usually electrostatic and two different approaches can be followed to enhance it: (*a*) the support surface chemistry (isoelectric point) needs to be matched to that of the coating species by chemical modifications (*i.e.*, by using SAMs), and (*b*) the growth of the MOF on the surface can be promoted by seeding with MOF nanocrystals and subsequent secondary growth. Based on our experience and literature, secondary growth seems to offer better possibilities for the formation of continuous coatings and that was the strategy followed in this work. [5, 21, 26, 40]

9.3.1. Seeds optimization

Traditional strategies for immobilizing catalysts on monoliths, such as suspension coating or slip–casting followed by fixation via calcination at high temperatures, cannot be applied with MOFs due to their relatively low thermal stability. [41, 42] Therefore, in order to avoid detachment of the coatings during operation, *in situ* growing strategies have to be developed.

Basically two lines can be followed: (*a*) direct nucleation and crystal (inter)growth on the support, and (*b*) a secondary growth after providing the surface with seeds.

In the first approach promoting nucleation on the support (by support surface modification) is essential for growing dense MOF coatings on surfaces. [43] In the second approach the size of the seed crystals and their interaction with the surface are critical to achieve dense coatings. Generally the smaller the crystal seeds the denser the synthesized coating, while the interaction can be influenced by surface modification thereby changing predominantly the electrostatic properties, [24, 25] approaches that are derived from the zeolite field.

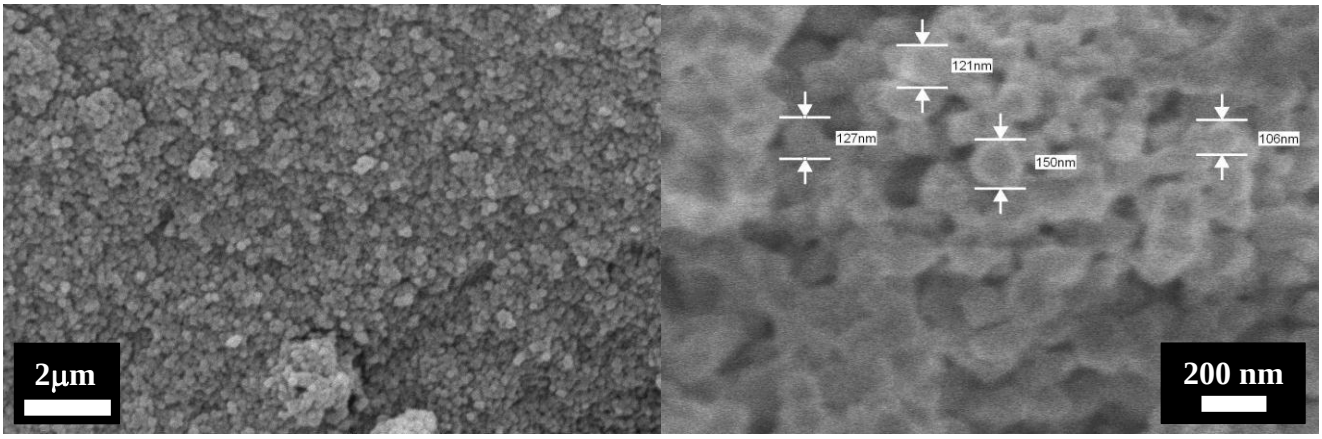

Figure 9 - 3 SEM micrograph for powder MIL–101(Cr) sample synthesized 2.5 times diluted.

In the case of MIL–101(Cr), fast nucleation is essential in order to obtain nanocrystals useful as seeds. This fast nucleation can be promoted by using microwave irradiation instead of conventional heating. The concentration of the reaction mixture is also crucial to achieve small particles. Gascon *et al.* [21] demonstrated that for HKUST–1 coatings on α–alumina, the final size of the crystals also depends on the concentration of the different reactants. The more concentrated the solution the larger the crystals, in clear contrast to zeolitic materials.

In order to examine whether the reaction concentration influence can be extended to other MOF topologies, the synthesis of MIL–101(Cr) was performed with different concentrations of reactants (described in the experimental part). SEM and dynamic light scattering were used to measure the particle size distribution of each sample, displaying the same trend found for HKUST–1. In the case of the most diluted solution an average crystal size of 150 nm was found, an appropriate crystal size to use for seeding (see Fig. 9–3). [21] PXRD, Raman spectroscopy and nitrogen adsorption confirmed the presence of MIL–101(Cr) structure as well as its remaining textural properties. Therefore, these smallest crystals (~150 nm) were used as seeds for both discs and monoliths coating.

9.3.2. MIL–101(Cr) coated α–alumina disc

α–alumina discs were used as model system for studying and understanding the growth of the MIL–101(Cr) crystals on the surface, as a basis to successful preparation of the MOF coated monoliths.

9.3.2.1. Dip coating

The discs seeded by dip coating were immersed in a fresh synthesis solution to carry out the secondary growth. The resulting materials were analyzed by scanning electron microscopy.

Figure 9–4 shows the cross section images of the discs together with the energy dispersive spectroscopy mapping in order to map the chemical composition along the cross section. From the figure it can be concluded that, if present, the thickness of the MOF layer is below the SEM resolution.

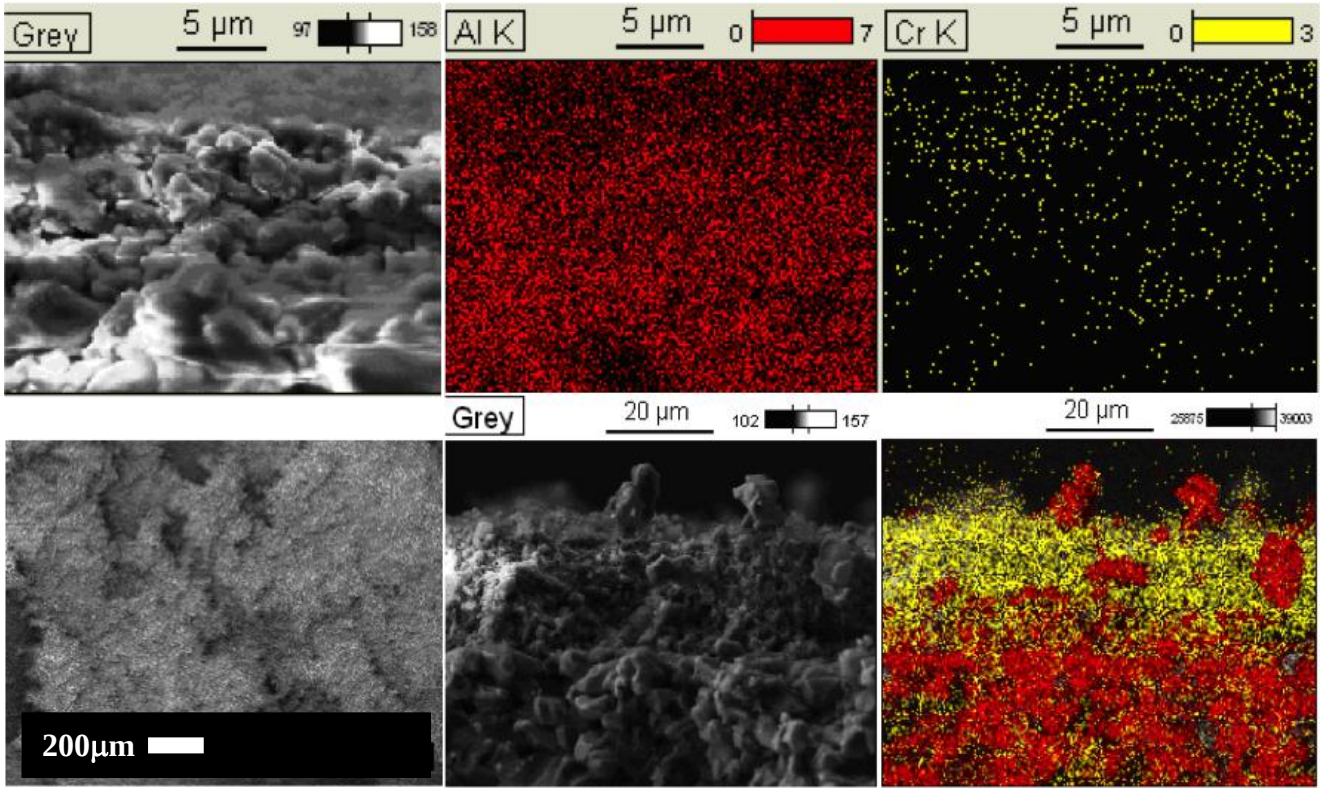

Figure 9 - 4 Top view and cross section with EDS mapping (red = Al; yellow = Cr) of the discs after secondary growth. (*Top*) Dip coating seeding top views. (*Bottom*) Spin coating seeding: top view (*left*) and cross sectional views (*middle and right*).

A similar conclusion can be drawn from the XRD patterns shown in Figure 9–5. Seeding the discs using dip coating did not result in sufficient loadings, probably due to the weak interaction with the surface. [24, 25]

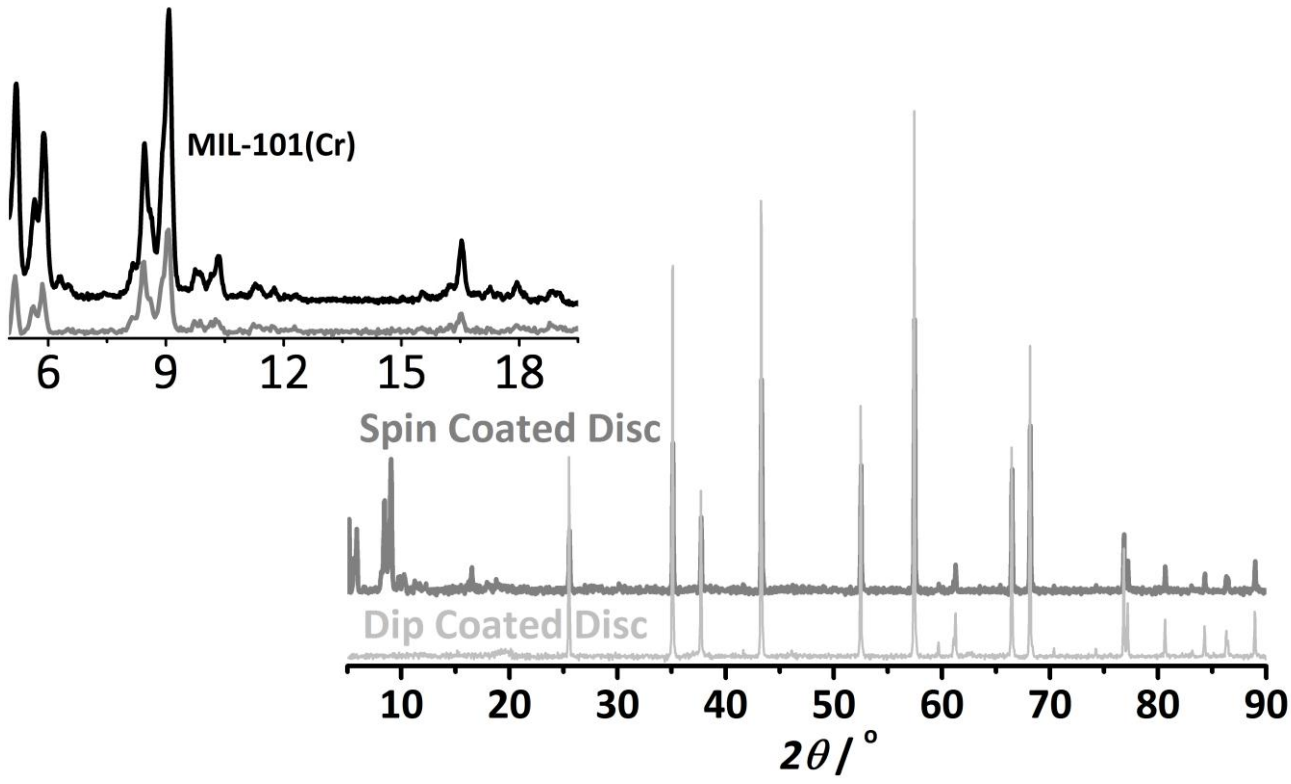

Figure 9 - 5 XRD pattern of discs after secondary growth: dip coated (*light grey*), spin coated (*dark grey*) as well as the MIL–101(Cr) crystal (*black line*).

9.3.2.2. Spin coating

When using spin coating the density of seeds on the support surface is much higher. The fast evaporation of the solvent during spinning leads to an even distribution. Figure 9–4 shows the SEM micrographs of the top view, cross section and the EDS mapping of the samples after the secondary growth. The top view shows a large amount of crystals well distributed all over the support. The EDS mapping of the cross section also shows a high concentration of Cr (yellow dots) over the alumina (Al–red dots). Figure 9–5 displays the XRD pattern of the sample compared with the pristine MIL–101(Cr). The MIL–101(Cr) reflections are narrow and well developed, a clear indication of the good crystallinity of the immobilized crystals. During the secondary growth the presence of nuclei on the support is essential to promote local growth. In the absence of these seeds nucleation on the substrate is not promoted, and mainly takes place in the liquid phase and no coating is formed on the support. In addition, the seeds seem to have a good interaction with the support since no detachment from the surface during secondary growth is observed.

9.3.1. MIL–101(Cr) coated cordierite monoliths

The results obtained on the disc supports indicate that spin coating and a fast evaporation of the solvent produce a good coverage and anchoring of the nanocrystals onto the surface.

In order to simulate a spin coating on the monoliths, a dip coating combined with soaking the monoliths under stirring in a seed solution (similar to the one used for the discs) for 1 h was performed. After that, the monolith was taken out from the solution and dried under vacuum during another hour at room temperature, in order to induce a controlled evaporation of the solvent. Then, the remaining ethanol adsorbed on the monolith is removed in an oven at 373 K.

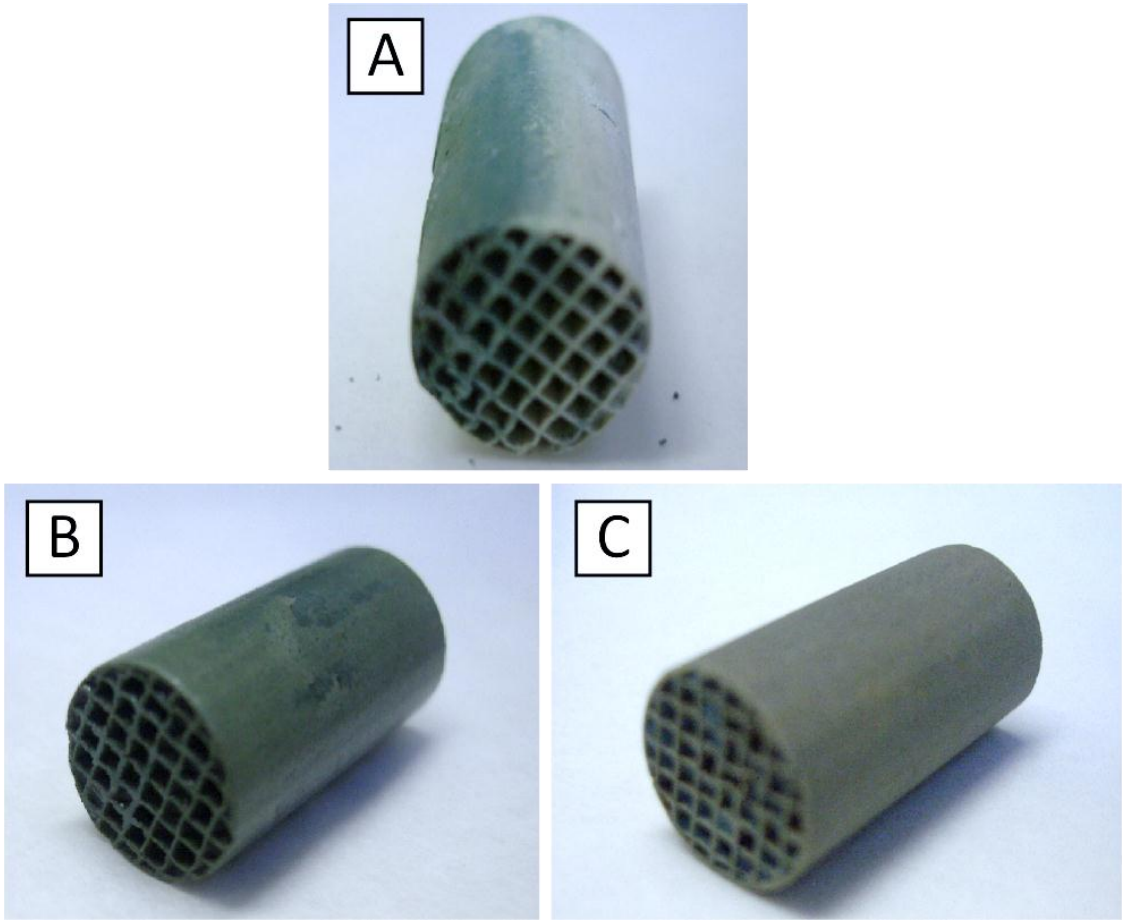

Figure 9 - 6 Images of the coated monolith prepared right after the synthesis. (A) Static synthesis. (B) Rotational synthesis *procedure A*. (C) Rotational synthesis *procedure B*.

The second procedure consisted of coating α–alumina and the MOF crystals together on the cordierite monolith, thereby simulating the application of a washcoat in order to promote that the crystals remain attached to the surface. [39, 41, 44]

These seeded samples were then subjected to a secondary growth approach following the procedure described before. Secondary growth performed in a static autoclave resulted in a non–uniform crystal distribution probably due to a concentration gradient in the synthesis (see Fig. 9–6A). Rotating the autoclave resulted in much more homogeneous coatings (see Fig. 9–6B&C). Synthesis with continuous surface refreshment turned out crucial to obtain homogeneous coatings. Slicing the samples prepared under rotational conditions revealed a homogeneous coating at all channel walls inside the monolith.

9.3.2. Monolith characterization

The presence of MIL–101(Cr) on the monoliths was studied by several techniques. Figure 9–7 shows the Raman spectra of the interior channel wall of the monolith. Similar scatter bands for MIL–101 (Cr) powder and the coated monolith wall are obtained, in good agreement with those reported in literature. [45] Bands at 1612 and 1454 cm^{-1} are associated with C=O and C–O stretching modes of the carboxylates, respectively. The bands at 1143, 866 and 633 cm^{-1} also correspond to the linker.

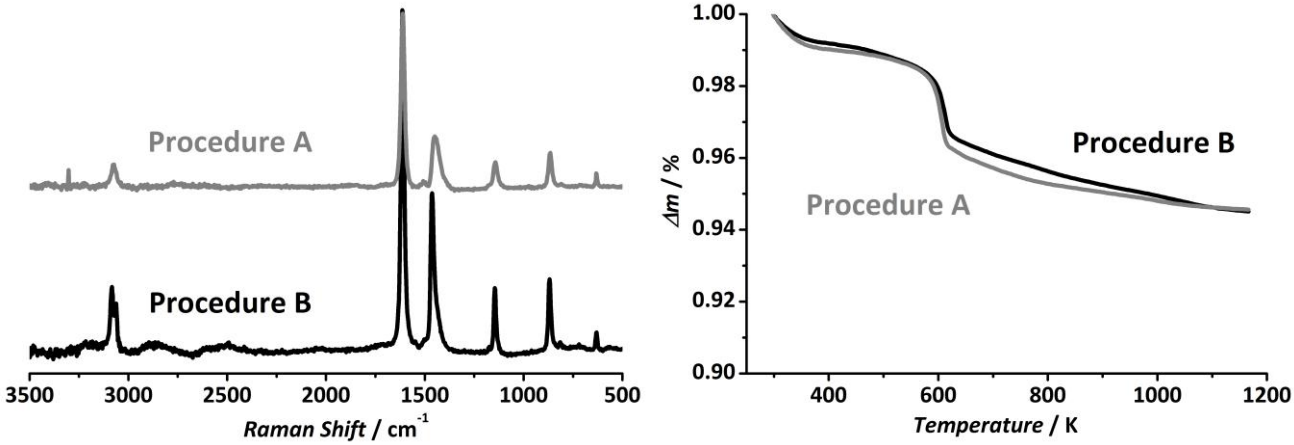

Figure 9 - 7 Raman spectra of the interior monolith channel walls for procedures A (*grey*) B (*black*).

The amount of MIL–101(Cr) immobilized on the monolith was quantified by TGA under an air flow. Figure 9–7 also shows the TG sample profiles obtained following both seeding procedures. These samples exhibit a step decrease corresponding to the linker decomposition of MIL–101(Cr) at around 648 K. After this step there is still a continuous mass decrease until 1073 K that can be assigned to slowly oxidizing carbonaceous residues stemming from decomposition of organic matter of the MOF. The rate of mass loss is proportional to the amount of MOF present in the monolith, resulting in a 9 wt% loading of MIL–101(Cr) for both procedures, a typical loading in catalytic applications. [41] Both synthesis procedures resulted in dense coatings of MIL–101(Cr). However, procedure B is simpler, since only one pre–treatment step is needed: the MIL–101(Cr) seeding is done at the same time as the alumina wash–coating. Therefore, procedure B was chosen as the standard procedure for the preparation of MIL–101 monoliths.

SEM micrographs of a monolith synthesized following procedure B are presented in Figure 9–8. Dense, uniform coatings of ~10 μm sized MIL–101(Cr) crystals are obtained on the channel walls of the monolith. The bipyramidal morphology of the crystals immobilized on the substrate corresponds with the typical crystal shape of the MIL–101(Cr). Furthermore, the crystal distribution is very homogeneous all over the channels. These results demonstrate that a high loading of MIL–101(Cr) can successfully be obtained.

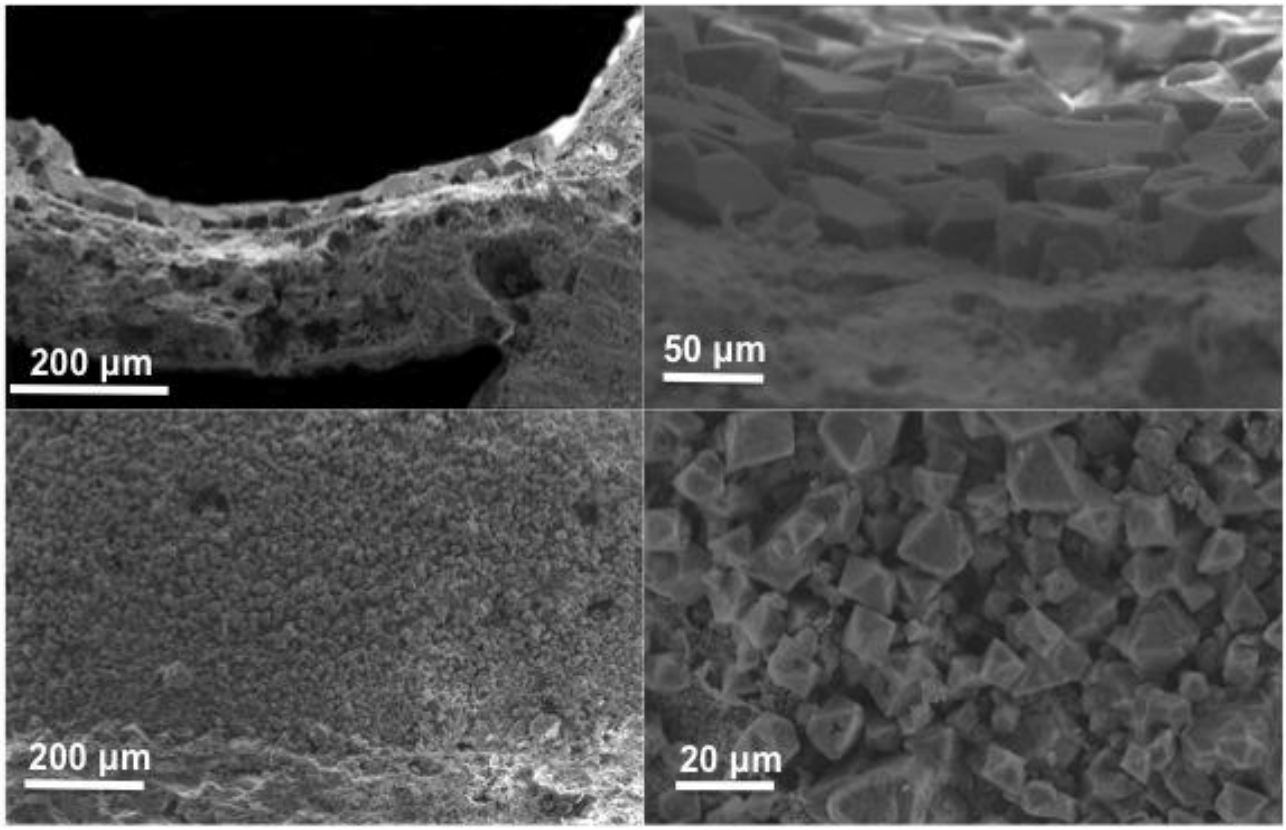

Figure 9 - 8 Cross section of a monolith channel (*top*) and top views of coated wall (*bottom*) at different magnifications for the synthesis procedure B.

9.3.3. Catalytic performance: selective tretralin oxidation

Tetralin oxidation with *t*–butyl hydroperoxide has been chosen as a good model reaction to study the catalytic performance of the monolith and its reusability, since extensive studies have reported on the good oxidation performance of MIL–101(Cr) in slurry operation. [32, 34, 35, 46]

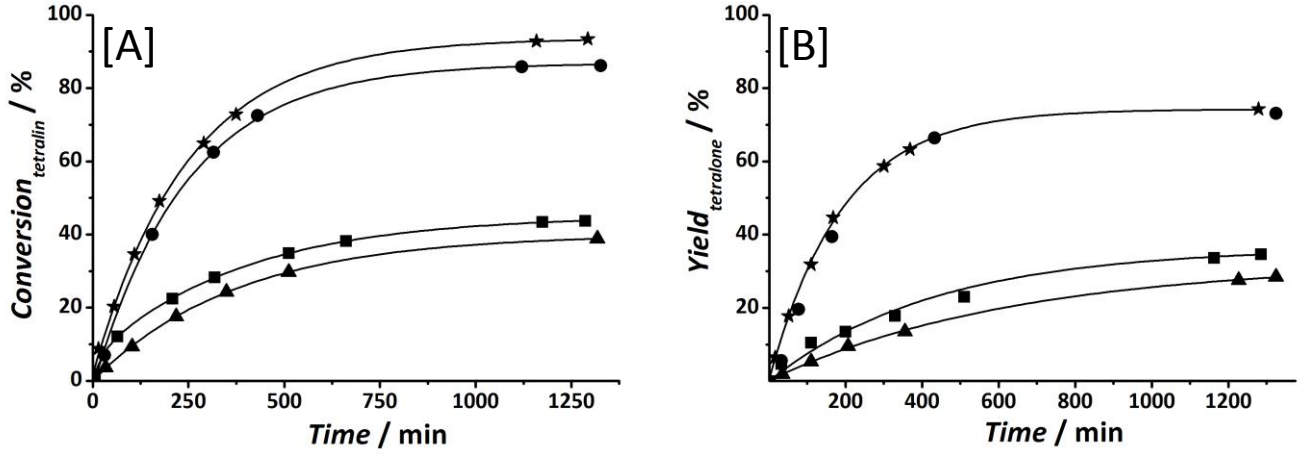

Figure 9 - 9 [A] Tetralin conversion [B] Yield of 1–tetralone. Comparison of MIL–101(Cr) performance in slurry mode (●) and coated on monolith (★). Blank experiments are presented for comparison, Al_2O_3 in the monolith (■), and standard reaction without catalyst (▲). Reaction conditions: 8 mmol tetralin, 16 mmol *t*–BuOOH, 50 mL chlorobenzene, *T* = 353 K, *m(catalyst)* = 50 mg.

Figure 9–9 shows the comparison of the catalytic performance of crystals in a slurry reactor and the performance of the monolithic stirrer reactor for the oxidation of tetralin at 353 K. [32, 47] As reference an α–alumina washcoated monolith (without MOF) was used, while the blank run was performed without solids. The latter two gave similar and low conversion trends, so there is hardly any influence of the monolith and alumina on the reaction. The experiments with the catalysts presented significantly higher activities and selectivity to 1–tetralone. The MIL–101(Cr) coated monolith shows a slightly higher activity than the crystals in the slurry, even though the MIL–101 crystals on the monolith are 10 times larger. The presence of α–alumina or cordierite in the monolith hardly affects the selectivity. Considering the yield towards the desired product 1–tetralone (Fig. 9–9), the catalytic behavior of both crystals and coated monolith is exactly the same. Apparently, the alumina mainly catalyzes some minor formation of undesired products.

Table 9 - 1 Parameter values used for *Carberry* and *Wheeler–Weisz* criterion.

	parameter	value	units
n	order of reaction	1	—
d_p	particle diameter (assumed sphere)	10	μm
a'	$A_p/V_p = 6/d_p$	6.0 E05	m^{-1}
L	$V_p/A_p = d_p/6$	1.67 E–06	M
r_{obs}	initial reaction rate	0.63	mol h^{-1} kg_{MOF}^{-1}
ρ	density MOF	439.7	kg m^{-3}
C_b, C_s	concentration in bulk and surface	—	mol m^{-3}
k_f	mass transfer coefficient $Sh = k_f d_p / D_{iff} \sim 2$	0.002	m s^{-1}
D_{iff}	diffusion coefficient (estimated)	1 E–08	m^2 s^{-1}
D_{eff}	effective diffusion coefficient $D_{eff} = D_{iff} \frac{\varepsilon_t(porosity)}{\tau(tortuosity)} = D_{iff} \frac{0.4}{3}$	1.33 E–09	m^2 s^{-1}

This demonstrates that the catalytic performance of MIL–101(Cr) supported on the monolith does not change with respect to that of the powders. The monolithic stirrer reactor can be viewed then as an immobilized–slurry reactor. The short internal diffusion distances in the washcoat layer in comparison with pellets and the large external surface area of the crystals are retained, but many of the problems of

handling a suspension of the fine catalyst are eliminated: the monoliths are easily recovered from the reaction mixture, while a 20% of the slurry powder was lost in the filtration step.

Table 9 - 2 ***Carberry* number and *Wheeler–Weisz* parameter to verify absence of transport limitations in the MOF crystals supported on the monolithic stirrer reactor.**

	C_o	*Carberry number*	*Wheeler–Weisz parameter*
	[mol m^{-3}]	$Ca = \frac{r_{obs}\,\rho}{a' k_f C_b} < \frac{0.05}{n}$	$\Phi = \eta_i \phi^2 = \frac{r_{obs}\,\rho\,L^2}{D_{eff}\,C_s}\left(\frac{n+1}{2}\right) < 0.15$
tetralin	160	4.01 E–07	1.00 E–06
t–BuOOH	320	2.00 E–07	5.01 E–07

The fact that the performance of the monolith reactor is very similar as that of the slurry reactor, even though crystals on the monolith are one order of magnitude bigger than those of the MIL–101 powder, evidences the good contact between liquid phase and solid in the monolithic reactor and the fast diffusional transport in the crystals. In addition, *Carberry* and *Wheeler–Weisz* parameters satisfy the criterion for the absence of transport limitations in the crystals of the monolithic stirrer reactor.

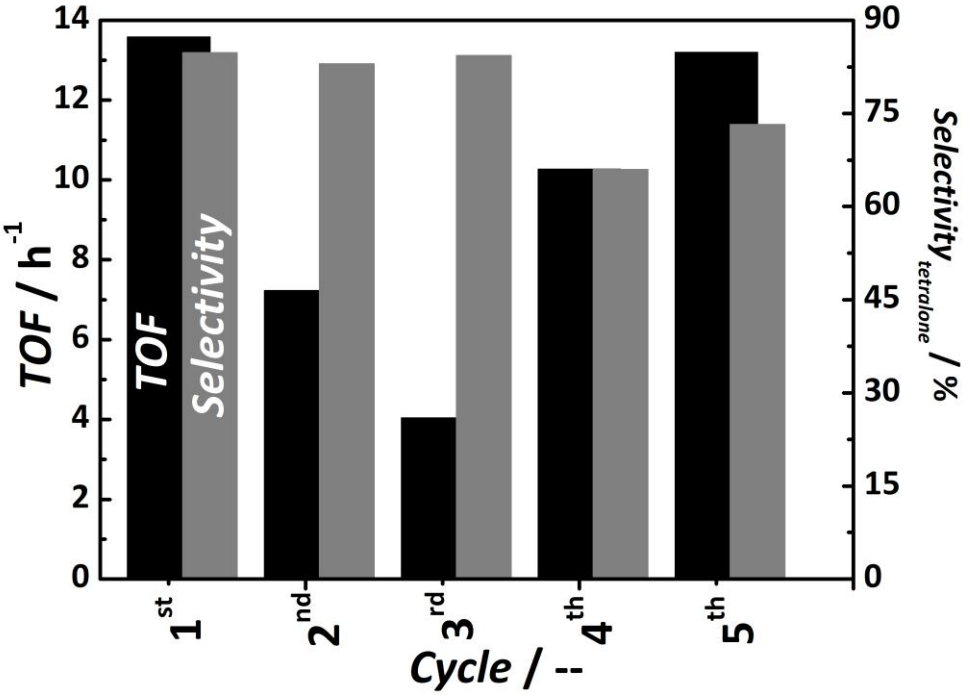

Figure 9 - 10 ***TOF*** **(mol$_{\text{tetralin converted}}$ mol$_{\text{active Cr}}^{-1}$ h^{-1}) and selectivity to 1–tetralone at 90% of conversion for five consecutive runs in the monolithic stirrer reactor after different regeneration procedures (reaction conditions as in Fig. 9–9). Pretreatment: (*1st run*) fresh sample, (*2nd run*) overnight 423 K in air, (*3rd run*) 24 h in boiling chlorobenzene, (*4th run*) as 3rd run plus overnight 473 K in air, (*5th run*) as 3rd run plus overnight 523 K in air.**

Figure 9–10 shows *TOF* values for tetralin conversion after the different regeneration procedures, assuming that 2 out of 3 chromium moles have coordinatively unsaturated sites (CUS) which are responsible for the catalytic behavior (after removal of adsorbed components, usually water). For the reuse of the monolithic stirrer reactor the reactivation and long–term utilization were investigated by a series of consecutive runs. Regeneration of the coated catalyst is needed due to strong adsorption of products on the active sites, which consists of applying pre–treatments of increasing severity, mainly based on washing in boiling organic solvents (chlorobenzene) and varying the temperature of the treatment in air (423–523 K).

Washing in boiling chlorobenzene together with overnight treatment in air at 523 K led to the full regeneration of the catalyst, although a slightly lower overall selectivity to 1–tetralone was obtained in the fifth run, caused by a possible generation of defects that are more active but less selective. These results point out the importance of the regeneration step in MOFs with open metal sites (*TOF* values might be reduced to half) and demonstrates the stability of MIL–101(Cr) upon regeneration between catalytic cycles. The presented results on the coated monolithic stirrer reactor indicate the beginning for potential industrial applications of catalysis with MOFs avoiding important problems like regeneration and attrition. [36]

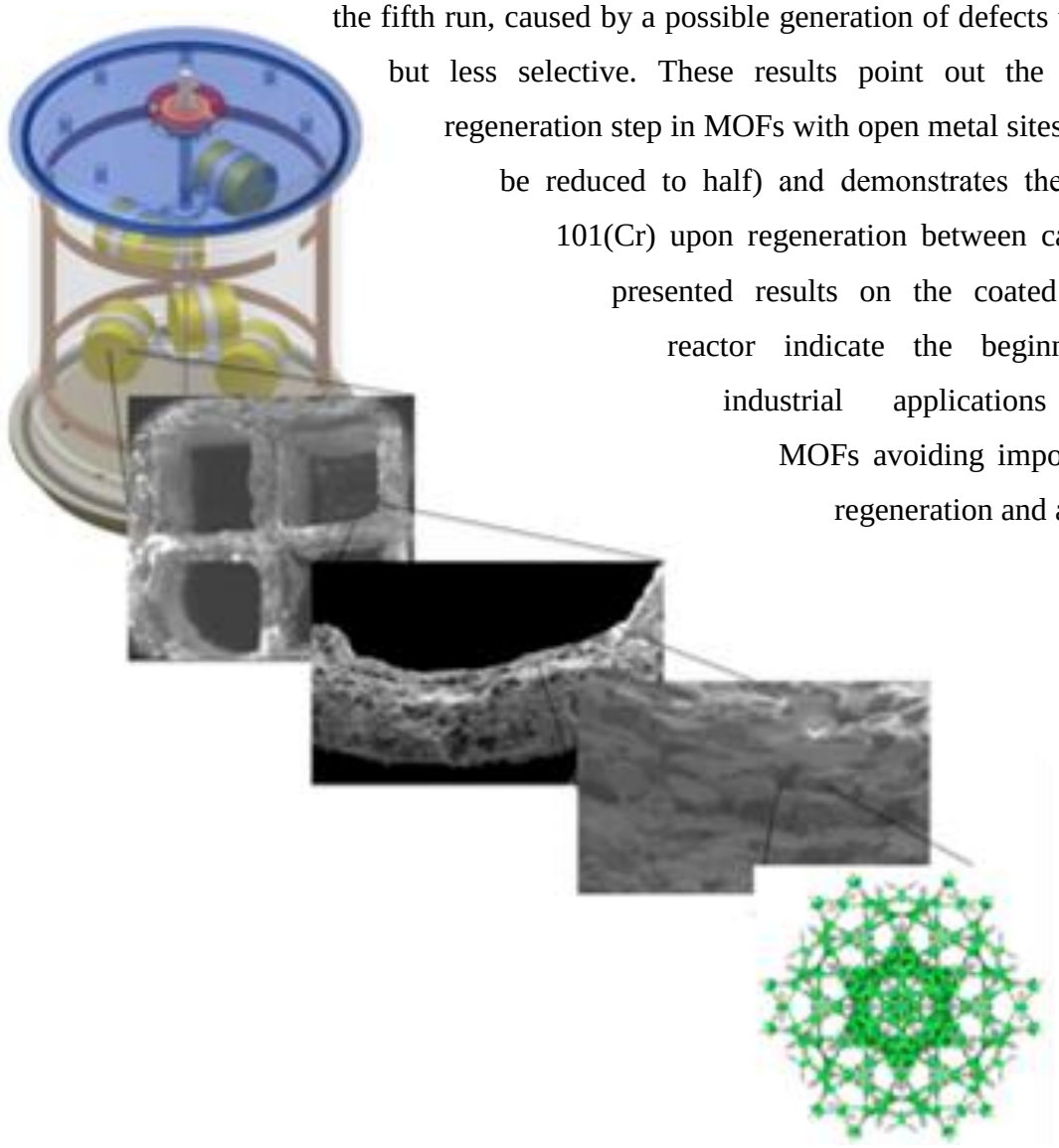

Figure 9 - 11 Overview of the monolithic stirrer reactor zoomed at the coated crystals of MIL–101(Cr) and the representation of one of the MOF cages.

9.4. CONCLUSION

The catalytic performance of MIL–101(Cr) immobilized on a monolith structure has been presented. A monolithic stirrer reactor has been used as playground for exploring reusability of MIL–101 during the liquid phase selective oxidation of tetralin. The presented results confirm the long–term stability of the catalyst and the absence of any transport limitations.

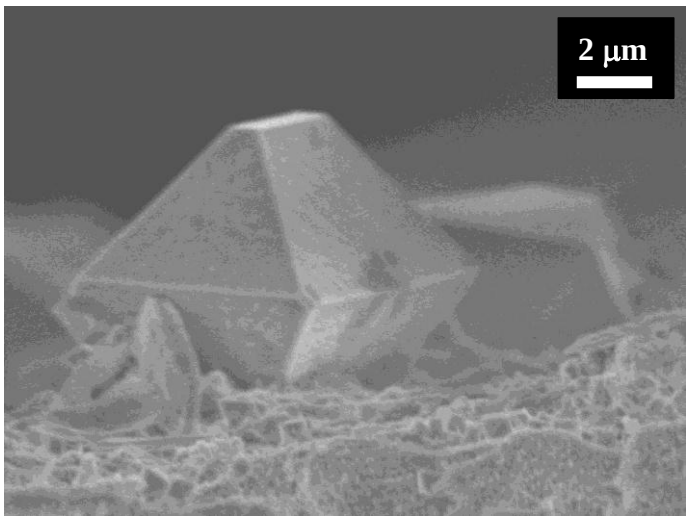

Figure 9 - 12 MIL–101(Cr) crystals on the surface of the monolithic support

The easy recovery of the catalyst allows performing as many reuses as necessary, something impossible to realize when working in the often–practiced slurry operation mode. The reported results demonstrate that MIL–101(Cr) undergoes reversible deactivation attributed to the strong adsorption of products on the Cr sites. Applying the proper regeneration procedure the initial performance is fully recovered. Regarding the synthesis of the supported MOF, it has been shown that the secondary growth approach is the most adequate to obtain uniform, dense coatings of this catalytic material in the monolith channels. The seeding step and the size of the seeds used are the critical elements in this process.

REFERENCES

[1] M.P. Suh, H.J. Park, T.K. Prasad, D.-W. Lim, Hydrogen storage in metal-organic frameworks, Chemical Reviews, 112 (2011) 782-835.
[2] A. Corma, H. García, F.X. Llabrés i Xamena, Engineering metal-organic frameworks for heterogeneous catalysis, Chemical Reviews, 110 (2010) 4606-4655.
[3] A. Fateeva, P.A. Chater, C.P. Ireland, A.A. Tahir, Y.Z. Khimyak, P.V. Wiper, J.R. Darwent, M.J. Rosseinsky, A water-stable porphyrin-based metal-organic framework active for visible-light photocatalysis, Angewandte Chemie - International Edition, 51 (2012) 7440-7444.
[4] M. Arnold, P. Kortunov, D.J. Jones, Y. Nedellec, J. Kärger, J. Caro, Oriented crystallisation on supports and anisotropic mass transport of the metal-organic framework manganese formate, European Journal of Inorganic Chemistry, (2007) 60-64.
[5] M. Shah, M.C. McCarthy, S. Sachdeva, A.K. Lee, H.K. Jeong, Current status of metal-organic framework membranes for gas separations: Promises and challenges, Industrial and Engineering Chemistry Research, 51 (2012) 2179-2199.
[6] Z.-Y. Gu, C.-X. Yang, N. Chang, X.-P. Yan, Metal-organic frameworks for analytical chemistry: from sample collection to chromatographic separation, Accounts of Chemical Research, 45 (2012) 734-745.
[7] Z.Y. Gu, X.P. Yan, Metal-organic framework MIL-101 for high-resolution gaschromatographic separation of xylene isomers and ethylbenzene, Angewandte Chemie - International Edition, 49 (2010) 1477-1480.
[8] L.E. Kreno, K. Leong, O.K. Farha, M. Allendorf, R.P. Van Duyne, J.T. Hupp, Metal-organic framework materials as chemical sensors, Chemical Reviews, 112 (2011) 1105-1125.
[9] N. Stock, S. Biswas, Synthesis of metal-organic frameworks (MOFs): Routes to various MOF topologies, morphologies, and composites, Chemical Reviews, 112 (2012) 933-969.
[10] A. Bétard, R.A. Fischer, Metal-organic framework thin films: from fundamentals to applications, Chemical Reviews, 112 (2011) 1055-1083.
[11] E.A. Flugel, A. Ranft, F. Haase, B.V. Lotsch, Synthetic routes toward MOF nanomorphologies, Journal of Materials Chemistry, 22 (2012) 10119-10133.
[12] D. Bradshaw, A. Garai, J. Huo, Metal-organic framework growth at functional interfaces: Thin films and composites for diverse applications, Chemical Society Reviews, 41 (2012) 2344-2381.
[13] J. Gascon, F. Kapteijn, B. Zornoza, V. Sebastián, C. Casado, J. Coronas, Practical approach to zeolitic membranes and coatings: State of the art, opportunities, barriers, and future perspectives, Chemistry of Materials, 24 (2012) 2829-2844.
[14] C. Munuera, O. Shekhah, H. Wang, C. Wöll, C. Ocal, The controlled growth of oriented metal-organic frameworks on functionalized surfaces as followed by scanning force microscopy, Physical Chemistry Chemical Physics, 10 (2008) 7257-7261.
[15] S. Hermes, F. Schröder, R. Chelmowski, C. Wöll, R.A. Fischer, Selective nucleation and growth of metal-organic open framework thin films on patterned $COOH/CF_3$-terminated self-assembled monolayers on Au(111), Journal of the American Chemical Society, 127 (2005) 13744-13745.
[16] O. Shekhah, K. Hirai, H. Wang, H. Uehara, M. Kondo, S. Diring, D. Zacher, R.A. Fischer, O. Sakata, S. Kitagawa, S. Furukawa, C. Wöll, MOF-on-MOF heteroepitaxy: Perfectly oriented $[Zn_2(ndc)_2(dabco)]_n$ grown on $[Cu_2(ndc)_2(dabco)]_n$ thin films, Dalton Transactions, 40 (2011) 4954-4958.
[17] B. Liu, O. Shekhah, H.K. Arslan, J. Liu, C. Wöll, R.A. Fischer, Enantiopure metal-organic framework thin films: Oriented SURMOF growth and enantioselective adsorption, Angewandte Chemie - International Edition, 51 (2012) 807-810.
[18] J. Yao, D. Dong, D. Li, L. He, G. Xu, H. Wang, Contra-diffusion synthesis of ZIF-8 films on a polymer substrate, Chemical Communications, 47 (2011) 2559-2561.
[19] A. Huang, F. Liang, F. Steinbach, J. Caro, Preparation and separation properties of LTA membranes by using 3-aminopropyltriethoxysilane as covalent linker, Journal of Membrane Science, 350 (2010) 5-9.
[20] A. Huang, W. Dou, J. Caro, Steam-stable zeolitic imidazolate framework ZIF-90 membrane with hydrogen selectivity through covalent functionalization, Journal of the American Chemical Society, 132 (2010) 15562-15564.
[21] J. Gascon, S. Aguado, F. Kapteijn, Manufacture of dense coatings of $Cu_3(btc)_2$ (HKUST-1) on α-alumina, Microporous and Mesoporous Materials, 113 (2008) 132-138.
[22] V.V. Guerrero, Y. Yoo, M.C. McCarthy, H.K. Jeong, HKUST-1 membranes on porous supports using secondary growth, Journal of Materials Chemistry, 20 (2010) 3938-3943.
[23] Y. Hu, X. Dong, J. Nan, W. Jin, X. Ren, N. Xu, Y.M. Lee, Metal-organic framework membranes fabricated via reactive seeding, Chemical Communications, 47 (2011) 737-739.
[24] Y.S. Li, F.Y. Liang, H. Bux, A. Feldhoff, W.S. Yang, J. Caro, Molecular sieve membrane: Supported metal-organic framework with high hydrogen selectivity, Angewandte Chemie - International Edition, 49 (2010) 548-551.
[25] H. Bux, F. Liang, Y. Li, J. Cravillon, M. Wiebcke, J. Caro, Zeolitic imidazolate framework membrane with molecular sieving properties by microwave-assisted solvothermal synthesis, Journal of the American Chemical Society, 131 (2009) 16000-16001.

[26] A. Sachse, R. Ameloot, B. Coq, F. Fajula, B. Coasne, D. De Vos, A. Galarneau, *In situ* synthesis of Cu-btc (HKUST-1) in macro-/mesoporous silica monoliths for continuous flow catalysis, Chemical Communications, 48 (2012) 4749-4751.
[27] S. Aguado, J. Canivet, Y. Schuurman, D. Farrusseng, Tuning the activity by controlling the wettability of MOF eggshell catalysts: A quantitative structure-activity study, Journal of Catalysis, 284 (2011) 207-214.
[28] S.E. Dapurkar, H. Kawanami, T. Yokoyama, Y. Ikushima, Highly selective oxidation of tetralin to 1-tetralone over mesoporous CrMCM-41 molecular sieve catalyst using supercritical carbon dioxide, New Journal of Chemistry, 33 (2009) 538-544.
[29] J. Muzart, Chromium-catalyzed oxidations in organic synthesis, Chemical Reviews, 92 (1992) 113-140.
[30] R.A. Shaikh, G. Chandrasekar, K. Biswas, J.-S. Choi, W.-J. Son, S.-Y. Jeong, W.-S. Ahn, Tetralin oxidation over chromium-containing molecular sieve catalysts, Catalysis Today, 132 (2008) 52-57.
[31] N.I. Kuznetsova, L.I. Kuznetsova, V.A. Likholobov, Catalytic properties of Cr-containing heteropolytungstates in H_2O_2 participated reactions: H_2O_2 decomposition and oxidation of unsaturated hydrocarbons with H_2O_2, Journal of Molecular Catalysis A: Chemical, 108 (1996) 135-143.
[32] J. Kim, S. Bhattacharjee, K.E. Jeong, S.Y. Jeong, W.S. Ahn, Selective oxidation of tetralin over a chromium terephthalate metal organic framework, MIL-101, Chemical Communications, (2009) 3904-3906.
[33] N.V. Maksimchuk, K.A. Kovalenko, V.P. Fedin, O.A. Kholdeeva, Heterogeneous selective oxidation of alkenes to α,β-unsaturated ketones over coordination polymer MIL-101, Advanced Synthesis and Catalysis, 352 (2010) 2943-2948.
[34] N.V. Maksimchuk, K.A. Kovalenko, V.P. Fedin, O.A. Kholdeeva, Cyclohexane selective oxidation over metal-organic frameworks of MIL-101 family: superior catalytic activity and selectivity, Chemical Communications, 48 (2012) 6812-6814.
[35] Y.K. Hwang, D.Y. Hong, J.S. Chang, H. Seo, M. Yoon, J. Kim, S.H. Jhung, C. Serre, G. Férey, Selective sulfoxidation of aryl sulfides by coordinatively unsaturated metal centers in chromium carboxylate MIL-101, Applied Catalysis A: General, 358 (2009) 249-253.
[36] J. Gascon, U. Aktay, M.D. Hernandez-Alonso, G.P.M. van Klink, F. Kapteijn, Amino-based metal-organic frameworks as stable, highly active basic catalysts, Journal of Catalysis, 261 (2009) 75-87.
[37] C. Férey, C. Mellot-Draznieks, C. Serre, F. Millange, J. Dutour, S. Surblé, I. Margiolaki, Chemistry: A chromium terephthalate-based solid with unusually large pore volumes and surface area, Science, 309 (2005) 2040-2042.
[38] S.H. Jhung, J.H. Lee, J.W. Yoon, C. Serre, G. Férey, J.S. Chang, Microwave synthesis of chromium terephthalate MIL-101 and its benzene sorption ability, Advanced Materials, 19 (2007) 121-124.
[39] A.F. Pérez-Cadenas, F. Kapteijn, J.A. Moulijn, Tuning the morphology of monolith coatings, Applied Catalysis A: General, 319 (2007) 267-271.
[40] S. Aguado, J. Canivet, D. Farrusseng, Engineering structured MOF at nano and macroscales for catalysis and separation, Journal of Materials Chemistry, 21 (2011) 7582-7588.
[41] T.A. Nijhuis, A.E.W. Beers, T. Vergunst, I. Hoek, F. Kapteijn, J.A. Moulijn, Preparation of monolithic catalysts, Catalysis Reviews - Science and Engineering, 43 (2001) 345-380.
[42] A.F. Pérez-Cadenas, M.M.P. Zieverink, F. Kapteijn, J.A. Moulijn, High performance monolithic catalysts for hydrogenation reactions, Catalysis Today, 105 (2005) 623-628.
[43] M.C. McCarthy, V. Varela-Guerrero, G.V. Barnett, H.K. Jeong, Synthesis of zeolitic imidazolate framework films and membranes with controlled microstructures, Langmuir, 26 (2010) 14636-14641.
[44] J.A. Moulijn, M.T. Kreutzer, T.A. Nijhuis, F. Kapteijn, Monolithic Catalysts and Reactors. High Precision with Low Energy Consumption, in, 2011, pp. 249-327.
[45] J. Juan-Alcañiz, E.V. Ramos-Fernandez, U. Lafont, J. Gascon, F. Kapteijn, Building MOF bottles around phosphotungstic acid ships: One-pot synthesis of bi-functional polyoxometalate-MIL-101 catalysts, Journal of Catalysis, 269 (2010) 229-241.
[46] Z. Saedi, S. Tangestaninejad, M. Moghadam, V. Mirkhani, I. Mohammadpoor-Baltork, MIL-101 metal-organic framework: A highly efficient heterogeneous catalyst for oxidative cleavage of alkenes with H_2O_2, Catalysis Communications, 17 (2012) 18-22.
[47] K.M. De Lathouder, T.M. Fló, F. Kapteijn, J.A. Moulijn, A novel structured bioreactor: Development of a monolithic stirrer reactor with immobilized lipase, Catalysis Today, 105 (2005) 443-447.

Summary

This thesis primarily focuses on the development of new approaches for the incorporation of catalytic functionalities in MOFs and their use as heterogeneous catalysts. Therefore, **Chapter 1** gives a general introduction about the concept of metal–organic frameworks, and reviews extensively the most interesting approaches for the functionalization of MOFs towards catalysts.

In **Chapter 2**, a new strategy has been developed for the direct encapsulation of polyoxometalates (POMs) into MIL–101(Cr). The addition of phosphotungstic acid (PTA) to the synthesis mixture of MIL–101 yields the direct encapsulation and good distribution of PTA over the MOF crystals. X–ray diffraction ensures the formation of the right MOF structure despite the POM presence. ICP–OES and TGA demonstrate the presence of PTA in the sample, while vibrational spectroscopy (DRIFT, Raman, UV–Vis) reveals the structural changes after washing with NH_4F. When this one–pot approach is followed, POM units not only occupy the large cages of MIL–101 (similar to impregnation procedures) but also medium–sized cavities are filled, with pentagonal windows smaller than PTA. These new catalysts show the highest activities reported to date at 313 K for the Knoevenagel condensation of benzaldehyde with ethyl cyanoacetate when using apolar toluene as solvent, as well as, when using polar DMF and ethanol, with TOFs exceeding 900 h^{-1}. In contrast, poor or absent activity was found from the catalysts prepared via the impregnation of the polyoxometalate in MIL–101, where the agglomeration of the POM only on the large cages deteriorates the catalytic performance. In addition, the systems exhibit a remarkable activity in two acid–catalyzed reactions, the esterification of 1–butanol with acetic acid in liquid phase slurry operation and the dimethyl ether production from methanol in a fixed bed gas phase operation. The strong interaction between the guest species and the MOF host, however, deteriorates the acidic properties of the encapsulated polyoxometalates. No leaching is observed.

Chapter 3 investigates the templating effect of PTA during the synthesis of NH_2–MIL–101(Al) by means of *in situ* small– and wide–angle X–Ray scattering (SAXS/WAXS). Efficient PTA encapsulation has been observed upon crystallization. The WAXS range displays attenuation of specific diffraction peaks associated with the entrapped PTA molecules in the medium and large cages of this MOF. In addition, the performance of PTA as a nucleation site has been unraveled, leading to a complete model for the encapsulation mechanism. Initial time evolution at the SAXS regime suggests both surface and mass fractal substance when PTA is present, while smooth surface morphology is observed for bare NH_2–MIL–101(Al). Stabilization of the intermediate precursor phase NH_2–MOF–

235(Al) is the initial step of the encapsulation process, since low temperature synthesis with PTA leads to the formation of only the intermediate phase. In contrast, in the absence of PTA, NH_2–MIL–101(Al) is the only product under the same reaction conditions. Kinetics of growth and nucleation have been determined in the presence and absence of PTA, and surprisingly little differences have been found.

The effect of synthesis conditions in the one–pot encapsulation of PTA in MIL–100(Cr) has been studied in **Chapter 4**. Both conventional and microwave heating methods have been explored in three different solvent systems: pure aqueous or organic (DMF) phase and biphasic mixtures (water/2–pentanol). Biphasic systems yielded crystals with similar textural properties as those formed in water. The use of DMF as solvent promotes the formation of gel–like solids with dual porosity and enhanced accessibility. The addition of PTA to the MIL–100(Cr) synthesis mixture results in its direct encapsulation, confirmed by ^{31}P MAS NMR, elemental analysis, N_2 adsorption and DRIFT analysis, while PTA loadings has been tuned by modifying initial concentrations in the reaction mixture to obtain 15 and 30 wt%. The best combination for PTA/MIL–100(Cr) formation was obtained under microwave irradiation in the biphasic solvent. Microwave irradiation decreases the time of synthesis (from 4 days to 3 hours) while the use of biphasic media preserves PTA's integrity without affecting the MOF structure formation. The interaction of PTA with MIL–100(Cr) results in a loss of framework Lewis acidity, while the Brønsted acidity of the MOF structure is hardly affected. Although PTA is considered as a super Brønsted acid molecule, after encapsulation in MIL–100(Cr) hardly any additional acidity is observed.

The synthesis, characterization (FT–IR, XPS, NMR, UV–Vis), and catalytic performance of Pt supported on PTA/NH_2–MIL–101(Al) materials has been explored in **Chapter 5**. The highly dispersed PTA units encapsulated in NH_2–MIL–101(Al) cages by one–pot synthesis, act as anchoring sites for the Pt precursor. After different post–treatments, the performance of the resulting catalysts has been tested in the oxidation of CO, the preferential CO oxidation in the presence of H_2, and in the hydrogenation of toluene. Reduction at 473 K results in the formation of both small Pt^0 clusters and Pt^{2+} species. Reduction at 573 K induces the formation of intermetallic Pt–W^{5+} species, which exhibit the best CO oxidation activity and in the presence of H_2 a higher selectivity towards CO_2 than Pt supported on alumina, resembling the combination of a noble metal on a reducible support. In toluene hydrogenation, the MOF catalysts perform worse than Pt on alumina, which is ascribed to the very small size of the Pt ensembles formed in the MOF catalysts.

Chapter 6 explores the inclusion of free sulfonic acid groups in, *a priori*, highly stable MOFs and their application as heterogeneous catalysts in a model esterification reaction. Two metal organic frameworks bearing sulfonic acid moieties are investigated: HSO_3–MIL–101(Cr) synthesized

following different approaches and a new, not yet resolved structure, based on HSO_3–BDC and Zr. The acidic properties, catalytic performance, deactivation and stability of the different structures is critically evaluated. In case of MIL–101(Cr), deactivation of the sulfonic acid groups via formation of butyl sulfonic esters has been observed. Due to the strong interaction between $–SO_3^-$ and the Cr open metal site where usually fluoride is located in the structure, the HSO_3–MIL–101(Cr) catalysts are not stable under acidic regeneration conditions. When using Zr as metal node, a new and stable sulfonic acid containing porous structure was synthesized. This structure showed high activity and full re–usability in the esterification of 1–butanol with acetic acid. In this case, deactivation of the catalyst due to sulfonic ester formation could be reversed by reactivation under acidic conditions.

Chapter 7 illustrates the development of a new post–functionalization method to introduce acidity in several MOFs for their use in catalysis. Upon treatment with a mixture of triflic anhydride and sulfuric acid, chemically stable MOF structures MIL–101(Cr) and MIL–53(Al) can be sulfated, resulting in a Brønsted hydrogen sulfate group attached to, up to 20 and 50% of the aromatic terephthalate linkers of the structure, respectively. The sulfated samples have been extensively characterized by MAS NMR, XANES, and FTIR spectroscopy. The functionalized acidic frameworks show catalytic activity similar to that of acidic polymers like Nafion® NR50 in the esterification of 1–butanol with acetic acid (*TOF* ~ 1.75 min^{-1} @ 343 K). Water adsorbs strongly up to 4 molecules per sulfoxy acid group, and an additional 2 molecules are taken up at lower temperatures in the 1D pore channels of sulfated MIL–53(Al). The high water content and Brønsted acidity provide the sulfated MIL–53(Al) structure with elevated proton conductivity up to moderate temperatures.

Chapter 8 presents the results of a new consecutive pre– and post– functionalization approach for the coordination of catalytically active metals in MIL–101(Cr) through oxamate complexation. The starting MOF, NO_2–MIL–101(Cr) was successfully synthesized in short periods (8 h) under acidic conditions. In a first post–synthesis step, Sn_2Cl reduction of the NO_2 moieties leads to the formation of NH_2–MIL–101(Cr). The second functionalization step consists of a straightforward condensation of the amino groups of the ligand with ethyl chloro–oxoacetate resulting in free oxamate groups attached to the linker. Two different copper complexes have been coordinated through the oxamate ligand, attaining loadings as high as 9 wt% and showing similar performance as previously reported copper MOFs (HKUST–1, [Cu(2–pymo)$_2$] and [Cu(im)$_2$]) in "click chemistry" catalysis (1,3–dipolar cycloaddition reactions) and multicomponent coupling reactions (propargylamine formation). Palladium and gold in a highly dispersed form can be incorporated and stabilized by the oxamate ligand. The resultant catalysts are very active and selective in the Suzuki–Miyaura condensation and in the oxidation of benzyl alcohol (BA), respectively. However, palladium leaching is observed. After

reduction, immobilized gold nanoparticles are formed, that maintain a good performance in BA oxidation to benzaldehyde for at least 4 consecutive runs. No side reactions (hydrolysis) are observed, attributed to the absence of any cationic gold species. TEM analysis and DRIFTS analysis of CO adsorption show the very uniform size of ~2 nm, similar as the cage size, and the metallic character of these gold particles, encapsulated in the MIL–101 cages.

Structuring heterogeneous catalysts from the nano– to the macro–level is essential for efficient catalyst utilization. Therefore, the optimized synthesis and the catalytic performance of MIL–101(Cr) immobilized on a monolithic structure are presented in **Chapter 9**. Secondary seeded growth is the optimal procedure to obtain uniform coatings of ~9 wt% inside the monolith channels. A monolithic stirrer reactor has been used as playground for exploring the catalytic performance of MIL–101(Cr) in the liquid phase of selective tretralin oxidation, with *TOF* values around 4.5 h^{-1} and 75% selectivity to 1–tetralone. The presented results confirm the stability of the catalyst and coating, and the absence of any transport limitations in this reaction (*Ca* and Φ criteria). The easy recovery of the catalyst allows simple reusability, something impossible to realize when working in the often–practiced slurry operation mode. The reported results demonstrate that MIL–101(Cr) undergoes reversible deactivation attributed to the relatively strong adsorption of products on the Cr sites. Applying the proper regeneration procedure (washing in chlorobenzene and air treatment @ 523 K) the initial performance is fully recovered.

In retrospect, these results confirm the successful development of catalytic functionalities in MOFs to transform them into catalysts. Several approaches have been successfully implemented for the incorporation of catalytically active functionalities in the MOF structures, namely (*i*) coordinatively unsaturated sites in metal clusters, (*ii*) pre– and post– functionalization of the organic MOF linkers, and (*iii*) encapsulation of active guest species like polyoxometalates and nanoparticles. This work provides elements for the foreseen further development of multi–functional MOF catalysts. And last but not least, this research emphasises the necessity to engineer MOF catalysts from the nano– to the macro–scale, where structured supports should be used as fixed bed reactors instead of slurry reactors to industrially apply MOF structures.

Samenvatting

Dit proefschrift richt zich primair op de ontwikkeling van nieuwe benaderingen om katalytische functionaliteiten in te bouwen in MOFs (metal–organic frameworks) en deze te gebruiken als heterogene katalysatoren. In **Hoofdstuk 1** wordt daarom een algemene inleiding gegeven in het onderwerp van MOFs en een overzicht van de meest interessante benaderingen om MOFs te functionaliseren naar katalysatoren.

In **Hoofdstuk 2** is een nieuwe strategie ontwikkeld om heteropolyzuren (HPA's) in te bouwen in MIL–101(Cr). Toevoegen van het heteropolyzuur van fosfor–wolfraam (phosphotungstic acid, PTA) aan het synthese mengsel resulteert in de directe inkapseling van PTA én een goede verdeling over de MOF kristallen. Røntgen diffractie (XRD) bevestigt de vorming van de juiste MOF structuur ondanks de aanwezigheid van PTA. Element analyse met ICP–OES en thermogravimetrische analyse (TGA) bevestigen de aanwezigheid van PTA in het monster, terwijl vibratie spectroscopie (DRIFT, Raman, UV–Vis) structuurveranderingen laat zien na wassen met NH_4F.

Na deze één–pots–synthese bezetten de PTA moleculen niet alleen de grote kooien in de structuur van MIL–101 (zoals na impregnatie verkregen wordt), maar zijn ook aanwezig in de middelgrote kooien die vijf–ringstoegangsopeningen hebben kleiner dan PTA.

Deze nieuwe katalysatoren vertonen de hoogste activiteiten ooit gerapporteerd bij 313 K in de Knoevenagel condensatie van benzaldehyde met ethylcyanoacetaat in tolueen als apolair oplosmiddel, maar ook in het polaire dimethylformamide (DMF) en ethanol, met turn–over frequencies (*TOFs*) groter dan 900 h^{-1}. Katalysatoren bereid via impregnatie van PTA in MIL–101 hebben daarentegen een lage of geheel afwezige activiteit. Agglomeratie van PTA in de grote kooien verknoeit de katalytische activiteit. Verder vertonen de één–pots katalysatoren een opmerkelijke activiteit in twee zuur-gekatalyseerde reacties, de verestering van 1–butanol met azijnzuur in een slurry operatie en de vorming van dimethylether (DME) uit methanol in een vast-bed gasfase operatie. De sterke interactie tussen de gast–species en de MOF gastheer leidt echter tot een sterke vemindering van de zure eigenschappen van de PTA. Uitloging van PTA is niet waargenomen.

In **Hoofdstuk 3** wordt het effect van PTA als mal (templaat) op de synthese van NH_2–MIL–101(Al) bestudeerd door middel van *in situ* small– and wide–angle X–Ray scattering (SAXS/WAXS). Tijdens kristallisatie wordt een efficiënte inkapseling van PTA waargenomen. In WAXS wordt de waargenomen vermindering van de diffractie intensiteit geassocieerd met de ingekapselde PTA moleculen in de grote en middelgrote kooien van deze MOF. PTA gedraagt zich als een nucleatiekern voor de MOF, wat de inkapseling verklaart. De SAXS metingen suggereren dat in het begin van de

synthese en in aanwezigheid van PTA fractale oppervlakte- en bulkstructuren aanwezig zijn, terwijl in afwezigheid van PTA een gladde oppervlakte morfologie waargenomen wordt voor NH_2–MIL–101(Al). De eerste stap in het inkapselingsproces is de stabilisering van een intermediaire precursor fase NH_2–MOF–235(Al), aangezien bij lagere temperatuur alleen deze fase wordt gevormd in aanwezigheid van PTA. In afwezigheid van PTA is NH_2–MIL–101(Al) het enige product dat gevormd wordt onder dezelfde reactiecondities. De nucleatie- en groeikinetiek van de MOF zijn bepaald voor aan– en afwezigheid van PTA. Verrassenderwijs zijn er weinig verschillen gevonden.

De invloed van de synthesecondities op de één-pots inkapseling van PTA in MIL–100(Cr) is beschreven in **Hoofdstuk 4**. Zowel conventionele als magnetron verwarming is onderzocht voor drie oplosmiddelsystemen: puur water of een organisch (DMF) oplosmiddel en twee–fasige mengsels (water/2–pentanol). Twee-fasige systemen leverden kristallen op met dezelfde textuureigenschappen als de synthese in water.

Het gebruik van DMF als oplosmiddel stimuleert de vorming van gel-achtige materialen met een bimodale porositeit en betere toegankelijkheid. Toevoegen van PTA aan het MIL–100(Cr) synthese mengsel geeft direct inkapseling, wat bevestigd is met ^{31}P MAS NMR, element analyse, N_2 adsorptie and DRIFTS analyse. Door variatie van de beginconcentratie in het reactiemengsel konden PTA beladingen van 15 en 30 gewichts% bereikt worden. De beste combinatie voor PTA/MIL–100(Cr) vorming werd gevonden voor een tweefasig oplosmiddel en magnetron opwarming. Magnetron opwarming verkort de syntheseduur (van 4 dagen tot 3 uur), terwijl in het tweefasige oplosmiddel de integriteit van het PTA behouden blijft en de vorming van de MOF structuur niet beïnvloed wordt. De interactie van PTA met MIL–100(Cr) resulteert in het verlies van de Lewis zure eigenschappen van de MOF, terwijl de Brønsted zure eigenschappen nauwelijks veranderen. PTA wordt als een super Brønsted zuur beschouwd, maar na inkapseling wordt nauwelijks enige toename van de zure eigenschappen van MIL–100(Cr) gevonden.

De synthese, karakterisering (FT–IR, XPS, NMR, UV–Vis) en katalytische eigenschappen van Pt op PTA/NH_2–MIL–101(Al) zijn onderzocht in **Hoofdstuk 5**. De hoog–disperse PTA in de NH_2–MIL–101(Al) kooien, verkregen via één–pots synthese, is een uitstekende verankeringsplaats voor de Pt–precursor. Na verschillende nabehandelingen zijn de resulterende katalysatoren onderzocht op hun gedrag in the oxidatie van CO, de selectieve oxidatie van CO in de aanwezigheid van H_2, en in de hydrogenering van tolueen. Reductie bij 473 K met waterstof resulteert in de vorming van zowel kleine Pt^0 clusters als Pt^{2+} species. Reductie bij 573 K induceert de vorming van of intermetallische Pt–W^{5+} species, resulterend in de hoogste CO oxidatie activiteit en in aanwezigheid van H_2 een hogere selectiviteit naar CO_2 dan Pt op alumina. Dit lijkt op de combinatie van een edelmetaal op een

reduceerbare drager. In de hydrogenering van tolueen zijn de MOF systemen minder actief dan Pt op alumina, toegeschreven aan de zeer kleine Pt clusters in de MOF systemen.

De inbouw van sulfonzure groepen in *a priori* zeer stabiele MOFs wordt beschreven in **Hoofdstuk 6** en de toepassing als heterogene katalysator in een modelreactie voor verestering. Twee MOFs met sulfonzure groepen zijn onderzocht: HSO_3–MIL–101(Cr) gesynthetiseerd volgens verschillende procedures, en een nieuwe MOF, gebaseerd op HSO_3–BDC en Zr, waarvan de structuur nog niet is opgehelderd. De zure eigenschappen, katalytisch gedrag, deactivering en stabiliteit van de verschillende structuren is kritisch geëvalueerd. In het geval van MIL–101(Cr) is deactivering van de sulfonzure groepen gevonden door vorming van sulfonzure esters van 1–butanol. De HSO_3–MIL–101(Cr) katalysatoren zijn niet stabiel onder de vereiste zure regeneratiecondities door de sterke interactie tussen $–SO_3^-$ de Cr open metal site waar gewoonlijk fluor is gebonden. Na gebruik van Zr als metal node, werd een nieuwe poreuze en stabiele MOF structuur met sulfonzure groepen gesynthetiseerd. Deze vertoonde een hoge activiteit en kon volledig worden hergebruikt voor de verestering van 1–butanol met azijnzuur. In dit geval kon de deactivering door sulfonzure estervorming worden opgeheven door reactivering onder zure condities. **Hoofdstuk 7** illustreert de ontwikkeling van een nieuwe post-synthetische methode om zure eigenschappen te introduceren in verschillende MOFs voor katalytische toepassing. Door behandeling met een mengsel van triflic acid en zwavelzuur, kunnen de chemisch stabiele MOF structuren MIL–101(Cr) en MIL–53(Al) worden gesulfateerd, resulterend in een Brønstedzure sulfoxygroep aan respectievelijk 20 en 50% van de aromatische tereftaalzuur linkers. De gesulfateerde monsters zijn uitgebreid gekarakteriseerd met MAS NMR, XANES en FTIR spectroscopie. De gefunctionaliseerde MOFs vertonen in de verestering van 1–butanol met azijnzuur een katalytische activiteit gelijkaan dat van zure polymeren zoals Nafion® NR50 (TOF ~ 1.75 min^{-1} @ 343 K). Water adsorbeert sterk, tot 4 moleculen per sulfoxygroep, en bij lagere temperaturen worden nog eens 2 moleculen meer opgenomen in de 1–dimensionale poriestructuur van de gesulfateerde MIL–53(Al). Het hoge watergehalte en Brønstedzure karakter geven een hoge protongeleiding van gesulfateerd MIL–53(Al) tot matig hoge temperaturen.

Hoofdstuk 8 beschrijft een nieuwe meerstaps pre– en post–functionaliseringsmethode voor het coördineren van katalytisch actieve metalen in MIL–101(Cr) via oxamate complexering. De uitgangs MOF, NO_2–MIL–101(Cr), kon succesvol gesynthetiseerd worden in korte tijd (8 uur) onder zure condities. In een eerste post–synthese stap leidt de reductie van de NO_2 species tot de vorming van NH_2–MIL–101(Cr). De tweede functionaliseringsstap is een simpele condensatie van de amino groep van het ligand met ethyl–chloor–oxoacetaat, wat resulteert in vrij oxamaat gebonden aan de linker.

Twee verschillende koper complexen zijn aan het oxamaat gecoördineerd, tot beladingen van 9 gew.%

Cu, wat zelfde activiteiten opleverde als eerder gerapporteerde koper MOFs (HKUST–1, [Cu(2–pymo)$_2$] en [Cu(im)$_2$]) in "click chemistry" katalyse (1,3–dipolaire cycloaddities) en multicomponent koppelingsreacties (propargylamine vorming). Palladium en goud kunnen in een hoogdisperse vorm worden ingebouwd en worden gestabiliseerd door het oxamaat ligand. De gevormde katalysatoren zijn erg actief en selectief in respectievelijk de Suzuki–Miyaura condensatie en in de oxidatie van benzyl alcohol (BA). Er wordt echter palladium uitloging waargenomen. Na reductie worden nanodeeltjes goud gevormd die een goede performance vertonen in de BA oxidatie naar benzaldehyde voor tenminste vier achtereenvolgende runs. Geen zijreacties (hydrolyse) zijn waargenomen, toegeschreven aan de afwezigheid van kationische goud species. TEM analyse en DRIFTS analyse van CO adsorptie wijzen opeen zeer uniforme afmeting van ~2 nm, gelijk aan de afmeting van de kooien, en tonen het metallische karakter van deze gouddeeltjes, ingekapseld in de MIL–101 kooien.

Structurering van heterogene katalysatoren van de nano– tot de macro–schaal is essentieel voor een efficiënte katalysatortoepassing. Daarom wordt in **Hoofdstuk 9** de geoptimaliseerde synthese en performance van MIL–101(Cr) gepresenteerd, geïmmobiliseerd op een monoliet structuur. Secundaire groei na enten van kiemen is de optimale procedure om een uniforme coating van ~9 gew.% te bereiken op de wanden van de monolietkanaaltjes. Een monolitische roerreactor is gebruikt om de katalytische performance van MIL–101(Cr) te exploreren in de selectieve oxidatie van tretraline in de vloeistoffase, met *TOF* waarden rond 4.5 h^{-1} en 75% selectiviteit tot 1–tetralone.

De gepresenteerde resultaten bevestigen de stabiliteit van de katalysator en de coating, en de afwezigheid van transportlimiteringen tijdens deze reactie (*Ca* en Φ criteria). De eenvoudige terugwinning van de katalysator maakt een eenvoudig hergebruik mogelijk, iets wat onmogelijk is met de vaak gebruikte slurry operatie. MIL–101(Cr) ondergaat een reversibele deactivering, toegeschreven aan de sterke adsorptie van produkten aan de Cr–sites. De originele activiteit wordt teruggekregen met de juiste regeneratie procedure (wassen in chloorbenzeen en behandelen in lucht @ 523 K).

Terugkijkend bevestigen de resultaten de succesvolle inbouw van katalytische functies in MOF, teneinde deze laatste in katalysatoren te transformeren. Verschillende benaderingen zijn gebruikt om dit te bereiken, namelijk (*i*) gebruik van coördinatief onverzadigde sites in metaal clusters, (*ii*) pre– and post– functionalisering van de organische linkers in de MOF en (*iii*) inkapseling van actieve gast–species zoals heteropolyzuur en nanodeeltjes. Dit werk verschaft bouwstenen voor de geanticipeerde verdere ontwikkeling van multifunctionele MOF katalysatoren. En tenslotte illustreert dit onderzoek de noodzaak om MOFs te 'engineeren' van nano– tot macroschaal, onder gebruikmaking van gestructureerde dragers in plaats van gebruik in slurry systemen, teneinde MOF katalysatoren industrieël toe te passen.

Outlook

MOFs offer unique advantages and opportunities for heterogeneous catalysis. The combination of an almost unlimited number of topologies with mild synthetic procedures and the absence of structure directing agents opens the door to the creation of catalytic functionalities by: (*i*) engineering metal clusters or connectors, (*ii*) designing organic functional ligands, and (*iii*) the encapsulation of almost every molecule, macromolecule or even nanoparticle of choice. In this sense, the methodologies developed in this Thesis will certainly contribute to the development of the topic and highlight that the work presented so far is only the "tip of the iceberg". During the next few years we will witness an even faster development of MOF catalysis.

In the near future, research into MOF catalysis should focus on the combination of different functionalities within one single framework. Multifunctional MOF catalysts will allow an efficient process intensification, for instance through multi–step tandem reactions. An excellent example has been recently published by Arnanz *et al.*, who performed tandem Sonogashira/click reactions with HKUST–1 with grafted Pd complex. [1] Another fine example has been lately described by Cirujano *et al.* with the incorporation of Pd and Pt as hydrogenation/reduction centres inside the cavities of MIL–101(Cr). The combination of either isolated metal complexes or encapsulated metal nano–particles with the coordinatively unsaturated Cr^{3+} of MIL–101(Cr) acting as Lewis acids resulted in outstanding performance in several cascade reactions. [2, 3]. Savonnet *et al.*, by using the mixed linker approach, also reported the synthesis of bifunctional MOFs with very high activities in transesterification. [4]

In addition, we should not forget the almost limitless possibilities that MOFs offer for chiral catalysis. MOFs offer great potential as enantioselective catalysts, a topic for which zeolites could hardly be adapted. Asymmetric syntheses are routinely practised in the synthesis of drugs, and these reactions are almost completely performed using expensive homogeneous catalysts. The use of chiral ligands will provide a vast number of new MOF catalysts available to be tested in this field. For example, the combination of different stereoselective organocatalysts as ligands and triphenylamine photoredox groups grafted into a single framework is a brilliant approach recently reported by Wu *et al*. [5] In addition, the incorporation of ligands with transition metal complexes (TMC) [6] will form structures with multi–metallic sites at a controlled distance with molecular confinement in the pores, mimicking the (design) catalytic behaviour of enzymes. [7]

Regarding encapsulation, POMs have shown to serve as excellent anchoring points for homogeneous catalysts, [8] metal nanoparticles and even intermetallic species. [9] The combination of the redox

properties of POMs with stereo–selective moieties or metal nanoparticles might contribute to create more efficient heterogeneous catalysts, as we have recently shown. [10]

Last but not least, the need for diminishing attrition problems caused by MOFs in slurry reactors has directed the studies towards shaping MOFs into structured supports. Plenty of work has focused on growing MOFs in thin films and membranes, [11] as well as onto the monolithic stirrer reactor described in this Thesis. [12] However, still more work needs to be done in engineering MOFs at the macro–scale levels into structured reactors for its appropriate implementation in industrial catalytic applications.

Summarizing, during the last years the necessary synthetic tools that allow precise engineering of metal–organic frameworks for catalysis have been developed. This is only the beginning: in the next decade we will witness a rapid development of multifunctional MOFs that might eventually end up in their industrial implementation. The poor thermal stability compared to inorganic materials, diminishes their application in bulk chemistry or petrochemical industries, where often robust systems are needed. Long–term stability and regeneration studies of MOF catalysts have been largely unexplored, and future work needs to be developed in this direction. The plethora of possibilities for designing MOFs with a combination of functional sites will find the highest interest on the heterogenization of homogeneous and organo– catalysts. Fine–tuning of MOF structures will avoid leaching, deactivation and facilitate recovery from the homogeneous and bio– catalytic systems used up to date. Therefore, maximum interest will be developed in fields like pharmaceutics and fine and agro–chemistry. [13, 14]

Moreover, the methodologies developed will also give chemists and material scientists a good alternative to new synthesis methods of producing an enormous variety of functional materials, with a wide range of applications (from optoelectronics to adsorption, membranes, medical applications and advanced LEDs). Certainly, this possibility for rational design in catalysis will importantly contribute to various fields of science.

REFERENCES

[1] A. Arnanz, M. Pintado-Sierra, A. Corma, M. Iglesias, F. Sánchez, Bifunctional metal organic framework catalysts for multistep reactions: MOF-Cu(btc)-[Pd] catalyst for one-pot heteroannulation of acetylenic compounds, Advanced Synthesis and Catalysis, 354 (2012) 1347-1355.

[2] F.G. Cirujano, F.X. Llabrés i Xamena, A. Corma, MOFs as multifunctional catalysts: One-pot synthesis of menthol from citronellal over a bifunctional MIL-101 catalyst, Dalton Transactions, 41 (2012) 4249-4254.

[3] F.G. Cirujano, A. Leyva-Pérez, A. Corma, F.X. Llabrés i Xamena, MOFs as Multifunctional Catalysts: Synthesis of Secondary Arylamines, Quinolines, Pyrroles, and Arylpyrrolidines over Bifunctional MIL-101, ChemCatChem, 5 (2013) 538-549.

[4] M. Savonnet, A. Camarata, J. Canivet, D. Bazer-Bachi, N. Bats, V. Lecocq, C. Pinel, D. Farrusseng, Tailoring metal-organic framework catalysts by click chemistry, Dalton Transactions, 41 (2012) 3945-3948.

[5] P. Wu, C. He, J. Wang, X. Peng, X. Li, Y. An, C. Duan, Photoactive chiral metal-organic frameworks for light-driven asymmetric α-alkylation of aldehydes, Journal of the American Chemical Society, 134 (2012) 14991-14999.

[6] M.C. Das, S. Xiang, Z. Zhang, B. Chen, Functional mixed metal-organic frameworks with metalloligands, Angewandte Chemie International Edition, 50 (2011) 10510-10520.

[7] R.W. Larsen, L. Wojtas, J. Perman, R.L. Musselman, M.J. Zaworotko, C.M. Vetromile, Mimicking heme enzymes in the solid state: metal-organic materials with selectively encapsulated heme, Journal of the American Chemical Society, 133 (2011) 10356-10359.

[8] Y. Chen, V. Lykourinou, C. Vetromile, T. Hoang, L.-J. Ming, R.W. Larsen, S. Ma, How Can Proteins Enter the Interior of a MOF? Investigation of Cytochrome c Translocation into a MOF Consisting of Mesoporous Cages with Microporous Windows, Journal of the American Chemical Society, 134 (2012) 13188-13191.

[9] N. Janssens, L.H. Wee, S. Bajpe, E. Breynaert, C.E.A. Kirschhock, J.A. Martens, Recovery and reuse of heteropolyacid catalyst in liquid reaction medium through reversible encapsulation in $Cu_3(btc)_2$ metal-organic framework, Chemical Science, 3 (2012) 1847-1850.

[10] E.V. Ramos-Fernandez, C. Pieters, B. Van Der Linden, J. Juan-Alcañiz, P. Serra-Crespo, M.W.G.M. Verhoeven, H. Niemantsverdriet, J. Gascon, F. Kapteijn, Highly dispersed platinum in metal-organic framework NH_2-MIL-101(Al) containing phosphotungstic acid - Characterization and catalytic performance, Journal of Catalysis, 289 (2012) 42-52.

[11] A. Bétard, R.A. Fischer, Metal-organic framework thin films: from fundamentals to applications, Chemical Reviews, 112 (2011) 1055-1083.

[12] E.V. Ramos-Fernandez, M. Garcia-Domingos, J. Juan-Alcañiz, J. Gascon, F. Kapteijn, MOFs meet monoliths: Hierarchical structuring metal organic framework catalysts, Applied Catalysis A: General, (2010).

[13] M.J. Climent, A. Corma, S. Iborra, Homogeneous and heterogeneous catalysts for multicomponent reactions, RSC Advances, 2 (2012) 16-58.

[14] M.J. Climent, A. Corma, S. Iborra, Heterogeneous catalysts for the one-pot synthesis of chemicals and fine chemicals, Chemical Reviews, 111 (2011) 1072-1133.

About the Author

Jana Juan Alcañiz was born on the 13th of February 1985 in Elche, Spain. After finishing her high school in 2003, she started Chemical Engineering at the University of Alicante (UA). However, after one year she continued the same studies in the Technical University of Valencia (UPV). During this education she was awarded with two grants for the best students offered by Torrecid S.A. (ceramic sector), and she had the possibility to do two internships in this company at the R&D section in Castellon (Spain) and Tomaszow Mazowiecki (Poland).

She obtained her Msc degree in Chemical Engineering in 2009, after completing the final graduation project at the Delft University of Technology in the Catalysis Engineering section (TNW–ChemE) on "*Development of Metal Organic Frameworks for acid and basic catalysis*". On April 2009 she started her PhD project at the Delft Univesity of Technology. She worked in the Catalysis Engineering section, under the supervision of Dr. Jorge Gascon and Prof. Dr. Freek Kapteijn, in the field of nano–structured catalysts in a project entitle "*Engineering of Metal Organic Framework Catalysts*". During this work she has (co)supervised 5 MSc, 2 BSc, 2 guest PhD students. She also instructed 2 LO1 and 2 LO2 groups of undergraduate students (Leren Onderzoeken). She collaborated with several (international) groups and training programs (IRTG/ENMIX/NIOK), with the opportunity of working as guest student in excellent research groups such as the Inorganic Chemistry section at Alicante University, the Institute of Chemical Technology at the Technical University of Valencia, and the Institute Lavoisier at the University of Versailles St–Quentin–En–Yvelines. In addition, she also contributed several times in experiments at the European Synchrotron Radiation Facilities in Grenoble (France), and the National Synchrotron Light Source in Brookhaven (USA).

The results described in this Thesis and the multiple collaborations, with colleagues from the TU Delft and abroad, have led to fourteen publications in international journals (two more papers submitted and one book chapter), and have been presented at numerous (international) conferences and workshops in the form of oral or poster presentations. These investigations have also received a number of awards within the scientific community: best poster prize at the 3rd International MOF Conference, most cited authors 2011 in Journal of Catalysis, most downloaded articles 2012 in Journal of Catalysis, hot–

feature articles April 2012 in Journal of Material Chemistry, and most accessed articles February and March 2012 in the New Journal of Chemistry.

Recently this year, she received the first Scopus Dutch Young Researcher Award 2013 in the category of Science & Engineering. The award was granted by the Publisher Elsevier B.V. in order to recognize and reward the talent, knowledge and experience of young scientists around the world. Specially it was mentioned in the press release: *"The Spanish winner, in a category dominated by men, also gave the evidence that the great amount of foreign talent that comes to the Netherlands to continue his/her academic career here can claim the prize just as much as their Dutch colleagues."*

During this period she combined the research focus with the president role in the NIOK (Netherlands Institute for Catalysis Research) PhD platform, the representing board for the PhDs working in the field of catalysis research in the Netherlands. She worked in the organization of social and professional activities to enhance integration between the NPP members, and the students with NIOK board and the Chemical Industry.

Since 1st June 2013, she is working at Albemarle Corp. as R&D scientist for the development of a new generation of hydroprocessing catalysts.

List of publications

H-index **8**

Total number of citations **223**

Journals

Juan-Alcañiz, J., Ferrando-Soria, J., Luz, I., Serra-Crespo, P., Skupien, E., Pardo, E., Llabrés i Xamena, F.X., Corma, A., Kapteijn, F., Gascon, J., "*The oxamate route, a versatile post-functionalization for metal incorporation in MIL-101(Cr): Catalytic applications of Cu, Pd and Au"*, submitted

Szilágyi, P.A., **Juan-Alcañiz, J.**, Serra-Crespo, P., Grzech, A., de Respinis, M., Trześniewski, B.J., Kapteijn, F., van de Krol, R., Geerlings, H., Gascon, J., Dam, B., *"Boosting ambient-temperature hydrogen storage: post-synthetically modified multivariate MIL-101(Cr) MOFs"*, submitted

[1] **Juan-Alcañiz, J.**, Gielisse, R., Lago, A.B., Ramos-Fernandez, E.V., Serra-Crespo, P., Devic, T., Guillou, N., Serre, C., Kapteijn, F., Gascon, J., "*Towards acid MOFs – Catalytic performance of sulfonic acid functionalized architectures"* (**2013**) Catal. Sci. Technol. *DOI: 10.1039/C3CY00272A*

[2] Szilágyi, P.A., Lutz, M., Gascon, J., **Juan-Alcañiz, J.**, Geerlings, H., Dam, B., van Esch, J., Kapteijn, F., van de Krol, R., "*MOF@MOF core-shell vs Janus particles and the effect of strain: potential for guest sorption, separation and sequestration*" (**2013**) CrystEngComm *DOI: 10.1039/C3CE40653A*

[3] Goesten, M.G., Stavitski, E., **Juan-Alcañiz, J.**, Martinez-Joaristi, A., Petukhov, A.V., Kapteijn, F., Gascon, J., "*Small-angle X-ray scattering documents the growth of metal-organic frameworks*" (**2013**) Catalysis Today, 205 pp. 120-127

[4] Serra-Crespo, P., Gobechiya, E., Ramos-Fernandez, E.V., **Juan-Alcañiz, J.**, Martinez-Joaristi, A., Stavitski, E., Kirschhock, C.E.A., Martens, J.A., Kapteijn, F., Gascon, J., "*Interplay of metal node and amine functionality in NH_2-MIL-53(Al): Modulating breathing behaviour through intra-framework interactions*" (**2012**) Langmuir, 28 (35) pp. 12916-12922

[5] Martinez-Joaristi, A., **Juan-Alcañiz, J.**, Serra-Crespo, P., Kapteijn, F., Gascon, J., "*Electrochemical synthesis of some archetypical Zn^{+2}, Cu^{+2}, and Al^{+3} metal-organic frameworks*" (**2012**) Crystal Growth and Design, 12 (7) pp. 3489-3498

[6] **Juan-Alcañiz, J.**, Gascon, J., Kapteijn, F., "*Metal-organic frameworks as scaffolds for the encapsulation of active species: state of the art and future perspectives*" (**2012**) Journal of Material Chemsitry, 22 (20) pp. 10102-10119

[7] Ramos-Fernandez, E.V., Pieters, C., Van der Linden, B., **Juan-Alcañiz, J.**, Serra-Crespo, P., Verhoeven, M.W.G.M., Niemantsverdriet, H., Gascon, J., Kapteijn, F., "*Highly dispersed platinum in metal-organic framework NH_2-MIL-101(Al) containing phosphotungstic acid – Characterization and catalytic performance*" (**2012**) Journal of Catalysis, 289 pp. 42-52

[8] Couck, S., Gobechiya, E., Kirschhock, C.E.A., Serra-Crespo, P., **Juan-Alcañiz, J.**, Martinez-Joaristi, A., Stavitski, E., Gascon, J., Kapteijn, F., Baron, G.V., Denayer, J.F.M., "*Adsorption and separation of light*

gases on na amino-functionalized metal-organic framework: An adsorption and in situ XRD study" (**2012**) ChemSusChem, 5 (4) pp. 740-750

[9] **Juan-Alcañiz, J.**, Goesten, M.G., Ramos-Fernandez, E.V., Gascon, J., Kapteijn, F., "*Towards efficient polyoxometalate encapsulation in MIL-101(Cr): Influence of synthesis conditions*" (**2011**) New Journal of Chemsitry, 36 (4) pp. 977-987

[10] Stavitski, E., Goesten, M.G., **Juan-Alcañiz, J.**, Martinez-Joaristi, A., Serra-Crespo, P., Petukhov, A.V., Gascon, J., Kapteijn, F., "*Kinetic control of metal-organic framework crystallization investigated by time-resolved in situ X-ray scattering"* (**2011**) Angewandte Chemie – International Edition, 50 (41) pp. 9624-9628

[11] **Juan-Alcañiz, J.**, Goesten, M.G., Martinez-Joaristi, A., Stavitski, E., Petukhov, A.V., Gascon, J., Kapteijn, F., "*Live encapsulation of a Keggin polyanion in NH2-MIL-101(Al) observed by in situ time resolved X-ray scattering"* (**2011**) Chemical Communications, 47 (30) pp. 8578-8580

[12] Goesten, M.G., **Juan-Alcañiz, J.**, Ramos-Fernandez, E.V., Sai Sankar Gupta, K.B., Stavitski, E., Van Bekkum, H., Gascon, J., Kapteijn, F., "*Sulfation of metal-organic frameworks: Opportunities for acid catalysis and proton conductivity*" (**2011**) Journal of Catalysis, 281 (1) pp. 177-187

[13] Ramos-Fernandez, E.V., Garcia-Domingos, M., **Juan-Alcañiz, J.**, Gascon, J., Kapteijn, F., "*MOFs meet monoliths: Hierarchical structuring metal-organic framework catalysts*", Applied Catalysis A: General, 391 (1-2) pp. 261-267

[14] **Juan-Alcañiz, J.**, Ramos-Fernandez, E.V., Lafont, U., Gascon, J., Kapteijn, F., "*Building MOF bottles around phosphotungstic acid ships: One-pot synthesis of bi-functional polyoxometalate-MIL-101 catalysts*" (**2010**) Journal of Catalysis, 269 (1) pp. 229-241

Book Contributions

[1] **Juan-Alcañiz, J.**, Ramos-Fernandez, E.V., Kapteijn, F., Gascon, J., Chapter 10: Metal-Organic Frameworks as nano-reactors in "*Metal Organic Frameworks as Heterogeneous Catalysts*", Francesc X. Llabrés i Xamena and Jorge Gascon, Eds. RSC Catalysis Series (**2013**) **ISBN:** 978-1-84973-572-8

Oral presentations

[1] **Juan-Alcañiz, J.**, Ferrando-Soria, J., Luz-Minguez, I., Serra-Crespo, P., Skupien, E., Pardo, E., Llabres i Xamena, F.X., Corma, A., Gascon, J., Kapteijn, F., "*Metal complex incorporation in MIL-101(Cr) through oxamate post-functionalization: opportunities for catalysis",* XIV Netherlands' Catalysis and Chemistry Conference (**2013**) Noordwijkerhout, The Netherlands

[2] **Juan-Alcañiz, J.**, Ramos-Fernandez E.V., van der Linden, B., Gascon, J., Kapteijn, F., "*Polyoxometalate Templated MOFs as Supports for Highly Dispersed Metal Nanoparticles: Mechanism of Templation and Catalytic Applications*", XIII Netherlands' Catalysis and Chemistry Conference (**2012**) Noordwijkerhout, The Netherlands

[3] **Juan-Alcañiz, J.**, Gascon, J., Kapteijn, F., "*Towards efficient encapsulation of Polyoxometalates in MOFs: synthesis and catalytic performance*", 13th International Research Training Group: Diffusion in Porous Materials (**2011**) Leipzig, Germany

[4] **Juan-Alcañiz, J.**, Goesten, M.G., Ramos-Fernandez E.V., Gascon, J., Kapteijn, F., "*Super-Acidity in MOFs*", 12th International Research Training Group: Diffusion in Porous Materials (**2010**) Utrecht, The Netherlands

[5] **Juan-Alcañiz, J.**, Goesten, M.G., Ramos-Fernandez E.V., Gascon, J., Kapteijn, F., "*Building MOF bottles around phosphotungstic acid ships: One-pot synthesis of polyoxometalate/MIL-101 catalysts*", 11th International Research Training Group: Diffusion in Porous Materials (**2010**) Leipzig, Germany

[6] **Juan-Alcañiz, J.**, Goesten, M.G., Ramos-Fernandez E.V., Martinez-Joaristi, A., Gascon, J., Kapteijn, F., "*Building MOF bottles around phosphotungstic acid ships: One-pot synthesis of bi-functional polyoxometalate-MIL-101 catalysts*", XI Netherlands' Catalysis and Chemistry Conference (**2010**) Noordwijkerhout, The Netherlands

Poster presentations

[1] **Juan-Alcañiz, J.**, Ferrando-Soria, J., Serra-Crespo, P., Pardo, E., Gascon, J., Kapteijn, F., "*Metal complex incorporation in MIL-101(Cr) through oxamate post-functionalization and its catalytic opportunities",* 3rd International Conference on Metal-Organic Frameworks and Open Framework Compounds (**2012**) Edinburgh, United Kingdom

[2] **Juan-Alcañiz, J.**, Ramos-Fernandez E.V., Gascon, J., Kapteijn, F., "*Evidence for Polyoxometalates Encapsulation in the Mesocavities of MIL-101(Cr) and its Excellent Performance as Catalyst*", 5th International FEZA Conference (**2011**) Valencia, Spain

[3] **Juan-Alcañiz, J.**, Goesten, M.G., Ramos-Fernandez E.V., Gascon, J., Kapteijn, F., "*Towards efficient polyoxometalate encapsulation in MOFs: influence of synthesis conditions and catalytic performance*", XII Netherlands' Catalysis and Chemistry Conference (**2011**) Noordwijkerhout, The Netherlands

[4] **Juan-Alcañiz, J.**, Goesten, M.G., Ramos-Fernandez E.V., Martinez-Joaristi, A., Gascon, J., Kapteijn, F., "*New generation of super-acid heterogeneous catalysts based on functionalized Metal-Organic Frameworks*", 1st International Workshop ENMIX (**2010**) Antwerpen, Belgium

[5] **Juan-Alcañiz, J.**, Ramos-Fernandez E.V., Goesten, M.G., Martinez-Joaristi, A., Gascon, J., Kapteijn, F., "*New generation of super-acidic solid catalysts based on one-pot encapsulation of heterpoly-acids in Metal-Organic Frameworks*", 2nd International Conference on Metal-Organic Frameworks and Open Framework Compounds (**2010**) Marseille, France

[6] **Juan-Alcañiz, J.**, Goesten, M.G., Ramos-Fernandez E.V., Martinez-Joaristi, A., Gascon, J., Kapteijn, F., "*New generation of super-acidic solid catalysts based on functionalized Metal-Organic Frameworks*", 16th International Zeolite Conference (**2010**) Sorrento, Italy

Awards

- **Scopus Dutch Young Researcher Award 2013:** granted by **Publisher Elsevier B.V.** based on a first selection from the Elsevier's Scopus database followed by a thorough review by a professional jury of independent experts in the matter. The jury members rated the candidates at various points, including: number of publications and citations, the spread and quality of journals published, frequency of first authorship and the relevance of the research field for future.

- **Most Cited Authors 2011 [Journal of Catalysis] – Juan-Alcañiz, J.**, Ramos-Fernandez, E.V., Lafont, U., Gascon, J., Kapteijn, F., "*Building MOF bottles around phosphotungstic acid ships: One-pot synthesis of bi-functional polyoxometalate-MIL-101 catalysts*", Journal of Catalysis, 269 (1) pp. 229-241
- **Poster Prize [3rd MOF Conference 2012] – Juan-Alcañiz, J.**, Ferrando-Soria, J., Serra-Crespo, P., Pardo, E., Gascon, J., Kapteijn, F., "*Metal complex incorporation in MIL-101(Cr) through oxamate post-functionalization and its catalytic opportunities"* (2012) Edinburgh, United Kingdom
- **Most Downloaded Articles 2012 [Journal of Catalysis] –** Ramos-Fernandez, E.V., Pieters, C., Van der Linden, B., **Juan-Alcañiz, J.**, Serra-Crespo, P., Verhoeven, M.W.G.M., Niemantsverdriet, H., Gascon, J., Kapteijn, F., "*Highly dispersed platinum in metal-organic framework NH_2-MIL-101(Al) containing phosphotungstic acid – Characterization and catalytic performance*", Journal of Catalysis, 289 pp. 42-52
- **Hot Feature Articles April 2012 [Journal of Material Chemistry] – Juan-Alcañiz, J.**, Gascon, J., Kapteijn, F., "*Metal-organic frameworks as scaffolds for the encapsulation of active species: state of the art and future perspectives*", Journal of Material Chemsitry, 22 (20) pp. 10102-10119
- **Most Downloaded Articles 2012 [New Journal of Chemistry] – Juan-Alcañiz, J.**, Goesten, M.G., Ramos-Fernandez, E.V., Gascon, J., Kapteijn, F., "*Towards efficient polyoxometalate encapsulation in MIL-101(Cr): Influence of synthesis conditions*", New Journal of Chemsitry, 36 (4) pp. 977-987

Acknowledgments

First of all, I would like to thank my promotors, Freek Kapteijn and Jorge Gascon, for their constant support. Their trust in my aptitudes and capability permitted me to stay in the Netherlands after my Master Thesis, and their assistance and encouragement helped me to be successful during the conformation of this book. Freek, I want to specially thank you for your continuous guidance and useful advice, especially when I struggle getting a message through, such as in presentations, publications or parts of this thesis composition. Jorge, I cannot thank you enough for your immense effort and determination on my work, and for granting me with great challenges and new experiences. I will always be thankful to you for giving me the exceptional opportunity of sharing and learning all these four years from both of you, and I hope it is not the last time I can share scientific discussions with you. I would also like to thank the rest of the groups' staff, Michiel Makkee and Patricia Kooyman for useful discussions, especially regarding safety and TEM.

I acknowledge the committee members of my PhD defense, Prof. Ulf Hanefeld, Prof. Herman van Bekkum, Prof. Norber Stock, Dr. Francesc X. Llabres I Xamena and Dr. Shushei Furukawa. Thank you for accepting my invitation, even though some of you come from very far away, and for the attention you conferred to my thesis and all the valuable comments. Especially to Herman van Bekkum for his level of detail and his previous contributions to my work.

Besides, I would like to thank those whose I have had the pleasure to collaborate with, even though their contribution is in this thesis or in common publications, I have learnt from everyone and shared great moments. My first collaboration abroad was at the University of Alicante, Inorganic Chemistry department, where I am really thankful to Francisco Reinoso for the excellent opportunity. I want to thank Ana and Joaquin Silvestre for their help and discussions during my experiments, but also the whole group for giving me a very pleasing stay. Then, I had the opportunity to spend some time at the Institute Lavoisier in Versailles, were I was fortunate to share time and learn from Christian Serre, Patricia Horcajada, Natalie Guillou and specially Thomas Devic, but also the group was very nice and extremely helpful during this period. I want to specially thank Ana Lago for showing me everything you had developed, and being a great company; and the Renaud's family where I was living for making my time outside work very enjoyable. The last collaboration abroad was at the Technical University of Valencia, Technological Institute of Chemistry, where I had the great pleasure to work in an excellent environment of people willing to help and discuss at any moment. Special thanks to Ignacio Luz that facilitated me the experimental work and continued with the experiments after I left,

and thanks to Francesc X. Llabres I Xamena for his frequent guidance. I would like to thank the people from Belgium, Elena Gobechiya, C.E.A. Kirschhock, Sara Couck, Joery Denayer; from Spain, Jesus Ferrando and Emilio Pardo; and the Netherlands, Andrei Petukhov, Sai Sankar Gupta, M. Verhoeven, Hans Niemantsverdriet, for their valuable discussions and the excellent work. Likewise, I would like to thank the colleagues at TU Delft for their contribution to this book: Emmanuel, Vera, Maarten, Ugo Lafont, and Eli Stavitski. I want to thank also Petra for her attitude, time, conversation, shared experience, the tremendous job done and the great times outside work, I wish you the best in life. And, I also want to specially thank Zoi for the long talks during your time at the CE department, I enjoyed very much your company and all the moments we spent together.

Furthermore, I would like to thank the secretary support, Els Arkesteijn, Elly Hilkhuijsen and Caroline Mona for their time and effort in making easier the work in the group, specially Els for all her help at any stage of the process. I am very thankful to the technical support, Bart, Harrie, Kevin, Willy and Oscar, that have been extremely helpful solving day to day problems at the CE section, and taking care of the facilities to give our best at work. But I also want to include Joop Padmos in charge of ICP techniques, Ben Norder regarding XRD, Kristina Djanashvili for the NMR, and Ruben Abellon for the UV-VIS measurements, in the ChemE department.

My special thanks to all the students I have had the pleasure to work with: Mariana, Stefan, Cyriel, Ravi, Robin and Marion; it has been an excellent experience to be part of your learning process, while I have also been taught by you plenty of times. In addition, I would like to thank the four LO (Leren Onderzoeken) groups, that I have been able to guide and go through very interesting experiences: Enes, Eric, David, Gerrit, Weiyi, Bahija, Kevin and Kim. I wish you a very successful future. In addition, I want to thank all the colleagues from the CE section: Abrar, Martijn, Pita, Sina, Anastasiya, Maxim, Hossein, Irina, Sumit, Emmanuel, Beatriz, Elena, Soren and Tania for their contribution to a nice working environment, as well as the former colleagues, Bandar, Jianrong, Malles, Jasper, Leticia, Ana Rita, Christa, Christian, Johan, Joanna, Pedro, Loli, Kshitij, Dirk, Natalie, Guliz, Carmen, Mila and Erisa. I want to thank you for the great moments, the shared experiences and significant discussion.

I would like to specially thank my dear office mates: Alberto, Enrique and Canan. You have been an incredible support for me, I enjoyed every moment of our technical and personal discussions, you are among the best people I have ever met and you will always have me as a friend. This work would not have been the same if you weren't there with me through all this period, you have not only been my colleagues but my friends, my confidents and my family. Specially Enrique, this thesis is also yours. I want to particularly thank you for you effort, time and patience. Your knowledge and experience, that you have been always willing to share, have helped me tremendously to achieve this book. I also want

to include Vicky in these lines, since I really appreciate her friendship and positivism during all this period.

Thanks to Dirk I had the opportunity to be the President of the NIOK PhD Platform (NPP) during two excellent years, where I had the possibility to work with Evelien. I want to particularly thank you for the great time together. It has been an brilliant experience, working that close to you as a real team. Thank you for been so responsible, easy to work with and fun, I wish you all the success in the future. Although I did not meet you many times in person, I want to thank Irene and Arlette for their excellent work at the NIOK secretary, you made my time in this organization very easy and pleasant.

Doing the PhD abroad makes you realize how important friends and family are. I want to thank my friends in the Netherlands for making my life more interesting and being there to support each other. Specially foreign people have come and gone and come back, but we always found moments to enjoy together. As well as my Spanish friends, you have always been a very important support.

Finally, I want to than my family, they are the reason why I am here and why I am this way. No tengo palabras suficientes para agradecer todo lo que habéis hecho por mí, y todo el amor que os tengo. Papa, eres la mejor persona que conozco, y me encanta tu positivismo. Te admiro y te quiero mucho, aunque siempre estés con tus mentiras piadosas que me sacan de quicio, no hubiera podido imaginar un padre mejor. Mama, siempre has estado para escucharme y me has dado todo el consejo, amor y comprensión que necesitaba. Eres toda una inspiración para mi, y espero hacer tan buen trabajo con mis hijos en un futuro como has hecho tu conmigo. Keko, es toda una satisfacción tenerte como hermano pequeño. Espero que siempre podamos contar el uno con el otro, como hemos hecho hasta ahora y quiero que sepas que estoy muy orgullosa de ti.

Quiero agradecer también a toda mi familia más cercana. A mis tíos Juan Antonio, Inma, Jose Antonio, Esther, Paco, y en especial a mi tía Juani por su fortaleza, de la que aprendo todos los días. A mis primos Jose Manuel, Mireia, Laura, Lourdes, Esther, y los pequeñines de la familia Andrea y Pau, porque me hacen increíblemente feliz, el poco tiempo que puedo pasar con ellos. Y sobre todo a mis abuelos, Josefa, Antonia y Juan Bautista por vuestro amor incondicional y vuestra sabiduría, y en especial a mi abuelo Jacinto con el que no puede pasar mucho tiempo en vida, pero que me ha enseñado muchísimo, y siempre ha estado presente a través de su recuerdo y sus cuentos.

Por último a Pablo, gracias por ser mi amigo, mi confidente y mi compañero. Nadie me ha conocido, entendido, apoyado y querido como tú. Admiro muchísimo tu forma de ser, sobretodo porque haces que quiera ser mejor persona cada día. Eres uno de los pilares más importantes de mi vida, y espero que estés siempre en mi futuro. Muchas gracias por tu compresión, por tu paciencia y por todos tus consejos. No hubiera llegado a estar donde estoy, ni ser la persona que soy, de no ser por ti. Te quiero.